Hydrocarbon source and migration pathway identification through basin & petroleum systems modelling and mineral magnetism: a case study on the Beatrice Field, Inner Moray Firth, UK North Sea

Joseph Richard Perkins

Thesis presented for the degree of
Doctor of Philosophy (PhD)

The Department of Earth Science & Engineering
Imperial College London

2018-2022

DECLARATIONS

DECLARATION OF ORIGINALITY

I hereby declare that this thesis, entitled "*Hydrocarbon source and migration pathway identification through basin & petroleum systems modelling and mineral magnetism: a case study on the Beatrice Field, Inner Moray Firth, UK North Sea*", and the accompanying work reported within, originates entirely from me. Any further information included within that derive from alternate sources and authors, both published and unpublished, are acknowledged and cited where appropriate, and listed within the bibliography of this work.

Joseph Richard Perkins
19.09.2022

COPYRIGHT DECLARATION

The copyright of this thesis rests with the author. Unless otherwise indicated, its contents are licensed under a Creative Commons Attribution-Non Commercial-No Derivatives 4.0 International Licence (CC BY-NC-ND). Under this licence, you may copy and redistribute the material in any medium or format on the condition that; you credit the author, do not use it for commercial purposes and do not distribute modified versions of the work. When reusing or sharing this work, ensure you make the licence terms clear to others by naming the licence and linking to the licence text. Please seek permission from the copyright holder for uses of this work that are not included in this licence or permitted under UK Copyright Law.

ABSTRACT

This research builds on past studies analysing the relationship between the presence, formation, and alteration of magnetic minerals with hydrocarbons by investigating the poorly understood petroleum system of the Inner Moray Firth. This research shows the Inner Moray Firth differs from the Central North Sea through both its petroleum system and its magnetic mineral assemblage.

Magnetic mineral analysis provides extensive evidence of magnetite, goethite, and siderite alongside more minor lepidocrocite and iron sulphides, differing from the iron sulphide-rich magnetic mineral assemblages of the Central North Sea. Furthermore, this research shows two magnetic mineral behaviours around oil-water contacts in wells of the Inner Moray Firth, resulting from varying magnetic mineralogy. Most wells show continuous presence of goethite, which alters into magnetite towards the oil-water contacts, creating a strong magnetic enhancement directly below the contact. In contrast, wells bearing extensive iron sulphides experience magnetic enhancement directly above the oil-water contact, produced by the iron sulphides.

Basin and petroleum systems modelling shows basin-wide maturity of Type I, Devonian-age, and Type II-III Mid Jurassic-age source rocks whilst dispelling the hypothesis of extensive Kimmeridge Clay Formation-sourced hydrocarbons due to limited maturation. Modelling shows evidence of widespread lateral and vertical hydrocarbon migration and that extensive faulting, alongside the late-stage Cenozoic tilting of the basin, combine to heavily constrain and drastically reduce the trapping success of the petroleum system.

Connections between the magnetic mineral analysis and modelling show direct correlations between vertical migration and siderite presence, alongside the preferential formation of iron sulphides over other magnetic minerals when sulphur is present. When sulphur is not present, magnetite typically forms through the alteration of goethite around oil-water contacts. Furthermore, this study demonstrates direct connections between iron sulphide presence and Type II source rocks, and between iron hydroxide presence and Type I and Type II-III source rocks.

PUBLICATIONS

FIRST AUTHOR PUBLICATIONS

Perkins, J. R., Fraser, A. J., Muxworthy, A. R., Neumaier, M., Schenk, O. **2022**. Utilising basin and petroleum systems modelling to characterise multi-source hydrocarbon generation, identify migration pathways, and unravel hydrocarbon mixing ratios in a poorly-understood basin: A case study on the Inner Moray Firth, UK North Sea. *Marine and Petroleum Geology*. *Submitted, in review*.

Perkins, J. R., Muxworthy, A. R., Fraser, A. J., Hu, P. **2022**. Magnetic mineral assemblage analysis and the implications for petroleum systems and source rocks: A study on the Inner Moray Firth, UK North Sea. *Geophysical Journal International*. *In prep*.

Perkins, J. R., Sims, M., Muxworthy, A. R., Fraser, A. J., Badejo, S. A., Lagroix, F. **2022**. Preferential suspension of magnetic minerals within hydrocarbon fractions. *In prep*.

NAMED AUTHOR PUBLICATIONS

Badejo, S. A., Fraser, A. J., Neumaier, M., Muxworthy, A.R., and Perkins, J.R. **2021**a. 3D petroleum systems modelling as an exploration tool in mature basins: A study from the Central North Sea, UK. *Marine and Petroleum Geology*. 133: 1-15. doi: 10.1016/j.marpetgeo.2021.105271.

Badejo, S. A., Muxworthy, A. R., Fraser, A. J., Neumaier, M., Perkins, J. R., Stevenson, G. R., and Davey, R. **2021**b. Using magnetic techniques to calibrate hydrocarbon migration in petroleum systems modelling: A case study from the Lower Tertiary, UK Central North Sea. *Geophysical Journal International*. 227 (1): 617-631. doi:10.1093/gji/ggab236.

ACKNOWLEDGEMENTS

Firstly, I would like to thank the Engineering and Physical Sciences Research Council (EPSRC) for providing me with the funding to complete my research and this project. I would also like to that my supervisors Professor Adrian Muxworthy and Professor Al Fraser for constant input, guidance and wisdom throughout my PhD and developing a base of research from which this project has bloomed. I would also like to thank my external supervisor Dr Martin Neumaier for his invaluable experience and knowledge in Basin and Petroleum Systems Modelling, and Dr Oliver Schenk, who provided critical insight and wisdom on the inner workings of Schlumberger's Petromod software.

My thanks go to the British Geological Survey and those working at its Core Store in Keyworth, Nottingham, UK, for their assistance and experience in providing me with cores across the study area for sampling and core logging. For laboratory experiments, I must thank Dr Pengxiang Hu for conducting low-temperature measurements on samples from this study in Professor Andrew Roberts' laboratory at the Australian National University in Canberra, Australia. I am also indebted to members of the Institute for Rock Magnetism (IRM) at the University of Minnesota, Minneapolis, USA. Firstly to the Review & Advisory Committee for granting me two Visiting Fellowships to conduct laboratory experiments, but secondly to the staff at the IRM in accommodating my need to conduct measurements during the COVID-19 pandemic, resulting in them measuring the samples on my behalf. Consequently, my thanks go directly to Maxwell Brown, Professor Dario Bilardello and Peter Solheid for their time and experience, alongside Professor Joshua Feinberg and Professor Bruce Moskowitz for their interpretations and insights.

Throughout my time at Imperial College, I have made good friends in the Department of Earth Science and Engineering, and the support, thoughts and ideas from all were invaluable during my PhD. My special thanks go to all of the Natural Magnetism Group (NMG), including my desk neighbours Tom North, Evie Baker and Jack Turney, and Maryam Abdulkarim. Furthermore, I want to thank past PhD students and NMG members Dr Charlie Penny and Dr Sope Badejo, as well as Dr Francesco Palci, for helping me through my first few months at Imperial whilst they themselves were working tirelessly to finish their own projects. I must also thank the other members of the Basin Modelling Group, Michael Sims and Dr Bhavik Lhodia for their knowledge, and Tim Wigan for listening to my harebrained ideas and offering more reasonable responses.

Lastly, and most importantly, I want to thank my family and friends for their love and support during these nearly four years of hard work. Firstly, to my dad, Richard, and sister, Eleanor, for their unwavering belief in me, despite my ability to disappear into my work, and my girlfriend Elle for her non-stop support through all the long hours and ever-increasing number of grey hairs. I thank my house- and flat-mates throughout the years for not complaining at my strange working hours and long working days, especially during the writing of this Thesis, and my friends outside of Imperial College, not only those in academia who have provided me with geological insights, but also those whose presence, encouragement and moral support was necessary when escaping the world I was in during this project, I could not have done it without any of them.

CONTENTS

Declarations i

Abstract ii

Publications iii

Acknowledgements iv

Contents v

List of Figures vii

List of Tables xxiv

List of Abbreviations xxix

Magnetism Definitions xxx

1 Introduction 1

1.1 Study rationale . . . 2

1.2 Aims and objectives . . . 4

1.3 Chapter overview . . . 5

2 Magnetism Review 7

2.1 Introduction . . . 8

2.2 Magnetisation principles . . . 8

2.3 Ferromagnetic minerals . . . 13

2.4 Magnetic minerals and hydrocarbons . . . 17

3 Geological Review 20

3.1 Introduction . . . 21

3.2 Geological principles . . . 21

3.3 Location of study area . . . 24

3.4 Inner Moray Firth Basin formation . . . 25

3.5 Inner Moray Firth Basin stratigraphy . . . 27

3.6 Beatrice Field . . . 31

3.7 Summary . . . 46

4 Methodologies 47

4.1 Introduction . . . 48

4.2 Magnetic analyses . . . 48

4.3 Geological analyses and model formation . . . 53

5 Geological Appraisal 56

5.1 Introduction . . . 57

5.2 Well log analysis . . . 63

5.3 Seismic data analysis . . . 76

5.4 Conclusion . . . 91

6 Magnetic Analysis 92

6.1 Introduction . . . 93

6.2 Basin-wide magnetism . . . 95

6.3 Well Analysis . . . 99

6.4 FORC Principal Component Analysis . . . 146
6.5 Discussion . . . 164
6.6 Conclusion . . . 176
7 Basin & Petroleum Systems Modelling 178
7.1 Introduction . . . 179
7.2 Key components of the model . . . 179
7.3 One-dimensional Modelling . . . 185
7.4 Multi-dimensional Modelling . . . 190
7.5 Discussion . . . 212
7.6 Conclusion . . . 215
8 Discussion 217
8.1 Introduction . . . 218
8.2 Well-scale magnetism-BPSM correlations . . . 218
8.3 Hydrocarbon Prospectivity . . . 222
8.4 Comparisons to other work . . . 224
8.5 Summary . . . 228
8.6 Conclusion . . . 229
9 Conclusions 231
9.1 Introduction . . . 232
9.2 Geological Appraisal . . . 232
9.3 Magnetic Analysis . . . 232
9.4 Basin and petroleum systems modelling . . . 234
9.5 Connections between magnetism and modelling . . . 236
Bibliography 238
Appendix 252
A.1 BPSM Framework . . . 253
A.2 BPSM Field Volumetric Extents . . . 268
A.3 BPSM Scenario Testing . . . 269
A.4 Well logs . . . 280
A.5 Complete magnetic dataset access . . . 288
A.6 Basin and petroleum systems model access . . . 288

List of Figures

1.1 Map of the Inner Moray Firth, the area of investigation within this study, highlighting the locations of the known hydrocarbon fields within the region. Also shown is a map of the UK (inset) with the study area highlighted. The majority of the Inner Moray Firth is located within North Sea Quadrants 11, 12, 17 and 18, with the Outer Moray Firth beginning in Quadrants 13 and 19. 3

2.1 Flow diagram outlining the identification of the different moments seen in different ferromagnetic minerals and their relative directional strength. Modified from Badejo (2019); Tauxe (2009). 9
2.2 Schematic hysteresis loop identifying the major magnetic properties derived from it. Modified from Dunlop and Özdemir (1997). 9
2.3 Schematic diagrams of the three dominant grain domain types: SD (a), PSD (b) and MD (c). Arrows show direction of magnetisation within the domain, positive and negative signs represent dipole orientation, and dashed lines are domain walls. Modified from Dunlop and Özdemir (1997). 11
2.4 FORC diagram measurement. a) Measurement an individual FORC, commencing at specified B_r, ending at M_s. b) Suite of FORCs within the pre-defined hysteresis loop, with the rectangle defining the area in c). c) Gridded area of FORCs displaying how $\rho(B_r,B)$ is calculated. d) A typical FORC Diagram, showing a non-interacting SD grain and an SP grain. Modified from Roberts *et al.* (2014) and Roberts *et al.* (2018). Note scales, diagrams and results are not accurate, just a visual aid. 12
2.5 Example FORC diagrams showing the different results created by the FORCs from varying magnetic grain domains, and thus how they are interpreted. Modified from Roberts *et al.* (2018). 14
2.6 Flow chart summarising the alteration processes observed in nature between numerous ferromagnetic minerals. Note that given the right circumstances and environments, all minerals will eventually alter to magnetite and then to hematite. See text for information and accompanying references. Modified from Badejo (2019). 15

3.1 Schematic diagram of a petroleum system and its major processes, showing the different stages of hydrocarbon expulsion out of source rock, migration into reservoir rock and accumulation in a trap below a sealing rock. From Perkins (2017). 22
3.2 Map of the study area in the Inner Moray Firth highlighting the positions of known hydrocarbon fields in the Inner and Outer Moray Firths and the wells used in this study. 24
3.3 Structural map of the IMF showing the hydrocarbon fields. See Figure 3.6 for cross sections. BF = Banff Fault; GGF = Great Glen Fault; HF = Helmsdale Fault; IMF = Inner Moray Firth Basin; OMF = Outer Moray Firth Basin. Modified from Linsley *et al.* (1980) and Roberts *et al.* (1990). 25

3.4 Bouguer gravity anomaly map across the IMF, showing clear negative gravity responses across the Inner Moray Firth in comparison to more positive responses towards the Central North Sea, where crust is known to have thinned. Clear alignments can be seen between fault locations in Figure 3.3 and the contours of the gravity map. Modified from Andrews *et al.* (1990). 26

3.5 Extents of the NSD shown through subcrops attributed to the Mid-Cimmerian Unconformity. Solid lines indicate known subcrop boundaries, dashed are inferred. From Underhill and Partington (1993). 27

3.6 Cross-sections across the south-east Inner Moray Firth, see Figure 3.3 for locations, showing major sediment packages and faults. Per = Permian; Tri = Triassic; DuG = Dunrobin Bay Group; FlG = Fladen Group; BrF = Brora Formation. The faults vary in age from Devonian to Cretaceous, with activity on the large, Devonian-age faults (e.g. the Great Glen Fault) through the basin's entire history. From Andrews *et al.* (1990) and Underhill (1991). . . . 28

3.7 Stratigraphic column from west to east (Inner to Outer Moray Firth) highlighting the main sedimentary and stratigraphic bodies within the area. HG = Heron Group; DuG = Dunrobin Bay Group; FlG = Fladen Group. Modified from Glennie *et al.* (2003), Harker and Rieuf (1996) and Whitbread and Kearsey (2016). 30

3.8 Tectonostratigraphic column of the IMF identifying key petroleum system intervals. The existence of four potential source rocks contributing to the Early and Middle Jurassic reservoir sequences offers the central investigation into the IMF. Modified from Peters *et al.* (1989). 32

3.9 Stratigraphic column of lithology seen within the Beatrice Field and sea level curve identifying dominant events related to unconformities seen within the Field. The Callovian-Ryazanian transgression is a flooding event caused by the formation of the North Sea Dome. DuG = Dunrobin Bay Group; DHFm = Devils Hole Formation; CrSa = Cromarty Sand Member; NBSh = Nigg Bay Shale Member; FaSh = Farclas Sand Member; BuSh = Burghie Shale Member; FiSa = Fiddich Sand Member; BrCo = Brora Coal; LiSa = Livet Sand Member; MoSa = Morangie Sand Member; LWSh = Lady's Walk Shale; GrSa = Grant Sand Member; Du = Dullan Member; StCh = Stotfield Cherty Rock. Modified from Stevens (1991) and Underhill and Partington (1993). 33

3.10 Photograph of a section of core from the J Sand, Well 11/30-2, Beatrice Field from 7152.83 to 7153.75 ft MD (2180.12-2180.46 m MD). Core shows basal silt grading into mixed silty sand to sands, indicative of what is typically seen in the basin in the Dunrobin Bay Formation. 34

3.11 Photographs of sections of core from the H (left) & I (right) Sands, Well 11/30-2, Beatrice Field, from 6937.83-6938.42 ft MD (2114.65-2114.83 m MD) and 7007.83-7008.42 ft MD (2135.99-2136.17 m MD), respectively. The I Sand shows higher clay and silt content compared to the clean, but oil-stained H Sand core, except for the silty section in the shallowest region of the core. 35

3.12 Facies model of the Early Jurassic, lower reservoir sequences of the Dunrobin Bay and Beatrice Formations, identifying the alluvial flood plain, crevasse splay, lagoonal, deltaic environments of deposition. The alluvial deposits came from the NW of the IMF, over the Great Glen Fault, into the basin. Modified from Andrews *et al.* (1990); Paleoservices (1978). 36
3.13 Photographs of sections of core from the Pentland Formation, Well 11/30-2, Beatrice Field from 6523-6523.67 ft MD (1988.21-1988.41 m MD) and 6729.5-6730 ft MD (2051.15-2051.30 m MD). The presence of silty, verging on clay-rich, oil-stained sands in the shallower section and the shallowest section of the deeper core show the in-formation reservoir, and migration pathways from the hydrocarbon-producing TOC-rich shales, as seen in the lower region of the deeper core. 37
3.14 Facies model of the Middle Jurassic, upper reservoir sequences of the Pentland and Brora Formations, identifying the alluvial flood plain, lagoonal, delta and beach bar and barrier depositional environments, and the transitional shelf zone of the Heather Formation. The alluvial deposits came from the NW of the IMF, over the Great Glen Fault, into the basin. Modified from Andrews *et al.* (1990); Paleoservices (1978). 38
3.15 Photographs of sections of core from the A (left) & B (right) Sands, Well 11/30-2, Beatrice Field from 6336.67-6337.25 ft MD (m MD) and 6384.82-6385.17 ft MD (m MD), respectively. Both cores show consistent sand presence, but the B Sand shows more influx of silt, especially towards its base when it transitioned from the Pentland Formation into the B Sand. 39
3.16 a) Contour map showing top of pay (A Sand) in the Beatrice Field, and b) associated cross-section through the Beatrice Field, outlining major faults and sediment packages seen. Note that contour depths are in feet. A = A Sand, MSh = Mid Shale, B = B Sand, Pent = Pentland Formation, H = H Sand, I = I Sand, LW = Lady's Walk Shale, J = J Sand, RB = Red Beds, Tr = Triassic Chert. From Linsley *et al.* (1980) and Stevens (1991). 40
3.17 Maps showing assumed (dashed line) and known (solid line) depositional extents of a) Lower and Middle Devonian Old Red Sandstone (ORS); b) Brora Coal Formation; and c) Kimmeridge Clay, in which TOC trends are shown. Modified from Brown *et al.* (1988) and Evans *et al.* (2003). 41
3.18 Graphs of monthly production rates (black) of the hydrocarbon fields within the IMF, with calculated rates (blue) via best fit curves. Missing data is due to a lack of reported production rates, not breaks in production. Data from Kilvington and Gallivan (1983) and Oil and Gas Authority (2018). 46

5.1 Map of the study area in the Inner Moray Firth highlighting the positions of known hydrocarbon fields in the Inner and Outer Moray Firths and the wells used in this chapter's analysis. 57
5.2 Map outlining locations of wells and seismic lines in the IMF used within this study. . . . 58
5.3 Depth distribution diagrams of wells across Quadrants 11 and part of 12. 60
5.4 Depth distribution diagrams of wells across part of Quadrant 12, Quadrants 13, 18 and 19. 61
5.5 Example well log responses derived by the geology of the IMF, evidenced by the well log from Well 11/30a-10 located in the Beatrice Field, with depth in metres MD brt. 65

5.6 Gamma ray well log and interpreted log through the reservoir section of Well 11/30-2 within the Beatrice Field, logged using symbols from Tucker (2011). Depths in feet MD brt. . . . 67
5.7 Gamma ray well log and interpreted log through the reservoir section of Wells 11/30a-8 and 11/30a-B10 in the Beatrice Field, logged using symbols from Tucker (2011). Depths in feet MD brt. . . . 68
5.8 Example well log from Well 11/30a-8 showing resistivity logs and their use in estimating the well's OWC. . . . 69
5.9 Annotated photograph of core from the IMF, showing the variations seen in oil- and water-saturated sands and the location of the OWC. . . . 69
5.10 Map of the IMF showing the selected wells with OWCs, as per Table 5.3. . . . 70
5.11 Map showing the location and line of the wells used in the well log correlation in Figure 5.12 relatively to the IMF, the hydrocarbon fields and the BPSM model. . . . 71
5.12 Log correlation across the wells identified in Figure 5.11, showing the consistent presence of formations in the IMF, controlled mainly by depth not thickness. Depth is in metres MD brt. . . . 72
5.13 Petrophysical crossplots of the *M-N* ratio in the formations within the IMF. a) shows all datapoints across all formations, b) shows the mean values and tie lines of sand-shale relationships of the reservoir formations, c) shows the non-reservoir formations' means and sand-shale tie lines. The following sequence of plots show formation-separated data distributions. . . . 75
5.14 Well-seismic tie of Well 11/30a-10, showing the well log plots, the synthetic seismic trace and the relevant position within the seismic survey, with additional traces either side, shown for context. . . . 78
5.15 Well-seismic tie across the reservoir section of the IMF, their synthetic seismic trace and the associated seismic section showing the comparatively low seismic resolution, limiting interpretation of the formations within the reservoir section. . . . 79
5.16 Map showing locations of the interpreted seismic lines in Figures 5.17, 5.18, 5.19 & 5.20. . 80
5.17 Seismic Line 1 from the SW section of the IMF, both uninterpreted (above) and interpreted (below), identifying the main lithology packages. BlS = Black Shales, Hea = Heather, Res = Reservoir, Tri = Triassic, Zec = Zechstein. GGF = Great Glen Fault, SB = Smith Bank Fault, CRF = Central Ridge Fault, LF = Lossiemouth Fault. Syn-rift deposition of the KCF and erosive and fault removal of post-KCF sediment. Note a ∼4x vertical exaggeration. . . 81
5.18 Seismic Line 2 from the central section of the IMF, both uninterpreted (above) and interpreted (below), identifying the main lithology packages. BlS = Black Shales, Hea = Heather, Res = Reservoir, Tri = Triassic, Zec = Zechstein, Rot = Rotliegend. GGF = Great Glen Fault, SB = Smith Bank Fault, CRN = Northern Central Ridge Fault, CRF = Central Ridge Fault, LF = Lossiemouth Fault. Continued evidence of syn-rift deposition within the KCF in the Great Glen Sub-basin, but Cromer Knoll sediments at seabed across the rest of the section. Note a ∼4x vertical exaggeration. . . . 82

5.19 Southern half of Seismic Line 3 from the NE section of the IMF, both uninterpreted (above) and interpreted (below). KCF = Kimmeridge Clay, BlS = Black Shales, Hea = Heather, Res = Reservoir, Tri = Triassic, Zec = Zechstein, Rot = Rotliegend. GGF = Great Glen Fault, SB = Smith Bank Fault, CRF = Central Ridge Fault, LF = Lossiemouth Fault, BF = Buckie Fault. The Banff Sub-basin shows more stability than the other regions of the IMF, suggesting that the Lossiemouth and Buckie Faults are the southern edge of the syn-rift IMF basin. Note a ∼4x vertical exaggeration. 83

5.20 Northern half of Seismic Line 3 from the NE section of the IMF, both uninterpreted (above) and interpreted (below). KCF = Kimmeridge Clay, BlS = Black Shales, Hea = Heather, Res = Reservoir, Tri = Triassic, Zec = Zechstein, Rot = Rotliegend. GGF = Great Glen Fault, SB = Smith Bank Fault, CRF = Central Ridge Fault, LF = Lossiemouth Fault, BF = Buckie Fault. Further evidence of extensive syn-rift deposition of the KCF, loss of post-KCF sediments to the north of the KCF and variable thicknesses of Cromer Knoll sediment across the section. Note a ∼4x vertical exaggeration. 84

5.21 Contour maps showing the depth to the top of all main sediment packages in the IMF, bar the seabed. All sediment packages are heavily fault-controlled, bar the Devonian and Basement as these formed predominantly prior to the IMF formation. X and Y Cells refer to the cells of the BPSM. 85

5.22 Contour maps showing the thicknesses of all main formation packages within the IMF, bar the basement. Whilst the thicknesses of the Cromer Knoll, Rotliegend and Devonian are skewed due to the removal of surficial sediments during late stage rifting, and the infill the pre-existing Caledonian-Orogeny formed basin, respectively, the syn-rift sedimentation of the KCF is clear to see in its thickness map. This is in stark contrast to the majority of sediment packages through the central section of the IMF. X and Y Cells refer to the cells of the BPSM. 88

5.23 GDE Map of the KCF, showing the extensively thickened regions around the basin-forming faults where the majority of the sands were deposited during its syn-rift formation, with the model extent outlined on the GDE Map. Black dots indicate location of wells that drill through the KCF, which is all wells in the IMF. X and Y Cells refers to the cells of the BPSM. 89

5.24 Map showing the faults across the IMF, coloured solely for clarity, annotated with the main basin-forming and controlling faults. Image extracted from Petrel (Schlumberger, 2015). . 90

6.1 Map of the Inner Moray Firth, highlighting the extent of the basin and petroleum systems model, the positions of the known hydrocarbon fields in the region and showing the locations of the wells where sampling of cores was possible, delineated by the number of samples from each well. Note that not all wells in the study area were sampled, see Chapter 3 for the complete well dataset. 93

6.2 Example hysteresis loop data from room temperature analysis carried out in this study. The hysteresis loops show examples of a) typical high quality data; b) most typical, mode quality data; and c) low quality data. Note that the grey loop is the uncorrected hysteresis loop, and the black loop is the corrected hysteresis loop. 95

6.3 Series of data plots comparing the various room temperature magnetic characteristics of samples across the IMF, delineated as a function of formation and by saturating fluid. a) shows a Day Plot (Day *et al.*, 1977), comparing M_r/M_s against B_{cr}/B_c; b) shows M_r/M_s against B_c; and c) to j) are a series of plots showing the relationships between M_r, M_s, B_c, B_{cr} and H_{fs}. The data spread across all formations and saturating fluids is relatively continuous with no initially observable patterns as a result of either saturating fluid or lithological formation. 97

6.4 Series of plots showing the mean room temperature magnetic mineral properties of key geological formations within the IMF, differentiated by age. The plots show that the Middle Jurassic formations have the greatest mean M_s and high M_r responses, with the Lower Jurassic formations having the lowest mean M_s and M_r responses. The formations with the greatest sampling density (A and B Sands) show the greatest data variance. 98

6.5 Map of the IMF and study area, outlining the location of the selected wells where samples were taken for room- and high-temperature magnetic analysis, with a reference to the location of the basin and petroleum systems model created in this study. 100

6.6 Series of data plots comparing the room temperature magnetic characteristics of samples across the formations in the IMF, delineated by well and by saturating fluid. a) shows a Day Plot (Day *et al.*, 1977), comparing M_r/M_s against B_{cr}/B_c; b) shows M_r/M_s against B_c; and c) to j) are a series of plots showing the relationships between M_r, M_s, B_c, B_{cr} and H_{fs}. The Day Plot (a) shows a linear range of data with most wells spread across it, but with the Wells 11/24a-2 and 12/21-2 having lower B_{cr}/B_c and M_r/M_s ratios than the others, reflected in the B_c data in plots b, d, e and i. 103

6.7 Series of plots showing the mean room temperature magnetic mineral properties of several wells across the IMF, differentiated by location. The plots show that Well 11/24a-2 shows the highest mean M_s and M_r responses, with Well 11/30-2 having the greatest error bars, due to sampling limitations. 104

6.8 Series of high-temperature susceptibility curves showing examples of the responses formed by the six individual magnetic minerals identified in this study that are present across the IMF. 105

6.9 Map of the IMF and study area, showing the location of Well 11/24-1 in Lybster Field. . . 106

6.10 Plots of magnetic results against depth within Well 11/24-1, with gamma ray and resistivity well log data used to identify formations and fluids. Well shaded in red is oil-saturated, blue is water-saturated, purple is within the OWC zone, with the OWC zone shown. M_s = saturation magnetisation; M_r = remanent magnetisation; B_c = magnetic coercivity; B_{cr} = coercivity of remanence; and H_{fs} = high field slope, HT susceptibility-identified magnetic minerals at each sample are shown. 107

6.11 Series of high temperature susceptibility curves and room temperature FORC diagrams of selected samples, as located on the gamma ray well log plot, across various depths and saturated by both oil and water, in Well 11/24-1. The high temperature plots show a defined change in magnetic mineralogy between saturating fluids that is not as well represented in the FORC diagrams. Goe = goethite, He = hematite, Lep = lepidocrocite, Mag = magnetite, Pyrr = pyrrhotite, Sid = siderite 108
6.12 Series of low temperature ZFC, FC and RT Curves of select samples across the OWC zone seen in Well 11/24-1, used to identify the magnetic mineral assemblages within the samples through identification of mineral-specific behaviours. Early and sharp T_V responses (e.g. ii, iii) are expected errors in measurements, as they are typically smoother (e.g. i). Note the increasing remanence values measured towards the OWC, and immediately below it (ii, iii), which is indicative of increasing magnetite content. Goe = goethite, Sid = siderite, T_V = Verwey Transition indicative of Mag (magnetite). 109
6.13 Map of the IMF and study area, showing the location of Well 11/24a-2 in the basin's NE. . 110
6.14 Plots of magnetic results against depth within Well 11/24a-2, with gamma ray and resistivity well log data used to identify formations and fluids. Well shaded in red is oil-saturated, blue is water-saturated, with the OWC shown. M_s = saturation magnetisation; M_r = remanent magnetisation; B_c = magnetic coercivity; B_{cr} = coercivity of remanence; and H_{fs} = high field slope, HT susceptibility-identified magnetic minerals at each sample are shown. . . . 110
6.15 Series of high temperature susceptibility curves and room temperature FORC diagrams of selected samples, as located on the gamma ray well log plot, across various depths and saturated by both oil and water, in Well 11/24a-2. The high temperature plots show a defined change in magnetic mineralogy between saturating fluids that is not as well represented in the FORC diagrams. Mag = magnetite, Pyr = pyrite, Pyrr - pyrrhotite. 111
6.16 Map of the IMF and study area, showing the location of Well 11/30-2 in Beatrice Field. . . 112
6.17 Plots of magnetic results against depth within Well 11/30-2. Well shaded in red is oil-saturated, blue is water-saturated, with the OWCs shown. M_s = saturation magnetisation; M_r = remanent magnetisation; B_c = magnetic coercivity; B_{cr} = coercivity of remanence; and H_{fs} = high field slope, HT susceptibility-identified magnetic minerals at each sample are shown. 113
6.18 Series of high temperature susceptibility curves and room temperature FORC diagrams of selected samples, as located on the gamma ray well log plot, across various depths and saturated by both oil and water, in Well 11/30-2. The high temperature plots show limited variation in magnetic mineralogy between saturating fluids. Goe = goethite, He = hematite, Mag = magnetite, Sid = siderite. 114
6.19 Series of low temperature ZFC, FC and RT Curves of select samples across the lower OWC seen in Well 11/30-2, used to identify the magnetic mineral assemblages within the samples. Goe = goethite, T_V = Verwey Transition indicative of Mag (magnetite). 115
6.20 Map of the IMF and study area, showing the location of Well 11/30-5 in Beatrice Field. . . 116

6.21 Plots of magnetic results against depth within Well 11/30-5, with gamma ray and resistivity well log data used to identify formations and fluids. Well shaded blue is water-saturated. M_s = saturation magnetisation; M_r = remanent magnetisation; B_c = magnetic coercivity; B_{cr} = coercivity of remanence; and H_{fs} = high field slope, HT susceptibility-identified magnetic minerals at each sample are shown. 116

6.22 Series of high temperature susceptibility curves and room temperature FORC diagrams of selected samples, as located on the gamma ray well log plot, across various depths and saturated by water, in Well 11/30-5. All high temperature plots show consistent magnetic mineralogy, but FORCs show some variation between SD and MD/PSD behaviours. Goe = goethite. 117

6.23 Series of low temperature ZFC, FC and RT Curves of select samples in Well 11/30-5, used to identify the magnetic mineral assemblages within the samples through identification of mineral-specific behaviours. Goe = goethite, T_V = Verwey Transition indicative of Mag (magnetite), Sid = siderite. 118

6.24 Map of the IMF and study area, showing the location of Well 11/30a-8 in Beatrice Field. . 119

6.25 Plots of magnetic results against depth within Well 11/30a-8, with gamma ray and resistivity well log data used to identify formations and fluids. Well shaded in red is oil-saturated, blue is water-saturated, with the OWC shown. M_s = saturation magnetisation; M_r = remanent magnetisation; B_c = magnetic coercivity; B_{cr} = coercivity of remanence; and H_{fs} = high field slope, HT susceptibility-identified magnetic minerals at each sample are shown. . . . 120

6.26 Series of high temperature susceptibility curves and room temperature FORC diagrams of selected samples, as located on the gamma ray well log plot, across various depths and saturated by both oil and water, in Well 11/30a-8. Goe = goethite, He = hematite, Lep = lepidocrocite, Mag = magnetite, Pyr = pyrite, Pyrr = pyrrhotite, Sid = siderite. 121

6.27 Series of low temperature ZFC, FC and RT Curves of select samples across the OWC and within the water-saturated section of Well 11/30a-8. Note the increasing remanence values measured towards the OWC (1-3), which is indicative of increasing magnetite content. Goe = goethite, Sid = siderite, T_V = Verwey Transition, for Mag (magnetite). 122

6.28 Room and low temperature Mössbauer spectra of samples from 7021 (H in Figure 6.26 and 5 in Figure 6.27) and 7024 ft in Well 11/30a-8. 123

6.29 SEM images from various samples within the water and oil columns of Well 11/30a-8. Sd = siderite, Ma = magnetite, Go = Goethite. Samples a, b, c, g and h are from the oil column samples (6900, 6906 and 6913 ft), whilst sample d is from 7019 ft, e, f and i are from 7021 and 7024 ft. 124

6.30 Map of the IMF and study area, showing the location of Well 11/30a-B10 in Beatrice Field. 125

6.31 Plots of magnetic results against depth within Well 11/30a-B10, with gamma ray and resistivity well log data used to identify formations and fluids. Well shaded in red is oil-saturated, blue is water-saturated, with the OWCs shown. M_s = saturation magnetisation; M_r = remanent magnetisation; B_c = magnetic coercivity; B_{cr} = coercivity of remanence; and H_{fs} = high field slope, HT susceptibility-identified magnetic minerals at each sample are shown. 126

6.32 Series of high temperature susceptibility curves and room temperature FORC diagrams of selected samples, as located on the gamma ray well log plot, across various depths and saturated by both oil and water, in Well 11/30a-B10. Goe = goethite, Lep = lepidocrocite, Pyr = pyrite, Pyrr = pyrrhotite, Sid = siderite. 127
6.33 Series of low temperature ZFC, FC and RT Curves of select samples across the two OWCs seen in Well 11/30a-B10, used to identify the magnetic mineral assemblages within the samples through identification of mineral-specific behaviours. Note the increasing remanence values measured towards the OWC (i-iii), which is indicative of increasing magnetite content. Goe = goethite, T_V = Verwey Transition indicative of Mag (magnetite), Sid = siderite. 128
6.34 Map of the IMF and study area, showing the location of Well 12/21-2 in Jacky Field. . . . 129
6.35 Plots of magnetic results against depth within Well 12/21-2, with gamma ray and resistivity well log data used to identify formations and fluids. Well shaded in red is oil-saturated, blue is water-saturated, with the OWC shown. M_s = saturation magnetisation; M_r = remanent magnetisation; B_c = magnetic coercivity; B_{cr} = coercivity of remanence; and H_{fs} = high field slope, HT susceptibility-identified magnetic minerals at each sample are shown. . . . 130
6.36 Series of high temperature susceptibility curves and room temperature FORC diagrams of selected samples, as located on the gamma ray well log plot, across various depths and saturated by both oil and water, in Well 12/21-2. Goe = goethite, He = hematite, Lep = lepidocrocite, Mag = magnetite, Sid = siderite. 131
6.37 Series of low temperature ZFC, FC and RT Curves of select samples across the OWC seen in Well 12/21-2, used to identify the magnetic mineral assemblages within the samples through identification of mineral-specific behaviours. Early and sharp T_V responses (e.g. iv, v) are expected errors in measurements, as they are typically smoother (e.g. i). Note the increasing remanence values measured towards the OWC (i-iii), which is indicative of increasing magnetite content. Goe = goethite, T_V = Verwey Transition indicative of Mag (magnetite), Sid = siderite. 132
6.38 Map of the IMF and study area, showing the location of Well 12/21-4 in the centre of the IMF. 133
6.39 Plots of magnetic results against depth within Well 12/21-4, with gamma ray and resistivity well log data used to identify formations and fluids. Well shaded in blue is water-saturated. M_s = saturation magnetisation; M_r = remanent magnetisation; B_c = magnetic coercivity; B_{cr} = coercivity of remanence; and H_{fs} = high field slope, HT susceptibility-identified magnetic minerals at each sample are shown. 133
6.40 Series of high temperature susceptibility curves and room temperature FORC diagrams of selected samples, as located on the gamma ray well log plot, across various depths and saturated by water, in Well 12/21-4. The high temperature susceptibility plots show relative consistency across the samples, matched in the consistent FORC diagrams. Goe = goethite, He = hematite, Lep = lepidocrocite. 134
6.41 Map of the IMF and study area, showing the location of Well 12/25-3 in the east of the IMF, on the border of the Inner and Outer Moray Firth Basins. 135

6.42 Plots of magnetic results against depth within Well 12/25-3, with gamma ray and resistivity well log data used to identify formations and fluids. Well shaded in red is oil-saturated, blue is water-saturated, with the OWC shown. M_s = saturation magnetisation; M_r = remanent magnetisation; B_c = magnetic coercivity; B_{cr} = coercivity of remanence; and H_{fs} = high field slope, HT susceptibility-identified magnetic minerals at each sample are shown. . . . 136
6.43 Series of high temperature susceptibility curves and room temperature FORC diagrams of selected samples, as located on the gamma ray well log plot, across various depths and saturated by oil, in the upper section of Well 12/25-3. The magnetic mineralogy is relatively consistent across the oil-saturated upper section of the well. Goe = goethite, Mag = magnetite, Sid = siderite. 137
6.44 Series of high temperature susceptibility curves and room temperature FORC diagrams of selected samples, as located on the gamma ray well log plot, across various depths and saturated by both oil and water, in the lower section of Well 12/25-3. The high temperature plots show relatively consistent magnetic mineralogy with the upper section of the well. Goe = goethite, Mag = magnetite, Pyr = pyrite, Pyrr = pyrrhotite, Sid = siderite. 138
6.45 Map of the IMF and study area, showing the location of Well 12/27-1 in the SE of the basin. 139
6.46 Plots of magnetic results against depth within Well 12/27-1, with gamma ray and resistivity well log data used to identify formations and fluids. Well shaded in red is oil-saturated, blue is water-saturated, purple is within the OWC zone, with the OWC zone shown. M_s = saturation magnetisation; M_r = remanent magnetisation; B_c = magnetic coercivity; B_{cr} = coercivity of remanence; and H_{fs} = high field slope, HT susceptibility-identified magnetic minerals at each sample are shown. 140
6.47 Series of high temperature susceptibility curves and room temperature FORC diagrams of selected samples, as located on the gamma ray well log plot, across various depths and saturated by both oil and water, in Well 12/27-1. The high temperature plots show a defined change in magnetic mineralogy across the section. Goe = goethite, He = hematite, Mag = magnetite, Maghe = maghemite, Sid = siderite. 141
6.48 Map of the IMF and study area, showing the location of Well 12/27-2 in the SE of the basin. 142
6.49 Plots of magnetic results against depth within Well 12/27-2. Well shaded in red is oil-saturated, blue is water-saturated, with the OWC shown. M_s = saturation magnetisation; M_r = remanent magnetisation; B_c = magnetic coercivity; B_{cr} = coercivity of remanence; and H_{fs} = high field slope, HT susceptibility-identified magnetic minerals at each sample are shown. 142
6.50 Series of high temperature susceptibility curves and room temperature FORC diagrams of selected samples, as located on the gamma ray well log plot, across various depths and saturated by both oil and water, in Well 12/27-2. There is limited magnetic mineralogy variation between the saturating fluids. Goe = goethite, He = hematite, Lep = lepidocrocite, Mag = magnetite, Sid = siderite. 143
6.51 Map of the IMF and study area, showing the location of Well 12/29-1 in the SE of the basin. 144

6.52 Plots of magnetic results against depth within Well 12/29-1. Well shaded in red is oil-saturated, blue is water-saturated, with the OWC shown. M_s = saturation magnetisation; M_r = remanent magnetisation; B_c = magnetic coercivity; B_{cr} = coercivity of remanence; and H_{fs} = high field slope, HT susceptibility-identified magnetic minerals at each sample are shown. 144
6.53 Series of high temperature susceptibility curves and room temperature FORC diagrams of selected samples, as located on the gamma ray well log plot, across various depths and saturated by both oil and water, in Well 12/29-1. The high temperature plots do not show a defined change in magnetic mineralogy across the well. Goe = goethite. 145
6.54 Series of plots summarising the identification of the three PCA end-members identified within this study's FORC diagram analysis. Upper left shows the scree plot of the PCA components and eigenvalues produced, upper right is a PCA plot of all the data points used in the PCA, with the end-members identified. Lower left, middle and rift are the three end-members identified in this study's PCA, present in the FORC diagrams of the samples of the IMF – PSD, MD and SD, respectively. 147
6.55 PCA plots of all samples analysed in this study's FORC PCA, delineated by saturation of oil and water, through two perspectives – well (left) and formation (right). The two perspectives allow analysis into both geographical variations, through investigations into the variations between wells, and geological variations, through investigations into the variations between formations. 148
6.56 PCA plot of samples, and depth plot showing EM contributions and mass-corrected proportions of the samples in Well 11/24-1. 152
6.57 PCA plot of samples, and depth plot showing EM contributions and mass-corrected proportions of the samples in Well 11/24a-2. 153
6.58 PCA plot of samples, and depth plot showing EM contributions and mass-corrected proportions of the samples in Well 11/30-5. 154
6.59 PCA Plot of samples from Well 11/30a-8, separated by formation and saturating fluid. . . . 155
6.60 Depth plot showing mass-corrected proportions of the grain domains seen in samples in Well 11/30a-8. 155
6.61 PCA Plot of samples from Well 11/30a-B10, separated by formation and saturating fluid. . 156
6.62 Depth plot showing mass-corrected proportions of grain domains seen in samples in Well 11/30a-B10. 156
6.63 PCA Plot of samples from Well 12/21-2, separated by formation and saturating fluid. . . . 157
6.64 Depth plot showing mass-corrected proportions of the grain domains seen in samples in Well 12/21-2. 157
6.65 PCA plot of samples, and depth plot showing EM contributions and mass-corrected proportions of the samples in Well 12/21-4. 158
6.66 PCA plot of samples, and depth plot showing EM contributions and mass-corrected proportions of the samples in Well 12/25-3. 159

6.67 PCA plot of samples, and depth plot showing EM contributions and mass-corrected proportions of the samples in Well 12/27-1. 160
6.68 PCA plot of samples, and depth plot showing EM contributions and mass-corrected proportions of the samples in Well 12/27-2. 161
6.69 PCA plot of samples, and depth plot showing EM contributions and mass-corrected proportions of the samples in Well 12/29-1. 162
6.70 Map showing the IMF, with pie charts from each well magnetically analysed showing the relative presence of each magnetic mineral identified within this study, ignoring the ubiquitous magnetite, split into oil- and water-saturated samples. Values are relative percentages of samples from each well and saturating fluid that show evidence of the respective minerals, to remove the bias caused by varying sample numbers. 164
6.71 Series of plots showing the room temperature M_s values, FORC PCA endmember contributions, and the high temperature susceptibility-identified minerals present in samples across wells in the IMF that both bear OWCs (highlighted) and show mineralogical variation. Note that the depth (Y axis) are not consistent between wells. 168
6.72 Schematic showing how magnetic minerals interact around oil-water contacts in the IMF. Wells dominated by goethite (Goe, G) see decreasing goethite signals towards the OWC in tandem with increasing magnetite (Mag) presence towards the contact, with siderite (S) present in wells that experience extensive vertical migration of the hydrocarbons. Wells with low concentrations of goethite see this same pattern, but with increasing iron sulphide (FeS)-presence towards the OWC. 170

7.1 Series of boundary condition plots of the three components and their properties used within the BPSM in this study. The paleo-water depth is a direct estimation on the water level of the area throughout time, and correlatable to the facies seen in the basin, whilst sediment-water interface temperatures relate to the temperature at seabed, thus is related to the PWD. Heat flow is directly connected to the basin's geological history and periods of rifting and instability that increase the temperatures across the basin, and the events seen in the IMF are visible in it. Conditions were collated and derived from Allen and Allen (2005); Andrews *et al.* (1990); Brown *et al.* (1988) and Wygrala (1989). 181
7.2 Map showing the locations of the wells used to create the erosion map used for the late-stage uplift in the BPSM, including the reference well within Cromarty Field. Wells were selected through data availability, with limitations in certain regions as a result of reduced data coverage. 183
7.3 Map showing the amount of sediment eroded across the IMF during the late stage Cenozoic uplift and erosion, estimated through well log analysis and calculations based on the work of Thomson (1993), with the locations of the wells used and the basin-bounding faults from which the erosion is centred. The majority of the erosion is bound to the Great Glen Fault (GGF) and the greatest volume of lost sediment occurs in the Sutherland Terrace to the north of the GGF. 184

7.4 Map of the IMF showing the location of the wells used for 1D modelling calibrations. The well distribution across the IMF is generally strong, however the wells available are limited to those with calibration data. 185
7.5 Burial history plots of the formations seen in the IMF, created in this study, from Wells 11/24-1, in the Lybster Field, 11/30-5 in Beatrice Field, and 12/27-1 in the south west of the IMF. The burial histories in these three wells are the same throughout the Devonian-Triassic sequence, prior to variations from the Late Jurassic into the Cenozoic, where the influence from the erosion maps occurs. 186
7.6 Well calibration plots of calculated vitrinite reflectance curves (lines) plotted against the core sample tested vitrinite reflectance data (crosses) from the calibration wells used within the IMF model. Note that the model base is 6km, but the plots are limited to the drilled depths of the wells. The different calculated lines represent different calculation techniques from Burnham *et al.* (2016) (blue), Nielsen *et al.* (2015) (orange) and Sweeney and Burnham (1990) (black). 188
7.7 Map of the IMF showing the wells used for calibration and their success in matching calibration data to calculated values against the backdrop of the depth map of the Top Reservoir. The majority of the wells see strong calibration between the simulated results and the calibration data, however several around the perimeter of the Smith Bank High, suggesting the formation of this horst. 189
7.8 Schematic diagrams showing how BPSMs recreate fault-lithology relationships compared to an idealised real-world example, and the potential for erroneous accumulations within the reservoir layer in the footwall of the modelled fault. 190
7.9 Maps showing the average transformation ratio (TR) in the model cells of the four source rocks of the IMF at present day, and time plot showing the source rock maturity via generation mass, in Mtoe, through time across the entire IMF. The maps show how for the non-Devonian source rocks, the Great Glen Sub-basin is the main centre of maturity for the source rocks. For the generation mass, indicative of the ever-increasing maturity of a source rock, is that the Devonian Fish Beds begin to mature in the late-Carboniferous during the early basin-forming inversion, however, the bulk of maturity in the Fish Beds, alongside the other source rocks, occurs from approximately 150 Ma, due to the deposition of large volumes of sediment alongside the mid- and late-Jurassic rifting events. 192
7.10 Time plots of expulsion mass, in million tons of oil equivalent, of the three effective source rocks in the IMF, the Devonian Fish Beds, Pentland Formation and the Kimmeridge Clay Black Shales, alongside the immature Brora Coal. The expulsion masses of hydrocarbons broadly reflect the generation masses of the source rocks, outlined in Figure 7.9, but with a delay due to the time needed to generate and then expel the matured hydrocarbon. The expulsion masses show how there was an early stage of hydrocarbon production of the Devonian Fish Beds, but the vast majority of hydrocarbons were expelled after 150 Ma, especially in the Pentland Formation and Kimmeridge Clay Black Shales. 195

7.11 Figure showing the Devonian Fish Beds and the expulsion onset time of the hydrocarbons generated in the source rock, alongside the migration vectors of the Devonian-sourced hydrocarbons within the Devonian ORS flagstones, Rotliegend and Zechstein sediment packages. Migration occurs laterally through the flagstones prior to seeing more vertical migration during the more permeable and porous sediments that overlay them. Green indicates oil migration and red indicates gas migration. 196
7.12 Figure showing the Pentland Formation and the expulsion onset time of the hydrocarbons generated in the source rock, alongside the migration vectors of the Pentland-sourced hydrocarbons within the Pentland, Brora Coal, B and A Sand sediment packages. Migration occurs overwhelmingly vertically through the section. Green indicates oil migration and red indicates gas migration. 198
7.13 Figure showing the Kimmeridge Clay Black Shales and the expulsion onset time of the hydrocarbons generated in the source rock, alongside the migration vectors of the Black Shale-sourced hydrocarbons within the Black Shales and Kimmeridge Clay Formation sediment packages. Migration occurs overwhelmingly vertically through the section but with lateral migration within the Black Shales initially due to the high clay and shale content. Green indicates oil migration and red indicates gas migration. 199
7.14 Maps of the IMF showing the structure of the basin through a Top Reservoir depth map (left) and the regions of different migration methods used to determine the charge history of the known hydrocarbon accumulations in the basin (right). The deepest regions of the basin, through the Great Glen, Wick and Lossiemouth Sub-basins, are where the source rocks of the IMF reach highest maturity, but, as discussed, large swathes of the basin reach maturity in both the dominant source rocks. 200
7.15 Time plot showing the filling history, in mass (million tons of oil equivalent) of the three known accumulations in the IMF – Beatrice (top), Jacky (middle) and Lybster (bottom) Fields. The fields filled at varying rates throughout geological time, post-deposition of the sealing Heather Formation, with the filling histories split into the hydrocarbon components and their relative contributions, as calculated by the final model produced in the BPSM. . . 202
7.16 Series of maps showing the changes in petroleum saturation percentage, above a threshold of 30 %, across the Beatrice and Jacky Field region of the IMF through geological time. The maps show the early stages of charging (120 Ma), through to the peak of filling (66 Ma), the significant losses post-uplift commencement, and then through to present day. 204
7.17 Time plots from Beatrice Field showing the proximal and deep-basin migration mixing of the Devonian Fish Beds and Pentland Formation through time. The plots show both the regions and source rocks of the IMF where hydrocarbons migrated from and the combined totals of each migration region, in accumulated mass and relative percentages. The influence of deep-basin hydrocarbons is greatest prior to the opening of the faults at 66 Ma, before the dominance of proximal charge becomes clear. 205

7.18 Time plots from Jacky Field showing the proximal and deep-basin migration mixing of the Devonian Fish Beds and Pentland Formation through time. The plots show both the regions and source rocks of the IMF where hydrocarbons migrated from and the combined totals of each migration region, in accumulated mass and relative percentages. The relative influence of both migration types is somewhat consistent through the charge history after the initial dominance of deep-basin Devonian, with the migration mix post-66 Ma being relatively even across. 206

7.19 Time plots from Lybster Field showing the proximal and deep-basin migration mixing of the Devonian Fish Beds and Pentland Formation through time. The plots show both the regions and source rocks of the IMF where hydrocarbons migrated from and the combined totals of each migration region, in accumulated mass and relative percentages. There is a near-total dominance on the charge by proximal migration until the faults open at 66 Ma, when the deep-basin migration charge enters and the two combine to create a near-even mix. 207

7.20 Map of the study area within the IMF, containing a boundary identifying the region of the BPSM, showing petroleum saturation percentages of reservoir formations within the basin. Highlighted on the map are the known hydrocarbon accumulations (Beatrice, Jacky and Lybster Fields), the fifteen potential unknown accumulations identified in this study, and the 2D line extracted and shown in Figure 7.22. UA = unknown accumulation. 209

7.21 Time plot showing the filling history of the unknown accumulation UA 15, in the northern region of the Great Glen Sub-basin, split into the relative hydrocarbon source rock contributions. 211

7.22 Two 2D lines extracted from the central northern region of the IMF, see Figure 7.20, across the Great Glen Sub-basin, highlighting UAs 6 and 15, and Jacky Field. The upper 2D extraction shows the lithologies and structures present, and the lower 2D extraction shows the petroleum saturation of the section, highlighting the locations of accumulated modelled hydrocarbons. 213

8.1 Systematic figure outlining the method of delineating the region around each well for hydrocarbon mixing ratio analysis. The accurate extraction of a precise area around each well on a small scale within the BPSM is not possible, thus delineating the area based on the BPSM cells is the more accurate method, despite variations in distance from wells occurring in different directions. 219

8.2 Maps of the IMF identifying the regions separated for deep basin and proximal hydrocarbon charging, highlighting the Great Glen Sub-basin (GG SB) and the Lossiemouth Sub-basin (Loss. SB), and the wells utilised in this analysis. The majority of wells are located within the shallower, proximally charged regions of the basin, however two, Wells 12/27-2 and 12/29-1, sit within the deep basin-charge region of the Lossiemouth Sub-basin. 222

8.3 Contour maps of varying sequences through the BPSM of the IMF showing the maximum temperature reached across the basin, highlighting the highest and lowest maximum temperatures reached. These temperatures are derived from the BPSM and show that all sequences exist within the magnetite-formation window between 85-250 °C defined by Aubourg *et al.* (2008, 2012), Aubourg and Pozzi (2010) and Kars *et al.* (2012, 2014). KC Bl. Sh. = Kimmeridge Clay Black Shale. 226
8.4 Cross-section across the Great Glen Sub-basin showing the relationships and behaviours between the petroleum system and the hydrocarbon-generating source rocks, and the magnetic minerals within the basin. 229

A.1 Map of the Inner and Outer Moray Firths, and Northern North Sea showing the locations of the wells used to build the erosion map of the sediments removed during the late-stage rifting event in the IMF. Highlighted are the hydrocarbon fields across the region, and the positions of the wells cused to calculate the erosion volume and the location of the non-erosion impacted reference well, 13/30-3. 259
A.2 Sonic-Depth plot of all wells used to calculate apparent erosion, and both their original sonic velocities (grey) and rolling average results (coloured), alongside their *m* gradient line. Note reference Well 13/03-3 is plotted in yellow, and its midpoint sonic velocity is highly correlatable with the Athy's Law calculation estimate. The reference well is significantly deeper but has a slower relative sonic velocity than the wells from the IMF. 260
A.3 Map showing the calculated variation in volume of eroded material across the IMF and the locations of the wells used to calculate it, based on the offset from the relevant wells in the IMF to the reference well, 13/30-3 in the Outer Moray Firth. Locations of the wells used to develop the map are shown, including locations of the known hydrocarbon fields within the IMF, and the basin-forming faults that the erosion is influenced by. Note that X and Y Cells refers to the grid of the BPSM. 262
A.4 Series of boundary condition plots of the three components and their properties used within the BPSM in this study. The paleo-water depth is an estimation on the water level of the area throughout time, and somewhat correlatable to the facies seen in the basin, whilst sediment-water interface temperatures relate to the temperature at seabed, thus is related to the PWD. Heat flow is connected to the basin's geological history and periods of rifting that increase the temperatures across the basin, and the rifting events seen in the IMF are visible in it, and is estimated from work by Allen and Allen (2005). 264
A.5 Figures showing the published (upper; red) and this study's (lower; blue) delineations of the three hydrocarbon fields within the IMF for accurate volumetric comparisons against the greatest petroleum saturation volume created in BPSM testing. 268
A.6 Flow chart outlining the iterative processes involved in the creation of this study's final 3D BPSM. ThK refers to thermal conductivity and Φ refers to porosity. 269
A.7 Series of depth plots from Well 12/16-1, in the North of the IMF, showing the results of varying thermal conductivities on calculated vitrinite reflectance curves and their relationships to calibration data. 271

A.8 Graph showing the transformation ratios and the temperatures they require of the different kinetics used to test hydrocarbon generation in the Pentland Formation, and their associated maps showing the degrees of maturity the Pentland Formation reached using them, based on the final model's Pentland Formation TOC of 4 %. 275

A.9 Series of maps over Beatrice and Jacky Fields in the centre of the IMF showing the petroleum saturation percentage of each cell, over a threshold of 25%, developed via various FCP and permeability scenarios, with consistent TOC values of 4 % and 5.5 % for the Pentland and Devonian, respectively. The threshold is to remove any unsaturated cells from the figures, which show how much influence the fault properties have on the accumulations. 276

A.10 Map over Beatrice and Jacky Fields showing the petroleum saturation percentage of each cell, over a threshold of 25%, of the final model derived through the FCP 2.5 MPa model, with consistent TOC values of 4 % and 5.5 % for the Pentland and Devonian, respectively. 277

A.11 Time plots showing the accumulation history of Beatrice Field throughout geological time, post-deposition of the sealing Heather Formation, under various FCP and fault permeability conditions. The initial filling of the field occurs at the same rate regardless of fault properties due to it occurring during a period of stability and closed fault properties. Beyond 66 Ma, when the faults open to varying degrees, based on their properties, the significant difference in accumulation volumes caused by the faults becomes clear. 278

List of Tables

2.1 Magnetic properties of selected terrestrial ferromagnetic (sensu lato) minerals. T_C = Curie Temperature, T_N = Néel Temperature, IO = iron oxides, IOH = iron oxyhydroxides, IS = iron sulphides, IC = iron carbonates. From Butler (1982), Dunlop and Özdemir (1997), Evans and Heller (2003), Lanza and Meloni (2006), Ponomar *et al.* (2017), Roberts *et al.* (2011) and Schröder *et al.* (2020). 15

3.1 Table summarising geochemical results of the IMF hydrocarbons and other source samples, derived by Peters *et al.* (1989). The IMF hydrocarbons and Middle Jurassic bitumen samples were both collected from Well 11/30-2 within the Beatrice Field, the Kimmeridge Clay and Devonian Type II samples were taken from Well 12/27-1, with the Devonian Type II originating from Early Devonian organic-rich siltstones, and the Devonian Type I source being collected from similar Middle Devonian organic-rich siltstones at Holborn Head Quarry on onshore Scotland (Peters *et al.*, 1989). Note biomarkers are denoted by their presence (Y) or absence (N). 44

4.1 Table summarising the input parameters of the room temperature Vibrating Sample Magnetometer (VSM) analytical laboratory methods used for the ascertainment of key magnetic properties within prepared samples. 50

4.2 Table summarising the input parameters of the room temperature FORC and remFORC analytical laboratory methods used for the ascertainment of FORC diagram data of prepared samples carried out in a VSM. 51

5.1 List of wells in the IMF used in this chapter and study, delineated by the North Sea Quadrant in which they exist. 59

5.2 Table outlining the average responses of the well logs across formations in the IMF, from all the wells analysed in this study. The reservoir sands in the Mid Jurassic show generally much lower gamma ray responses that the other clay-rich formations such as the Devonian, LW Shale, Mid Shale and KC Black Shales. 64

5.3 Table outlining the wells containing OWCs that were selected for analysis in this study. . . 70

5.4 Table showing the data input numbers and resultant outputs of the *M*-*N* calculations carried out on the formations within the IMF. Note that the *M* and *N* values are dimensionless. . . 74

5.5 Table outlining the minimum, maximum and average present day depths of all formations in the IMF, bar the seabed. The depths of the source rocks within the IMF indicate that the deeper regions of the Black Shales may reach maturity, but not the entirety of the formation, similarly to the Pentland Formation. In comparison the Devonian Fish Beds are well in the maturation window. 86

5.6 Table outlining the minimum, maximum and average depths of formations in the IMF. The majority of the basin's thickness is contributed by Cromer Knoll, Kimmeridge Clay, Rotliegend and Devonian sediments, all formed via pre-existing basin infill and periods of syn-rift sedimentation. 89

6.1 Table outlining the amount of core-derived samples collected from numerous wells across the IMF, delineated by both formation and well. The majority of samples are centered around the Middle Jurassic reservoir section due to this being the most heavily cored section of the wells, but other formations and sediment packages are sampled, however below the Lower Jurassic sediments there are few due to the limited numbers of wells that were drilled, much less cored. 94

6.2 Table outlining the mean magnetic results from all samples from all wells in the IMF, alongside one standard deviation (σ), through the Cretaceous Cromer Knoll to the Lower Jurassic, delineated by geological formation and saturating fluid. As the results are a function of formation, they show geological variations but through all wells across the basin, therefore results do not show the lateral variations across the IMF. O = oil, W = water. 96

6.3 Table outlining the mean magnetic results from all samples from all wells in the IMF, alongside one standard deviation (σ), delineated by well and saturating fluid. Results of each well are grouped across all formations sampled throughout, so results are a function of the magnetic mineral assemblage across the entire section, thus the results are skewed to the most magnetic formations. O = oil, W = water. 101

6.4 Table outlining the breakdown of samples across formations and wells within the IMF, used for Principal Component Analysis within this study. Due to the coring patterns in the wells of the basin, sample numbers are skewed towards the upper reservoir sequence of the A and B Sands. 146

6.5 Summary table outlining the varying PCA end-member presence across the formations analysed in the IMF, delineated by saturating fluid. There are little clear trends present within the data, though this is likely a result of the formation-based analysis grouping all well-derived results together, limiting clarity towards geographical variations. 151

6.6 Table summarising the FORC PCA results from the analysed wells across the IMF in this study alongside the magnetic minerals identified in each well, highlighting the end-members seen in both oil- and water-saturated samples, in order of presence from highest to lowest, where applicable. 163

6.7 Table showing the wells in the IMF that were magnetically analysed in this study, highlighting the total number of samples, and the number of samples within each saturating fluid containing the relevant magnetic mineral, identified through high temperature susceptibility curves. Mag = magnetite, Goe = goethite, Sid = siderite, Lep = lepidocrocite, FeS = iron sulphides, grouping pyrite and pyrrhotite, and Mgh = maghemite. 165

6.8 Table the shallowest and deepest presence of each non-magnetite magnetic mineral seen within the IMF in this study 166

6.9 Table summarising the OWC locations and depths (in MD, bar 11/30a-B10 which is TVD), magnetic responses and magnetic minerals present the wells studied in the IMF, ignoring the pervasive magnetite, separated by saturating fluid, and the classification of each OWC-bearing well, based on its characteristics. Goe = goethite, FeS = iron sulphides, Lep = lepidocrocite, Sid = siderite, Mgh = maghemite. 169

7.1 Table outlining the ages and main events assigned to the BPSM of the IMF in this study, and the facies assigned to layers. The facies are derived from the properties available within PetroMod, including mixing multiple facies, determined through core and wireline log analysis, and, where required, supported by literature (Andrews *et al.*, 1990; Brown *et al.*, 1988; Glennie *et al.*, 2003; Linsley *et al.*, 1980; Roberts *et al.*, 1990; Stevens, 1991). 180

7.2 Table of properties applied to the source rocks of the IMF in the BPSM. TOC and HI were derived from well report core analysis and Peters *et al.* (1989), and then back-calculated to define an original TOC (TOC_O) and HI (HI_O) value, using Jarvie *et al.* (2007), whilst the 4-component source rock kinetics were taken from the work of Baur (2019) (Ba) and di Primio and Horsfield (2006) (DP). 182

7.3 Table of properties applied to the faults within the IMF BPSM, showing the variation in fault behaviour – more closed during basin stability, thus acting as fluid migration barriers; and semi permeable-to-open during periods of rifting and instability, where the faults act as fluid pathways. 183

7.4 Table showing the rounded results from the final model of source rock hydrocarbon totals, generation, expulsion and accumulation totals across the entirety of the IMF, in gigatons of oil equivalent (Gtoe) and converted billion barrels of oil equivalent (Bboe), due to the very large totals involved, based on the conversion rate of 1 toe = 7.142857 boe. Results are rounded due to the degree of accuracy available in the BPSM. 193

7.5 Table outlining the results of the differential migration methods used to analyse the hydrocarbon charging of the three known hydrocarbon accumulations within the IMF (Beatrice, Jacky and Lybster Fields). The table shows the split between deep-basin migration from the sub-basins, and proximal migration from beneath alongside the relevant contribution of each source rock to the field's hydrocarbon mixing ratio. Note that the relevant migration totals, or source contributions, in Lybster Field do not sum to 100 % due to the 1 % influence of the Kimmeridge Clay Black Shales. 200

7.6 Table showing the basin and petroleum systems model simulated hydrocarbon mass (in million tons of oil equivalent; Mtoe), equivalent calculated volume (in million barrels of oil equivalent; Mboe) and hydrocarbon mixing ratio results from the three known accumulations within the IMF, Beatrice, Jacky and Lybster Fields, alongside their published estimated volumes, and mixing ratio, from Izundu (2008); Offshore Magazine (2012); Oil and Gas Authority (2018); Peters *et al.* (1989); Stevens (1991). Volume calculations are based on the conversion rate of 1 toe = 7.142857 boe. Bl. Sh. refers to the Kimmeridge Clay Black Shales. 201

7.7 Table showing the basin and petroleum systems model simulated hydrocarbon masses (in Mtoe) and equivalent calculated volume (in Mboe) at both present day and at the peak of hydrocarbon charging, at 66.01 Ma, prior to faults opening during the late-stage uplift event in the IMF. Volume calculations are based on the conversion rate of 1 toe = 7.142857 boe. . 203

7.8 Table outlining the properties of the various potential previously-unidentified accumulations highlighted within the BPSM of the IMF in this study. Volume calculations are based on the simulated mass, converted to barrels of oil through the conversion rate of 1 toe = 7.142857 boe. 210

8.1 Table summarising the hydrocarbon mixing ratios and magnetic minerals present in the wells sampled for magnetic analysis in the IMF that contain both oil- and water-saturated samples, and the dry well 12/21-4, for reference. The mixing ratios are calculated in the BPSM and the magnetic mineral presence is the percentage of samples containing the relevant magnetic mineral against the total number of samples in each well, note that minerals can occur concurrently within samples. Dashes indicate no presence of relevant magnetic mineral. Dev. = Devonian Fish Beds, Pent. = Pentland Formation, Bl. Sh. = Kimmeridge Clay Black Shales, Goe = goethite, Sid = siderite, FeS = iron sulphides (either pyrite or pyrrhotite), Lep = lepidocrocite, Mgh = maghemite. 220

8.2 Table outlining the comparison between the mixing ratio contributions of the Devonian Fish Beds and Pentland Formation source rocks and the relative abundance of goethite, lepidocrocite and maghemite in oil-saturated samples in wells across the IMF. The mixing ratios are calculated from the BPSM and the relative abundance is investigated through the presence in each sample of one of the three minerals, roughly equating to abundance in the magnetic mineral assemblages in each sample, as direct abundance estimates are not possible. Note that multiple minerals can occur concurrently within samples, but this does not impact the count. Dev. = Devonian Fish Beds, Pent. = Pentland Formation, Bl. Sh. = Kimmeridge Clay Black Shales, Goe = goethite, Lep = lepidocrocite, Mgh = maghemite. . 221

8.3 Table outlining the source rock mixing percentages, mixing percentages of the source locations of the Devonian and Pentland source rocks, and magnetic mineral presence at wells across the IMF. The mixing ratios and migration ratios are calculated in the BPSM and the magnetic mineral presence is the percentage of samples containing the relevant magnetic mineral against the total number of samples in each well, note that minerals can occur concurrently within samples. Dashes indicate no presence of relevant magnetic mineral. Dev. = Devonian Fish Beds, Pent. = Pentland Formation, Bl. Sh. = Kimmeridge Clay Black Shales, O = oil, W = water, Goe = goethite, Sid = siderite, FeS = iron sulphides (either pyrite or pyrrhotite), Lep = lepidocrocite, Mgh = maghemite. 223

A.1 Table outlining the ages and main events assigned to the BPSM of the IMF in this study, and the facies assigned to layers. The facies are derived from the properties available within PetroMod, including mixing multiple facies, determined through core and wireline log analysis, and, where required, supported by literature (Andrews *et al.*, 1990; Brown *et al.*, 1988; Glennie *et al.*, 2003; Linsley *et al.*, 1980; Roberts *et al.*, 1990; Stevens, 1991). 255

A.2 Table of the fault property framework in the BPSM, from which testing was carried out. Testing was based on the correlation between faults becoming more permeable and more capable of migrating fluids during periods of basin rifting and instability, and faults being less permeable and more of a barrier to fluids during periods of stability. 256
A.3 Table outlining the facies assigned to layers in the BPSM, derived from the properties available within PetroMod. All facies, such as sandstone, shales, carbonates, etc. are assigned geological properties in PetroMod, produced through calculations and literature, and mixing these facies will create new ones with updated and refined properties reflective of the lithologies they replicate. 257
A.4 Table outlining the inputs to calculate the apparent erosion within the Cenozoic of the IMF used in the BPSM, and the reference well (13/30-3) alongside the Athy's Law calculation used to confirm the lack of erosion in the reference well. 261
A.5 Table outlining the calibration data, and wells containing it, within this study. 267
A.6 Table outlining the components and variables tested within the modelling carried out in this study, with variables in bold italics being those used in the successful final model. 270
A.7 Table showing the results of varying FCP and fault permeability scenarios in the Beatrice Field in both BPSM-simulated masses and calculated converted volume, based on the conversion rate of 1 toe = 7.142857 boe, and the percentage contributions of each source rock to the accumulation. Bl. Sh. = Kimmeridge Clay Black Shales. 276
A.8 Table showing the results of scenario tests of Pentland TOC in the Beatrice Field, with a FCP of 2 MPa and Devonian TOC of 5.5%, through the BPSM-simulated hydrocarbon mass and the calculated converted volume, based on the conversion rate of 1 toe = 7.142857 boe. . . 279

List of Abbreviations

Magnetism

CRM	Chemical Remanent Magnetisation
B_c	Coercivity
B_{cr}	Coercivity of remanence
T_C	Curie Temperature
EM	Endmember
EDX	Energy dispersive x-ray analysis
FC	Field-cooled curves
FORC	First Order Reversal Curve
Goe	Goethite
He	Hematite
H_{fs}	High-field slope
HT	High temperature
B	Induced field strength
B_i	Interaction field distribution
FeS	Iron sulphides
IS	Isomer Shift
IRM	Isothermal Remanent Magnetisation
Lep	Lepidocrocite
LT	Low temperature
Mgh	Maghemite
Mag	Magnetite
M	Magnetisation
m	Magnetic moment
χ	Magnetic mass susceptibility
MD	Multi domain
NRM	Natural Remanent Magnetisation
T_N	Néel Temperature
PC	Principal component
PCA	Principal component analysis
PSD	Pseudo-single domain
QS	Quadrupole split
M_r	Remanent magnetisation
B_r	Reversal field
RT	Room temperature
M_s	Saturation magnetisation
SEM	Scanning electron microscopy
Sid	Siderite
SD	Single domain
TRM	Thermoremanent Magnetisation
ZFC	Zero field-cooled curves

Petroleum Geoscience

API	American Petroleum Institute
boe	Barrels of oil equivalent
bopd	Barrels of oil per day
BCU	Base Cretaceous Unconformity
BPSM	Basin & petroleum systems modelling
brt	Below Rotary Table datum
Bboe	Billion barrels of oil equivalent
Btoe	Billion tons of oil equivalent
LLD	Deep resistivity well log
GR	Gamma ray well log
Gtoe	Gigatons of oil equivalent
GGF	Great Glen Fault
RHOB	Grain density well log
HF	Heat flow
IMF	Inner Moray Firth
KB	Kelly Bushing datum
KCF	Kimmeridge Clay Formation
MD	Measured depth
MSFL	Micro-spherical focused resistivity log
MMBBL	Million barrels of oil
Mboe	Million barrels of oil equivalent
Mtoe	Million tons of oil equivalent
NPHI	Neutron porosity
NSD	North Sea Thermal Dome
OWC	Oil-water contact
ORS	Old Red Sandstone
PWD	Paleo-water depth
SWIT	Sediment-water interface temperature
LLS	Shallow resistivity well log
DT or ΔT	Sonic transit time well log
STBBL	Standard barrel
SCF	Standard cubic feet
toe	Tons of oil equivalent
TOC	Total organic carbon
TVD	Total vertical depth
TVSS	Total vertical depth sub-surface
TR	Transformation ratio
UA	Unknown accumulation
R_o	Vitrinite reflectance

MAGNETISM DEFINITIONS

- E_{anis} – Anisotropy Energy – Due to the orientation of the magnetisation with respect to the crystallographic axes of the material
- B_c – Coercivity – The magnetic field required to bring the magnetisation of the material to zero.
- B_{cr} – Coercivity of Remanence – The field required to reduce a material's magnetic remanence to zero.
- T_C – Curie Temperature – The temperature above which materials lose their permanent magnetic properties, at which point they become paramagnetic.
- E_d – Demagnetisation Energy – The interaction of a materials atomic magnetic moment with itself.
- E_{ex} – Exchange Energy – The (quantum mechanical exchange coupling) between two interacting atomic spins.
- H_{fs} – High-field slope – This is the angle of the slope on the hysteresis loop when in a high magnetic field, i.e. it is the high-field susceptibility (κ).
- M_{in} – Induced magnetism – The magnetism of a material caused by an external field, described by the strength of the applied field multiplied by magnetic susceptibility.
- m – Magnetic moment – The strength and direction of a material's magnetism, and can be both microscopic (at atomic level) and macroscopic (magnetism per unit volume).
- κ – Magnetic susceptibility – The degree of magnetisation a material undergoes in response to a magnetic field. This is strictly speaking volume susceptibility, despite it being dimensionless.
- χ – Mass susceptibility – The magnetic susceptibility (κ) divided by density, with units of m^3kg^{-1}.
- T_M – Morin Transition – A low-temperature ($\sim$260 K) phase transition that affects the magnetic properties of hematite. Above the transition the magnetic spins are not perfectly anti-parallel, and this slight canting leads to a change from antiferromagnetism to "parasitic" ferromagnetism.
- T_N – Néel Temperature – The temperature above which an antiferromagnetic material becomes paramagnetic. This is analogous to the Curie Temperature for ferromagnetic materials.
- M – Net magnetisation – Akin to macroscopic magnetic moment: the average, volume-dependant sum of the microscopic magnetic moments within a material. It can also be described by the sum of remanent and induced magnetism.
- M_r – Remanent magnetism – The remaining magnetism of a material after an external magnetic field is removed. Natural Remanent Magnetism is the permanent magnetism of a geological material.
- M_s – Saturation magnetisation – The magnetism of a material when all the atomic magnetic moments are aligned.
- T_V – Verwey Transition – A low-temperature ($\sim$120 K) phase transition that affects the magnetic, electrical and thermal properties of magnetite. Heating above the transition the most clear change is in the crystal lattice structure, which changes from monoclinic to cubic inverse spinel.

Chapter 1 | Introduction

1.1 | STUDY RATIONALE

The relationships between magnetic minerals and hydrocarbons are long-established but relatively poorly explored in comparison to other areas of geoscience. This study aims to both build the knowledge between magnetic mineral presence, formation, and alteration with hydrocarbons, as well as establish how an under-studied and little understood petroleum system evolved and exists. Furthermore, this work scrutinises the relationship between the two components of its study to investigate the potential for magnetic mineral behaviour and therefore refine and improve the insight into the petroleum system within the basin.

Research, beginning with Donovan *et al.* (1979, 1982), indirectly connects hydrocarbons to magnetic signatures, however, works by Elmore *et al.* (1987), Elmore and Crawford (1990), Kilgore and Elmore (1989) and Emmerton *et al.* (2012, 2013) have proven the presence of direct relationships. This research mainly relates magnetic susceptibility anomalies to hydrocarbons via hypotheses that suggest magnetic minerals are chemical byproducts of iron oxides exposed to a hydrocarbon-created reducing environment. Furthermore, they hypothesise that secondary magnetite appears as framboidal aggregates formed through inorganic processes associated with either hydrocarbon presence or oil biodegradation (Elmore *et al.*, 1987; Elmore and Crawford, 1990; Kilgore and Elmore, 1989; Elmore *et al.*, 2001; Costanzo-Álvarez *et al.*, 2006; Elmore *et al.*, 2012). Machel (1995) discussed how magnetite and pyrrhotite are more stable under reducing conditions, and goethite and hematite are more stable under oxidizing conditions. Magnetic minerals were first proposed as a tool for hydrocarbon exploration in tandem with the discovery of "geochemical plumes" of reducing conditions caused by seepages above hydrocarbon accumulations (Elmore *et al.*, 1987; Machel and Burton, 1991a,b). Aeromagnetic surveys alongside soil, sediment, and drill cutting analyses were considered as exploration tools to identify the shallow, microseepage-induced magnetic signatures (Donovan *et al.*, 1982; Elmore *et al.*, 1987; Díaz *et al.*, 2000; González *et al.*, 2002; Aldana *et al.*, 2003; Costanzo-Álvarez *et al.*, 2006; Aldana *et al.*, 2011). However, relationships between magnetic anomalies and hydrocarbon presence are not necessarily direct, with anomalies potentially deriving from geological variations or other external sources, thus requiring further investigation (Elmore *et al.*, 1987; Costanzo-Álvarez *et al.*, 2006).

This study builds upon research by the Natural Magnetism Group (NMG) at Imperial College London by Emmerton *et al.* (2012, 2013), followed by Abubakar *et al.* (2015, 2020), Badejo *et al.* (2021a,b,c) and Abdulkarim *et al.* (2022a,b,c), among other research. Past research has focussed on known petroleum systems and how the magnetic minerals fit into the previously established knowledge. Consequently, this work differs through its investigation of a largely unknown petroleum system and its examination of the potential for magnetic mineral behaviour to enhance and aid the understanding of that system.

The Inner Moray Firth is in the third arm of the North Sea trilete rift system (Figure 1.1). However, it formed through a different evolutionary process than the other parts of the North Sea (Andrews *et al.*, 1990; Barr, 1985; Johnson *et al.*, 2005; McQuillin *et al.*, 1982; Roberts *et al.*, 1990; Underhill, 1991). The basin contains sediments in ages from the Devonian to present day, with several organic matter-rich formations possibly capable of charging the petroleum system (Aalund, 1983; Andrews *et al.*, 1990;

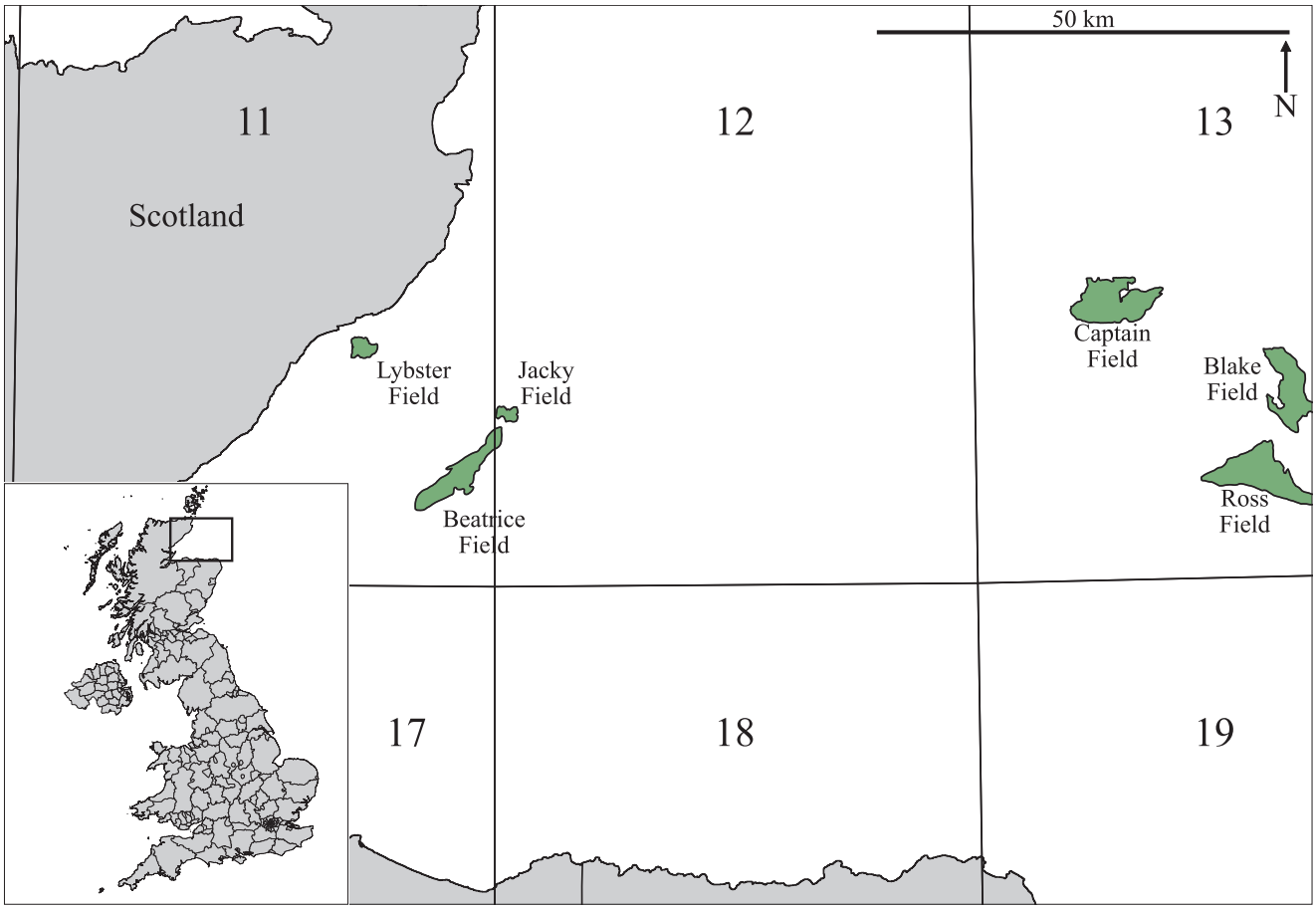


Figure 1.1: *Map of the Inner Moray Firth, the area of investigation within this study, highlighting the locations of the known hydrocarbon fields within the region. Also shown is a map of the UK (inset) with the study area highlighted. The majority of the Inner Moray Firth is located within North Sea Quadrants 11, 12, 17 and 18, with the Outer Moray Firth beginning in Quadrants 13 and 19.*

Brown *et al.*, 1988; Evans *et al.*, 2003; Greenhalgh, 2016; Linsley *et al.*, 1980; Mackenzie *et al.*, 1983; Peters *et al.*, 1989; Stevens, 1991), with varying publications suggesting not only different source rock contributions, but also different source kitchen regions capable of organic matter maturation and hydrocarbon generation (Linsley *et al.*, 1980; Mackenzie *et al.*, 1983; Peters *et al.*, 1989; Stevens, 1991). The Inner Moray Firth represents an interesting study area due to the lack of widespread acceptance and consistent knowledge on both its source rock(s) and region(s) of maturation. Furthermore, extensive core availability and the likely presence of non-Kimmeridge Clay-sourced hydrocarbons make the Inner Moray Firth ideal for comparative magnetic analysis of differently-sourced petroleum systems.

This study also looks to build on previous work investigating the relationships between hydrocarbons and magnetic minerals in relation to different petroleum systems. Previous work by the NMG at Imperial College London has investigated the Central North Sea petroleum systems (Abdulkarim *et al.*, 2022a,b,c; Badejo *et al.*, 2021a,b,c). Comparing these regions to the Inner Moray Firth which has evidence of a non-Kimmeridge Clay-sourced petroleum system (Peters *et al.*, 1989), builds the understanding of how different source rock properties and depositional environments may vary the magnetic mineral assemblages.

1.2 | AIMS AND OBJECTIVES

As discussed, this study uses the petroleum system of the Inner Moray Firth, UK North Sea, as a case study of the relationship between magnetic minerals and hydrocarbons. The basin contains a two-source, mixed hydrocarbon system (Peters *et al.*, 1989), with no currently defined proof of the two source rock kitchens (Greenhalgh, 2016), nor a definitive assertion on the kerogen types used to form the hydrocarbons (Peters *et al.*, 1989), meaning this research is more complex than previous works which examined better-understood petroleum systems. This research builds on previous work by modelling source rock maturation, hydrocarbon migration pathways and accumulations in the Inner Moray Firth, to define the kerogen type(s) and kitchen locations of the source rock(s), and the extent to which these source rocks contribute to hydrocarbon mixing ratios. Furthermore, investigations into the basin and petroleum systems modelling and magnetic analyses identify to what extent the magnetic minerals are impacted by the components of the petroleum system.

This study achieves these outcomes through room-, high-, and low-temperature magnetic analyses of core samples, in tandem with basin and petroleum systems modelling created through in-depth seismic data, well log, and core analysis. Several key questions are at the forefront of this analysis:

- How has the petroleum system of the Inner Moray Firth evolved?
- To what extent does the Inner Moray Firth's petroleum system differ to those in the Central North Sea?
- To what extent do the known source rocks of the Inner Moray Firth contribute to the hydrocarbon accumulations?
- Can any future unidentified hydrocarbon prospects be identified through the basin and petroleum systems modelling
- Do magnetic mineral assemblages of petroleum systems charged with different types of source rocks correlate or contrast?
- Is it possible to constrain a petroleum system through understanding of the magnetic mineral assemblages within the region?

To answer these questions, this study conducts and covers the entire sequence of analysis and interpretation of both the magnetic mineral behaviour and geological basin investigation. The initial two review chapters cover, firstly, the principles of magnetic mineral analysis and magnetic behaviours within geoscience, and secondly, the geological history and the sediments within the Inner Moray Firth study area. Following these, an appraisal chapter explores the production of a geological model and sample location identification for magnetic analysis, through seismic data interpretation, well log data processing and investigation, and core logging and analysis. Beyond this appraisal are the two main components of this study, a chapter covering the magnetic mineral behaviours of the core samples, and an additional chapter on the basin and petroleum systems modelling carried out on the geological model of the Inner Moray Firth. The outcomes of these investigations are then collated and analysed in discussion and conclusion chapters.

1.3 | CHAPTER OVERVIEW

The first review chapter covers magnetic mineralogy principles, the behaviours associated with various magnetic minerals and magnetic mineralogy's relationship with hydrocarbons, and presents and portrays the basic theories and knowledge associated with magnetism in relation to this study. An introduction to magnetism and its founding principles are built upon by an explanation of magnetic data presentation, prior to a summary of significant and study-relevant magnetic minerals and the interactions they share. Following this, a brief literature review presents past research into the relationships discovered and evolved between magnetic minerals and hydrocarbons, to give a rounded view of the impacts this study has, and the work it is building from.

The second review chapter begins with an introduction to basin analysis and petroleum geoscience, and their associated datasets. Following this, a geological insight into the Inner Moray Firth is presented, outlining the geological history and structural evolution of the study area, the sediments, and key formations that infill the basin, and the hydrocarbons discovered within it. The chapter ends with a review of the geochemical analysis conducted within the study area on the hydrocarbons present, as a basis for the basin and petroleum systems modelling (BPSM). This chapter presents a critical summary of the knowledge of the Inner Moray Firth, built on the necessary analytical principles, from which this study's modelling and conclusions are made.

The methodology chapter covers all of the requisite analytical techniques utilised within this study. It displays the sample collection and preparation techniques alongside room-, low-, and high-temperature magnetic mineral measurement constraints and properties, as well as the microscopy analysis. Furthermore, it covers the techniques and processes involved in collating, processing, and building both the geological model and the BPSM.

The first of the analytical chapters covers the geological appraisal of the Inner Moray Firth through various datasets, including seismic data, well logs, and core analysis. This chapter builds from initial literature from the previous chapters, drawing conclusions based on the data available, and producing a geological model which then evolves into a BPSM in the following chapters. This analysis is of critical importance to the study, as whilst it does not itself produce key findings or directly answer the questions posed in this introductory chapter, it is the foundation not only of the BPSM and the results therein, but also directs and refines the sampling locations required for magnetic mineral analysis.

The magnetic analysis chapter initially details the basin-wide room temperature magnetic behaviour of the study area, before presenting and analysing the room-, low-, and high-temperature behaviours of samples at well scale, to give insight into localised magnetic mineral assemblages, behaviours, and variations. Well-scale first order reversal curve (FORC) principal component analysis (PCA) is analysed in detail to further understand the magnetic mineral grain behaviour across the Inner Moray Firth. The implications of this body of analysis are considered not only for the wider understanding of magnetism, but for the study area and the petroleum system and associated BPSM in this study.

The basin and petroleum systems modelling chapter covers the production, inputs, testing, and results surrounding one-, two-, and three-dimensional modelling of the Inner Moray Firth from a petroleum

systems perspective. This chapter is focused on producing a functioning BPSM that can be used to refine the understanding of the study area and how the petroleum system within it has formed and evolved through its geological history. The chapter is concluded with a discussion both analysing the BPSM results and their implications, and the impact the results may have with the magnetic mineral analysis.

This thesis is concluded with a discussion chapter that collates the analysis carried out within the preceding three chapters and combines them to produce answers on the critical questions posed in the introduction. The discussion chapter also produces crucial knowledge and development into the relationship between magnetic minerals and hydrocarbons. The thesis is then summarised within a concluding chapter. Further analysis and data for rounding and deepening knowledge can also be found in the Appendix, where the theories, framework, and scenario testing within the BPSM analysis are presented, alongside the well logs used within this study. The Appendix also directs access to repositories containing the data produced within this study, as well as including copies of the publications produced within this research.

Chapter 2 | Magnetism Review

2.1 | INTRODUCTION

This chapter will cover the theories surrounding mineral magnetism which are applied in this study. The chapter details the principles required as a foundation for the rest of the review, and examines the properties of a select group of magnetic minerals relevant to the study, and to mineral magnetism as a whole. Finally, it reviews past and present research investigating the relationship between hydrocarbons and mineral magnetism, one of the foundations that this study is focussed on and looking to build beyond.

2.2 | MAGNETISATION PRINCIPLES

2.2.1 | MAGNETISATION

Bleaney and Bleaney (2013) defines magnetisation (M) as the net magnetic moment (m) per unit volume with dimensions of amperes per metre (A m^{-1}). This is the overarching property under which rock magnetism is analysed. Rock-forming materials subjected to the Earth's magnetic field are categorised as dia-, para- or ferro-magnetic, with all materials being diamagnetic (lacking a permanent magnetic moment) to some extent (Dunlop and Özdemir, 1997; Lanza and Meloni, 2006). Materials that possess other magnetism forms have negligible diamagnetism, thus are classified as either para- or ferro-magnetic (Dunlop and Özdemir, 1997; Emmerton *et al.*, 2012; Lanza and Meloni, 2006). Paramagnetic materials have permanent microscopic magnetic moments partially aligned to an applied external field, and ferromagnetic materials (*sensu latu*) have long-range ordered (strong alignment across a large atomic distance), causing permanent magnetic moments (Dunlop and Özdemir, 1997). Paramagnetic materials lose their macroscopic magnetisation when the external magnetic field is removed, whereas ferromagnetic materials contain measurable remanent magnetisation (M_r) when the external field is removed due to exchange coupling (Butler, 1992).

Ferromagnetism (*sensu lato*) is subdivided into four variants (Figure 2.1). i) ferromagnetism (*sensu strictu*) itself has parallel neighbour moments that produce strong net magnetisations, e.g. elemental iron; ii) antiferromagnetism has anti-parallel neighbour moments creating a zero net magnetisation (Butler, 1992); iii) ferrimagnetism has anti-parallel neighbour moments, e.g. iron(II,III) oxides, but with one direction being stronger, creating a small net magnetisation; and iv) canted antiferromagnetism has antiparallel neighbour moments that are subtly angled in a direction orthogonal to the main magnetic moment, creating a weak net magnetisation in that angled direction, e.g. hematite (Dunlop and Özdemir, 1997).

Applying a magnetic field to a ferromagnet increases its total magnetic energy, causing the sample to become magnetised and changing its domain structure to accommodate the increase in energy (Dunlop and Özdemir, 1997; Emmerton, 2012). The intensity of this new magnetisation is dependent on: mineralogy, domain state, temperature and field; the response of the material to both changes in temperature and induced field are typically represented in a hysteresis loop (Figure 2.2; Tauxe (2009)).

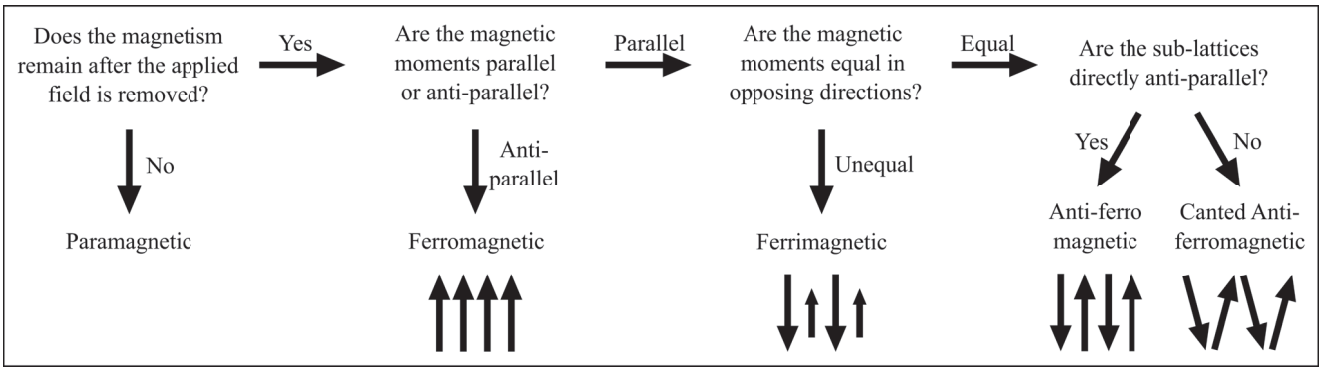


Figure 2.1: *Flow diagram outlining the identification of the different moments seen in different ferromagnetic minerals and their relative directional strength. Modified from Badejo (2019); Tauxe (2009).*

When a ferromagnet is subjected to a saturating magnetic field it acquires a saturation magnetisation (M_s; Figure 2.2). Once this field is removed, the remaining remanence is termed saturation remanent magnetism (M_r). This is where grains show different responses: I) SD grains gain M_r through the rotation of the grains' magnetic moments to the direction of the induced field; and II) MD grains whose behaviour is governed by domain wall movement (Dunlop and Özdemir, 1997; Evans and Heller, 2003). Further properties are also identified, with coercivity (B_c), the field needed to reduce the material's magnetisation to zero, and the negative field required to reduce a material's remanence to zero is the coercivity of remanence (B_{cr}) also produced on the loop (Dunlop and Özdemir, 1997).

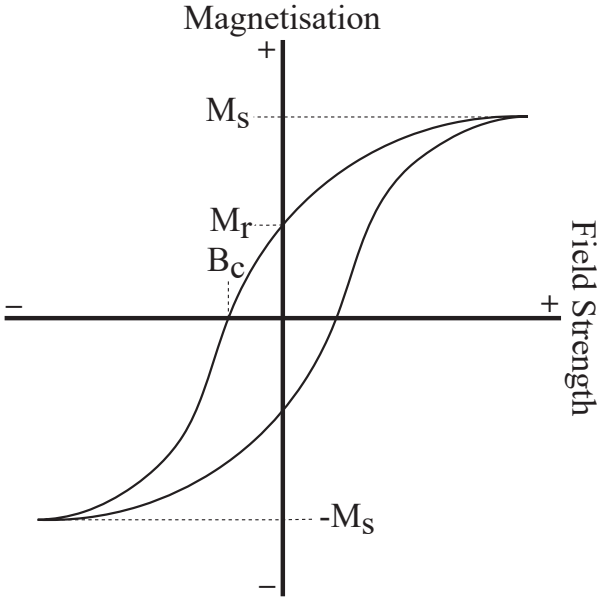


Figure 2.2: *Schematic hysteresis loop identifying the major magnetic properties derived from it. Modified from Dunlop and Özdemir (1997).*

2.2.2 | Magnetic Remanence

The remanent magnetisation (M_r), as discussed previously, is the magnetism remaining within a sample after it has been subjected to a magnetic field, and is typically derived from a variety of sources. Overprinting of this magnetism is common within geology due to the processes and associated environments that minerals are subjected to within the rock cycle, such as subduction, uplift and erosion. The types of M_r typically seen within this system, as well as within a laboratory setting, are outlined below.

2.2.2.1 | Natural Remanent Magnetisation (NRM)

NRM is the natural magnetism of a sample dependant on the strength of the geomagnetic field imposed on it during the rock's formation (Primary NRM) and throughout its history (Secondary NRM). Overprinting or obscuring of the primary NRM by the secondary NRM is an issue facing many paleomagnetists who's research demands the analysis of primary NRM only (Tauxe, 2009).

2.2.2.2 | THERMOREMANENT MAGNETISATION (TRM)

TRM is a result of the cooling of a sample from high temperatures above minerals' Curie Temperature, causing re-writing of the sample's pre-existing magnetism and the imposing of a new magnetism aligned to the ambient magnetic field during cooling (Tauxe, 2009). TRM is very common in igneous and metamorphic rocks due to the temperatures associated with both geological processes, for example, both processes can produce temperatures that surpass magnetite's Curie Temperature of ∼580 °C, and is typically stable over geological time periods due to the high energy barriers at ambient temperatures (Tauxe, 2009).

2.2.2.3 | CHEMICAL REMANENT MAGNETISATION (CRM)

CRM is acquired when the local environment forms or alters magnetic minerals at or below their blocking temperature whilst in the presence of a magnetic field (Dunlop and Özdemir, 1997). Typically, chemical alteration within geology comes in the form of either the formation of new minerals or sufficient alteration of pre-existing minerals (Dunlop and Özdemir, 1997). This is a very relevant and common magnetisation within a geological context due to the high frequency of chemical alteration present in geological systems, e.g. diagenesis and changing conditions between oxidising and reducing.

2.2.2.4 | ISOTHERMAL REMANENT MAGNETISATION (IRM)

IRM is typically acquired when a sample is kept at a constant temperature and subjected to a strong magnetic field (Tauxe, 2009). If the sample reaches magnetic saturation during this process, IRM transforms into saturation isothermal remanent magnetisation (SIRM) (Tauxe, 2009). It can occur naturally, due to lightening strikes.

2.2.3 | MAGNETIC DOMAINS

A material's magnetic behaviour and structure is determined by its total magnetic energy, which is controlled by the sum total of the demagnetisation, anisotropy, exchange and external field energies (Kittel, 1949). If a ferromagnet is below its Curie Temperature (T_C) and above a critical size, it is energetically favourable for the material's magnetic structure to break up into patterns known as domains (Kittel, 1949). Domain theory states that magnetic moments within a domain are parallel aligned, but change direction across domain walls, either sharply or through gradual moment rotation depending on wall width and material magnetic properties (Kittel, 1949). The variation in domain walls cause three types of domains: single domain (SD), pseudo-single domain (PSD) and multi-domain (MD; Figure 2.3; Tauxe (2009)).

SD grain sizes exist below critical size (e.g. ∼80 nm for magnetite, Muxworthy and Williams (2006)) so cannot form domain walls, thus all moments are aligned, resulting in uniform magnetism when the grain reaches saturation magnetisation (M_s; Kittel (1949)). SD grains are magnetically hard and stable and have high M_r/M_s ratios and coercivity (B_c), making them ideal for magnetism studies (Stacey and Banerjee, 1974). When the demagnetisation energy is too great for the grain to remain stable, the domain can split, causing a change in structure to MD/PSD (Butler and Banerjee, 1975).

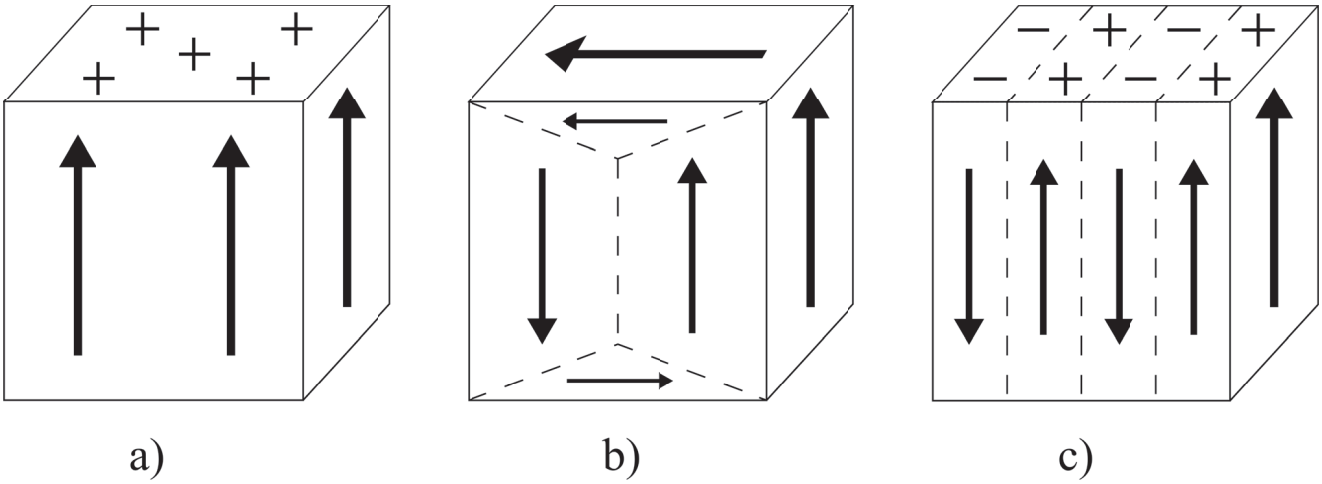


Figure 2.3: *Schematic diagrams of the three dominant grain domain types: SD (a), PSD (b) and MD (c). Arrows show direction of magnetisation within the domain, positive and negative signs represent dipole orientation, and dashed lines are domain walls. Modified from Dunlop and Özdemir (1997).*

PSD grains have a few domains and exhibit a mixture of both SD- and MD-like behaviour – high M_r/M_s ratios and low B_c respectively – and are seen as a transition zone between SD and MD (Butler, 1992; Roberts *et al.*, 2017; Tauxe, 2009). The transition from SD to PSD is sharp, but PSD towards MD is gradual, and highly dependant on grain size and shape (Roberts *et al.*, 2017).

MD behaviour exists when a grain has several domains, resulting in magnetically soft characteristics with low M_r/M_s ratios and B_c (Evans and Heller, 2003). When the grain grows beyond a critical size (making MD grains typically larger than SD grains), it splits into equally-magnetised domains. However, moving a domain wall can change the magnetisation of the grain and the domain sizes, and a larger MD grain may have more easily-movable domain walls, and thus a less stable M_r, than an SD grain (Lowrie, 2012).

2.2.3.1 | Identifying domain states through First Order Reversal Curves

First order reversal curves (FORCs) and the diagrams that they are used to construct are used to identify magnetic mineral domain states within analysed samples (Roberts *et al.*, 2000). FORCs directly relate to the domain behaviour of the magnetic minerals in the samples they are dervied from, and they are constructed from partial magnetic hysteresis loops (Roberts *et al.*, 2000). A FORC is the forward magnetisation curve measured between a specific reversal field value (B_r) and the sample's magnetic saturation, with the magnetisation value of the FORC at any point along this curve being denoted by $M(B_r,B)$, where B is the induced field strength (Figure 2.4a; Roberts *et al.* (2014)). Multiple, evenly-spaced FORCs are measured within the sample's hysteresis loop, forming a grid of magnetic measurements used to create the FORC diagram (Figures 2.4b-c), with neighbouring points on consecutive FORCs being used to determine the FORC distribution ($\rho(B_r,B)$, Equation 2.1; Roberts *et al.* (2014)). Because reversible magnetisation components (dia- or para-magnetism) do not exhibit hysteresis, these components will be eliminated by the equation and will not contribute to a sample's FORC diagram (Roberts *et al.*, 2014), thus the magnetisation produced during FORC diagram development is a function of the ferromagnetic (*sensu latu*) minerals only.

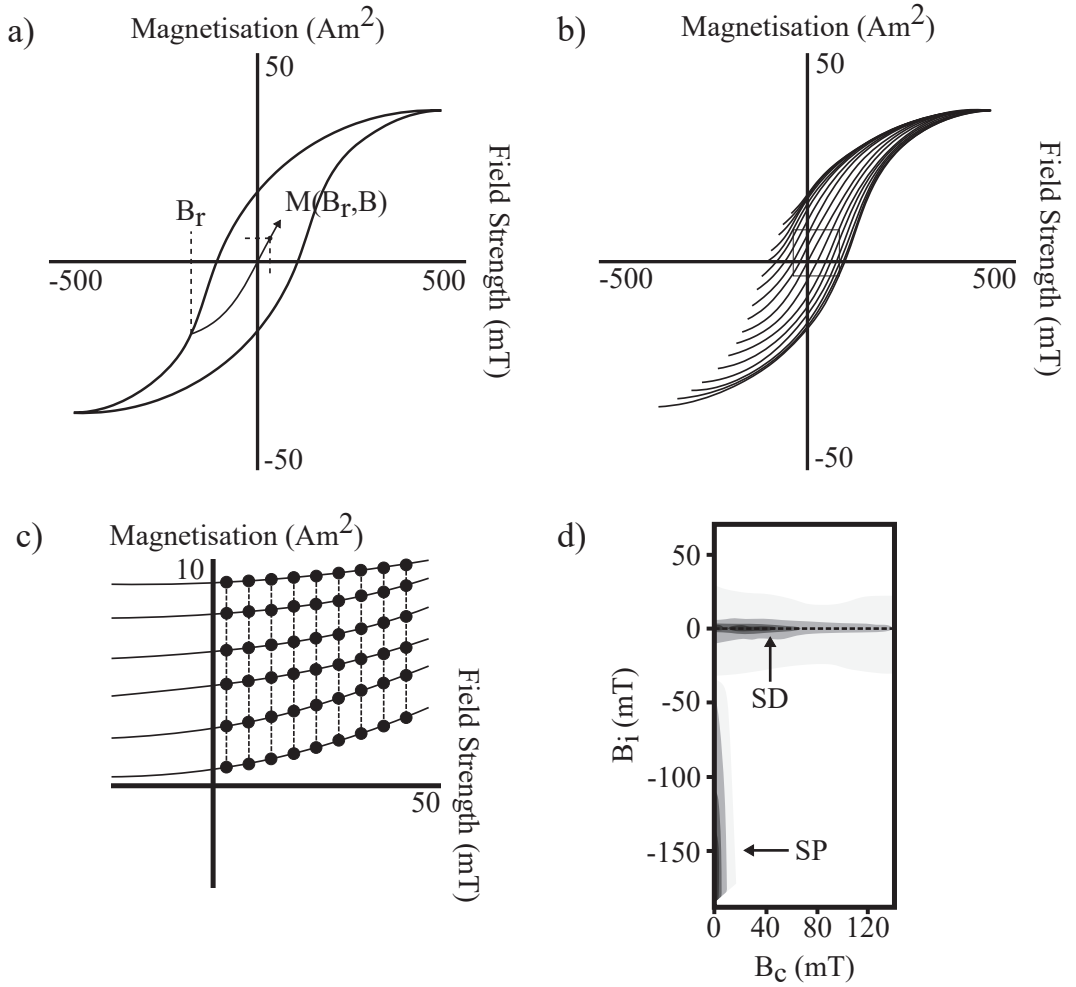


Figure 2.4: *FORC diagram measurement. a) Measurement an individual FORC, commencing at specified B_r, ending at M_s. b) Suite of FORCs within the pre-defined hysteresis loop, with the rectangle defining the area in c). c) Gridded area of FORCs displaying how $\rho(B_r,B)$ is calculated. d) A typical FORC Diagram, showing a non-interacting SD grain and an SP grain. Modified from Roberts* et al. *(2014) and Roberts* et al. *(2018). Note scales, diagrams and results are not accurate, just a visual aid.*

$$\rho(B_\mathrm{r},B) = -\frac{1}{2}\frac{\delta^2 M(B_\mathrm{r},B)}{\delta B_\mathrm{r}\delta B} \tag{2.1}$$

FORC diagram axes are rotated from (B_r,B) to (B_c,B_i) (Equations 2.2 and 2.3), with B_c the coercivity distribution and B_i the interaction field distribution (Figure 2.4d; Dodrill (2015); Roberts *et al.* (2014); Tauxe (2009)). Rotation is because $B \geq B_r$, resulting in the FORC distribution being only well defined where $B_c \geq 0$, thus confining the diagram to the positive half of the plane (Roberts *et al.*, 2014).

$$B_\mathrm{c} = \frac{B_\mathrm{r} - B}{2} \tag{2.2}$$

$$B_\mathrm{i} = \frac{B_\mathrm{r} + B}{2} \tag{2.3}$$

A simple interpretation of FORC diagrams, is that the x-axis corresponds to the coercivity distribution, and the y-axis the magnetostatic interaction field, with this field being either inter-grain interaction fields or internal MD interaction fields (Roberts *et al.*, 2000). Interpretations of the produced FORC diagram will offer insight into the dominant grain domain state(s) seen within the tested sample, as each domain will produce different relationships between the coercivity and the interaction field distributions.

2.2.3.2 | FORC DIAGRAM INTERPRETATION

Interpretation of FORC diagrams is subjective, resulting in possible issues between interpreters. The development of a machine learning-derived FORC interpretation system is the most ideal analytical tool to remove human-induced errors, however this is not a simple task. There are a range of generally accepted interpretation rules that can be applied to FORC diagrams (Figure 2.5):

- Ridge-like distributions along the B_i=0 axis suggest the presence of non-interacting SD grains (Figure 2.5a; Pike *et al.* (1999)).
- A positive peak below the B_i=0 axis suggests the presence of thermally relaxing SD grains (SP grains, Figure 2.5a; Roberts *et al.* (2014)).
- Concentric peaks with vertical spread on the B_i axis suggests the presence of interacting SD grains (Figure 2.5b-c; Roberts *et al.* (2000)).
- A negative peak below the B_i=0 axis suggests the presence of an SD assemblage (Figure 2.5c; Muxworthy *et al.* (2004).
- A steeply dipping negative region either side of a peak is likely due to either multiaxial anisotropy (Harrison and Lascu, 2014; Valdez-Grijalva and Muxworthy, 2019) or SD vortex behaviour (Figure 2.5c-d; Lascu *et al.* (2018); Valdez-Grijalva *et al.* (2018)).
- A consistent vertical spread along the B_c axis suggests the presence of MD grains (Figure 2.5e; Roberts *et al.* (2000)).
- A combination of vertical spread along the B_c axis and a peak at the B_c axis suggests the presence of PSD grains (Figure 2.5f; Roberts *et al.* (2017)).

2.3 | FERROMAGNETIC MINERALS

To successfully identify the different minerals within analysed samples, their individual behaviours and structures must be understood. This section investigates the most common and potentially relevant magnetic minerals to this study, however this list is not exhaustive.

2.3.1 | IRON & TITANIUM OXIDES

Iron and titanium iron oxides are the most important group of terrestrial magnetic minerals, consisting of magnetite (Fe_3O_4), hematite (α-Fe_2O_3), maghemite (γ-Fe_2O_3), titanomagnetite ($Fe_{2-x}Ti_xO_4$) and titanohematite ($Fe_{2-\gamma}Ti_\gamma O_3$; Table 2.1; Dunlop and Özdemir (1997)). This group can be split into two structural types: strongly magnetic cubic oxides of titanomagnetites (including magnetite) and titanomaghemites, and weakly magnetic rhombohedral minerals of solid solution titanohematites and hematites (Dunlop and Özdemir, 1997; Evans and Heller, 2003). Magnetite is critical to magnetic studies due to its magnetic strength and abundance – it contributes the dominant magnetic signature in the majority of rocks (Emmerton *et al.*, 2012). Magnetite is ferrimagnetic, as Fe^{3+} and Fe^{2+} cations exist in two interstitial sites between face-centered oxygen anions within its cubic structure (Emmerton, 2012). The moments of the two Fe^{3+} cations cancel out, resulting in the grain's magnetic moment deriving

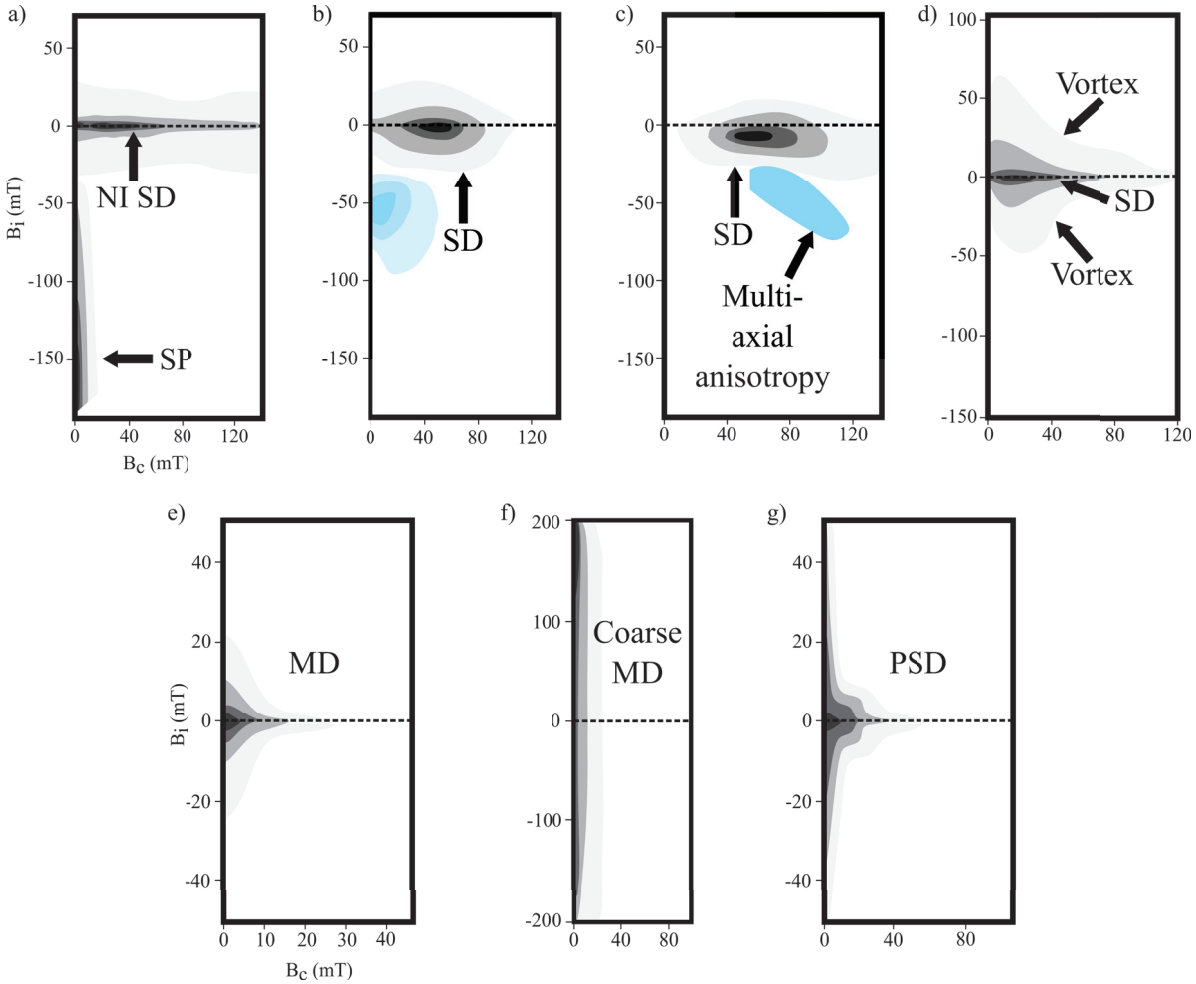


Figure 2.5: *Example FORC diagrams showing the different results created by the FORCs from varying magnetic grain domains, and thus how they are interpreted. Modified from Roberts* et al. *(2018).*

from the Fe^{2+} ions (Emmerton, 2012). In the ambient environment, magnetite is unstable and gradually oxidises to maghemite via low-temperature crystal-surface maghematisation, then to hematite through prolonged oxidation or heating (Figure 2.6; Dunlop and Özdemir (1997); Evans and Heller (2003)).

Magnetite experiences variation via titanium replacement of iron, creating the titanomagnetite solid-solution series between endmembers of magnetite (Fe_3O_4) and ulvospinel (Fe_2TiO_4) (Dunlop and Özdemir, 1997; Evans and Heller, 2003). Low temperature, partially-oxidized titanomagnetites transform into metastable titanomaghemites, and can invert to more stable titanohematite, but can also be reduced to magnetite (Figure 2.6; Dunlop and Özdemir (1997); Evans and Heller (2003)).

Hematite is ferromagnetic and typically SD, but often experiences significant impurities and crystal defects within its antiferromagnetic, rhombohedral structure (Dunlop and Özdemir, 1997). Hematite shows a net M_r perpendicular to two sub lattices, and at room temperature, it has a very high B_c compared to relatively-sized magnetite grains (Dunlop and Özdemir, 1997). Titanohematites are also rhombohedral and have compositions on the tie-line between endmembers of hematite (α-Fe_2O_3) and ilmenite ($FeTiO_3$), and are similar to titanomagnetites in that solid-solution is only complete at high temperatures (Dunlop and Özdemir, 1997). Hematite is the end product in systems with open contact to oxygen, but when oxygen is excluded pyrrhotite (providing sulphur is present) and magnetite, along with elemental iron, are the final products (Figure 2.6: Dekkers *et al.* (2000)).

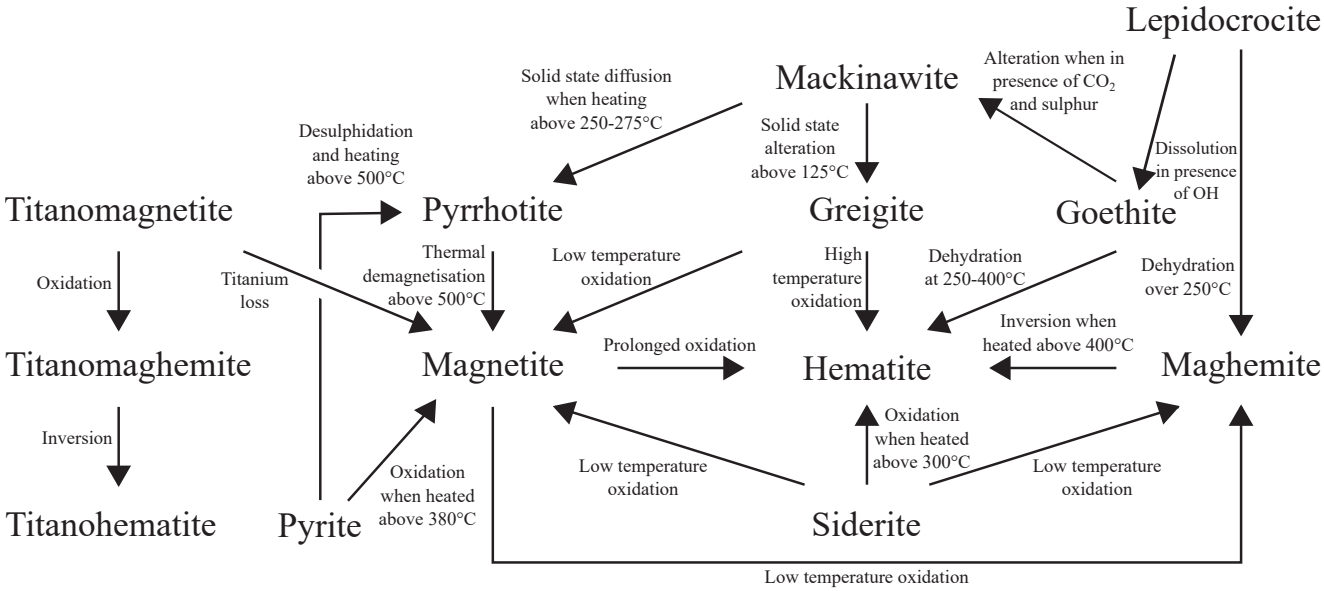


Figure 2.6: *Flow chart summarising the alteration processes observed in nature between numerous ferromagnetic minerals. Note that given the right circumstances and environments, all minerals will eventually alter to magnetite and then to hematite. See text for information and accompanying references. Modified from Badejo (2019).*

Table 2.1: *Magnetic properties of selected terrestrial ferromagnetic (*sensu lato*) minerals. T_C = Curie Temperature, T_N = Néel Temperature, IO = iron oxides, IOH = iron oxyhydroxides, IS = iron sulphides, IC = iron carbonates. From Butler (1982), Dunlop and Özdemir (1997), Evans and Heller (2003), Lanza and Meloni (2006), Ponomar* et al. *(2017), Roberts* et al. *(2011) and Schröder* et al. *(2020).*

Group	Mineral	Formula	Magnetism type at room temperature	T_C (°C)	T_N (K)
IO	Magnetite	Fe_3O_4	Ferromagnetic	580	-
	Hematite	α- Fe_2O_3	Canted-antiferromagnetic	675	948
	Maghemite	γ- Fe_2O_3	Ferromagnetic	590-675	-
IOH	Goethite	αFeOOH	Canted-antiferromagnetic	120	393
	Lepidocrocite	γFeOOH	Canted-antiferromagnetic	–196	∼–50
IS	Greigite	Fe_3S_4	Ferrimagnetic	>330	-
	Pyrrhotite	Fe_7S_8	Ferrimagnetic	320	-
	Pyrite	FeS_2	Paramagnetic	-	-
	Mackinawite	$Fe_{1+x}S$, x = 0-0.11	?Paramagnetic	-	-
IC	Siderite	$FeCO_3$	Paramagnetic	-	–38

Maghemite is magnetically similar to magnetite, and is body-centred-cubically structured (Dunlop and Özdemir, 1997). It is metastable at room temperature but inverts to weakly magnetic hematite above 300-600 °C (Figure 2.6), causing issues in deriving an accurate T_c (Evans and Heller, 2003).

2.3.2 | IRON OXYHYDROXIDES

Iron oxyhydroxides are often collectively classed as limonite (Fe,O,OH,H_2O), but the most important is the imperfect-antiferromagnetic, weakly-ferromagnetic, orthorhombic goethite (α-FeOOH; Dunlop and Özdemir (1997)). Goethite dehydrates in the temperature range of 250-400 °C to form superparamagnetic, remanence-lacking hematite (Figure 2.6; Dunlop and Özdemir (1997)). Lepidocrocite (γ-FeOOH) is more minor than goethite, and also antiferromagnetic, but its Néel Temperature (T_N) is far below 0 °C (Table 2.1), thus lepidocrocite at room temperature is paramagnetic (Dunlop and Özdemir, 1997). Lepidocrocite dehydrates to strongly magnetic maghemite when heated to above 250 °C (Figure 2.6; Dunlop and Özdemir (1997)).

2.3.3 | IRON SULPHIDES

There are two dominant ferromagnetic iron sulphides – greigite (Fe_3S_4) and pyrrhotite (Fe_7S_8; Dunlop and Özdemir (1997)). Pyrite (FeS_2) is also an abundant iron sulphide, but is paramagnetic (Evans and Heller, 2003), thus has limited use in paleo-magnetic research, although it is often present and is important in understanding iron and sulphur presence in natural systems. Pyrite often alters, environment-depending, to either magnetite (below 400 °C) or pyrrhotite (at approximately 535 °C; Li and Zhang (2005); Wang *et al.* (2008); Waters *et al.* (2008)). Greigite is the sulphide counterpart of magnetite, having the same inverse spinel structure, is common in sediments deposited in anoxic environments, and can also be biomineralised by magnetotactic bacteria (Dunlop and Özdemir, 1997; Evans and Heller, 2003). Greigite is ferromagnetic, however, its M_s is approximately 57 % that of magnetite (Li *et al.*, 2014). Greigite also has the ability to alter into a variety of other ferromagnetic minerals, with oxygen presence often the determining factor (Figure 2.6; Dekkers *et al.* (2000)).

Naturally-occurring pyrrhotite is a mix of ferrimagnetic, monoclinic Fe_7S_8 and antiferromagnetic, hexagonal phases such as Fe_9S_{10} and $Fe_{11}S_{12}$ (Dunlop and Özdemir, 1997; Evans and Heller, 2003). The observed deficiency of Fe^{2+} is accounted for by lattice vacancies and ordering, which gives rise to different numbers of Fe^{2+} ions in Fe_7S_8 on its two sublattices (Volk *et al.*, 2016). This makes monoclinic pyrrhotite similar to maghemite in that its ferromagnetism is due to cation deficiency and vacancy ordering. During thermal demagnetisation above 500 °C, pyrrhotite irreversibly transforms to magnetite, or hematite at higher temperatures (Figure 2.6; Table 2.1; Bina and Daly (1994); Dekkers (1990); Dunlop and Özdemir (1997); Evans and Heller (2003)).

Another commonly identified but not fully characterised iron sulphide is the typically metastable, tetragonal, iron (II) monosulphide mackinawite ($Fe_{1+x}S$, x=0-0.11). Mackinawite is the naturally occurring end member of the mackinawite-pyrrhotite-smythite-greigite phase relationship, with the other end being non-naturally occurring, pure ferric monosulphide γ-Fe_2S_3 (Evans *et al.*, 1964; Krupp, 1994; Rickard, 2013; Vaughan and Craig, 1978). Mackinawite's magnetic properties are a cause of debate and discussion, with no conclusive definitions of its structure, properties or behaviour at any temperature range. Some argue that mackinawite is paramagnetic (Schröder *et al.*, 2020), others that it is antiferromagnetic (Kwon *et al.*, 2011),whilst its properties at low temperatures are unknown, and at high temperatures it alters, environmentally-depending, to either greigite at 125 °C (Hunger and Benning,

2007; Lennie *et al.*, 1997) or pyrrhotite at 250-275 °C (Lennie *et al.*, 1995), limiting further knowledge of its properties (Figure 2.6). Mackinawite typically forms via hydrogen sulphide (HS^-) reacting with iron, either as Fe^{2+} or Fe metal, but can also alter from goethite when in an environment containing both a sulphur source and carbon dioxide (Lennie *et al.*, 1997; Vaughan and Craig, 1978; Wang *et al.*, 2015).

2.3.4 | Iron Carbonates

Siderite ($FeCO_3$) is common in carbonates, but is paramagnetic at low temperatures, thus carries no natural magnetic remanence, however, it is identifiable by its T_C (Dunlop and Özdemir, 1997). At room temperature, natural siderites oxidise by measurable amounts when exposed to air, but when heated, rapid oxidation to magnetite or maghemite occurs, then ultimately to hematite above 300 °C (Figure 2.6; Dunlop and Özdemir (1997)).

2.4 | Magnetic minerals and hydrocarbons

Early research (Donovan *et al.*, 1979, 1982) indicated indirect connections between hydrocarbon presence and magnetic signatures, but as research rapidly progressed, direct relationships were established (Elmore *et al.*, 1987; Elmore and Crawford, 1990; Kilgore and Elmore, 1989). The majority of research connects hydrocarbon presence to magnetic susceptibility anomalies, with suggestions that magnetic minerals are chemical byproducts of iron oxides exposed to reducing environments (Elmore *et al.*, 1987, 2001, 2012; Elmore and Crawford, 1990; Kilgore and Elmore, 1989). This reducing environment is created by the influx of hydrocarbons into a region, and further processes including hydrocarbon biodegradation can further produce new, or alter pre-existing magnetic minerals (Costanzo-Álvarez *et al.*, 2006; Elmore *et al.*, 1987; Machel, 1995). The predictions of Machel (1995) suggest that differing magnetic minerals are more or less stable in different conditions produced by hydrocarbon presence, offering magnetite and pyrrhotite as stable under reducing conditions, compared to goethite and hematite in more oxidizing conditions.

The identification of the hydrocarbon-magnetic mineral relationship was swiftly followed by discussions over its potential for hydrocarbon exploration, with Elmore *et al.* (1987) and Machel and Burton (1991a,b) identifying the formation of reducing conditions over hydrocarbon accumulations as a result of seepages. The hydrocarbon exploration method was hypothesised to include aeromagnetic surveys alongside soil, sediment and drill cutting analysis, to identify these so-called "geochemical plumes" (Aldana *et al.*, 2003, 2011; Costanzo-Álvarez *et al.*, 2006; Díaz *et al.*, 2000; Donovan *et al.*, 1982; Elmore *et al.*, 1987; González *et al.*, 2002). Although, as with other hydrocarbon exploration methods, drawbacks from these potential hydrocarbon-derived magnetic anomalies include their formation through a wide variety of non hydrocarbon-derived sources (Costanzo-Álvarez *et al.*, 2006; Elmore *et al.*, 1987).

The properties and contents of hydrocarbons themselves are another source of derived magnetic anomalies, with all fluids in a hydrocarbon accumulation showing diamagnetism, with crude oil showing a much more negative susceptibility than formation waters (Ivakhnenko and Potter, 2004). Variations in magnetic signatures from hydrocarbons predominantly relate to their density, residue content, API gravity, viscosity, sulphur content and metal concentrations, with light crude being the most diamagnetic

(Ivakhnenko and Potter, 2004). Furthermore, the biodegradation of hydrocarbons can impact magnetic anomalies, as Fe^{2+}-oxidizing and Fe^{3+}-reducing microorganisms create newly formed, predominantly SD magnetite (Rijal *et al.*, 2010, 2012) and iron sulphides (Badejo *et al.*, 2021a,b,c).

Grains formed within shales that are subjected to a magnetic field acquire a chemical remanent magnetisation and a thermoviscous magnetisation that both align parallel to the applied field. Furthermore, these are predominantly impacted by thermal effects and hydrothermal alteration, suggesting that any shales within, or passing through, oil window temperatures ($\sim$100 °C) can be remagnetised due to thermal imprinting (Aubourg *et al.*, 2008). Typically these grains are magnetite and hematite, formed at the expense of pyrite and by oxidation of the newly-formed magnetite, respectively, however, relative ratios of pyrrhotite and magnetite at low temperatures ($<$250 °C) can be utilised as a paleo-temperature geothermometer to aid maturity and paleo-maturity analysis (Aubourg *et al.*, 2008; Aubourg and Pozzi, 2010). At low temperatures (40-85 °C) pyrrhotite dominates magnetic mineral assemblages, but above this, up to 250 °C, the neoformation of magnetite increasingly overshadows the presence of pyrrhotite (Aubourg and Pozzi, 2010). Beyond 250 °C, pyrrhotite formation occurs at the expense of magnetite, and pyrite when $>$320 °C, creating a paleo-burial model (Aubourg *et al.*, 2012; Rochette, 1987). Relative presences of various minerals within remagnetised shales give a proxy for burial depth via temperature, from greigite at the subsurface, to magnetite at $>$2 km depth and pyrrhotite at $>$6 km depth (Aubourg *et al.*, 2012).

Costanzo-Álvarez *et al.* (2019) identified that organic matter free radicals (Fe^{3+} an Mn^{2+}), derived from thermal degradation of slightly-biodegraded kerogens, react with iron oxides and sulphides present in the area within two diagenetic stages. The first of these stages partially dissolves the iron oxides and sulphides, resulting in a relative decrease in both magnetic susceptibility and natural remanent magnetisation, and relative increase in the free radicals (Costanzo-Álvarez *et al.*, 2019). The second diagenetic stage exists in a zone of increased hydrocarbon content (at $\sim$2680 m), and results in the partial replacement of framboidal pyrite by authigenic pyrrhotite, causing a direct increase in magnetic susceptibility and natural remanent magnetisation compared to the increase in free radicals, suggesting this replacement is caused by the presence of hydrocarbons (Costanzo-Álvarez *et al.*, 2019).

Biodegradation impacts the relative abundances of aliphatic compounds and polar components in hydrocarbons, in turn impacting magnetic anomalies (Emmerton *et al.*, 2012, 2013). Biodegradation destroys aliphatic compounds, giving greater relative abundances of polar components and asphaltenes, and preferentially removing SD grains, creating a relative increase of MD grain presence (Costanzo-Álvarez *et al.*, 2006; Emmerton *et al.*, 2013). Preferential removal of SD grains results in lower quality hydrocarbons giving lower magnetic susceptibility readings, and a greater anomaly in high quality, less biodegraded hydrocarbons (Costanzo-Álvarez *et al.*, 2006; Emmerton *et al.*, 2013). Hydrocarbon generation also aids the creation of magnetic minerals, as proven by Abubakar *et al.* (2015) when pyrolyzing source rocks from the Wessex Basin, UK in hydrocarbon-forming conditions. In tandem with this, Abubakar (2015) and Abubakar *et al.* (2020) also concluded that variations in magnetic mineralogy occur along oil migration pathways. This is through dominance of magnetite in the proximal hydrocarbon plume and pyrrhotite in the distal plume, with a mix of both in the shallow proximal plume environment.

Badejo (2019) and Badejo *et al.* (2021a,b,c) identify a magnetic coercivity increase along a ∼30 km lateral-migration pathway in Early Tertiary intervals in the Central North Sea, which suggests an increasing presence of iron sulphides that correlate to greigite being identified only within hydrocarbon-bearing wells. The increase in iron sulphide presence along the migration pathway, reflected in a proximal siderite-rich signal, mixed middle-distance signal, to a distal iron sulphide-rich signal is proposed to be caused by either: I) an organic mechanism of biodegradation by anaerobic sulphate-reducing bacteria leading to increased greigite precipitation in the shallower, distal regions of the migration pathway; or II) an inorganic mechanism of greigite grain precipitation during generation and expulsion of early mature oil followed by migration up the fill-spill chain along the migration pathway, resulting in increasingly greater greigite accumulations in distal regions. Scenario I is suggested as the more likely as biodegradation is cited as the cause of decreasing oil APIs up the distally-shallowing migration pathway.

No conclusive variation of saturation or remanent magnetisation is observed by Badejo (2019) and Badejo *et al.* (2021a,b,c) along the migration pathways of the petroleum system, however peaks in both, as well as mass-dependant susceptibility, were identified at both gas-oil and oil-water contacts. The peaks are attributed to SD magnetite or greigite presence caused by diagenetic alteration, or biodegradation causing precipitation of extra- or intra-cellular magnetite/greigite, at the interfaces.

Most recently, a study from Abdulkarim *et al.* (2022a) has showed siderite presence in a hydrocarbon system can be deduced as a proxy for vertical migration. This follows work by Badejo *et al.* (2021a) who also shows this evidence, and theorised it was caused by vertical hydrocarbon charging, not lateral migration. Furthermore, Abdulkarim *et al.* (2022b) and Abdulkarim *et al.* (2022c) present extensive iron sulphide and lepidocrocite presence in the Central North Sea, and offer these as possible proxies for oil-water contact depth caused by variations in degrees of biodegradation.

CHAPTER 3 | GEOLOGICAL REVIEW

3.1 | INTRODUCTION

This chapter covers the literature on the study area from a geological perspective, discussing the basics of petroleum systems before reviewing the Inner Moray Firth (IMF), its formation and the stratigraphy within it. Furthermore, a review of the hydrocarbon geochemistry of the basin from past investigations is discussed, due to the potential for multiple source rocks and hydrocarbon source regions, alongside the associated hydrocarbon mixing ratios present within the basin. Beyond this, the production history of the three fields (Beatrice, Jacky and Lybster) is analysed. The review will offer insights into where potential source regions should be and where to focus investigations within the model, as well as estimating hydrocarbon volumetrics within the fields.

3.2 | GEOLOGICAL PRINCIPLES

3.2.1 | HYDROCARBON FORMATION

Petroleum is a mixture of hydrocarbon molecules (both oil and hydrocarbon gas) and small quantities of metals and organic molecules containing sulphur, oxygen and nitrogen (Gluyas and Swarbrick, 2004). Petroleum is a hydrocarbon that originates from aquatic organic matter that gets buried and preserved by sediment (Bjorlykke, 2010). The organic matter is typically algal or planktonic, though a variety of different organic matter contributes to a range of different hydrocarbons (Bjorlykke, 2010; Kumar, 2012). Once organic matter has sunk through an anaerobic water column, it is buried by rapid sedimentation (Bjorlykke, 2010). Sand- and larger-sized grains more-readily allow oxygen diffusion between them, hindering preservation of the underlying organic matter, consequently burial by clay- and silt-size sediment is necessary for organic matter preservation (Bjorlykke, 2010).

After initial organic matter burial, kerogen can be formed through a sequence of reactions occurring over extensive time periods, during which the organic matter undergoes compaction, heating, further burial and diagenesis (Bjorlykke, 2010; Kumar, 2012). Initially, bacterial oxidation and fermentation converts lipids and lignins into simple molecules, methane and carbon dioxide, followed by these simple molecules undergoing polymerisation to become organic acids and then increased diagenesis of the acids after this results in the formation of kerogen (Bjorlykke, 2010). Once kerogen is formed, further heating and pressure converts it into oil or gas, depending on the conditions within the rock (the “oil window”) (Bjorlykke, 2010; Gluyas and Swarbrick, 2004).

3.2.2 | PETROLEUM SYSTEMS

Petroleum systems require a specific sequence of components to exist, and typically occur in depressional basins where deposition is stratigraphic and sediment is contained (Bjorlykke, 2010; Dembicki Jr, 2017; Gluyas and Swarbrick, 2004). The sequence begins with an underlying source rock, in which hydrocarbons are generated and matured, then expelled (Figure 3.1; Gluyas and Swarbrick (2004)). Migration of the hydrocarbons occurs along pressure gradients into porous and permeable reservoir rocks, at which point they are halted by the presence of an impermeable seal constricted into a hydrocarbon

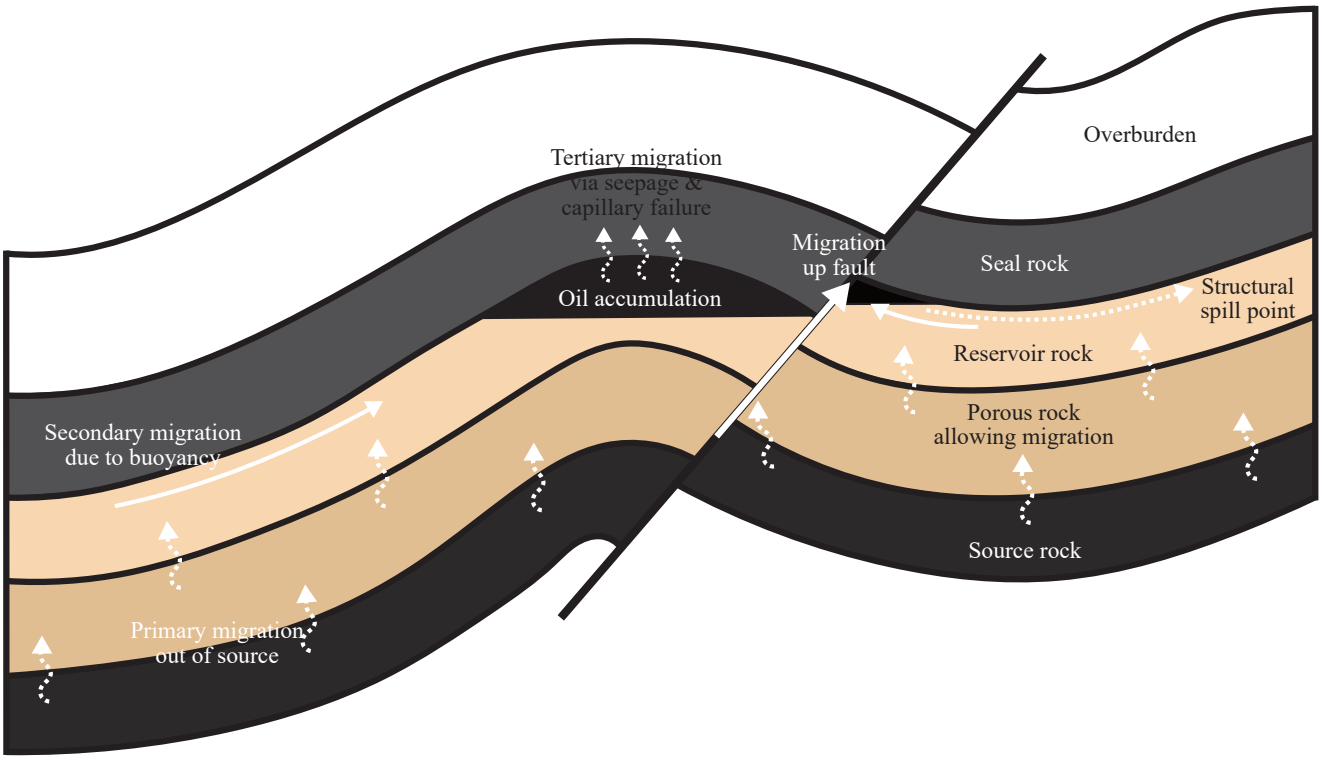


Figure 3.1: *Schematic diagram of a petroleum system and its major processes, showing the different stages of hydrocarbon expulsion out of source rock, migration into reservoir rock and accumulation in a trap below a sealing rock. From Perkins (2017).*

trap (Figure 3.1; Bjorlykke (2010); Dembicki Jr (2017); Gluyas and Swarbrick (2004)). This trap and seal combination prevents further flow of hydrocarbon fluids resulting in an accumulation within the reservoir rock, although seepage and spill may occur laterally, due to structural spill, or vertically, due to capillary failure (Figure 3.1; Bjorlykke (2010); Dembicki Jr (2017); Gluyas and Swarbrick (2004)).

3.2.3 | Reservoir Characterisation Techniques

To obtain sufficient and relevant data to understand and model a hydrocarbon field and its enclosing basin, characterisation must occur through a variety of methods (Gluyas and Swarbrick, 2004). This often begins with remote sensing, the cheapest investigation technique, through satellite imaging, gravity surveys, and magnetic surveys (Gluyas and Swarbrick, 2004). Remote sensing typically encompasses the entire basin, analysing structure, architecture and filling sediments, with satellite imaging gathering spectral data on varying wavelengths and direct images of basins (Gluyas and Swarbrick, 2004). Gravity surveys identify regional tectonic regimes via gravity anomalies analysed through density differences observed in gravimetric data, and magnetic surveys assess magnetic anomalies and variations caused by lithology, and typically are used to define basin shape and size (Gluyas and Swarbrick, 2004).

3.2.3.1 | Seismic Surveys

Following remote sensing, a series of other techniques are used, with increasing degrees of focus into specific basinal regions and hydrocarbon prospect(s). Firstly, seismic surveys are undertaken across an area, aimed at analysing sub-surface structure, potential petroleum system components and delineating

a prospect's borders (Gluyas and Swarbrick, 2004; Veeken, 2007; Bjorlykke, 2010). Seismic surveys are individually taken as two-dimensional "slices" of an area, to create a cross-sectional appearance, but are often taken in a grid to form a three-dimensional survey (Bjorlykke, 2010; Gluyas and Swarbrick, 2004). Four-dimensional surveys can also be taken repeatedly over a period of time to analyse sub-surface fluid movement and impacts any infrastructure may cause, however these require fixed receptors on the surface, increasing survey times and costs (Bjorlykke, 2010; Gluyas and Swarbrick, 2004). Seismic surveys characterise a reflection coefficient at a lithological boundary, derived from contrasting seismic velocities and lithological densities across the boundary, refer to widespread literature for further detail, including Bjorlykke (2010), Gluyas and Swarbrick (2004), Veeken (2007) and Yilmaz (2001).

3.2.3.2 | Development & appraisal wells

Once seismic data has been used to identify a potential prospect, wells are drilled within the prospect's borders to ascertain: I) if the prospect is oil-bearing (development well) and II) to delineate the field if it is (appraisal well; Gluyas and Swarbrick (2004)). These wells are used alongside cores and well logs to improve knowledge on the field (Gluyas and Swarbrick, 2004).

3.2.3.3 | Cores

Core samples are taken down-well so sections can be analysed *ex situ*, allowing for direct study of lithological intervals of interest, and for testing that is not otherwise possible, predominantly assessing permeability (Gluyas and Swarbrick, 2004). Cores are either whole sections of well, comprised of the entire well or selected intervals, or plugs – 3cm sections taken at uniform intervals along the well's sidewall, removed post-drilling (Gluyas and Swarbrick, 2004). Plugs are cheaper than whole cores, however they do not offer the same level of information due to their spacing and the selectivity of samples, thus do not represent the entirety of their source interval (Gluyas and Swarbrick, 2004).

3.2.4 | Well logs

Geophysical equipment is passed down a well to ascertain numerous petrophysical characteristics that form a geostatistical recreation of the field when correlated across multiple wells (Gluyas and Swarbrick, 2004). Well logs assess a wide-range of properties aimed at identifying lithologies, alongside fluid volumes and fluid contacts within a reservoir (Bjorlykke, 2010; Ellis and Singer, 2007; Gluyas and Swarbrick, 2004). Initially caliper, spontaneous potential and gamma ray logs are run to analyse well conditions, formation water, and basic lithology (Bjorlykke, 2010; Ellis and Singer, 2007; Gluyas and Swarbrick, 2004). These more accurately determine the depths of the field's critical components to prevent logging the entire well with significantly costlier techniques (Bjorlykke, 2010).

The desired intervals are then concurrently analysed through resistivity, density and neutron logs to assess and estimate lithology, porosity, permeability, fluid contacts and fluid saturations (Bjorlykke, 2010; Ellis and Singer, 2007; Gluyas and Swarbrick, 2004). Porosity can be further analysed through sonic and nuclear magnetic resonance logs, with sonic logs also used to assess reservoir overpressure (Ellis and Singer, 2007; Gluyas and Swarbrick, 2004). Acoustic, dipmeter and image logs are also

available to test well conditions, investigate sedimentary features and directly image the lithology, respectively (Bjorlykke, 2010; Ellis and Singer, 2007; Gluyas and Swarbrick, 2004).

3.2.4.1 | WELL-SEISMIC TIES

Well logs and seismic surveys can be tied by creating a log-derived synthetic seismic trace utilising wave velocities and lithological densities from sonic and density logs (Veeken, 2007). This trace is tied to the equivalent depth in a seismic survey, allowing for correlation and seismic calibration to each lithology, improving interpretations (Veeken, 2007).

3.3 | LOCATION OF STUDY AREA

The IMF is located in the outer margins of the western arm of the North Sea Rift, has an average water depth of 45 m, and contains three known, produced, and now abandoned hydrocarbon fields; Beatrice, Jacky and Lybster Fields (Figure 3.2; Linsley *et al.* (1980); Stevens (1991)). Beatrice Field is the significantly larger accumulation, containing estimated reserves of 480 MMBBLs, compared to Jacky's 5.2 MMBBLs and Lybster's 40 MMBBLs (Linsley *et al.*, 1980; Stevens, 1991). Due to its size, Beatrice Field contains numerous wells and is the focus around which this study builds, however the consistent structure and stratigraphy that contains all three fields offers the opportunity to understand basin-wide variations in the petroleum system derived from non-lithological impactors.

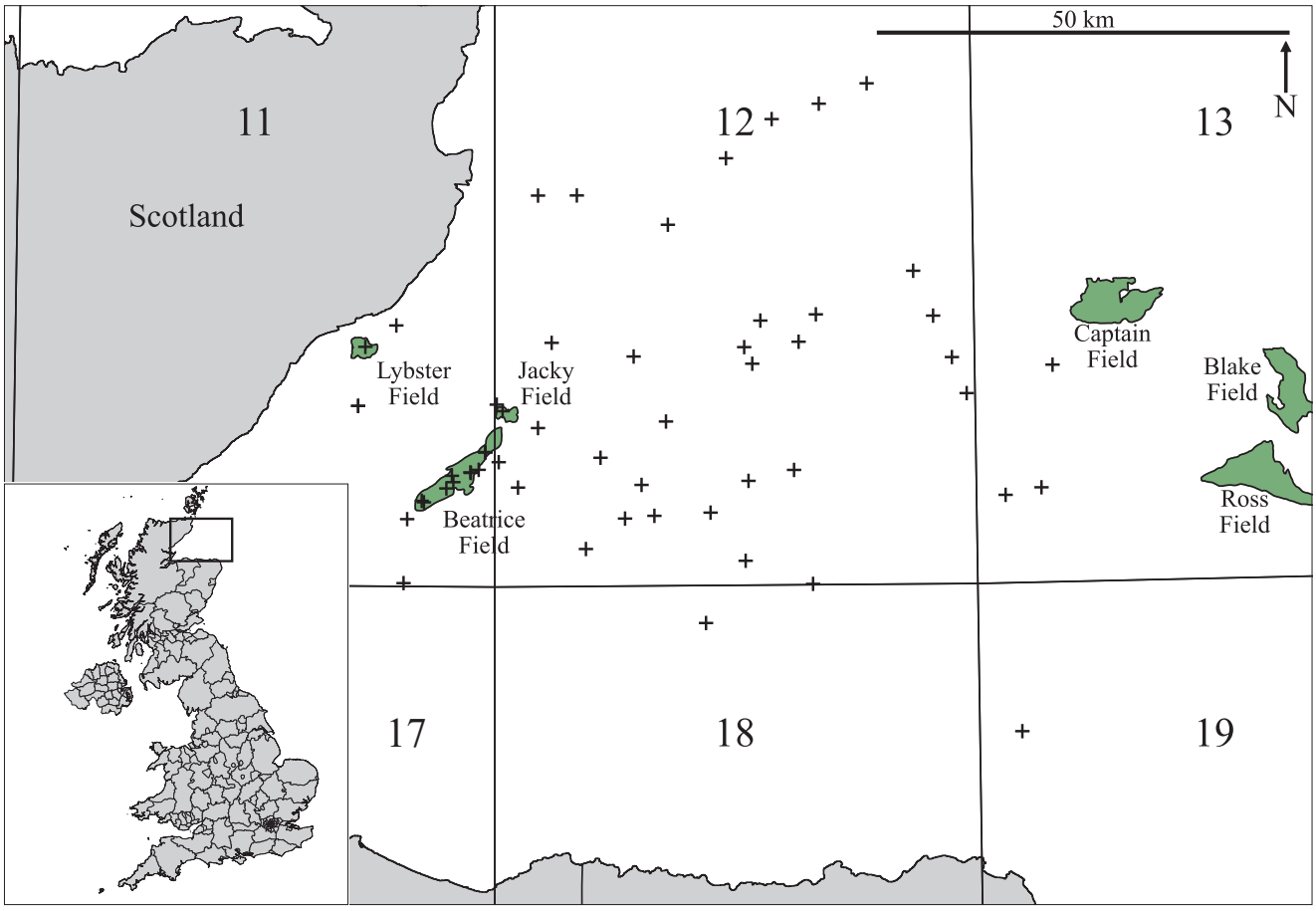


Figure 3.2: *Map of the study area in the Inner Moray Firth highlighting the positions of known hydrocarbon fields in the Inner and Outer Moray Firths and the wells used in this study.*

3.4 | INNER MORAY FIRTH BASIN FORMATION

The IMF forms the western arm of the trilete North Sea Rift, opening in the Permian via strike-slip motion on the sub-vertical Great Glen Fault (GGF) Zone, pinned at the intersection with the Wick Fault, continuing until stabilisation in the Cretaceous (Barr, 1985; Johnson *et al.*, 2005; McQuillin *et al.*, 1982; Roberts *et al.*, 1990; Underhill, 1991). The basin overlies the pre-existing Caledonian Orogeny-formed Orcadian Basin and is developed on a steep planar and listric ramp fault system linked to complex arrays associated with the GGF and flat detachment faults at 20-25 km depth (Andrews *et al.*, 1990; Barr, 1985; Bird *et al.*, 1987). The IMF is bound by the Helmsdale and Wick Faults to the north, the GGF to the north-west and the Banff Fault to the south (Figure 3.3; Roberts *et al.* (1990); Underhill (1991)).

The basin is isostatically uncompensated and, in association, has not experienced crustal thinning, resulting in a crustal thickness of 26-27 km, evidenced by Bouguer gravity anomaly analysis (Figure 3.4). This gravity data shows strong negative responses within the IMF, indicative of thicker crust, compared to more positive values eastwards away from the basin, towards the Central North Sea (Andrews *et al.*, 1990). The gravity data shows clear alignment between the gravity response and the positions of the larger scale faults within the basin, such as the Great Glen, Wick and Lossiemouth Faults, indicating critical involvement in the basin structure (Figure 3.4). Deep detachment faults impeded crustal thinning, through transferring stress, and therefore lower crustal and upper mantle extension, out of the

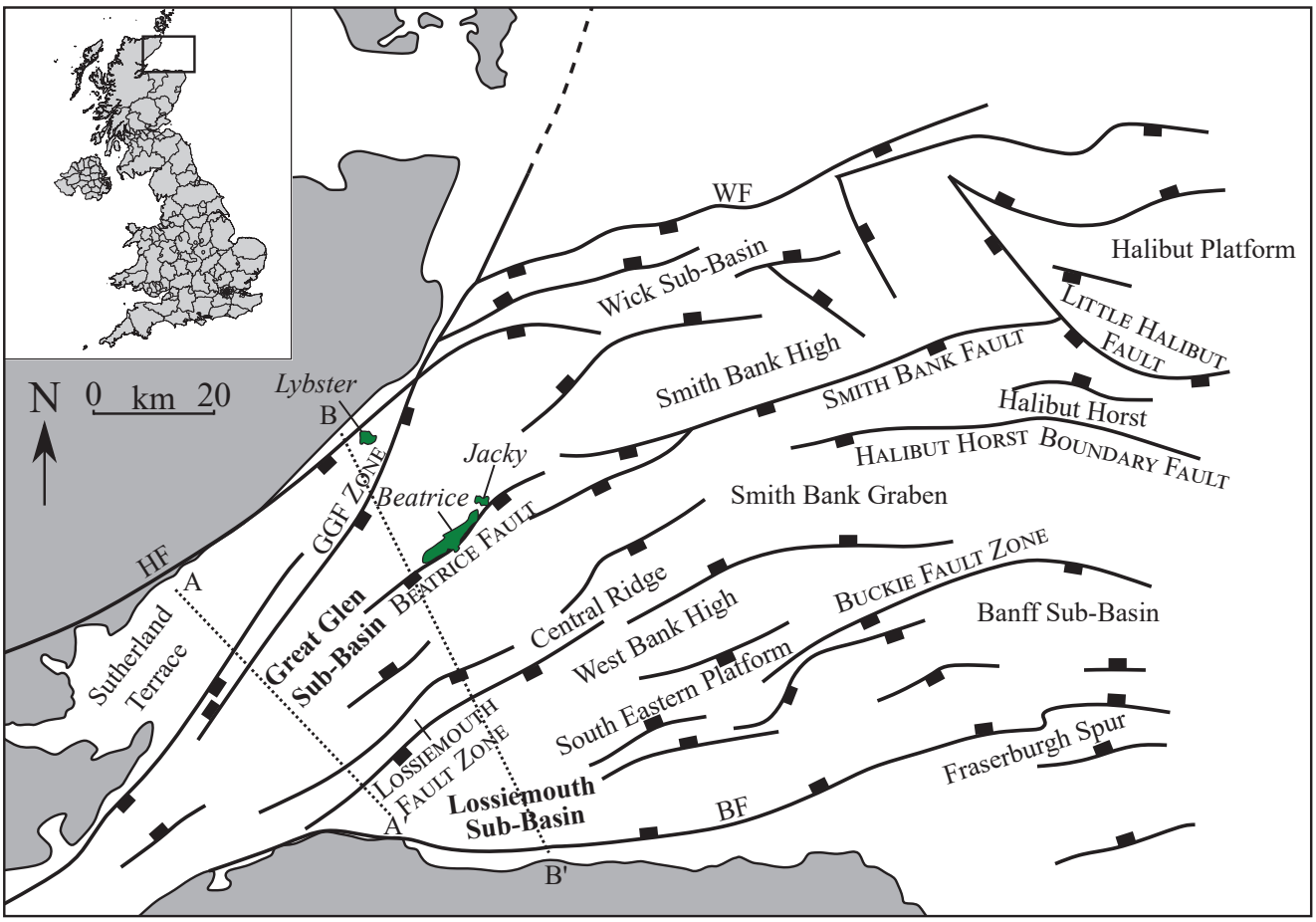


Figure 3.3: *Structural map of the IMF showing the hydrocarbon fields. See Figure 3.6 for cross sections. BF = Banff Fault; GGF = Great Glen Fault; HF = Helmsdale Fault; IMF = Inner Moray Firth Basin; OMF = Outer Moray Firth Basin. Modified from Linsley* et al. *(1980) and Roberts* et al. *(1990).*

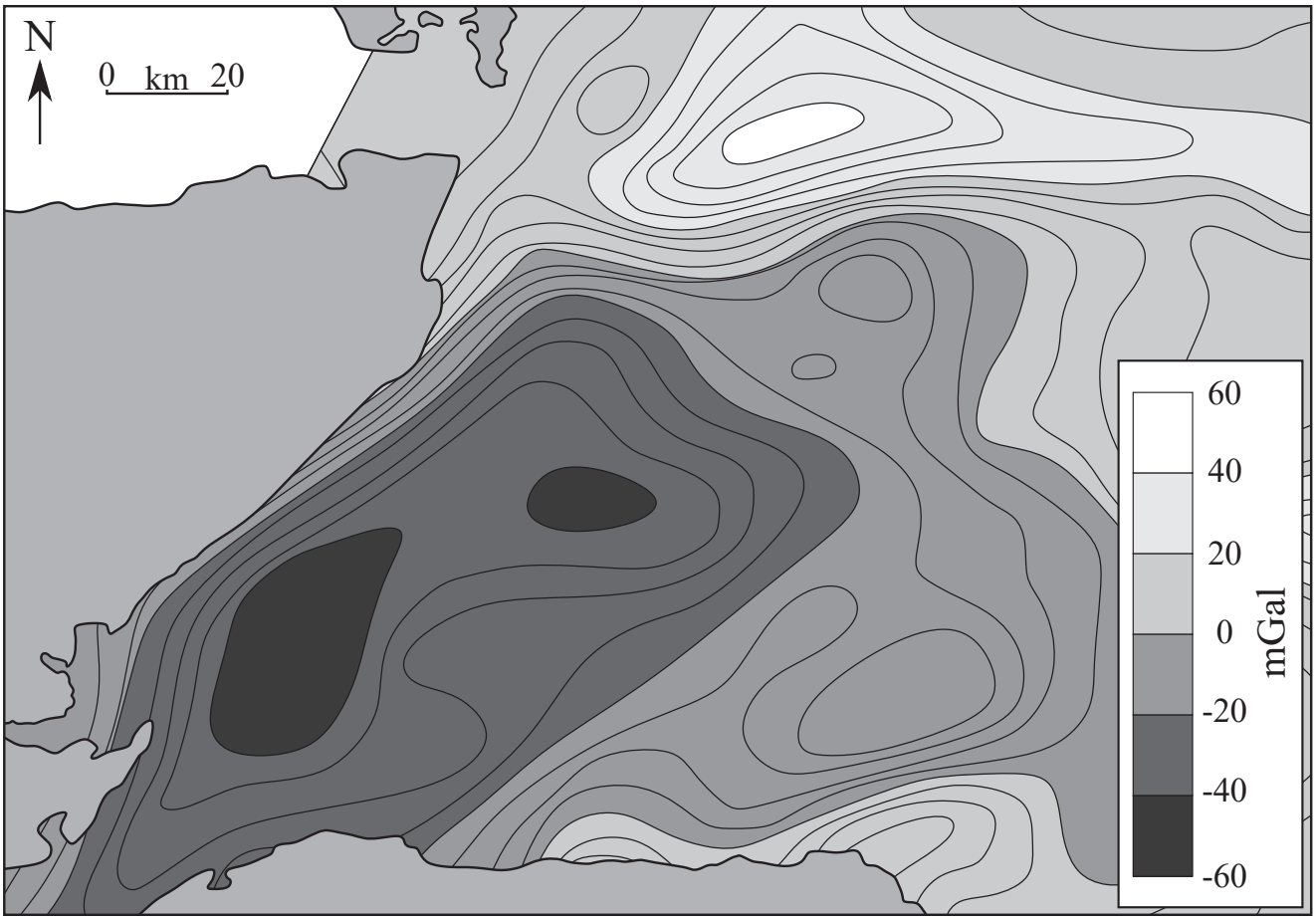


Figure 3.4: *Bouguer gravity anomaly map across the IMF, showing clear negative gravity responses across the Inner Moray Firth in comparison to more positive responses towards the Central North Sea, where crust is known to have thinned. Clear alignments can be seen between fault locations in Figure 3.3 and the contours of the gravity map. Modified from Andrews* et al. *(1990).*

basin (Andrews *et al.*, 1990; Barr, 1985; Roberts *et al.*, 1990). Consequently, despite being structurally related to the other arms of the North Sea Rift, the IMF developed in an entirely different four-stage sequence (Andrews *et al.*, 1990; Barr, 1985; McQuillin *et al.*, 1982; Roberts *et al.*, 1990). Permo-Triassic inversion and half-graben block rotation was followed by Jurassic-Early Cretaceous tectonic subsidence caused by extensional separation of boundary faults, then Early Cretaceous-Cenozoic epeirogenic subsidence and Cenozoic uplift and erosion caused by crustal flexure (Greenhalgh, 2016; McQuillin *et al.*, 1982). The IMF contains two overarching sub-basins, the Great Glen and Lossiemouth Sub-Basins, separated by the ENE-WSW-trending Central Ridge horst, and smaller-scaled grabens and half-grabens separated by structurally higher horsts or footwall highs (Figures 3.3 & 3.6; Andrews *et al.* (1990); Argent *et al.* (2002); Dimitropoulos and Donato (1981); McQuillin *et al.* (1982); Roberts *et al.* (1990)). The basin is dominated by tilted fault blocks and oblique-slip faults, and the fault system experienced early generation of its main faults, with strain progressively localising onto these larger faults away from smaller faults. This has resulted in the basin being constrained, filled and formed by large-scale faulting, suggesting a fully evolved, interconnected fault system (Dimitropoulos and Donato, 1981; Roberts *et al.*, 1990; Walsh *et al.*, 2002).

The IMF is a predominantly strike-slip system, containing flower geometries, *én echelon* folding and faulting, pull apart systems, inversion structures, lateral stratigraphy offsets and ordered combinations of

extensional and compressional faults that include major and listric faults, alongside sedimentary wedges within significantly extended rotational structures (Argent *et al.*, 2002; Bird *et al.*, 1987; Roberts *et al.*, 1990). These all developed as an array of linked, shaped faults with several levels of detachment related to the GGF, with faults trending perpendicular to the GGF (ESE-WNW) evolving as dip-slip (Argent *et al.*, 2002; Bird *et al.*, 1987; Roberts *et al.*, 1990).

Two episodes of regional thermal subsidence occurred in the Early-Middle Jurassic, prior to the deflation of the Central North Sea Thermal Dome (NSD; Figure 3.5), and were succeeded by a second major phase of rifting that activated deep-rooted extensional tilted fault blocks, as well as thermal subsidence and pulses of transpression during the Cretaceous (Johnson *et al.*, 2005; Underhill, 1991; Underhill and Partington, 1993). Cenozoic inversion was caused by the basin attempting isostatic equilibrium due to the lack of crustal thinning, and resulted in the removal of $\sim$1 km of post-Early Cretaceous sediments, prior to covering by $\leq$100 m of Quaternary sediments (Andrews *et al.*, 1990; Argent *et al.*, 2002; Barr, 1985; Hillis *et al.*, 1994; Roberts *et al.*, 1990).

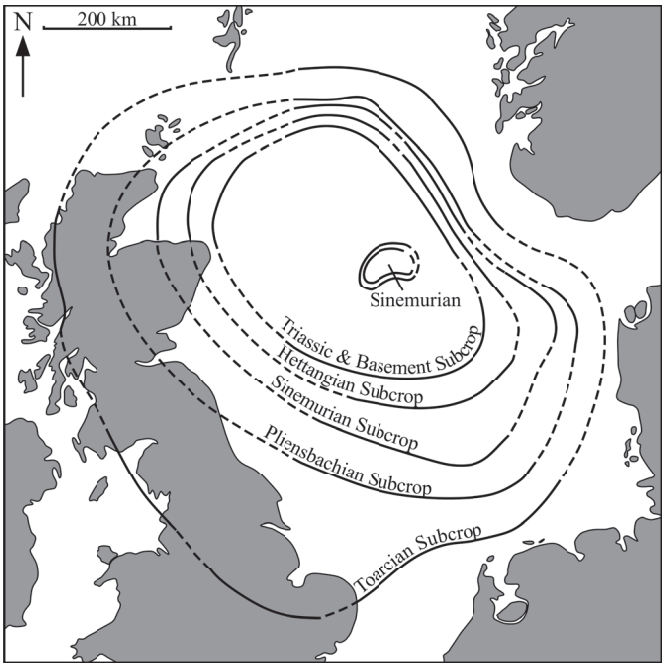


Figure 3.5: *Extents of the NSD shown through subcrops attributed to the Mid-Cimmerian Unconformity. Solid lines indicate known subcrop boundaries, dashed are inferred. From Underhill and Partington (1993).*

The NSD caused transgressive flooding in the IMF during the Mid-Cimmerian Unconformity, initiated the North Sea rift and affected heat flows through uplift and mantle pluming within the central North Sea (Underhill and Partington, 1993). The NSD affected structural evolution and pre-existing hydrocarbon accumulations, typically causing those nearer its centre to crack to gas or become overmature. This is unlike those in the IMF, which sits in the outer reaches of the NSD (Figure 3.5), thus likely did not experience the impacts to the same extent, however did experience a local unconformity and hiatus (Underhill and Partington, 1993).

Faulting in the IMF predominantly occurred syn-sedimentation, with sedimentation rates being greater than fault growth and sedimentary wedges and condensed sequences showing against fault hanging walls and footwalls, respectively (Roberts *et al.*, 1990; Thomson and Hillis, 1995; Walsh *et al.*, 2002). During the Triassic, sediment movement into the Beatrice Field region shows thickening trends from the SW and SE, whilst in the Jurassic sediment thickens across all major faults associated with the basin (Roberts *et al.*, 1990).

3.5 | Inner Moray Firth Basin stratigraphy

Sediment in the IMF is sequenced from Devonian to Cretaceous, lacking Carboniferous intervals, deposited syn- or post-upper crustal stretching (Andrews *et al.*, 1990; Roberts *et al.*, 1990). Uncon-

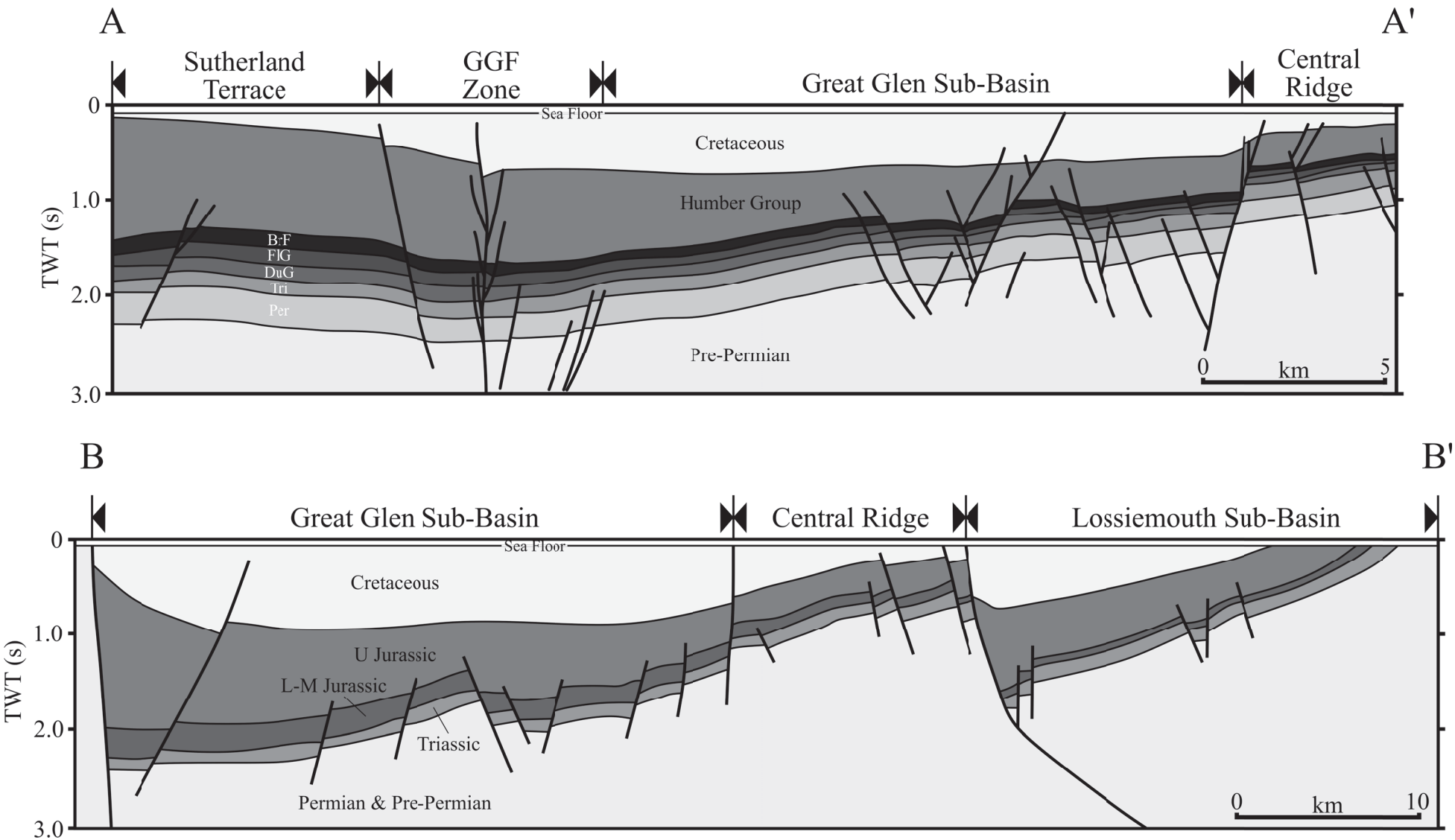


Figure 3.6: *Cross-sections across the south-east Inner Moray Firth, see Figure 3.3 for locations, showing major sediment packages and faults. Per = Permian; Tri = Triassic; DuG = Dunrobin Bay Group; FlG = Fladen Group; BrF = Brora Formation. The faults vary in age from Devonian to Cretaceous, with activity on the large, Devonian-age faults (e.g. the Great Glen Fault) through the basin's entire history. From Andrews* et al. *(1990) and Underhill (1991).*

formably overlying basement metasediments and granites within the underlying Orcadian Basin are basal Devonian Lower, Middle and Upper Old Red Sandstones (ORS; Figure 3.7; Andrews *et al.* (1990); Brown *et al.* (1988)). The Lower ORS is a locally-variable and isolated lacustrine-environment deposited sequence of siltstones and mudstones, with the Middle ORS being a similar lacustrine environment but with a much greater distribution across the northern North Sea, whilst the Upper ORS is an occasionally oil stained sandstone (Brown *et al.*, 1988). Fault activity and extensive erosion in the Early Permian caused the complete loss of Carboniferous sediments (Andrews *et al.*, 1990; Brown *et al.*, 1988; Johnson *et al.*, 2005; Newman and Dean, 2005; Roberts *et al.*, 1990; Whitbread and Kearsey, 2016).

The Permian consists of the Early Permian Rotliegend Group and Late Permian Zechstein Group (Figure 3.7; Andrews *et al.* (1990); Brown *et al.* (1988); Roberts *et al.* (1990)). The Rotliegend contains approximately 500 m of red beds, a sequence of three facies – very fine to fine grained, well sorted, red-brown sandstones, with frequent 2 m-thick dark red-brown, non-calcareous, occasionally anhydrite-bearing claystone intervals; overlain by a tripartite division of basal fine-grained sandstone, a siltstone-claystone unit and an interbedded sandstone-siltstone-claystone unit; and topped by a grey to red-brown dolomitic shale with thin, anhydrite nodule-bearing, dolomitic and micaceous sandstone stringers (Andrews *et al.*, 1990; Brown *et al.*, 1988). The boundary between the Early and Late Permian saw rapid transgression and deposition of the Kupferschiefer Formation, a thin dark greyish-brown to black, laminated, sapropelic, pyritic, dolomitic mudstone, with high concentrations of copper, lead and zinc sulphides (Brown *et al.*, 1988; Johnson *et al.*, 1994; Roberts *et al.*, 1990). The Moray Firth Zechstein was predominantly constrained to 50-150 m thick deposits in a carbonate-sulphate platform and a south-eastern deep hypersaline basin, with the development of clastic, carbonate, anhydrite and halite lithofacies (Brown *et al.*, 1988).

The Triassic unconformably overlies the Zechstein and has constant internal bed thicknesses around faults (Brown *et al.*, 1988). The Early Triassic consists of the Lossiehead Formation (Heron Group) – a lower grey, brown to orange-red, fine-coarse grained sandy unit, and an upper interbedded fine-grained sandstone, siltstone and reddish-brown, anhydrite-bearing claystone unit (Brown *et al.*, 1988). This is capped by 11-12 m of locally microcrystalline silica- and sand grain-bearing Cherty Rock, that is dominantly tan-coloured micritic limestone with chert inclusions and relic concretionary layering (Brown *et al.*, 1988).

Jurassic sediments contain all Beatrice Field reservoir units (detailed in Section 3.6.1), as well as the Kimmeridge Clay Formation. The Early Jurassic consists of minor sands, the Mid Jurassic of upward-coarsening paralic and interbedded sandstone sequences, and the Late Jurassic of shallow marine sands and some spiculitic sands (Figure 3.7; Andrews *et al.* (1990); Brown *et al.* (1988); Linsley *et al.* (1980); Roberts *et al.* (1990); Stevens (1991)). The Kimmeridge Clay sequences of the IMF are dominated by shales yet experience extensive sand input, predominantly from turbidites and fault-derived gravity flow sands, which formed injected sand cones within the Kimmeridge Clay, caused by forcibly emplaced 70-100 °C fluids, hotter than typical strata temperatures of 50-60 °C, along the Helmsdale Fault and GGF in response to Cenozoic-age dextral strike-slip motion (Andrews *et al.*, 1990; Davies *et al.*, 1996; Harker and Rieuf, 1996; Jonk *et al.*, 2003; Whitbread and Kearsey, 2016).

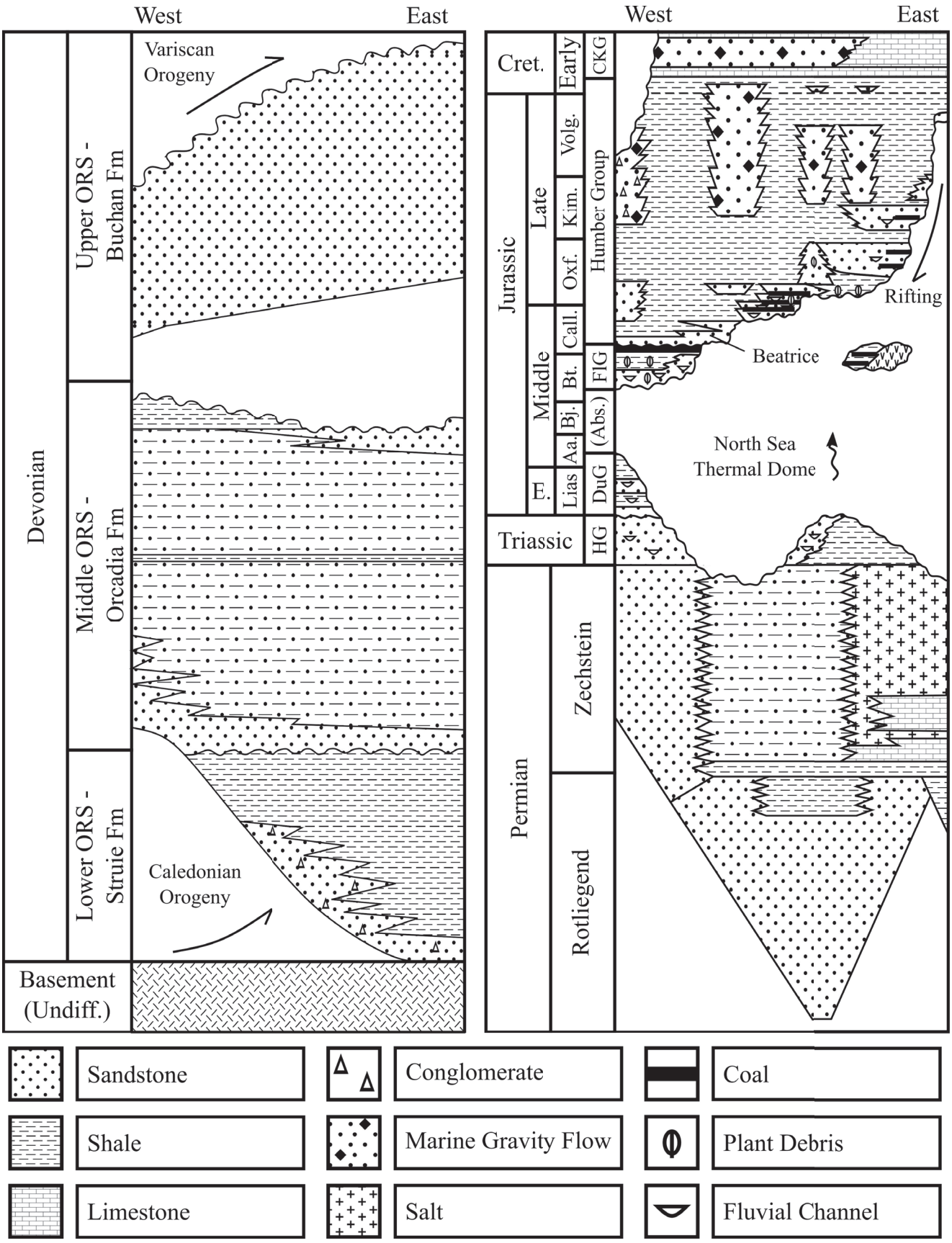


Figure 3.7: *Stratigraphic column from west to east (Inner to Outer Moray Firth) highlighting the main sedimentary and stratigraphic bodies within the area. HG = Heron Group; DuG = Dunrobin Bay Group; FlG = Fladen Group. Modified from Glennie* et al. *(2003), Harker and Rieuf (1996) and Whitbread and Kearsey (2016).*

The Early Cretaceous is represented by the Cromer Knoll Group, and is subdivided into the Valhall, Sola and Rodby Formations. Observing the subdivision is difficult in the IMF, with deposition controlled by relative sea level change and tectonic activity (Andrews *et al.*, 1990; Brown *et al.*, 1988). The Valhall Formation is mainly calcareous mudstones and marls, the Sola Formation a non-calcareous, dark grey, organic-matter-rich claystone with thin limestone and siltstone beds, and the Rodby Formation is dominated by grey to red-brown sandy marls and calcareous shales (Brown *et al.*, 1988). The Cromer Knoll Group has a high sandstone content in the IMF, with strong tectonic controls on deposition clearly marked along the Halibut and Smith Bank Faults. Due to Cenozoic uplift and associated erosion, the Cromer Knoll Group is the surficial formation in the Inner Moray Firth, other than overlying Quaternary sediments (Andrews *et al.*, 1990; Brown *et al.*, 1988).

3.6 | BEATRICE FIELD

Beatrice Field's existence was confirmed by well 11/30-1 in July 1976, and exploration wells constrained the field at approximately 24 km^2, with an estimated 146 MMBBL recoverable oil from approximately 480 MMBBL in-place (Stevens, 1991). The Jurassic-age reservoir intervals (Figure 3.8) are filled with 38 °API, highly viscous (2.23 mPa·s, or 2.23 cP), highly waxy (17 %), low sulphur, high pour point (18.3 °C), paraffinic crude oil that has a low bubble point pressure (4.38 MPa), low formation volume factor (1.09) and a low gas-oil ratio (126 SCF/STBBL) (Linsley *et al.*, 1980; Stevens, 1991). The field has a low energy, with initial pressures of 19.98 MPa at 1981 m and poor aquifer influx, requiring water injection from the start of production (Stevens, 1991).

The field sits on a structural high in a tilted, NE-SW-trending fault block, trapped by a three-way dip closed and fault-bounded anticlinal trap, with some slight dip reversal being caused by drape over the underlying fault block and fault drag (Barr, 1985; Linsley *et al.*, 1980; Stevens, 1991). The reservoir sequence contains a series of layered, potentially parasequenced, fully correlatable Early-Mid Jurassic sandstones (A, B, H, I and J Sands), interspersed with two shale horizons, and an internally-uncorrelatable, interbedded sandstone and shale unit that is a potential source rock (Stevens, 1991). The reservoir has an average gross thickness of 335 m and a net sand thickness of 137 m (a net-to-gross of 41 %), the crest sits at ∼1800 m TVSS, whilst the oil-water contact (OWC) occurs at 2068 m, with an average water saturation of 21.5 % (Stevens, 1991). The reservoir sands display porosity and permeability ranges of 13-22 % and 1-4000 mD, respectively, with oil recovery varying between 12-45 % (Stevens, 1991). Cementation has greatly decreased pore space below the OWC, but the oil column above appears to have limited cementation, preserving porosity and permeability (Linsley *et al.*, 1980).

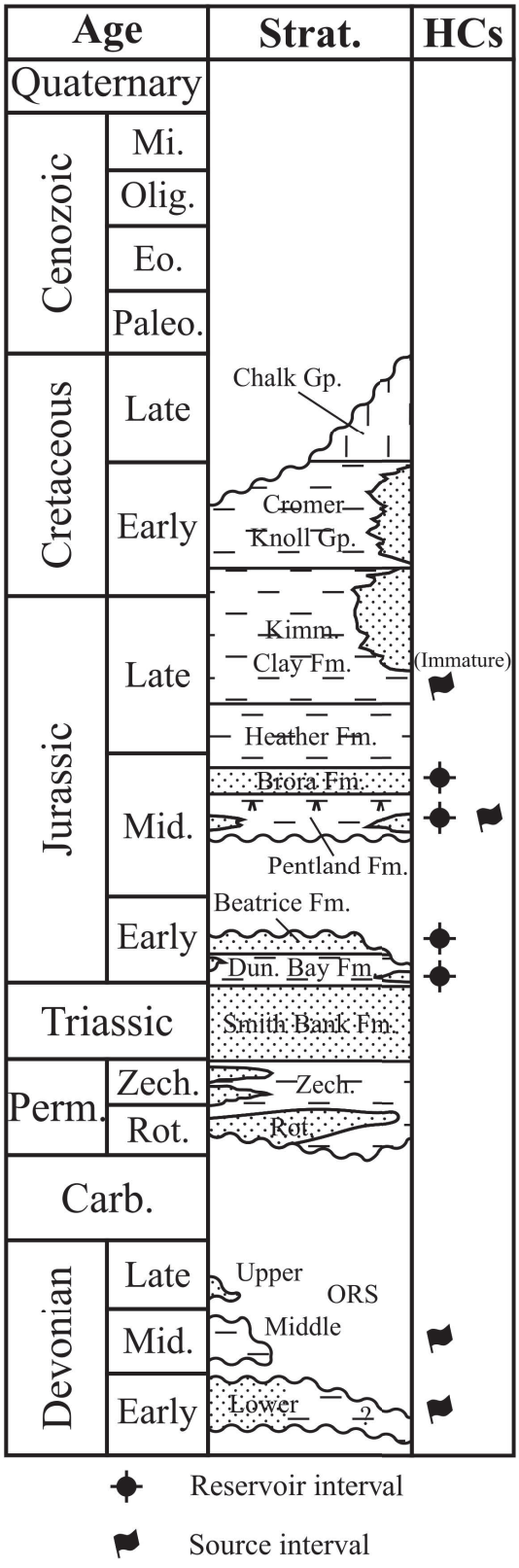


Figure 3.8: *Tectonostratigraphic column of the IMF identifying key petroleum system intervals. The existence of four potential source rocks contributing to the Early and Middle Jurassic reservoir sequences offers the central investigation into the IMF. Modified from Peters* et al. *(1989).*

3.6.1 | RESERVOIR STRATIGRAPHY

The Beatrice Field reservoir section is bound below by the Triassic-age Stotifeld Cherty Rock and above by the Late Jurassic-age Heather Formation (Figure 3.9). The stratigraphy outside of the Early-Middle Jurassic has been outlined previously (Section 3.7). The following are the reservoir intervals seen within the Beatrice Field, as well as the Early-Middle Jurassic across the Inner Moray Firth.

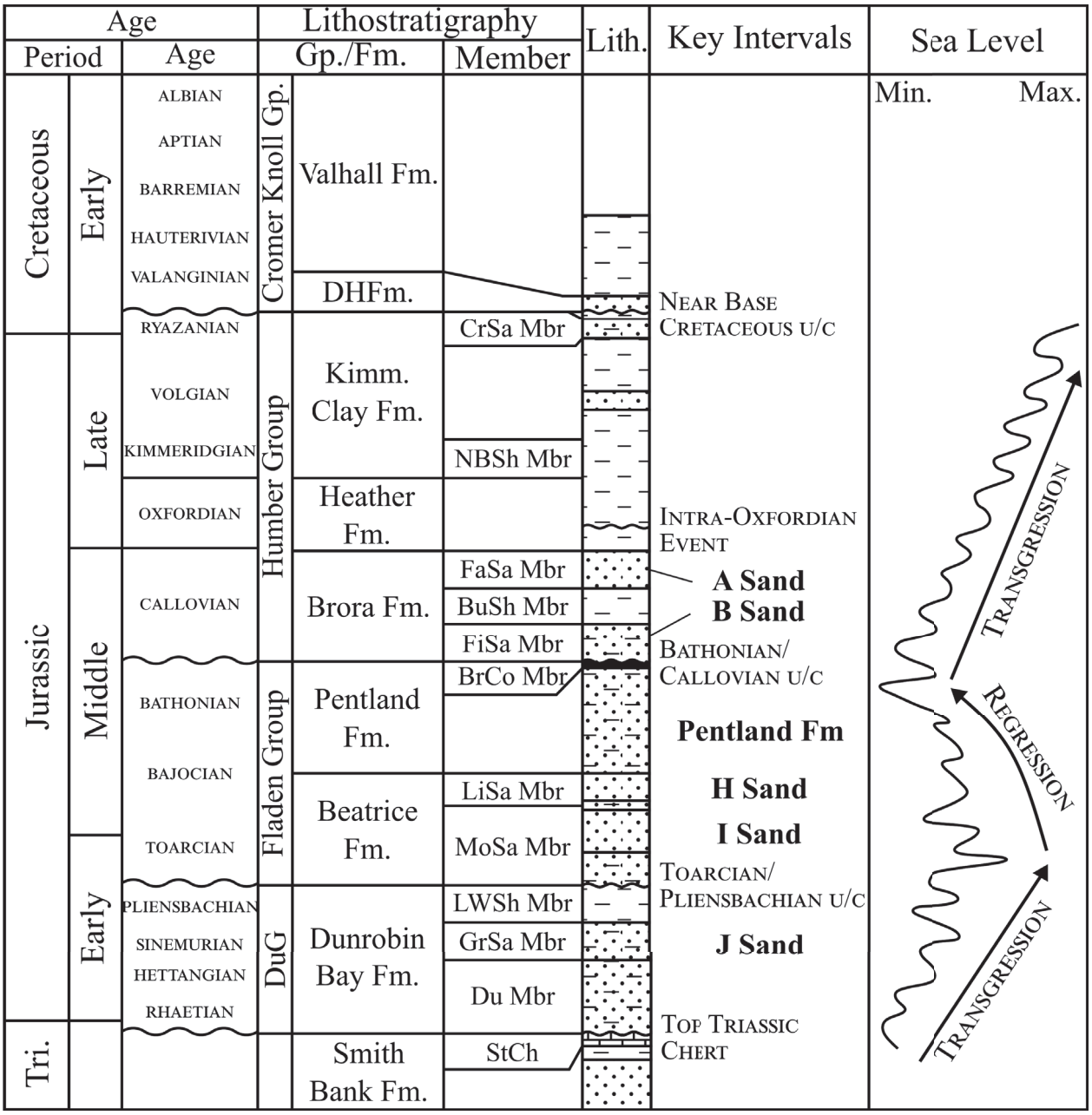


Figure 3.9: *Stratigraphic column of lithology seen within the Beatrice Field and sea level curve identifying dominant events related to unconformities seen within the Field. The Callovian-Ryazanian transgression is a flooding event caused by the formation of the North Sea Dome. DuG = Dunrobin Bay Group; DHFm = Devils Hole Formation; CrSa = Cromarty Sand Member; NBSh = Nigg Bay Shale Member; FaSh = Farclas Sand Member; BuSh = Burghie Shale Member; FiSa = Fiddich Sand Member; BrCo = Brora Coal; LiSa = Livet Sand Member; MoSa = Morangie Sand Member; LWSh = Lady's Walk Shale; GrSa = Grant Sand Member; Du = Dullan Member; StCh = Stotfield Cherty Rock. Modified from Stevens (1991) and Underhill and Partington (1993).*

3.6.1.1 | DUNROBIN BAY FORMATION (DUNROBIN GROUP) – J SAND

The basal J Sand of the Dunrobin Bay Formation overlies the Triassic Stotfield Cherty Rock, averages 15 % porosity and 400 mD permeability (Figure 3.10), and was deposited within an alluvial flood basin and levee-crevasse (Linsley *et al.*, 1980; Stevens, 1991). The J Sand consists of fine grained, moderately sorted, occasionally calcareous silty sandstones and sandy siltstones interbedded with, and grading into, mottled and veined grey-green shales (Dullan and Grant Sand Members; Figure 3.12) (Linsley *et al.*, 1980; Stevens, 1991). Beds are rarely thicker than 1.5 m, with sandstones being moderately-well cemented by authigenic silica and containing rare shell and ostracod fragments, alongside planar and ripple cross-beds, whilst the shales show rootlet horizons, rare plant material and desiccation cracks (Linsley *et al.*, 1980).

Up-sequence, a transition from brackish to more marine conditions is reflected in a change from shales to organic-rich black shales (Linsley *et al.*, 1980). Thicker and coarser-grained sandstones are distributary channel-deposited, with minor zones becoming rich in carbonate/dolomite, transitioning to sandy limestone (Linsley *et al.*, 1980). Overlying these is the Lady's Walk Shale – a series of transgressive, calcareous muds containing thin-shelled pectens, crinoid fragments and ammonoids and mottled, basally-burrowed siltstones (Linsley *et al.*, 1980; Stevens, 1991).



Figure 3.10: *Photograph of a section of core from the J Sand, Well 11/30-2, Beatrice Field from 7152.83 to 7153.75 ft MD (2180.12-2180.46 m MD). Core shows basal silt grading into mixed silty sand to sands, indicative of what is typically seen in the basin in the Dunrobin Bay Formation.*

3.6.1.2 | BEATRICE FORMATION (FLADEN GROUP) – H & I SANDS

The H and I Sands of the Beatrice Formation unconformably overlay the Early Jurassic sediments and average 17 % porosity, but due to variations in sand types and diagenetic histories, permeability varies between 1-20 mD and 500-2000 mD (Linsley *et al.*, 1980; Stevens, 1991). The formation represents the beginning of a high energy, regressive deltaic sand sequence containing massive, fine-medium grained sandstones (Figure 3.11) with 10-12 % feldspar and 15-18 % clays with extensive variation in sorting and degrees of cementation (Linsley *et al.*, 1980). The diagenetic cement cycle shows initial

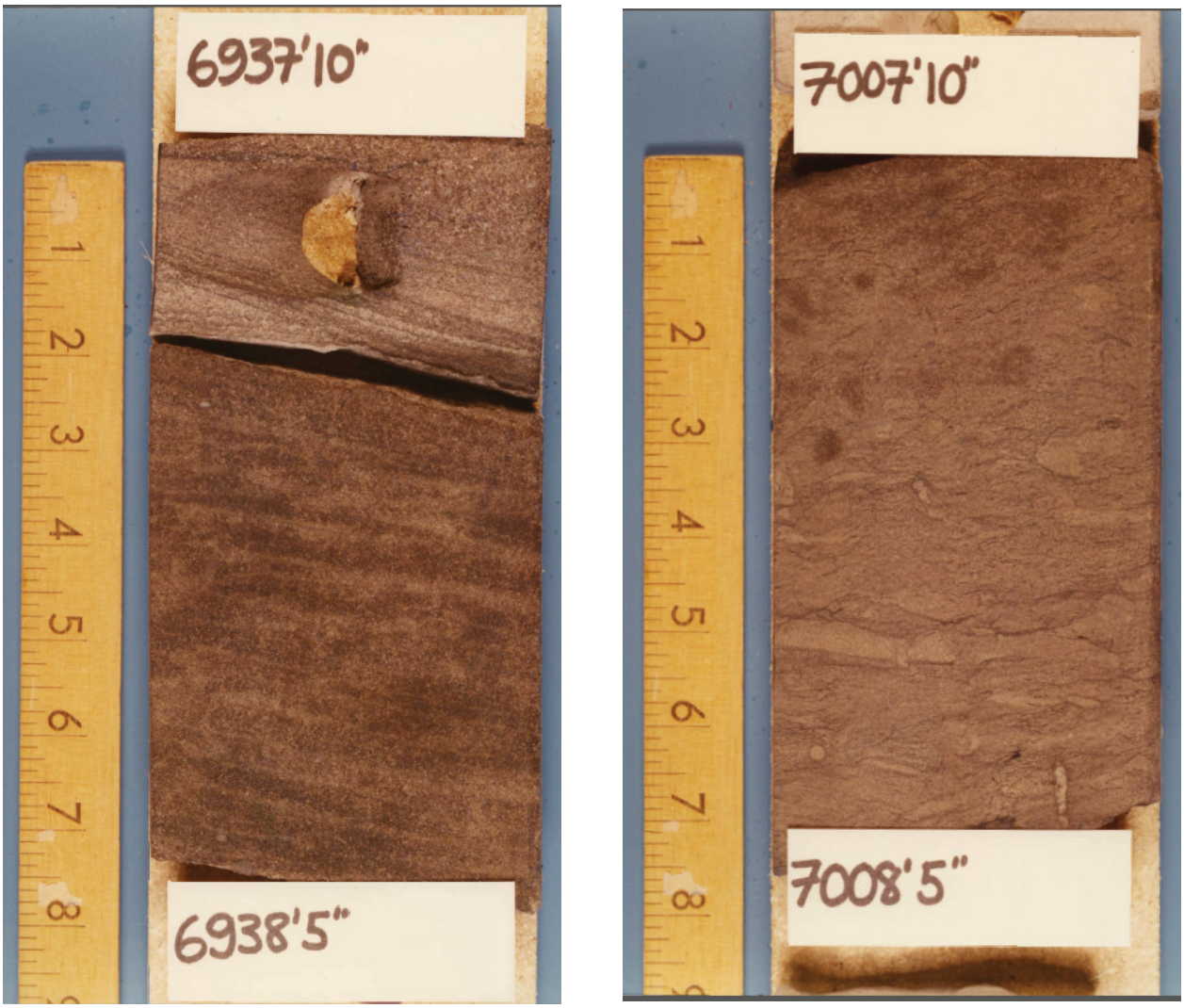


Figure 3.11: *Photographs of sections of core from the H (left) & I (right) Sands, Well 11/30-2, Beatrice Field, from 6937.83-6938.42 ft MD (2114.65-2114.83 m MD) and 7007.83-7008.42 ft MD (2135.99-2136.17 m MD), respectively. The I Sand shows higher clay and silt content compared to the clean, but oil-stained H Sand core, except for the silty section in the shallowest region of the core.*

syntaxial authigenic quartz growth, developing into authigenic kaolinite then amorphous silica (Linsley *et al.*, 1980). The depositional sequence contains two broadly coarsening-up cycles overlain by lagoonal-delta-top clays that contain marine acritarchs-dinocysts and thin coal and rootlet horizons, then major distributory channel sands (Figure 3.12; Linsley *et al.* (1980)).

3.6.1.3 | Pentland Formation (Fladen Group)

The Pentland Formation is a conformably overlying cyclical sequence of alluvial flood-plain deposits that average 16.5 % porosity, however, sand thickness variations cause permeability variations between effectively zero and up to 320 mD (Figure 3.13; Linsley *et al.* (1980)). Within this unit there are five major sandstone bodies, however a single interbed sequence typically contains more than one depositional cycle (Linsley *et al.*, 1980). A single depositional cycle consists of a sharply-based, well sorted, cross-bedded, ripple-laminated authigenic silica-cemented alluvial point-bar sandstone, typically about 6m thick, fining-up into a mottle and veined siltstone, then a flood basin-levee-crevasse, carbonaceous, waxy claystone (Figure 3.14; Linsley *et al.* (1980); Richards *et al.* (1993); Stevens (1991)). This cy-

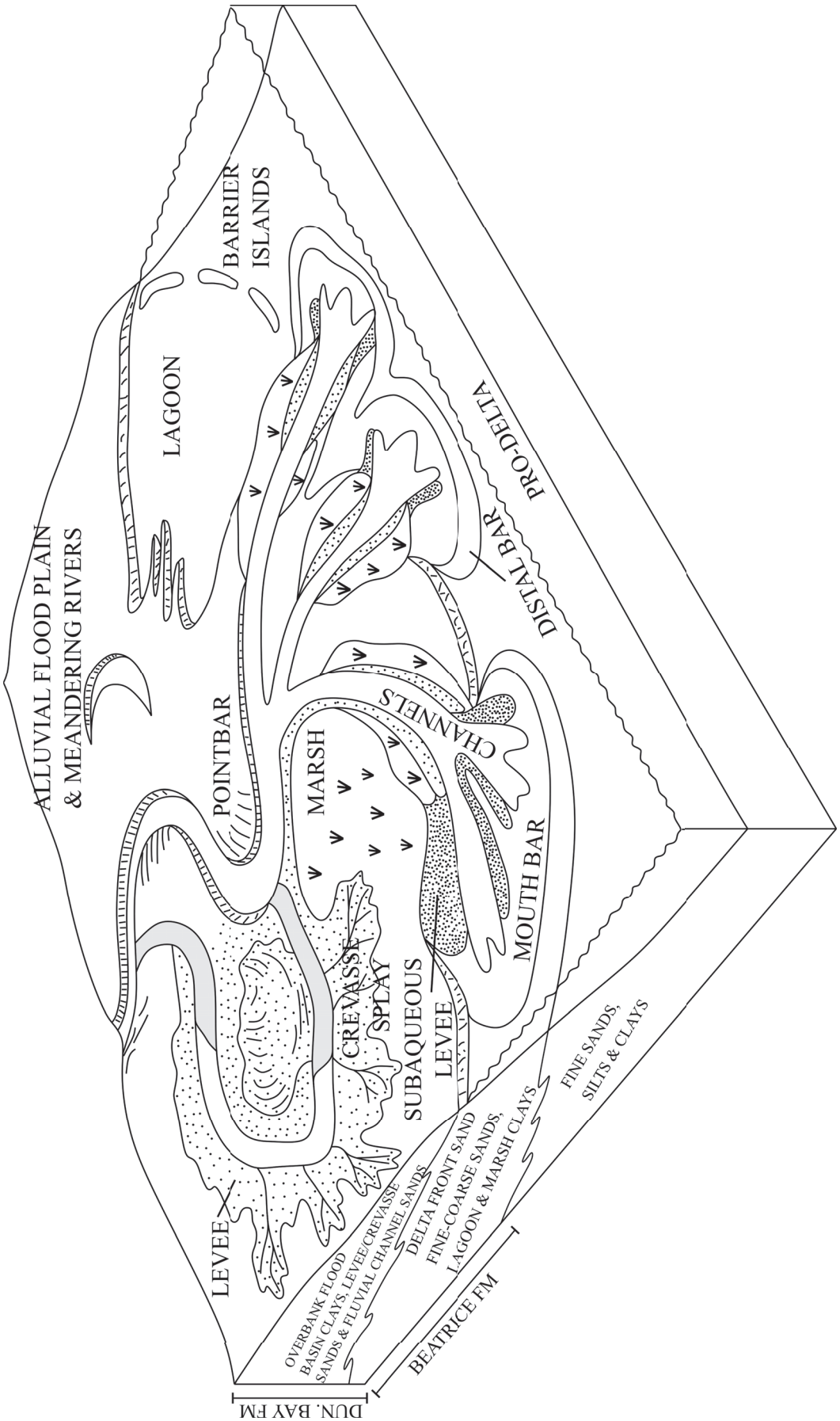


Figure 3.12: *Facies model of the Early Jurassic, lower reservoir sequences of the Dunrobin Bay and Beatrice Formations, identifying the alluvial flood plain, crevasse splay, lagoonal, deltaic environments of deposition. The alluvial deposits came from the NW of the IMF, over the Great Glen Fault, into the basin. Modified from Andrews* et al. *(1990); Paleoservices (1978).*

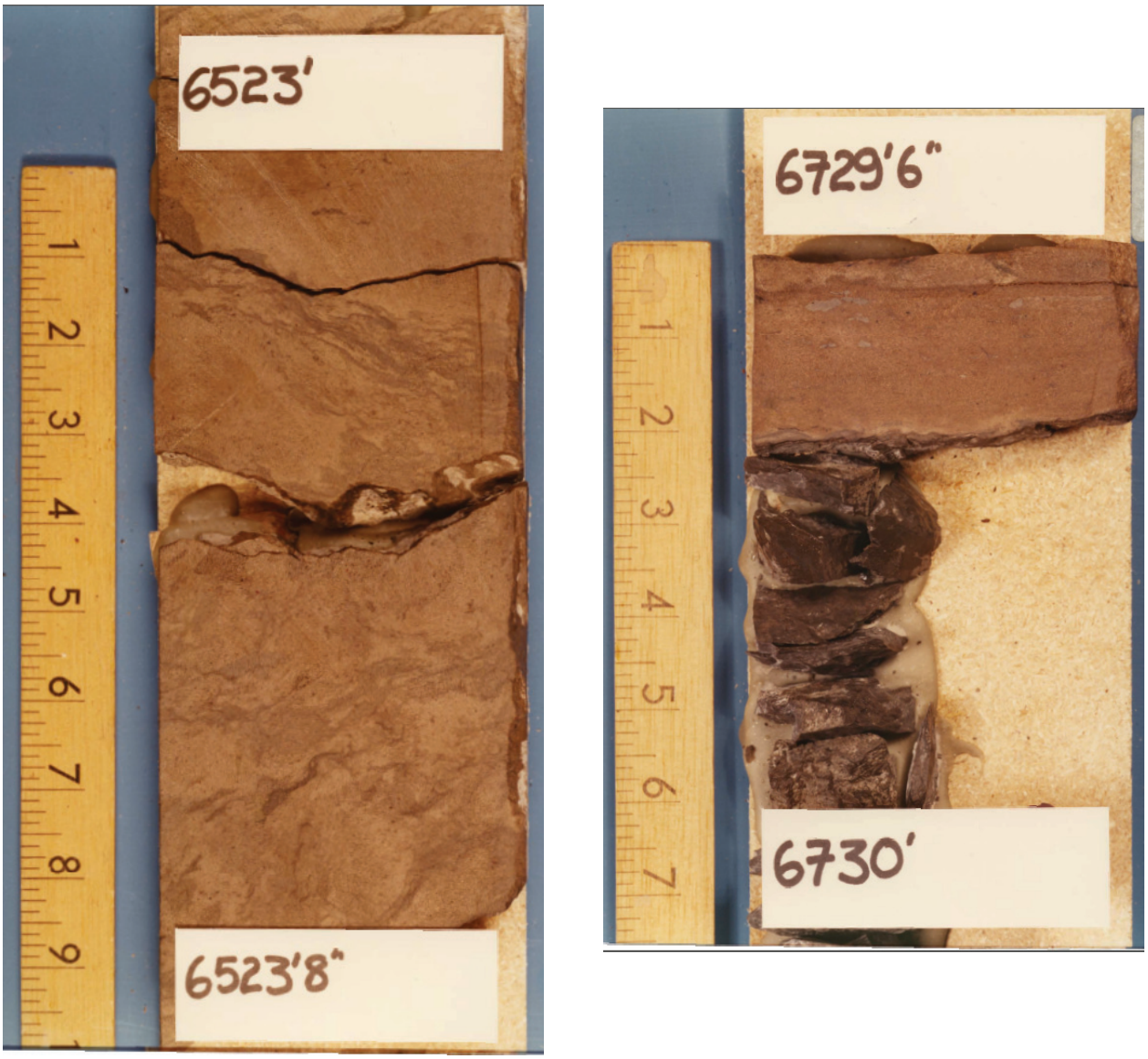


Figure 3.13: *Photographs of sections of core from the Pentland Formation, Well 11/30-2, Beatrice Field from 6523-6523.67 ft MD (1988.21-1988.41 m MD) and 6729.5-6730 ft MD (2051.15-2051.30 m MD). The presence of silty, verging on clay-rich, oil-stained sands in the shallower section and the shallowest section of the deeper core show the in-formation reservoir, and migration pathways from the hydrocarbon-producing TOC-rich shales, as seen in the lower region of the deeper core.*

clothem is topped by a silty claystone with rootlets and the Brora Coal, assumed to have been deposited within an extensive lagoonal coastal swamp (Linsley *et al.*, 1980; Richards *et al.*, 1993).

3.6.1.4 | Brora Formation (Humber Group) – A & B Sands

A transgression overlaid the Brora Coal, and is followed by a cycle of alternating, coarsening-up, transgressive-regressive marine shales and sideritic sandstones (Figure 3.15; Linsley *et al.* (1980)). The cycle averages 16 % porosity and permeabilities of 50-500 mD, and consists of fine grained, silty, shelly, bioturbated, *Rhaxella* spicule-containing sandstones grading into silty, shelly shelf muds, overlain by fine grained flasar-bedded, ripple laminated, silty sandstones that coarsen-up into clean, fine-medium grained, cross-bedded or bioturbated beach or barrier sandstone (Figure 3.14; Linsley *et al.* (1980)).

The Early Callovian-age B Sand typically shows three cycles in an average 15 m section, conse-

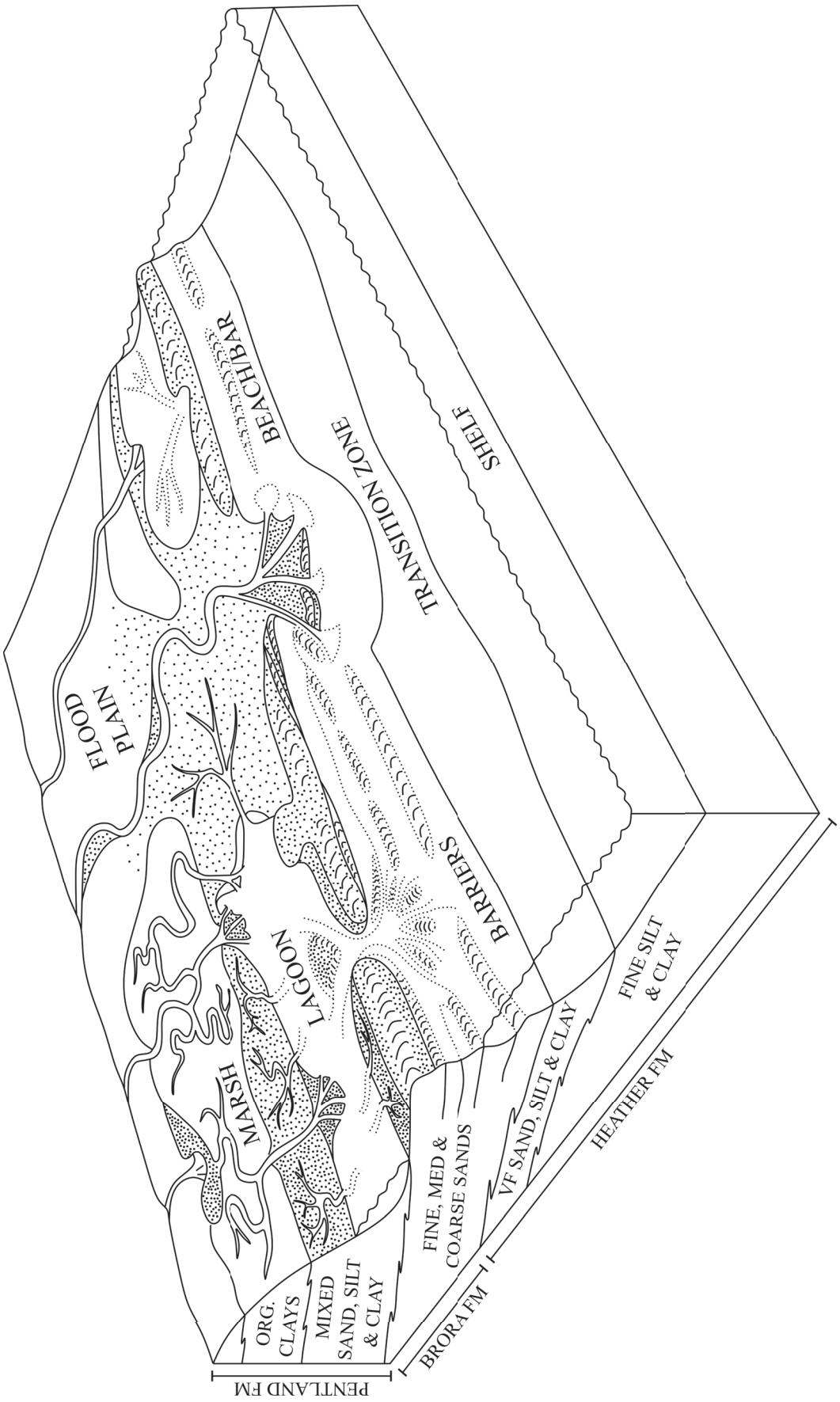


Figure 3.14: *Facies model of the Middle Jurassic, upper reservoir sequences of the Pentland and Brora Formations, identifying the alluvial flood plain, lagoonal, delta and beach bar and barrier depositional environments, and the transitional shelf zone of the Heather Formation. The alluvial deposits came from the NW of the IMF, over the Great Glen Fault, into the basin. Modified from Andrews* et al. *(1990); Paleoservices (1978).*

quently sand bodies are relatively thin, with common calcite cement, however in the Late Callovian-age A Sand, a single depositional cycle is typically 30 m thick, resulting in thick sand sequences and making it the dominant component of the Beatrice reservoir (Linsley *et al.*, 1980; Stevens, 1991). Above the A Sand, a belemnite-guard rich sandstone occurs, and shows some current orientation (Linsley *et al.*, 1980). The sandstone transitions into overlying shelf muds of the sealing Heather Formation (Linsley *et al.*, 1980; Stevens, 1991).

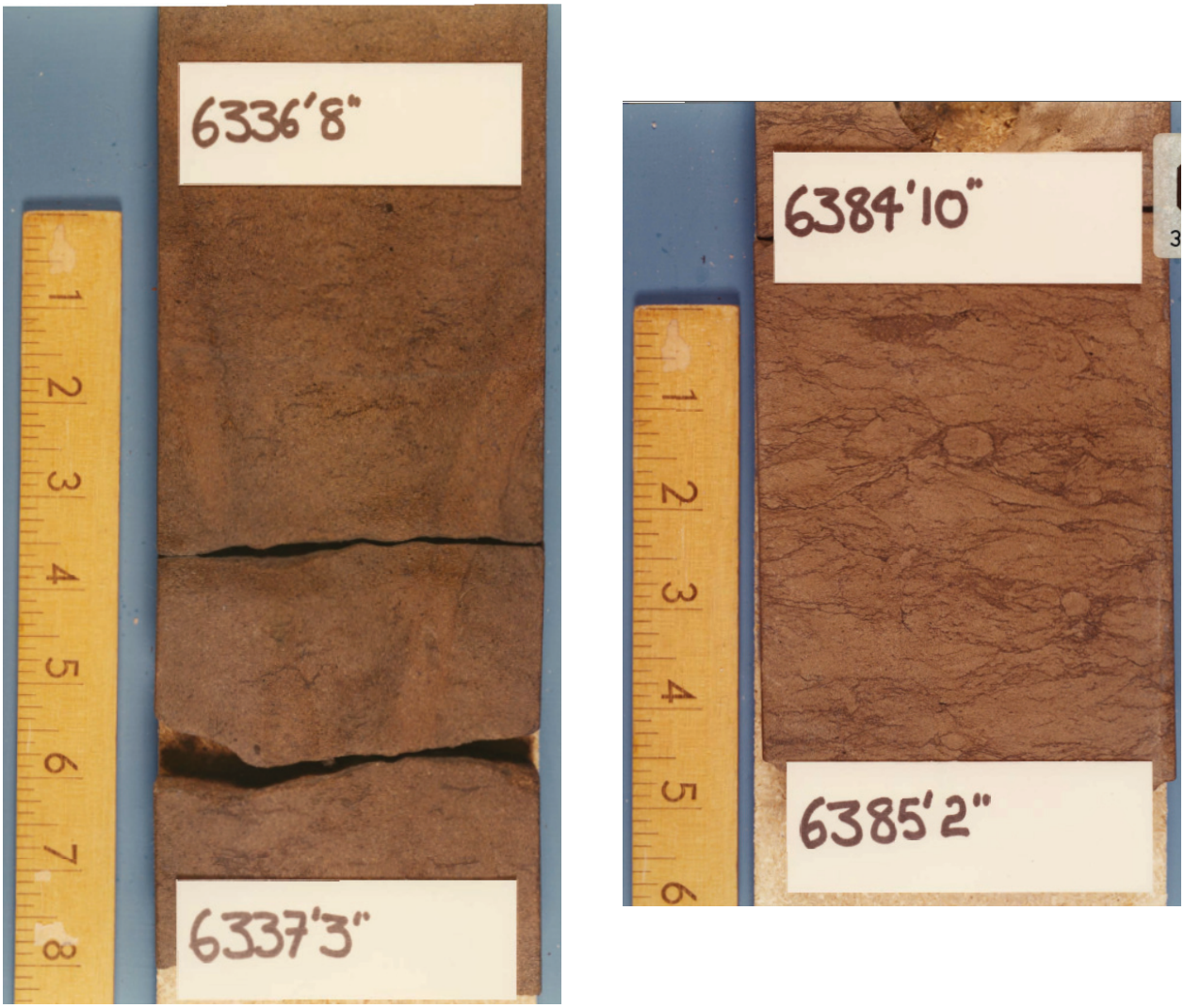


Figure 3.15: *Photographs of sections of core from the A (left) & B (right) Sands, Well 11/30-2, Beatrice Field from 6336.67-6337.25 ft MD (m MD) and 6384.82-6385.17 ft MD (m MD), respectively. Both cores show consistent sand presence, but the B Sand shows more influx of silt, especially towards its base when it transitioned from the Pentland Formation into the B Sand.*

3.6.2 | FIELD STRUCTURE

The development of Beatrice's structure and trap is closely linked to formation of the IMF, with Barr *et al.* (1985) suggesting the trap is derived from the basin's isostatic disequilibrium, and the majority of faults in the field being normal but being controlled by pre-existing strike-slip fault trends attributed to the rejuvenation of Caledonian faults during Permian-Triassic continental rifting (Linsley *et al.*, 1980; Stevens, 1991). Most Beatrice-related faulting is thought to be constrained to the Late

Oxfordian, critically including the field-bounding and -trapping Beatrice Fault, and had ceased by the Mid-Kimmeridgian, however the Beatrice Fault may have continued its development until the Ryazanian, akin to other major basin faults (Linsley *et al.*, 1980; Stevens, 1991). Barr *et al.* (1985) state that a sub-horizontal, deep-rooted detachment system beneath the IMF, combined with a lack of deep-rooted steep faults that would have facilitated isostatic recovery, and a lack of lithospheric thinning, as proven by Dimitropoulos and Donato (1981), has the ability to cause the three-way dip closure system trapping Beatrice (Figure 3.16).

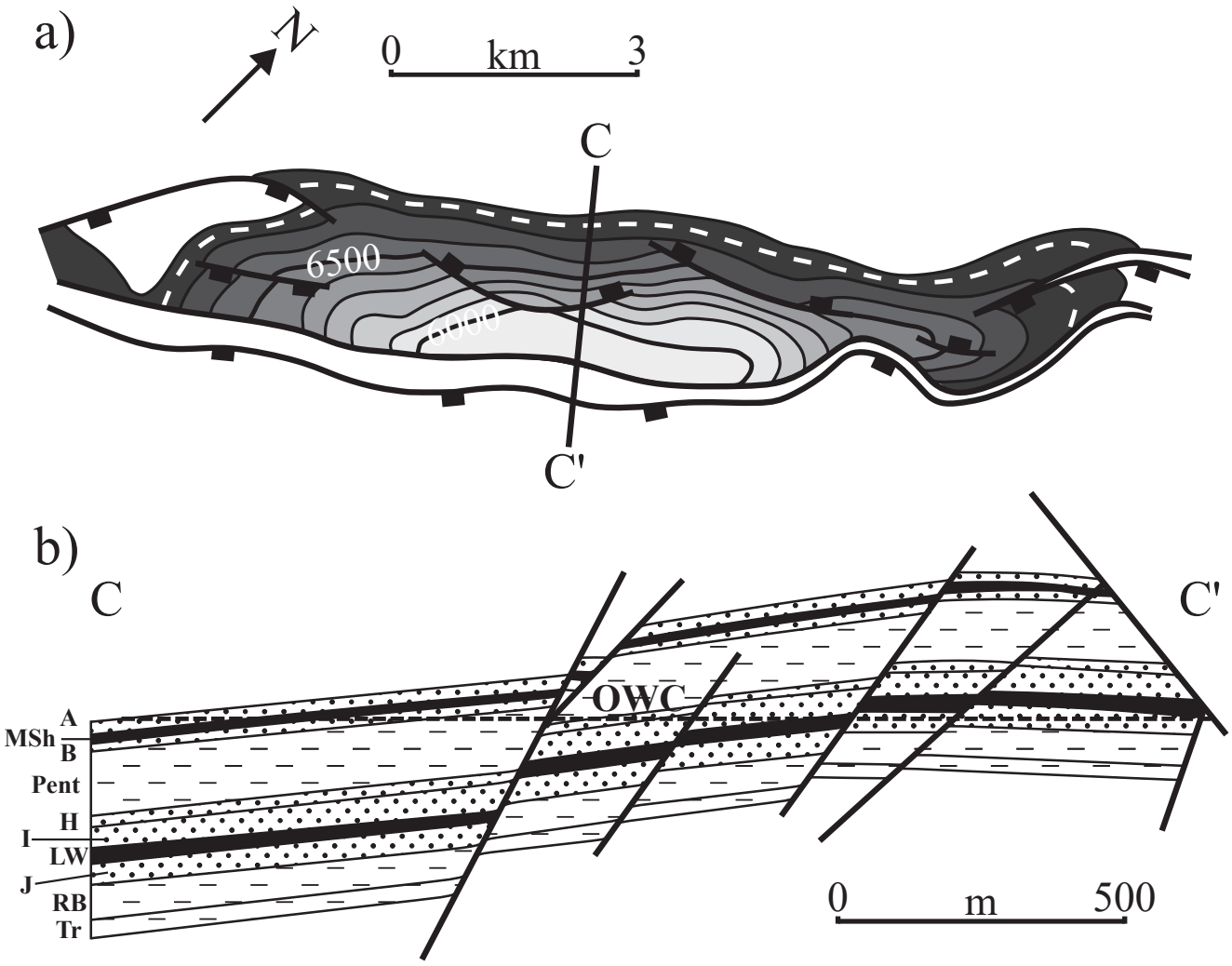


Figure 3.16: *a) Contour map showing top of pay (A Sand) in the Beatrice Field, and b) associated cross-section through the Beatrice Field, outlining major faults and sediment packages seen. Note that contour depths are in feet. A = A Sand, MSh = Mid Shale, B = B Sand, Pent = Pentland Formation, H = H Sand, I = I Sand, LW = Lady's Walk Shale, J = J Sand, RB = Red Beds, Tr = Triassic Chert. From Linsley* et al. *(1980) and Stevens (1991).*

3.6.3 | FIELD SOURCE ROCKS

Five dominant source rocks exist in the northern North Sea: the Early Devonian Struie Formation; the Middle Devonian Orcadia Formation; the Carboniferous Firth Coal Formation; the Middle Jurassic Pentland Formation; and the Late Jurassic Kimmeridge Clay Formation (Greenhalgh, 2016). In the IMF, the Firth Coal Formation is not present due to Early Permian removal of Carboniferous sediment, and the

Kimmeridge Clay, despite containing high TOC, is believed to be too shallow and immature to produce oil (Figure 3.17c; Greenhalgh (2016); Mackenzie *et al.* (1983); Peters *et al.* (1989)). Consequently, current theories and geochemical research (Peters *et al.*, 1989) infer that the IMF hydrocarbons is a non-biodegraded co-sourced mix of both Devonian and Middle Jurassic sources (Stevens, 1991).

The Devonian source rock flagstones sit within the Old Red Sandstone (ORS) and were deposited

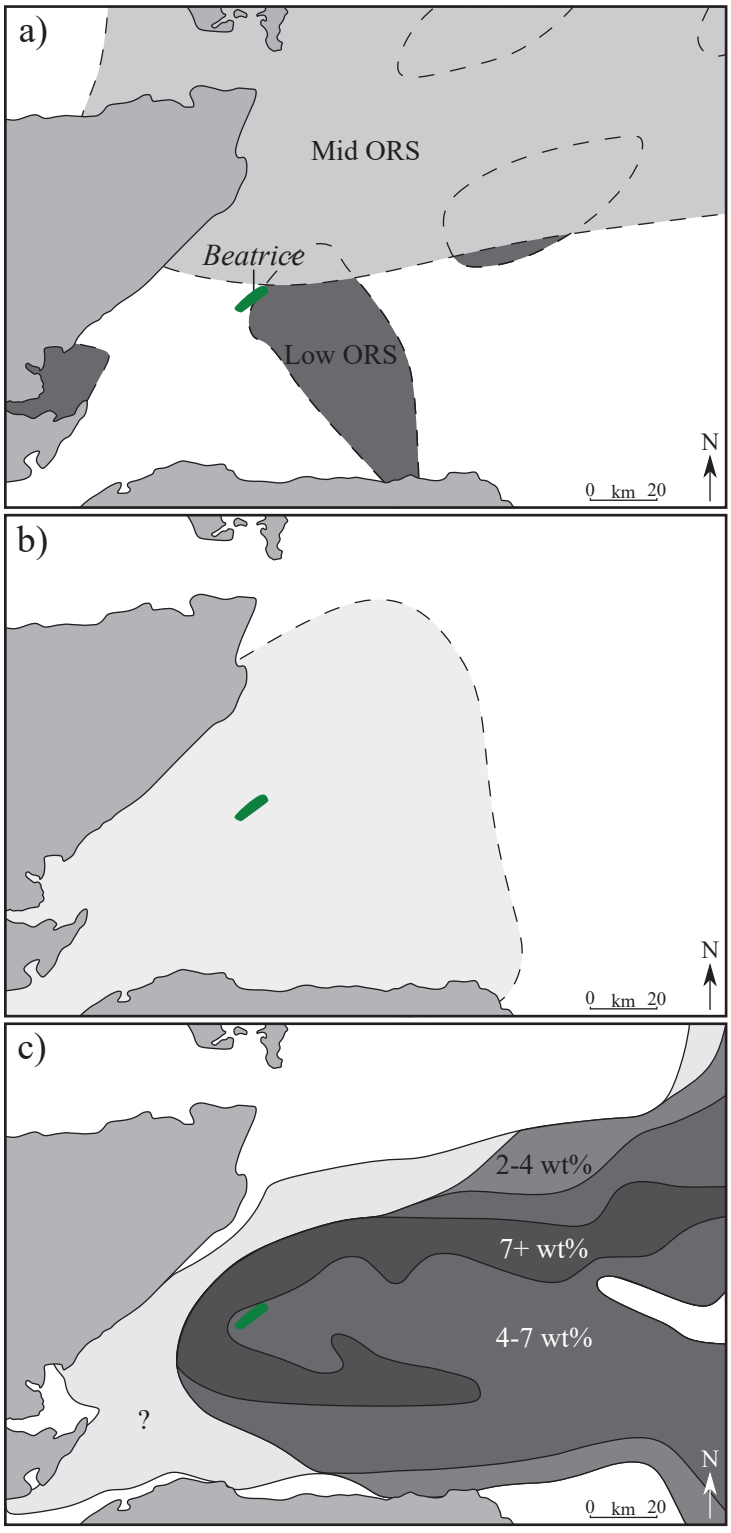


Figure 3.17: *Maps showing assumed (dashed line) and known (solid line) depositional extents of a) Lower and Middle Devonian Old Red Sandstone (ORS); b) Brora Coal Formation; and c) Kimmeridge Clay, in which TOC trends are shown. Modified from Brown* et al. *(1988) and Evans* et al. *(2003).*

in an extensive lacustrine region known as the Orcadian Lake (Brown *et al.*, 1988), and are rich in Type I amorphous kerogen, but also contain more minor Type II source material. The lacustrine environment varies in consistency across the basin, being isolated in the Early Devonian before becoming more widespread in the Middle Devonian, and the extent of the lake is difficult to define, although it is thought that during the Middle Devonian it extended across the entire northern North Sea (Figure 3.17a; Brown *et al.* (1988); Greenhalgh (2016); Peters *et al.* (1989)). Sources are non-uniformally distributed, dark, organic rich, laminated units, with the best source potential in thin, continuous, highly TOC-rich Fish Beds within the flagstones, which were deposited during sea level-fluctuation-forced extinction events (Greenhalgh, 2016; Trewin, 1989). In contrast, the Pentland Formation is a Type II-III source restricted to the Moray Firth (Figure 3.17b; Curry and Fisher (1982); Linsley *et al.* (1980); Richards *et al.* (1993)). The formation is a coastal, alluvial flood-plain deposit in a freshwater swamp environment that experienced periodic marine-brackish influences (Curry and Fisher, 1982; Linsley *et al.*, 1980; Richards *et al.*, 1993), see Section 3.6.1.3 for further detail.

3.6.3.1 | HYDROCARBON GEOCHEMISTRY

Biomarker and isotope analysis proves a non-correlative relationship between Kimmeridge Clay bitumen and the IMF hydrocarbons, but does show a correlation between IMF hydrocarbons and both Devonian siltstones and Pentland shales and coals (Table 3.1; Mackenzie *et al.* (1983); Peters *et al.* (1989)). Furthermore, IMF hydrocarbons have a significantly higher wax content, higher pour point and lower sulphur content than most other North Sea oils, which are typically Kimmeridge Clay-sourced (Aalund, 1983). Despite a potential influx of plant matter into the IMF during the Late Jurassic causing differing Kimmeridge Clay composition in the region to that of the rest of the North Sea, Mackenzie *et al.* (1983) suggests that the Kimmeridge Clay could require a further 3 km of burial to reach maturity, although this seems excessive. Extensive burial of the Kimmeridge Clay is rare in the IMF, however, it possibly has occurred adjacent to the GGF to the NW of the Beatrice Field, thus offering a potential source location if the Kimmeridge Clay contributed to the IMF hydrocarbons, although evidence suggests this contribution is unlikely (Mackenzie *et al.*, 1983).

Peters *et al.* (1989) propose a Devonian:Pentland source-mixing ratio of 60:40 within the IMF hydrocarbons, however they state that thermal maturity biomarkers indicate that IMF hydrocarbons are more mature than any potential sources, giving unreliable conclusions. The Devonian sources also contain an unknown ratio of Type I and II oils, causing further source-mixing uncertainties resulting in Devonian:Pentland ratios potentially varying between 58:42 (fully Type I) and 66:34 (fully Type II; Peters *et al.* (1989)). This complexity suggests a history much more convoluted than initially believed, with maturation, migration, mixing and charging histories yet to be fully unravelled.

The minimal presence of desmethyl C_{30}-steranes in IMF hydrocarbons suggests partially marine conditions, however strong perhydro-β-carotene signatures in both the IMF hydrocarbons and Devonian bitumen samples suggests a more saline lacustrine environment (Peters *et al.*, 1989). The presence of gammacerane and carotene in the Devonian kerogen indicates an algal source in a high salinity, anaerobic environment (Duncan and Hamilton, 1988; Greenhalgh, 2016). Maceral analysis and terpane diagrams show similarities between IMF hydrocarbons and Devonian bitumens, however, carbon isotopes

suggest the Devonian cannot be the sole source (Peters *et al.*, 1989). Mass chromatograms show matching peaks between Pentland bitumen and IMF hydrocarbons of 1,2-benzopyrene and 3,4-benzopyrene, proven to not be derived from anthropogenic contamination (Peters *et al.*, 1989). The percentage of normal paraffins within IMF hydrocarbons and the Middle Jurassic bitumens are significantly greater than the other samples, and the mixing of Middle Jurassic and Devonian sources would generate a waxy oil similar to that seen in Beatrice (Peters *et al.*, 1989).

In summary, Peters *et al.* (1989) suggest a mix of a lacustrine source (Devonian) dominated by non-marine organic matter alongside a marginal marine-to-fluvial source (Pentland) dominated by degraded marine planktonic organic matter. Erosion and rifting events in the Permian likely significantly reduced the volume of hydrocarbons generated in the Palaeozoic due to the lack of seals and faults, however most Devonian oil is thought to have reached mid-late maturity by the Late Palaeozoic (Greenhalgh, 2016; Trewin, 1989). Significant Mesozoic maturity most likely occurred in regions where oil did not reach maturity during the Palaeozoic, with this inferred for the IMF hydrocarbons, and likely caused by the North Sea Dome (Hogan *et al.*, 1978). Cracking to gas would have been likely if IMF hydrocarbons was emplaced earlier and within elevated pressure and temperature conditions for an extended time period (Greenhalgh, 2016). This later heating may be the reason IMF hydrocarbons shows a higher level of maturity than the inferred sources.

3.6.3.2 | SOURCE KITCHEN LOCATIONS

Due to the limitations in constraining the Orcadian Lake, the low mobility of the Pentland Formation-sourced hydrocarbons, the extent and connection to any potential Kimmeridge Clay maturation, the basin's complex tectonic history, extensive regional and local facies variabilities and thermal maturity inequalities, defining the source regions and migration history of the Beatrice Field has not yet been successfully accomplished (Greenhalgh, 2016). Due to its low mobility, long-range migration of the Pentland Formation hydrocarbons is strongly doubted and its presence within the Beatrice Field (proven by cores and well logs) suggests a more proximal kitchen than that of any other source (Hogan *et al.*, 1978). Conversely, two different arguments exist for the Devonian source kitchen. Marshall (1998) offers evidence for the overprinting of an initially steep geothermal gradient, caused by deep burial in the Palaeozoic, which deflectes away from a potential Devonian source kitchen close to Beatrice Field, but Curran (1987a) and Underhill (1991) suggest long-ranged migration of Devonian hydrocarbons occurred. However these differ, with Curran (1987a) proposing that the area around Well 12/27-1 (20 km SE of Beatrice) shows optimum conditions for a Devonian source kitchen, due to the presence of the source intervals in logs and cores, whereas Underhill (1991) suggests optimum Devonian oil production would have occurred in the north of the Sutherland Terrace, 20 km NW of Beatrice. Despite this uncertainty, hydrocarbon generation modelling consistently infers that oil maturation occurred in the Early Cretaceous (Greenhalgh, 2016; Robertson Research International, 2001).

In attempts to constrain the locations of IMF source kitchens, Parnell *et al.* (2017) and Peters *et al.* (1998) followed Underhill (1991) by analysing organic-rich veins within the Caledonian-age granitic basement in the Helmsdale region, and oil-cemented fractures in brecciated sandstone clasts likely derived from Helmsdale Fault gouge breccia, respectively. Geochemical analysis by Peters *et al.* (1998)

Table 3.1: *Table summarising geochemical results of the IMF hydrocarbons and other source samples, derived by Peters* et al. *(1989). The IMF hydrocarbons and Middle Jurassic bitumen samples were both collected from Well 11/30-2 within the Beatrice Field, the Kimmeridge Clay and Devonian Type II samples were taken from Well 12/27-1, with the Devonian Type II originating from Early Devonian organic-rich siltstones, and the Devonian Type I source being collected from similar Middle Devonian organic-rich siltstones at Holborn Head Quarry on onshore Scotland (Peters* et al., *1989). Note biomarkers are denoted by their presence (Y) or absence (N).*

	Geochemistry Results								Biomarkers						
	$\delta^{13}C$ (‰)	Wt% S	TOC (%)	R_o	Wax (%)	S_2 (mg HC/g rock)	HI (mg HC/g TOC)	OI (mg CO_2/g TOC)	Perhydro-β-carotene	Desmethyl C_{30}-steranes	Terpanes	1,2-Benzopyrene	3,4-Benzopyrene	28,30-Bisnorhopane	25,28,30-Trisnorhopane
IMF hydrocarbons	-31.77	0.11	-	-	21	-	-	-	Y	Y	Y	Y	Y	N	N
Kimmeridge Clay Bitumen	-38.32	2.58	5.78	0.54	12	22.38	387	50	N	Y	N	N	N	Y	Y
Middle Jurassic Bitumen	-27.42	-	3.40	0.53	24	7.56	222	8	N	Y	N	Y	Y	N	N
Devonian Bitumen Type I	-33.98	0.08	4.68	0.61	11	43.69	933	3	Y	N	Y	N	N	N	N
Devonian Bitumen Type II	-34.94	0.62	1.11	0.45	12	6.77	609	59							

shows the presence of 24-*n*-propylcholestanes and β-carotenes, suggesting both marine and lacustrine source rocks, respectively, inferring a mixed oil similar to that of Beatrice Field hydrocarbons, plus a suite of biomarkers that indicate both mild and heavy biodegradation. Analysis also reveals the presence of oleanane, typically suggesting a post-Cretaceous paralic marine shale source or, more rarely, an effective oleanane-bearing Pentland Formation marine source (Peters *et al.*, 1998). Mass spectrometry of the Pentland Formation in Well 11/30-2 confirms the presence of oleanane in the formation, therefore inferring that fractures along the Helmsdale Fault were filled with forcibly-emplaced, heavily biodegraded, co-sourced oils that closely resemble oil seen in Beatrice Field (Peters *et al.*, 1998).

Parnell *et al.* (2017) conclude that both Devonian and Jurassic sources were possible in the organic-rich sediment veins within the granitic basement, but sterane compositions relate the organic matter to a Jurassic shale. Parnell *et al.* (2017) state that the veins were forcefully emplaced, and that oil was present during sediment vein emplacement, potentially reflecting high fluid pressures associated with post-Jurassic movement along the Helmsdale Fault. The presence of high-pressured fluids in the basin is evidenced by Jonk *et al.* (2003) and specifically in the Helmsdale Fault by Parnell *et al.* (2017), with these hydrofractures and faults potentially acting as conduits facilitating primary hydrocarbon migration, with high fluid pressures capable of producing open fractures and dilatant faults at all depths associated with hydrocarbons (Aydin, 2000).

3.6.4 | IMF HYDROCARBON PRODUCTION HISTORY

Production of Beatrice Field came online in September 1981, but due to low field pressures, caused by the low gas-oil ratio, poor aquifer influx and high oil viscosity due to its wax content, enhanced oil recovery was necessary from the beginning, involving both electrical submersible pumping (ESP) and water injection, chosen over gas injection due to the low gas-oil ratio in the field (Chorneyko, 2006; Clifford and Duthie, 1987; Fielder and Johnson, 1986; Kilvington and Gallivan, 1983; Kilvington *et al.*, 1987; Stevens, 1991). Furthermore, due to the high wax content, giving high viscosity and high pour point oil, pour point depressants (PPDs) and associated solvents were also utilised from the beginning of production to reduce the oil viscosity and lower the pour point to a more viable temperature (Chorneyko, 2006; Clifford and Duthie, 1987; Fielder and Johnson, 1986; Kilvington and Gallivan, 1983; Kilvington *et al.*, 1987; Linsley *et al.*, 1980; Stevens, 1991). Across the life of the reservoir, production rates dropped dramatically from an initially strong rate of 30-40,000 barrels of oil per day (bopd) through the first two years of production (1981-1983) down to less than 1000 bopd at the end of the field's life in the early 2010s (Figure 3.18; Kilvington and Gallivan (1983); Oil and Gas Authority (2018)). There is limited information regarding both the Lybster and Jacky Fields, however there is data that shows production, which occurred from mid-2012 to late-2017, and mid-2009 to mid-2014, respectively, was initially strong before dramatically dropping off much quicker than Beatrice Field (Figure 3.18; Oil and Gas Authority (2018)). Lybster Field had much lower production rates compared to the other fields, due to low reservoir pressures, and the field was only viable due to its proximity to the coast and pre-existing infrastructure, resulting in very low production costs. In comparison, whilst Jacky Field has much smaller reserves it is under high pressure and thus production rates were initially high and the field benefited from being in close proximity to the infrastructure developed for Beatrice Field.

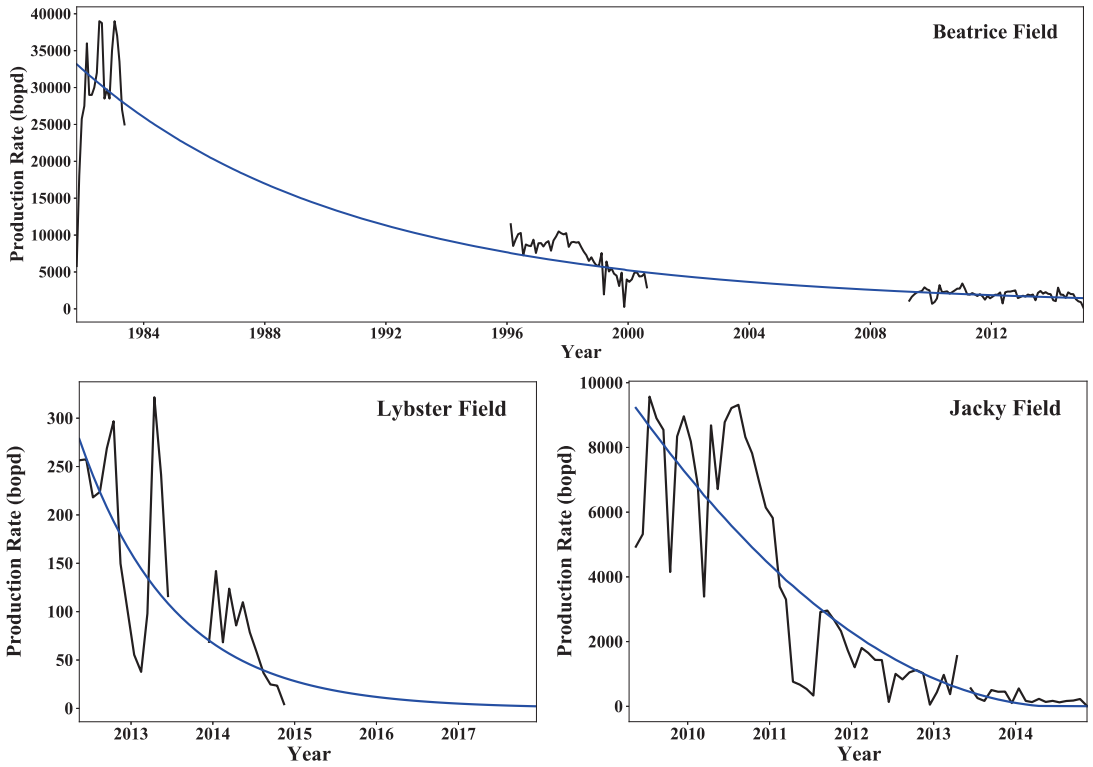


Figure 3.18: *Graphs of monthly production rates (black) of the hydrocarbon fields within the IMF, with calculated rates (blue) via best fit curves. Missing data is due to a lack of reported production rates, not breaks in production. Data from Kilvington and Gallivan (1983) and Oil and Gas Authority (2018).*

3.7 | SUMMARY

This chapter has shown how the IMF has formed and evolved through its geological history, which has differentiated the basin from other more Central North Sea depocentres. This evolutionary variation offers this study the ability to compare the findings to other North Sea petroleum systems, as well as those in other areas. Further variations are seen in the petroleum system, most clearly found within the source rocks, where an apparent lack of Kimmeridge Clay-sourced hydrocarbons further differentiates the IMF from the other North Sea regions, as does a likely mixed source hydrocarbon accumulation. With only three known hydrocarbon fields in the IMF, understanding the petroleum system, through the work in this study, offers the opportunity to investigate both the possible reasons why the basin has a lower number of hydrocarbon accumulations compared to other reasons of the North Sea, and if any previously unidentified accumulations exist.

Chapter 4 | Methodologies

4.1 | INTRODUCTION

This chapter covers the various methodologies used across this study, separated into magnetic analyses and modelling analyses, both geological interpretations and basin and petroleum systems modelling. Whilst there are overlaps between the two overarching analytical techniques used in this study, they are two very different disciplines so have been separated accordingly.

4.2 | MAGNETIC ANALYSES

The magnetic analyses used throughout Chapter 6 were carried out in an overarching two step process - initially, samples were collected and processed according to what analytical technique was to be carried out, and then the analysis itself. These two processes are outlined within this section.

4.2.1 | SAMPLING AND PROCESSING

4.2.1.1 | BGS CORE STORE SAMPLE COLLECTION

As part of all UK North Sea drilling licensing agreements, half of all core drilled (separated vertically) is given to the British Geological Survey (BGS) upon extraction, and is then stored at the BGS Core Store in Keyworth, Nottingham, offering the opportunity to sample across large swathes of core. To select the sections of core most suitable for magnetic analysis, composite well logs were used to initially identify the stratigraphy present in each well, and then to determine relevance to the petroleum system, including key aspects of the reservoir body, most critically the oil-water contact(s).

Sample collection was done at the BGS Core Store, with samples being selected based on maximising the spread of samples across all reservoir intervals whilst also accruing samples around critical research areas like the oil-water contact. Samples taken are between 2 cm and 7 cm in size, taken at intervals of 1 m (3 ft) in reservoir sections and 30 cm (1 ft), or smaller, intervals in critical areas.

4.2.1.2 | SAMPLE PREPARATION - CUTTING & CORING IN ROCK PREP LAB

Due to the well consolidated nature of the sand samples, all samples that were structurally strong enough were cored into 5 mm diameter cores in the Imperial College Department of Earth Science and Engineering's Rock Preparation Laboratory. These samples were then trimmed to 1 cm length using a water-cooled circular saw. Samples were then weighed and stored in sample containers at the Natural Magnetism Group (NMG) Laboratory at Imperial College London ready for analysis.

4.2.1.3 | SAMPLE PREPARATION - GRINDING IN NMG LABORATORY

Samples that were not suitable for coring, such as poorly consolidated sands and clays, were ground in a quartz mortar and pestle in the Imperial College Department of Earth Science and Engineering's NMG Laboratory. These samples were then weighed and stored within sample bags at the NMG Laboratory ready for analysis.

Samples that had core taken from them are also required to produce some ground samples for high

and low temperature analyses. These were prepared in the same way as the non-cored samples. Samples also sent to the Institute for Rock Magnetism (IRM) in Minneapolis, USA and Australia National University (ANU) in Canberra, Australia magnetism laboratories were prepared in this way, with samples being ground, weighed and bagged before being sent to the relevant institutions.

4.2.2 | Laboratory methods

4.2.2.1 | Magnetic Analyses

Hysteresis Measurements

Room temperature hysteresis measurements were undertaken with a Princeton Vibrating Sample Magnetometer at the NMG Laboratory at Imperial College in White City, London to produce datasets outlining the room temperature properties of the samples, to deduce grain size and magnetic mineralogy within the samples. This magnetic analysis was done to determine the saturation magnetisation (M_s), remanent magnetisation (M_{rs}), coercivity (B_c), coercivity of remanence (B_{cr} and high-field slope (H_{fs}) of each sample via the formation of a hysteresis loop. Alongside the hysteresis loop, backfield curve and isothermal remanent magnetisation (IRM) measurements were also carried out to further the analysis of each sample. See Table 4.1 for information on the input controls of this analysis.

Furthermore, on the Princeton VSM at the NMG Laboratory, room temperature First Order Reversal Curve (FORC) data was collected in two forms - as standard FORC analysis, as developed by Roberts *et al.* (2000), and as a remFORC measurement (set up within this study as an NMGremFORC; Muxworthy and Baker (2022)). These processes are carried out at room temperature and produce similar results through similar techniques however differ in one major way – FORC analysis measures the points along the magnetisation curve ($M(B_r,B)$) in-field, whereas remFORCs, also known as remanence FORCs, measure $M(B_r,B)$ out of field, thus giving a remanence measurement for each $M(B_r,B)$ point. This is beneficial as comparisons allow further analysis, and remFORCs offer the opportunity to measure noisy samples that otherwise would produce chaotic FORC diagrams. However, as the applied field has to continuously switch from a specified value to zero then back, it takes significantly longer than a standard FORC, approximately double the time (Zhao *et al.*, 2017). The analytical techniques for both FORCs and remFORCs are similar, albeit with slightly differing inputs. Both have been run on the VSM at room temperature, with similar input parameters (see Table 4.2 for information on the input controls of the analysis), however remFORCs require the input of a python-written script on the Princeton system. All samples underwent FORC analysis, however only the noisiest and most important samples underwent remFORC analysis due to the timescales involved.

Low temperature analysis via MPMS

Low temperature measurements were carried out on Magnetic Property Measurement Systems (MPMS) at the IRM and ANU. the low temperatures (10-300 K) are used to identify nanometric particles ($\leq$30 nm) that are hard to identify at room temperature (superparamagnetic minerals; Dunlop and Özdemir (1997)), and to classify the magnetic minerals in the samples through identification of crystallographic transitions seen in certain minerals that occur below room temperature. The transitions include the Ver-

Table 4.1: *Table summarising the input parameters of the room temperature Vibrating Sample Magnetometer (VSM) analytical laboratory methods used for the ascertainment of key magnetic properties within prepared samples.*

Input controls	Hysteresis Loop	Backfield Curve	IRM
Sensitivity	5-10 μAm^2	20-50 nAm^2	20-50 nAm^2
Applied field maximum	300 mT	-	-
Applied field increment	3.75 mT	-	-
Averaging time	250 ms	-	-
Pause at maximum field	1 s	-	-
Averages	1	-	-
Sequence	-	Nonlinear	Nonlinear
Initial field	-	1 mT	1 mT
Final field	-	500 mT	500 mT
Number of points	-	40	40
Saturating field (DCD)	-	1 T	1 T
Pause at saturation	-	1 s	1 s
Averaging time	-	5 s	5 s
Pause at applied field	-	1 s	1 s
Pause at zero field	-	1 s	1 s
Slew rate to applied field	-	1 T/s	1 T/s
Commence demagnetizing at	-	-	550 mT
Exit demagnetizing at	-	-	0 T
Field decrement (% of field)	-	-	5 %
Limit slew rate to $\leq$	-	-	200 mT/s
Limit slew time to $\geq$	-	-	300 ms
Pause at each applied field	-	-	60 ms

wey Transition within magnetite at 120-125 K (Verwey, 1939), the Morin Transition in hematite at 263 K (Morin, 1950) and the Besnus Transition in monoclinic pyrrhotite at 30-34 K (Besnus and Meyer, 1964; Rochette *et al.*, 1990).

Three low temperature magnetisation analyses were run on the MPMS to identify these mineral transitions within samples. Low temperature demagnetisation analysis was carried out, where samples

Table 4.2: *Table summarising the input parameters of the room temperature FORC and remFORC analytical laboratory methods used for the ascertainment of FORC diagram data of prepared samples carried out in a VSM.*

Input controls	FORC	NMG remFORC
Sensitivity	2 μAm^2	-
Saturating field	+1 T	-
B_i (min)	-40 mT	-
B_i (max)	+40 mT	-
B_c (min)	0 T	-
B_c (max)	+80 mT	-
Averaging time	250 ms	-
Field increment	1.93 mT	-
Number of FORCs	100	-
Allow for smoothing factor of	7	-
Pause at saturating field	1 s	-
Pause at calibration field	1 s	-
Pause at reversal field	1 s	-
Slew rate limit	1 T/s	-
Number of measurements	1	-
Pause	-	250 ms
Average time	-	2 s
B_r max	-	120 mT
B min	-	100 mT
Max field	-	1 T
Number of FORCs	-	70

were subjected to a strong applied field at room temperature to reach SIRM before being cooled to 20 K and warmed back to 300 K in a zero-field, generating two curves known as cycling cooling and cycling warming curves. Field cooled (FC) and zero-field cooled (ZFC) warming curves were also carried out, where an applied field produces an SIRM at 10 K, and then is warmed in a zero-field to 300 K. These two analyses differ through how the SIRM is reached – FC scenarios cool the sample whilst subjecting it to an applied field, whereas ZFC scenarios cool the sample to 10 K in a zero-field.

HIGH TEMPERATURE SUSCEPTIBILITY VIA KAPPABRIDGE

High temperature susceptibility measurements were carried out using a Kappabridge system at the NMG Laboratory. Susceptibility is used to determine the mineralogy of samples based on their Curie Temperatures via identification of sample thermomagnetic behaviour (Dunlop and Özdemir, 1997). Samples were heated from room temperature to 700 °C within a non-reactive argon atmosphere.

4.2.2.2 | LOW AND ROOM TEMPERATURE MÖSSBAUER SPECTROSCOPY

Mössbauer spectroscopy was carried out at the IRM in Minneapolis, at both room and low (20 K) temperatures. Mössbauer spectroscopy is used to assess mineral assemblages in samples, and was first identified by Mössbauer (1958). A source produces gamma rays which are absorbed by iron as a function of the iron mineral lattice, enabling the differentiation between minerals. It is typically done at low temperatures for weakly magnetic samples, and up to room temperature for more strongly magnetic particles. Natural samples, typically having low iron content, are rarely successful due to their weak magnetism, and this also means measurements take 3-4 days to complete.

4.2.2.3 | SCANNING ELECTRON MICROSCOPY AND ENERGY DISPERSIVE X-RAY ANALYSIS

Samples for Scanning Electron Microscopy (SEM) analysis were pre-processed prior to imaging – initially, whole-rock samples were crushed as per Section 4.2.1.3, before being sieved through a 500 μm brass sieve. The sieved samples were then magnetically separated using the Frantz LB-1 Magnetic Barrier Laboratory Separator located in the Department of Earth Science and Engineering at Imperial College London. The samples were run through the separator three times to refine the volume of magnetic material. The non-magnetic separated sample was kept but is now no longer useful in the study. The magnetic grains were then crushed again as per Section 4.2.1.3 to ensure as fine a texture as possible. These samples were then mounted on microscopy stubs using carbon tape before being coated with 15 nm of chromium within a Quorum Q150T S turbomolecular coater.

SEM imaging and Energy Dispersive X-ray (EDX) analysis were carried out in the Imperial College London Centre for Electron Microscopy. SEM imaging was conducted on samples with a Zeiss Auriga Cross Beam SEM system, which contains a Schottky field emission gun, Gemini electron column and three detectors - a standard in-chamber ET detector and two in-column detectors, one secondary electron detector and an energy selective backscattered electron detector. The system also has a Ga+ ion focused ion beam (FIB), however this was not used. The SEM system operates between 100 V and 30 kV resulting in spatial resolutions of 1.0 nm and has imaging resolution to 2.5 nm. EDX analysis was conducted through the SEM that is connected to the Oxford Instruments INCA EDS analysis system.

4.3 | GEOLOGICAL ANALYSES AND MODEL FORMATION

4.3.1 | SEISMIC INTERPRETATION

Seismic interpretation is critical in the development of a geological model, and is used within Chapters 5 & 7, as it produces horizon surfaces and faults within the confines of the data area that are then used to build the model. The seismic data acquired was depth converted prior to acqusition for this study, thus no time-depth conversion was necessary during this project. Seismic horizon interpretation was carried out using Schlumberger's Petrel (Schlumberger, 2015) software and was undertaken using a combination of manual, two-dimensional guided and three-dimensional guided interpretation techniques. Guided autotracking methods utilise a manual input point from the interpreter that the software uses as a basis for automated picking, which can be done in two and three dimensions depending on the seismic data being interpreted. Fault interpretation is wholly manual and is dependant on the interpreter's abilities. Both seismic and fault interpretations are then quality checked to ensure that both the manual and automated picking are accurate.

4.3.2 | WELL LOG ANALYSIS

Well log data is used to tie seismic interpretations with proven data, as well as offering the opportunity to draw conclusions on the lithologies seen around the wells through petrophysical analysis, as shown in Chapter 5. Well log data was both purchased from IHS Markit and acquired under academic licence from the Oil and Gas Authority (OGA) National Data Repository (Oil and Gas Authority, 2021). This data is used to create well correlations, petrophysical analysis and well-seismic ties. Well correlations and well-seismic ties were carried out in Petrel, where stratigraphic well tops, the depths at which specified lithological units occur, are compared to each other in terms of depth and petrophysical properties seen in each unit in each well to determine consistency and continuity of units across the study area, including lithological variation within units.

Petrophysical analysis was carried out in Interactive Petrophysics (IP; Lloyd's Register (2018)) and Schlumberger's Petrel where ".las" petrophysical data files for each well are loaded and interpreted in regards to their lithologies and relevant stratigraphy, geological properties, e.g. porosity and clay content, and petroleum system components, such as present hydrocarbons, oil-water contacts and organic content of source rocks. Petrophysical analysis commences from the initial suite of data, such as gamma ray, density and resistivity logs that are then implemented into a series of equations used to determine petrophysical properties that cannot be acquired directly from the well log, such as porosity.

4.3.3 | CORE ANALYSIS

This research carried out no original core analysis due to original post-drilling analysis producing all the core data necessary for this project. Core analysis is used to accurately determine properties that well log analysis can only estimate, such as porosity and permeability, and is also used to analyse source rock properties. The core data required for this project, used to calibrate the models and log analysis,

was taken from well reports. The properties acquired from the reports are porosity and permeability for reservoir sequences, and total organic carbon (TOC) and vitrinite reflectance in source rocks.

4.3.4 | GEOLOGICAL MODEL FORMATION

The conversion from a geological model in Schlumberger's Petrel to a basin and petroleum system model (BPSM) in Schlumberger's PetroMod (Schlumberger, 2020) is the aggregation of all interpreted surfaces and faults, petrophysical data and well top data and converting these into gridded objects. The horizon interpretations were converted into 50 m resolution grid cells and faults were converted into a Fault Framework that has gridded faults and analysed fault-fault relationships. The Fault Framework was then utilised during the creation of a Fault History table that outlines the properties of the faults and the ages at which the faults were active. This is critical in the petroleum system model, and specifically within this project, as migration pathways are highly dependant on fault activity and fault properties. Stratigraphic columns are formed to define the ages of each interpreted horizon with the gridded surfaces then linked to the stratigraphic column during the exporting process. Facies modelling is also done within Petrel, where lithology specified in the PetroMod project is used to develop a group of facies that are then assigned to each stratigraphic interval.

4.3.5 | BASIN AND PETROLEUM SYSTEMS MODEL FORMATION

Once the geological model is created in Petrel, it then must be exported to PetroMod at which point it becomes a BPSM. All surfaces must be assigned ages from the stratigraphic column which leads to the formation of units between them which are filled with facies. Faults, their properties and periods of activity are also included in this initial exporting sequence, as are the assignment of erosion maps where appropriate. Erosion maps are model-sized maps that identify any past thickness existing at a specific ages that have been eroded away from the present day geometry.

Boundary conditions are some of the most critical parameters within the model, are the final inputs into the BPSM and are heat flow (HF), paleo-water depth (PWD) and sediment-water interface temperature (SWIT). HF is the basal heat flow of sub-model geology, encompassing the heat flow of everything beneath the model (e.g. basement lithologies, crustal heat and mantle heat; Hantschel and Kauerauf (2009)). Controlling the amount of heat entering the model through the base, HF is heavily dependant on rifting events and is the dominant control on model temperatures, which in turn controls the maturation of source rocks and the existence of the oil/gas window(s) (Allen and Allen, 2005). PWD is the past, and present, depth of the water body above the model (most frequently sea) and controls the depth of the top of the model, which has a level of control on maturity and depths of all lithologies. SWIT is the temperature of the model at its surface, thus corresponds to the PWD and controls the heat entering the model from the surface. SWIT is significantly less impactful on the model than HF (Allen and Allen, 2005), and is typically unknown but is often calculated through AutoSWIT, based on the calculations of Wygrala (1989). AutoSWIT takes the model's PWD and latitude, and assigns variable temperatures throughout time based on known or assumed temperatures at the specified latitude across the history of the model. See Appendix Section A.1 for further detail.

4.3.5.1 | BPSM SIMULATION

Once the BPSM has all parameters and inputs acquired, the model is then simulated to create outputted data showing overarching events and properties such as paleogeometry, basin formation, basin temperatures and erosive events, alongside petroleum system events and properties, such as source rock maturation and hydrocarbon formation, migration and trapping. These output give rise to accumulations and potential undiscovered reservoirs, as well as offering interpretable components that can be used to understand and define the charge history of the basin.

Simulation options control what inputs and outputs can be used, specifically what migration methods and calibration outputs (e.g. vitrinite reflectance curves). One dimensional models were run on a local computer but two- and three-dimensional models were run on Imperial College's High Powered Computing (HPC) cluster. This required the creation of the models locally prior to copying to a server and the creation and submission of job scripts to the cluster. Use of the HPC both allowed computing-intensive processes to be run externally, freeing up local computing power for other activities, and the use of up to 512 times the processing power (up to 16 nodes each with 32 cores), speeding up the modelling times, however is limited to the number of software licenses available, with one being required for each additional instance of the software used within simulation on the HPC cluster.

4.3.5.2 | MODEL CALIBRATION

Once models have been simulated, calibration must be carried out to ensure accuracy of the results and to allow accurate modelling of planned variables to test different scenarios in the basin. Model calibration is typically done through comparisons between calculated output well data and core or well analysis data, most commonly temperature, vitrinite reflectance, pressure and porosity curves. Core and well data is inputted into PetroMod and produces data points along well paths within the models and are matched against the calculated data curves. Temperature and vitrinite data is most heavily dependant on the HF inputs as well as paleogeometry and erosive thicknesses, whereas the other parameters are heavily reliant on compaction, lithological and facies variations and erosive events. See Appendix Section A.3 for further detail.

CHAPTER 5 | GEOLOGICAL APPRAISAL

5.1 | INTRODUCTION

In this chapter, analysis of geological and geophysical datasets builds the understanding of the Inner Moray Firth's (IMF) geology (Figure 5.1). The end goal of this chapter is to create a geological framework model of the IMF using well log and seismic data interpretation, aided by core data and literature, and to then fill this framework with data relating to the formations and facies seen within the layers produced. To do this, extensive well log and seismic data has been collated from various sources, leading to an in-depth dataset that builds the model through data-driven properties.

This study used 40 two dimensional (2D) seismic lines, 8 SW-NE inlines, 32 NW-SE crosslines, totalling more than 2500km of seismic data and a 22 by 11 km three dimensional (3D) seismic cube to develop the geological model within the basin's geographical limits (Figure 5.2). Due to data availability, only seismic data that had been depth converted prior to being supplied was accessible, therefore this study was unable to both verify the accuracy of the depth conversion, and thus the interpretations resulting from the seismic data, or to depth convert the data directly. Whilst this is not a major issue, the lack of verification on the accuracy of the depth conversion should be mentioned as a possible flaw in the appraisal of the basin geology. Alongside the seismic data, 57 wells distributed across the eastern two-thirds of the basin were used to correlate facies, formations and depths across the IMF (Figures 5.1 & 5.2; Table 5.1). Due to exploration limitations, no wells have ever been drilled within the south-westerly region of the basin (Quadrant 17), and consequently, this area has no well-derived model constraints.

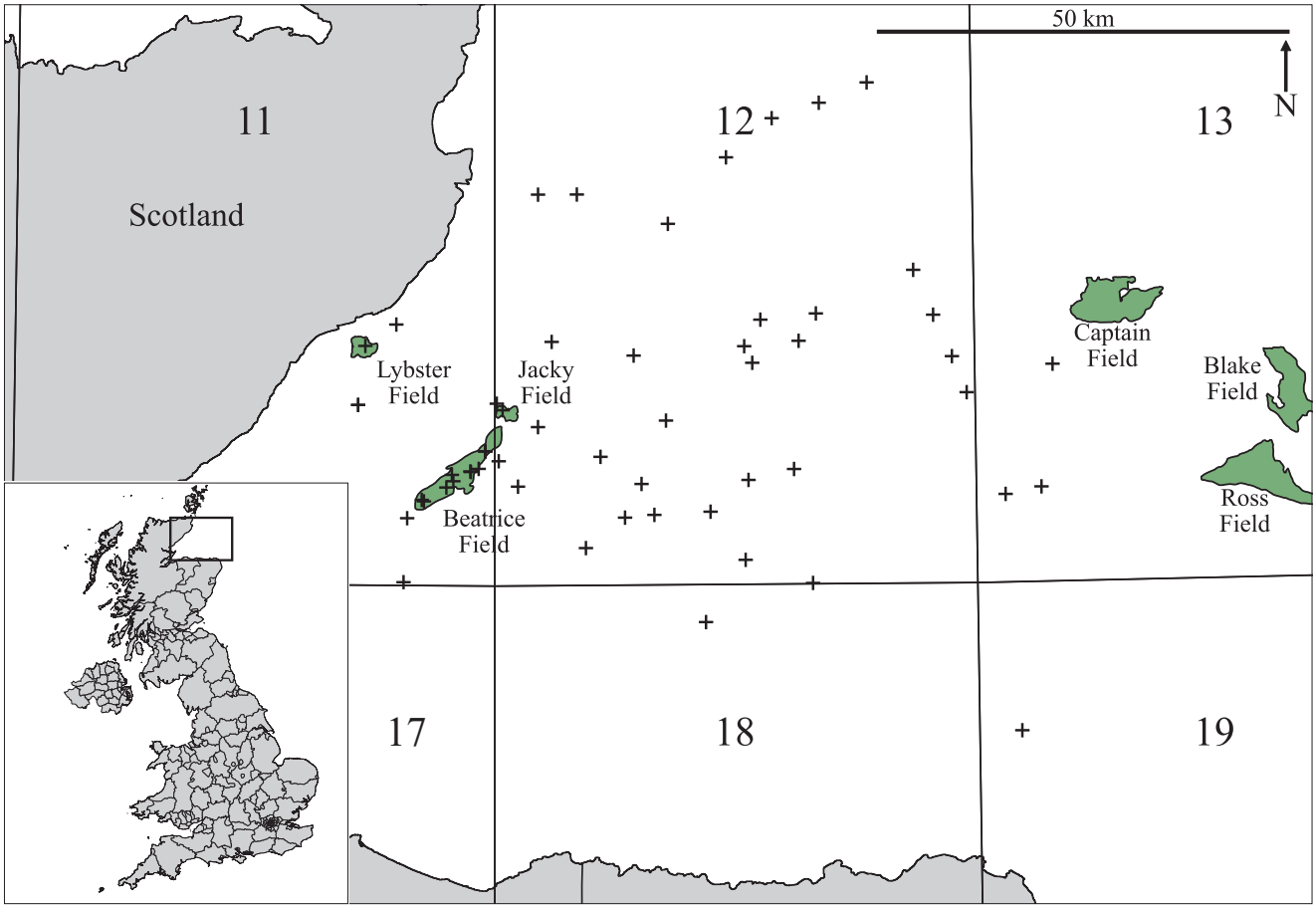


Figure 5.1: *Map of the study area in the Inner Moray Firth highlighting the positions of known hydrocarbon fields in the Inner and Outer Moray Firths and the wells used in this chapter's analysis.*

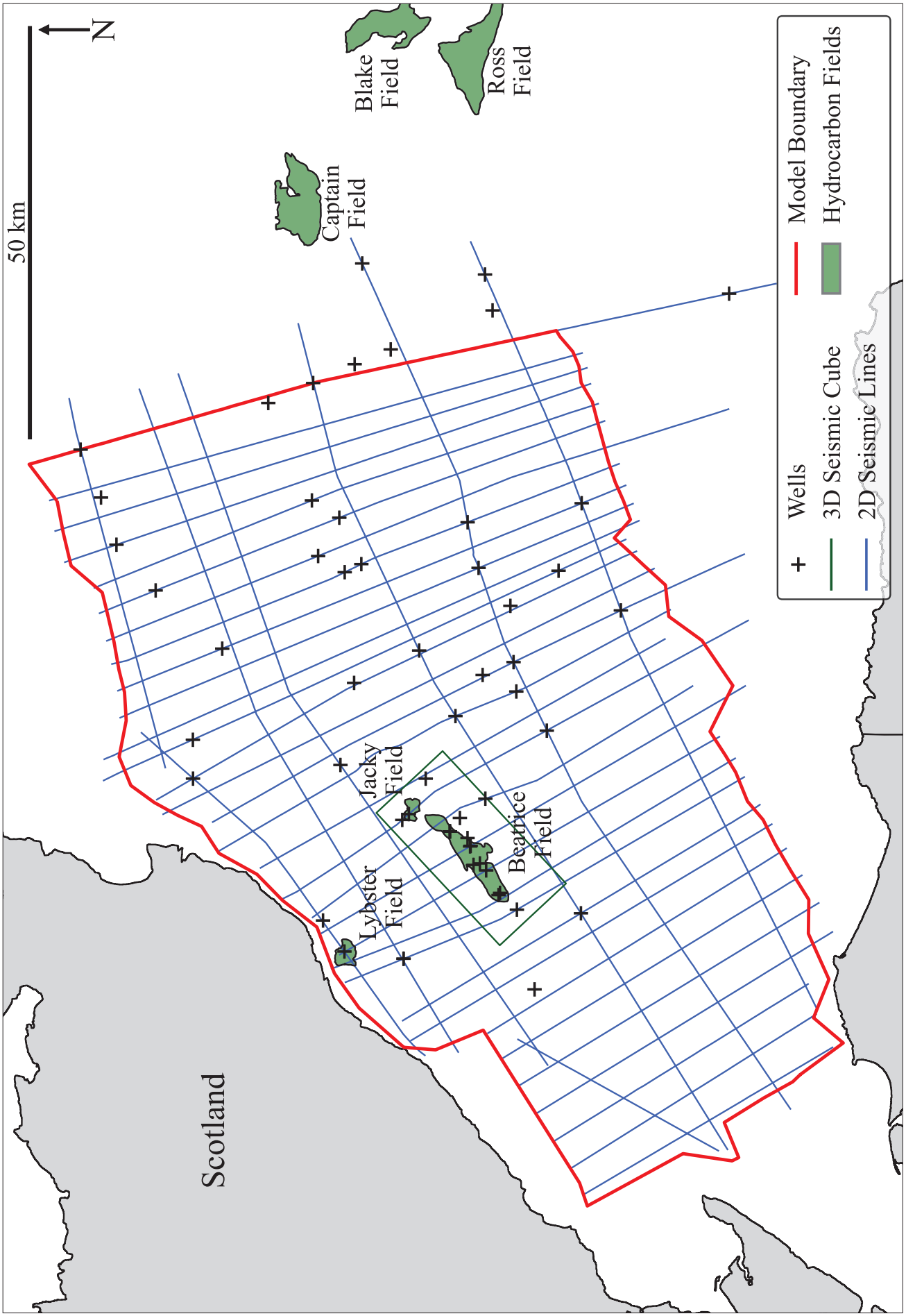


Figure 5.2: *Map outlining locations of wells and seismic lines in the IMF used within this study.*

Table 5.1: *List of wells in the IMF used in this chapter and study, delineated by the North Sea Quadrant in which they exist.*

Quadrant 11	Quadrant 12		Quadrant 13	Quadrant 18	Quadrant 19
11/24-1	12/13-1	12/24-1	13/21b-2	18/03-1	19/01-1
11/24a-2	12/14-1	12/24-3	13/26-1		
11/24b-4	12/14-2	12/25-1	13/26b-3		
11/29-1	12/16-1	12/25-2	13/30-3		
11/30-1	12/16-2	12/25-3			
11/30-2	12/17b-1	12/26-1			
11/30-4	12/18-1	12/26-2			
11/30-5	12/20b-1	12/26c-5			
11/30-6	12/21-1	12/27-1			
11/30-7	12/21-2	12/27-2			
11/30a-8	12/21-4	12/27a-3			
11/30a-9	12/21-5	12/27-4			
11/30a-10	12/22-1	12/28-1			
11/30a-A4	12/22a-4	12/28-2			
11/30a-B7	12/23-1	12/28-3			
11/30a-B9	12/23-2	12/29-1			
11/30a-B10	12/23-3A	12/29-2			

Within the IMF, there is a good distribution of wells in terms of both location and depth, with numerous wells running through the basin's entire stratigraphy from the Quaternary sediments to the Devonian and sometimes the Caledonian Basement. Depth is generally interest-dependant, with the majority of central IMF wells around Beatrice Field only drilled until they reach the Triassic, or wells along the Inner-Outer Moray Firth border which drill through the Cretaceous then stop in the Kimmeridge Clay or Heather Formations (Figures 5.3 & 5.4). Within this study, the wells of interest are all found in Quadrants 11 and 12, with Quadrant 17 not containing any wells, and all of 13, 18 and 19 being on the Inner-Outer Moray Firth border and out of seismic, and therefore model, range, thus ending up out of the study's area of interest.

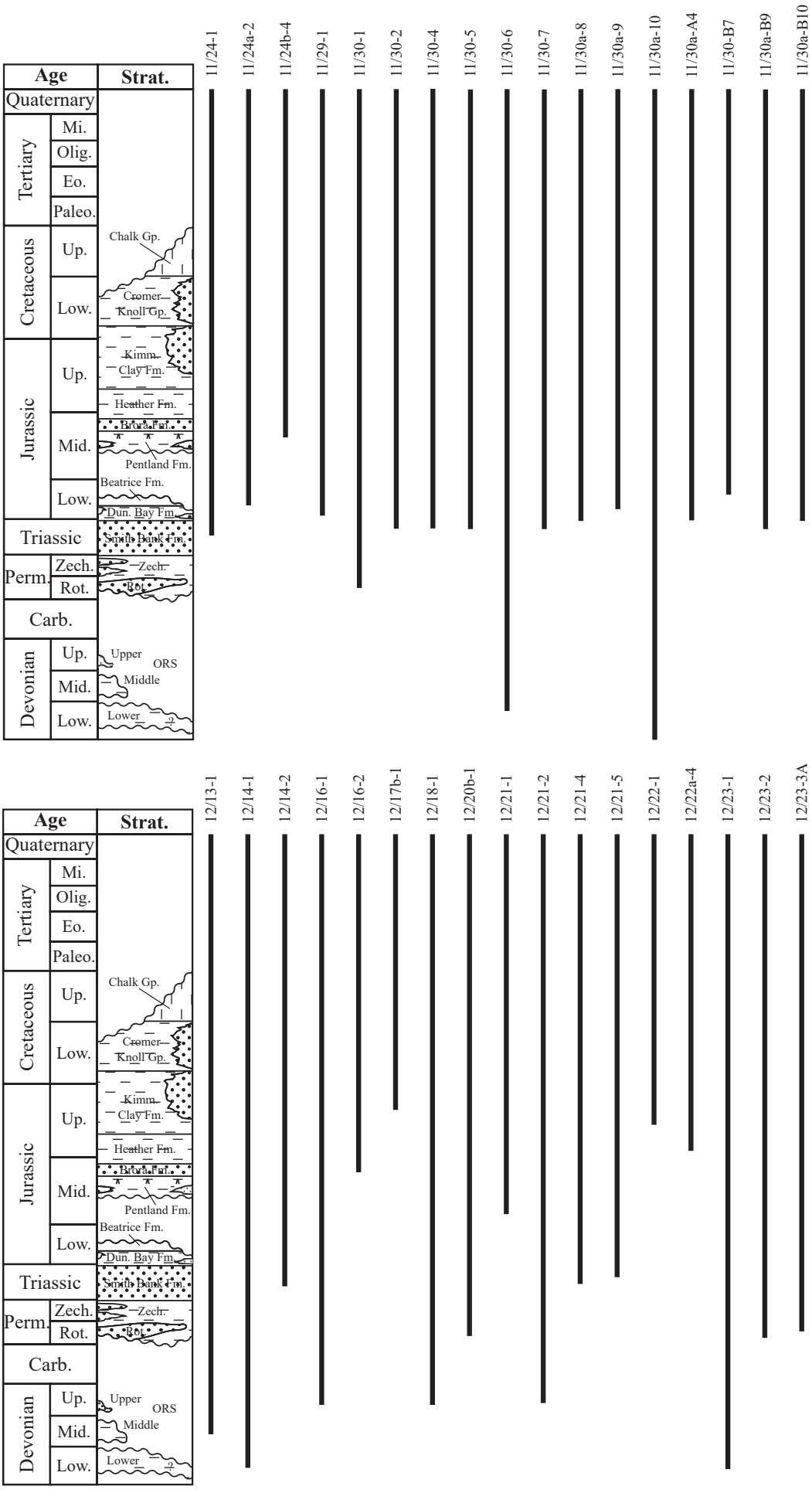


Figure 5.3: *Depth distribution diagrams of wells across Quadrants 11 and part of 12.*

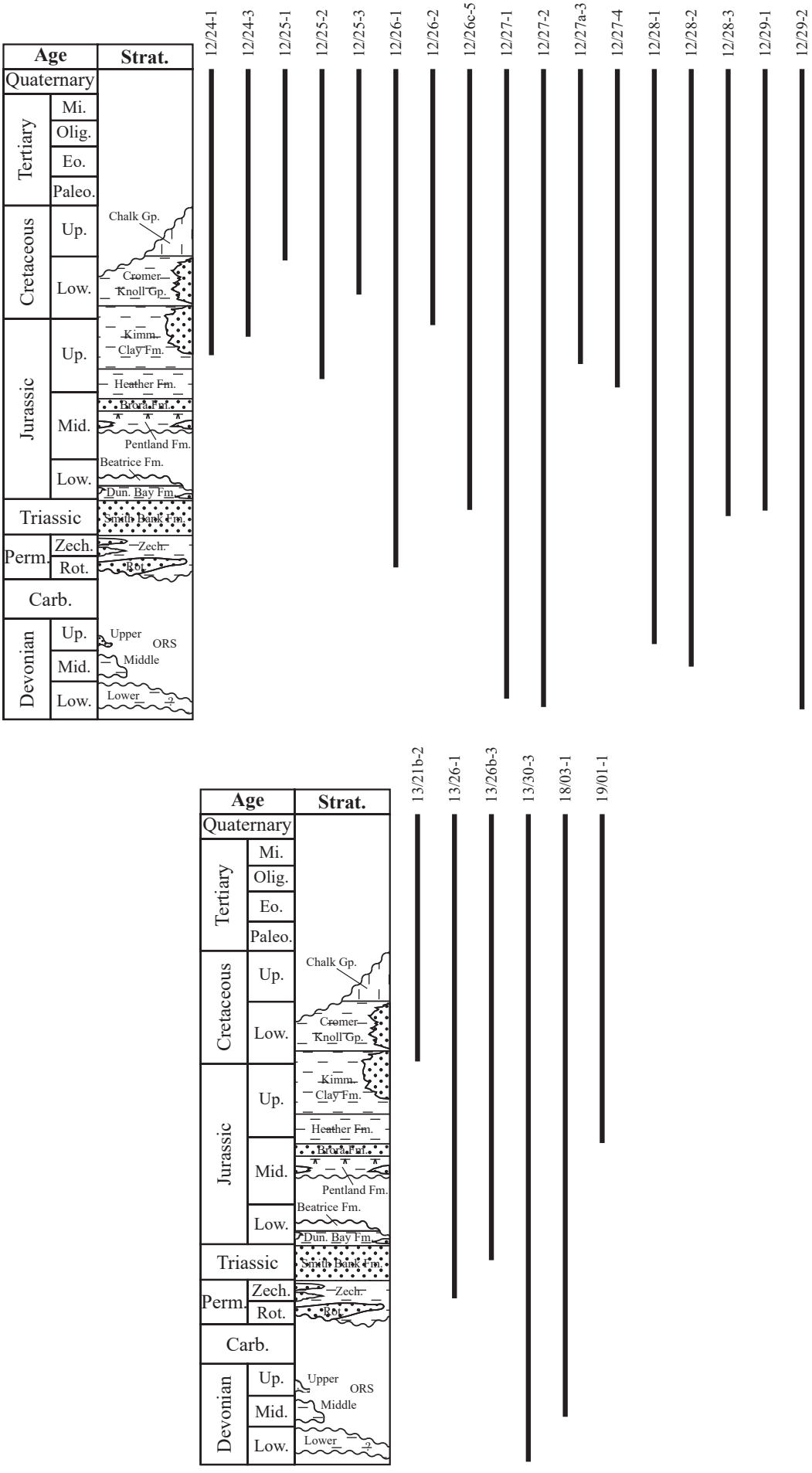


Figure 5.4: *Depth distribution diagrams of wells across part of Quadrant 12, Quadrants 13, 18 and 19.*

Within this chapter, a series of abbreviated terms are used in the various plots to identify the formations and age groupings being displayed. These are outlined here:

- **CKn** – Cromer Knoll
- **WSa** – Wick Sand
- **KCF** – Kimmeridge clay Formation
- **BlS** – Kimmeridge Black Shale
- **Hea** – Heather
- **ASa** – A Sand
- **MSh** – Mid Shale
- **BSa** – B Sand
- **BCo** – Brora Coal
- **Pnt** – Pentland
- **HSa** – H Sand
- **ISa** – I Sand
- **LWS** – Lady's Walk Shale
- **JSa** – J Sand
- **RBd** – Red Beds
- **Cht** – Stotfield Chert
- **Tri** – Triassic
- **Zec** – Zechstein
- **Rot** – Rotliegend
- **Dev** – Devonian

- **URe** – Upper Reservoir (A to B Sands, inclusive)
- **LRe** – Lower Reservoir (H Sand to Red Beds, inclusive)

5.2 | WELL LOG ANALYSIS

Well log analysis is a critical focus of geological appraisal as it is one direct way of analysing the formations seen within the study area through interpretable geophysical data. The data are collected in drilled wells, and comes in a variety of forms, though typically is presented in five major ways – gamma ray, sonic transit time, grain density, neutron porosity and fluid resistivity. Gamma ray logs show the measured volume of radioactive particles within the formation, and is the key method of analysing lithology, as shales and igneous and metamorphic rocks have high gamma ray values, whereas sands and carbonates have low gamma ray values (Bjorlykke, 2010; Gluyas and Swarbrick, 2004). Sonic velocity is the speed at which a sonic wave passes through the formation, and is used to test porosity and cementation, as increased grain or cement density will decrease both porosity and sonic velocity (Bjorlykke, 2010; Gluyas and Swarbrick, 2004). Density and neutron porosity have an inverse relationship, where density is the calculated density of the lithology and neutron porosity is the estimation of the percentage of pore space between grains, through the calculation of the volume of hydrogen atoms, which occur most typically in fluids held in the pore spaces, but can also be used to assess fluid types (Bjorlykke, 2010; Gluyas and Swarbrick, 2004). As such, increased density will typically result in decreased porosity and neutron porosity, and therefore these are plotted inversely to each other on log plots. Resistivity is the calculation of the electrical resistance caused by various fluids within different regions of the formation, and as such, is used to determine fluid contacts (e.g. the oil-water contact; OWC) (Bjorlykke, 2010; Gluyas and Swarbrick, 2004). This is done through two or three resistivity logs, one in the shallow, "invaded zone", typically in the first few inches of the formation away from the well, where water-based drilling mud has flushed the formation with water, and one in the deep, "virgin zone" where the pre-existing fluids are unimpeded by drilling activity (Bjorlykke, 2010). These two values can also be joined by a medium resistivity, but the variation between the two, or three, resistivities is what is interpreted - water has a lower resistivity than hydrocarbons (both oil and gas) and therefore where hydrocarbons exist, the deeper resistivity log will show higher responses than the shallow log, and the point where the two logs meet is the oil- or gas-water contact.

5.2.1 | LOG FORMATION INTERPRETATION

As shown in Figures 5.3 and 5.4, the majority of wells are drilled through the Jurassic reservoir and into the Triassic. Typically the Cretaceous deposits of the Cromer Knoll and Wick Sands are characterised by low gamma ray values indicative of very sandy lithologies, with the Kimmeridge Clay and Heather Formations showing higher gamma ray values indicative of shales (Table 5.2 & Figure 5.5). Within the reservoir section, from the A Sand into the Red Beds, the boundaries between the shales and the sands within the section are easily identified through the variations in gamma ray readings, as clearly seen at the boundary of the Heather Formation and A Sand at approximately 1860 m (Table 5.2 & Figure 5.5).

Within the lithology below the reservoir, from the Triassic into the Devonian, shales are dominant but interspersed with sands. Directly below the reservoir section, the Triassic is topped with the Stotfield Cherty Rock that acts as a clear marker bed for the remainder of the shale-dominated lithology (Figure

5.5). Whilst the Triassic and Permian sequences are shale-sand mixtures, there is a definitive change in gamma response at the Rotliegend-Devonian boundary, shown by a marked increase in gamma ray response seen in high-TOC shales. The only sequence with higher gamma ray responses is the basement, which is predominantly granitic (Table 5.2 & Figure 5.5).

The stratigraphy of the IMF is relatively consistent and the log responses seen within Figure 5.5 are commonplace across the well logs in the study. There is minimal variation in formation presence or log response, with the only clear variations being formation thickness and resistivity variations caused by the saturating fluids. Due to the consistency of the formations and the variations seen across the basin, averages of the logs across the IMF are also consistent, with the sandy formations consistently having gamma ray responses below 50 API, and shales increasing up to, and beyond 100 API (Table 5.2).

Table 5.2: *Table outlining the average responses of the well logs across formations in the IMF, from all the wells analysed in this study. The reservoir sands in the Mid Jurassic show generally much lower gamma ray responses that the other clay-rich formations such as the Devonian, LW Shale, Mid Shale and KC Black Shales.*

Formation	Gamma Ray (API)	Sonic (µs/ft)	Density (g/cm^3)	Neutron Porosity (dec)
Cromer Knoll	44.953	130.546	2.230	0.323
Wick Sand	54.174	115.392	2.272	0.294
Kimmeridge Clay	61.902	98.606	2.346	0.277
KC Black Shales	86.775	97.281	2.370	0.334
Heather	68.579	89.365	2.442	0.281
A Sand	36.194	72.169	2.448	0.142
Mid Shale	85.854	88.603	2.441	0.337
B Sand	49.944	77.037	2.466	0.222
Brora Coal	64.598	89.374	2.188	0.360
Pentland	65.204	76.311	2.434	0.233
H Sand	36.595	74.142	2.429	0.150
I Sand	39.438	73.924	2.443	0.150
LW Shale	85.960	77.408	2.500	0.252
J Sand	57.729	78.937	2.407	0.207
Red Beds	78.806	82.497	2.468	0.262
Stotfield Chert	50.932	85.170	2.369	0.191
Triassic	69.945	79.746	2.475	0.198
Zechstein	67.091	76.032	2.521	0.156
Rotliegend	53.584	77.094	2.414	0.156
Devonian	94.021	63.195	2.592	0.116
Basement	161.192	54.926	2.642	0.041

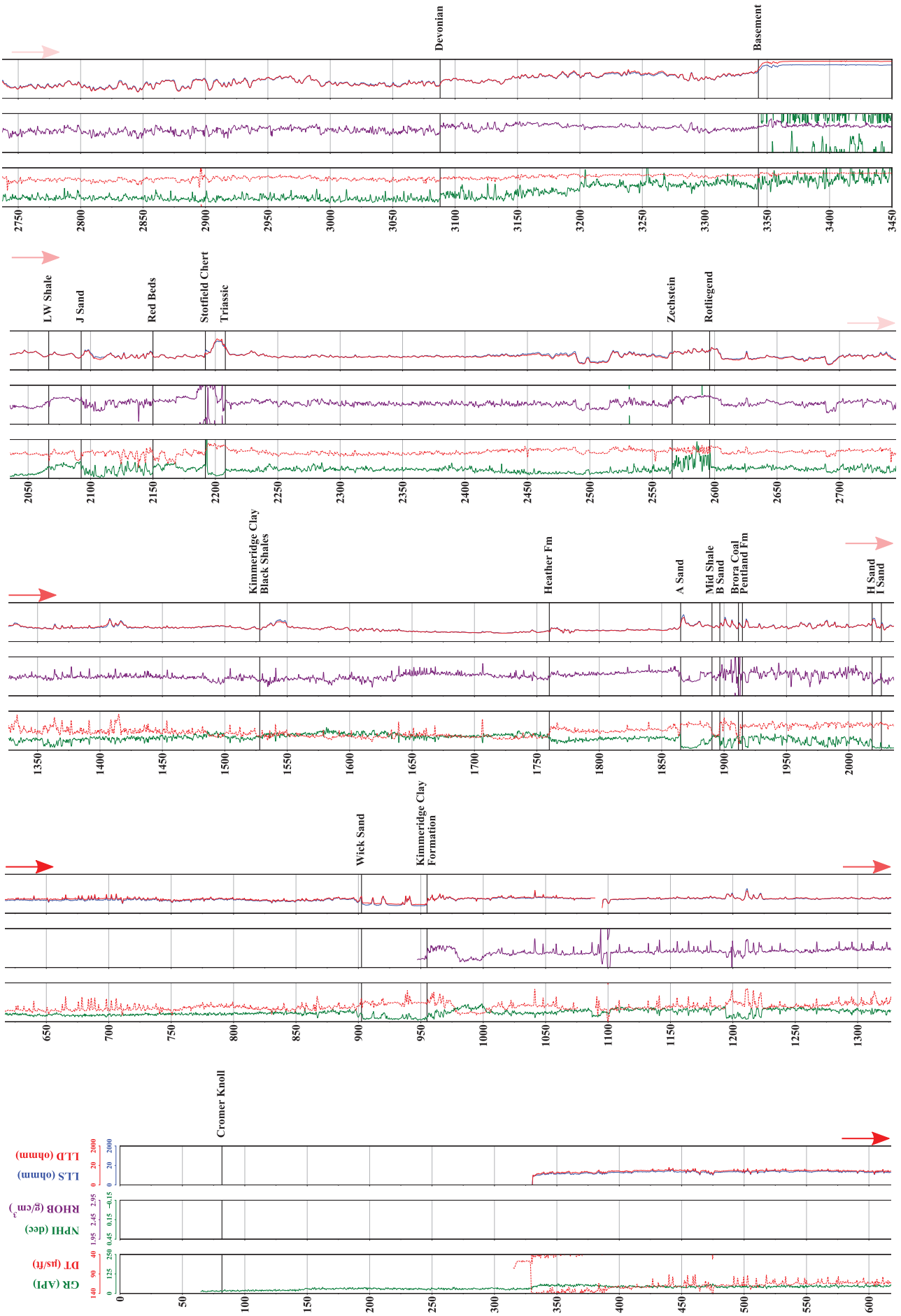


Figure 5.5: *Example well log responses derived by the geology of the IMF, evidenced by the well log from Well 11/30a-10 located in the Beatrice Field, with depth in metres MD brt.*

5.2.2 | SEDIMENTARY LOGGING

To ensure that the well log analysis accurately reflects the geology of the system, sedimentary logs were taken from several wells within the Beatrice Field region of the IMF from cores at the British Geological Survey's Core Store in Keyworth, UK. These were logged to analyse and interpret the lithology of the reservoir formations and to calibrate and correlate the well log analysis to direct observations within the basin. In total, three wells were logged – Wells 11/30-2, 11/30a-8 and 11/30a-B10 – however of these wells, only 11/30-2 was cored throughout the entirety of the reservoir section, with the core availability of the others being constrained to either the upper reservoir (11/30a-8) or the lower reservoir (11/30a-B10). Note that due to the age of the wells, wells drilled in the late 1960s and mid-late 1970s were measured in feet and all logging and sampling was carried out in feet, not metres, thus this has been continued both in the logging here and in the magnetic sampling in Chapter 6.

Within Well 11/30-2, the Heather Formation is quite fossil rich, containing belemnites, bivalves and evidence of ammonite imprinting, very similar to the Mid Shale that sits between the two uppermost reservoir sands, however, this also sees a shell bed and is more brown-grey rather compared to the Heather Formation's dark grey nature (Figure 5.6). The upper reservoir A and B Sands are somewhat similar, in that they contain shell beds and are mostly heavily oil-stained, fine to medium grained sands that grade into silts at their base (Figure 5.6). The Pentland Formation, topped by the coal-bearing Brora Coal, is dominated by clay particles within hard, fissile, mid- to light-grey shales, with increasing sand interbeds as it increases with depth.

Below the Pentland Formation in Well 11/30-2, within the lower reservoir section, good quality sands dominate the H Sand, with these grading into shell bed-rich I Sand silts which grade into the dark grey shales and clays of the Lady's Walk Shale (Figure 5.6). The J Sand, whilst showing sand, appears to contain more silt content and what sands exist are consolidated and likely cemented. Overall, the log reflects a distinctive lower reservoir quality than the upper reservoir section, however the beds are thicker and the H Sand does offer some good reservoir properties.

Within the other wells, 11/30a-8 and 11/30a-B10, the lithologies seen within the logged core is broadly similar to those in Well 11/30-2 (Figure 5.7). The Heather Formation is fossil-bearing shale, the A Sand is a high quality reservoir sand and the B Sand is of mixed quality, whilst the Pentland Formation is a mix of sands and shales, and the lower reservoir is mixed quality also. The main difference in the wells seems to be the varying sand-silt mix within the H and I Sands, the fossil presence within the Lady's Walk Shale in Well 11/30a-B10, and the higher quality reservoir sands in the J Sand of 11/30a-B10 (Figure 5.7).

The sedimentary logs align very well with the well log gamma ray data, with the varying lithologies initially analysed in the well logs being reflected in the cores. The variable reservoir quality seen within the J Sand, as well as the Pentland Formation, which despite being a source has the sand interbeds that act as reservoir units, is reflected in both analytical methods, and the lack of logged cores across the rest of the basin is not significant.

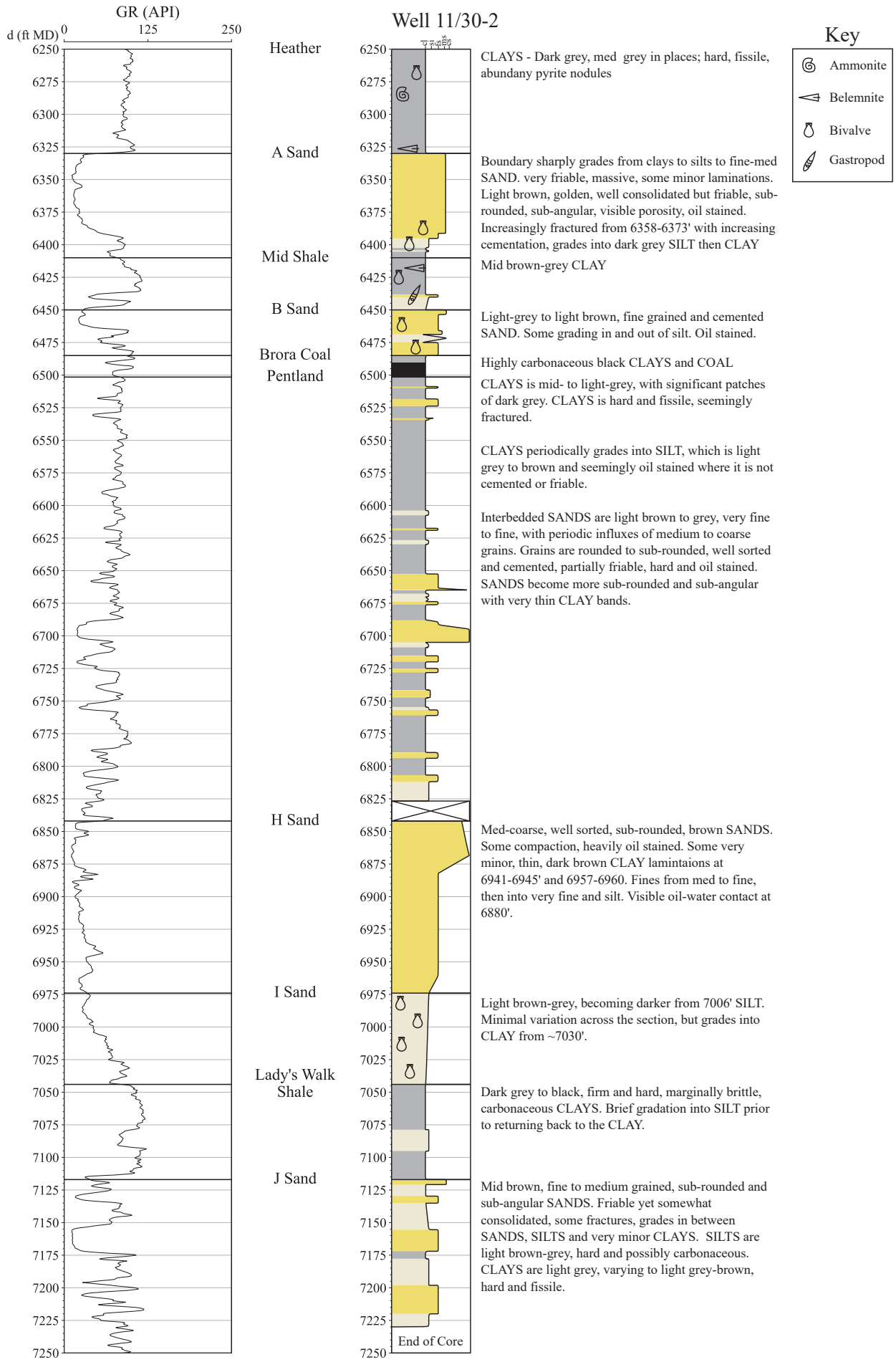


Figure 5.6: *Gamma ray well log and interpreted log through the reservoir section of Well 11/30-2 within the Beatrice Field, logged using symbols from Tucker (2011). Depths in feet MD brt.*

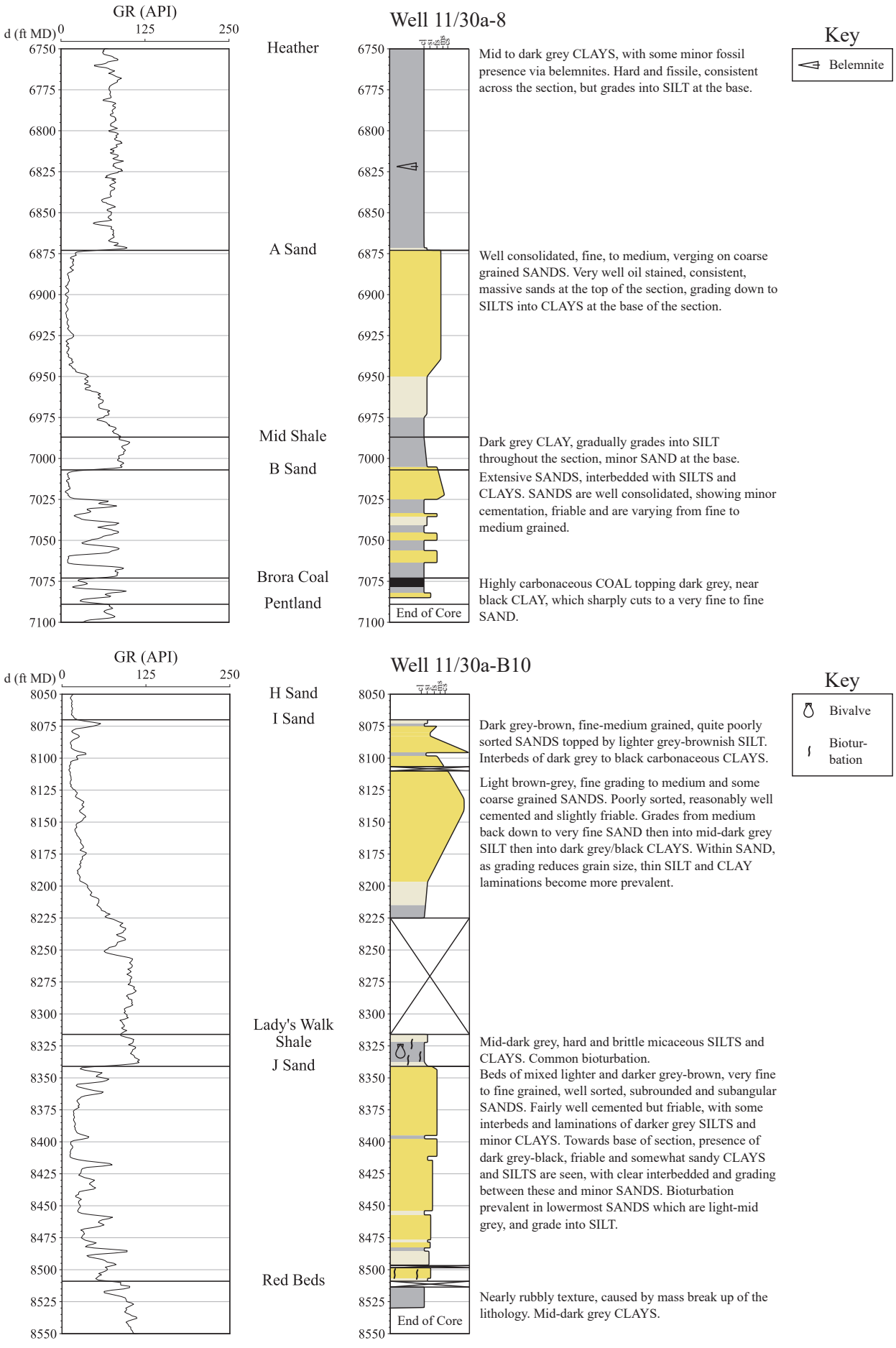


Figure 5.7: *Gamma ray well log and interpreted log through the reservoir section of Wells 11/30a-8 and 11/30a-B10 in the Beatrice Field, logged using symbols from Tucker (2011). Depths in feet MD brt.*

5.2.3 | OWC INTERPRETATION

Identification of OWCs within the wells of the IMF was critical to this study, both to understand how the magnetic minerals vary across the fluid contacts, but also to control and analyse the petroleum systems modelling results. Interpretation of the OWCs was carried out in two forms - firstly through analysis of well logs, and secondarily through visual analysis of core. Well log OWC interpretation, as outlined previously, can be done through repeat formation tests, but in this study is done through resistivity logs, where a separation in deep (higher, hydrocarbon-saturated) and shallow (lower, water-saturated) resistivity logs indicates a difference in formation fluids, and where these meet is the OWC (Figure 5.8; Bjorlykke (2010)). Whilst this is a good method of identifying OWCs, it ideally needs thick sand bodies, it can be open to interpretation, and localised sand bodies can create misleading contacts away from the main OWC. Furthermore, well log resolution is typically 0.5 ft (15 cm), which is coarser than magnetic variations, which can occur on a centimetre scale. As such, where possible, core analysis was used to identify OWCs, and where required, both calibrates and supersedes the well log interpretation.

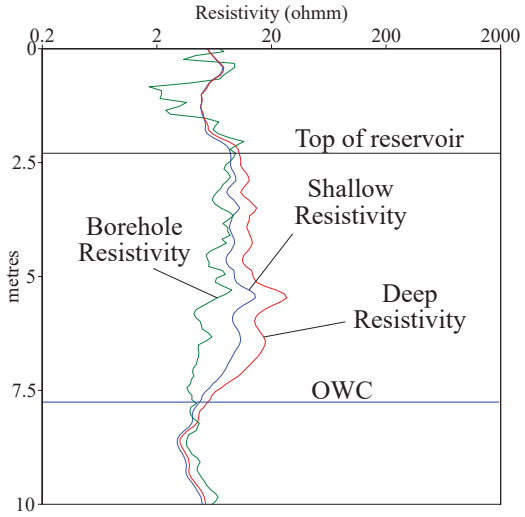


Figure 5.8: *Example well log from Well 11/30a-8 showing resistivity logs and their use in estimating the well's OWC.*

Across the cores analysed, the variation between visual and logged OWCs was minimal (within 1 m), however this, as previously mentioned, can cause issues with magnetic analysis sampling. Within visual analysis, the change in saturating fluid is very obvious, as oil-saturated sands are a dark brown, verging on black, and smell heavily of hydrocarbons, whereas clean (water-saturated) sands are a pale yellow, or sometimes golden colour, although this varies by lithology. When analysing the core, OWC identification is simply a case of finding the boundary between the oil-stained and clean sands (Figure 5.9), which can either be very sharp, with a gradational boundary less than 2 cm wide, or more of a zone, which can be up to 5 m or greater.



Figure 5.9: *Annotated photograph of core from the IMF, showing the variations seen in oil- and water-saturated sands and the location of the OWC.*

In this study, several wells from across the basin were highlighted and sampled to carry out the magnetic analysis shown in Chapter 6. The majority of these wells were chosen as they contain visible OWCs that could be sampled, that were caused by both reservoir trapping and localised lithological trapping, although other non-OWC-bearing wells were also analysed. Chapter 6 will cover this in greater detail, however Table 5.3 outlines those OWC-bearing selected wells, the depths of the OWCs and what formations they exist within, whilst Figure 5.10 shows their locations.

Table 5.3: *Table outlining the wells containing OWCs that were selected for analysis in this study.*

Well	Region of the IMF	Formation(s) containing the OWC	OWC depth, ft MD (& m TVD)
11/24-1	Lybster Field	B Sand	4948.0 (1506.65)
11/24a-2	Central NW	A Sand	6130.0 (1863.02)
11/30-2	Beatrice Field	A Sand & H Sand	6385.0 (1943.65) & 6879.0 (2094.22)
11/30a-8	Beatrice Field	A Sand	6925.0 (2110.24)
11/30a-B10	Beatrice Field	I Sand & J Sand	6643.0 (1716.15) & 6753.0 (1740.46)
12/21-2	Jacky Field	B Sand	7118.0 (2169.27)
12/25-3	East IMF, on OMF border	Cromer Knoll	5603.0 (1706.29)
12/27-1	South-east of IMF	Pentland	3735.8 (1138.47)
12/27-2	South-east of IMF	B Sand	5207.8 (1587.09)
12/29-1	South-east of IMF	Heather	6921.95 (2109.75)

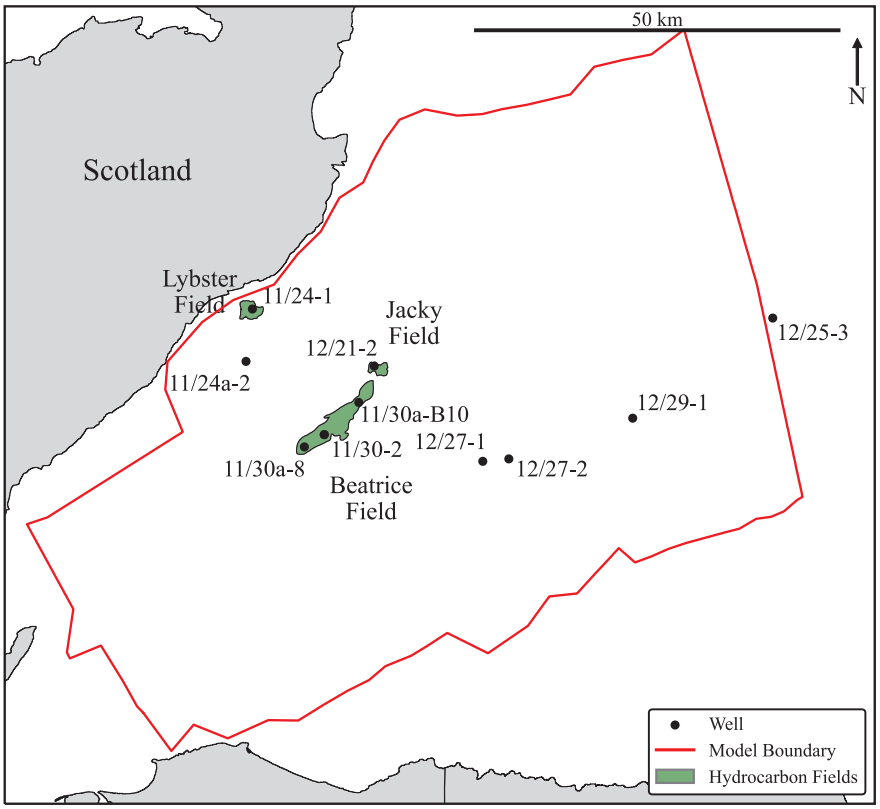


Figure 5.10: *Map of the IMF showing the selected wells with OWCs, as per Table 5.3.*

5.2.4 | LOG CORRELATION

Well correlation is critically important to determine how lithologies vary across the study area, and most crucially within this study it focusses on a NW-SE transect through the centre of the basin, cutting orthogonally across the IMF (Figure 5.11). Due to the lack of wells drilled in the SW area of the basin, correlation here was not possible, and as a result, correlation is heavily skewed by the significant depth variations produced by the structurally complex nature of the eastern half of the basin. Correlation, therefore, focusses on a series of four wells through the centre of the basin – from Well 11/24-1 in Lybster Field, through Well 11/30a-10 in Beatrice Field, towards 12/27-1 then 12/29-1 in the SE of the basin.

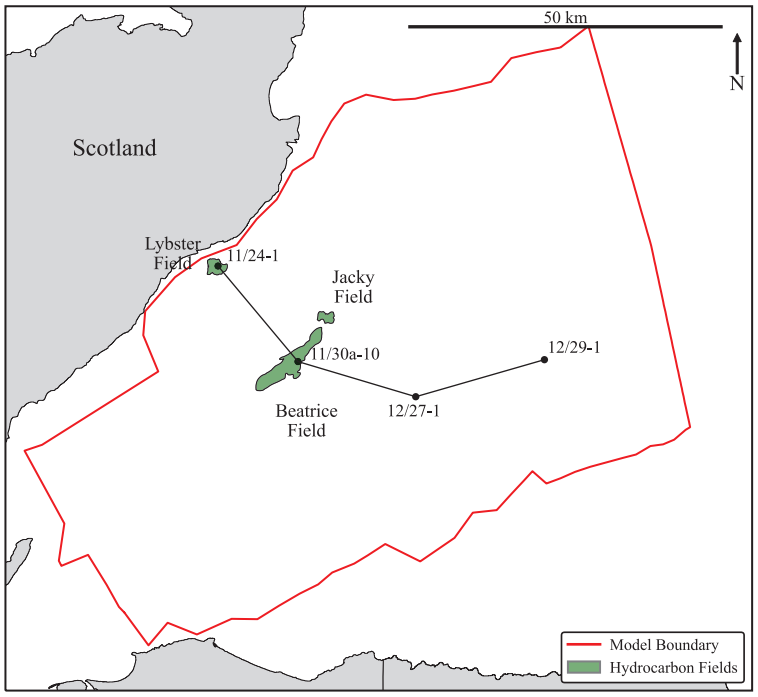


Figure 5.11: *Map showing the location and line of the wells used in the well log correlation in Figure 5.12 relatively to the IMF, the hydrocarbon fields and the BPSM model.*

Well correlation shows consistency in all lithologies regardless of location, with the dominant variations in the formations being thickness and depth, caused by the basin's structure (Figure 5.12). The Cromer Knoll Group and Kimmeridge Clay Formation are a mix of sandy shales and clay-rich sands, separated by the clean sand of the Wick Sand at the Base Cretaceous Unconformity (BCU). The Kimmeridge Clay Black Shales show high gamma ray responses, typical of an organic-rich shale, and overlay the sandy, shale-dominant, hydrocarbon-sealing Heather Formation. Below these are the relatively much thinner, clean upper reservoir sands, with the Pentland Formation and Lower Reservoir sections showing comparatively increased shale content. Below these is the very thin chert of the Stotfield Chert which sharply transitions into sandy Triassic sediments, shale- and salt-rich Zechstein lithologies and then clay-rich sands and sand-rich shales of the Rotliegend lithologies. Beyond the Rotliegend, the Devonian flagstones and fish beds are strongly clay and organic matter-dependant, resulting in the high gamma ray responses, followed by the even higher gamma ray responses of the basement.

Despite the main difference being formation thickness and depth, another clear difference is the lack of post-Kimmeridge Clay sediments in Well 11/24-1 (Figure 5.12). This is due to movement of the GGF and associated loss of shallow sediments during the late stage erosion. Furthermore, minor variations are seen within the lithologies, predominantly in those above the reservoir, with the Heather in Well 11/24-1 being a lot sandier than in the other wells, but still being based by a hydrocarbon-sealing shale. The Kimmeridgian Black Shales also vary in gamma ray response, likely as a result of varying organic matter maturity between the shallower, less mature regions, and the deeper, more mature regions.

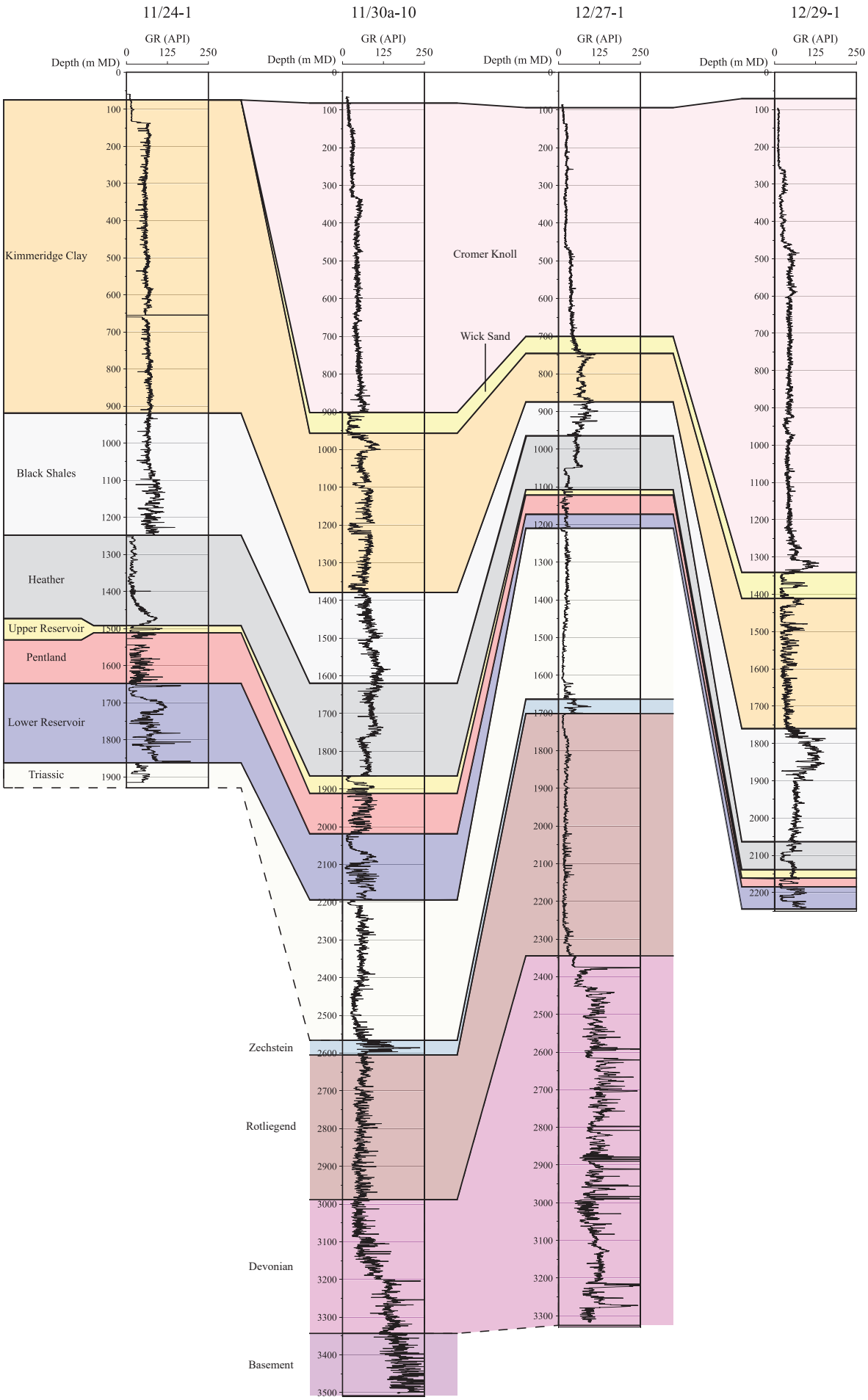


Figure 5.12: *Log correlation across the wells identified in Figure 5.11, showing the consistent presence of formations in the IMF, controlled mainly by depth not thickness. Depth is in metres MD brt.*

5.2.5 | LOG CROSSPLOTS

Well log crossplots are used widely in geological analyses as a method of double-checking well log interpretations and refining the understanding of formations and how they vary. Crossplots aim to identify the formation variations in broad senses, showing the variations across the entirety of the basin through gamma ray (GR), sonic transit time (DT), density (RHOB) and neutron porosity (NPHI) well log data. The majority of lithologies in the IMF are consistent across the basin, with little lithological variation, however minor localised changes are expected and seen, such as alterations in sand-clay ratios within the reservoirs, evidenced by changes in GR and DT responses, increasing cementation at depth, evidenced by varying DT responses, varying total organic carbon (TOC) through source rocks, evidenced by GR and RHOB variations, and sand influxes into sealing shale formations. *M-N* plots investigate lithological variations through multiple well log datasets, through the difference between sonic velocity-estimated porosity (M) and neutron porosity-estimated porosity (N). Originally developed by Burke *et al.* (1969) and further outlined by Morton-Thompson *et al.* (1993), the *M-N* plot shows binary and ternary mixtures of minerals via well log data through two equations (Equations 5.1 & 5.2).

$$M = \frac{\Delta t_{fl} - \Delta t_{log}}{\rho_{log} - \rho_{fl}} \times 0.01 \qquad (5.1) \qquad\qquad N = \frac{\phi N_{fl} - \phi N_{log}}{\rho_{log} - \rho_{fl}} \qquad (5.2)$$

Δt_{fl} and Δt_{log} are the sonic velocities of the formation fluid and the logged lithological value, ρ_{fl} and ρ_{log} are the densities of the formation fluid and logged lithological value and ϕN_{fl} and ϕN_{log} are the neutron porosity values of the formation fluid and logged lithological value, respectively. In the M equation, multiplication of the result by 0.01 is to bring the value to the same order of magnitude as the N result. Fluid values are slightly different between freshwater and saltwater, where freshwater sonic velocity, density and neutron porosity are 189 µs/ft, 1.00 g/cm^3 and 1.00, respectively, whereas saltwater sees a slight change to 185 µs/ft, 1.1 g/cm^3 and 1.00, respectively (Burke *et al.*, 1969; Morton-Thompson *et al.*, 1993).

M-N plots in this study, based on freshwater formation fluid calculations, analyse the formations of the IMF split into both "sandy" (dot) and "shaley" (cross) log responses, using a gamma ray threshold value of 50 API to separate the sandier and carbonate components with the shalier and hard rock components of each formation (Table 5.4). The limitations of this *M-N* method are centred around not all formations having both "sandy" and "shaley" lithologies, skewing the average *M-N* values towards the smaller datasets, evidenced most clearly by the Devonian and Basement. Furthermore, not all formations are solely "sandy" or "shaley", exemplified by the Basement, Zechstein and Stotfield Chert formations, identifiable by granitic gneiss, salt and cherty components, respectively. As such, some inaccurate interpretations of these formations occur when analysing them within the plot (Table 5.4). Lastly, with not all wells drilled through all formations, sample numbers are skewed towards the wells where these formations have been drilled, limiting the ability to analyse cross-basin formation variations.

Despite the limitations, clear conclusions can be drawn from the *M-N* plots (Table 5.4; Figure 5.13). The mean M and N values of the reservoir sands all plot within the sandstone region, providing further evidence of their relatively clean sand nature (Figure 5.13b). However, as the various whole-data

Table 5.4: *Table showing the data input numbers and resultant outputs of the M-N calculations carried out on the formations within the IMF. Note that the M and N values are dimensionless.*

Formation	Number of data points			Sand		Clay	
	Total	Sand	Clay	M	N	M	N
Cromer Knoll	52297	35766	16531	0.571	0.588	0.329	0.509
Wick Sand	7584	4189	3395	0.777	0.597	0.361	0.513
Kimmeridge Clay	65990	23830	42160	0.722	0.595	0.643	0.509
KC Black Shales	21829	2968	18861	0.804	0.585	0.654	0.477
Heather	28738	9076	19662	0.819	0.592	0.641	0.466
A Sand	2563	1886	677	0.828	0.617	0.767	0.536
Mid Shale	1066	119	947	0.817	0.590	0.689	0.447
B Sand	2601	1413	1188	0.804	0.586	0.738	0.48
Brora Coal	753	207	546	0.914	0.623	0.900	0.551
Pentland	14024	4252	9772	0.805	0.594	0.806	0.522
H Sand	2259	1831	428	0.818	0.613	0.753	0.527
I Sand	3119	2350	769	0.816	0.617	0.748	0.515
LW Shale	2891	270	2621	0.764	0.576	0.755	0.498
J Sand	4759	1980	2779	0.825	0.611	0.766	0.538
Red Beds	4393	328	4065	0.772	0.552	0.734	0.505
Stotfield Chert	37706	19771	17935	0.804	0.598	0.705	0.583
Triassic	1714	308	1406	0.802	0.594	0.725	0.534
Zechstein	11659	3743	7916	0.774	0.563	0.733	0.555
Rotliegend	48010	19841	28169	0.805	0.595	0.788	0.602
Devonian	40269	2564	37705	0.816	0.613	0.795	0.556
Basement	1996	42	1954	0.763	0.422	0.819	0.589

plots show, there is some degree of fluctuation and periodic, localised drift into the shale region (Figure 5.13ASa, BSa, HSa, ISa and JSa). The results of several formations are inconclusive, due to both lithology variations not adhering to the plot segments (Chert, Zechstein), or vast number of data points (Cromer Knoll). Within numerous formations, there is evidence of both calcite and carbonates (most clear in the Chert, Zechstein and Rotliegend), as well as some evidence of secondary porosity (evidenced most clearly in the Brora Coal and Pentland). Curvature of the data points from the sand region into the shale infers the presence of increased cementation, with this identifiable most clearly here in the Chert and Zechstein, but also partially in the H, I and J Sands (Figure 5.13, Chakraborty *et al.* (2015)). The flagstone-dominated Devonian, containing the mixture of hydrocarbon-generating shales, carbonates and sands, is plotting mostly within the sand region, but shows influences of carbonates and most significantly, both secondary porosity and gas or salt. With no geological evidence of salt in the Devonian, it can be inferred that this data grouping is gas-enriched Devonian strata, formed as a result of overmaturing of the Devonian source rocks, and the secondary porosity may well be a result of weathering and/or erosion, suggesting that there could be some gas accumulations in the Devonian sequences in the IMF, although this plot is the only evidence for this (Figure 5.13Dev).

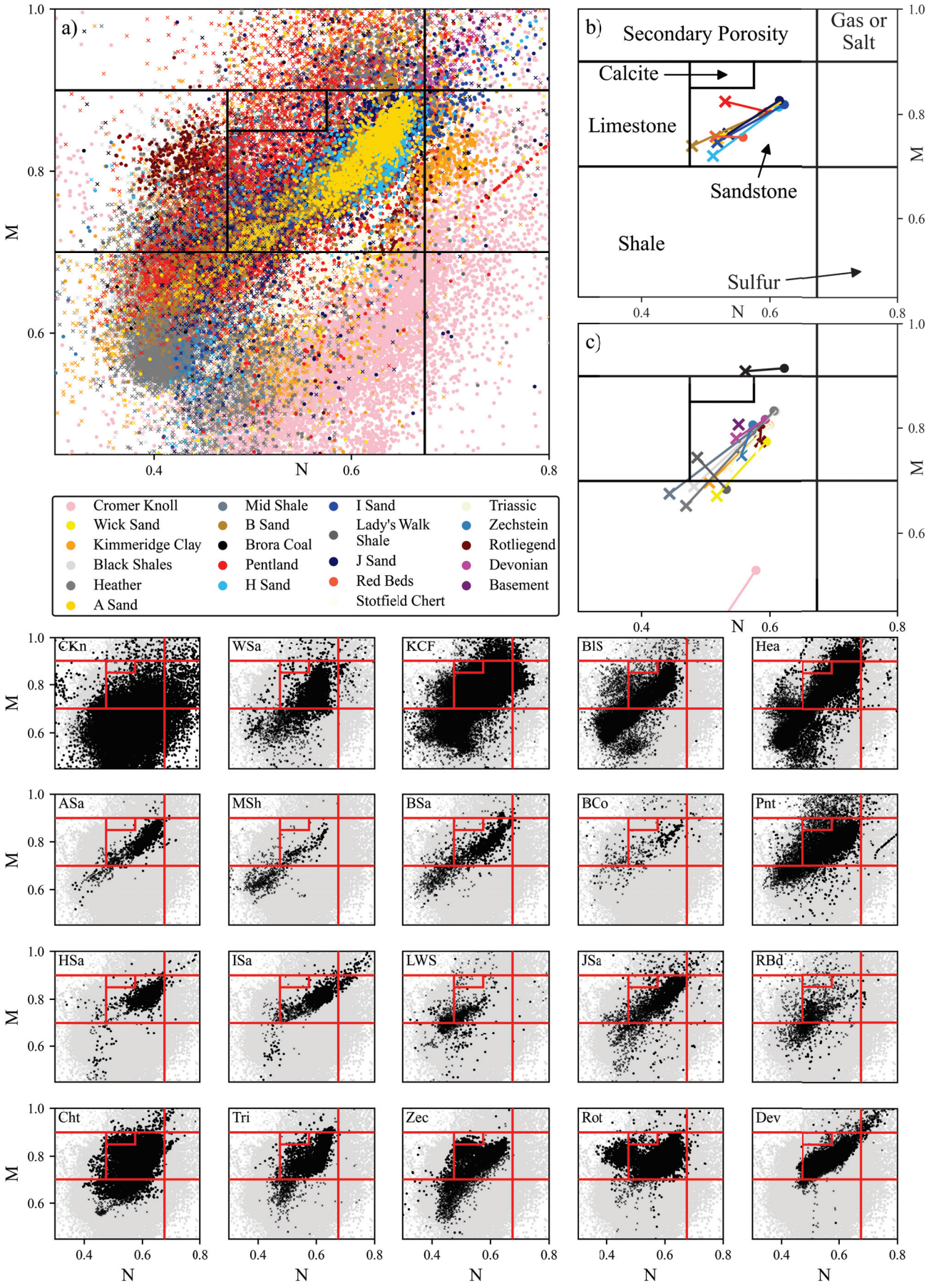


Figure 5.13: *Petrophysical crossplots of the M-N ratio in the formations within the IMF. a) shows all datapoints across all formations, b) shows the mean values and tie lines of sand-shale relationships of the reservoir formations, c) shows the non-reservoir formations' means and sand-shale tie lines. The following sequence of plots show formation-separated data distributions.*

5.3 | SEISMIC DATA ANALYSIS

Analysis of well log-calibrated seismic data is the foundation of both the geological and basin and petroleum systems models in this study. It involves the interpretation of seismic datasets to highlight faults and lithological packages, thus creating the framework of the basin within computational space, giving insight into the basin's structure and history, formation presence and thickness variation, and can also indicate any leaking hydrocarbons.

The seismic dataset, shown previously in Figure 5.2, was acquired in 1997 and comprises numerous two dimensional (2D) seismic lines across the majority of the IMF, and a three dimensional (3D) cube across the Beatrice and Jacky Field region. Due to the data being predominantly 2D, whilst there is good coverage across the basin, there are limitations surrounding the interpretations carried out due to the extensive and consistent gaps between the lines, potentially hiding crucial information such as an extra fault or formation pinch out.

This section covers seismic data interpretations and analyses done in this study, including showing select seismic lines and associated interpretations, indicating how the basin evolves as it stretches from near-coast in the west, through the basin centre and eastward towards the northern North Sea. Furthermore, it also shows the depth maps of the formations of the basin created as a result of the interpretations, and the fault framework which outlines the faults and their widespread presence across the basin.

5.3.1 | WELL-SEISMIC TIES

In geological analysis, it is important to connect the well analysis to the seismic analysis, as without this connection, incorrect interpretations and conclusions could be made. The method of connecting well and seismic data is through well-seismic ties, and the production of synthetic seismic traces from well log data. Well-seismic ties are also crucial to producing accurate time-depth conversions of seismic data, which is collected in a time domain and requires converting into metres depth below zero, however as the seismic data in this study was provided already depth-converted, as previously mentioned, this was not necessary here (Simm and Bacon, 2014).

The production of synthetic traces begins with sonic and density well logs, which are used to calculate acoustic impedance. Acoustic impedance is the resistance by the geology to the sound waves produced by the sonic log, which are typically continuously resampled during down-log calculations to remove minor anomalies (Badley, 1985; Becquey *et al.*, 1979; Simm and Bacon, 2014). The variations in the resampled acoustic impedance down-log are most often caused by changes in geology and bedding planes, with these commonly occurring at formation boundaries, and are then used to calculate a reflection coefficient. The reflection coefficient is the relative change in acoustic impedance down-well and directly leads into the formation of a synthetic trace. This synthetic trace can then be directly linked to its relative location within a seismic dataset and the interpretations taken from it and any initial seismic interpretations can be compared and used to improve either one, or to develop a time-depth relationship (TDR), which is required to depth-convert the seismic dataset (Simm and Bacon, 2014).

In this study, a well-seismic tie was undertaken on Well 11/30a-10, situated within the Beatrice

Field, with this well chosen for its location, in the centre of the basin, in an area of significant interest and on a 2D seismic line, and also because it was logged throughout the basin's entire section, from the surface to the Basement. Within the well-seismic tie, successful production of the synthetic trace resulted in strong correlation between the synthetic trace and the seismic data traces (Figure 5.14). The positive peaks and negative troughs of the reflection coefficient, and its produced synthetic trace, align with those seen in the seismic data, and both successfully align with the picked well tops and associated seismic interpretations. The main downside to the well-seismic tie within this study is the comparative resolutions between the well log data and the produced synthetic trace and the seismic data, the former of which is high quality, sub-1 m resolution, and the latter two are lower resolution, with resolutions closer to 20 m and greater, due to the lower relative resolution of the seismic dataset (Figure 5.14).

The resolution of the seismic data is approximately 20 m, lower than the reservoir features of the IMF (Figure 5.15). Due to the data being depth converted prior to being procured for this study, and a lack of processing report being available, accurate definition of the trace frequency and therefore resolution is not possible, due to a lack of the time data required to calculate the wavelength of the data. However, seismic resolution is calculated through the following equations, where λ is wavelength, V is wave velocity and F is frequency (Simm and Bacon, 2014):

$$\lambda = \frac{V}{F} \qquad (5.3) \qquad\qquad Resolution = \frac{\lambda}{4} \qquad (5.4)$$

Despite being unable to accurately calculate the resolution of the seismic survey, estimates can be gleaned by analysing the seismic data and measuring the thicknesses of the waves. Figure 5.15 shows that the wavelength between two peaks is approximately 80 m, and therefore, using Equation 5.4, the seismic resolution is approximately 20 m. Consequently, whilst this resolution is adequate for interpreting thick sequences, it lacks the refinement required to successfully differentiate the formations of the reservoir section, which is required for accurate modelling (Figure 5.15).

5.3.2 | SEISMIC DATA INTERPRETATION

Interpretation of the seismic data, through both well-seismic ties and seismic trace amplitude analysis, is a critical component of this study and was carried out on all forty 2D seismic lines and every tenth trace within the 3D cube. This section covers the results of the seismic analysis through three of the seismic lines, one through the south west of the IMF, one through the centre, and one through the north east (Figure 5.16). Seismic interpretation is reasonably clear and possible in the shallower formations, from the Cromer Knoll, at seabed, down to the Triassic, however the seismic quality decreases dramatically below this, with interpretations of the Devonian and Basement being difficult and relying heavily on well control. As previously discussed, seismic resolution is low and accurate interpretation of the reservoir sequences is difficult, thus the figures below only highlight the "reservoir section", which covers the sequences between the Top Reservoir (Top A Sand) and the base of the Red Beds (Top Triassic), however seismic interpretation was split into three sections – the Upper Reservoir, grouping the A Sand, Mid Shale and B Sand; the Pentland Formation; and the Lower Reservoir, grouping the H and I Sand, Lady's Walk Shale, J Sand and Red Beds.

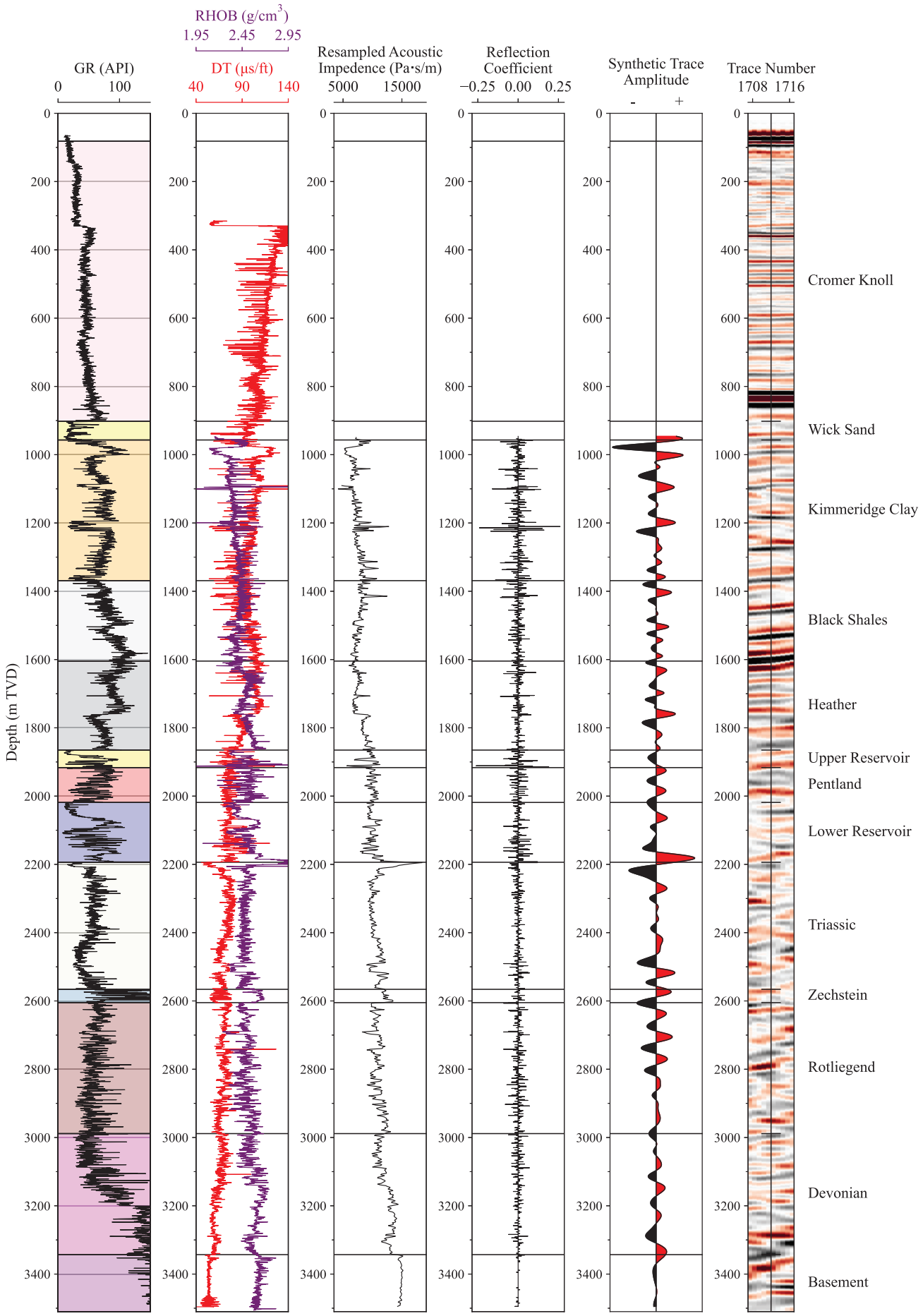


Figure 5.14: *Well-seismic tie of Well 11/30a-10, showing the well log plots, the synthetic seismic trace and the relevant position within the seismic survey, with additional traces either side, shown for context.*

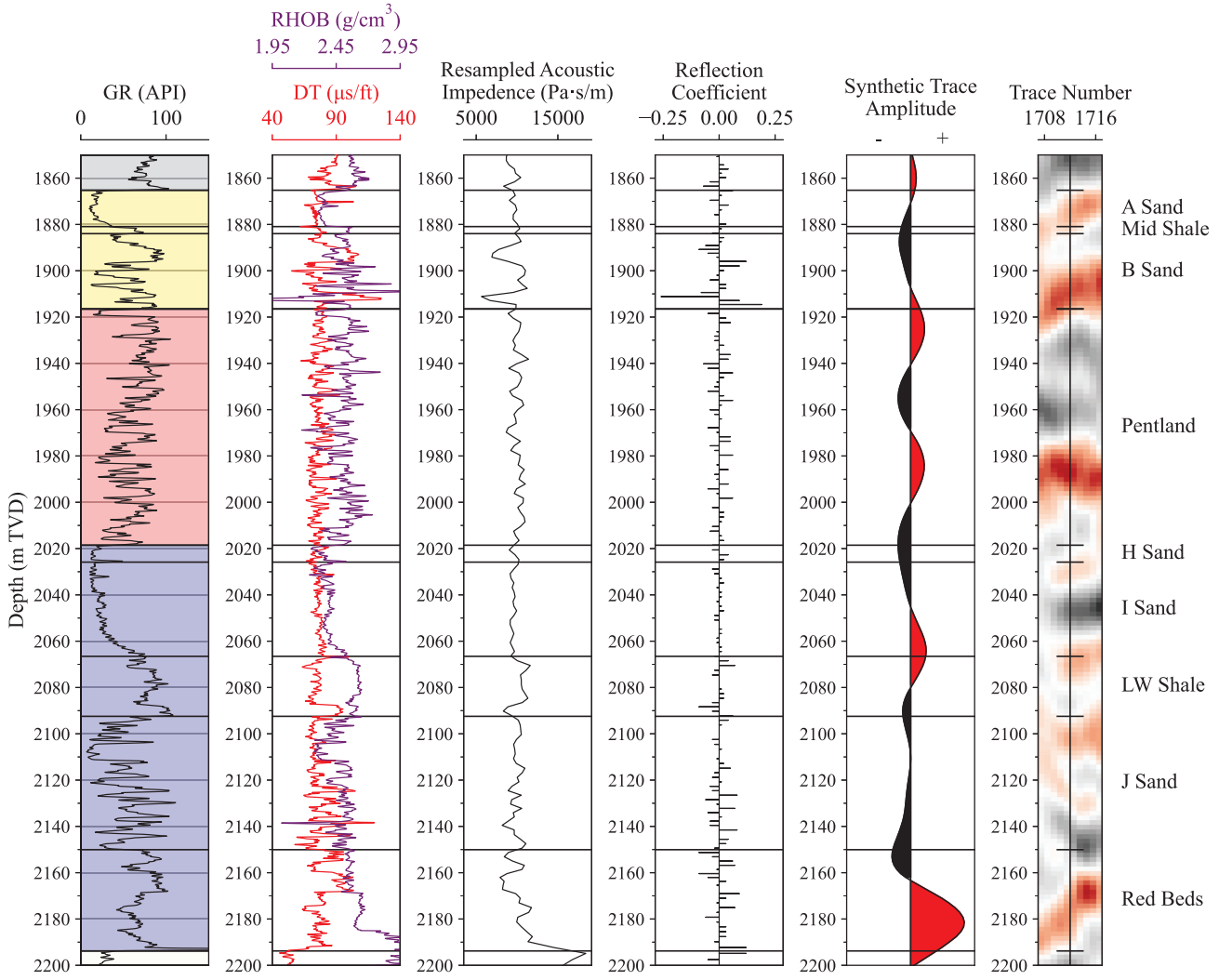


Figure 5.15: *Well-seismic tie across the reservoir section of the IMF, their synthetic seismic trace and the associated seismic section showing the comparatively low seismic resolution, limiting interpretation of the formations within the reservoir section.*

Within seismic Line 1 (Figure 5.17), the most south-westerly line discussed in this section, the formations appear as a relatively consistent layer-cake sequence. The bulk of the seismic within the line is comprised of the sub-Triassic packages - the pre-rift basement and Devonian, syn-rift Rotliegend and the post-rift Zechstein. The post-Triassic, mid-Jurassic reservoir sequence and Heather Formation sit alongside the Kimmeridge Clay Black Shales in the pre- and post-rift sequences deposited between the two major rifting sequences, in the Permian and Cretaceous (Andrews *et al.*, 1990; Roberts *et al.*, 1990). The syn-Late Jurassic-rift Kimmeridge Clay Formation (KCF) then comprises the majority of the sub-1000 m-depth upper sequence, which also sees areas of sediment loss at seabed, most clearly defined by the lack of Wick Sand or Cromer Knoll sequence to the north of the GGF, and around the Central Ridge and to the south of the Lossiemouth Fault.

Line 2, whilst maintaining similar characteristics to Line 1, does diverge in the thicknesses of the packages seen within the layer cake sequence (Figure 5.18). Line 2 also sees significantly less exposure at seabed of packages that are not Cretaceous Cromer Knoll, however it does also experience the KCF exposure to the north of the GGF. Within Line 2, the pre-Triassic sequences do not dominate the line to the same extent as seen in Line 1, but there is the same trend of pre-, syn- and post-rifting packages.

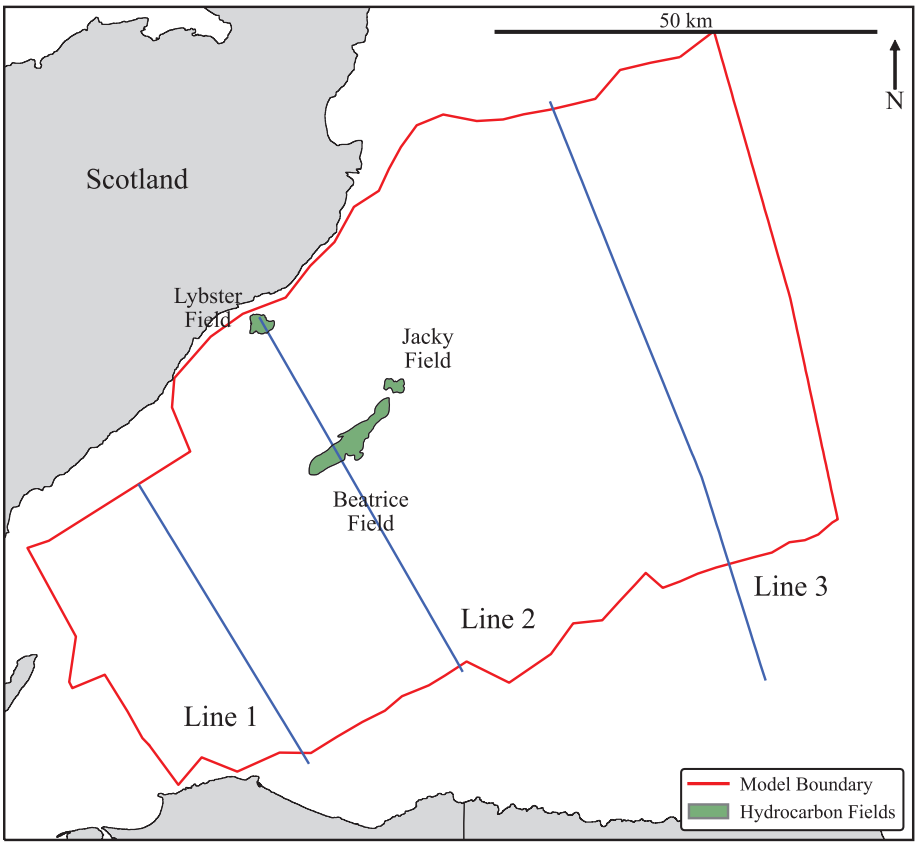


Figure 5.16: *Map showing locations of the interpreted seismic lines in Figures 5.17, 5.18, 5.19 & 5.20.*

Furthermore, another difference is seen by the structures creating the hydrocarbon traps of Beatrice and Lybster Fields, through which Line 2 intersects. The throw caused by the Smith Bank Fault at approximately Trace 2500 has given rise to the fault-trapped high in which Beatrice Field sits and small-scale faulting to the north of the GGF around Trace 4000 is where Lybster Field is situated, and neither of these are seen in Line 1. Within the Beatrice Field region, the juxtaposition of the reservoir intervals is also critical, as on Smith Bank Fault hanging wall, the reservoir sands are thrown against the sealing shales of the Heather Formation and Kimmeridge Clay Black Shales, creating a fully-formed trap, which again is not present within Line 1.

Line 3 continues the similar structure and sequences seen within the other lines outlined here (Figures 5.19 & 5.20). Structurally, there are some localised variations as a result of the large-scale, basin-forming faults present in this eastern part of the basin, namely the Wick Fault, however the packages and sequences seen within this line are consistent with the other lines in terms of layer cake sequencing. The reservoir sequence sees a mix of characteristics seen within the other lines, as, whilst the Beatrice Field region of the reservoir forms a high against the Smith Bank Fault, it throws against the sandy clays of the KCF, thus does not form a trap. In turn, in the Lybster Field region, there is, akin to Line 1, a lack of localised faults that are needed to create small traps within the reservoir sequence. Line 3 is one of the few lines within the seismic dataset that covers the region to the far south east of the Lossiemouth Fault, beyond the Lossiemouth sub-basin, and shows the Buckie Fault faulting out the reservoir sequence, so that the Banff sub-basin does not have any of the sequences where currently known accumulations exist. Furthermore, the Banff sub-basin is very heavily dominated by pre-Triassic sequences and shows very little thickness within the post-Jurassic packages, thus differs greatly to the rest of the IMF.

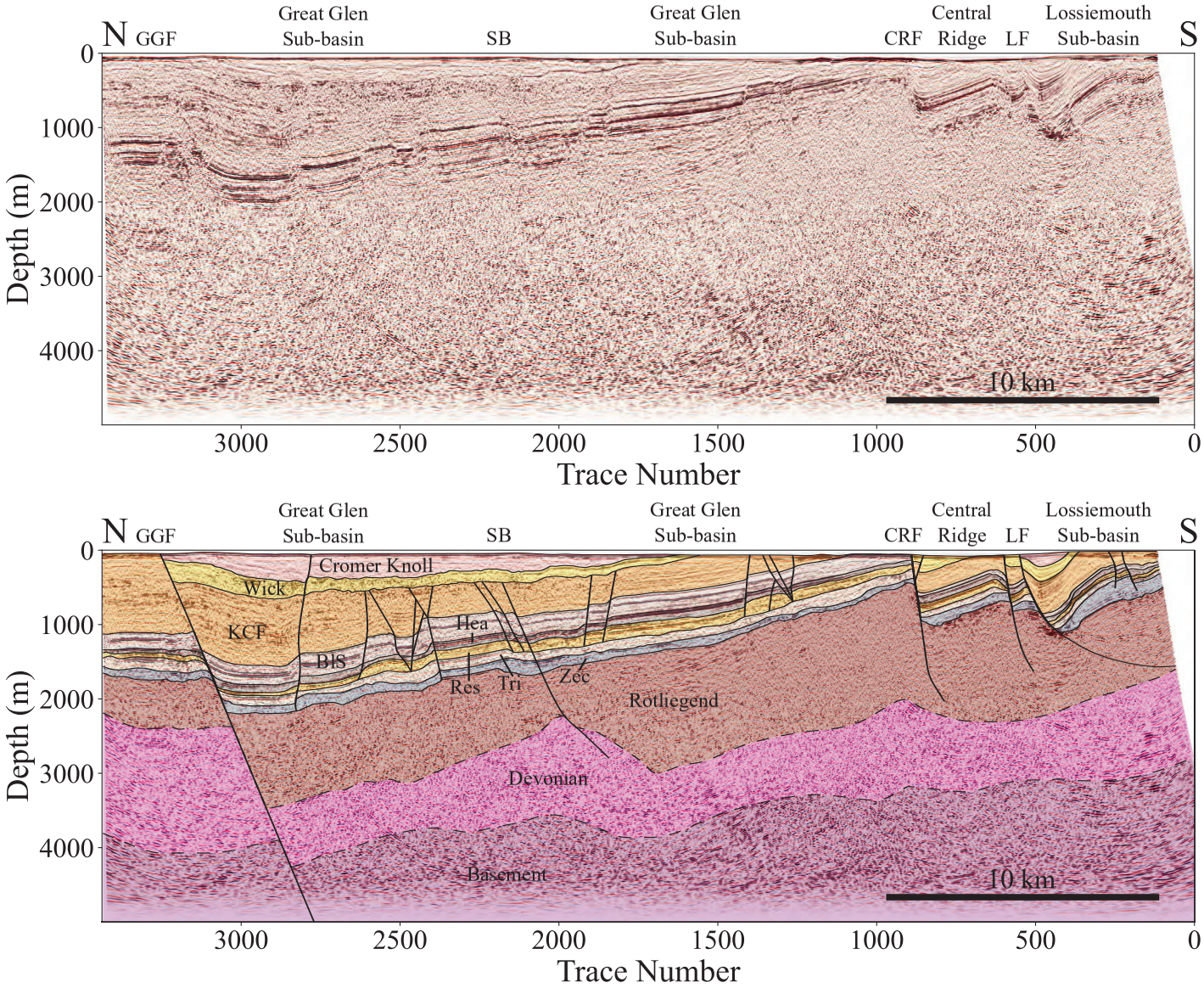


Figure 5.17: *Seismic Line 1 from the SW section of the IMF, both uninterpreted (above) and interpreted (below), identifying the main lithology packages. BlS = Black Shales, Hea = Heather, Res = Reservoir, Tri = Triassic, Zec = Zechstein. GGF = Great Glen Fault, SB = Smith Bank Fault, CRF = Central Ridge Fault, LF = Lossiemouth Fault. Syn-rift deposition of the KCF and erosive and fault removal of post-KCF sediment. Note a ~4x vertical exaggeration.*

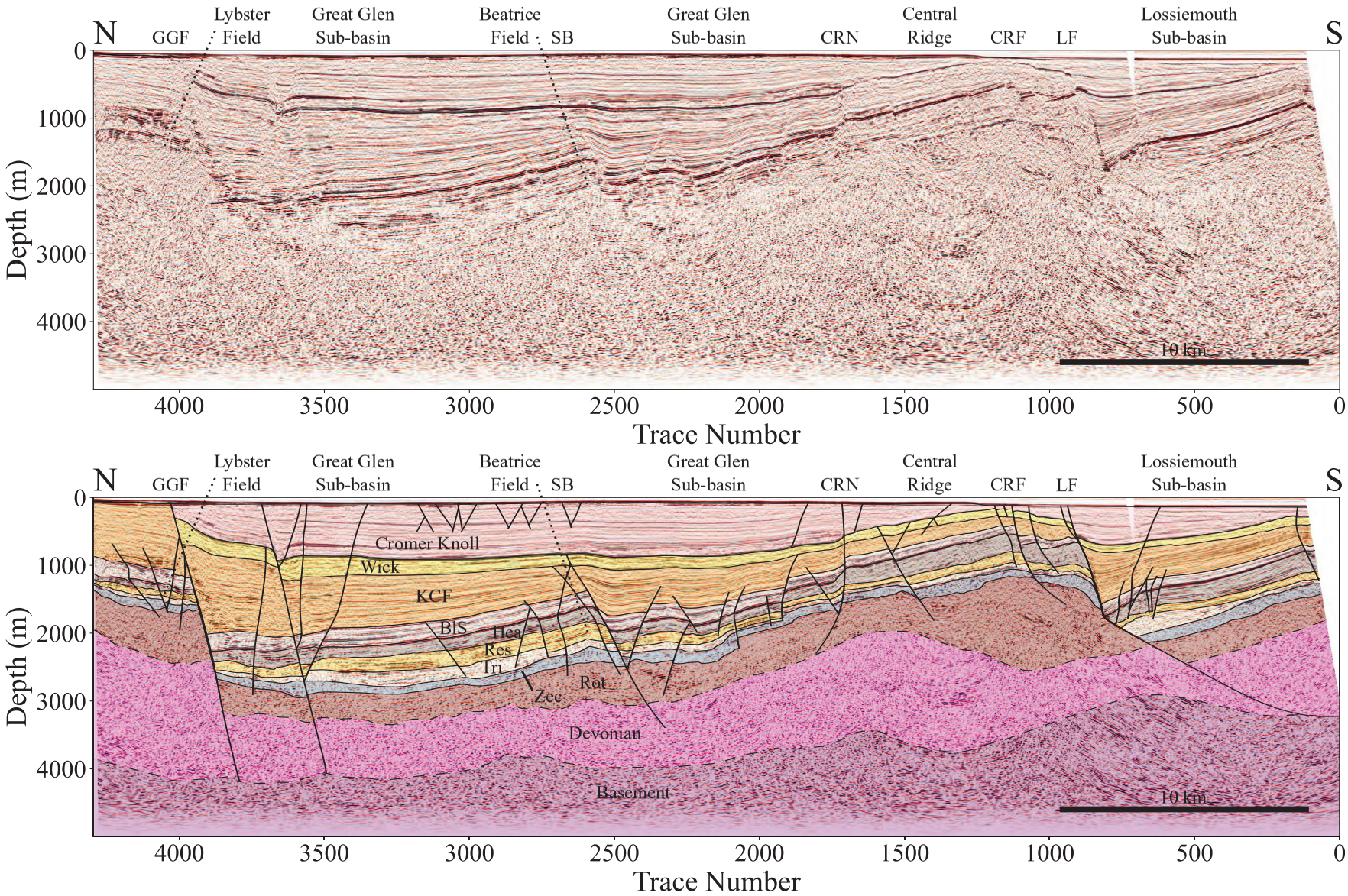


Figure 5.18: *Seismic Line 2 from the central section of the IMF, both uninterpreted (above) and interpreted (below), identifying the main lithology packages. BlS = Black Shales, Hea = Heather, Res = Reservoir, Tri = Triassic, Zec = Zechstein, Rot = Rotliegend. GGF = Great Glen Fault, SB = Smith Bank Fault, CRN = Northern Central Ridge Fault, CRF = Central Ridge Fault, LF = Lossiemouth Fault. Continued evidence of syn-rift deposition within the KCF in the Great Glen Sub-basin, but Cromer Knoll sediments at seabed across the rest of the section. Note a ~4x vertical exaggeration.*

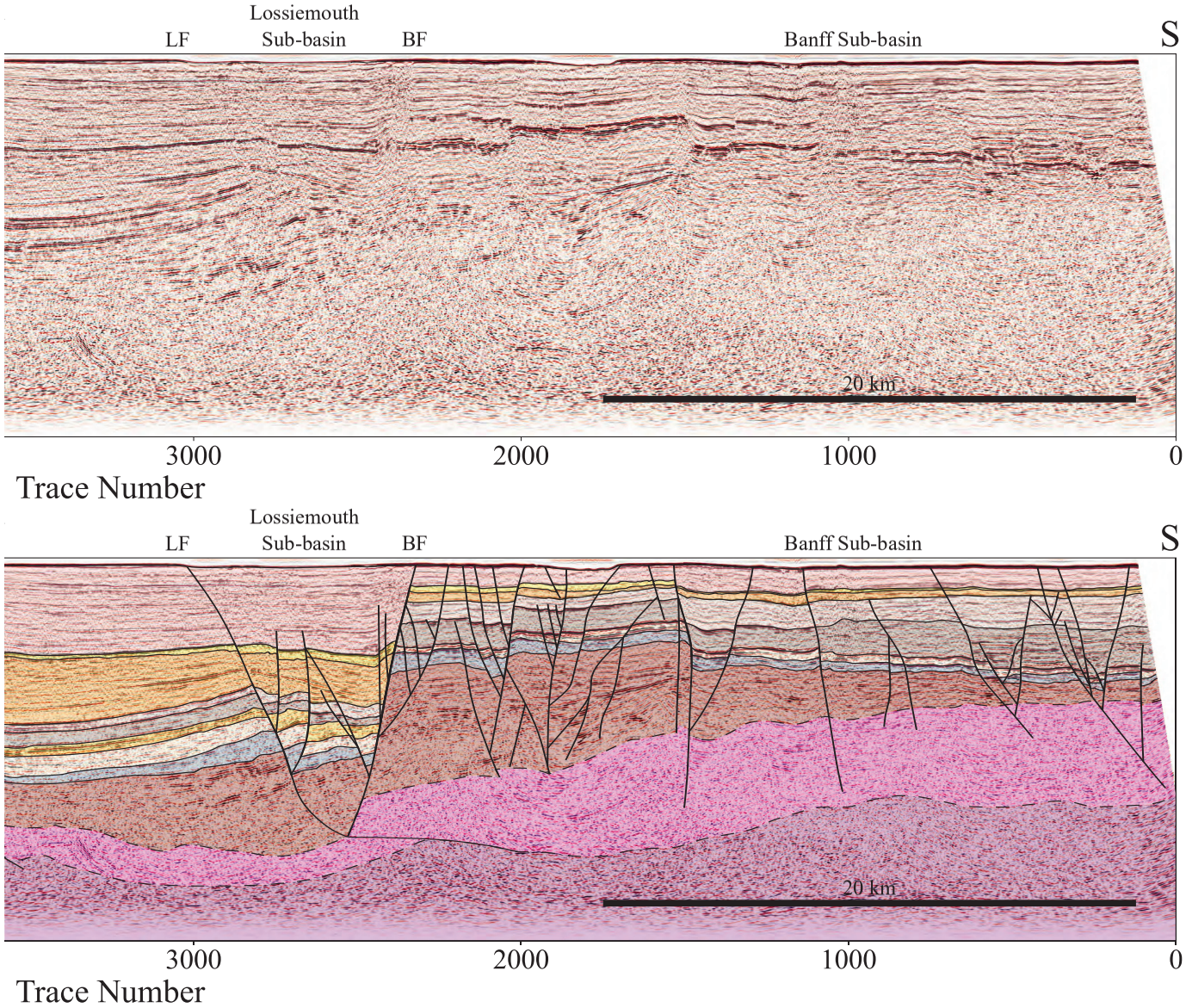


Figure 5.19: *Southern half of Seismic Line 3 from the NE section of the IMF, both uninterpreted (above) and interpreted (below). KCF = Kimmeridge Clay, BlS = Black Shales, Hea = Heather, Res = Reservoir, Tri = Triassic, Zec = Zechstein, Rot = Rotliegend. GGF = Great Glen Fault, SB = Smith Bank Fault, CRF = Central Ridge Fault, LF = Lossiemouth Fault, BF = Buckie Fault. The Banff Sub-basin shows more stability than the other regions of the IMF, suggesting that the Lossiemouth and Buckie Faults are the southern edge of the syn-rift IMF basin. Note a ~4x vertical exaggeration.*

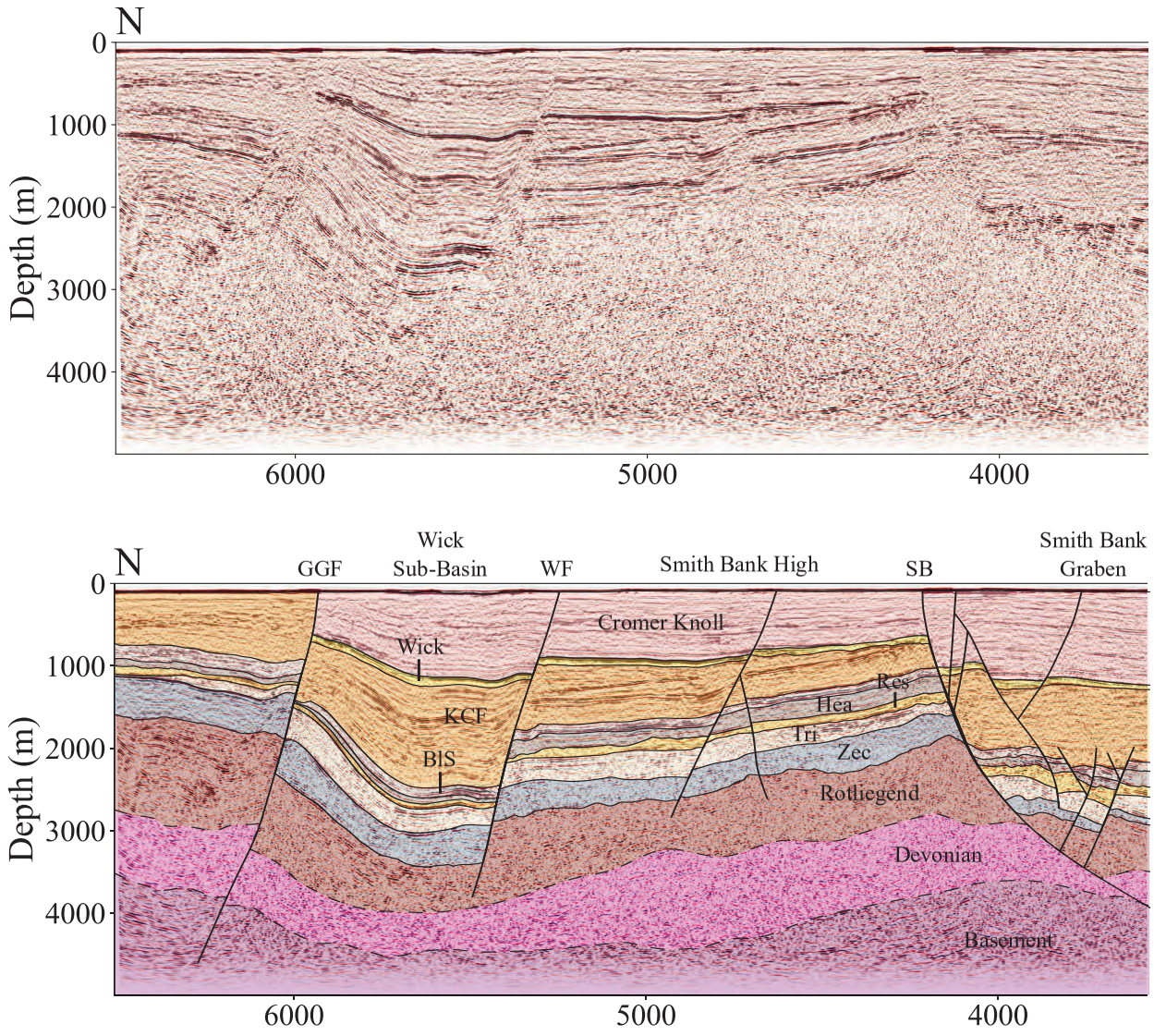


Figure 5.20: *Northern half of Seismic Line 3 from the NE section of the IMF, both uninterpreted (above) and interpreted (below). KCF = Kimmeridge Clay, BlS = Black Shales, Hea = Heather, Res = Reservoir, Tri = Triassic, Zec = Zechstein, Rot = Rotliegend. GGF = Great Glen Fault, SB = Smith Bank Fault, CRF = Central Ridge Fault, LF = Lossiemouth Fault, BF = Buckie Fault. Further evidence of extensive syn-rift deposition of the KCF, loss of post-KCF sediments to the north of the KCF and variable thicknesses of Cromer Knoll sediment across the section. Note a ∼4x vertical exaggeration.*

5.3.3 | DEPTH MAPS

Depth maps are the product of converting seismic interpretations into interpolated surfaces covering the entire study area (Hantschel and Kauerauf, 2009). They show the distinct structure of the basin exists within the vast majority of the formations (Figure 5.21). Whilst thicknesses vary across the basin,

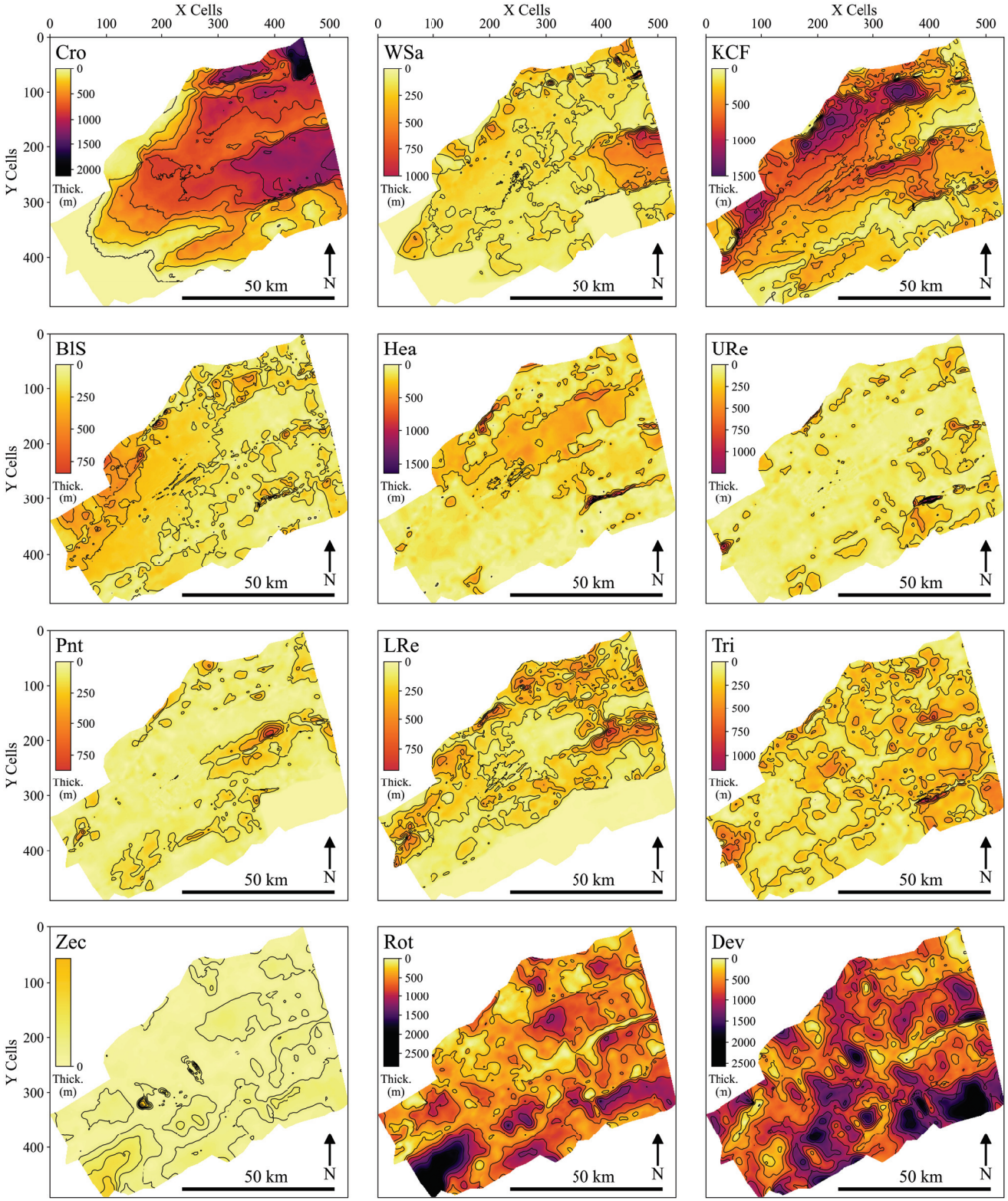


Figure 5.21: *Contour maps showing the depth to the top of all main sediment packages in the IMF, bar the seabed. All sediment packages are heavily fault-controlled, bar the Devonian and Basement as these formed predominantly prior to the IMF formation. X and Y Cells refer to the cells of the BPSM.*

the structure of each formation is relatively consistent, with only the pre-existing basement not showing any fault block systems. The formations show a series of tilted fault blocks and grabens in the eastern half of the basin, towards the Outer Moray Firth, all delineated and formed by the large, basin-bounding faults controlled by the underlying Caledonian structures previously outlined (Figures 5.17, 5.18, 5.19 & 5.20). These controlling faults in the east, the Wick, Smith Bank, Central, Lossiemouth and Buckie Faults, run to significant depths, and aid the structural formation of the Devonian, and thus also the basin as a whole, whilst producing the deepest regions of all formations (Table 5.5; Andrews *et al.* (1990); Roberts *et al.* (1990)). In the western half of the basin, towards coastal Scotland, there is much less fault control through the central regions of the basin, although to the northwestern edge, the IMF is heavily bound to the GGF through all formations. The Lossiemouth Fault, which runs through the south eastern section of the basin, does control the most south westerly quarter of the IMF, where the formations tend to reach their shallowest points, however due to its relatively small throws, despite its size, this is not picked up on the depth maps (Table 5.5).

The other depth map observation is source rock viability; however, as this is present day depth, not maximum burial, conclusions are only tentative and require further BPSM investigation. The Kimmeridge Clay Black Shales are generally too shallow for the organic content to mature, with its average depth to top of 1200 m and average temperature of approximately 50 °C, however in localised deeper regions it may experience some maturity, as it reaches depths of over 2700 m and temperatures up to 130 °C (Table 5.5). The Pentland Formation is similar, however its deeper average depth of about 1700 m and temperatures of 60-70+ °C suggests that it can reach low maturity. In comparison to both of

Table 5.5: *Table outlining the minimum, maximum and average present day depths of all formations in the IMF, bar the seabed. The depths of the source rocks within the IMF indicate that the deeper regions of the Black Shales may reach maturity, but not the entirety of the formation, similarly to the Pentland Formation. In comparison the Devonian Fish Beds are well in the maturation window.*

Formation	Minimum depth (m)	Maximum depth (m)	Average depth (m)
BCU	Seabed	2224.0	633.61
Kimmeridge Clay	Seabed	2308.0	801.82
KC Black Shales	22.0	2730.0	1244.94
Heather	119.0	3021.0	1427.73
Upper Reservoir	183.0	3181.0	1605.19
Pentland	209.0	3301.0	1725.66
Lower Reservoir	255.0	3490.0	1866.13
Triassic	261.0	3917.0	2033.17
Zechstein	394.0	4319.0	2269.24
Rotliegend	521.0	4327.0	2320.24
Devonian	861.0	5138.0	2920.05
Basement	2210.0	5273.0	3744.90

these, the Devonian is consistently at hydrocarbon-maturing depths, averaging over 2900 m depth to top. However, there is a different issue in the Devonian, in that it may become overmature and the oil cracks to gas, replacing the oil in any traps present in the system.

5.3.4 | THICKNESS MAPS

Thickness maps, calculated by the vertical distance between relevant depth maps, can be very helpful in identifying basin-forming events, locating petroleum system components and indicating other geological processes. Throughout the IMF, four formations show evidence for the basin-forming rifting events previously outlined by Andrews *et al.* (1990) and Roberts *et al.* (1990) (Figure 5.22; Table 5.6). The Devonian and Rotliegend were deposited on the pre-existing basement and during initial basin-forming rifting, respectively, thus show evidence of initial basin fill and syn-rift deposition during basin infill, shown as varying thicknesses across the basin within the thickness maps (Figure 5.22; Table 5.6; Andrews *et al.* (1990); Roberts *et al.* (1990)). During the periods of relative stability post-Triassic, which also shows some small-scale syn-rift deposition, the reservoir sequences, Heather and Black Shales all are relatively consistent in their thicknesses. Above the Black Shales, within the Kimmeridge Clay Formation proper, there is large-scale, basin-wide evidence for syn-rifting deposition, evidenced both in the thickness maps and in the cross sections, associated with the second basin-forming rifting event, the Jurassic-Early Cretaceous subsidence (Figures 5.17, 5.18, 5.19 & 5.20; Andrews *et al.* (1990); Roberts *et al.* (1990)). Wick Sand deposition occurred during relative stability prior to the Base-Cretaceous Unconformity (BCU), where a hiatus occurred. This was prior to a further syn-rift depositional event within the Cromer Knoll Group in the Early Cretaceous, where the third rifting stage occurred via epeirogenic subsidence. The fourth rifting stage during the Triassic is not visible within the depth or thickness maps, due to its occurrence within eroded sediments (Andrews *et al.*, 1990; Barr, 1985; McQuillin *et al.*, 1982; Roberts *et al.*, 1990). Note that Figure 5.22 does not show the basement as the depth to its base is unknown, thus within all the models created, it has a standardised depth of 6 km.

The KCF shows the most structurally-attributable thickness variations of any sediment package in the IMF (Figure 5.22). Whilst the Devonian and Rotliegend deposits vary across the basin, they infill the pre-existing basin, and despite the Cromer Knoll being deposited syn-rift, its thickness is heavily constrained by the late-stage erosion and removal of the sediments above it. In comparison, the sediments of the Zechstein, Triassic and Early-/Mid-Jurassic packages have consistent thicknesses across the basin. Consequently, the KCF is a good target for gross depositional environment (GDE) mapping to identify depositional variations between its deltaic, gravity flow, turbidite and crevasse splay sands and clay-rich shaley facies (Figure 5.23; Andrews *et al.* (1990)). The thickness and GDE maps show how the thickest sections of the KCF lay in the footwalls of the large, basin-bounding and basin-forming faults, most notably the GGF, Helmsdale, Smith Bank and Wick Faults (Figure 5.23). The shapes of these regions and their associations to the faults infers that these are large-scale clastic deposits, formed as a result of depositional flows along the fault hanging walls that breach the faults and flow into the deeper basinal regions during rifting. This clastic deposition appears to be occurring syn-sedimentation of the wider-spread clays and shales of shallow marine shelf and deeper marine environments that are prevalent within the KCF (Andrews *et al.*, 1990).

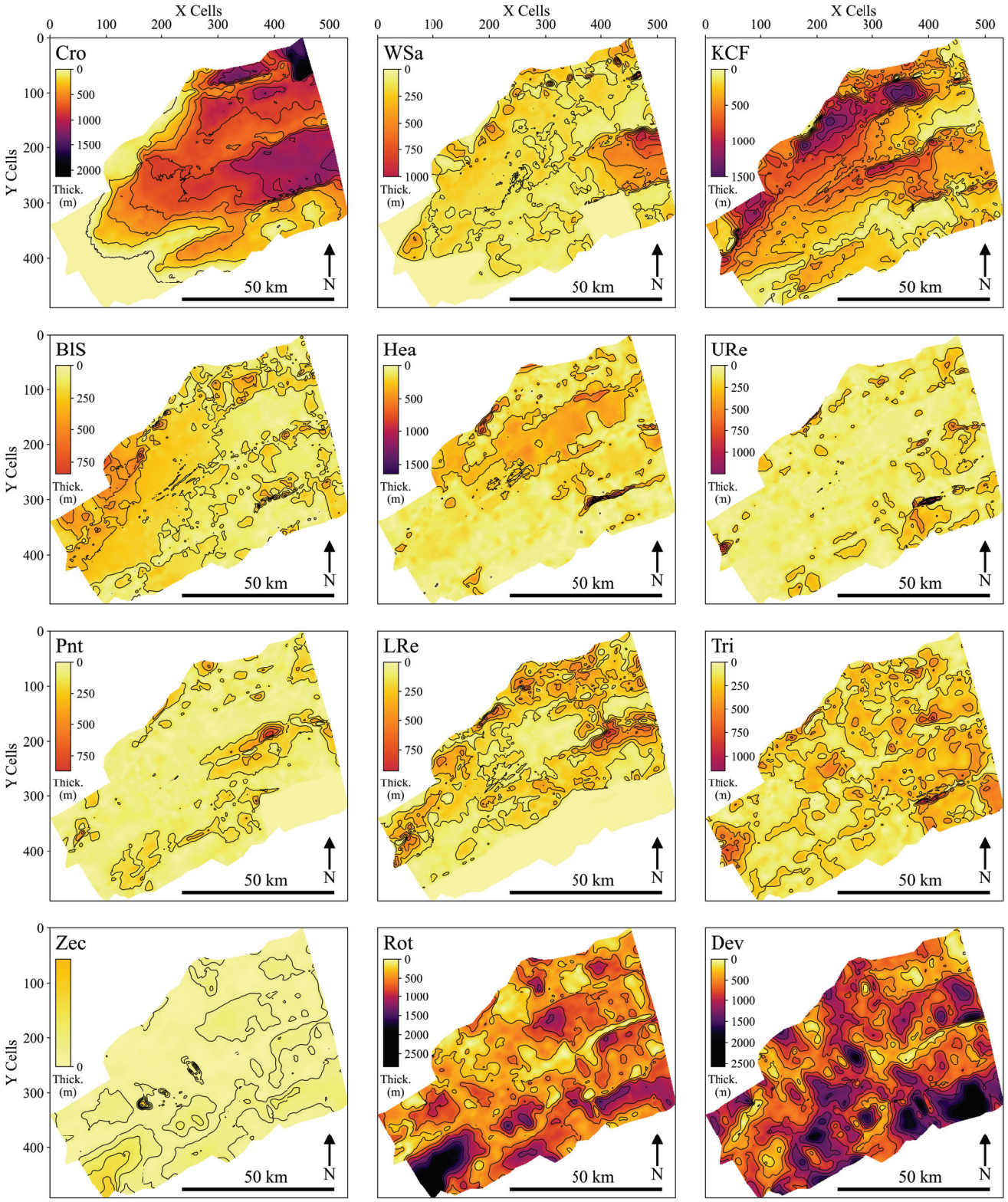


Figure 5.22: *Contour maps showing the thicknesses of all main formation packages within the IMF, bar the basement. Whilst the thicknesses of the Cromer Knoll, Rotliegend and Devonian are skewed due to the removal of surficial sediments during late stage rifting, and the infill the pre-existing Caledonian-Orogeny formed basin, respectively, the syn-rift sedimentation of the KCF is clear to see in its thickness map. This is in stark contrast to the majority of sediment packages through the central section of the IMF. X and Y Cells refer to the cells of the BPSM.*

Table 5.6: *Table outlining the minimum, maximum and average depths of formations in the IMF. The majority of the basin's thickness is contributed by Cromer Knoll, Kimmeridge Clay, Rotliegend and Devonian sediments, all formed via pre-existing basin infill and periods of syn-rift sedimentation.*

Formation	Minimum thickness (m)	Maximum thickness (m)	Average thickness (m)
Cromer Knoll	0.0	2122.0	552.11
Wick Sand	0.0	992.0	169.55
Kimmeridge Clay	0.0	1498.0	442.80
KC Black Shales	0.0	838.0	182.79
Heather	0.0	1639.0	177.46
Upper Reservoir	0.0	1243.0	121.47
Pentland	0.0	866.0	99.88
Lower Reservoir	0.0	926.0	167.99
Triassic	0.0	1148.0	226.06
Zechstein	0.0	311.0	49.00
Rotliegend	0.0	2845.0	599.81
Devonian	0.0	2570.0	824.85

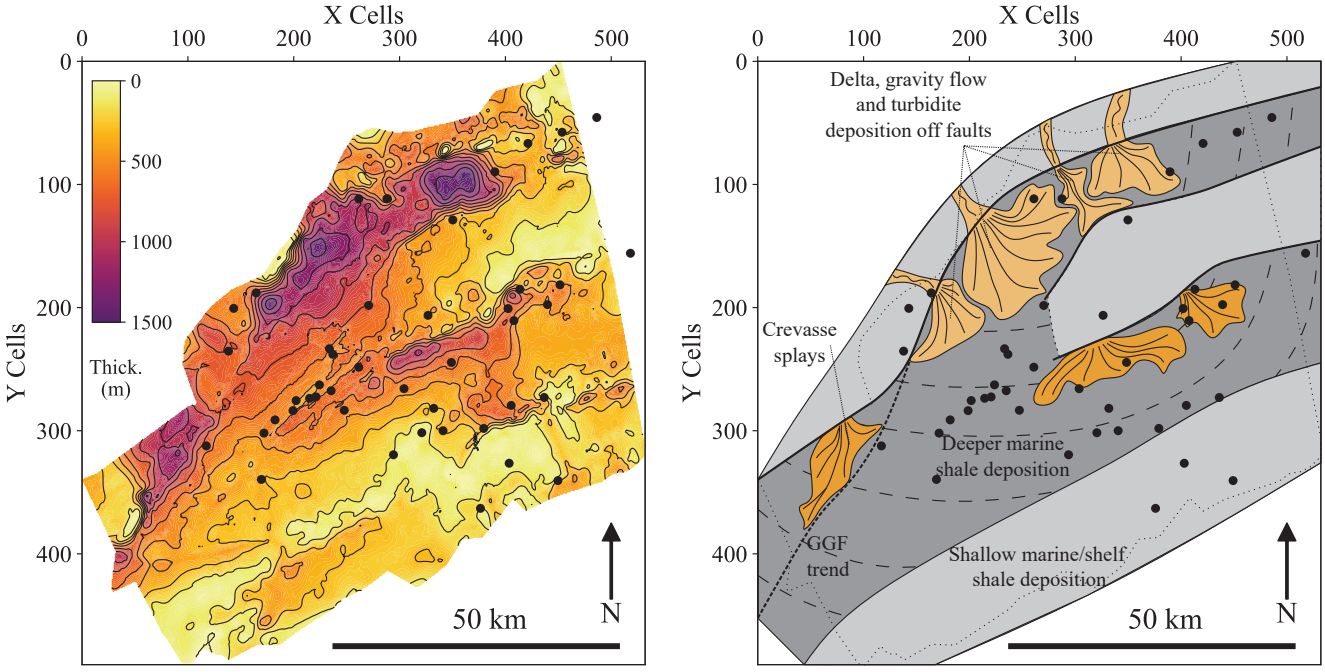


Figure 5.23: *GDE Map of the KCF, showing the extensively thickened regions around the basin-forming faults where the majority of the sands were deposited during its syn-rift formation, with the model extent outlined on the GDE Map. Black dots indicate location of wells that drill through the KCF, which is all wells in the IMF. X and Y Cells refers to the cells of the BPSM.*

5.3.5 | FAULT INTERPRETATIONS

The IMF is littered with both large-scale, basin-forming faults, and high numbers of smaller-scale faults that are typically related to the larger ones to some degree, be it in shape, depth to base, or direct connectivity (Figure 5.24). The faults within the IMF are crucial to its development as a basin as well as the petroleum system within it, as faults act as both fluid pathways and barriers, and as such, it is critical that they are understood, interpreted and built into the models. Within this study, 99 faults were interpreted and built into a fault framework, shown in Figure 5.24, all of which exist in tandem with each other and the formations that they intersect. The larger faults typically intersect all formations from the Devonian to the Cretaceous, and often to the seabed, whereas the smaller ones are typically constrained to the sequences between the BCU and the Triassic (Figures 5.17, 5.18, 5.19 & 5.20). The larger faults are crucial to the formation of the basin, but also to the migration of the Devonian-sourced hydrocarbons out of the deeper regions of the basin and into the Jurassic reservoir sequences, whilst the smaller ones undoubtedly control localised trapping and migration against and through the shalier formations within the reservoir section (the Pentland, Mid Shale and Lady's Walk Shale).

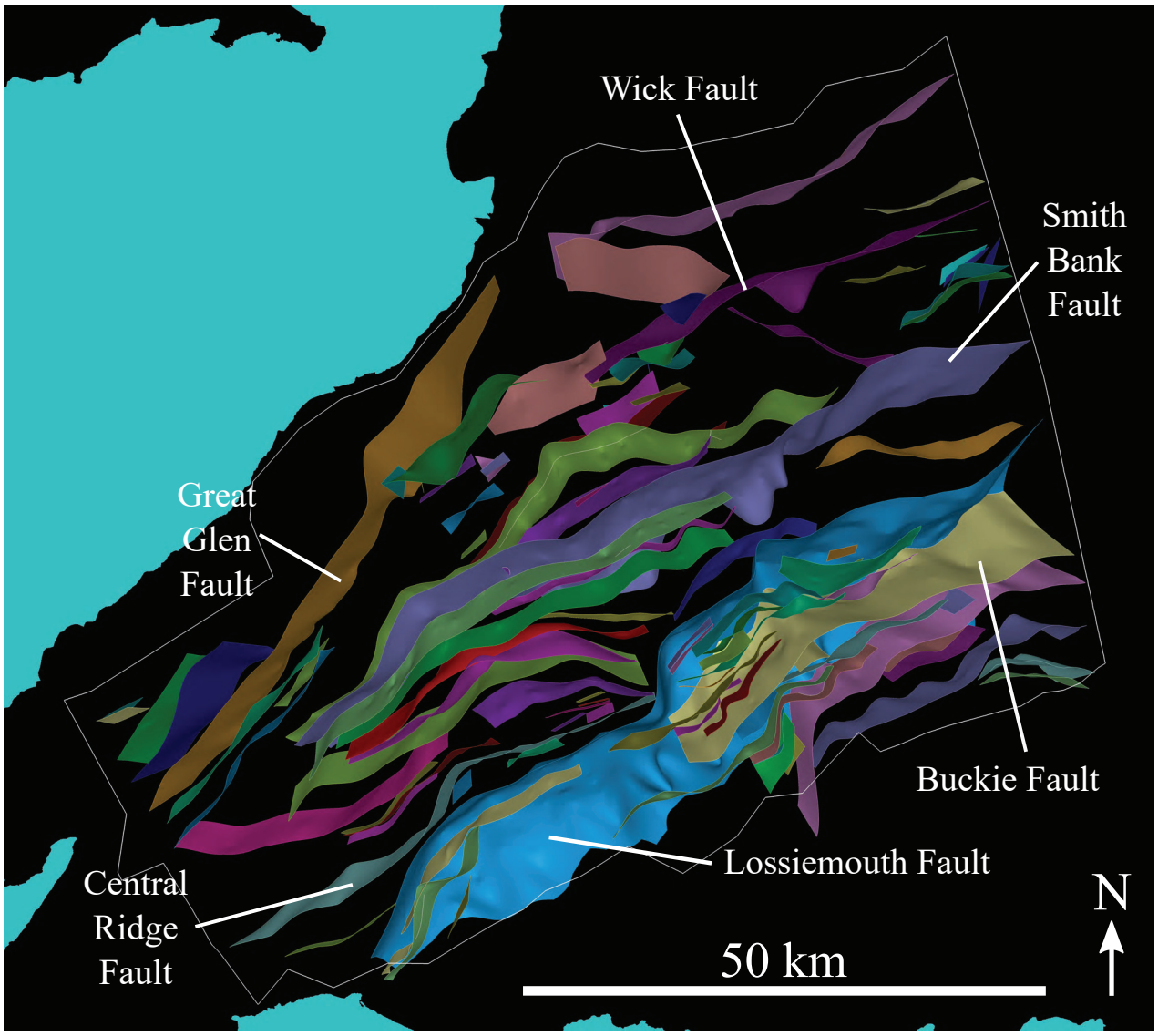


Figure 5.24: *Map showing the faults across the IMF, coloured solely for clarity, annotated with the main basin-forming and controlling faults. Image extracted from Petrel (Schlumberger, 2015).*

5.4 | CONCLUSION

Throughout this chapter, analysis of the geological data has resulted in an accurate three-dimensional recreation of the IMF in the form of a geological model. Through the interpretation of seismic data to form a surface and fault system, and analysis of well log data to determine the facies present within each sediment package, this work has developed an understanding both of the formations present within the IMF, but also how they relate, connect and change across the basin as a result of structural influences caused by the geological processes occurring throughout the basin's history. The analysis carried out in this chapter has provided the basis for the magnetic and petroleum systems modelling conducted in this study, both providing targets for magnetic mineral sampling and analysis, and to create the framework for the basin and petroleum systems model which leads into the understanding of the hydrocarbon generation, migration and accumulation patterns within the IMF.

Magnetic mineral analyses requires sampling of sand-rich lithologies due to the skewed results that occur within clay-rich formations. As such, well log analysis helps identify these, focussing sampling onto certain formations sand packages in shalier formations. This, in combination with the ability to identify oil-water contacts, makes well logs a valuable tool within magnetic mineral analysis. Whilst sampling mainly sand skews the results and analysis towards the thinner, less frequent sand bodies, such as the upper and lower reservoirs, the Wick Sand and parts of the Heather and Cromer Knoll, these are the areas of most interest.

Well log analysis has also refined the knowledge of the formations greater than analysis of literature can do, as it has improved the understanding of lithological variations across the IMF and through different formations. Lithological variations, such as the sandier components within the Heather Formation in Well 11/24-1, or the more shaley sections of the J Sand and Red Beds within Well 11/24-1 and Well 11/30a-10 (Figure 5.12), compared to the other wells, allows a much greater control of the facies within the basin and petroleum systems models.

The importance of faults within the BPSMs is made starkly clear by seismic analysis, as they undoubtedly contribute vastly to the basin's petroleum system. The faults initially formed the basin, and created the structural traps in which accumulations can occur, and furthermore, the large, deeply-penetrating faults potentially create pathways for hydrocarbons to migrate out of the Devonian source rocks, through the clay-rich Permian and Triassic strata and into the sandier reservoir sequences. These larger faults, and the smaller, more localised ones also offer routes to bypass the inter-reservoir shale formations, making them crucial to the migration pathways of the hydrocarbons across the IMF, and accurate interpretation and modelling of these is critical to a well-rounded understanding of the basin.

Interpretation and creation of depth maps and the associated creation of thickness maps, are also critical within the model, as they not only give indications of formation extent and location within the basin, but also aid initial investigations into source rock potential. At present day, the Kimmeridge Clay Black Shales appear mostly immature except within the deeper basin regions (Figure 5.21), whilst the Pentland Formation and Brora Coal are borderline. However, as the present day is not maximum burial, these findings are tentative.

Chapter 6 | Magnetic Analysis

6.1 | INTRODUCTION

Samples collected for magnetic analyses were taken from numerous wells across the study area, and, depending on core availability and quality, across as many formations within each well as possible (Figure 6.1). In total, 306 samples were collected, however due to various issues such as the sample magnetic intensity, composition and formation, 35 samples were not analysed, thus in total, 271 samples underwent room- (RT) and high-temperature (HT) magnetic analysis. The majority of the samples collected were within Jurassic-age sandstone bodies, as these are most likely to contain crucial information about the Jurassic-age reservoirs. However, with hydrocarbon migration very likely to have impacted a wider variety of formations, samples were also taken from key intervals across the rest of the geological section in the basin, including, where possible, source rocks from the Devonian Fish Beds, Pentland Formation and Kimmeridge Clay Black Shales, the breakdown of which can be seen in Table 6.1.

The majority of wells that were sampled were magnetically analysed (Figure 6.1; Table 6.1), however Wells 12/16-1, 18/03-1 and 19/01-1 had samples that were not analysable due to the lithologies cored. Sample distribution across the basin's geology is reasonably varied, but the reservoir section in the Middle Jurassic is the most heavily cored, and therefore sampled, region. This sampling is predominantly from the wells in the central IMF and around the Lybster Field in the north-west IMF, with shallower intervals being sampled towards the outer regions of the basin. The sampling distribution coincides with the geology of the IMF, with the outer regions showing more Upper Jurassic and Cretaceous formations in key depths and structures due to the shape of the basin.

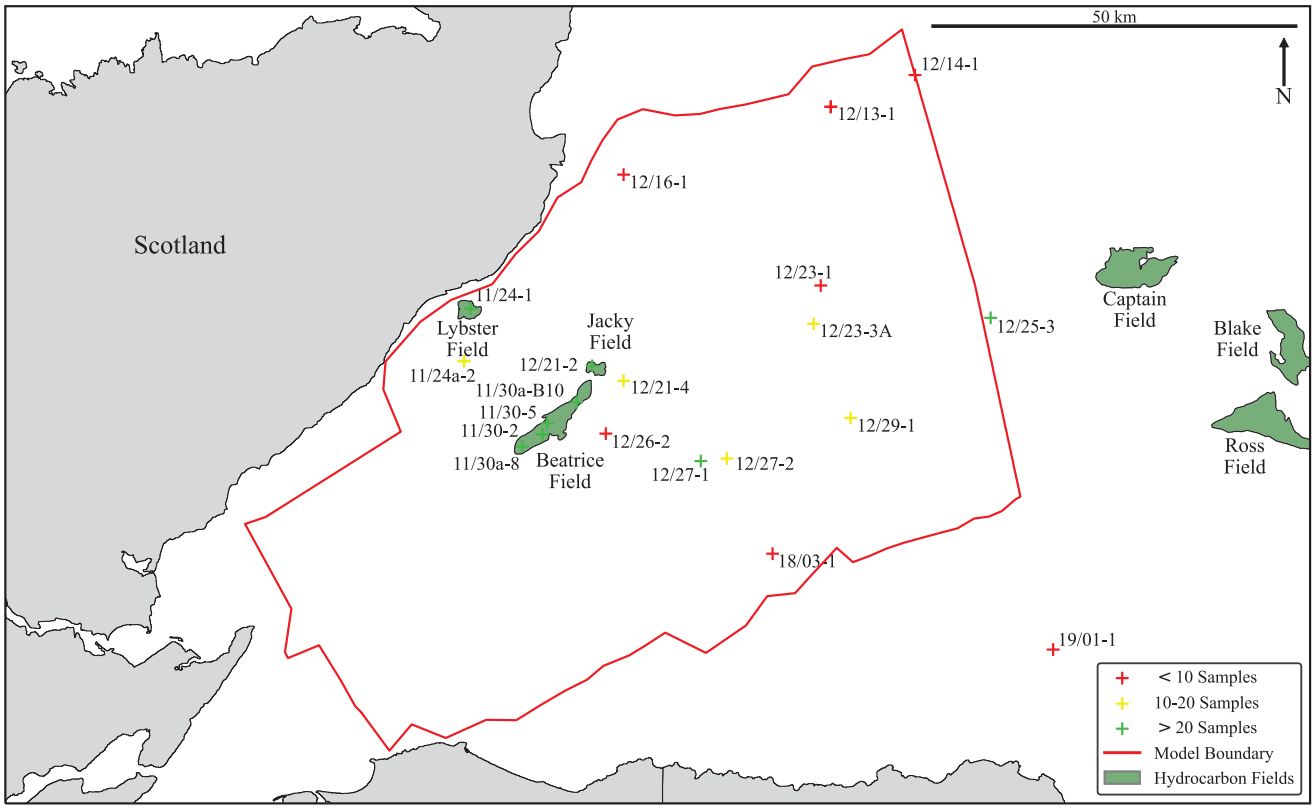


Figure 6.1: *Map of the Inner Moray Firth, highlighting the extent of the basin and petroleum systems model, the positions of the known hydrocarbon fields in the region and showing the locations of the wells where sampling of cores was possible, delineated by the number of samples from each well. Note that not all wells in the study area were sampled, see Chapter 3 for the complete well dataset.*

Table 6.1: *Table outlining the amount of core-derived samples collected from numerous wells across the IMF, delineated by both formation and well. The majority of samples are centered around the Middle Jurassic reservoir section due to this being the most heavily cored section of the wells, but other formations and sediment packages are sampled, however below the Lower Jurassic sediments there are few due to the limited numbers of wells that were drilled, much less cored.*

Age	Formation	Total Samples	NW IMF		Central IMF Fields					Central IMF				N IMF		E IMF			
			11/24-1	11/24a-2	11/30-2	11/30-5	11/30a-8	11/30a-B10	12/21-2	12/21-4	12/26-2	12/27-1	12/27-2	12/13-1	12/14-1	12/23-1	12/23-3A	12/25-3	12/29-1
Total Samples		271	28	16	18	9	33	32	33	11	3	23	12	3	7	3	10	20	10
K.	C. Knoll	20	-	-	-	-	-	-	-	-	-	-	-	-	-	-	-	20	-
Upper Jurassic	Wick Sand	7	-	-	-	-	-	-	-	-	3	-	-	-	4	-	-	-	-
	Kim. Clay	10	-	-	-	-	-	-	-	-	-	-	-	-	-	-	10	-	-
	Heather	21	4	-	1	-	3	-	-	-	-	-	-	-	3	-	-	-	10
Middle Jurassic	A Sand	63	7	16	3	-	19	-	10	7	-	-	-	-	-	-	-	-	-
	Mid Shale	6	-	-	-	-	-	-	1	3	-	2	-	-	-	-	-	-	-
	B Sand	50	9	-	2	-	11	-	12	1	-	3	12	-	-	-	-	-	-
	Pentland	33	8	-	1	-	-	-	10	-	-	14	-	-	-	-	-	-	-
Lower Jurassic	H Sand	10	-	-	6	4	-	-	-	-	-	-	-	-	-	-	-	-	-
	I Sand	19	-	-	-	5	-	14	-	-	-	-	-	-	-	-	-	-	-
	J Sand	23	-	-	5	-	-	18	-	-	-	-	-	-	-	-	-	-	-
Permian		2	-	-	-	-	-	-	-	-	-	-	-	-	-	2	-	-	-
Devonian ORS		8	-	-	-	-	-	-	-	-	-	4	-	3	-	1	-	-	-

This chapter covers the magnetic analysis undertaken on samples from the wells, though does not cover wells with less than ten samples, as no strong conclusions can be made from such a small sample set. Generally, closely-adjacent wells show similar sampling patterns, with this to be expected as sampling is heavily dependant on core availability. As coring reflects the technical and economic decisions made by the operators who drilled the wells, it results in sampling that is heavily skewed towards hydrocarbon-bearing locations. This economic decision is shown by only one well, Well 12/21-4, being described in the well report as dry and offering no evidence of any hydrocarbon influence in the sampled sections. As such, identifying a clear background signal has been difficult.

Room temperature magnetic property analysis was carried out through magnetic hysteresis data, with these providing initial assessments of the samples, and the formations and wells in which they are located. Data quality within these hysteresis loops varies, with examples of high quality, mode quality, and low quality hysteresis data presented in Figure 6.2.

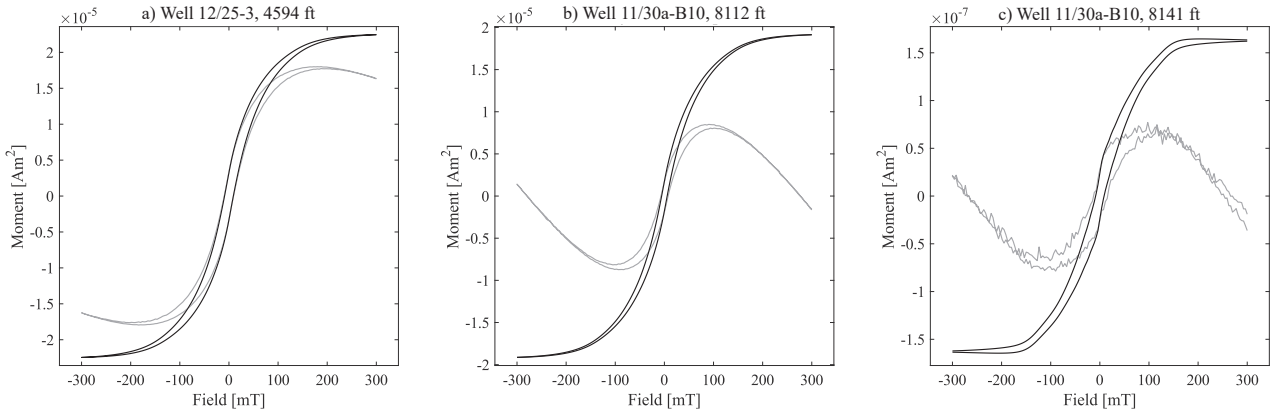


Figure 6.2: *Example hysteresis loop data from room temperature analysis carried out in this study. The hysteresis loops show examples of a) typical high quality data; b) most typical, mode quality data; and c) low quality data. Note that the grey loop is the uncorrected hysteresis loop, and the black loop is the corrected hysteresis loop.*

6.2 | BASIN-WIDE MAGNETISM

Analysing the basin-wide magnetism of the IMF through the magnetism of each formation (Table 6.2; Figures 6.3 and 6.4) and well offers an initial insight into the basin's magnetism. Whilst accurate conclusions can only be drawn from more localised analysis, an overview aids scrutiny. Table 6.2 shows how variable magnetic results are between different formations and between saturating fluids. The Cromer Knoll, H and I Sands show drastic increases in magnetisation (M_s) in oil-saturated samples compared to water-saturated ones, suggesting an increase in magnetic mineral abundance, whereas the other formations, bar A Sand, show relative M_s decreases in oil-saturated samples compared to water-saturated ones. The reverse of these trends tends to be seen in the coercivity (B_c) results, where formations with higher M_s responses in oil-saturated samples than water-saturated samples experience lower B_c, suggesting a decrease in magnetic grain size, responses in the oil-saturated samples than the water-saturated ones, and *vice versa*. Therefore, broadly speaking, formations experience an increase in magnetic mineral abundance alongside a decrease in magnetic grain size, or *vice versa*. The H Sands show significantly higher B_c responses in the water-saturated samples than their respective oil-saturated ones, which is a relationship not seen within any of the other reservoir formations (Table 6.2). In contrast, the I Sands see a much higher coercivity of remanence (B_{cr}) in the oil-saturated samples than the water-saturated ones Generally, the cleaner sands of the upper reservoir (A and B Sands) tend to have high B_{cr}/B_c ratios, i.e., more MD-like or SP-like, than the samples from other formations, including the deeper, slightly shalier sands of the lower reservoir (H, I and J Sands; Figure 6.3).

The Cromer Knoll samples generally follow the mean IMF magnetic results for all characteristics apart from remanent magnetisation (M_r), which, as Figure 6.3c shows, has a much steeper gradient than any other formation, forming the upper bound of the data. The other difference, though not as clearly defined, is that the high-field slope (H_{fs}) results plot only in the lower half of the data (Figure 6.3g-j). The cause of these differences is likely due to lithological variations between this Cretaceous formation and the others in the IMF that are Jurassic in age. As the Cromer Knoll is only sampled in one well, 12/25-3, the results will be investigated further in the depth-orientated analysis of that well.

Table 6.2: *Table outlining the mean magnetic results from all samples from all wells in the IMF, alongside one standard deviation (σ), through the Cretaceous Cromer Knoll to the Lower Jurassic, delineated by geological formation and saturating fluid. As the results are a function of formation, they show geological variations but through all wells across the basin, therefore results do not show the lateral variations across the IMF. O = oil, W = water.*

Age	Formation	Fluid	Number of samples	M_s (σ) (10^{-3} Am^2kg^{-1})	M_r (σ) (10^{-3} Am^2kg^{-1})	M_r/M_s (σ)	B_c (σ) (mT)	B_{cr} (σ) (mT)	B_{cr}/B_c (σ)	H_{fs} (σ) (10^{-3} Am^2kg^{-1})
K.	C. Knoll	O	14	1.37 (±0.69)	0.18 (±0.1)	0.13 (±0.02)	8.4 (±0.9)	48.6 (±6.1)	5.8 (±0.9)	3.7 (±2.3)
		W	6	0.89 (±0.29)	0.07 (±0.02)	0.08 (±0.01)	5.8 (±0.5)	56.8 (±2.3)	9.8 (±0.8)	-0.1 (±1.9)
Upper Jurassic	Kimm. Clay	O	10	2.85 (±1.7)	0.19 (±0.11)	0.07 (±0.01)	5.5 (±0.7)	56.9 (±5.1)	10.6 (±1.9)	11.3 (±4.6)
		W	0	-	-	-	-	-	-	-
	Heather	O	15	3.29 (±2.5)	0.21 (±0.13)	0.08 (±0.04)	5.7 (±3.4)	60.6 (±26.9)	14.3 (±14.9)	23.1 (±37.5)
		W	3	4.82 (±1.56)	0.25 (±0.05)	0.05 (±0.01)	4.5 (±0.7)	61.4 (±2.0)	14.0 (±1.9)	18.0 (±1.9)
Middle Jurassic	A Sand	O	34	5.70 (±5.73)	0.23 (±0.2)	0.05 (±0.03)	3.3 (±1.3)	50.9 (±13.9)	17.0 (±6.4)	4.3 (±16.7)
		W	28	4.05 (±7.34)	0.15 (±0.23)	0.10 (±0.06)	5.8 (±2.4)	48.0 (±13.7)	10.6 (±8.1)	29.5 (±107.5)
	B Sand	O	26	2.11 (±1.89)	0.12 (±0.07)	0.08 (±0.04)	6.0 (±2.9)	64.0 (±26.9)	13.1 (±8.2)	33.0 (±45.8)
		W	24	2.97 (±3.26)	0.16 (±0.18)	0.10 (±0.06)	6.0 (±3.6)	53.4 (±27.7)	13.3 (±11.9)	30.7 (±56.2)
	Pentland	O	10	1.37 (±0.67)	0.15 (±0.13)	0.11 (±0.05)	6.9 (±1.3)	44.6 (±13.7)	7.0 (±3.1)	13.1 (±30.3)
		W	23	2.69 (±1.92)	0.15 (±0.08)	0.07 (±0.03)	4.8 (±1.8)	58.3 (±36.9)	14.1 (±7.9)	23.3 (±53.4)
Lower Jurassic	H Sand	O	2	1.87 (±3.04)	0.12 (±0.19)	0.06 (±0.05)	4.1 (±1.7)	90.8 (±90.5)	28.0 (±32.3)	1.3 (±5.1)
		W	8	0.97 (±1.69)	0.04 (±0.07)	0.15 (±0.09)	12. (±10.8)	69.8 (±33)	10.8 (±10.2)	-1.7 (±6.2)
	I Sand	O	11	1.44 (±1.88)	0.12 (±0.18)	0.09 (±0.04)	6.0 (±2.4)	429.0 (±6.2)	8.3 (±4.1)	-6.1 (±2.8)
		W	8	0.35 (±0.36)	0.02 (±0.02)	0.08 (±0.03)	5.0 (±1.9)	50.0 (±8.7)	11.7 (±5.3)	-1.4 (±6.9)
	J Sand	O	11	0.19 (±0.07)	0.02 (±0.01)	0.16 (±0.02)	7.4 (±1.1)	40.6 (±2.9)	6.5 (±2.8)	-2.0 (±6.7)
		W	12	1.48 (±1.6)	0.09 (±0.09)	0.10 (±0.05)	6.6 (±2.2)	46.7 (±8.3)	8.4 (±3.9)	27.6 (±26.4)

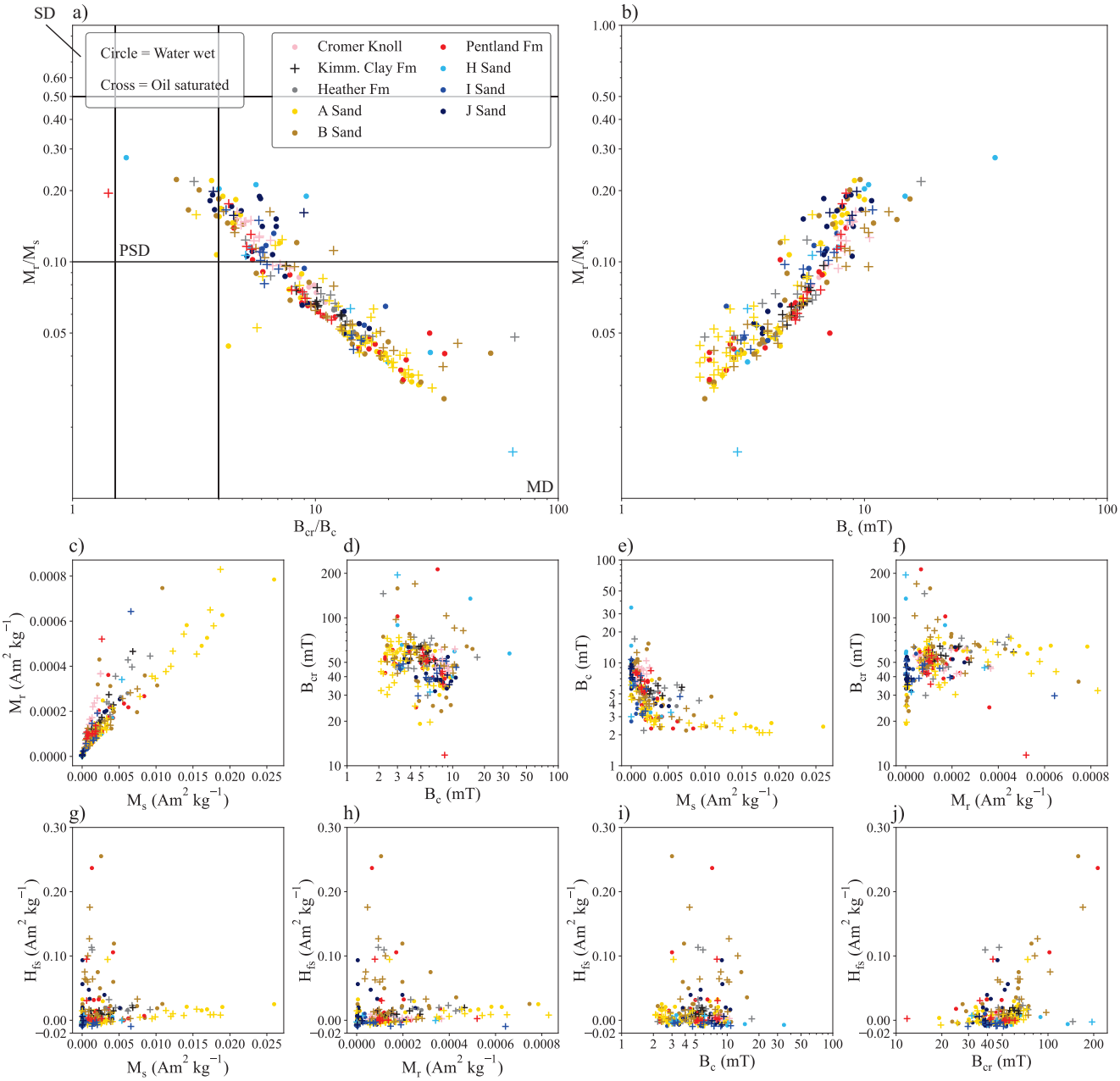


Figure 6.3: *Series of data plots comparing the various room temperature magnetic characteristics of samples across the IMF, delineated as a function of formation and by saturating fluid. a) shows a Day Plot (Day* et al.*, 1977), comparing M_r/M_s against B_{cr}/B_c; b) shows M_r/M_s against B_c; and c) to j) are a series of plots showing the relationships between M_r, M_s, B_c, B_{cr} and H_{fs}. The data spread across all formations and saturating fluids is relatively continuous with no initially observable patterns as a result of either saturating fluid or lithological formation.*

Whilst the Heather Formation is heavily shale-dominated, there are pockets of sand that have been sampled, and these sandier samples plot very centrally within the magnetisation and coercivity data (Figure 6.3a-f), however the H_{fs} results clearly group into the top half of the data (Figure 6.3g-j). Differences in the magnetic results from the Heather Formation compared to the other formations in the IMF are likely derived from lithological variations as the sands are isolated in pockets and do not act as continuous bands across the basin. Consequently, the Heather Formation sands are heavily influenced by the clays within the shales around them. The main contribution to the Heather Formation analysis is Well 12/29-1 (Section 6.3.13) and this will offer further insight into the magnetic assemblage(s) seen in

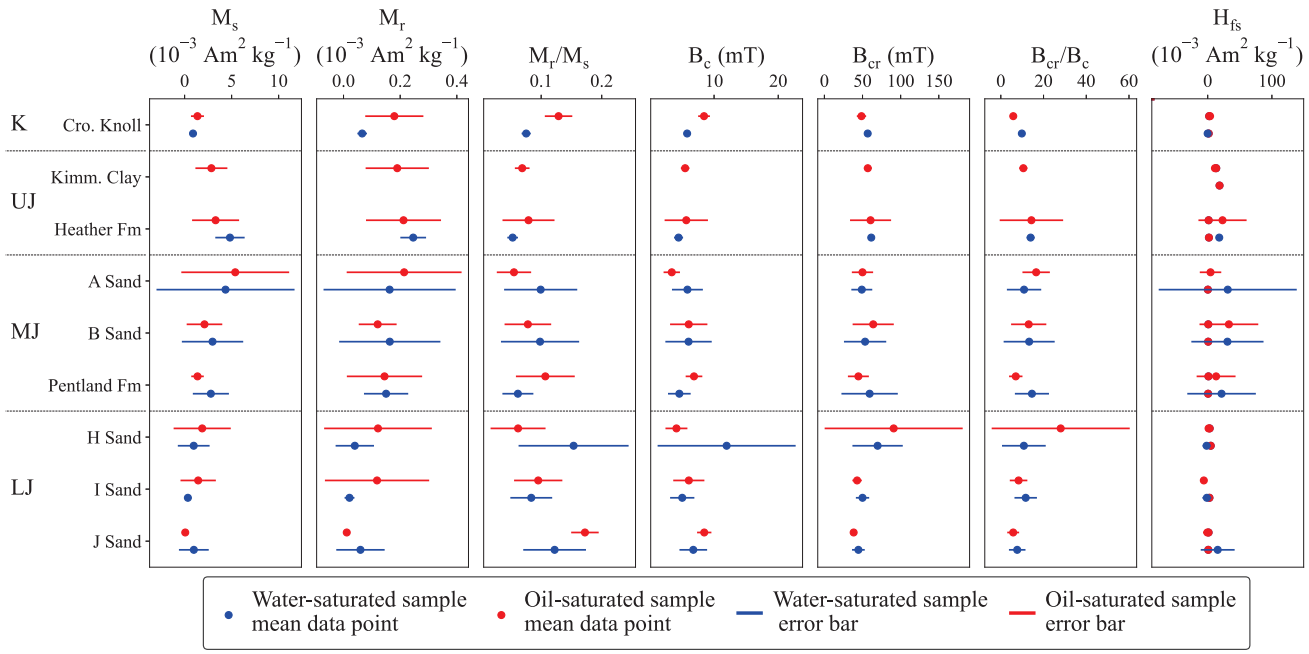


Figure 6.4: *Series of plots showing the mean room temperature magnetic mineral properties of key geological formations within the IMF, differentiated by age. The plots show that the Middle Jurassic formations have the greatest mean M_s and high M_r responses, with the Lower Jurassic formations having the lowest mean M_s and M_r responses. The formations with the greatest sampling density (A and B Sands) show the greatest data variance.*

the formation.

The diverse dataset of the A Sand shows magnetic fluctuation across the basin (Figure 6.3), despite the samples plotting linearly along the lower border of the M_s-M_r plot (Figure 6.3c), samples from Well 11/24a-2 have much higher M_s values than others (Figure 6.3c). Furthermore, samples from Well 12/21-2 have much lower B_c values than others, and both this well and 11/24a-2 have lower B_{cr} values than other wells (Figure 6.3d-f). In contrast, despite its proximity to Well 12/21-2, the dry well 12/21-4 has more similarity to wells within Beatrice Field (11/30-2 and 11/30a-8). All of the variations in oil- and water-saturated samples are indicative of differing magnetic assemblages across the basin, either as mineralogy or volume of magnetic material, and the main reservoir sand can be used to identify the causes behind them, as it is likely that there are multiple sources.

The B Sand has a similar data spread to the A Sand, with a mix of results from different wells, however the M_r, despite showing similar low values, does not extend as far into the upper reaches of the M_s like the A Sand does (Figure 6.3c). The formation does show a separation between different wells, with 12/21-2 showing lower coercivity than samples from Well 12/27-2 and a combination of other wells situated in between (Figure 6.3d-f). The variance between wells is continued in the H_{fs} plots (Figure 6.3g-j), with Well 12/27-2 showing an overall higher H_{fs} than the other wells, with 11/24-1 and 12/21-2 showing much lower values.

The Pentland Formation follows the same patterns as the A and B Sands regarding the separation of results between wells, but does differ in other aspects (Figure 6.3). Whilst Well 12/21-2 has A and B Sand similarities in the M_r by showing lower values, but the other samples show a much more concentrated grouping of results (Figure 6.3c). This disparity is matched in the coercivity results, but

is not reflected in the H_{fs} results which are widely spread and show no well-orientated correlations (Figure 6.3g-j). The Pentland Formation results differ to the other heavily clay-influenced formation, the Heather, as despite the magnetisation results being similar, the wider spread of H_{fs} in the Pentland does not align with the Heather grouping. That these formations do not fully correlate suggests that lithology is not the sole influence on magnetic assemblages.

The H Sand does not have a great number of sample points to analyse, however some tentative conclusions can be made from the data available - the formation shows no clear separation of oil-saturated magnetisation results compared to water-saturated ones (Figure 6.3c), although the water-saturated samples show lower M_s and M_r values than the oil-saturated samples. There are differences in samples from different wells, despite their close proximity, as although they show similar magnetisation results, there are differences in the coercivity values between Wells 11/30-2 (lower) and 11/30-5 (higher; Figure 6.3d-f). The H_{fs} results do not show much, however the results present do plot very centrally within the data (Figure 6.3g-j).

The I Sands shows two groupings of coercivity results and, bar one anomalous value, very low and concentrated magnetisation results (Figure 6.3a-f). The I Sand assemblage is similar to the H Sand in many aspects, but both these formations differ from J Sand with their saturating fluid responses. The cause of the data separation is unclear, as both saturating fluids are present in both groups.

The J Sand shows the clearest separation of oil- and water-saturated samples of all formations in the IMF, with oil-saturated samples having generally higher coercivity and M_r/M_s values than the water-saturated ones. Furthermore, the oil-saturated samples have a much tighter spread of H_{fs} data than the much more widespread water-saturated values. Akin to I Sands, the increased cementation associated with these deeper formations is likely to have impacted the magnetic assemblage, although the direct result is unclear. Alongside this, the J Sand has an increased clay content compared to the other formations, and it shows a similarity to the clay-rich Heather Formation samples through its middling alignment of the samples within the M_s-M_r plot (Figure 6.3c) and the more upper bound H_{fs} results (Figure 6.3g-j), suggesting that this could be a clay indicating characteristic.

6.3 | Well Analysis

Well-scale investigations into magnetic responses aid the understanding of magnetic mineralogy variations both across the IMF and caused by differing saturating fluids. Within this study, due to the limited sampling in numerous wells, as outlined previously in Table 6.1, select wells were identified for in depth analysis through room- and high-temperature methods, chosen through their locations, sample numbers and the formations sampled in each. In the north west of the IMF, Wells 11/24-1, in Lybster Field, and 11/24a-2 were selected, alongside the centrally-located Wells 11/30-2, 11/30-5, 1130a-8 and 11/30a-B10 in Beatrice Field, 12/21-2 in Jacky Field and 12/21-4, whilst Wells 12/27-1, 12/27-2 and 12/29-1 were selected in the south east of the IMF, and Well 12/25-3 in the east was chosen to investigate the boundary between the Inner and Outer Moray Firth Basins (Figure 6.5). The magnetic responses of the wells across the IMF vary somewhat, although there are minimal differences in the responses recorded in differing saturating fluids (Table 6.3 & Figure 6.6).

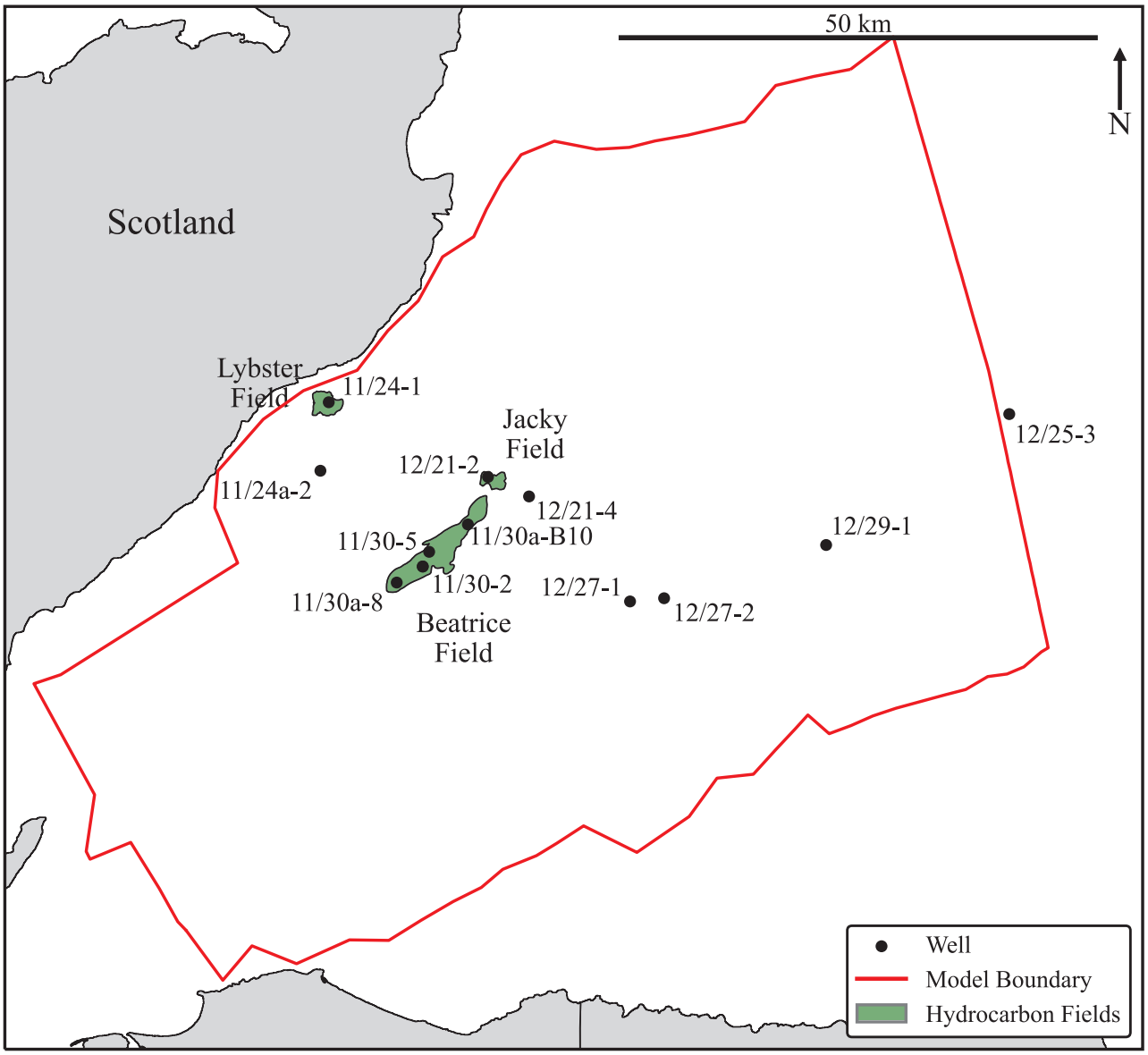


Figure 6.5: *Map of the IMF and study area, outlining the location of the selected wells where samples were taken for room- and high-temperature magnetic analysis, with a reference to the location of the basin and petroleum systems model created in this study.*

The mean well magnetism results show more similarities between oil- and water-saturated samples, likely due to the removal of geological variations by averaging samples across the entire well section. However, when plotted together, magnetic variations between the wells become clearer than between formations (Figure 6.6). Whilst the majority of wells broadly plot across the entire data spread, two wells are somewhat different, with Well 11/24a-2 having much lower B_c but relatively high M_s values compared to other wells, and Well 12/21-2 shows lower B_c values and has a spread of M_s data lower than the rest of the data (Figure 6.6a-c,e). There appears to be a very broad trend across the data, with the wells near Lybster Field (11/24-1 and 11/24a-2) and Jacky Field (12/21-2 and 12/21-4) having lower B_c and M_s values, those from around Beatrice Field (the 11/30 wells) showing more average values, and those from the south east of the IMF (Wells 12/27-1, 12/27-2 and 12/29-1) having higher values. From this basic magnetic data alone, it is not clear why this trend occurs, and requires further investigation through high temperature and FORC analysis.

Table 6.3: *Table outlining the mean magnetic results from all samples from all wells in the IMF, alongside one standard deviation (σ), delineated by well and saturating fluid. Results of each well are grouped across all formations sampled throughout, so results are a function of the magnetic mineral assemblage across the entire section, thus the results are skewed to the most magnetic formations. O = oil, W = water.*

	Well	Fluid	Number of Samples	M_s (σ) (10^{-3} Am^2kg^{-1})	M_r (σ) (10^{-3} Am^2kg^{-1})	M_r/M_s (σ)	B_c (σ) (mT)	B_{cr} (σ) (mT)	B_{cr}/B_c (σ)	H_{fs} (σ) (10^{-3} Am^2kg^{-1})
NW IMF	11/24-1	O	20	2.23 (±1.41)	0.11 (±0.05)	0.05 (±0.01)	4.2 (±1)	58.2 (±21.8)	14.5 (±12.5)	9.7 (±21.9)
		W	8	1.54 (±0.49)	0.10 (±0.05)	0.07 (±0.01)	5.3 (±0.8)	50.1 (±5.64)	9.7 (±2.5)	11.0 (±13.4)
	11/24a-2	O	11	13.27 (±3.66)	0.48 (±0.16)	0.04 (±0.01)	2.4 (±0.3)	54.1 (±11.9)	22.5 (±3.9)	8.5 (±4.4)
		W	5	18.44 (±4.56)	0.60 (±0.11)	0.03 (±0.01)	2.6 (±0.4)	62.5 (±3.1)	24.5 (±3.1)	19.8 (±3.8)
Central IMF Fields	11/30-2	O	4	1.44 (±2.24)	0.11 (±0.13)	0.10 (±0.08)	7.1 (±5.8)	77.8 (±66.5)	19.6 (±25.7)	0.8 (±4)
		W	14	1.90 (±1.5)	0.13 (±0.12)	0.10 (±0.06)	6.4 (±3.6)	64.0 (±31.6)	13.7 (±14)	75.9 (±159.8)
	11/30-5	O	0	-	-	-	-	-	-	-
		W	9	0.27 (±0.38)	0.01 (±0.02)	0.12 (±0.08)	9.6 (±10.1)	60.6 (±28.9)	10.5 (±6.1)	-4.8 (±4.5)
	11/30a-8	O	8	0.90 (±0.98)	0.07 (±0.06)	0.09 (±0.04)	5.3 (±1.1)	35.2 (±8.7)	7.4 (±3.2)	21.1 (±48.1)
		W	25	0.78 (±2.38)	0.06 (±0.17)	0.15 (±0.05)	7.6 (±2.3)	36.1 (±10)	5.5 (±4)	9.2 (±18)
	11/30a-B10	O	11	1.15 (±1.75)	0.09 (±0.17)	0.11 (±0.05)	6.5 (±2.4)	41.9 (±5.9)	7.6 (±3.9)	-5.2 (±4.3)
		W	10	0.64 (±1.36)	0.04 (±0.07)	0.13 (±0.05)	7.2 (±2)	43.1 (±7.5)	7.0 (±3.1)	14.8 (±27.3)
	12/21-2	O	17	3.08 (±1.43)	0.15 (±0.06)	0.05 (±0.01)	3.2 (±0.8)	51.7 (±15.8)	17.0 (±5.6)	1.4 (±7.1)
		W	16	4.72 (±2.69)	0.20 (±0.1)	0.05 (±0.02)	3.4 (±1.6)	66.0 (±42.5)	20.4 (±8.1)	28.3 (±61.3)

Table 6.3 (continued): *Table outlining the mean magnetic results from all samples from all wells in the IMF, alongside one standard deviation (σ), delineated by well and saturating fluid. Results of each well are grouped across all formations sampled throughout, so results are a function of the magnetic mineral assemblage across the entire section, thus the results are skewed to the most magnetic formations. O = oil, W = water.*

	Well	Fluid	Number of Samples	M_s (σ) (10^{-3} Am^2kg^{-1})	M_r (σ) (10^{-3} Am^2kg^{-1})	M_r/M_s (σ)	B_c (σ) (mT)	B_{cr} (σ) (mT)	B_{cr}/B_c (σ)	H_{fs} (σ) (10^{-3} Am^2kg^{-1})
Central IMF	12/21-4	O	0	-	-	-	-	-	-	-
		W	11	2.69 (±1.11)	0.13 (±0.04)	0.05 (±0.01)	4.2 (±0.8)	59.1 (±7)	14.7 (±3.6)	11.6 (±8.2)
	12/25-3	O	14	1.37 (±0.69)	0.18 (±0.1)	0.13 (±0.02)	8.4 (±0.9)	48.6 (±6.1)	5.8 (±0.9)	3.7 (±2.3)
		W	6	0.89 (±0.29)	0.07 (±0.02)	0.08 (±0.01)	5.8 (±0.5)	56.8 (±2.3)	9.8 (±0.8)	-0.1 (±1.9)
	12/27-1	O	15	1.30 (±0.63)	0.13 (±0.11)	0.11 (±0.05)	7.0 (±1.67)	60.0 (±58)	11.2 (±17.5)	50.6 (±145.2)
		W	4	2.19 (±1.12)	0.17 (±0.05)	0.09 (±0.04)	6.3 (±1.6)	52.0 (±9.9)	8.8 (±3.3)	1.7 (±5.1)
	12/27-2	O	8	0.78 (±0.36)	0.08 (±0.03)	0.11 (±0.04)	8.8 (±2.7)	83.0 (±39.9)	11.7 (±11.2)	91.6 (±41.4)
		W	4	2.94 (±1.65)	0.16 (±0.04)	0.07 (±0.05)	5.7 (±3.5)	63.2 (±12.4)	14.0 (±6.8)	56.6 (±49.9)
	12/29-1	O	7	5.21 (±2.29)	0.32 (±0.11)	0.06 (±0.01)	5.4 (±0.7)	64.9 (±9)	12.3 (±2.8)	18.8 (±7.5)
		W	3	4.82 (±1.56)	0.25 (±0.05)	0.05 (±0.01)	4.5 (±0.7)	61.4 (±2.0)	14.0 (±1.9)	18.0 (±1.9)

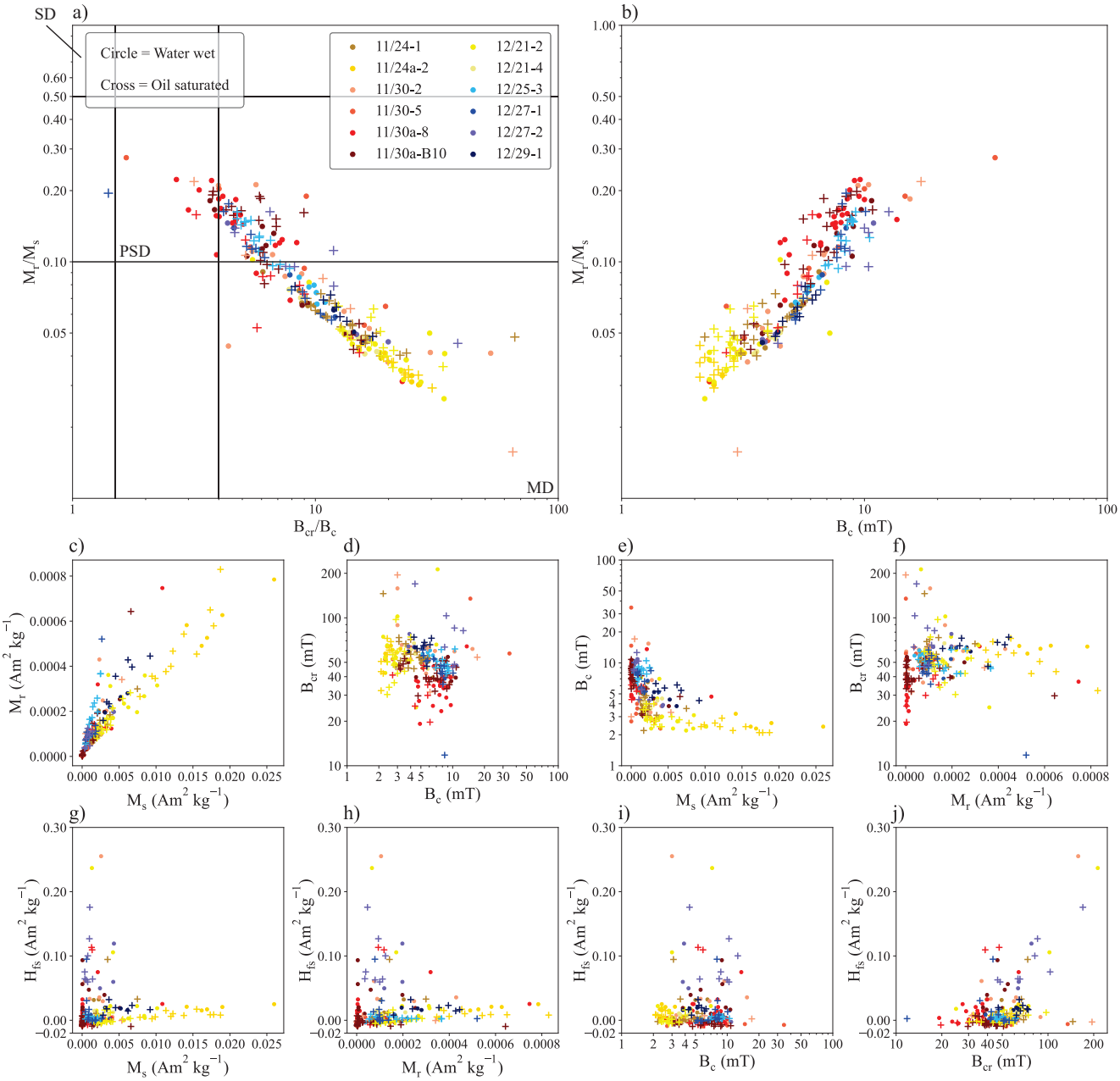


Figure 6.6: *Series of data plots comparing the room temperature magnetic characteristics of samples across the formations in the IMF, delineated by well and by saturating fluid. a) shows a Day Plot (Day* et al.*, 1977), comparing M_r/M_s against B_{cr}/B_c; b) shows M_r/M_s against B_c; and c) to j) are a series of plots showing the relationships between M_r, M_s, B_c, B_{cr} and H_{fs}. The Day Plot (a) shows a linear range of data with most wells spread across it, but with the Wells 11/24a-2 and 12/21-2 having lower B_{cr}/B_c and M_r/M_s ratios than the others, reflected in the B_c data in plots b, d, e and i.*

6.3.1 | High Temperature Mineral Interpretation

Within the well-scale analysis, high temperature susceptibility measurements were used to assist the identification of magnetic minerals alongside the room temperature analyses. The vast majority of samples contain weakly magnetic but ubiquitous magnetite, limiting the effective interpretation of the minerals at just room temperature, thus high temperature measurements are crucial to showing the minerals present through their susceptibility variations as they reach their various, identifiable magnetic unblocking temperatures. In this study, the high temperature measurements show evidence for at least seven magnetic minerals, with the majority of samples containing at least two in combination. As such,

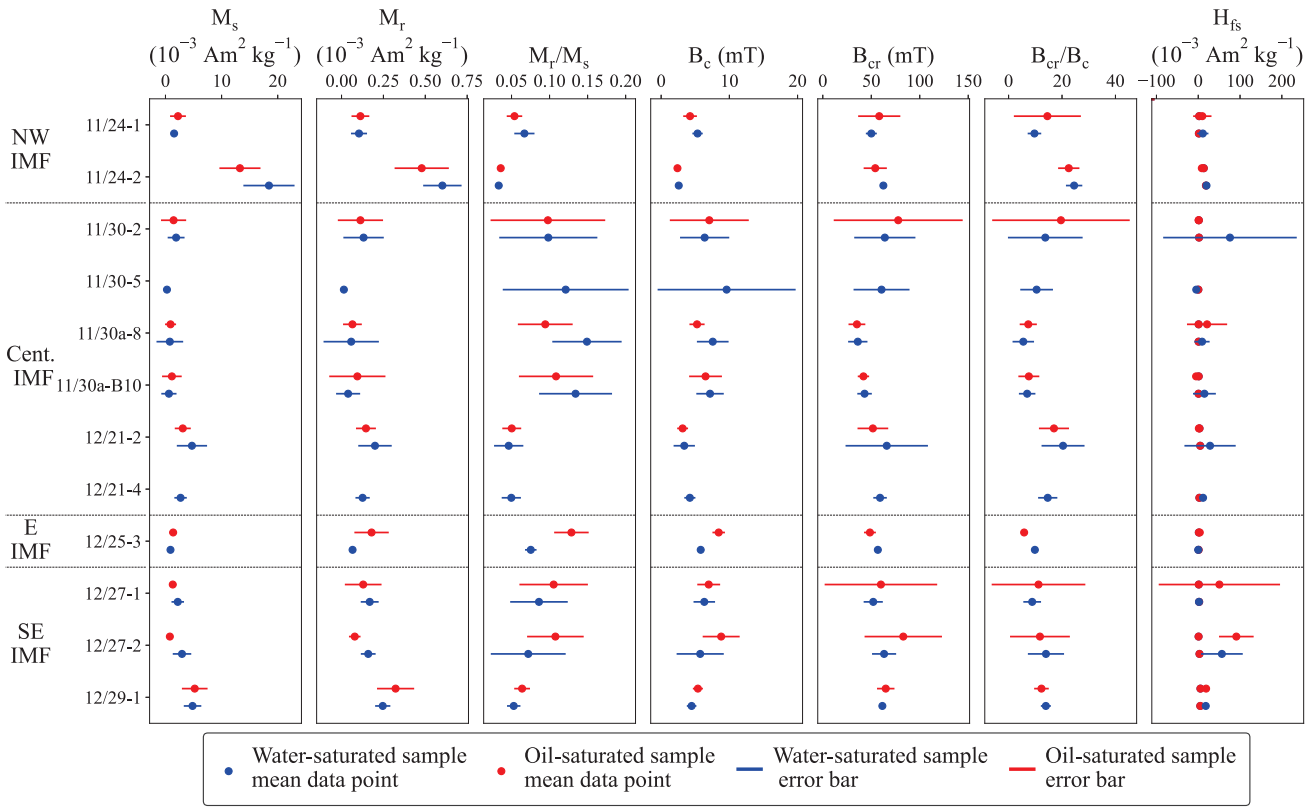


Figure 6.7: *Series of plots showing the mean room temperature magnetic mineral properties of several wells across the IMF, differentiated by location. The plots show that Well 11/24a-2 shows the highest mean M_s and M_r responses, with Well 11/30-2 having the greatest error bars, due to sampling limitations.*

there is extensive variety within the curves as the different minerals coexist in a variety of combinations, however when simplified and the curves are unmixed into their individual components, each mineral and the curves they are identified through become more clear. Throughout this section of the study, the minerals are identified and specified through the following series of high temperature susceptibility indicators:

- **Magnetite** (Fe_3O_4) – Figure 6.8a – Regardless of the activity on the heating curve, magnetite is identifiable by the sharp increase in susceptibility on the cooling curve as the temperature drops below its Curie Temperature of 580 °C (Dunlop, 2014; Dunlop and Özdemir, 1997; Kittel, 1967).
- **Goethite** (α-FeOOH) – Figure 6.8b – Goethite is evidenced by a double-jump in susceptibility as it is heated, firstly at about 250 °C, then again at around 300 °C as it alters, with its susceptibility peaking at around 450-500 °C. Typically, goethite alters into hematite via magnetite, and this results in the susceptibility at 700+ °C not returning to its initial baseline, along with often a small increase in susceptibility at the Curie Temperature of magnetite at 580 °C (Bustamante *et al.*, 2010; Dunlop and Özdemir, 1997; Liu *et al.*, 2006; Minyuk *et al.*, 2011). Note that the goethite-derived variation typically seen in magnetisation at 125 °C is not seen as these measurements are of susceptibility not direct magnetisation.
- **Siderite** ($FeCO_3$) – Figure 6.8c – Siderite shows an increasing susceptibility on the heating curve at around 400 °C, however beyond this temperature, siderite irreversibly alters to magnetite, so also shows a large increase in susceptibility at 590 °C as the newly-formed magnetite returns to

below it's Curie Temperature (Abdulkarim *et al.*, 2022a; Badejo *et al.*, 2021c; Emmerton *et al.*, 2012).

- **Pyrite** (FeS_2) – Figure 6.8d – As with other iron sulphides, pyrite is evidenced by a sharp increase in susceptibility peaking at approximately 300 °C, with minimal change on heating, but often with a clear indicator around 300 °C, typically pyrite alters to pyrrhotite (Fe_7S_8), producing the large susceptibility increase on the cooling curve (Dekkers, 1989; Minyuk *et al.*, 2013).
- **Lepidocrocite** (γ-FeOOH) – Figure 6.8e – This is a tricky mineral to identify as it shows a steep increase in susceptibility on heating beyond approximately 300 °C, similar to where goethite experiences an increase. However, lepidocrocite peaks at about 400 °C prior to showing an abrupt decrease in susceptibility back to baseline by about 480 °C (Gendler *et al.*, 2005).
- **Maghemite** (Fe_2O_3) – Figure 6.8f – Maghemite initially has relatively high susceptibilities, before seeing a valley between 200-500 °C during heating, typically before increasing again to approximately 550 °C then decreasing again as it passes through the Curie Temperature of magnetite which is has altered into (Gao *et al.*, 2019).
- **Hematite** (Fe_2O_3) – Hematite is very rarely seen present within samples, however is regularly present as an alteration product, commonly from goethite and magnetite, and it results in susceptibility curves that do not return to baseline when they reach 700 °C (Bustamante *et al.*, 2010; Dunlop and Özdemir, 1997; Minyuk *et al.*, 2011).

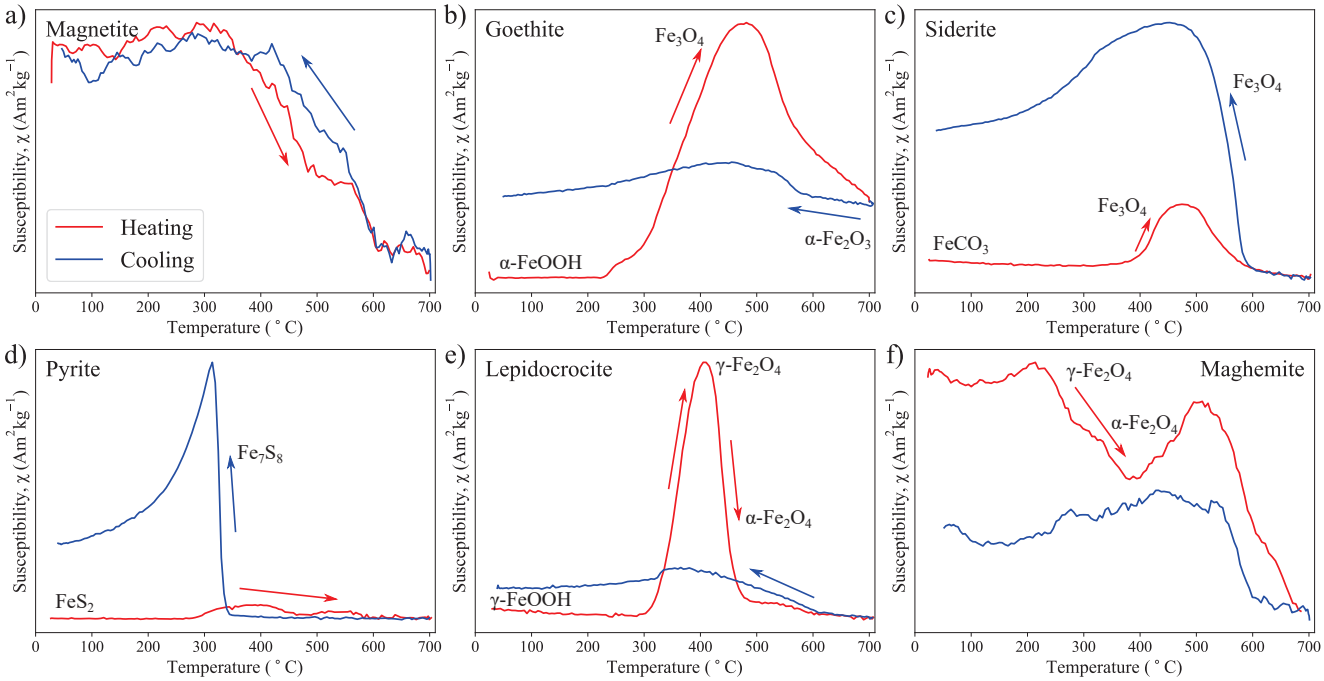


Figure 6.8: *Series of high-temperature susceptibility curves showing examples of the responses formed by the six individual magnetic minerals identified in this study that are present across the IMF.*

6.3.2 | WELL 11/24-1 - LYBSTER FIELD

Well 11/24-1 runs through the centre of Lybster Field in the north-west of the IMF (Figure 6.9), and has been drilled through the system into the Triassic, and has had Heather Formation, A and B Sands, Mid Shale and the Pentland Formation cored. From these intervals, 28 samples were taken and analysed at room temperature and high temperature to identify magnetic characteristics and mineralogy. Well 11/24-1 is one of the shallowest wells in the study, so is potentially impacted by biodegradation, and is located on the edge of the basin, thus may vary magnetically to more central-basin wells.

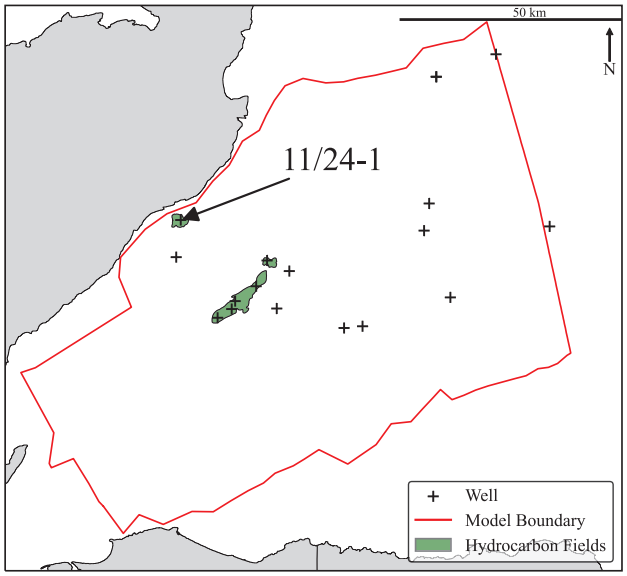


Figure 6.9: *Map of the IMF and study area, showing the location of Well 11/24-1 in Lybster Field.*

Well 11/24-1 has one of the best examples of magnetic enhancement seen at an OWC in this study, where the OWC zone between 4948-4955 ft experiences an abrupt increase in M_s, M_r and H_{fs}, but a decrease in B_c and B_{cr} immediately below the top of the OWC zone at 4949 ft (Figure 6.10). The increase at the contact is starkly different to the rest of the samples that stay relatively consistent throughout the rest of the well, only the B_c showing strong variations outside of the OWC zone.

The FORC assemblage broadly matches the direct magnetic results, with little variation from a strong PSD component throughout the well with some other domains offering minimal input, however, as Figure 6.11 shows, there is a difference in the FORC at the OWC enhancement which appears to be more PSD-dominant than others. The increase in PSD but not other domains at the enhancement would indicate an influx of solely-PSD grains in the formation water directly below the OWC. The HT susceptibility curves show a large dominance of both magnetite and goethite in both the oil- and water-saturated samples, as well as within the OWC zone (Figure 6.11A-G). There is minimal evidence of other minerals, however there are some minor indications of pyrrhotite in both the oil- and water-saturated samples, likely as a result of alteration of the goethite (Figure 6.11C), and siderite within the water-saturated Pentland Formation samples (Figure 6.11I,J). The assemblages in the oil-saturated and OWC zone samples are mostly consistent, however they do differ to the water-saturated samples, suggesting that there are variations between the saturating fluids.

In the low temperature curves of samples across the OWC zone, there is further evidence of goethite and magnetite in each sample, thus agreeing with the room- and high-temperature data that Well 11/24-1's magnetic assemblage is dominated by goethite and magnetite (Figure 6.12). Goethite is evidenced by a gap between the ZFC and FC curves until relatively high temperatures, approximately 200 K, and the presence of magnetite is seen by its Verwey transition at 120 K (Verwey, 1939). Furthermore, there is some evidence of siderite in the OWC zone (Figure 6.12iv,v), indicated by the sharp descent of the FC curve below 30 K, and magnetite in the samples around the OWC zone top (Figure 6.12ii,iii), evidenced

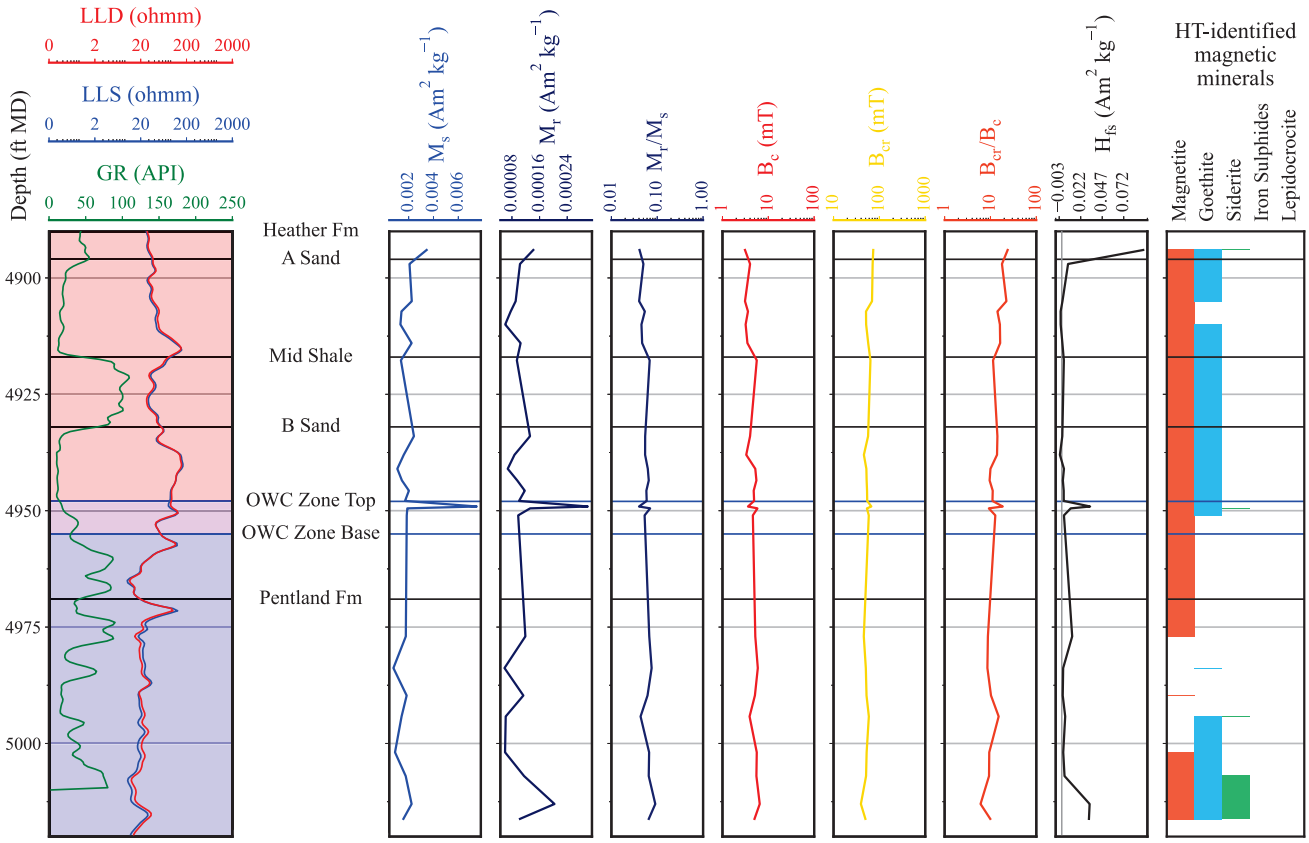


Figure 6.10: *Plots of magnetic results against depth within Well 11/24-1, with gamma ray and resistivity well log data used to identify formations and fluids. Well shaded in red is oil-saturated, blue is water-saturated, purple is within the OWC zone, with the OWC zone shown. M_s = saturation magnetisation; M_r = remanent magnetisation; B_c = magnetic coercivity; B_{cr} = coercivity of remanence; and H_{fs} = high field slope, HT susceptibility-identified magnetic minerals at each sample are shown.*

by the increased remanence.

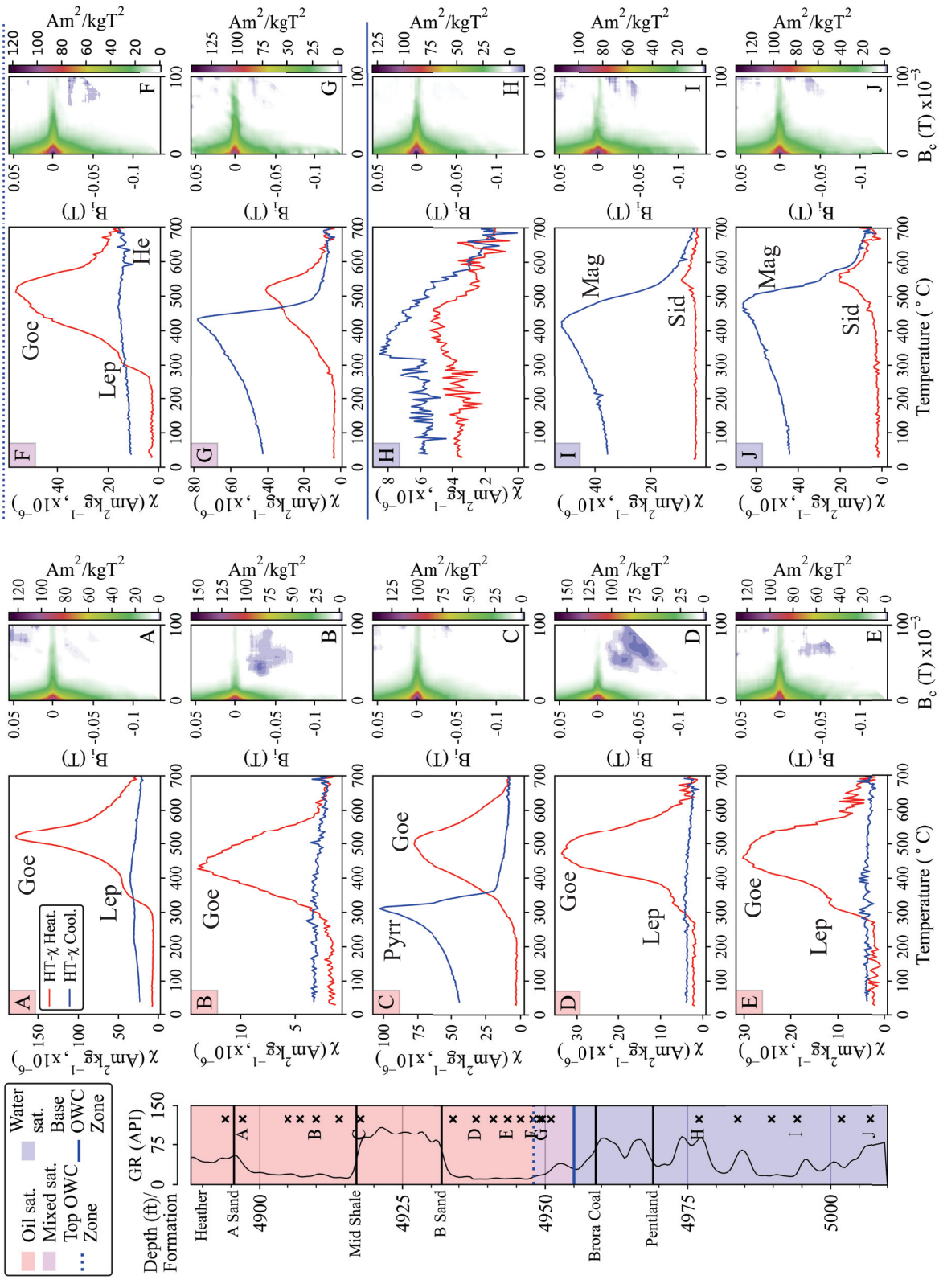


Figure 6.11: *Series of high temperature susceptibility curves and room temperature FORC diagrams of selected samples, as located on the gamma ray well log plot, across various depths and saturated by both oil and water, in Well 11/24-1. The high temperature plots show a defined change in magnetic mineralogy between saturating fluids that is not as well represented in the FORC diagrams. Goe = goethite, He = hematite, Lep = lepidocrocite, Mag = magnetite, Pyrr = pyrrhotite, Sid = siderite*

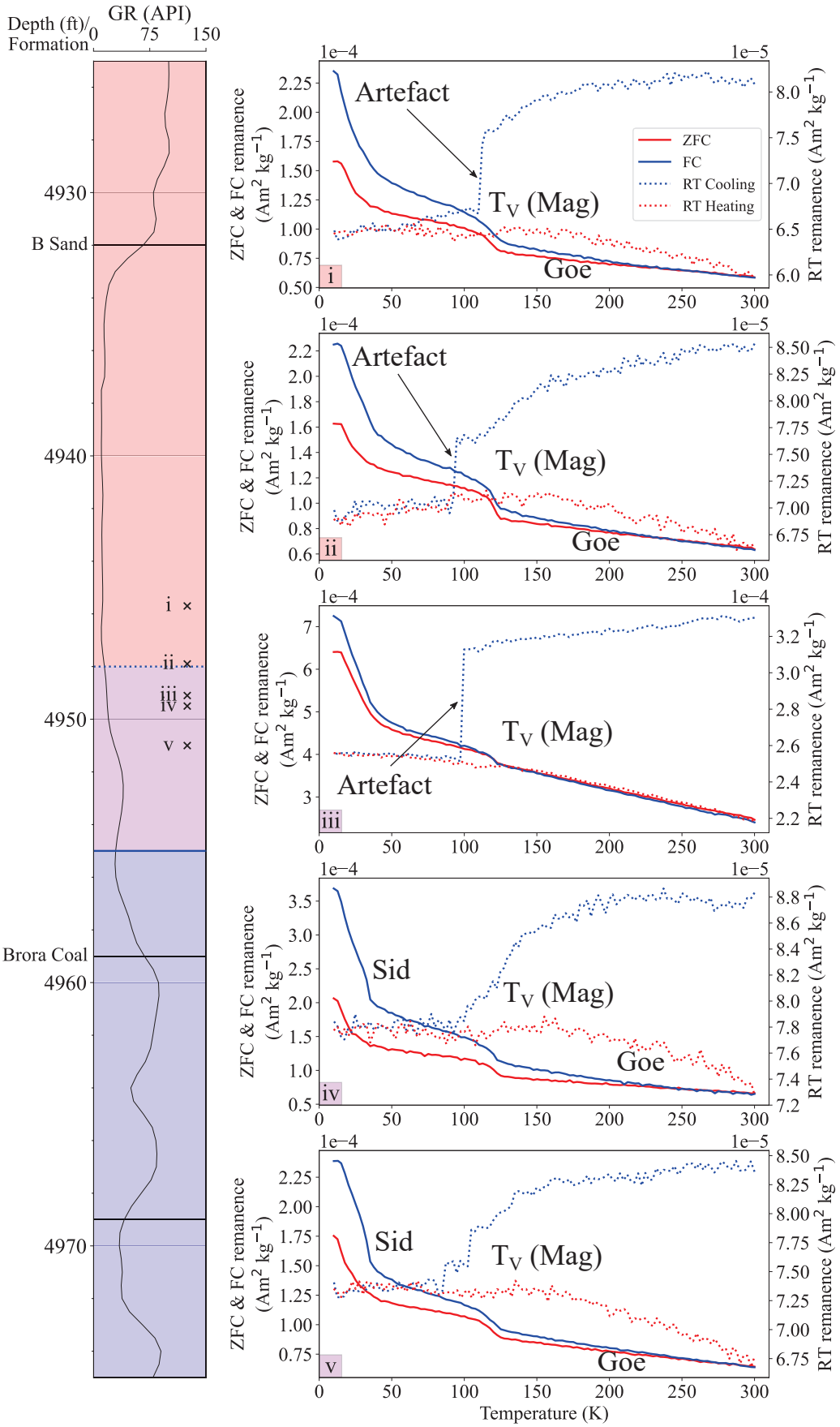


Figure 6.12: *Series of low temperature ZFC, FC and RT Curves of select samples across the OWC zone seen in Well 11/24-1, used to identify the magnetic mineral assemblages within the samples through identification of mineral-specific behaviours. Early and sharp T_V responses (e.g. ii, iii) are expected errors in measurements, as they are typically smoother (e.g. i). Note the increasing remanence values measured towards the OWC, and immediately below it (ii, iii), which is indicative of increasing magnetite content. Goe = goethite, Sid = siderite, T_V = Verwey Transition indicative of Mag (magnetite).*

6.3.3 | WELL 11/24A-2

Well 11/24a-2 is near Well 11/24-1 and Lybster Field in the NW IMF (Figure 6.13), drilled through a high created by the Great Glen Fault, it sits on the NW side of the basin-forming fault. It has been drilled through the entire reservoir section, however sampling was only available in the A Sand and the Mid Shale, with all 16 samples in this study taken from the A Sand. The sampled section is at a similar depth to wells in the central IMF around Beatrice Field, so any variation between the magnetic characteristics between the two are likely location- and hydrocarbon migration-derived rather than depth- and geologically-derived.

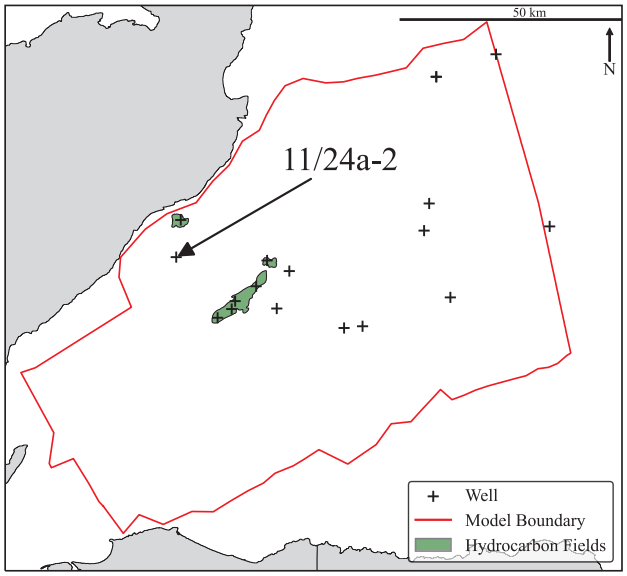


Figure 6.13: *Map of the IMF and study area, showing the location of Well 11/24a-2 in the basin's NE.*

The OWC in this well is less defined, and also shows reversed characteristics, than the OWC of 11/24-1. The M_s and M_r responses see a small increase above the contact at 6130 ft, and then a clear decrease below the contact, whilst the B_c, B_{cr} and H_{fs} decrease above the contact then sharply increase below (Figure 6.14). When looking at the magnetism as a whole, the oil-saturated samples show a generally lower magnetisation than the water-saturated samples, though only marginally (Figure 6.15).

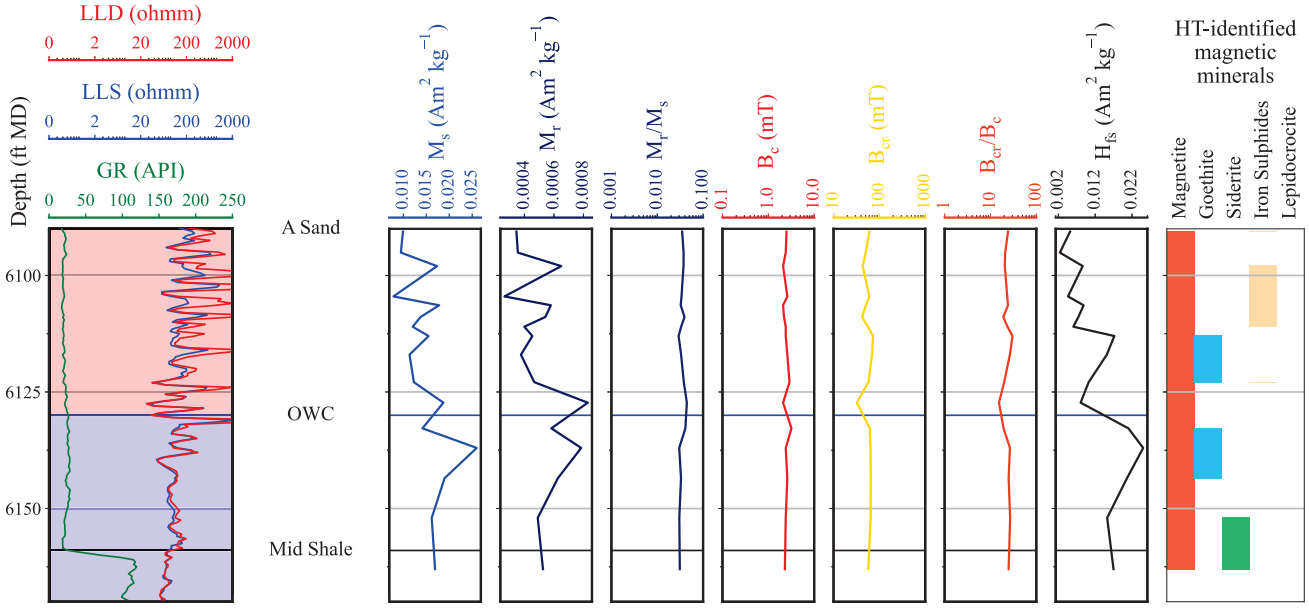


Figure 6.14: *Plots of magnetic results against depth within Well 11/24a-2, with gamma ray and resistivity well log data used to identify formations and fluids. Well shaded in red is oil-saturated, blue is water-saturated, with the OWC shown. M_s = saturation magnetisation; M_r = remanent magnetisation; B_c = magnetic coercivity; B_{cr} = coercivity of remanence; and H_{fs} = high field slope, HT susceptibility-identified magnetic minerals at each sample are shown.*

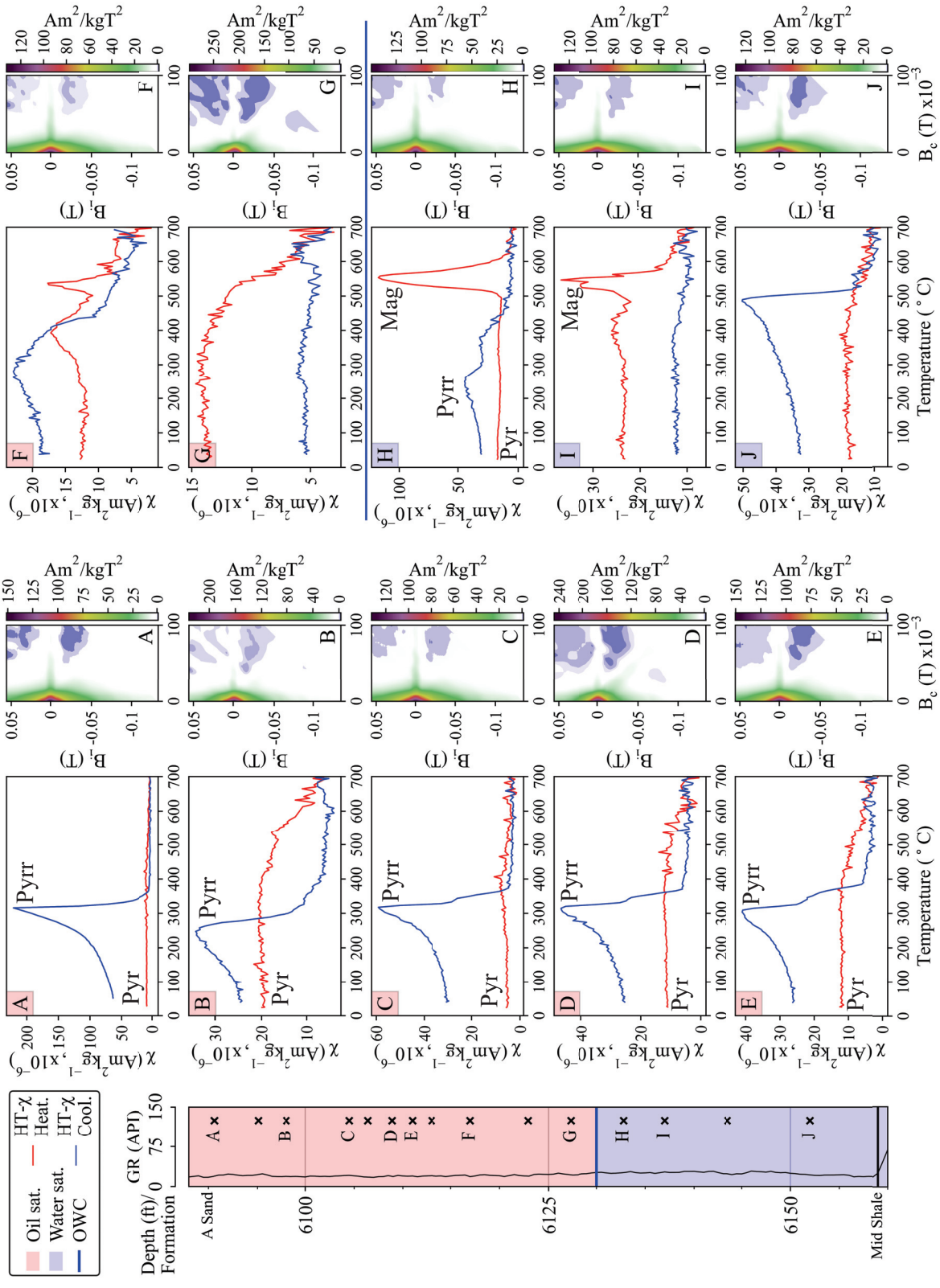


Figure 6.15: *Series of high temperature susceptibility curves and room temperature FORC diagrams of selected samples, as located on the gamma ray well log plot, across various depths and saturated by both oil and water, in Well 11/24a-2. The high temperature plots show a defined change in magnetic mineralogy between saturating fluids that is not as well represented in the FORC diagrams. Mag = magnetite, Pyr = pyrite, Pyrr - pyrrhotite.*

The FORC diagrams in this well differ to Well 11/24-1, but do show consistency with the magnetic response through variation between the samples above and below the OWC (Figure 6.15). The FORCs within the oil-saturated region and below the OWC are PSD-dominated, with some minor MD influence (Figure 6.15A-F). However, the FORC from just above the OWC (Figure 6.15G) shows a more MD-dominated assemblage with some evidence for vortex behaviour, suggesting that an accumulation of minerals different to the rest of the section is present just above the contact.

The continued difference in magnetic minerals between saturating fluids is further shown by the high temperature susceptibility curves (Figure 6.15), with a clear variation between the two fluids. Oil-saturated samples show unwavering evidence of pyrrhotite alongside pyrite and magnetite, with some potential for goethite in two of the eleven samples, whereas the water-saturated samples show evidence of goethite and magnetite, with some potential siderite in two of the samples. The extensive presence of iron sulphides in this well is different to all other wells within the IMF, and raises a question as to where the sulphur required to form them originated.

6.3.4 | Well 11/30-2 - Central Beatrice Field

Well 11/30-2, the centrally located well in Beatrice Field, is drilled through the Cretaceous-Triassic section, including the Jurassic-age reservoir (Figure 6.16). Due to sampling limits, only 18 samples were collected and analysed, split between the A, B H and J Sands, the Mid Shale and the Pentland Formation. The wells in Beatrice Field show evidence of two OWCs, likely due to localised trapping as a result of interbedded shales (the Mid Shale and Lady's Walk Shale) that exist within the reservoir section. Due to the sparse sampling distribution, clear analysis from this well's OWCs are difficult, however, the sampling of many formations within one well does offer cross-formation analysis and understanding of lithological variations within the same location.

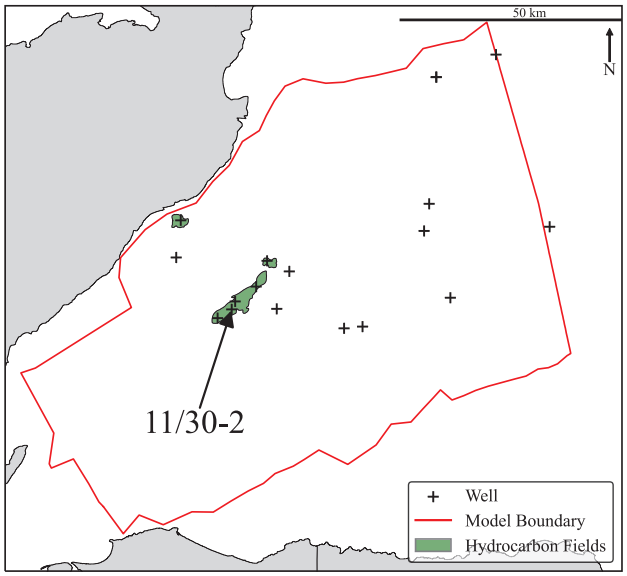


Figure 6.16: *Map of the IMF and study area, showing the location of Well 11/30-2 in Beatrice Field.*

The samples show strong consistency across the well, but with marginal fluctuations around the OWCs (Figure 6.17). Whilst the upper OWC, within the A Sand at 6385 ft, shows some variation and an increase below the OWC compared to above, the distance between the samples is too great to confirm a finely constrained enhancement similar to others in the study. In comparison, the lower OWC, in the H Sand at 6879 ft, shows a very distinct change in the magnetic response directly below the OWC, with the M_s, M_r and H_{fs} responses showing a decrease down to the OWC then minimal variation across it, but a clear increase below. In opposition to these, B_c sees a peak at the OWC before decreasing below and B_{cr} shows a clear increase directly below the OWC before decreasing.

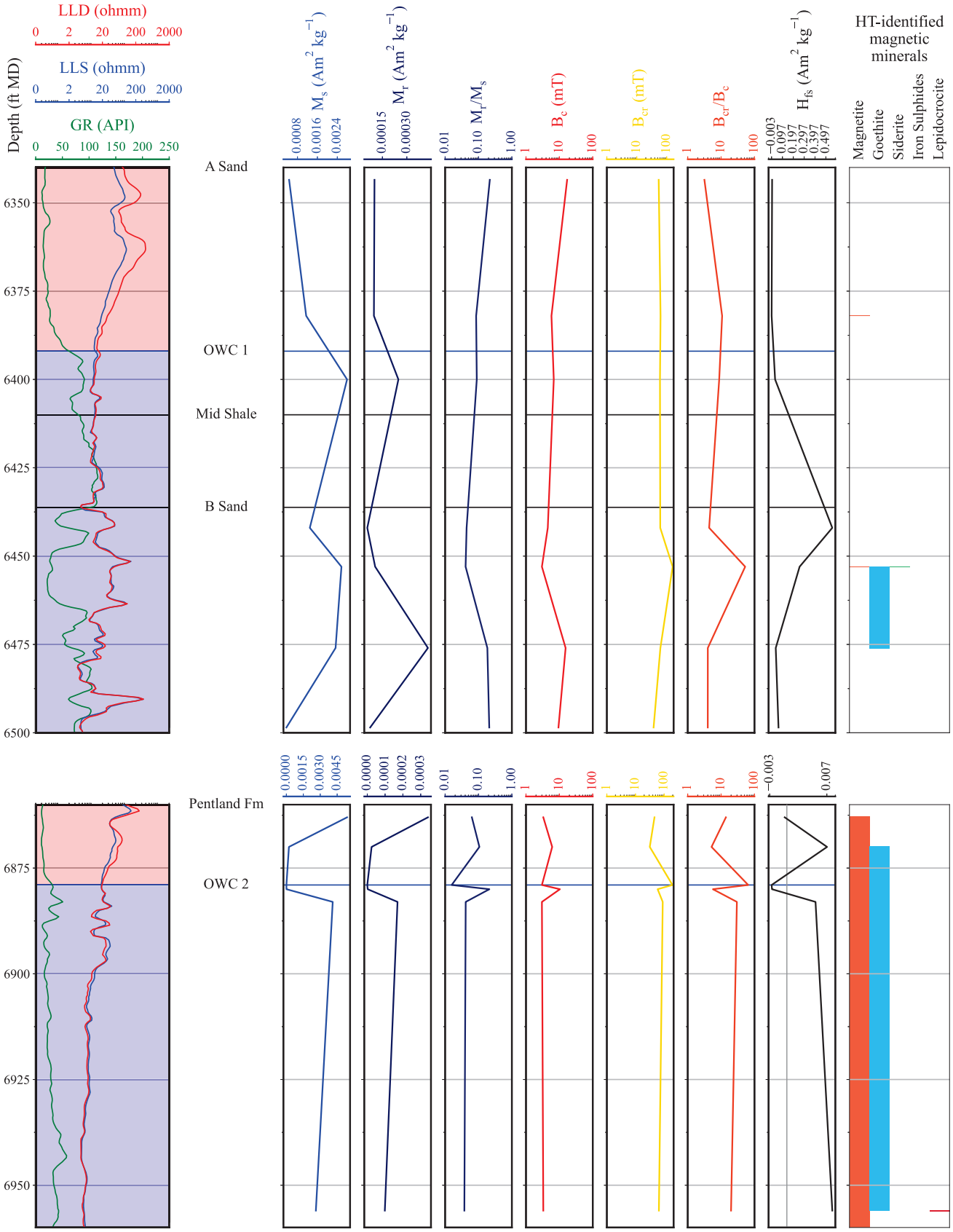


Figure 6.17: *Plots of magnetic results against depth within Well 11/30-2. Well shaded in red is oil-saturated, blue is water-saturated, with the OWCs shown. M_s = saturation magnetisation; M_r = remanent magnetisation; B_c = magnetic coercivity; B_{cr} = coercivity of remanence; and H_{fs} = high field slope, HT susceptibility-identified magnetic minerals at each sample are shown.*

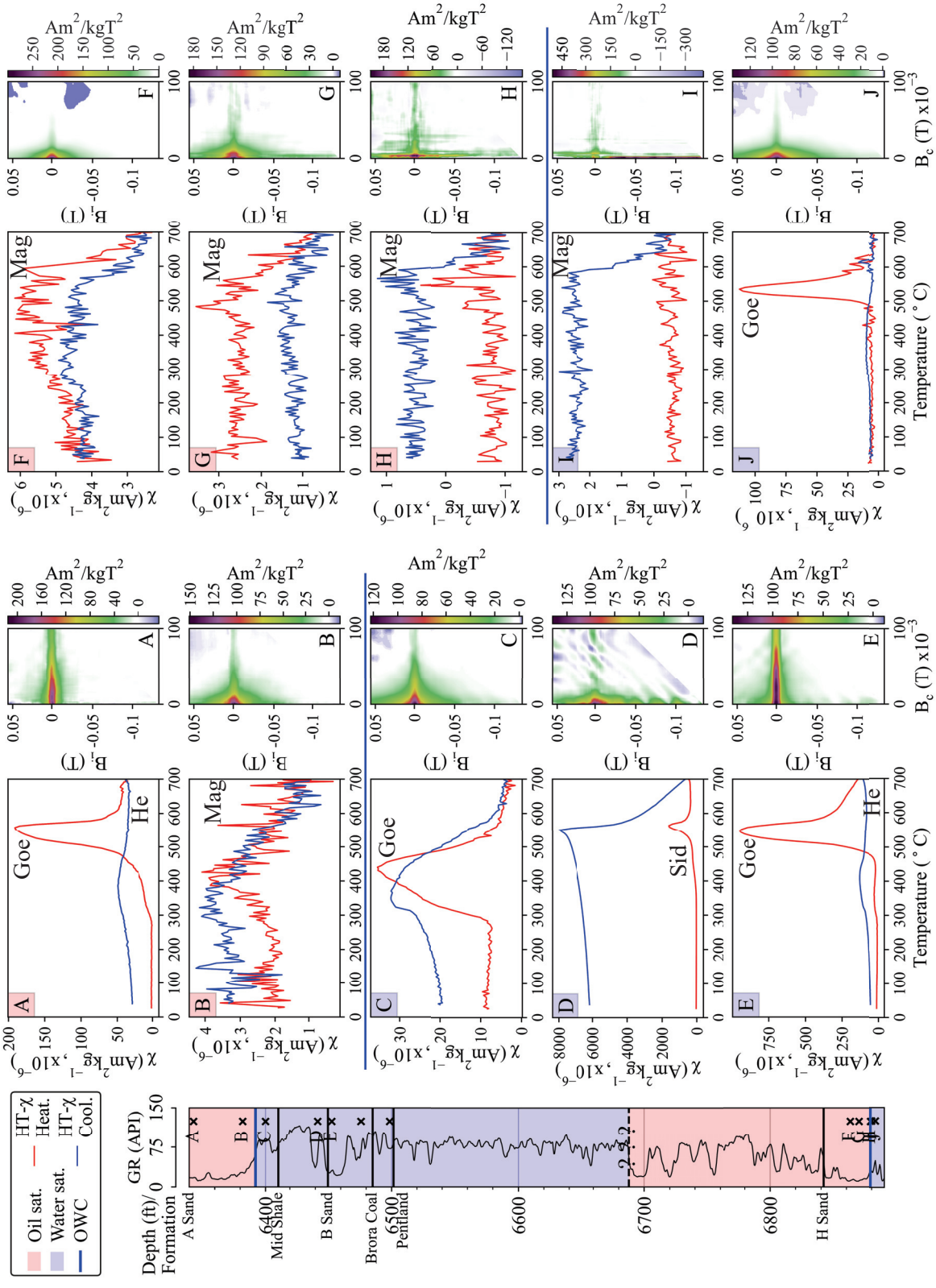


Figure 6.18: *Series of high temperature susceptibility curves and room temperature FORC diagrams of selected samples, as located on the gamma ray well log plot, across various depths and saturated by both oil and water, in Well 11/30-2. The high temperature plots show limited variation in magnetic mineralogy between saturating fluids. Goe = goethite, He = hematite, Mag = magnetite, Sid = siderite.*

Both oil- and water-saturated samples are similar, showing clear goethite and magnetite presence, but also indications of siderite, pyrite and potentially lepidocrocite (Figure 6.18). Generally the oil-saturated samples contain relatively more goethite than the water-saturated samples, however, goethite is not exclusive to either saturating fluid. The other minerals are not present within the oil-saturated samples, and are solely identified within water-saturated samples. The low temperature curves of samples across the upper OWC show some evidence of change across the contact, with the oil-saturated sample at 6870 ft showing evidence of magnetite, whilst the samples below the OWC, at 6879 and 6880 ft, show both evidence of magnetite and goethite (Figure 6.19).

OWC analysis is difficult due to the sampling limits and FORC diagram quality, however the FORC diagrams do show some saturating fluid-caused variations (Figure 6.18). Around the upper OWC, the FORC diagrams suggest varying levels of very PSD-dominated assemblages, but the sub-OWC FORC diagram (Figure 6.18E) shows more SD behaviour compared to the super-OWC FORC diagram (Figure 6.18B). In comparison, the lower OWC shows differing changes across it, with the super-OWC FORC diagram (Figure 6.18F) showing more MD influenced, PSD dominated behaviour than the sub-OWC FORC diagram (Figure 6.18J), which shows more PSD control with less MD influence.

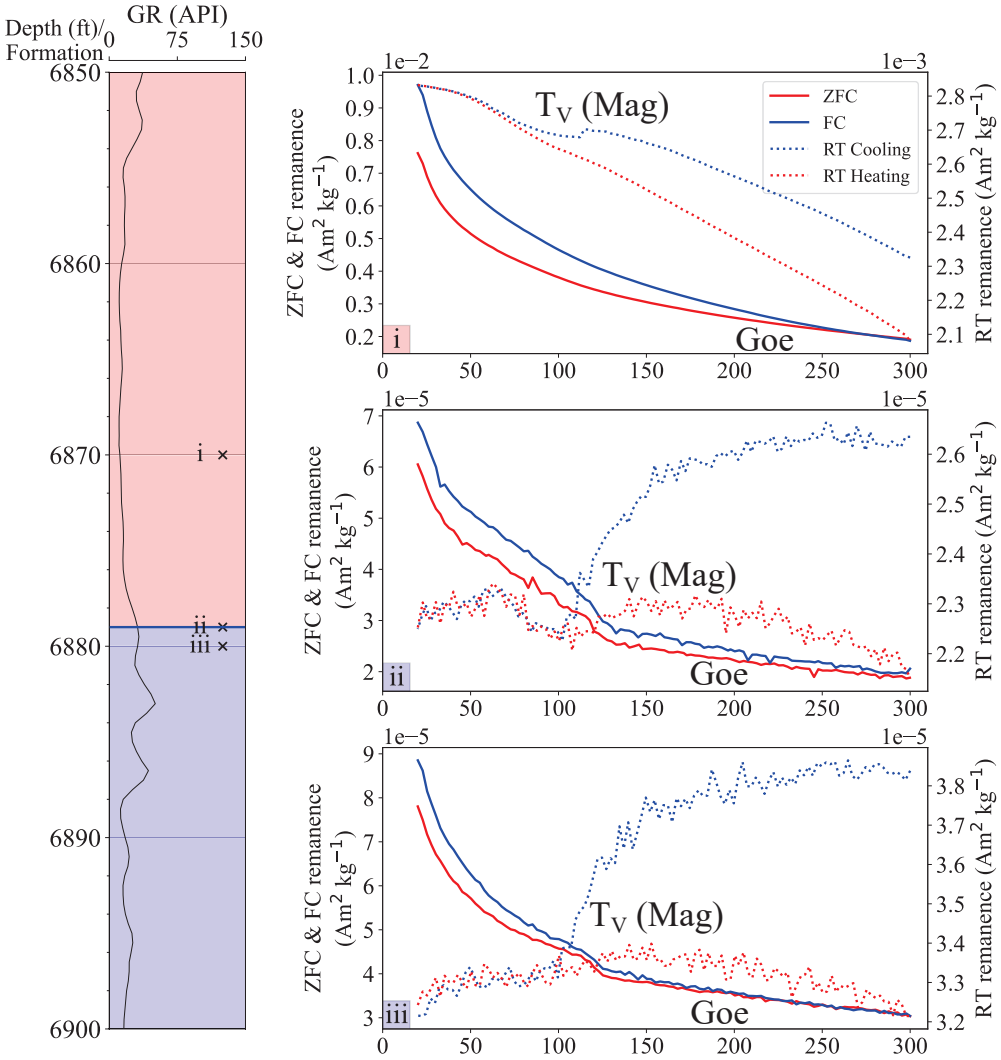


Figure 6.19: *Series of low temperature ZFC, FC and RT Curves of select samples across the lower OWC seen in Well 11/30-2, used to identify the magnetic mineral assemblages within the samples. Goe = goethite, T_V = Verwey Transition indicative of Mag (magnetite).*

6.3.5 | WELL 11/30-5 - CENTRAL BEATRICE FIELD

Well 11/30-5 is, akin to Well 11/30-2, located in the centre of Beatrice Field and is drilled through the Cretaceous-Triassic section, however can only be sampled from the lower reservoir H, I and J Sands (Figure 6.20). No OWC is present within the samples collected, as it exists within the upper reservoir, approximately 500 ft above the samples analysed in this study. Analysis of water-saturated samples below a hydrocarbon accumulation offers the opportunity to analyse formations that have experienced migration.

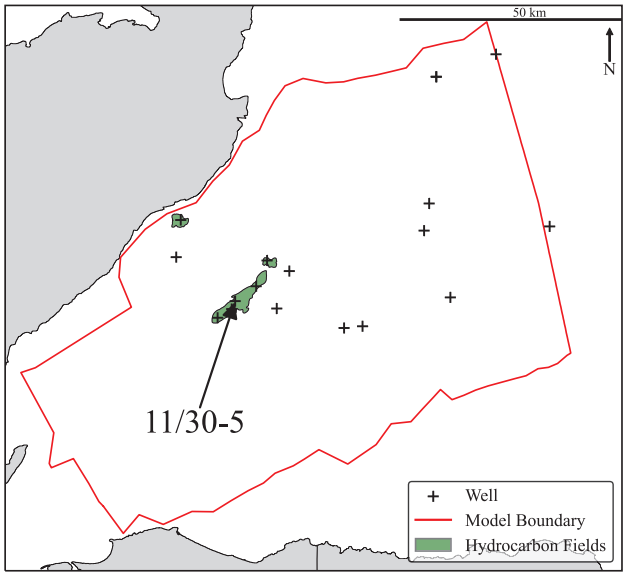


Figure 6.20: *Map of the IMF and study area, showing the location of Well 11/30-5 in Beatrice Field.*

Whilst the cored section of this well lacks an OWC, conclusions about the water-saturated samples of the central Beatrice Field, in which the samples are located, can be made, and these samples show relatively consistent results across the sampled section, with only two points either side of the H Sand-I Sand boundary offering drastic variation (Figure 6.21). The fluctuation seen across the formation change looks likely to be a result of lithology variation, as the increase in magnetisation seen at 7248 ft (sample point A) is accompanied by a clear increase in resistivity and the decrease at about

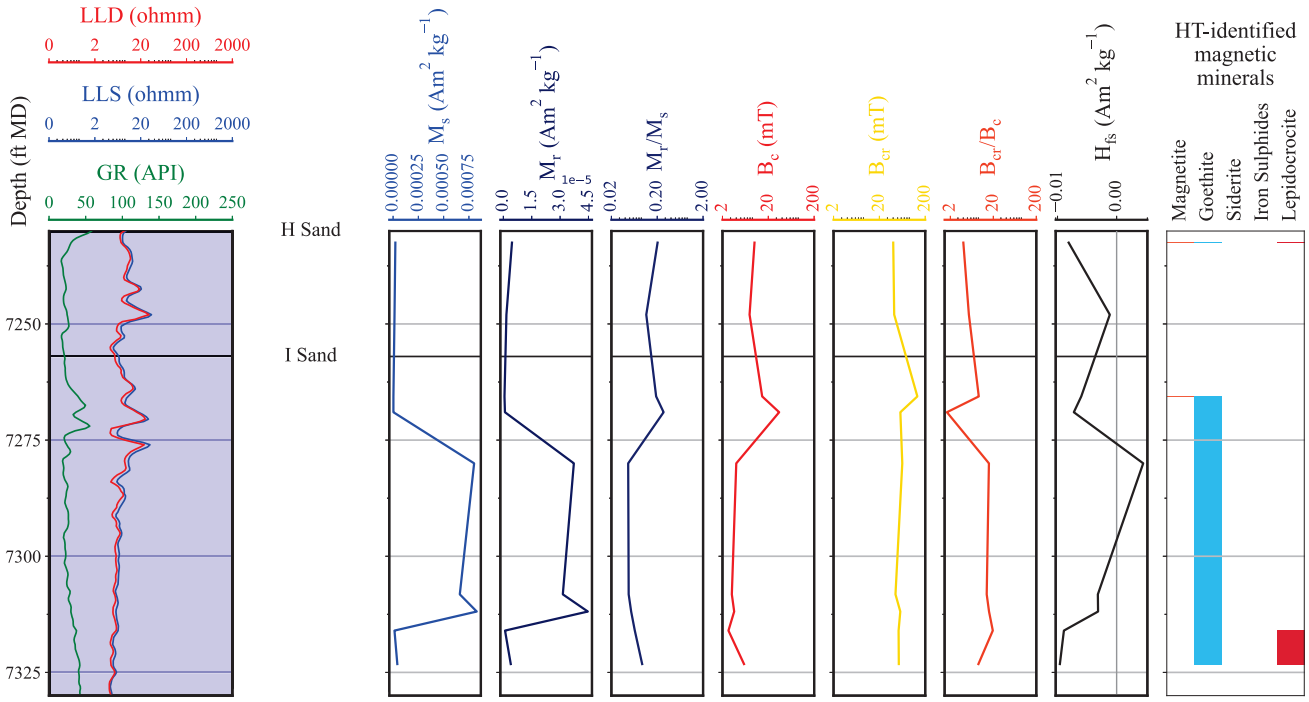


Figure 6.21: *Plots of magnetic results against depth within Well 11/30-5, with gamma ray and resistivity well log data used to identify formations and fluids. Well shaded blue is water-saturated. M_s = saturation magnetisation; M_r = remanent magnetisation; B_c = magnetic coercivity; B_{cr} = coercivity of remanence; and H_{fs} = high field slope, HT susceptibility-identified magnetic minerals at each sample are shown.*

7260 ft is associated with an increase in gamma ray response, both results of very localised lithology change, with the rest of the section being consistent across all magnetic properties.

The FORC diagrams in the well match the consistency of the magnetic properties with, accounting for data quality, very similar PSD-dominated, MD-influenced assemblages (Figure 6.22), although Figure 6.22B,C do show more SD and SP influences. The high temperature susceptibility curves within Well 11/30-5 are all consistent, showing strong goethite and magnetite presence, but with some potential minor pyrite or lepidocrocite (Figure 6.22). These curves are characteristic of many water-saturated samples seen within other wells across the IMF, and are indicative of samples that have seen hydrocarbon migration but little to no accumulation. As with other water-saturated samples in the other Beatrice Field wells, the low temperature ZFC and FC curves in Well 11/30-5 show definite evidence of goethite and magnetite (Figure 6.23). These reaffirm what the high-temperature susceptibility data shows, with widespread goethite and magnetite.

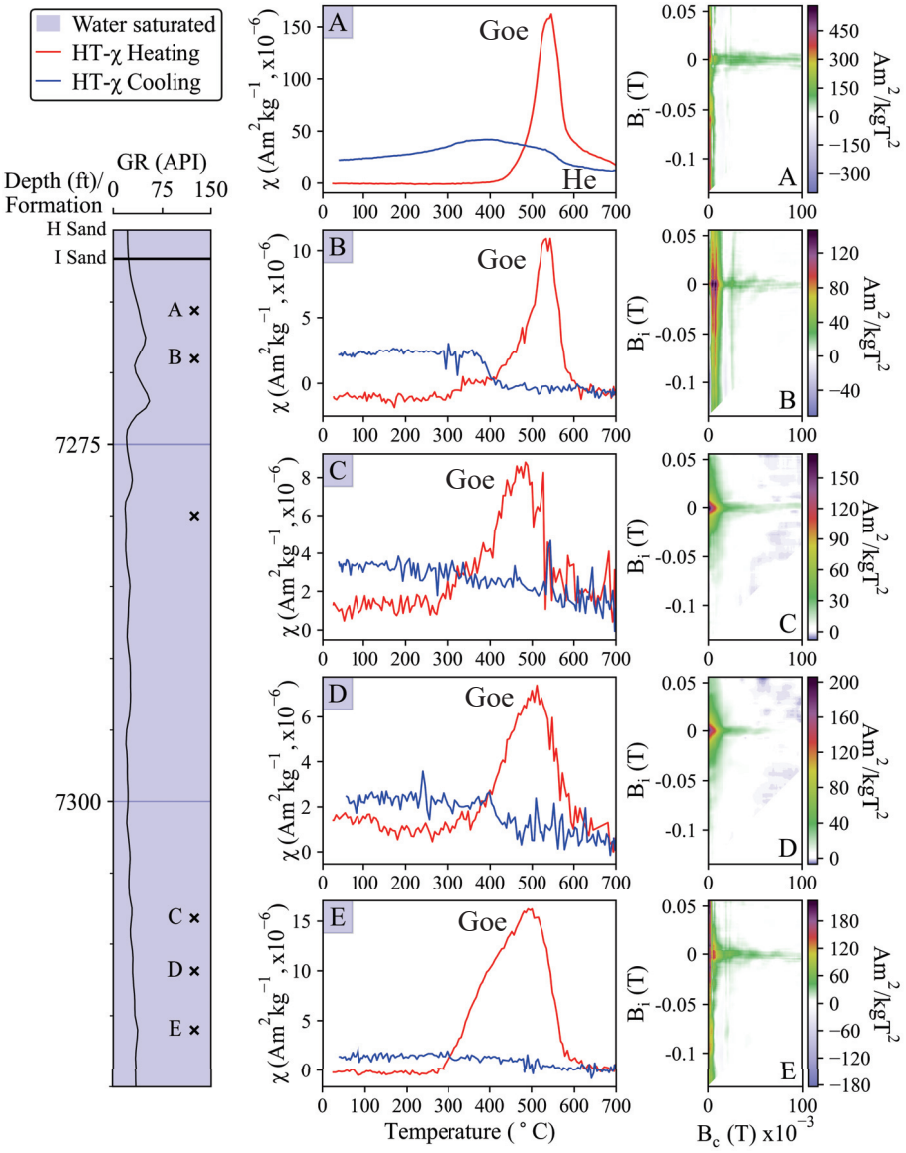


Figure 6.22: *Series of high temperature susceptibility curves and room temperature FORC diagrams of selected samples, as located on the gamma ray well log plot, across various depths and saturated by water, in Well 11/30-5. All high temperature plots show consistent magnetic mineralogy, but FORCs show some variation between SD and MD/PSD behaviours. Goe = goethite.*

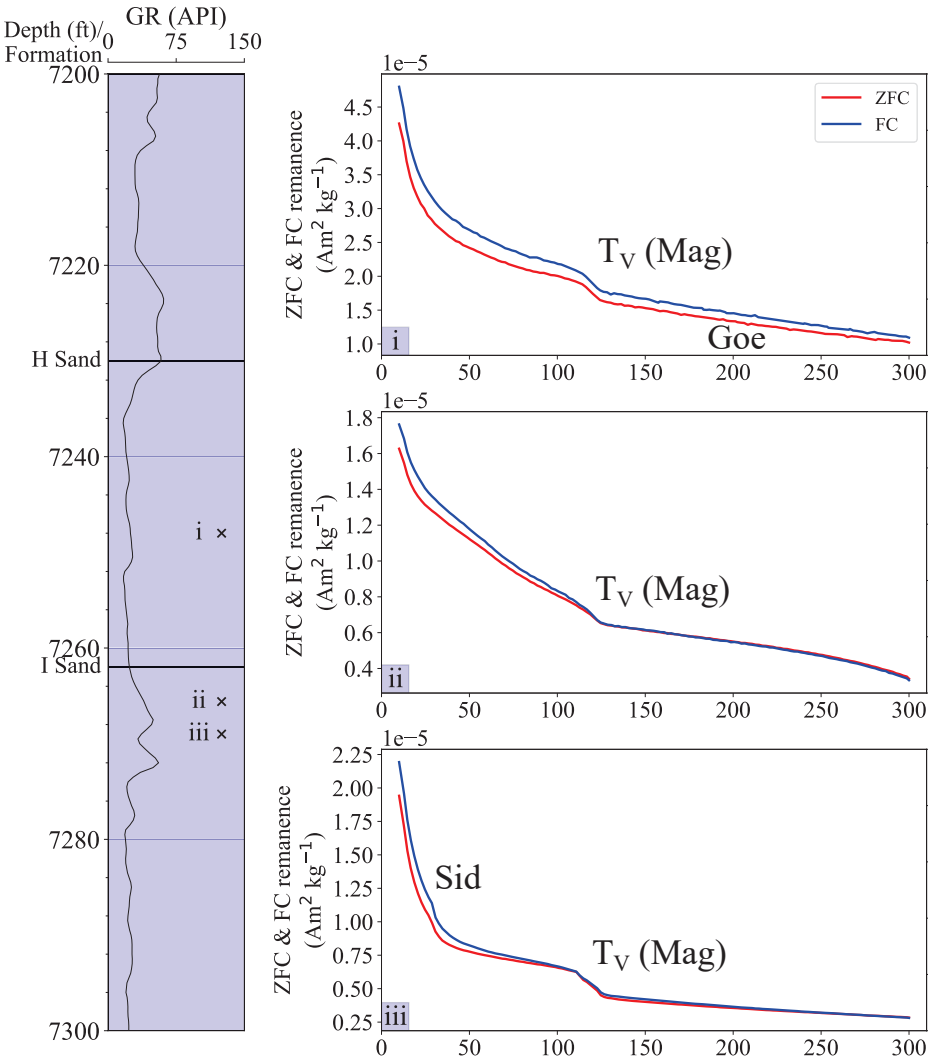


Figure 6.23: *Series of low temperature ZFC, FC and RT Curves of select samples in Well 11/30-5, used to identify the magnetic mineral assemblages within the samples through identification of mineral-specific behaviours. Goe = goethite, T_V = Verwey Transition indicative of Mag (magnetite), Sid = siderite.*

6.3.6 | WELL 11/30A-8 - SW BEATRICE FIELD

Well 11/30a-8 is in the very south western sector of the Beatrice Field, and, alongside the prior two wells 11/30-2 and 11/30-5, sits within the same section of the field's structure - the uppermost fault block of the Beatrice trapping system (Figure 6.24). 33 samples from Well 11/30a-8 were taken from the upper reservoir A and B Sands and cover an OWC in the A Sand.

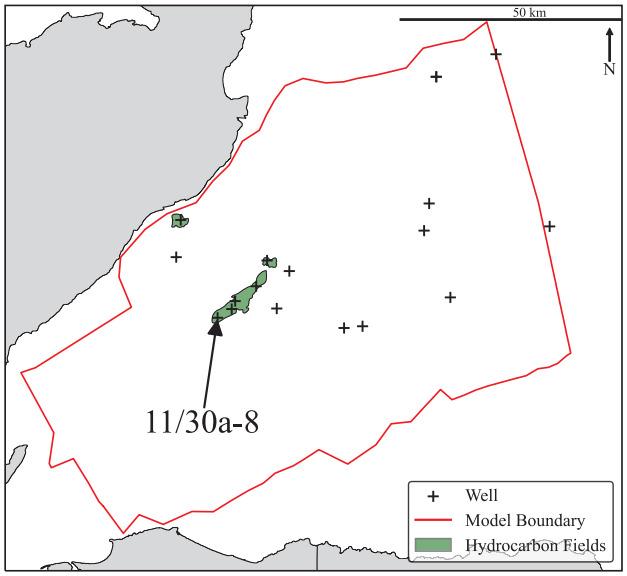


Figure 6.24: *Map of the IMF and study area, showing the location of Well 11/30a-8 in Beatrice Field.*

The OWC in Well 11/30a-8, at 6925 ft within the A Sand, shows surprising differences compared to other wells within the IMF, with a decrease in magnetic (M_s and M_r) responses below the OWC compared to above it, which is mirrored in the H_{fs} response (Figure 6.25). In opposition, the coercivity (B_c and B_{cr}) responses increase and the B_c response shows wild fluctuation within the few feet directly below the contact.

The FORC diagrams from the well show consistent PSD-dominant assemblages with minor MD influences (Figure 6.26). In the samples above the OWC, the heavily PSD-controlled assemblage shows a strong MD component that is immediately lost at and below the contact (Figure 6.26A-D). As with other wells in the IMF, Well 11/30a-8 is heavily magnetite- and goethite-rich, with minor evidence of lepidocrocite, siderite, pyrite and possible pyrrhotite (Figure 6.26). The water-saturated samples show the most variation however, unlike other wells, there is no localised changes around the OWC (Figure 6.26A-C), suggesting minimal change in mineralogy across the contacts and just enhancing pre-existing assemblages. Within the oil-saturated region of Well 11/30a-8, the low temperature ZFC, FC and RT curves show clear magnetite and goethite presence, with some siderite (Figure 6.27). The well also shows a marginal increase in remanence towards the OWC in the oil-saturated samples (Figure 6.27i-iii), with this an indication of ever-increasing magnetite content towards the contact.

Several Mössbauer spectra were taken from samples across 7019-7035 ft (Figure 6.28), where magnetisation variations suggest the potential for a paleo-OWC (Figure 6.25). Whilst this was initially considered due to the other oil-saturated wells in Beatrice Field contained two OWCs, the spike in magnetisation around this depth was the sole indication of any potential paleo-OWC, thus is attributed to lithological variation. The Mössbauer spectra have no evidence for the typically sextet-showing magnetite or goethite (Murad, 1982; Ristić *et al.*, 2017; Vandenberghe *et al.*, 1986), despite Fysh and Clark (1982) and de Grave and Vandenberghe (1986) showing that goethite in the presence of aluminium can form doublets similar to those seen in Doublet 1. The shape and isomer shift and quadrupole split values of Doublet 1 are most akin to an iron sulphide, probably pyrite (Evans *et al.*, 1982; Kar *et al.*, 2004), however this suggests that more localised iron sulphides are present through the well. Doublet 2 is most likely siderite, shown by the doublet behaviour and isomer shift and quadrupole split values akin to

those in the works of Antonova *et al.* (2020); Bill (2019); Ristić *et al.* (2017); Zavarzina *et al.* (2020), with this matching the samples' high temperature susceptibility responses.

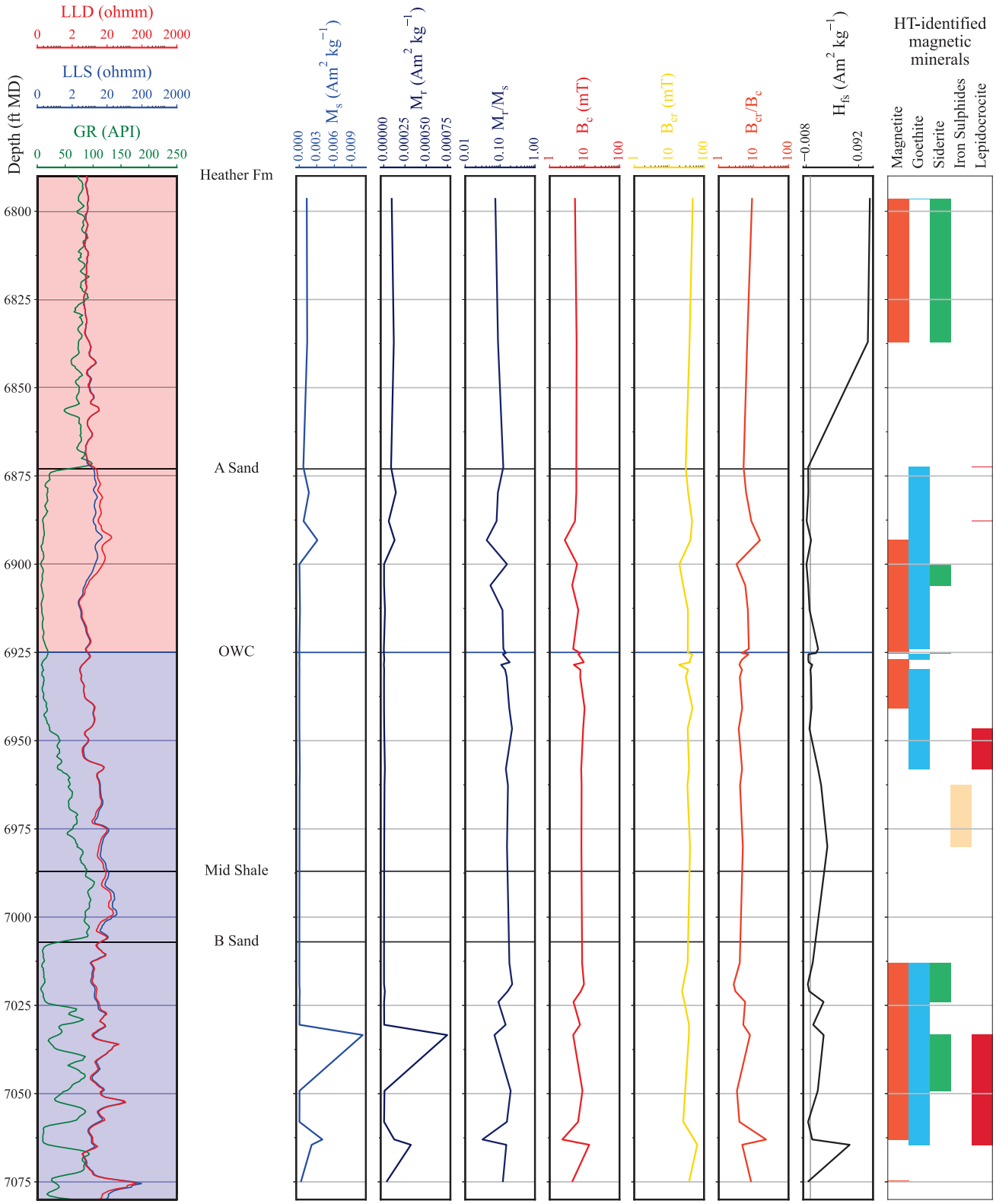


Figure 6.25: *Plots of magnetic results against depth within Well 11/30a-8, with gamma ray and resistivity well log data used to identify formations and fluids. Well shaded in red is oil-saturated, blue is water-saturated, with the OWC shown. M_s = saturation magnetisation; M_r = remanent magnetisation; B_c = magnetic coercivity; B_{cr} = coercivity of remanence; and H_{fs} = high field slope, HT susceptibility-identified magnetic minerals at each sample are shown.*

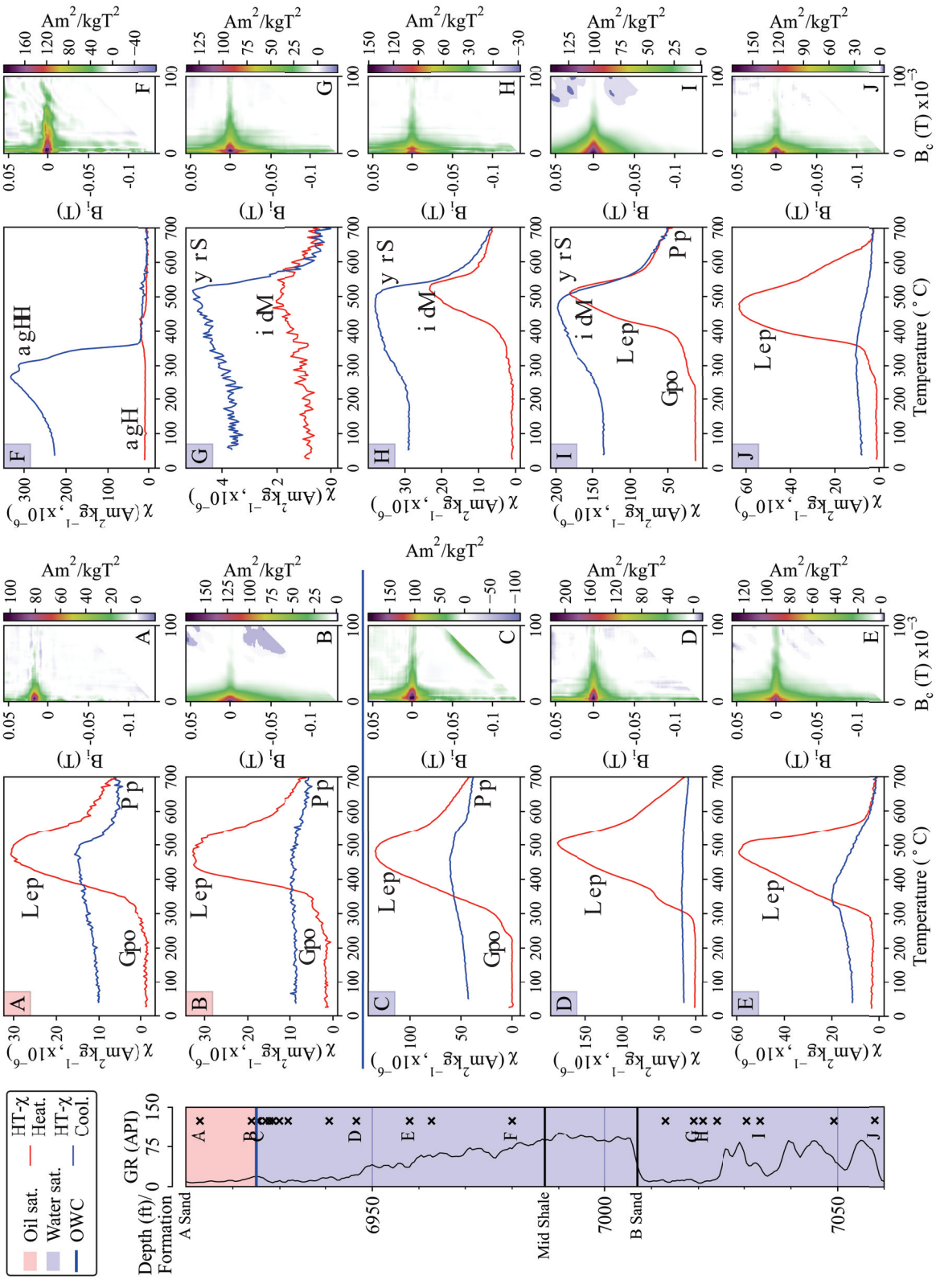


Figure 6.26: *Series of high temperature susceptibility curves and room temperature FORC diagrams of selected samples, as located on the gamma ray well log plot, across various depths and saturated by both oil and water, in Well 11/30a-8. Goe = goethite, He = hematite, Lep = lepidocrocite, Mag = magnetite, Pyr = pyrite, Pyrr = pyrrhotite, Sid = siderite.*

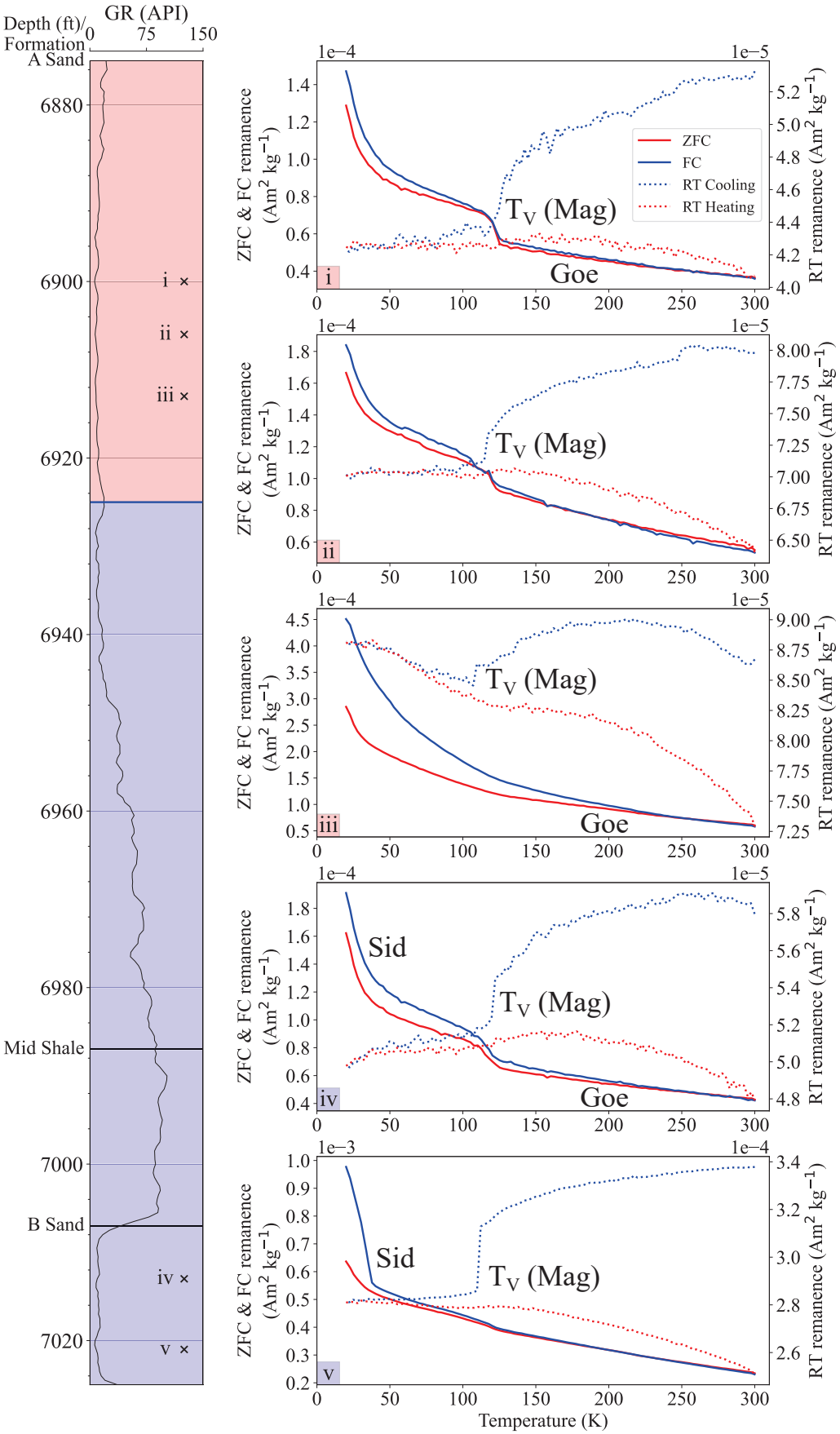


Figure 6.27: *Series of low temperature ZFC, FC and RT Curves of select samples across the OWC and within the water-saturated section of Well 11/30a-8. Note the increasing remanence values measured towards the OWC (1-3), which is indicative of increasing magnetite content. Goe = goethite, Sid = siderite, T_V = Verwey Transition, for Mag (magnetite).*

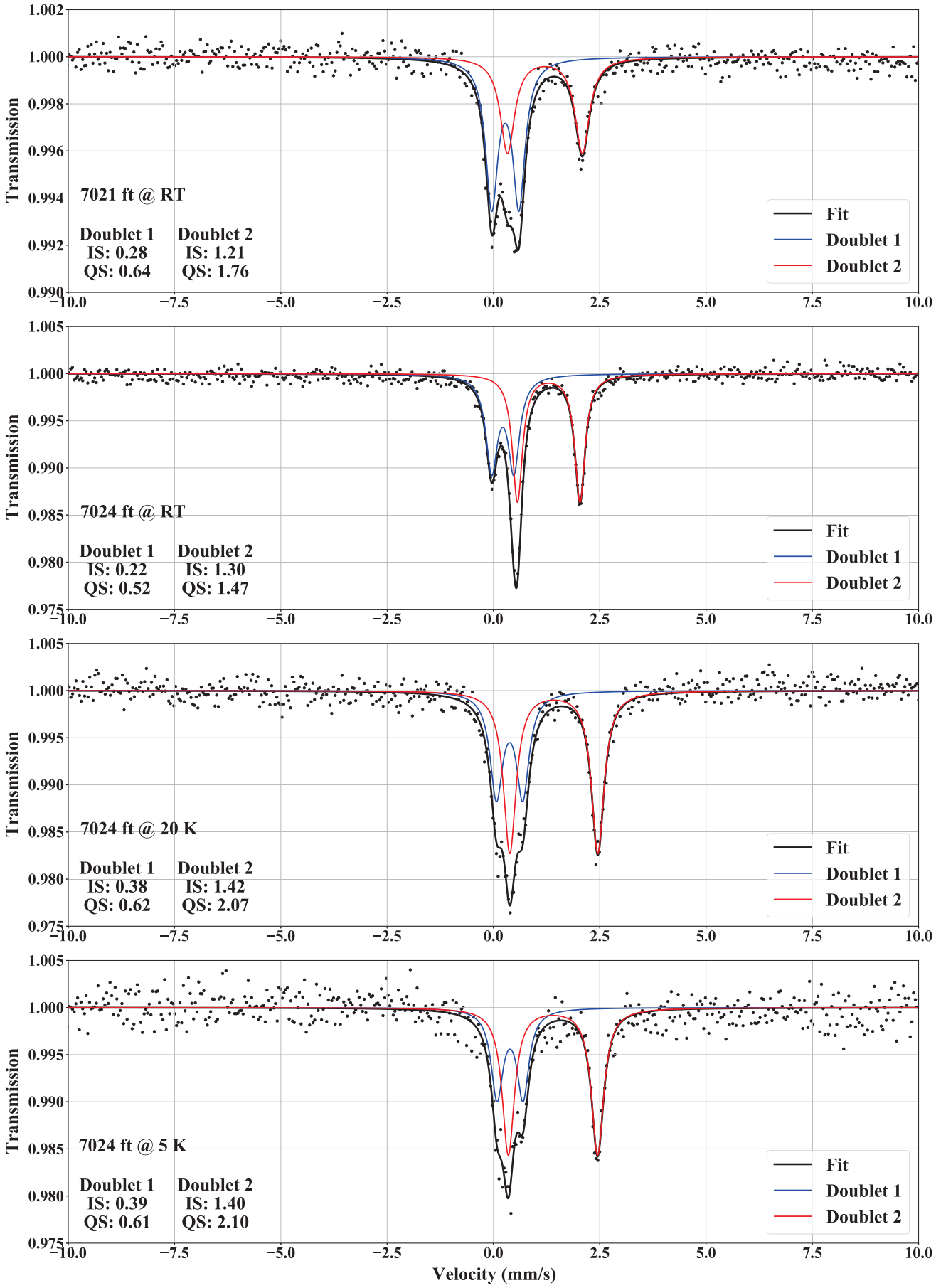


Figure 6.28: *Room and low temperature Mössbauer spectra of samples from 7021 (H in Figure 6.26 and 5 in Figure 6.27) and 7024 ft in Well 11/30a-8.*

Microscopy was carried out on three samples in the oil column, at 6900, 6906 and 6913 ft, and three samples in the water column at 7019, 7021 and 7024 ft, aiming to identify the magnetic minerals in the saturating fluids, however the assemblages were broadly consistent through both oil- and water-saturated samples. Within the microscopy assemblages, large siliceous grains of the sandstone were host to a wide variety of secondary minerals, including magnetic minerals. Within the images, several highly common grains were found: small (<1 μm) rod-like grains, small (<1 μm) globule-like grains, small (<1 μm) framboidal grains and larger (>10 μm) hexagonal plates (Figure 6.29a-f,i). Furthermore, there were several occurrences of a larger (>5 μm) framboidal grain formed of an amalgamation of partially cubic or tetragonal grains (Figure 6.29g,h), as well as rarer occurrences of a triagonal, almost tooth-like grain (Figure 6.29i). Identification of the minerals is based on both magnetic responses from other analyses as well as cross referencing literature, and suggests that the rod-like grains, globule-like grains and plates are most likely to be framboidal magnetite, but may well be goethite or siderite, whilst the small framboidal grains are most likely magnetite (Ai *et al.*, 2018; Carneiro *et al.*, 2013; Qu *et al.*, 2011; Zavarzina *et al.*, 2020). The large framboidal grains, as well as the tooth-like ones are identified as magnetite, however they could also be goethite or siderite (Elmore *et al.*, 1987; Ohfuji and Rickard, 2005; Qu *et al.*, 2011; Zavarzina *et al.*, 2020). Whilst energy dispersive x-ray (EDX) analysis was attempted on the samples, the responses were too heavily skewed to the backing carbon tape and siliceous sand grains to give accurate results.

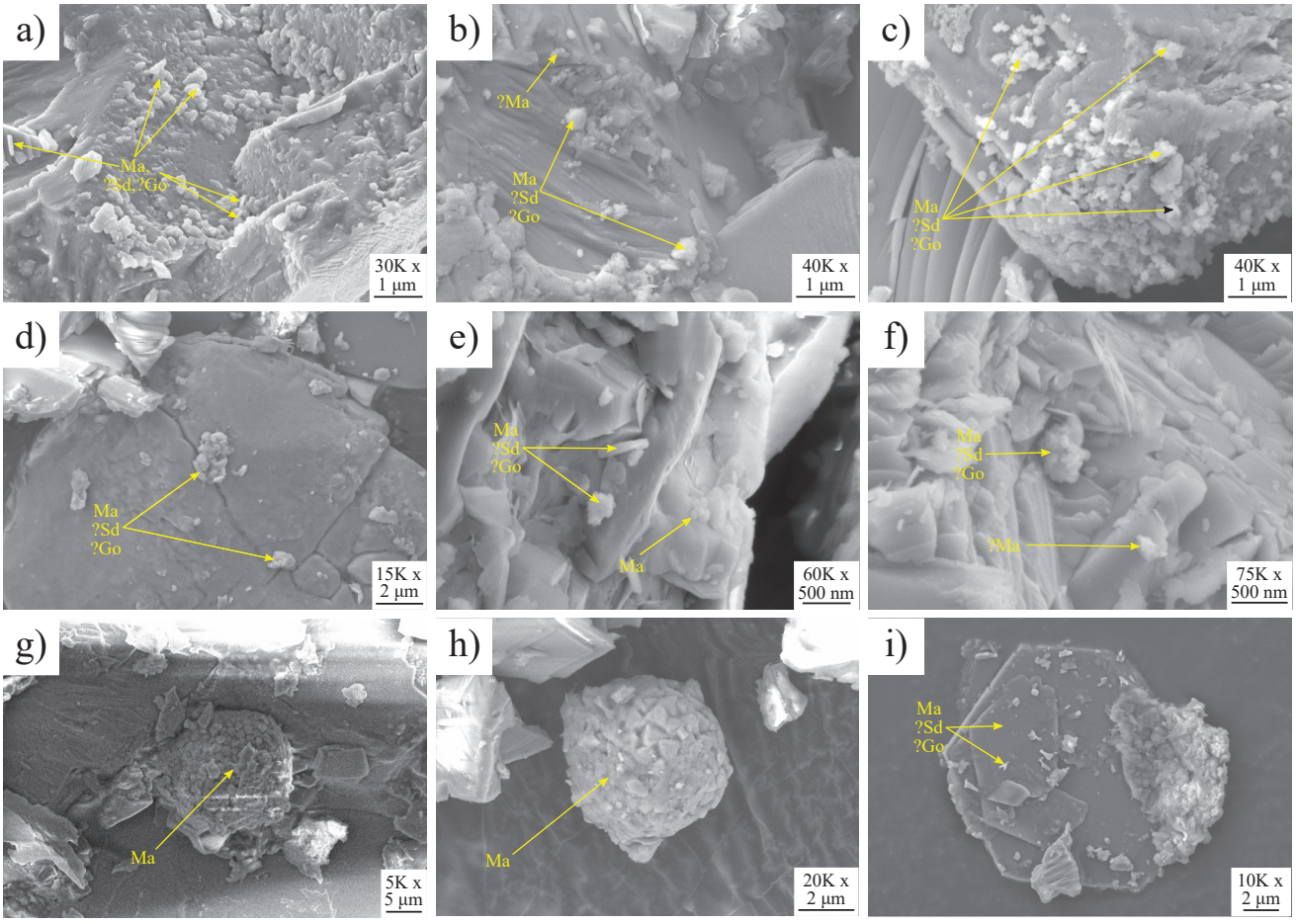


Figure 6.29: *SEM images from various samples within the water and oil columns of Well 11/30a-8. Sd = siderite, Ma = magnetite, Go = Goethite. Samples a, b, c, g and h are from the oil column samples (6900, 6906 and 6913 ft), whilst sample d is from 7019 ft, e, f and i are from 7021 and 7024 ft.*

6.3.7 | WELL 11/30A-B10 - NE BEATRICE FIELD

Well 11/30a-B10, in the north east end of Beatrice Field, has an OWC in the lower reservoir, as despite the OWC remaining at the same approximate depth across the field, the north east sector of the field is shallower than the rest of the field, likely due to fault block tilting (Figure 6.30). Sampling is constrained to the lower reservoir I and J Sands, with 32 samples collected and shows evidence of two OWCs, akin to Well 11/30-2. The depths of the samples is purely a result of the measured depth-vertical depth (MD-TVD) variation of the drilled well which was deviated from vertical, and as such, all samples are depth-defined by MD, which is approximately 1500 ft greater than the TVD.

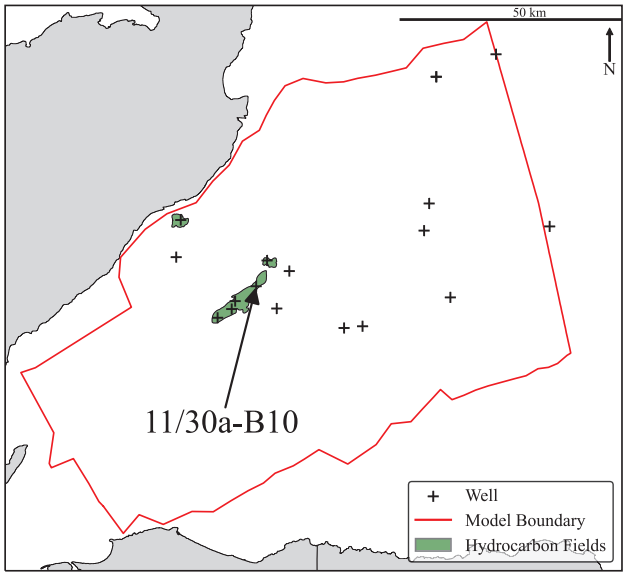


Figure 6.30: *Map of the IMF and study area, showing the location of Well 11/30a-B10 in Beatrice Field.*

Similarly to Well 11/30-2, the OWCs of Well 11/30a-B10 show differing enhancements to each other, with the upper of the two OWCs in Well 11/30a-B10, at 8196 ft MD (6643 ft TVD) in the I Sand, showing no discernible magnetic enhancement, whilst the lower OWC, at 8362.5 ft MD (6753 ft TVD), does (Figure 6.31). The lower OWC sees an increase in M_s and M_r below the contact having seen a sharp decrease immediately above the contact, but in turn shows a clear decrease in B_c, B_{cr} and H_{fs} below the contact. The H_{fs} response across the contact is interesting as within the bulk of the oil-saturated region it shows a negative response, but turns positive just above the contact, before returning back to negative below the contact. The presence of strong variations in magnetic properties within sample 8459 ft show no evidence of a paleo-OWC, and were fully water-saturated, thus has been attributed to lithological variation. The FORC diagrams show minimal change across the sampled sections, showing mostly PSD-focussed assemblages but with some MD, SD and SP influences in parts (Figure 6.32). There is also no clear variation across the OWCs, with the reason being unclear.

Within the high temperature susceptibility data, there is yet more clear evidence of magnetite and goethite within both oil- and water-saturated samples as well as potential lepidocrocite presence within several oil-saturated samples (Figure 6.32B). Furthermore, there is evidence of pyrite and pyrrhotite within two water-saturated samples (Figure 6.32G,H), as well as evidence of siderite within the water-saturated samples (Figure 6.32J). As with the other Beatrice Field low temperature analyses, there is mixed evidence of magnetite and goethite within both oil-saturated and water-saturated samples, and some siderite (Figure 6.33). There is also some increased magnetite presence in the samples around the OWC (Figure 6.12i,ii), evidenced by the marginal increase in remanence recorded by the samples.

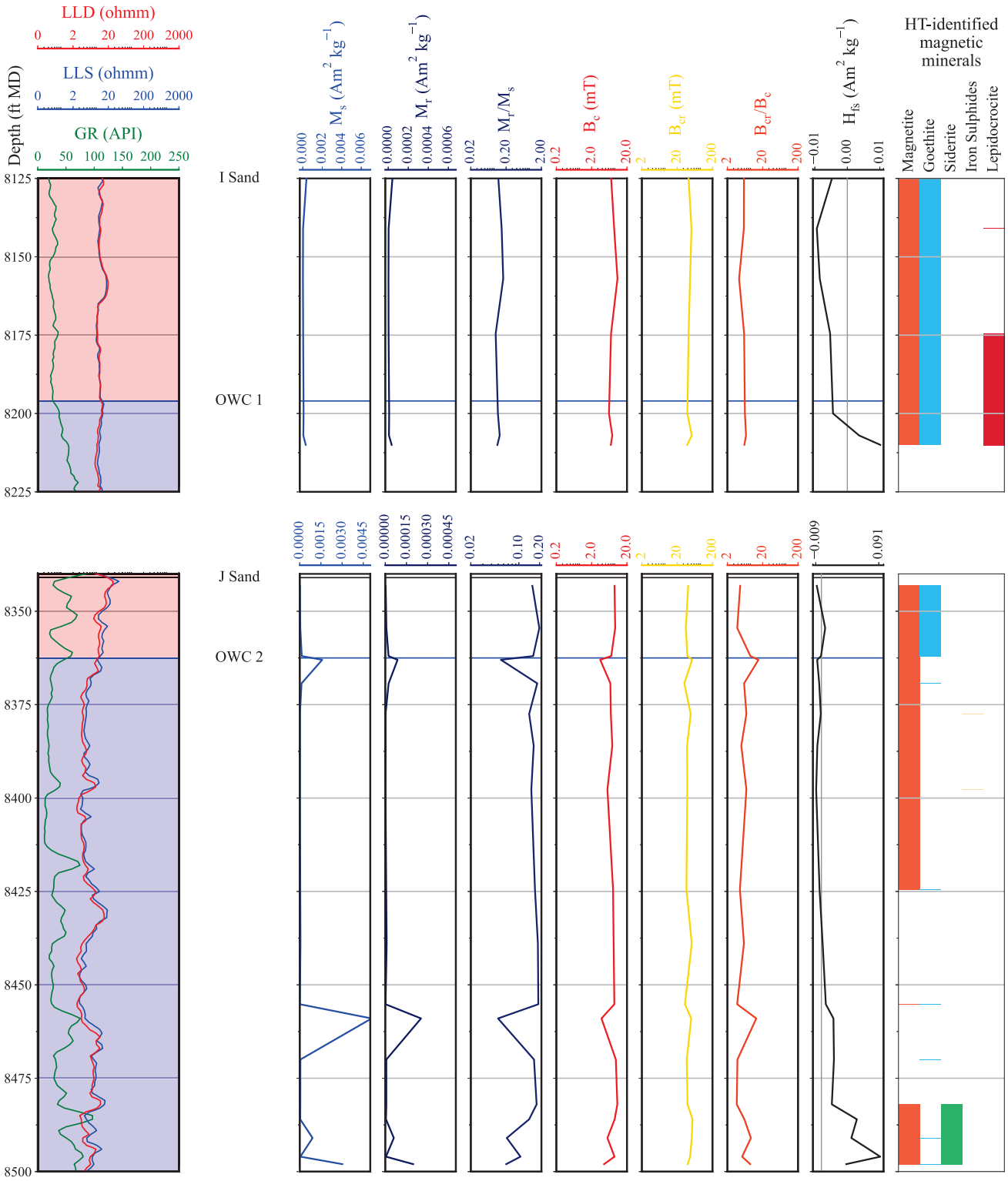


Figure 6.31: *Plots of magnetic results against depth within Well 11/30a-B10, with gamma ray and resistivity well log data used to identify formations and fluids. Well shaded in red is oil-saturated, blue is water-saturated, with the OWCs shown. M_s = saturation magnetisation; M_r = remanent magnetisation; B_c = magnetic coercivity; B_{cr} = coercivity of remanence; and H_{fs} = high field slope, HT susceptibility-identified magnetic minerals at each sample are shown.*

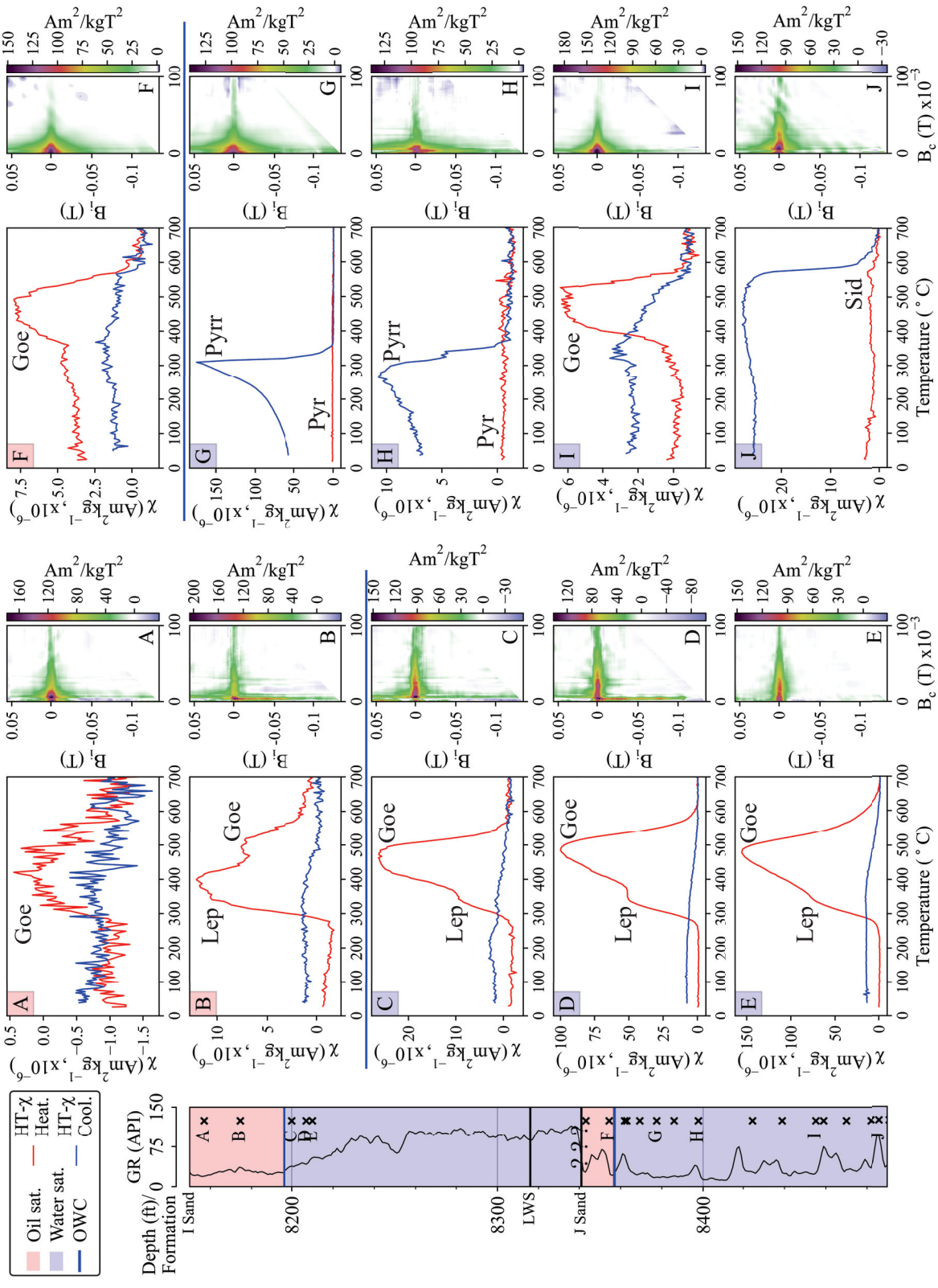


Figure 6.32: *Series of high temperature susceptibility curves and room temperature FORC diagrams of selected samples, as located on the gamma ray well log plot, across various depths and saturated by both oil and water, in Well 11/30a-B10. Goe = goethite, Lep = lepidocrocite, Pyr = pyrite, Pyrr = pyrrhotite, Sid = siderite.*

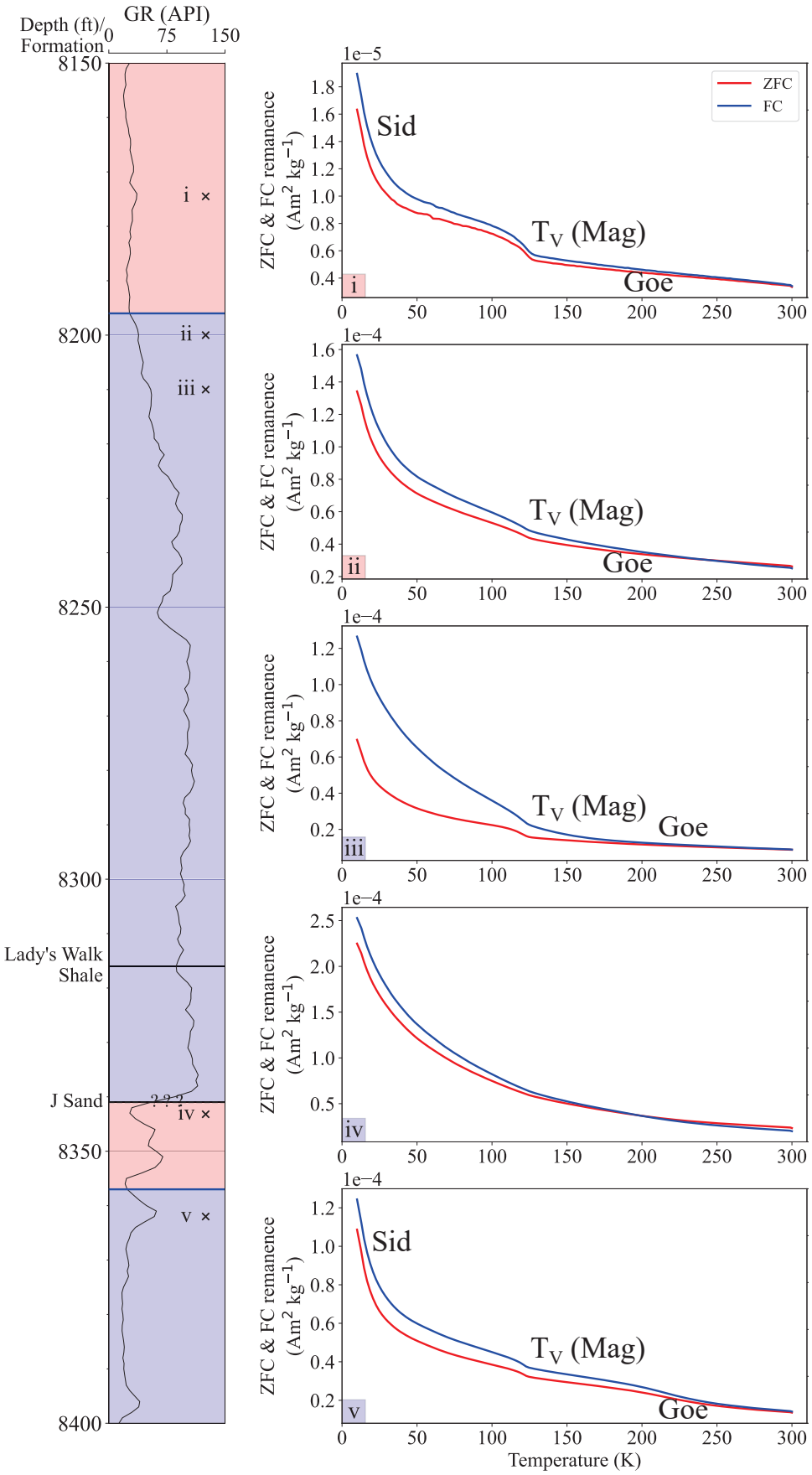


Figure 6.33: *Series of low temperature ZFC, FC and RT Curves of select samples across the two OWCs seen in Well 11/30a-B10, used to identify the magnetic mineral assemblages within the samples through identification of mineral-specific behaviours. Note the increasing remanence values measured towards the OWC (i-iii), which is indicative of increasing magnetite content. Goe = goethite, T_V = Verwey Transition indicative of Mag (magnetite), Sid = siderite.*

6.3.8 | WELL 12/21-2 - JACKY FIELD

Well 12/21-2 sits within Jacky Field, to the immediate north-east of Beatrice Field (Figure 6.34), and is drilled through the same Jurassic-age petroleum system at similar depths to the wells in the shallowest sections of the Beatrice Field. In total, 33 samples were collected from the well across the A and B Sands, Mid Shale and the Pentland Formation, offering the opportunity to magnetically compare Jacky and Beatrice Fields. As Jacky Field is under higher pressure than Beatrice, and is nearing being an overpressured system, any differences or similarities between Jacky Field and Beatrice Field could be crucial to understanding the connections between magnetic assemblages and hydrocarbon systems.

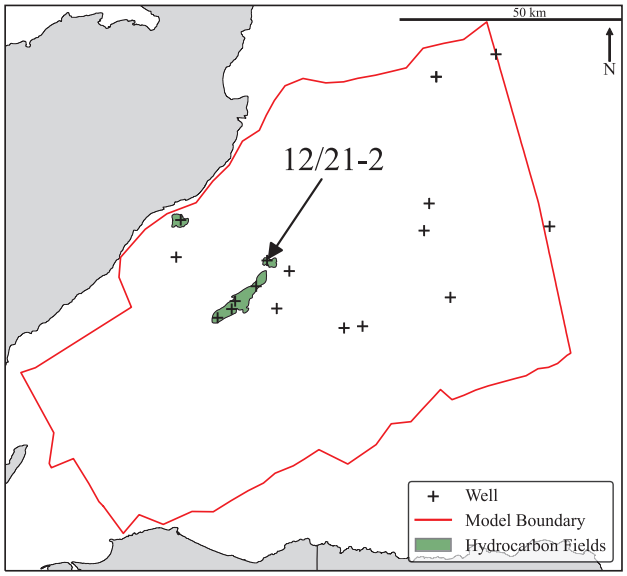


Figure 6.34: *Map of the IMF and study area, showing the location of Well 12/21-2 in Jacky Field.*

Well 12/21-2 has a very clear magnetic enhancement at the OWC, at 7118 ft in the B Sand, where all magnetic characteristics show a rapid increase in response in the few feet above the contact from within the oil column down to the OWC, at which point they all peak, then show sloped decreases in the samples across the uppermost water-saturated samples (Figure 6.35). Unlike many other examples in this study, all magnetic characteristics in Well 12/21-2 show increases directly below the OWC, apart from B_c which shows minimal variation. FORC diagram-derived domain assemblages are broadly consistent across the samples in Well 12/21-2, showing largely PSD-dominated samples (Figure 6.36). As with other wells in this study, the OWC enhancement is near-solely PSD grains, suggesting again that all enhancement at OWCs in the IMF are caused by an accumulation of PSD domain grains, and further analysis of the FORC diagrams from Well 12/21-2 can be seen in Section 6.4.1.7.

Akin to the other wells in the IMF, high temperature analysis Well 12/21-2 shows extensive presence of magnetite and goethite, but far more siderite than seen in the other fields (Figure 6.36). Whilst variations in ratios between the three minerals vary across the well, they occur in both oil- and water-saturated samples, but are more prevalent in the water-saturated section (Figure 6.36B,F). Beyond the three previously mentioned minerals, the only evidence of other minerals comes in the form of three samples containing lepidocrocite, in tandem with goethite (Figure 6.36E,G).

The low temperature ZFC, FC and RT curves from Well 12/21-2 show very similar results to the data collected from wells within Beatrice Field, with further extensive proof of goethite and magnetite, plus siderite (Figure 6.37). The siderite is not as prevalent in the low temperature results as it is in the high temperature results, however this is likely due to the disparity in sample numbers between the techniques. Siderite is identifiable in low temperature analysis through a sharply declining FC curve from 5 K to about 20 K, where is it joined by the ZFC curve and they track as a slower trend towards room temperature, and here is most clearly seen in the sample from 7118.5 ft (Figure 6.12iv). There is

also some increased magnetite presence in the samples around the OWC (Figure 6.12), evidenced by the marginal increase in remanence recorded by the samples trending towards the contact.

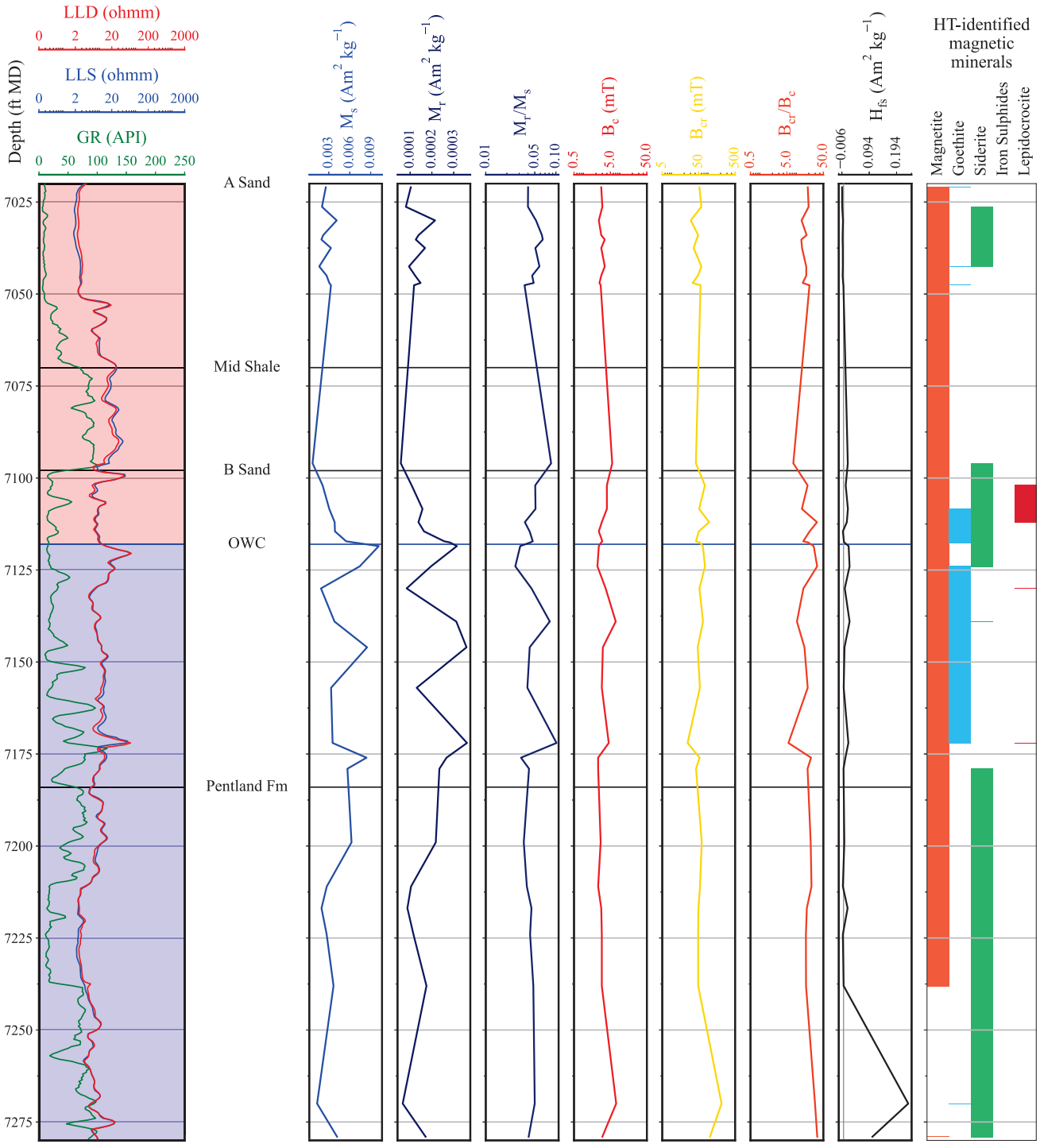


Figure 6.35: *Plots of magnetic results against depth within Well 12/21-2, with gamma ray and resistivity well log data used to identify formations and fluids. Well shaded in red is oil-saturated, blue is water-saturated, with the OWC shown. M_s = saturation magnetisation; M_r = remanent magnetisation; B_c = magnetic coercivity; B_{cr} = coercivity of remanence; and H_{fs} = high field slope, HT susceptibility-identified magnetic minerals at each sample are shown.*

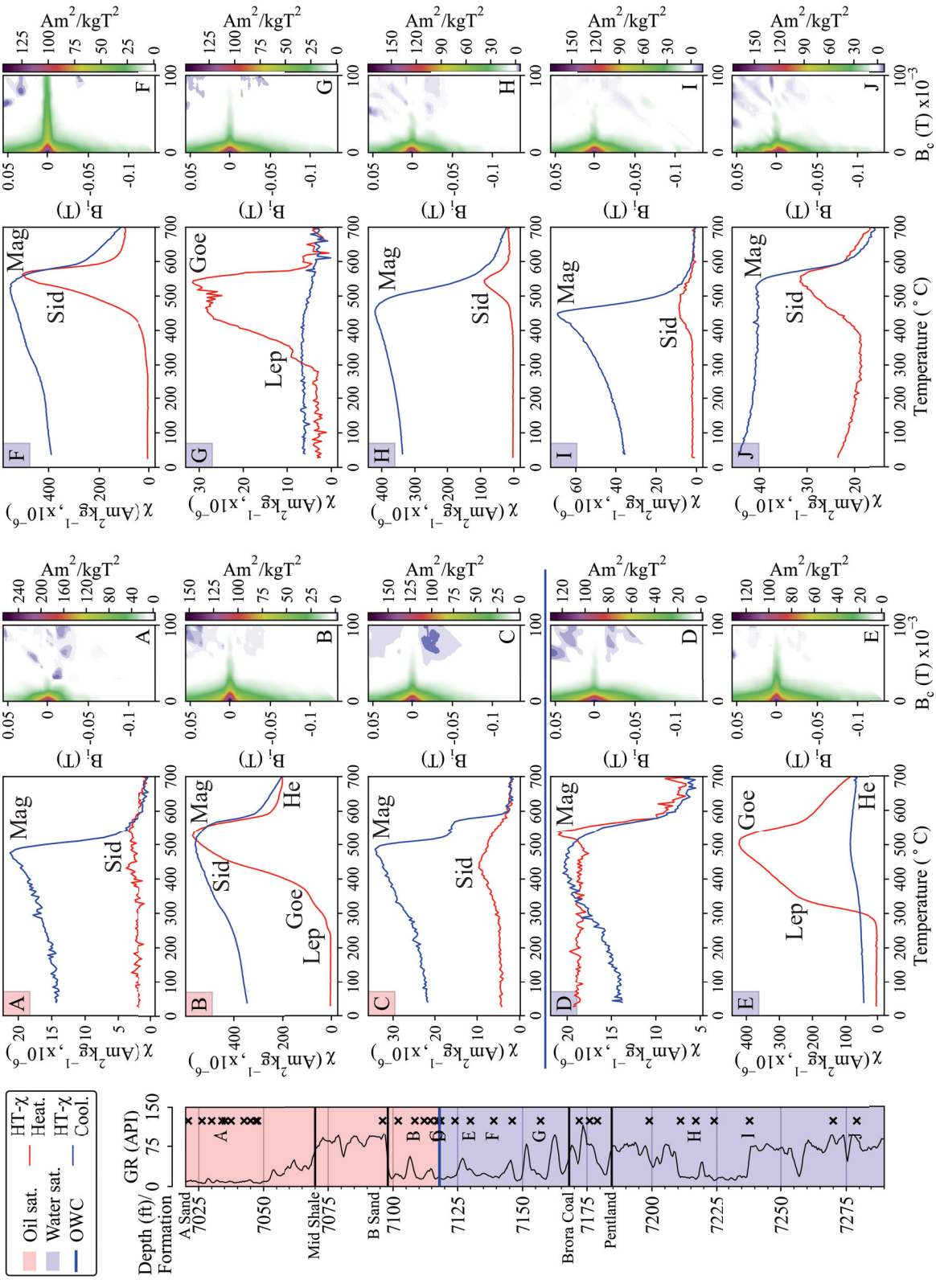


Figure 6.36: *Series of high temperature susceptibility curves and room temperature FORC diagrams of selected samples, as located on the gamma ray well log plot, across various depths and saturated by both oil and water, in Well 12/21-2. Goe = goethite, He = hematite, Lep = lepidocrocite, Mag = magnetite, Sid = siderite.*

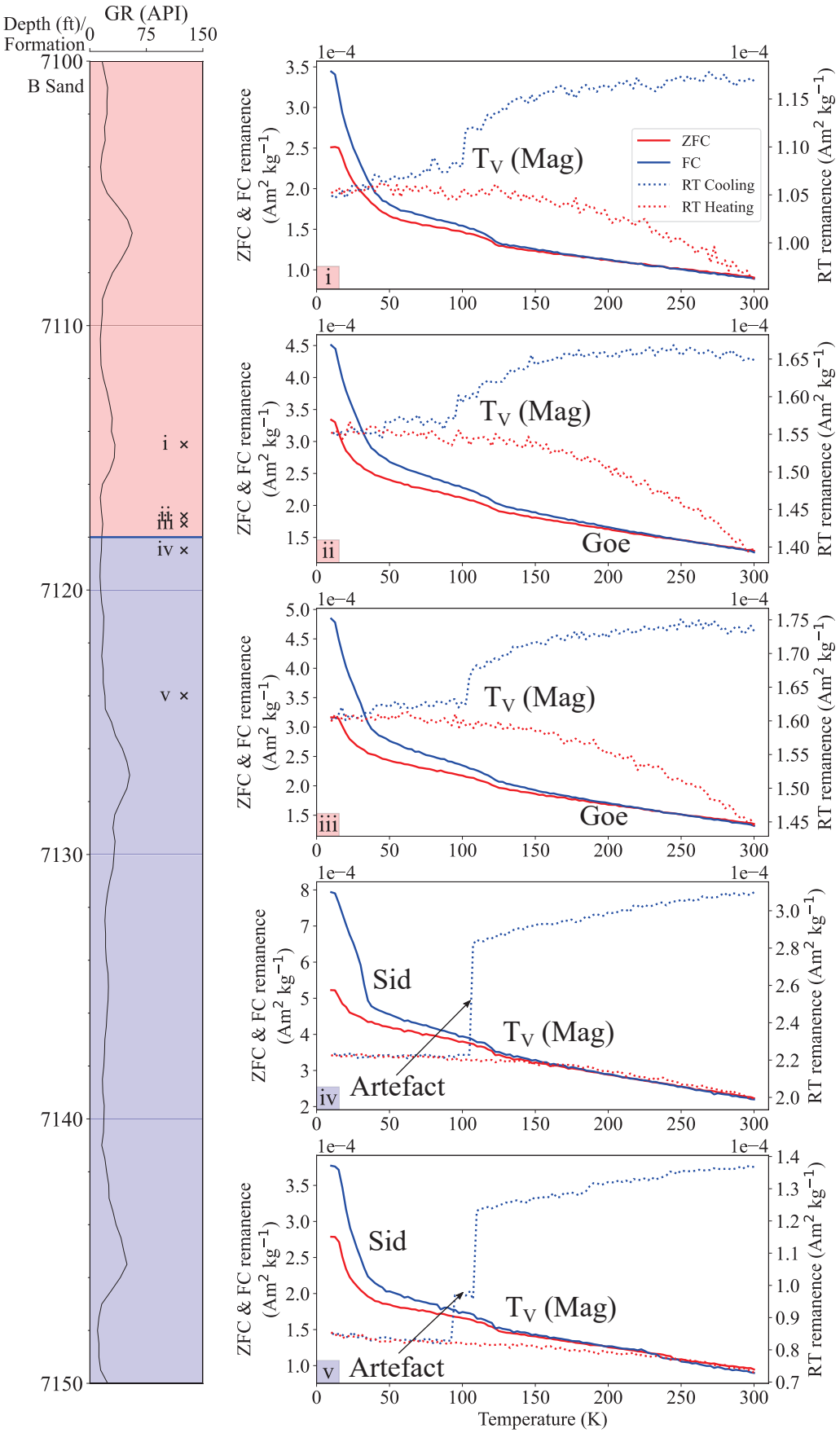


Figure 6.37: *Series of low temperature ZFC, FC and RT Curves of select samples across the OWC seen in Well 12/21-2, used to identify the magnetic mineral assemblages within the samples through identification of mineral-specific behaviours. Early and sharp T_V responses (e.g. iv, v) are expected errors in measurements, as they are typically smoother (e.g. i). Note the increasing remanence values measured towards the OWC (i-iii), which is indicative of increasing magnetite content. Goe = goethite, T_V = Verwey Transition indicative of Mag (magnetite), Sid = siderite.*

6.3.9 | WELL 12/21-4

Well 12/21-4, located to the south west of the Beatrice and Jacky Fields (Figure 6.38), is the only well in the IMF that this study found and sampled that was classed as dry by the drilling company. The well was drilled through the Jurassic-age reservoirs but found no oil or traces of oil, indicating no present or past interaction with hydrocarbons, as such, it makes a good well for analysing background samples of the IMF to compare against hydrocarbon-saturated wells. Within Well 12/21-4, 11 samples were collected from the upper reservoir A and B Sands, that are situated approximately 200 feet shallower than the Beatrice and Jacky Field equivalents.

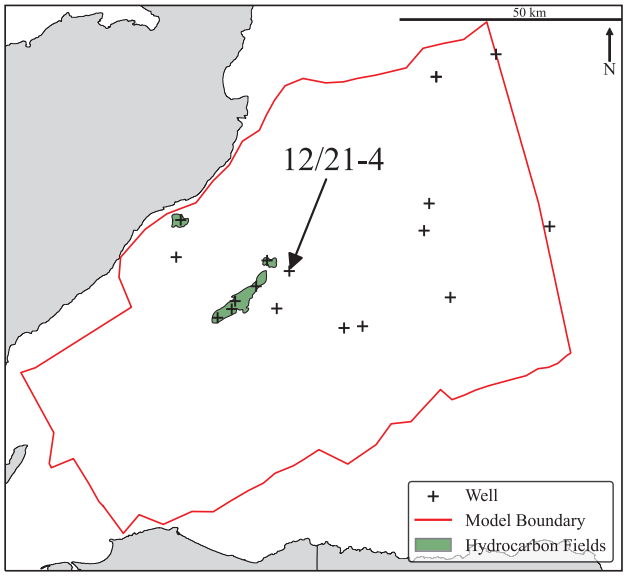


Figure 6.38: *Map of the IMF and study area, showing the location of Well 12/21-4 in the centre of the IMF.*

The samples from this solely water-saturated well shows that magnetic responses do vary regardless of saturating fluid, with lithology and formation water being the causes, as seen by the increasing responses as a result of clay content in the B Sand at approximately 6810 ft (Figure 6.39). Similarly, the FORC diagrams across the well are very similar, showing strongly PSD-dominated assemblages with some clear SD and SP influence throughout the samples analysed (Figure 6.40).

The high temperature analysis of the samples from Well 12/21-4 show extensive dominance not only

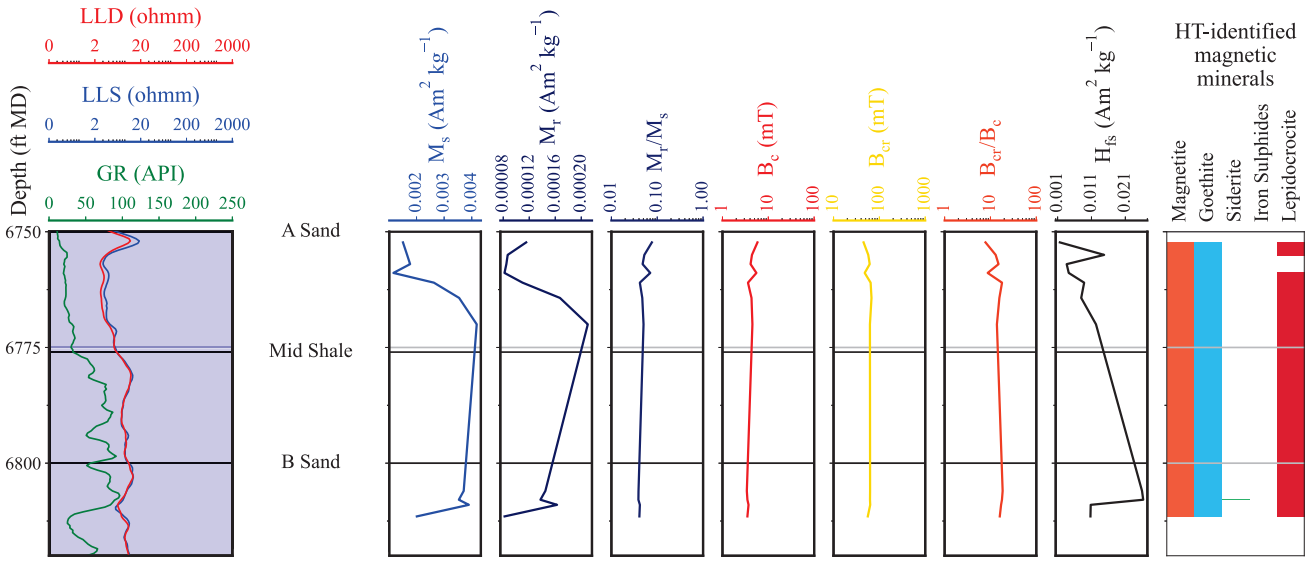


Figure 6.39: *Plots of magnetic results against depth within Well 12/21-4, with gamma ray and resistivity well log data used to identify formations and fluids. Well shaded in blue is water-saturated. M_s = saturation magnetisation; M_r = remanent magnetisation; B_c = magnetic coercivity; B_{cr} = coercivity of remanence; and H_{fs} = high field slope, HT susceptibility-identified magnetic minerals at each sample are shown.*

of magnetite, but of goethite and lepidocrocite (Figure 6.40A,D,E). The samples show no evidence of siderite, but some potential for iron sulphides, likely pyrrhotite, as an alteration product during high temperature susceptibility analysis (Figure 6.40C). The distinct lack of siderite would suggest that this well could possibly be completely dry; Abdulkarim *et al.* (2022a) indicates that siderite is a proxy for vertical hydrocarbon migration, however this requires connection with the basin and petroleum systems model to determine if it is truly non-hydrocarbon bearing.

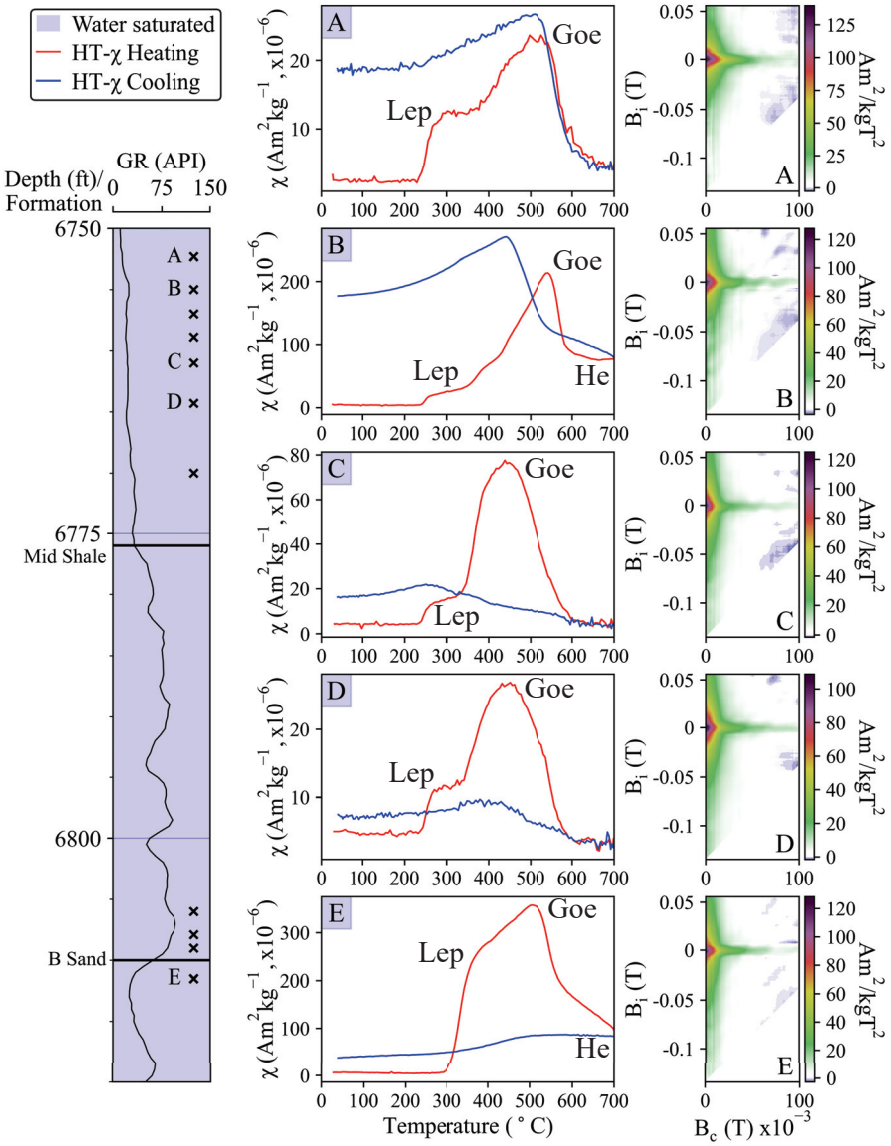


Figure 6.40: *Series of high temperature susceptibility curves and room temperature FORC diagrams of selected samples, as located on the gamma ray well log plot, across various depths and saturated by water, in Well 12/21-4. The high temperature susceptibility plots show relative consistency across the samples, matched in the consistent FORC diagrams. Goe = goethite, He = hematite, Lep = lepidocrocite.*

6.3.10 | WELL 12/25-3

Well 12/25-3 was sampled due to it bordering the edge of the study area, bounding the Outer and Inner Moray Firths, with the aim of analysing both the difference in assemblages on the IMF's perimeter and also the Cretaceous Cromer Knoll Group through which the well was drilled (Figure 6.41). The Cromer Knoll group in this region of the IMF is a potential reservoir due to the large volumes of sand between interbedded shales, whilst maintaining large lateral thicknesses. As such, Well 12/25-3 was drilled solely through the Cromer Knoll Group, and 20 samples were taken from two depth intervals. The upper sample grouping, within a sand pocket between 4510 and 4600 ft, are all oil-saturated, with the lower sample grouping showing a localised OWC, potentially caused by lithological trapping, that occurs at 5603 ft.

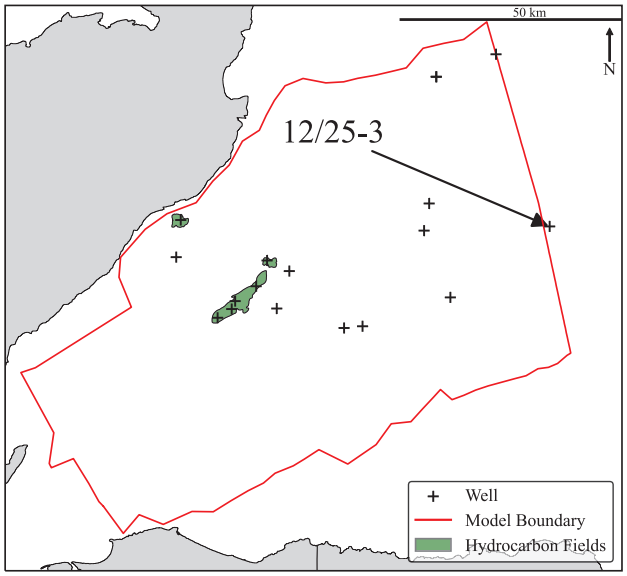


Figure 6.41: *Map of the IMF and study area, showing the location of Well 12/25-3 in the east of the IMF, on the border of the Inner and Outer Moray Firth Basins.*

The shallower Cromer Knoll samples are relatively magnetically consistent, both within themselves and with the deeper section, except for around the OWC (Figure 6.42). At the OWC at 5603 ft, there is a clear change in the magnetic response, with a sharp increase in M_s, M_r and B_c and decrease in B_{cr} immediately above the OWC that maintains to the OWC, with the OWC also seeing a peak in H_{fs}, before all properties rapidly drop below the OWC. The strong magnetic response seen within the oil column at 4571 ft shows no clear evidence of OWC behaviour, consequently is attributed to lithological variation.

The FORC diagrams in both sections of the well are relatively consistent, being heavily PSD-dominated, but some oil-saturated samples do show more SD components (Figure 6.43E,I) and water-saturated show more MD components (Figure 6.44P,Q,S), however these are more localised variations than widespread trends. In comparison, there are variations seen around the OWC, where directly above the contact there is evidence of more SP and vortex behaviours which are not seen in the slightly more MD-containing sample directly below (Figure 6.44M,N). High temperature susceptibility analysis shows that the majority of samples are magnetically quite weak but contain magnetite, siderite and goethite across both oil- and water-saturated samples (Figures 6.43 & 6.44). The majority of samples are consistent, however the samples immediately above the OWC show distinct presence of pyrite, unlike any other samples in the well, which is immediately lost when crossing the contact into the water-saturated samples.

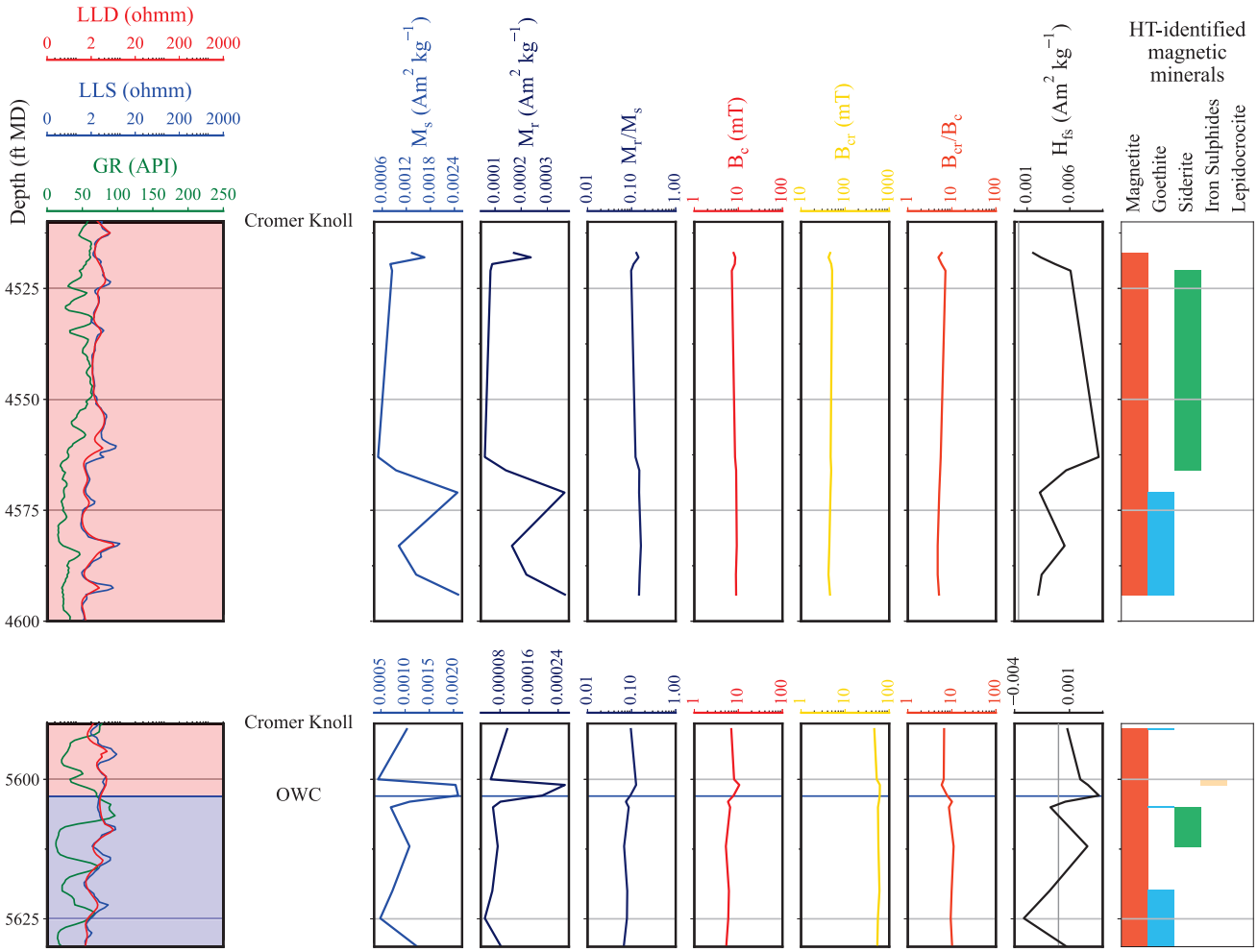


Figure 6.42: *Plots of magnetic results against depth within Well 12/25-3, with gamma ray and resistivity well log data used to identify formations and fluids. Well shaded in red is oil-saturated, blue is water-saturated, with the OWC shown. M_s = saturation magnetisation; M_r = remanent magnetisation; B_c = magnetic coercivity; B_{cr} = coercivity of remanence; and H_{fs} = high field slope, HT susceptibility-identified magnetic minerals at each sample are shown.*

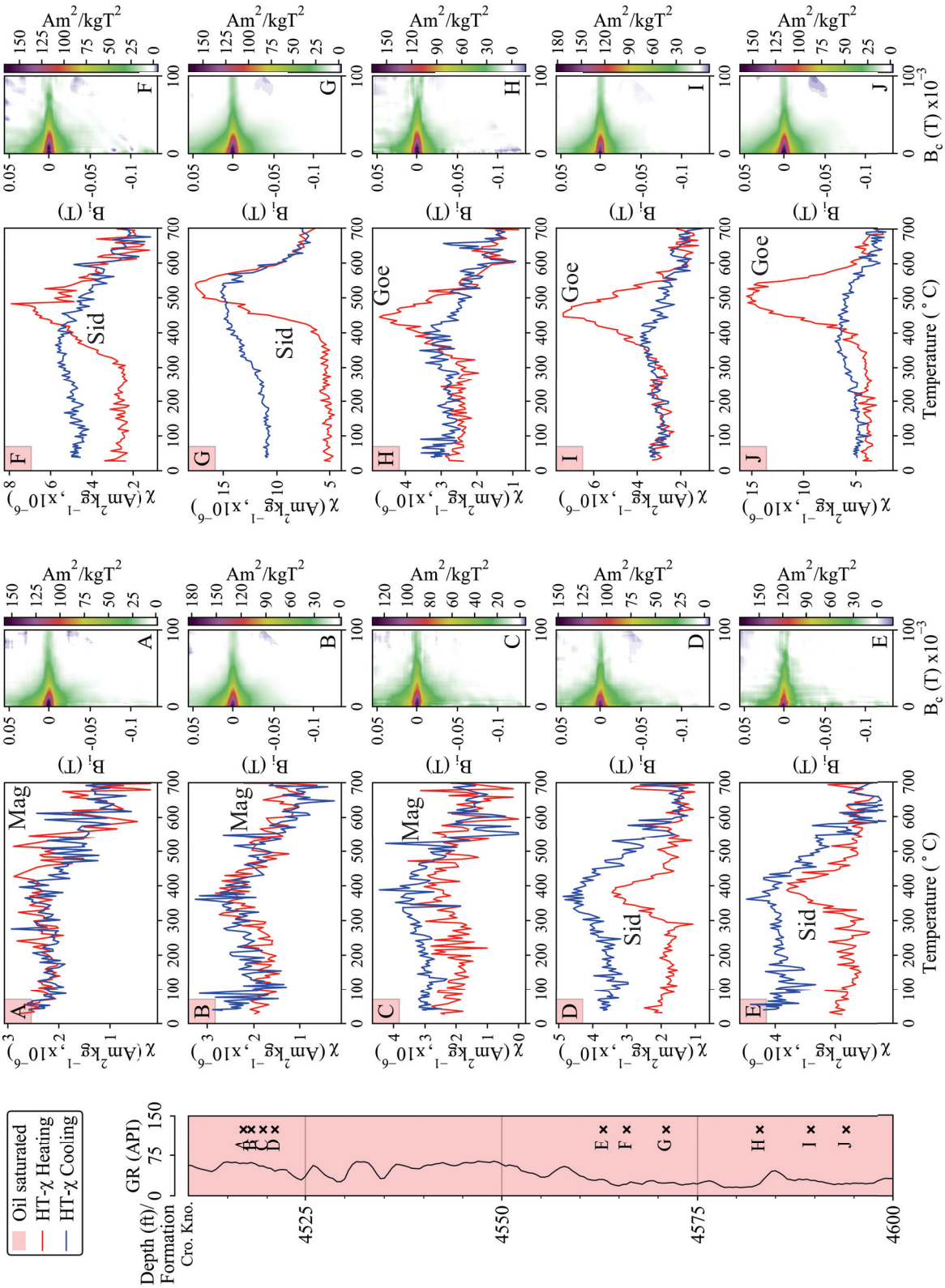


Figure 6.43: *Series of high temperature susceptibility curves and room temperature FORC diagrams of selected samples, as located on the gamma ray well log plot, across various depths and saturated by oil, in the upper section of Well 12/25-3. The magnetic mineralogy is relatively consistent across the oil-saturated upper section of the well. Goe = goethite, Mag = magnetite, Sid = siderite.*

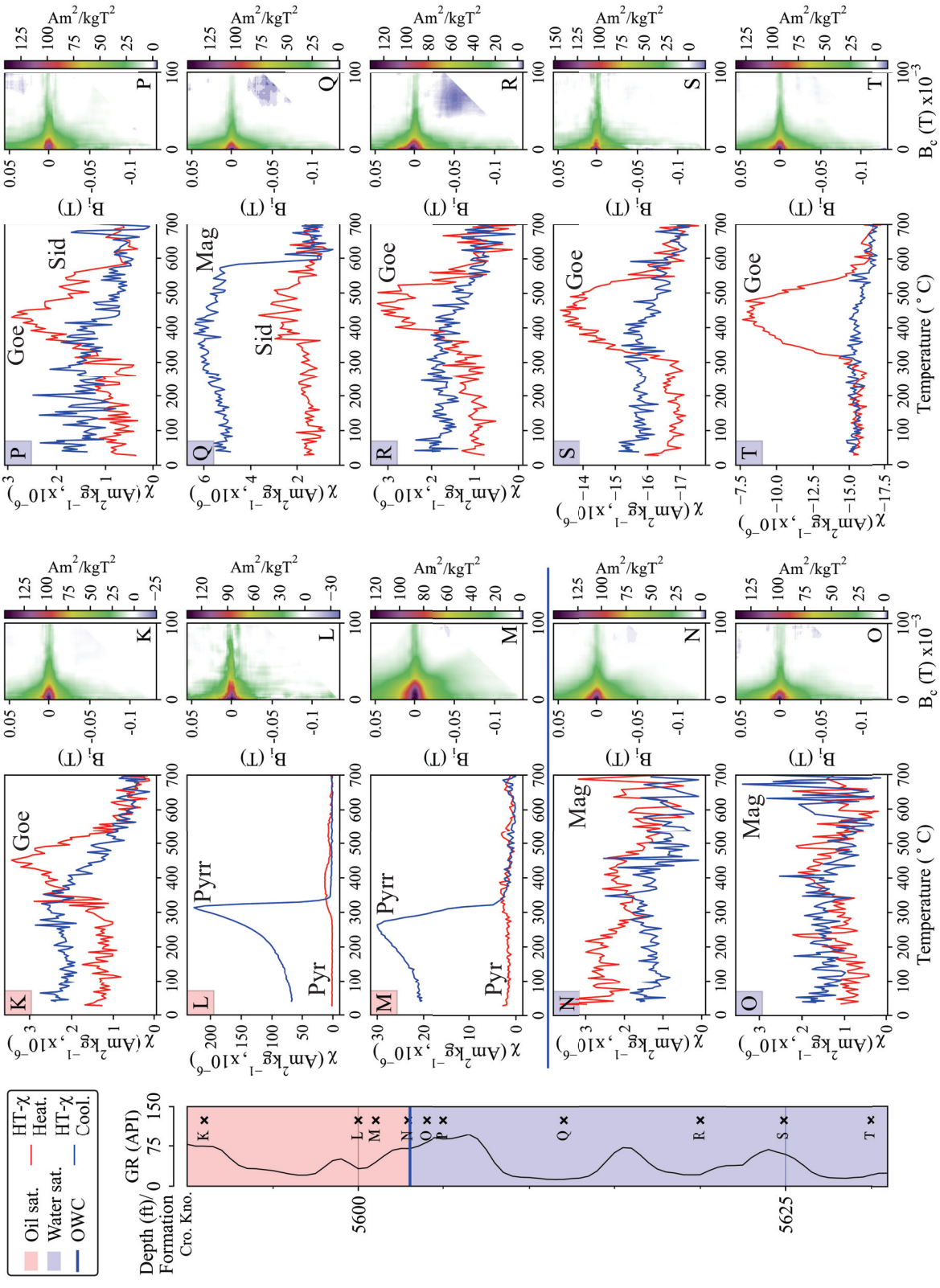


Figure 6.44: *Series of high temperature susceptibility curves and room temperature FORC diagrams of selected samples, as located on the gamma ray well log plot, across various depths and saturated by both oil and water, in the lower section of Well 12/25-3. The high temperature plots show relatively consistent magnetic mineralogy with the upper section of the well. Goe = goethite, Mag = magnetite, Pyr = pyrite, Pyrr = pyrrhotite, Sid = siderite.*

6.3.11 | WELL 12/27-1

Well 12/27-1 is situated in a shallower location in the south-south east of the IMF, south east of the Beatrice Field (Figure 6.45). The well has been drilled through the Jurassic-age reservoir section and down into the Devonian source rocks, with 23 samples taken, including four from the Devonian for analysis on the source rocks, however no true source rock (Devonian Fish Beds) were available to sample, so the analysis carried out on the Devonian Flagstones are not included in this section. The reservoir-equivalent section in the well is significantly shallower than the Beatrice Field, with the top of the reservoir sitting at approximately 3500 ft (approximately 1060 m), but does have an OWC occurring within the mid-Jurassic Pentland Formation.

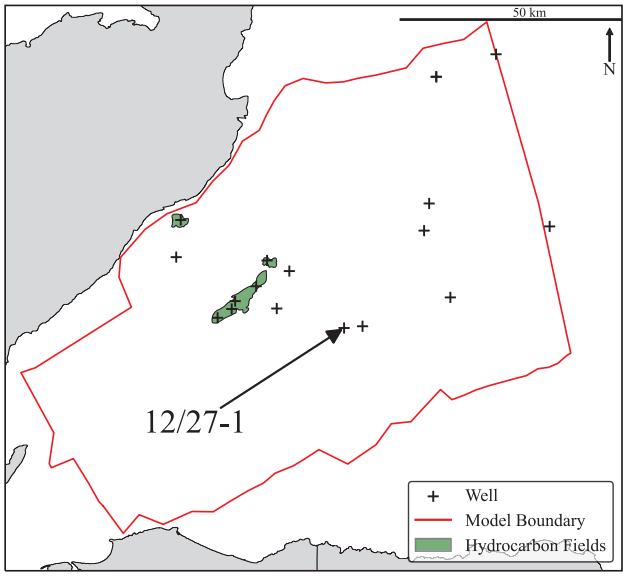


Figure 6.45: *Map of the IMF and study area, showing the location of Well 12/27-1 in the SE of the basin.*

The magnetic responses seen within the well are relatively consistent in both oil- and water-saturated samples except around the OWC zone at 3735.8-3745 ft (Figure 6.46). The magnetic properties show clear variations immediately below the top of the oil-water interface at the uppermost point of the OWC zone, with M_s, M_r and B_c showing strong increases with B_{cr} showing a strong decrease, whilst H_{fs} shows a very minimal increase. A secondary, although much more limited, enhancement also is apparent below the base of the OWC zone, which shows an increase in M_s and M_r, but negligible change in the other parameters. Well 12/27-1, along with Well 11/24-1, are the two best examples of very closely contained magnetic enhancement at the OWC, and interestingly are both within OWC zones.

The FORC diagrams show some variation between the oil- and water-saturated samples, with the oil-saturated samples showing a SD-SP-PSD assemblage (Figure 6.47). In comparison, below the OWC in the centre of the water-saturated section there is a much clearer PSD-dominant assemblage, and immediately below the OWC at the interface the increase in PSD grains compared to the oil-saturated section above becomes apparent.

The high temperature susceptibility curves of both oil- and water-saturated samples show strong variation, despite both containing magnetite, with the oil-saturated samples containing more goethite than the water-saturated samples, whilst also containing a high abundance of siderite (Figure 6.47A-E). In comparison, the water-saturated samples are heavily siderite-dominated with limited goethite present (Figure 6.47I,J), whilst the samples through the OWC zone deviate drastically from both the oil- and water-saturated samples, containing solely magnetite and maghemite (Figure 6.47F-H). This presence of maghemite diverges from the rest of well assemblages within the IMF, as it is not seen in any other well, with the reason for this unclear.

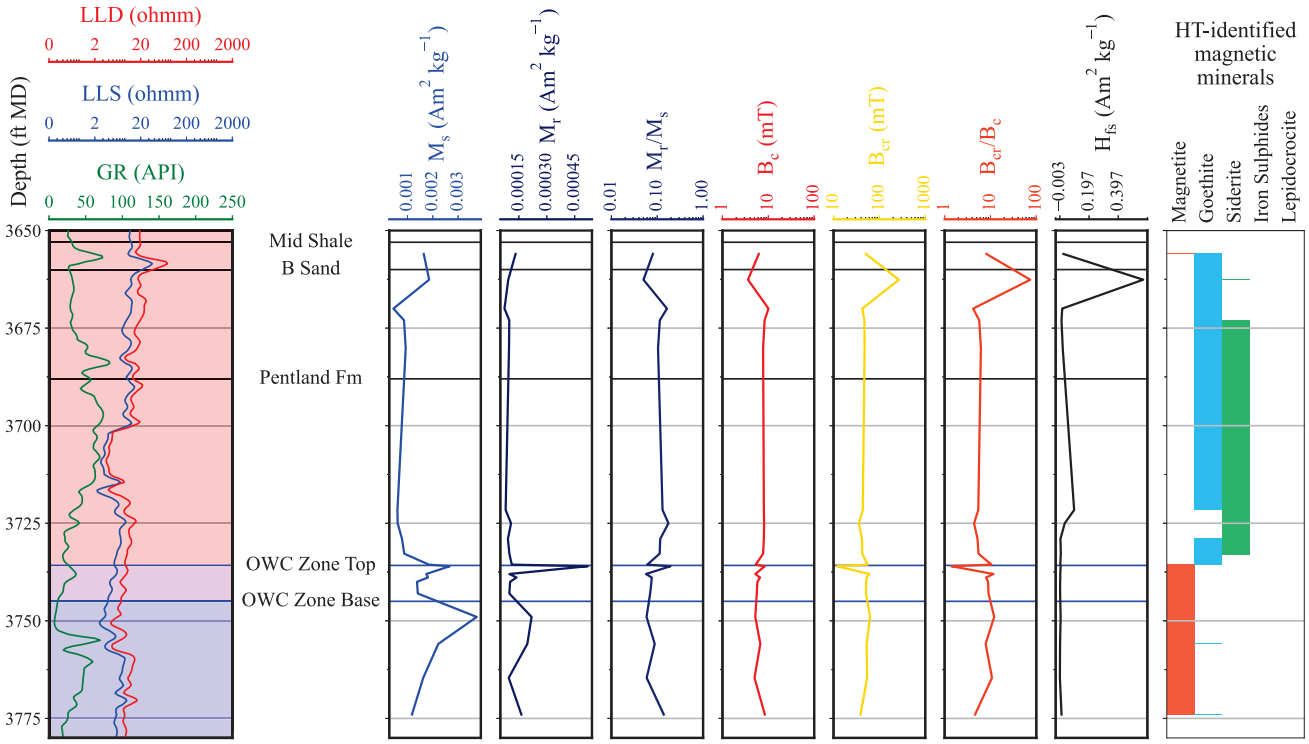


Figure 6.46: *Plots of magnetic results against depth within Well 12/27-1, with gamma ray and resistivity well log data used to identify formations and fluids. Well shaded in red is oil-saturated, blue is water-saturated, purple is within the OWC zone, with the OWC zone shown. M_s = saturation magnetisation; M_r = remanent magnetisation; B_c = magnetic coercivity; B_{cr} = coercivity of remanence; and H_{fs} = high field slope, HT susceptibility-identified magnetic minerals at each sample are shown.*

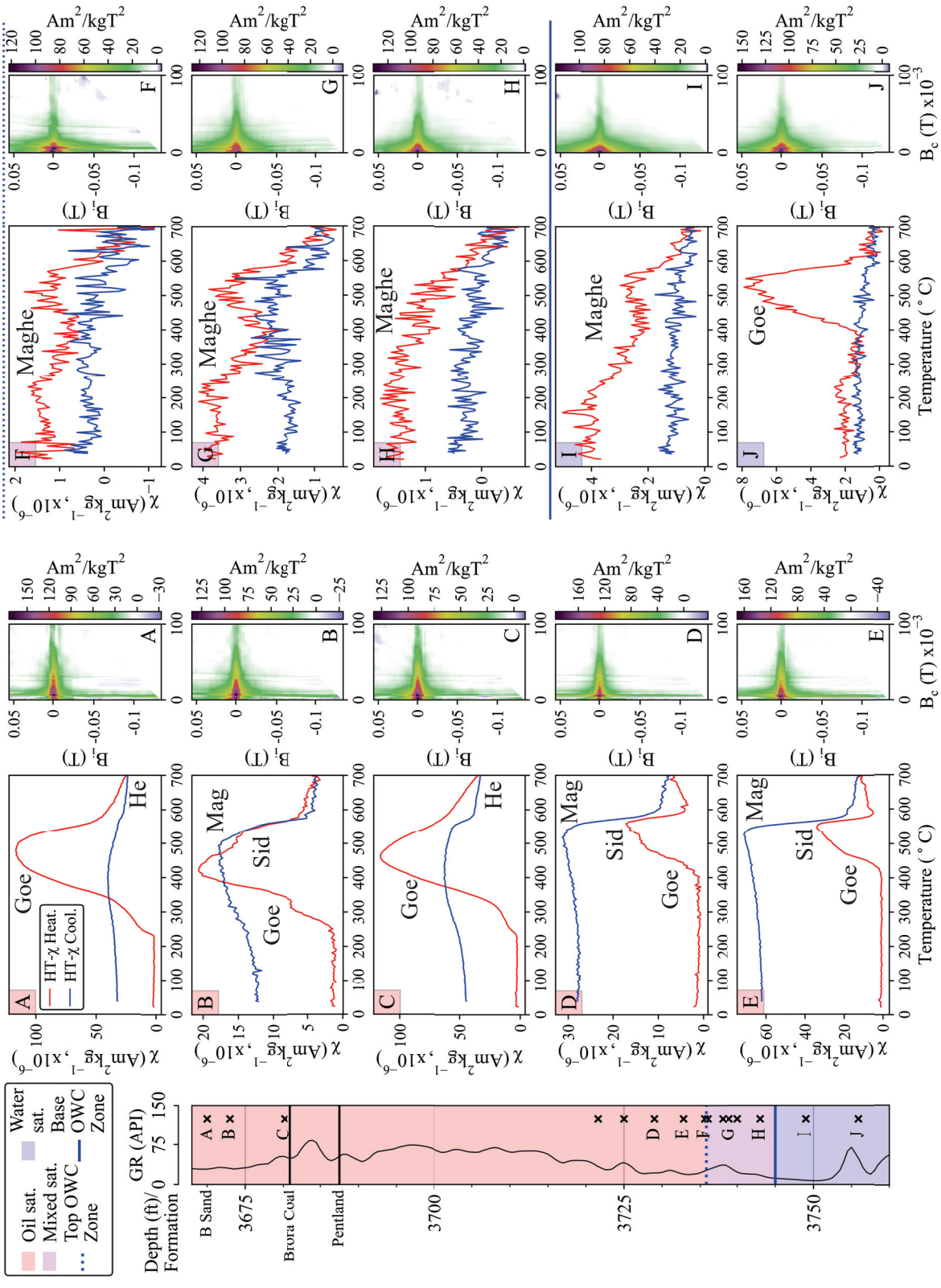


Figure 6.47: *Series of high temperature susceptibility curves and room temperature FORC diagrams of selected samples, as located on the gamma ray well log plot, across various depths and saturated by both oil and water, in Well 12/27-1. The high temperature plots show a defined change in magnetic mineralogy across the section. Goe = goethite, He = hematite, Mag = magnetite, Maghe = maghemite, Sid = siderite.*

6.3.12 | WELL 12/27-2

Well 12/27-2 neighbours Well 12/27-1 to its immediate north west, however the section is deeper here by approximately 1500 ft (Figure 6.48). This well was drilled throughout the entire Cretaceous to Devonian system, however sampling was limited to a very constrained area of the upper reservoir, as such, 12 samples were collected from the B Sands and the Pentland Formation. Due to its close proximity, and similar sampling distribution to Well 12/27-1, analysis of this well is useful to see how localised variations can be, and if, to what extent, depth can influence the magnetic assemblages.

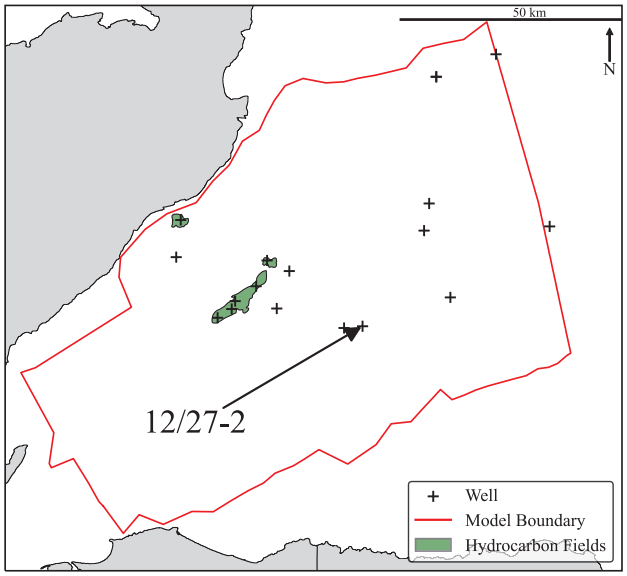


Figure 6.48: *Map of the IMF and study area, showing the location of Well 12/27-2 in the SE of the basin.*

Well 12/27-2 shows a strong magnetic enhancement at the OWC at 5207.8 ft, however this could be affected by the change in lithology approximately 3 ft below the OWC (Figure 6.49). Despite this, there is a clear increase in M_s, M_r and B_c immediately below the OWC, however this B_c increase is preceded by a rapid decrease immediately above the OWC, whilst H_{fs} shows a rapid increase above the contact followed by an immediate decrease. FORC diagrams across the samples all show varying degrees of PSD dominance, with oil-saturated samples showing some PSD, but more SD, SP and MD behaviour compared to the water-saturated samples that are more PSD (Figure 6.50). The high temperature susceptibility curves are, again similarly to Well 12/27-1, showing differences between the saturating fluids, with evidence for dominant goethite within oil-saturated samples alongside some siderite present in most samples, but water-saturated samples contain more evidence for solely containing siderite, alongside the ubiquitous magnetite (Figure 6.50). There are also two occurrences of lepidocrocite within the oil-saturated samples (Figure 6.50A).

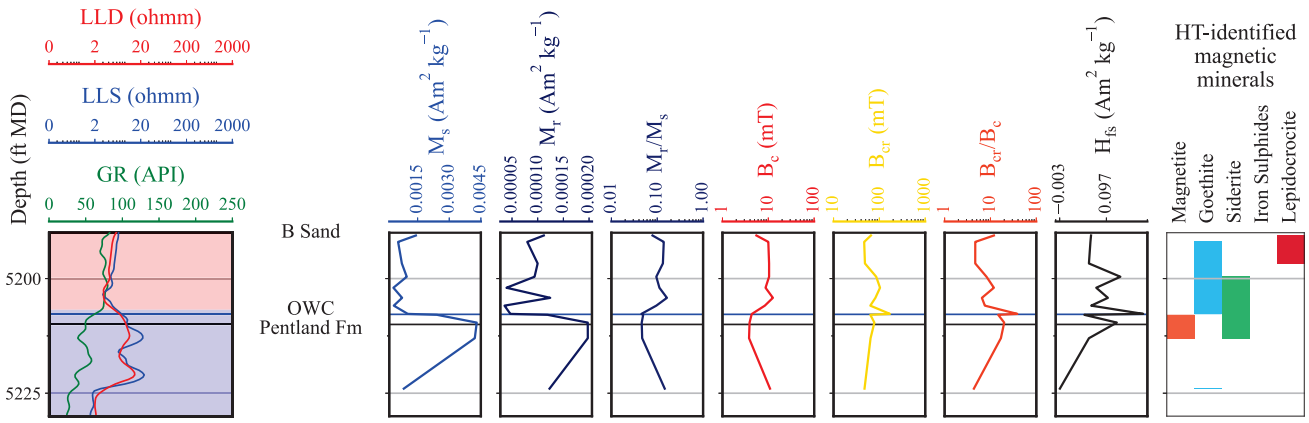


Figure 6.49: *Plots of magnetic results against depth within Well 12/27-2. Well shaded in red is oil-saturated, blue is water-saturated, with the OWC shown. M_s = saturation magnetisation; M_r = remanent magnetisation; B_c = magnetic coercivity; B_{cr} = coercivity of remanence; and H_{fs} = high field slope, HT susceptibility-identified magnetic minerals at each sample are shown.*

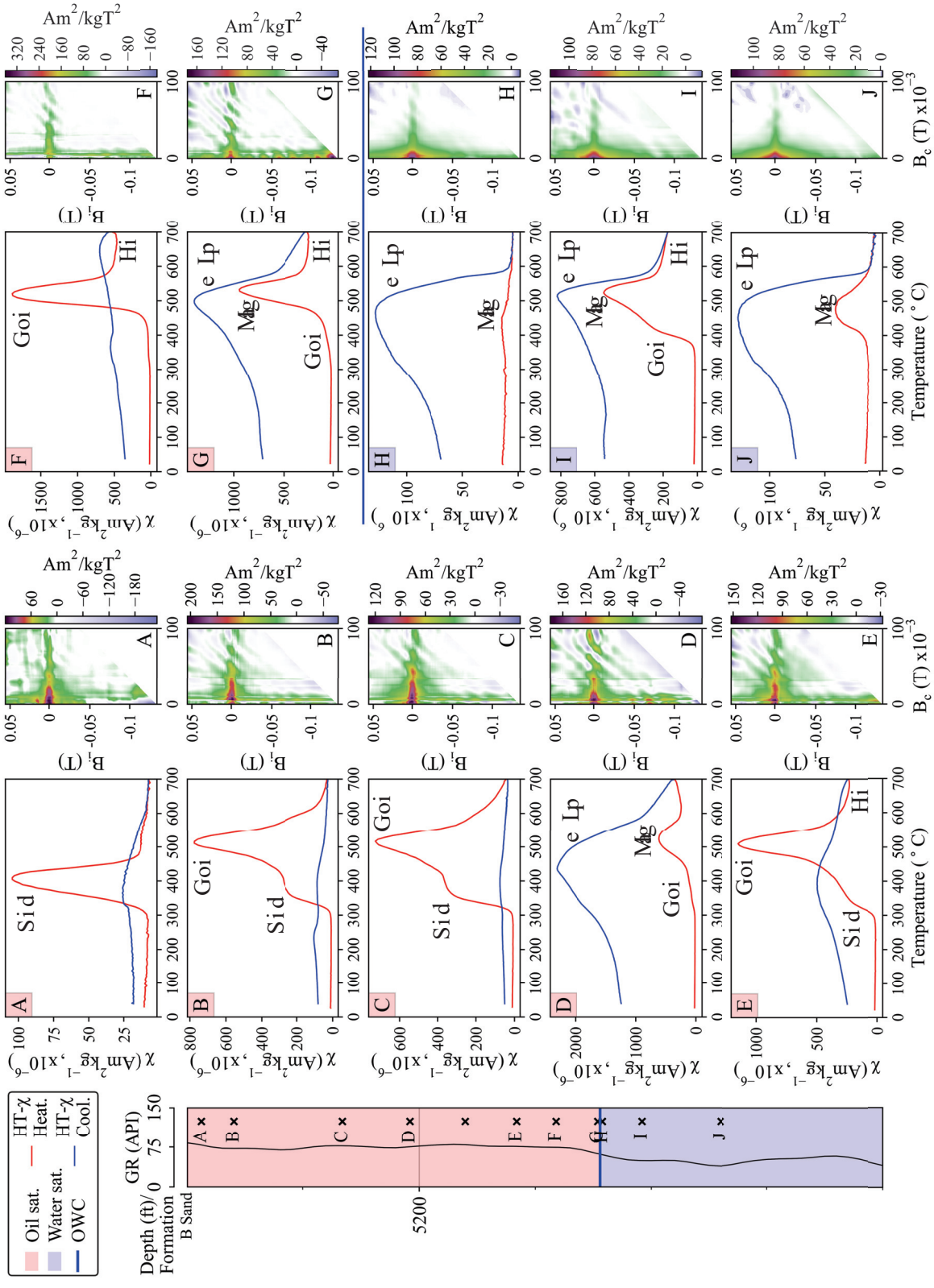


Figure 6.50: *Series of high temperature susceptibility curves and room temperature FORC diagrams of selected samples, as located on the gamma ray well log plot, across various depths and saturated by both oil and water, in Well 12/27-2. There is limited magnetic mineralogy variation between the saturating fluids. Goe = goethite, He = hematite, Lep = lepidocrocite, Mag = magnetite, Sid = siderite.*

6.3.13 | WELL 12/29-1

Well 12/29-1 is the most south easterly well magnetically analysed in this study, and despite being drilled through the entire Jurassic reservoir section, sampling is constricted to cores taken within the Heather Formation, in isolated sand bodies between the large-scale shale intervals (Figure 6.51). Consequently, the OWC in the well is most likely a lithological one, with hydrocarbons being trapped within a small sand body rather than within a larger, fault-controlled structural trap.

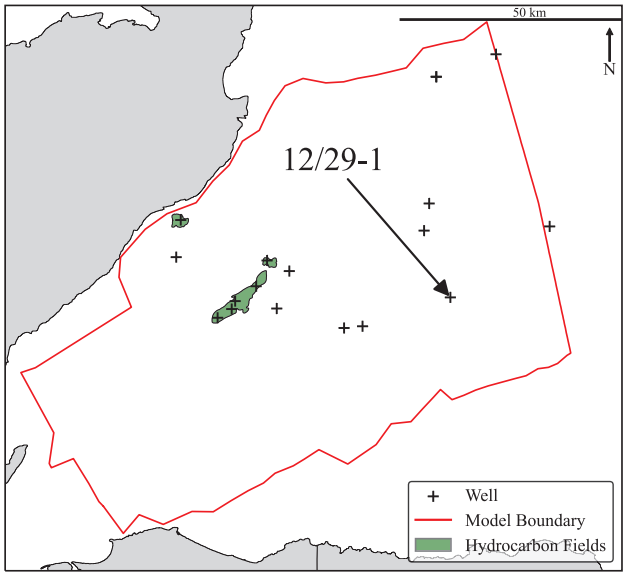


Figure 6.51: *Map of the IMF and study area, showing the location of Well 12/29-1 in the SE of the basin.*

Well 12/29-1 differs slightly to the majority of other wells in the IMF as it sees an increase in magnetisation (M_s and M_r) directly above the OWC, which sits at 6921.95 ft, prior to a drastic decrease below the OWC (Figure 6.52). In tandem with these properties, B_{cr} also shows an above-OWC increase followed by a below-OWC decrease, whereas B_c shows a rapid decrease above and increase below the OWC. These coercivity responses also differ to the majority of the other wells in that they are reversed, with most other wells showing matching magnetisation-B_c and opposing magnetisation-B_{cr} responses. The FORC assemblages within the well show minimal variations across the samples, with all showing strong PSD-dominance and limited influence of any other components (Figure 6.53). This continuity across the saturating fluids is seen within the high temperature susceptibility curves, where there is little variation in the magnetite-dominated assemblages, although all samples show evidence of what appears to be goethite (Figure 6.53).

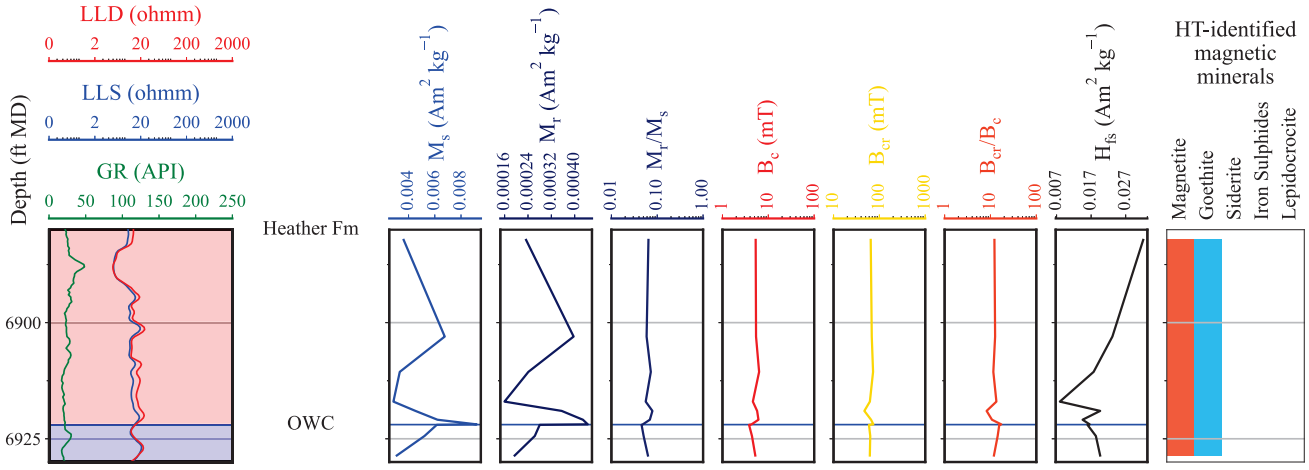


Figure 6.52: *Plots of magnetic results against depth within Well 12/29-1. Well shaded in red is oil-saturated, blue is water-saturated, with the OWC shown. M_s = saturation magnetisation; M_r = remanent magnetisation; B_c = magnetic coercivity; B_{cr} = coercivity of remanence; and H_{fs} = high field slope, HT susceptibility-identified magnetic minerals at each sample are shown.*

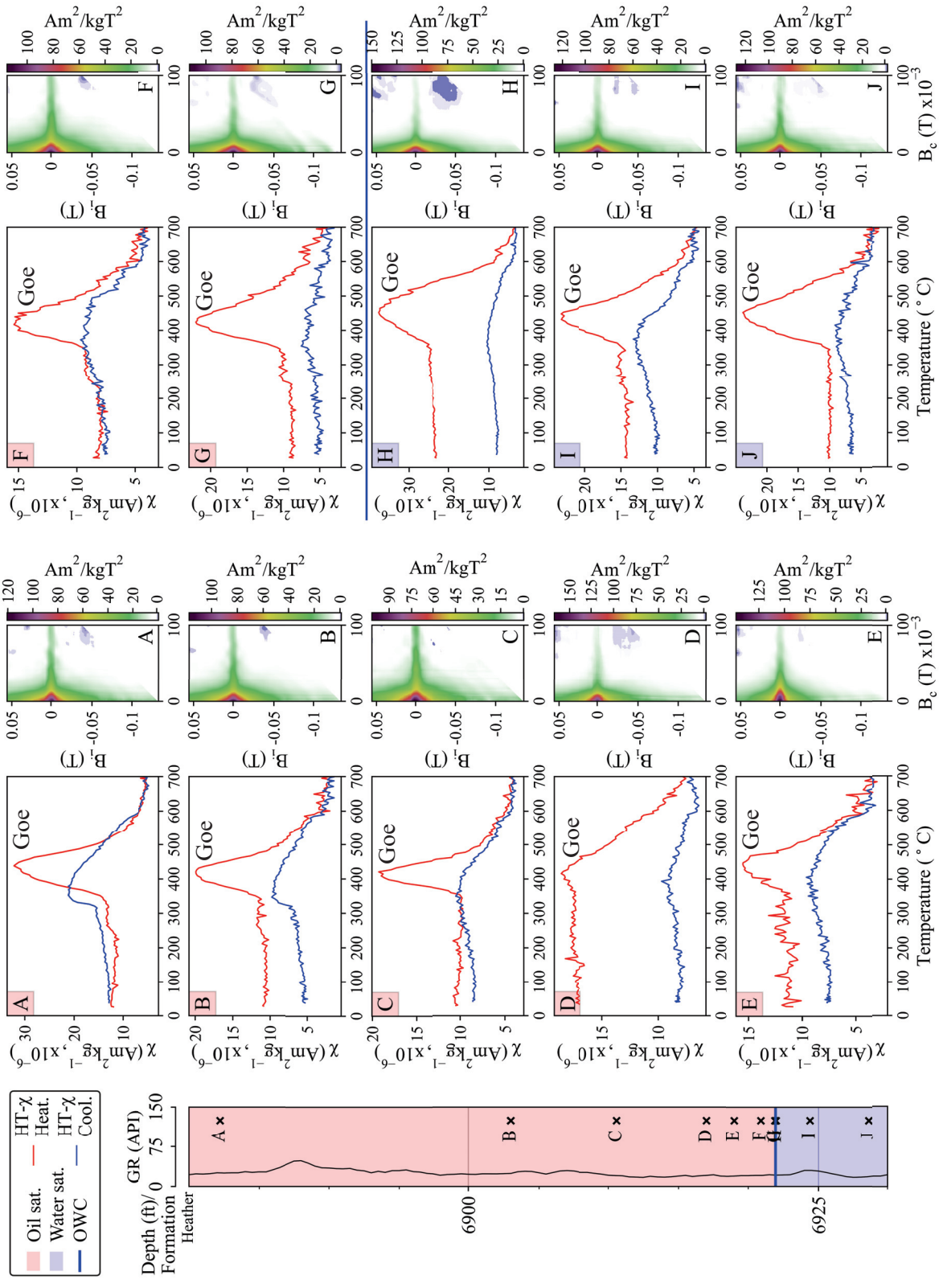


Figure 6.53: *Series of high temperature susceptibility curves and room temperature FORC diagrams of selected samples, as located on the gamma ray well log plot, across various depths and saturated by both oil and water, in Well 12/29-1. The high temperature plots do not show a defined change in magnetic mineralogy across the well. Goe = goethite.*

6.4 | FORC Principal Component Analysis

Principal Component Analysis (PCA) of FORC data is a common technique to identify the domain assemblages of samples through analysis of their FORC diagrams and was first proposed by Lascu *et al.* (2015) and evolved by Harrison *et al.* (2018). PCA is carried out by identifying the number of principal components (PCs) through a scree plot showing eigenvalues. Following the PC identification, endmember (EM) grain domains (PSD, MD, SD, etc.) are identified, which are always $EM = PCA + 1$, i.e., two principal components will have three endmembers, which is the case in the samples seen in the IMF. However, the IMF endmembers were picked predominantly through the planar distribution of samples (Figure 6.54), with the difficulty in developing and presenting FORC PCA data increasing dramatically beyond three endmembers, despite the potential for up to 5 or 6 endmembers based on the eigenvalues seen. EM definition is done by plotting all data points in principal component space, and picking the EMs through the spread of data, with each EM producing a clear domain-specific FORC diagram. EM proportions and absolute values at each data point, based on mass-normalising of the data, are then used to classify the domain assemblage at the points, which is then analysed for changes across variables such as location, depth, formation and fluid.

This study's FORC PCA data identifies grain assemblage changes between multiple variables. Within the samples analysed (Table 6.4), two principal components (PCs) and three endmembers (EMs; PSD, MD and SD) were identified (Figure 6.54). The PSD (EM1), MD (EM2) and SD (EM3) EMs were identified by through the PC plot and the idealised FORC diagrams for each EM, with the majority of

Table 6.4: *Table outlining the breakdown of samples across formations and wells within the IMF, used for Principal Component Analysis within this study. Due to the coring patterns in the wells of the basin, sample numbers are skewed towards the upper reservoir sequence of the A and B Sands.*

Age	Formation	Total Samples	NW IMF		Central IMF Fields					Central, SW & E IMF				
			11/24-1	11/24a-2	11/30-2	11/30-5	11/30a-8	11/30a-B10	12/21-2	12/21-4	12/27-1	12/27-2	12/25-3	12/29-1
Total Samples		219	23	16	16	7	30	24	32	8	20	14	12	10
K.	C. Knoll	20	-	-	-	-	-	-	-	-	20	-	-	-
U. J.	Heather	17	3	-	1	-	3	-	-	-	-	-	-	10
M. Jurassic	A Sand	61	6	16	3	-	19	-	10	7	-	-	-	-
	B Sand	50	9	-	2	-	11	-	12	1	-	3	12	-
	Pentland	30	8	-	-	-	-	-	10	-	-	12	-	-
L. Jurassic	H Sand	10	-	-	6	4	-	-	-	-	-	-	-	-
	I Sand	16	-	-	-	3	-	13	-	-	-	-	-	-
	J Sand	15	-	-	4	-	-	11	-	-	-	-	-	-

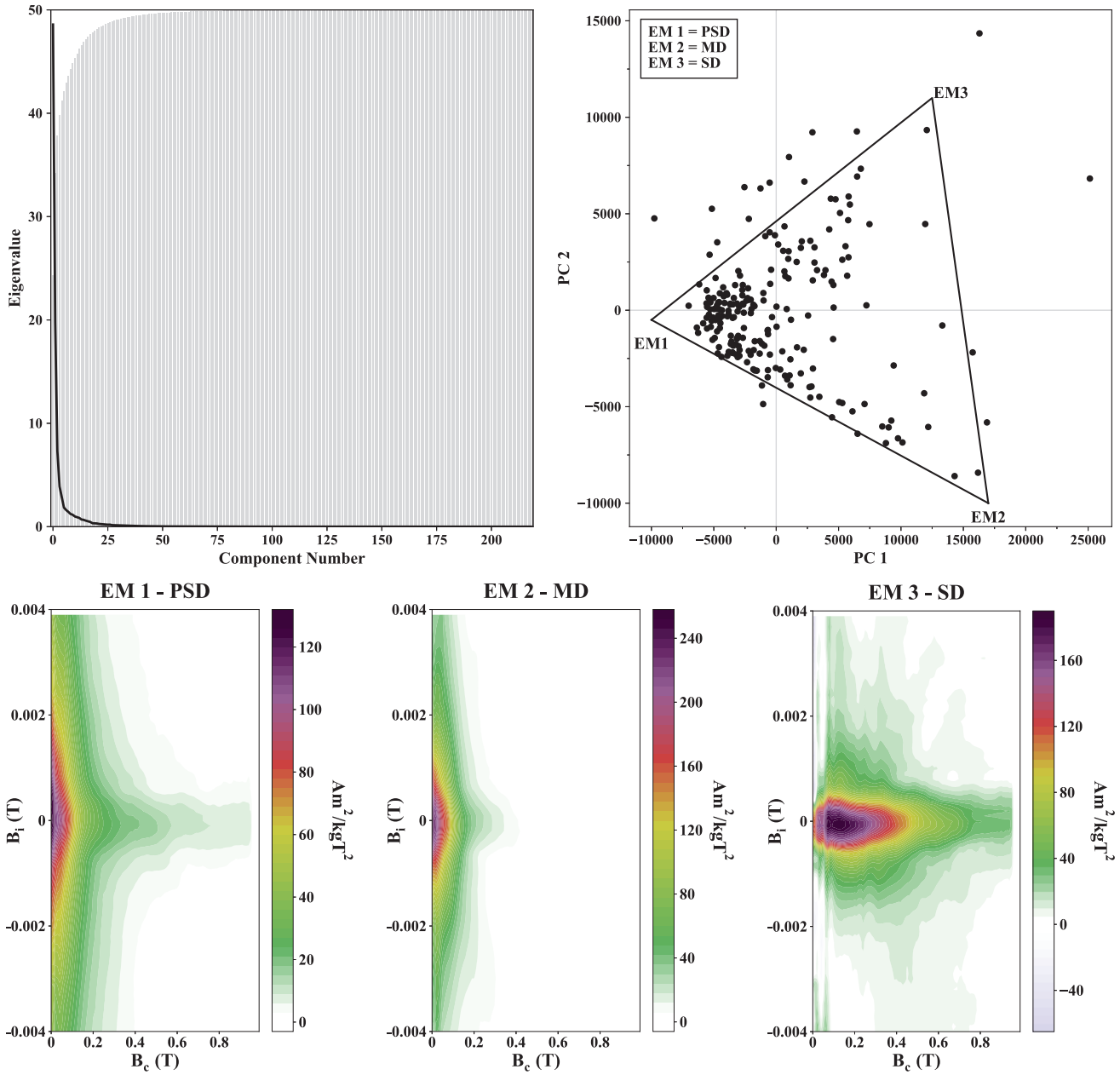


Figure 6.54: *Series of plots summarising the identification of the three PCA end-members identified within this study's FORC diagram analysis. Upper left shows the scree plot of the PCA components and eigenvalues produced, upper right is a PCA plot of all the data points used in the PCA, with the end-members identified. Lower left, middle and rift are the three end-members identified in this study's PCA, present in the FORC diagrams of the samples of the IMF – PSD, MD and SD, respectively.*

analysed samples showing similar characteristics to the idealised FORC diagrams, but with variations dependent on the sample domain assemblage. PSD grains dominate the samples analysed and are also somewhat MD-like, with fewer showing clear MD and SD behaviour (Figure 6.54).

With PCA requiring quality data across multiple sample points for accurate results, many of the samples that were magnetically characterised were not suitable for PCA. However, 219 of the original 271 samples through several formations were analysed across 12 wells within the IMF. The data spread across the samples and wells in the IMF for PCA is good, however the lack of quality samples in the mid-reservoir shales, Permian and Devonian means they were not analysed, and neither was the Upper Jurassic Wick Sand due to the lack of samples (Table 6.4). However, with 219 samples analysed, only

approximately 20 % of the samples collected were not used, and although there is a clear skew in sample numbers towards the A and B Sands, this is reflective of the overall sample distribution (Table 6.1).

Figure 6.54 shows that the majority of data points are strongly PSD, with ever-decreasing influence from MD and SD grains. However, Figure 6.54 shows all undifferentiated data from the PCA, which does not offer insight into localised changes in the assemblages. To identify variations caused by localised factors, Figure 6.55 shows the PCA results from two perspectives, formation and well, separated by saturating fluid type (oil and water). Any domain assemblage variations between formations, or across depth, saturating fluids or location in the IMF, should be identifiable through this separation of data. Formation analysis is also necessary to control data skews seen by anomalous data points in wells and to draw conclusions on how OWCs vary in assemblage based on the formation they occur in.

Figure 6.55 highlights that, whilst there are some similarities between well and formation results, there are also identifiable differences, with even clearer differences seen between the results from differing saturating fluids. Whilst there is an obvious grouping of PSD-dominated oil-saturated samples, there are numerous oil-saturated samples that show clear MD- and SD-dominance, whereas the majority of water-saturated samples are constrained into the PSD-dominated sector.

A further variation seen within well results is the difference in end members across samples in different locations around the IMF - Wells 11/24-1, 11/24a-2 and 12/21-2 strongly plot along the PSD-MD tie line, whereas wells 12/25-3, 12/27-1 and 12/27-2 plot along the PSD-SD tie line. In contrast, the remaining wells (11/30-2, 11/30-5, 11/30a-8, 11/30a-B10, 12/21-4 and 12/29-1) plot predominantly within the PSD space, and spread centrally through the plot, showing no major inclination towards either MD or SD dominance. The separation may be a result of the differing formations within each well, however this is where the formation-orientated PCA becomes crucial.

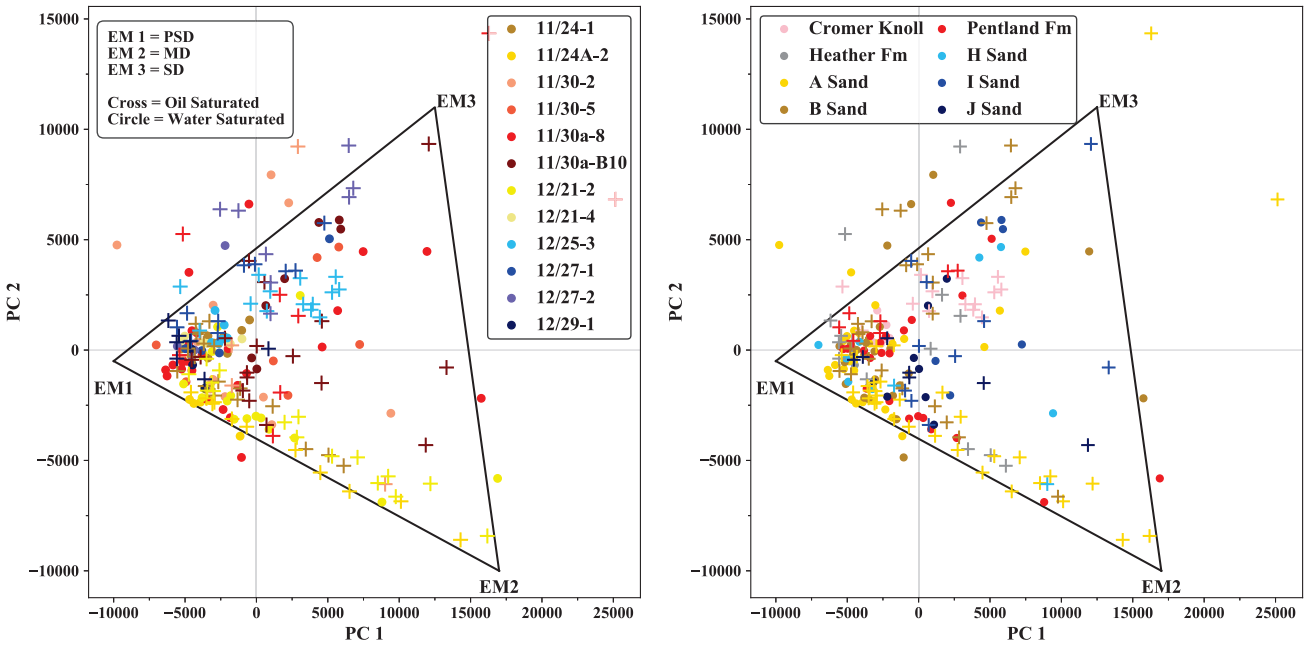


Figure 6.55: *PCA plots of all samples analysed in this study's FORC PCA, delineated by saturation of oil and water, through two perspectives – well (left) and formation (right). The two perspectives allow analysis into both geographical variations, through investigations into the variations between wells, and geological variations, through investigations into the variations between formations.*

PCA of the Cromer Knoll is limited due to all samples originating from the same well, 12/25-3, resulting in heavy bias towards local variations seen in the extremities of the outer IMF. The concentration of samples does not give a good data spread across the basin, and as such cannot be trusted to represent the entirety of the IMF. Despite this, conclusions can be drawn, and the majority of Cromer Knoll data points show PSD and SD domains, with nearly no MD influence (Figure 6.55). The data spread is different to the other formations seen within the IMF, with Cromer Knoll samples showing similarly high PC1 scores in both SD and MD domains, and much lower PC2 scores in MD domains. This domain distribution is quite different to deeper formations where, for the majority of formations, there is no score alignment between domains. Furthermore, when separated into oil- and water-stained samples, there is a very obvious difference, with all water-saturated samples tightly grouped in the PSD region, whereas the oil-saturated samples are much more SD-dominated, with some minor MD influence. The difference between fluids suggests that they are directly responsible for magnetic variations to some extent in the subsurface, but most definitely within the Cromer Knoll Group.

The Heather Formation is predominantly shales, as it acts as the petroleum system seal within the IMF, as such, there are few samples drawn from localised sandier intervals. The PCA data within these sands shows clear variations between wells (Figure 6.55), with 12/29-1 samples grouped in the PSD region and 11/24-1 more MD, whilst 11/30a-8 and 11/30-2 are more SD-leaning. The samples in the central IMF (11/30-2 and 11/30a-8) are less conclusive than the others from the basin-marginal wells, however this may be due to a lack of samples in 11/30-2, whilst those from 11/30a-8 mostly sit centrally within the end-member triangle, suggesting a more even influence between all three domains. Similar to the Cromer Knoll Group, the water-saturated samples from the Heather Formation, whilst there are not many, do group within the PSD region of the PCA plot, with other oil-saturated samples spreading towards more MD- and SD-influences. On the other hand, the water-saturated samples are from Well 12/29-1, and the oil-saturated samples from this well also plot in a very tight PSD-dominated grouping, unlike the Cromer Knoll Group from Well 12/25-3, suggesting that lithological variations may be having an effect on magnetic assemblage.

PCA of the A Sand broadly follows similar trends to the trends of the entire dataset PCA - water-saturated samples mostly clustering within the PSD sector and oil-saturated samples tracking along the tie lines between PSD and other EMs (Figure 6.55). Where A Sand differs is that all oil-saturated samples fall solely along the PSD-MD tie line. The oil-saturated samples can be roughly split along the tie line, with wells 11/24-1, 11/24a-2, 11/30-2 and 11/30a-8 remaining dominated by PSD grains, whereas Well 12/21-2 spreads extensively towards the MD EM. This difference is unclear, as Well 12/21-2 is geographically a lot closer to wells 11/30-2 and 11/30a-8 than Well 11/24a-2, so influences beyond regional variances must be the cause(s). Due to A Sand being the uppermost reservoir unit, most wells where sampling was possible have purely oil-saturated samples or an insufficient number of water-saturated samples to draw conclusions, thus deriving same-well fluid saturation variations in the A Sand is difficult. However, Well 11/30a-8 offers some insight, with the majority of the water-saturated samples are PSD-dominated, save for the three outliers that exist in the centre of the end members, whilst the oil-saturated samples plot along the PSD-MD tie line alongside the other oil-saturated samples.

Despite the B Sand being lithologically similar to A Sand, the PCA distributions differ (Figure 6.55).

Whilst most water-saturated samples are PSD dominated, like A Sand, there is a significant difference with the oil-saturated samples, which are much more SD dominated than the A Sand equivalents, and show little MD influence. The most obvious outliers in the B Sand samples are the oil-saturated ones from Well 12/21-2, that plot with ever-increasing MD influence, akin to those seen in the A Sand. Comparatively, the samples from Well 11/24-1 do not show formation-crossing patterns, as where the oil-saturated A Sand samples track from PSD to MD influence, those in B Sand track from PSD to SD, although it must be noted that a couple of samples do show significant MD influences. The difference in B Sand assemblage in the wells to the south east of the IMF (12/27-1 and 12/27-2) compared to the centre and north west is clear - the water-saturated samples are PSD-dominated, the oil-saturated samples trend along the PSD-SD tie line. Well 12/27-1 and 12/27-2 exist nearly adjacent to each other in the IMF and are lithologically and geologically near identical, suggesting that the differences they show compared to the rest of the wells in the IMF could be a result of localised variation.

The Pentland Formation, whilst sampling was from sands, is a very shale-dominated formation, and as such has lithological differences when compared to the reservoir sands, especially the A and B Sands. However, the PCA assemblage shows relatively similar results to the reservoir sands (Figure 6.55), which a general grouping of water-saturated samples in the PSD region, and oil-saturated samples leaning towards the SD region. The clearest outlier within the Pentland PCA is the water-saturated samples from Well 12/21-2, which show ever-increasing MD-influences, very similarly to the well's oil-saturated samples seen in the A and B Sands. The second most notable difference between this PCA and those in other formations is the spread of data spread through the water-saturated samples of Well 11/24-1 that show increasing SD influences. This is a departure from the water-saturated samples seen in B Sand, that were strongly clustered in the PSD sector, suggesting that some variation is occurring.

Due to limited sampling in the H Sand, it is difficult to draw widespread conclusions from the formation, as only a few samples from two adjacent wells offer PCA results. The majority of water-saturated samples show PSD-dominated results, however three water-saturated samples show a mix of both MD and SD influence (Figure 6.55). The two oil-saturated samples are relatively central within the PCA plot, showing no major end member dominance, suggesting that there is fluid influence on the magnetism, akin to the other formations, although it is less conclusive than others.

PCA of the I Sand differs to other formations in the IMF as water-saturated samples show MD or SD influence and the oil-saturated samples are PSD dominated (Figure 6.55). Due to limited samples, the difference may be a function of a lack of diversity, but similar assemblages are seen within the J Sand also, suggesting a degree of continuity and lithological influences on the magnetic assemblage. There is also a difference in assemblage within the two wells, 11/30-5 and 11/30a-B10, with the water-saturated 11/30-5 samples trending approximately along the PSD-MD tie line, whereas the samples from Well 11/30a-B10 show clear separations between water- and oil-saturated samples. Water-saturated 11/30a-B10 samples group tightly in the SD region, whereas the oil-saturated samples are widespread, though predominantly cluster in the PSD sector. The variation in assemblage between the wells is curious, as they are positioned very close to each other, and both sit within the Beatrice Field, the main difference in the two formations is the depth they occur at - the top of I Sand in Well 11/30-5 is at approximately 7260 ft (2210 m), whereas in Well 11/30a-B10 the top of the I Sand is at approximately 8080 ft (2460

m). The difference in depth, whilst not great, may be large enough to create lithological variations, such as an increase in cementation, that could cause differences in the magnetic assemblage.

Akin to I Sand, J Sand shows an inverse saturating fluid-PCA relationship, with most water-saturated samples showing MD and SD influences and oil-saturated samples being more PSD dominated (Figure 6.55). Also similar to I Sand is the variation between wells, with Well 11/30a-B10 containing SD water-saturated samples, while Well 11/30-2 contains more MD water-saturated samples. The depth variation between these formations across wells is similar to I Sand also, with the top of J Sand sitting at approximately 7120 ft (2170 m) and 8340 ft (2540 m) in Wells 11/30-2 and 11/30a-B10, respectively.

When analysing FORC PCA data as a function of formation, there are clear trends across both formation and location in the IMF (Table 6.5). The Cretaceous, Upper and Middle Jurassic formations have PSD dominated water-saturated samples and a mix of all domains in oil-saturated samples. In contrast, whilst the H Sand of the Lower Jurassic follows the patterns of the formations above, the I and J Sands are the opposite, with MD- and SD-dominated water-saturated samples and oil-saturated samples are PSD dominated. The cause of the shift in domain assemblage at depth is unclear, but with the H Sand being lithologically similar to the Pentland Formation sands, and the deeper I and J Sands being increasingly cemented and much shalier than than the shallower A and B Sands, the cause could well be lithological rather than fluid-related. In order to further identify the mineral assemblages and determine any causes of variations, analysing the FORC data through well bore-orientated analysis is crucial, and will be carried out in the following section.

Table 6.5: *Summary table outlining the varying PCA end-member presence across the formations analysed in the IMF, delineated by saturating fluid. There are little clear trends present within the data, though this is likely a result of the formation-based analysis grouping all well-derived results together, limiting clarity towards geographical variations.*

Age	Formation	Oil	Water
K.	**C. Knoll**	SD	PSD
U. J.	**Heather**	PSD, MD, SD	PSD
M. Jurassic	**A Sand**	PSD, MD	PSD
	B Sand	SD, (PSD, MD)	PSD
	Pentland	PSD, SD	PSD, MD
L. Jurassic	**H Sand**	Mix	PSD
	I Sand	PSD	SD, (PSD)
	J Sand	PSD	MD, SD

6.4.1 | WELL PCA

6.4.1.1 | WELL 11/24-1 - LYBSTER FIELD

The samples from Well 11/24-1 show an overall PSD grains domination in the assemblage, with SD and MD grains offering a significantly smaller proportion of the magnetic signal (Figure 6.56). Throughout the samples all points have generally consistent proportions, with PSD grains accounting for between 50 and 90 % of the magnetic mineral assemblage at each point. At the majority of points within the A and B Sands, PSD grains account for over 75 % of the assemblage, with both sand bodies having average PSD:MD:SD grain domain ratios of 76:12:12 % across their samples. This contrasts with the Pentland Formation that has a PSD:MD:SD ratio of 59:20:21 %.

The only clear departure from the trend seen across the well is just below the top of the OWC zone, at sample depth 4949.1 ft, where there is a huge increase in PSD grains relative to the assemblage, with PSD:MD:SD absolute values showing a 2.80:0.12:0.15 $Am^2T^{-2}g^{-1}$ ratio, equating to a 91 % domination of PSD grains in the assemblage, compared to the 4.0 % and 5 % contribution of MD and SD grains, respectively. The return to normalcy from samples at 4949.5 and 4951 ft show that this enhanced signal is very narrowly constrained to the top few centimetres of the contact zone, and suggests that the magnetic mineral accumulation was halted from further surface-ward movement by the fluid density differences between oil and water. Unfortunately, due to core constraints, the base of the OWC zone could not be sampled, and therefore it is not possible to ascertain if there is a secondary enhancement zone where hydrocarbons cease to be prevalent. The PSD enhancement at 4949.1 ft is directly comparable to the enhancement in magnetic moment and saturation magnetisation see in Section 6.3.2. This indicates that the increase in magnetisation is likely due to the formation or accumulation of solely PSD grains, as there is little fluctuation of SD and MD grain influence across the contact zone. This increase in PSD grain-derived magnetisation is likely a result of goethite altering to magnetite at the redox boundary caused by the OWC.

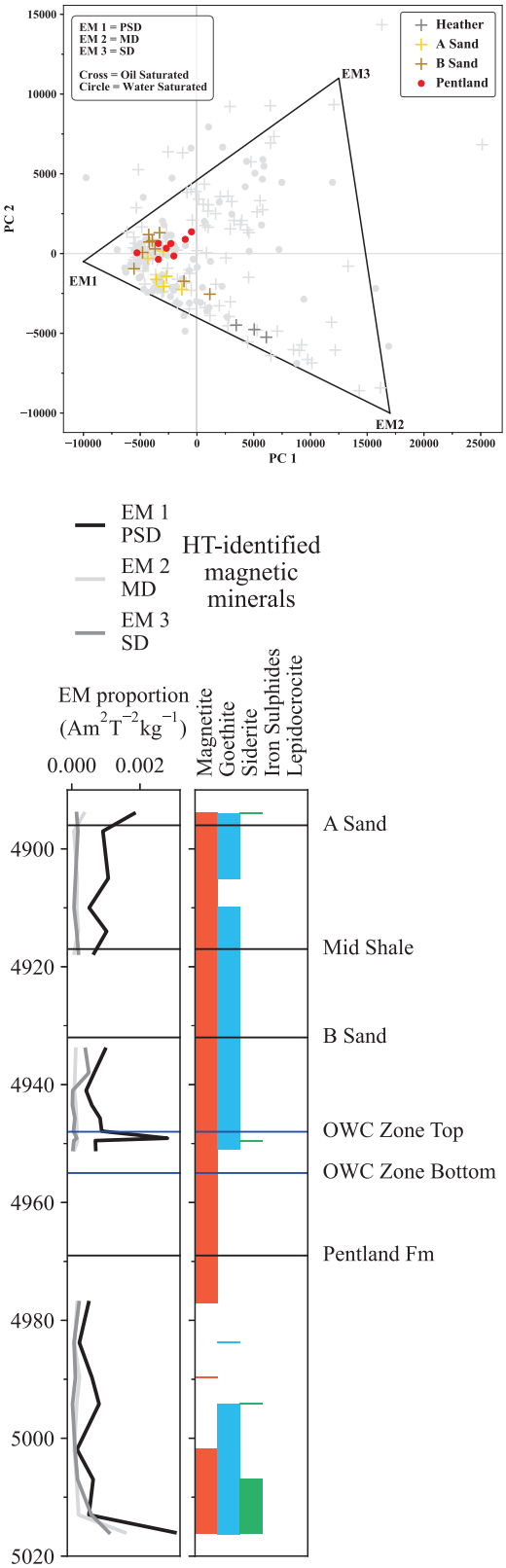


Figure 6.56: *PCA plot of samples, and depth plot showing EM contributions and mass-corrected proportions of the samples in Well 11/24-1.*

Samples from the Pentland Formation show a slightly different domain assemblage to that of the cleaner sands of the upper reservoir. The difference is likely to be a result of lithological variation, as, despite sampling in the Pentland being done within the sandy intervals, these intervals naturally contain a higher clay content than the reservoir sands. However, it is interesting that the domain assemblage is still PSD-dominant, with SD and MD offering approximately equal influence.

6.4.1.2 | Well 11/24a-2

Unlike the other wells in the IMF, Well 11/24a-2, in the NW flank of the basin, shows significantly greater MD grain behaviour (Figure 6.57). MD grains periodically match and exceed the magnetic contribution of PSD grains throughout the sampled interval within the A Sand, whilst SD grains maintain a similar low proportion, akin to the other wells. The variation in domains is seen in PSD:MD:SD ratios within the sampled section of 68:30:2 %, equivalent to mean absolute value ratios of 5.92:3.07:0.16 $Am^2T^{-2}g^{-1}$. Across the OWC at 6130 ft, there is a clear variation in domain assemblage, with the greatest proportion of MD grains seen within the well occurring above the contact at 6127.3 ft, and the largest PSD proportion occurring below the contact at 6137 ft, an increase on the emergence of PSD domination at 6132.8 ft. The PSD:MD:SD assemblage ratios at 6127.3 ft are 13:85:2 %, and at 6137 ft are 87:3:10 %. The assemblage variation matches the direct magnetic variations seen across the contact, as identified in Section 6.3.3, which gives further evidence of PSD, but locally MD, grains forming the bulk of the magnetic enhancement around OWCs.

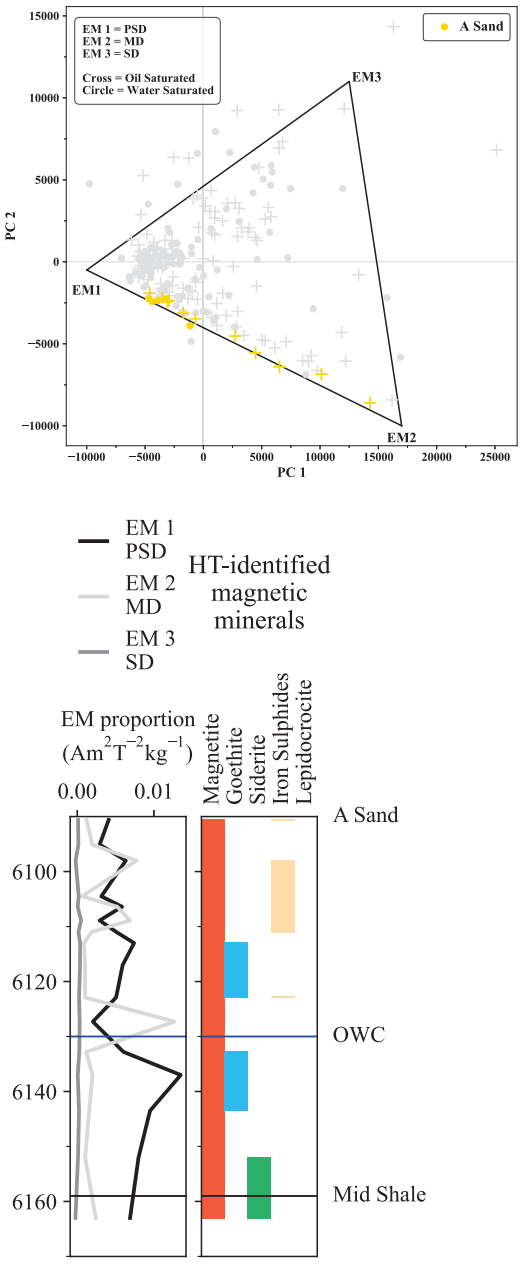


Figure 6.57: *PCA plot of samples, and depth plot showing EM contributions and mass-corrected proportions of the samples in Well 11/24a-2.*

The periodic influx of MD grains at varying points within the hydrocarbon column is unique to this well. In addition to this, the MD peak above the OWC in Well 11/24a-2 is not seen at any other location within the IMF, which would infer a localised variation in mineral assemblage, potentially as a result of its proximity to the Great Glen Fault. There is a chance that the periodic re-activation of the Great Glen Fault during rifting events (Andrews *et al.*, 1990) has caused intermittent, surface-ward fluid flow up the fault line. These periods of fluid flow could have created localised magnetic assemblage variations at points through the hydrocarbon column as the local area around Well 11/24a-2 filled with hydrocarbons. However, this requires testing through the basin and petroleum systems model. With the extensive presence of iron sulphides within

this well that is not seen elsewhere, it suggests that MD grains in this well are iron sulphides or potentially framboidal greigite.

6.4.1.3 | Well 11/30-2 - Beatrice Field

Despite Well 11/30-2 containing samples across multiple formations, due to sampling constraints they are too widely dispersed to accurately draw any conclusions from. Consequently, whilst the samples have been included in the formation analysis, they are not included in this section. The general trends of the well follow those seen elsewhere, with a broadly PSD-dominant assemblage throughout, and lesser MD and SD components, with an average PSD:MD:SD ratio of 49:27:24 %.

6.4.1.4 | Well 11/30-5 - Beatrice Field

Due to sampling limits, Well 11/30-5 was not sampled across the OWC. However, the samples across water-saturated H and I Sands do give some insight into the assemblage in the central regions of the Beatrice Field (Figure 6.58). The PSD:MD:SD ratio averages 43:36:21 % across all samples in well, but there are extensive variations, including large localised peaks in all three EMs at various data points. The small sample set in this well means limited conclusions can be taken from it, but the data spread is broadly similar to other regions.

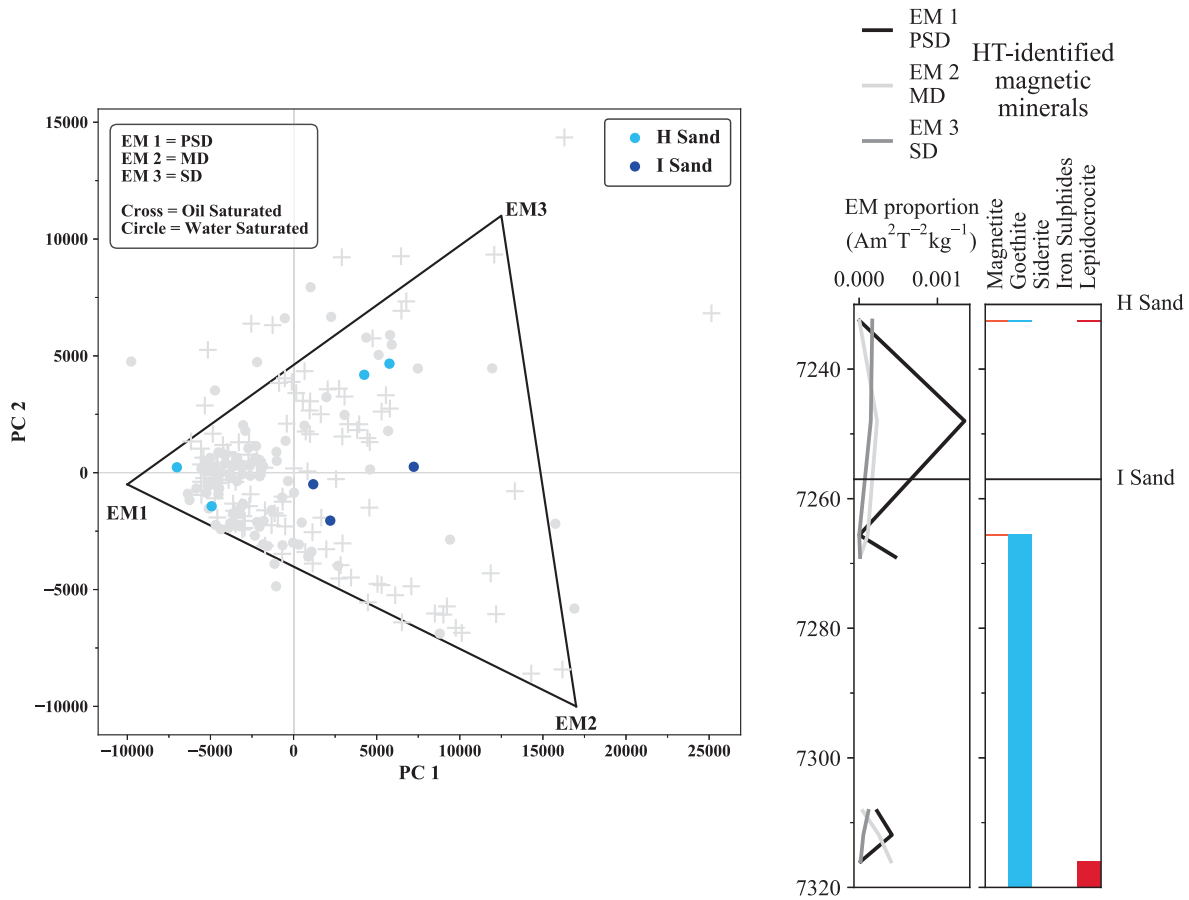


Figure 6.58: *PCA plot of samples, and depth plot showing EM contributions and mass-corrected proportions of the samples in Well 11/30-5.*

6.4.1.5 | Well 11/30a-8 - Beatrice Field

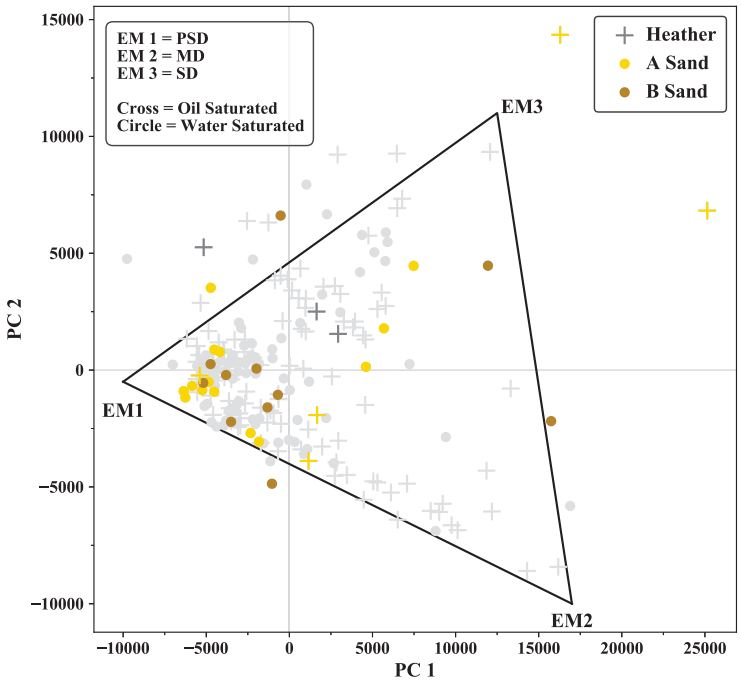


Figure 6.59: *PCA Plot of samples from Well 11/30a-8, separated by formation and saturating fluid.*

Well 11/30a-8 shows similar grain domain assemblages in A and B Sands to other wells across the IMF (Figures 6.59 & 6.60). PSD grains dominate the samples, with an average PSD:MD:SD ratio of 62:14:24 %, but with localised variation. Akin to other wells, there is variation in the assemblage across the OWC, as, despite the continued PSD control above and below the contact, directly above the contact there is a relatively great increase in MD influence, which then, alongside the PSD influence, drops off at the contact before increase again below.

Whilst the strong PSD component around the contact can be directly attributed to altered goethite-derived magnetite presence, similar to numerous other wells in the basin, the immediate drop in PSD contribution below the contact is different to the other wells. This directly correlates to a lack of identified magnetite but consistent presence of goethite in the sample. As goethite is typically antiferromagnetic and has a very big coercivity that does not saturate, it does not contribute to FORC PCA, resulting in this clear decrease. Furthermore, the sharp increase at 7030 ft relates to the hypothesised, but proven inconclusive, paleo-OWC, with the FORC PCA behaviour very similar to actual OWCs.

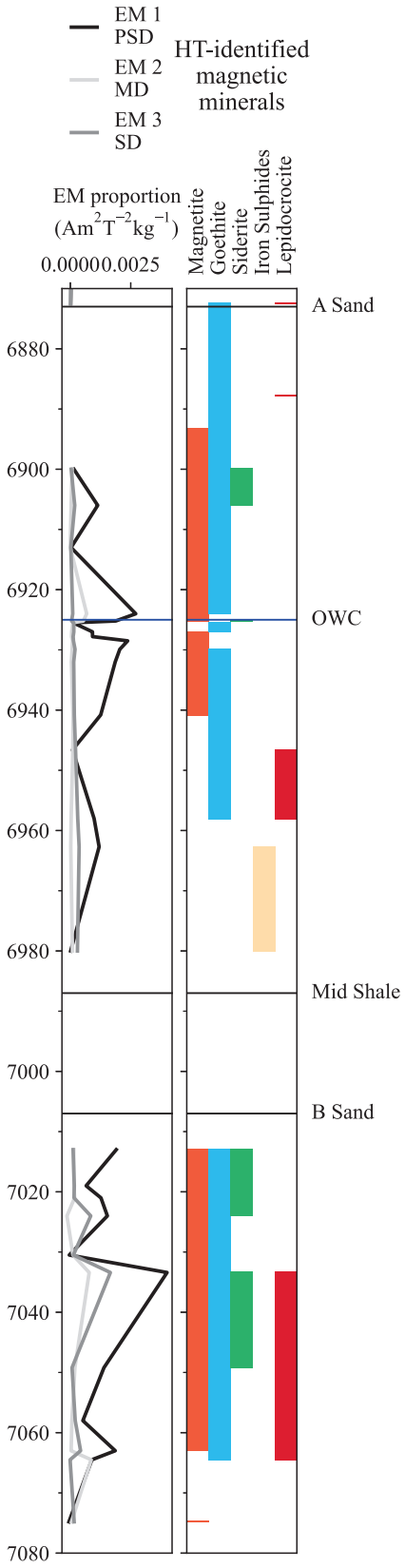


Figure 6.60: *Depth plot showing mass-corrected proportions of the grain domains seen in samples in Well 11/30a-8.*

6.4.1.6 | Well 11/30a-B10 - Beatrice Field

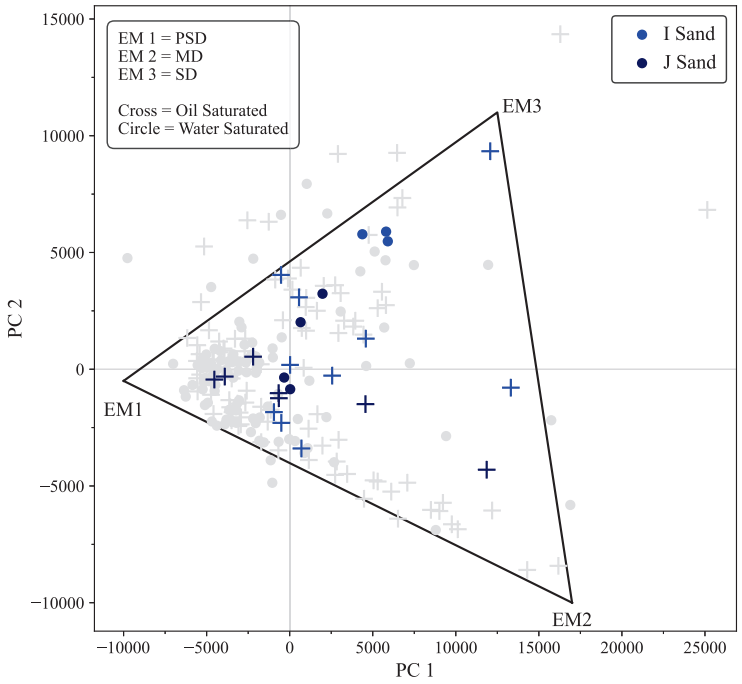


Figure 6.61: *PCA Plot of samples from Well 11/30a-B10, separated by formation and saturating fluid.*

Well 11/30a-B10 has an assemblage different to others in the Beatrice Field, with the upper sections of both formations differing to those of deeper areas, suggesting potential for the trapping of magnetic minerals at the top of each formation (Figures 6.61 & 6.62). The OWCs at 8196 ft and 8362.5 ft see the assemblages wholly change, with both seeing PSD dominance above and a more even distribution of all three domains below. The average PSD:MD:SD ratios of the upper region are 77:10:13 % and 53:30:17 % above and below the OWC, respectively, but in the lower region this ratio alters to 17:20:63 % and 27:33:40 %. The decline in PSD and relative increase in MD and SD grains below relatively similar depths in each formation bears little relation to the magnetic signals recorded and it is unclear why this occurs.

Well 11/30a-B10 differs to other wells through a lack of variation in assemblages across OWCs, with this likely caused by a lack of alteration of goethite into magnetite around the contacts. The upper OWC shows no variation in assemblage across it, whilst the lower OWC has an increase in PSD and marginal change in MD and SD influence below the contact compared to above, but they are nowhere near as clear as other examples seen within this study.

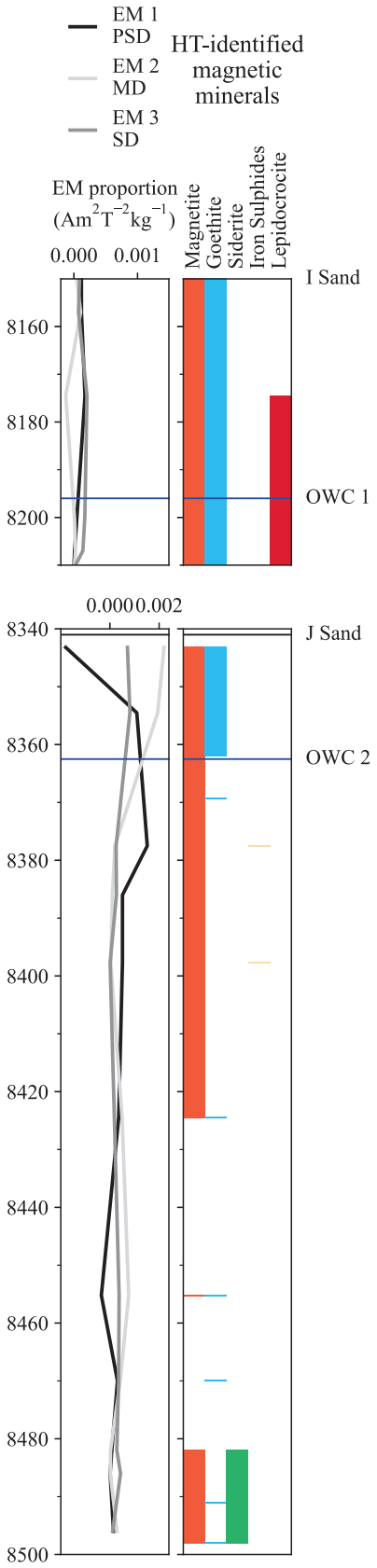


Figure 6.62: *Depth plot showing mass-corrected proportions of grain domains seen in samples in Well 11/30a-B10.*

6.4.1.7 | Well 12/21-2 - Jacky Field

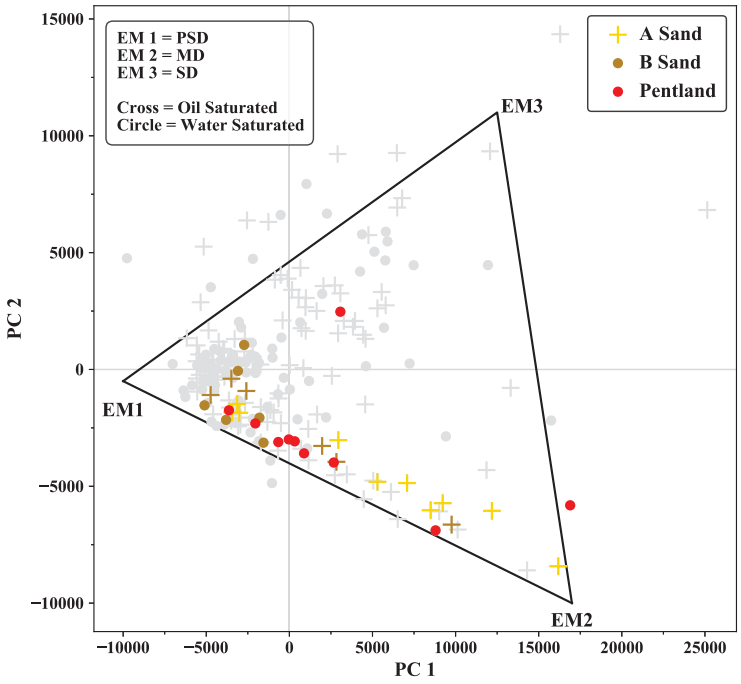


Figure 6.63: *PCA Plot of samples from Well 12/21-2, separated by formation and saturating fluid.*

Whilst the lower, water-saturated section of Well 12/21-2 in the Pentland Formation shows a more even distributions of domains, akin to wells in Beatrice Field, MD grains are more dominant, unlike the other locations, and the samples around the OWC at 7118 ft show further differences (Figure 6.64). Above the OWC, a sharp increase in SD and decrease in PSD influence follows a rapid increase in PSD and decrease in SD influence at the OWC and below the OWC, both PSD and SD influences decrease, but at vastly different values. The PSD:MD:SD ratios vary from: 4:2:94 % above; 82:1:17 % at; and average 75:8:17 % below the contact. Despite the SD-dominant assemblage at 7114.5 ft being potentially anomalous, the variation in average PSD:MD:SD assemblages above (56:6:38 %) and immediately below (76:7:17 %) the OWC show a definitive fluid-derived alteration. Whilst the differences between the B Sand and the Pentland Formation shows variation is largely a result of lithology, the increase in in PSD influence from below towards the OWC links directly to magnetite formation from goethite, producing both stronger magnetic signals as well as greater PCA contributions.

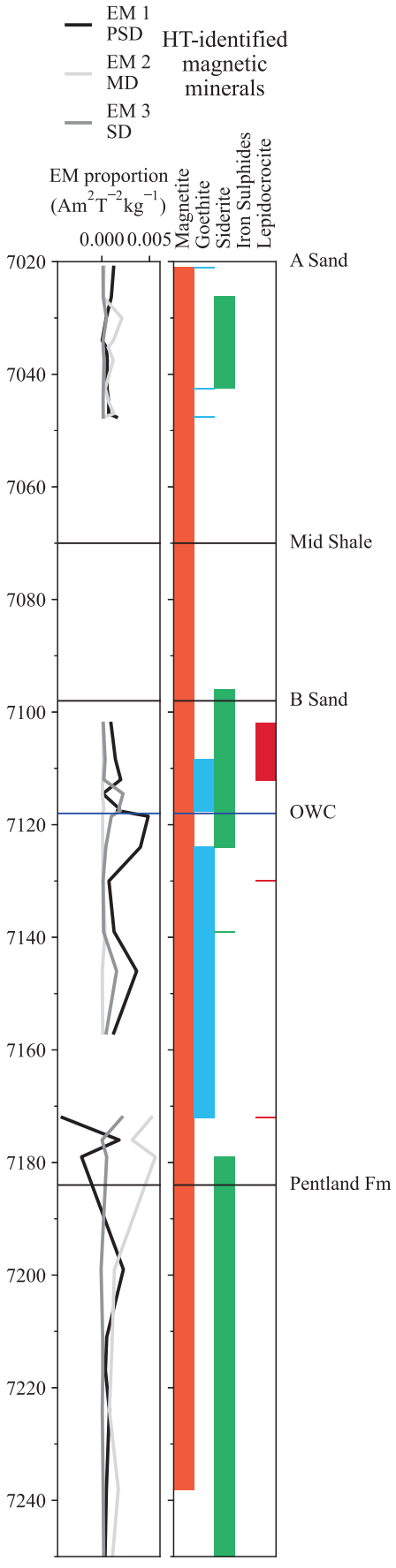


Figure 6.64: *Depth plot showing mass-corrected proportions of the grain domains seen in samples in Well 12/21-2.*

6.4.1.8 | WELL 12/21-4

Well 12/21-4, as the only completely dry, hydrocarbon-free well in the study area, provides information on the background magnetism seen in the geology of the IMF, although information is severely limited by the lack of samples, with only A Sand having any core (Figure 6.65). The A Sand of 12/21-4 does give an insight into the magnetic assemblage, however, with PSD grains still maintaining a strong dominance on the assemblage, however there are clear differences in this well compared to others regarding the MD and SD influences, with SD grains offering a larger component than the MD grains, unlike other wells within the IMF. On average, across the samples, the A Sand of Well 12/21-4 has a PSD:MD:SD ratio of 74:5:21 %.

The differing proportions of MD and SD grains compared to other locations within the IMF could be circumstantial, however it could suggest that hydrocarbons are either transporting, generating or altering grains that are of large enough size to be either MD or PSD in nature. Considering that other wells within the IMF are PSD-dominated, it is possible that hydrocarbon influx is responsible for the addition of MD grains into the magnetic assemblages in hydrocarbon-bearing regions of the IMF.

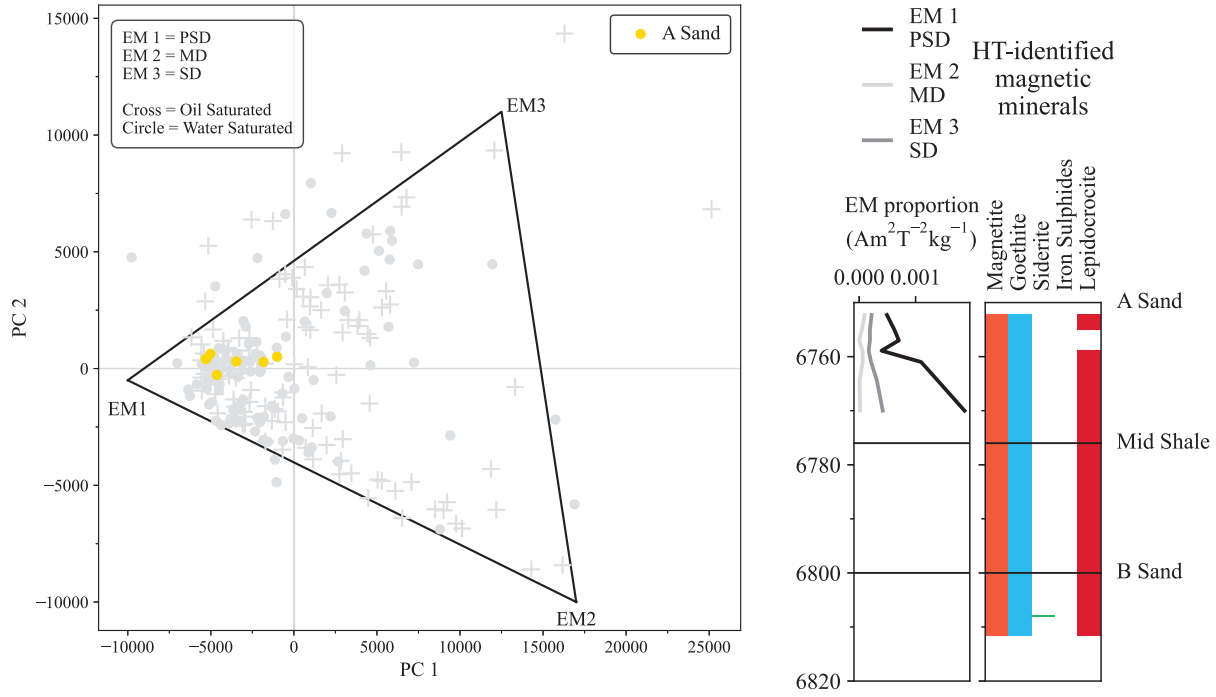


Figure 6.65: *PCA plot of samples, and depth plot showing EM contributions and mass-corrected proportions of the samples in Well 12/21-4.*

6.4.1.9 | WELL 12/25-3

Well 12/25-3 was sampled to investigate the differences between the Inner and Outer Moray Firth and the PCA analysis shows that there is a clear difference (Figure 6.66). Whilst the upper section of the Cretaceous Cromer Knoll Group maintains the IMF-like PSD grain domination, this changes in the lower section to a more MD-dominated assemblage, with a unique SD peak above the localised OWC, and increased MD presence across the contact. Akin to Well 11/24a-2, the presence of iron sulphides identified in the high temperature susceptibility analysis and the correlated presence of MD

grains here suggests that MD grains in this well are also iron sulphides, although the strong presence of iron sulphides align with the SD peak above the OWC.

The upper section of the Cromer Knoll is broadly reflective of the overall IMF assemblage, with an average PSD:MD:SD ratio of 74:20:6 % but with some variance across sample points, whereas the lower section differs drastically, with an average PSD:MD:SD ratio of 15:65:20 %. Across the samples encircling the localised OWC, the variation in assemblages is of stark difference to those elsewhere, with samples immediately above the OWC, at 5601 and 5602.9 ft, showing PSD:MD:SD ratios of 2:2:96 % and 4:43:53 %, respectively. Directly below the contact, at 5604 ft, the PSD:MD:SD ratio alters to 10:72:18 %, before it averages a 9:84:7 % ratio across the samples below.

The reasons behind the variation between the two Cromer Knoll regions is unclear, although it is likely due to lithological variations, with the upper section being a larger, more homogeneous sandstone body, whereas the lower section is more chaotically sand-and-shale interbedded. These interbeds are also likely to have caused the localised OWC, with large sections of shale existing above this small sand body likely trapping a small pocket of oil.

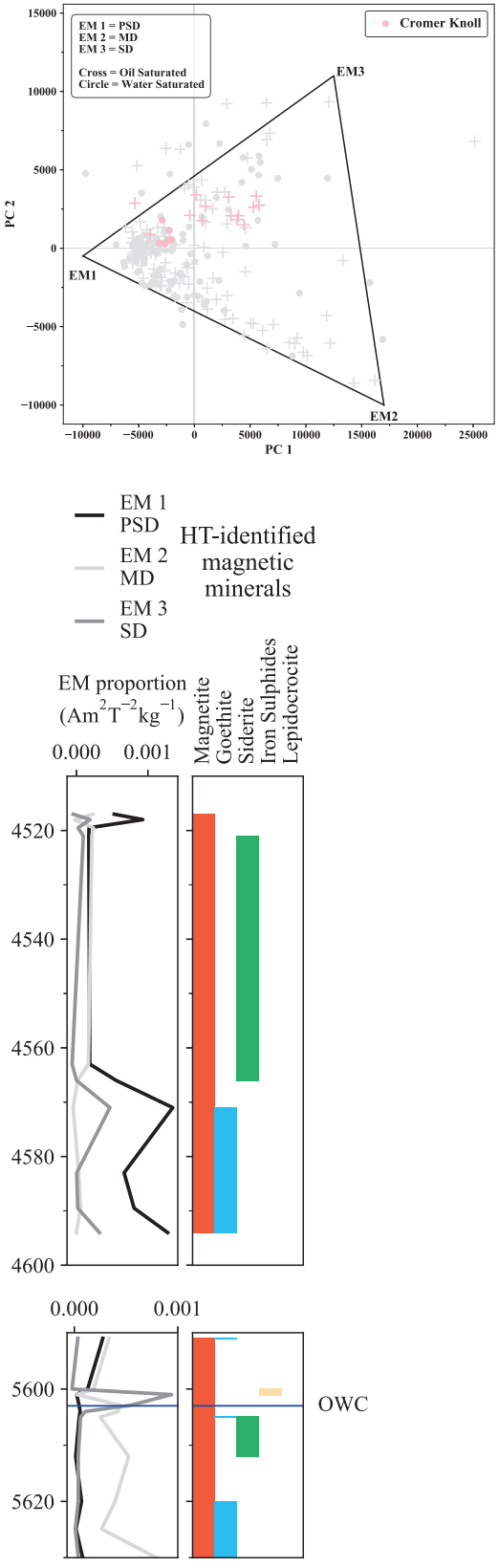


Figure 6.66: *PCA plot of samples, and depth plot showing EM contributions and mass-corrected proportions of the samples in Well 12/25-3.*

6.4.1.10 | Well 12/27-1

Well 12/27-1 follows the IMF pattern of magnetic assemblages, with a PSD dominance, and minor MD and SD components (Figure 6.67). However, the assemblage does vary compared to others nearby, such as Wells 12/27-2 and 12/21-4, in that it has an OWC zone, which sits between 3735.8 and 3745 ft, that shows two PSD increases below the beginning and end of the zone. Above the zone at 3735.6 ft, PSD:MD:SD ratios are 77:13:10 %, which then increases directly below the top of the zone at 3738 ft to 87:3:10 %. The PSD dominance then drops through the body of the contact zone, to an average PSD:MD:SD ratio of 68:8:24 %, before it increases again below the bottom of the zone at 3749 ft to 80:14:6 %. Akin to other wells, increased presence of PSD domain grains immediately below the contact likely relate to increased presence of magnetite as an alteration product of goethite. The marginal prominence of SD grains over MD grains in the oil-saturated section directly

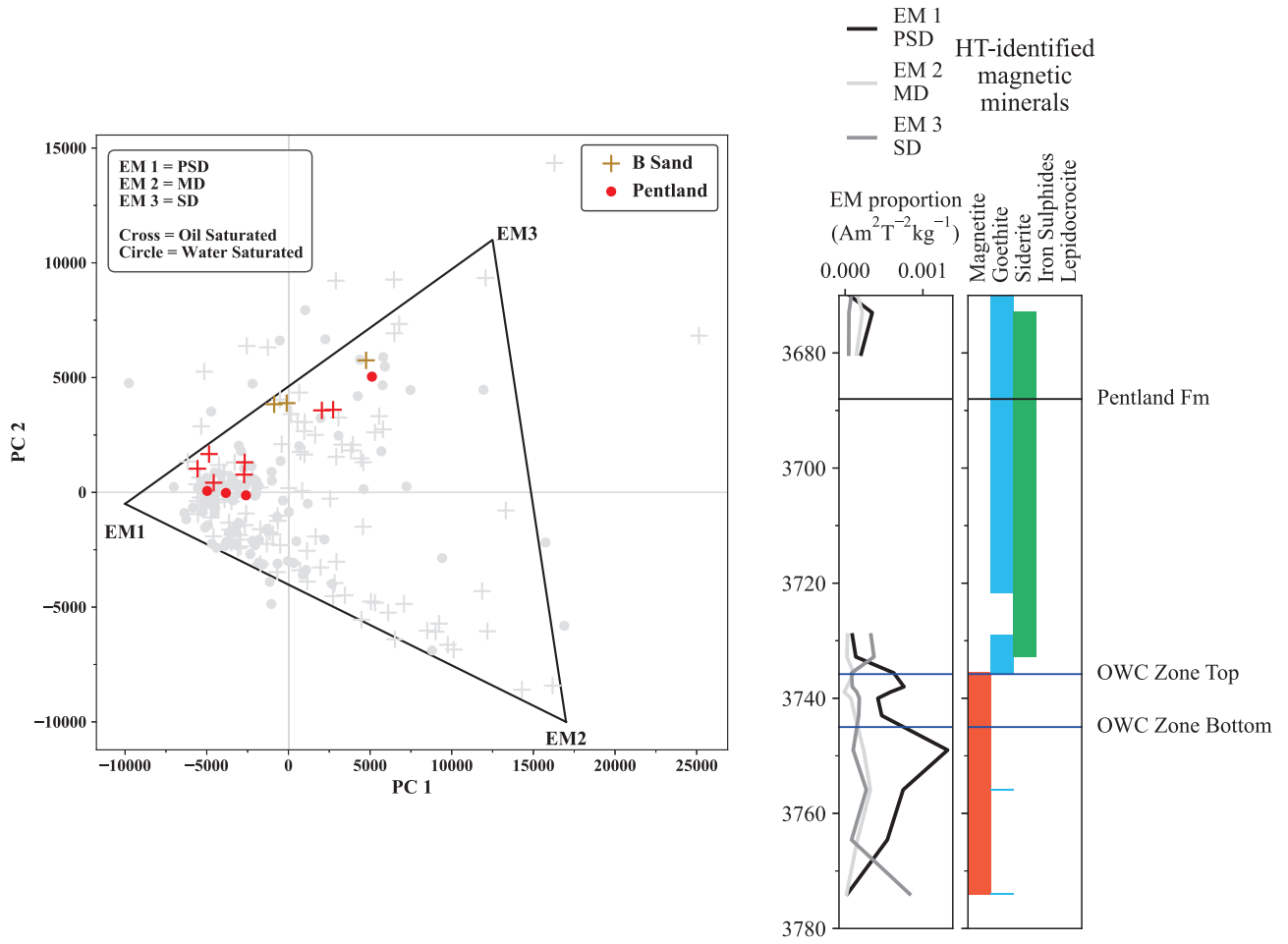


Figure 6.67: *PCA plot of samples, and depth plot showing EM contributions and mass-corrected proportions of the samples in Well 12/27-1.*

relate to the presence of siderite that is not seen within the water-saturated section which also sees no siderite.

6.4.1.11 | WELL 12/27-2

Well 12/27-2, whilst showing strong magnetic enhancement at the OWC (Section 6.3.12), shows consistent MD and SD contribution throughout the samples of the well, with the enhancement occurring through PSD domain grains (Figure 6.68). The lack of MD and SD variation significantly contrasts to the PSD component, which shows a massive influx at the OWC, linking to the increased magnetic enhancement over the contact. The assemblage has an average PSD:MD:SD ratio above the contact of 34:50:16 %, which contrasts to the post-contact assemblage ratio of 80:17:3 %. Whilst the oil column in the well shows unusually even domain distribution, the distinctly low magnetic signal is likely to be a cause, as most wells in the IMF have stronger signals accompanied by stronger PSD components. The heavy-PSD dominance in the assemblage, which links directly to the magnetic signal, is made even clearer at the contact, and this would suggest that PSD minerals are those most likely to have formed or accumulated directly below the OWC. The PSD accumulation would suggest, similar to other wells in the study area, this this well sees a connection between extensive goethite across the well being altered to magnetite around the OWC, causing the below-contact enhancement in PSD domain dominance.

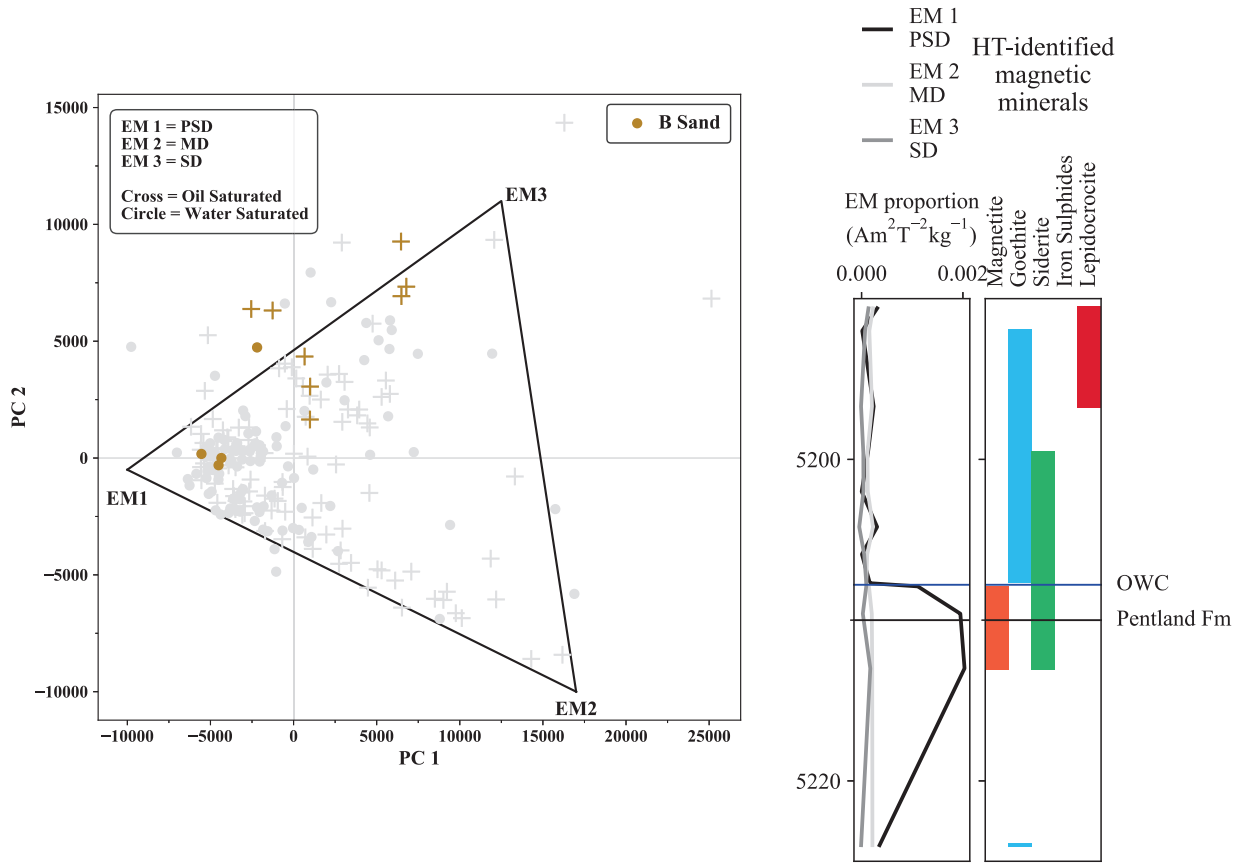


Figure 6.68: *PCA plot of samples, and depth plot showing EM contributions and mass-corrected proportions of the samples in Well 12/27-2.*

6.4.1.12 | WELL 12/29-1

The samples within the Well 12/29-1 differ to those in other study wells in the IMF as they are located within a localised sand body in the Heather Formation. The sand body has an OWC due to an apparent influx of hydrocarbons that were lithologically trapped into a small accumulation. The lithological difference is partially reflected in the domain assemblage, however generally, there is still a dominating PSD component, and smaller MD and SD components, reflected in an average PSD:MD:SD ratio of 74:16:10 % (Figure 6.69).

The most interesting difference between the assemblage in Well 12/29-1 and in other wells is the variation in components across the OWC. In 12/29-1, above the contact there is a sharp increase in both MD and SD grains at 6919 ft that corresponds to a relatively low PSD component, prior to an increase in PSD influence up to the contact at 6921.95 ft. The assemblage seen at 6919 ft is starkly different to anywhere else across the sampled area, with a PSD:MD:SD ratio of 37:35:28 %. Despite the PSD grains showing reduced influence in the samples above 6919 ft, up to 6903 ft, the relative percentage does not fluctuate massively, with a low of 70 % and a high of 86 %. This variation corresponds to the direct increase in magnetisation seen as depth increases up to the OWC, and would confirm that the PSD grains are providing a large majority of the magnetic component. Following the variation at 6919 ft, the other unique variation in this well is seen at the contact, where the PSD influence takes a clear drop from 2.77 $Am^2T^{-2}g^{-1}$ (85 %) above the contact at 6921.9 ft to 2.65 $Am^2T^{-2}g^{-1}$ (72 %) below the

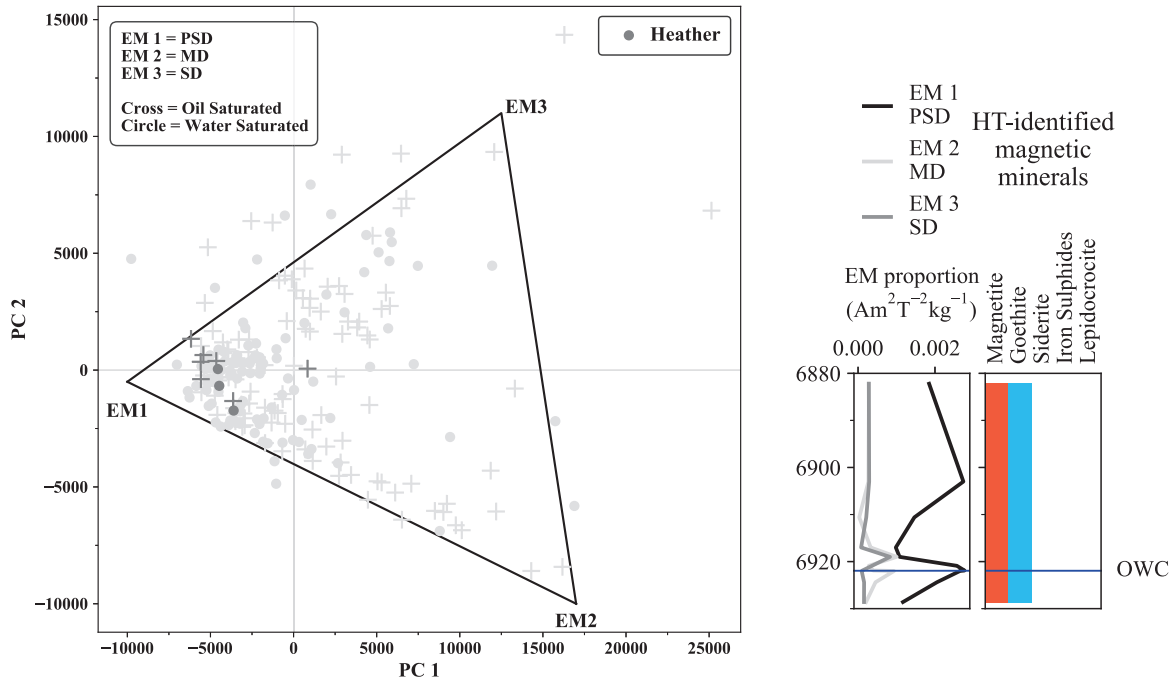


Figure 6.69: *PCA plot of samples, and depth plot showing EM contributions and mass-corrected proportions of the samples in Well 12/29-1.*

contact at 6922 ft. The decrease in PSD is opposed by an equal increase in MD influence across the same depths, from 0.39 $Am^2T^{-2}g^{-1}$ (12 %) above the contact to 0.94 $Am^2T^{-2}g^{-1}$ (25 %) below.

Whilst it is unclear what the cause of the MD and SD peak is at 6919 ft, the most likely scenario is lithological variation. The alternate is a shallower paleo-contact, with hydrocarbons locally filling, developing an assemblage showing an increased MD and decreased PSD variation similar to that of the present day OWC, then filling further with a secondary charge period. The main argument against this is the significant increase in SD grains seen at 6919 ft that is not reflected at the OWC, although there is a chance that a paleo-contact would have a differing assemblage to the present day contact. Interconnecting identified minerals, the sole presence of magnetite and goethite in the well suggest that these are the dominant contributors to the PSD grains.

6.4.1.13 | SUMMARY

The FORC PCA of the selected wells in the IMF show that all assemblages are dominated by PSD grains, with this most likely to be the pervasive magnetite, but with this magnetite also potentially derived from alteration of goethite (Table 6.6). Where enhancements at OWCs are seen, there are variations in which magnetic domain is enhanced, with no distinct observable patterns in the domain variations beyond the broadly consistent enhancement of PSD domain grains. In Wells 11/24-1, 12/27-1 and 12/27-2 PSD domain grains are enhanced with limited variation in the other domains, Well 11/24a-2 sees an MD enhancement above the contact but PSD below, 11/30a-8 sees a PSD and minor MD enhancement above the contact, 12/21-2 sees an SD enhancement above and PSD enhancement below, 12/25-3 sees a massive SD enhancement above the contact, with minor MD enhancement, and 12/29-1 sees an increase in PSD and SD above the contact and MD below.

Table 6.6: *Table summarising the FORC PCA results from the analysed wells across the IMF in this study alongside the magnetic minerals identified in each well, highlighting the end-members seen in both oil- and water-saturated samples, in order of presence from highest to lowest, where applicable.*

Region	Well	PCA domains		Identified minerals	
		Oil	Water	Oil	Water
NW IMF	**11/24-1**	PSD, SD, MD	PSD, SD, MD	Mag, Goe, Sid	Mag, Goe, Sid
	11/24a-2	PSD, MD, SD	PSD, MD, SD	Mag, Goe, FeS	Mag, Goe, Sid
Beatrice Field	**11/30-2**	PSD, MD, SD	PSD, MD, SD	Mag, Goe	Mag, Goe, Sid
	11/30-5	-	PSD, MD, SD	-	Goe, Mag, Lep
	11/30a-8	PSD, MD, SD	PSD, SD, MD	Sid, Goe, Mag, Lep	Sid, Goe, Mag, Lep, FeS
	11/30a-B10	PSD, SD, MD	PSD, MD, SD	Mag, Goe, Lep	Mag, Goe, Lep, FeS
Jacky & SE of Beatrice	**12/21-2**	PSD, SD, MD	PSD, SD, MD	Mag, Goe, Sid, Lep	Mag, Goe, Sid, Lep
	12/21-4	-	PSD, SD, MD	-	Mag, Goe, Lep, (Sid)
East IMF	**12/25-3**	PSD, SD, MD	MD, PSD, SD	Mag, Goe, Sid, FeS	Mag, Goe, Sid
SE IMF	**12/27-1**	PSD, SD, MD	PSD, MD, SD	Goe, Sid, (Mag)	Mag, Goe
	12/27-2	MD, PSD, SD	PSD, MD, SD	Goe, Sid, Lep	Sid, Mag, Goe
	12/29-1	PSD, SD, MD	PSD, MD, SD	Mag, Goe	Mag, Goe

The domains lack direct connectivity to the minerals present in the IMF, predominantly because goethite, siderite, lepidocrocite and pyrite do not contribute to FORC PCA, and with it being a pervasive mineral in the basin, this limits conclusions. However, there is consistent enhancement of PSD domain grains at the OWCs, which is connected to the increase in magnetic response seen in low temperature analysis, and is attributed to enhanced presence or magnetic response of magnetite, likely produced from alteration of goethite. Whilst it is difficult to determine if the three end-members individually represent one of the seven magnetic minerals identified (magnetite, hematite, goethite, siderite, lepidocrocite, iron sulphides and maghemite), because the minerals typically occur in a variety of domain states, broad interconnections are possible. PSD-dominated samples typically contain goethite and magnetite, whilst MD-dominated samples are strongly associated with iron sulphides, evidenced most clearly by Well 11/24a-2, and SD-dominated samples most readily contain one or multiple of siderite, goethite and lepidocrocite. However, due to the minerals other than magnetite lacking contributions to FORCs, it is not possible to directly connect the domain states and minerals.

6.5 | Discussion

6.5.1 | Magnetic mineral assemblages across the IMF

Magnetic mineral presence varies across the IMF, however the variation is primarily seen in mineral abundance rather than presence or absence, with the majority of magnetic minerals seen basin-wide. Due to magnetite's prevalence across the samples in the basin, for the purpose of clarity, focus is centred on the other magnetic minerals identified through the various analytical techniques and to what extent they influence the magnetic behaviours across the IMF. Beyond magnetite, goethite has widespread presence in nearly all samples in all wells (Figure 6.70; Table 6.7). In comparison, siderite and lepidocrocite are

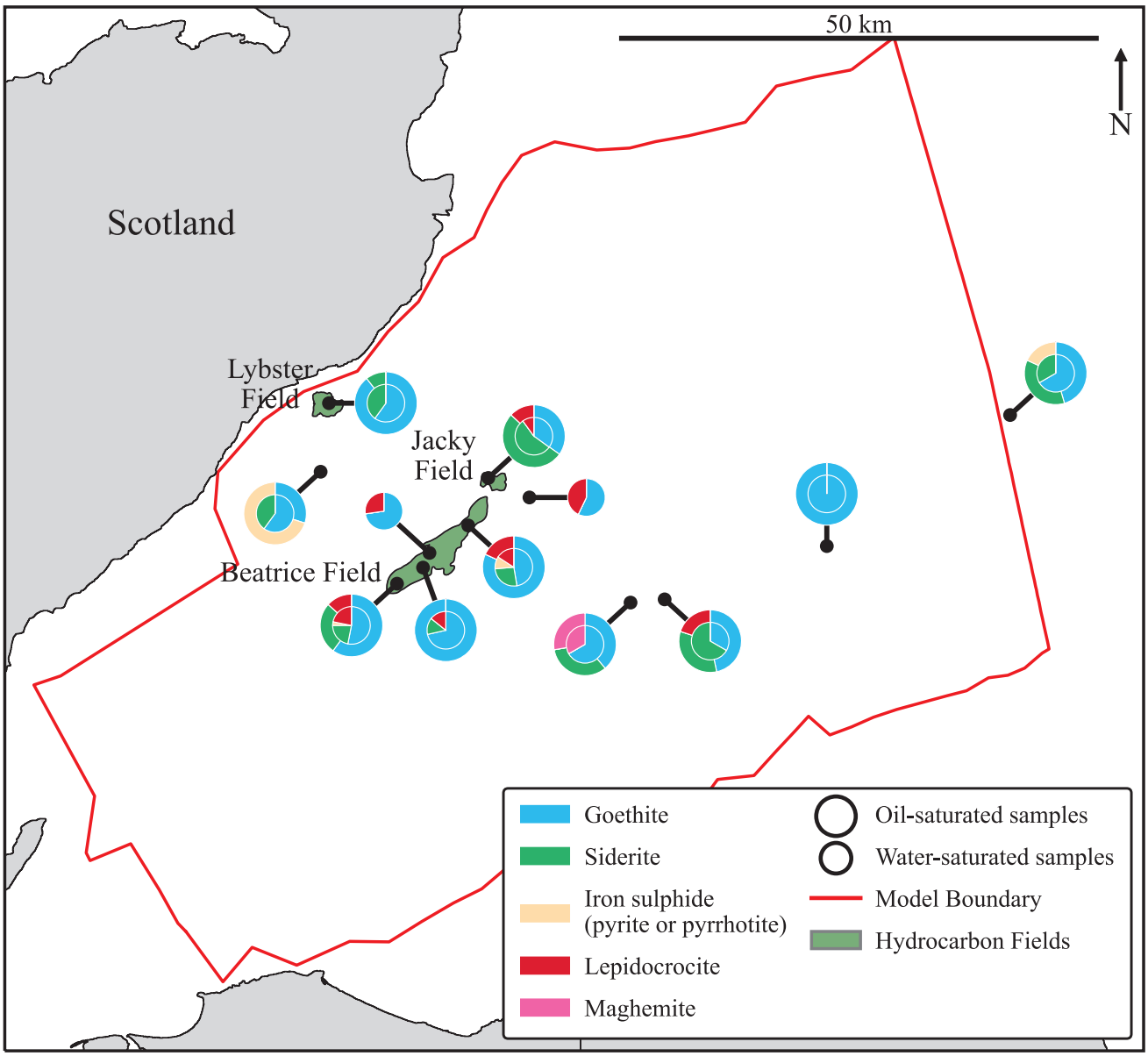


Figure 6.70: *Map showing the IMF, with pie charts from each well magnetically analysed showing the relative presence of each magnetic mineral identified within this study, ignoring the ubiquitous magnetite, split into oil- and water-saturated samples. Values are relative percentages of samples from each well and saturating fluid that show evidence of the respective minerals, to remove the bias caused by varying sample numbers.*

Table 6.7: *Table showing the wells in the IMF that were magnetically analysed in this study, highlighting the total number of samples, and the number of samples within each saturating fluid containing the relevant magnetic mineral, identified through high temperature susceptibility curves. Mag = magnetite, Goe = goethite, Sid = siderite, Lep = lepidocrocite, FeS = iron sulphides, grouping pyrite and pyrrhotite, and Mgh = maghemite.*

Well	Saturating Fluid	Total Samples	Number of occurrences					
			Mag	Goe	Sid	FeS	Lep	Mgh
11/24-1	Oil	20	20	17	2	0	0	0
	Water	8	6	6	4	0	0	0
11/24a-2	Oil	11	11	3	0	7	0	0
	Water	5	5	3	2	0	0	0
11/30-2	Oil	5	4	3	0	0	0	0
	Water	12	12	5	1	0	1	0
11/30-5	Oil	n/a	-	-	-	-	-	-
	Water	8	2	8	0	0	3	0
11/30a-8	Oil	10	7	9	4	0	2	0
	Water	23	18	17	7	1	7	0
11/30a-B10	Oil	12	12	9	0	0	2	0
	Water	18	16	9	5	2	3	0
12/21-2	Oil	16	16	8	12	0	3	0
	Water	16	15	7	11	0	2	0
12/21-4	Oil	n/a	-	-	-	-	-	-
	Water	8	11	8	0	0	6	0
12/25-3	Oil	14	14	5	4	2	0	0
	Water	6	6	4	2	0	0	0
12/27-1	Oil	13	7	7	6	0	0	5
	Water	4	4	2	0	0	0	1
12/27-2	Oil	8	0	7	5	0	3	0
	Water	4	3	1	2	0	0	0
12/29-1	Oil	7	7	6	0	0	0	0
	Water	3	3	3	0	0	0	0

present across the basin, but in significantly smaller quantities than either goethite or magnetite, and iron sulphides, both pyrite and pyrrhotite, are present in limited numbers, most extensively within Well 11/24a-2. There is one well, 12/27-1, that indicates the presence of maghemite, and solely around the

Table 6.8: *Table the shallowest and deepest presence of each non-magnetite magnetic mineral seen within the IMF in this study*

Magnetic Mineral		Shallowest presence, ft (& m) & Formation	Deepest presence, ft (& m) & Formation
Goethite		3656.0 (1114.4) Mid Shale	7323.2 (2232.1) I Sand
Siderite		3662.6 (1116.4) Mid Shale	11148.7 (3398.1) Devonian
FeS	Pyrrhotite	4917.7 (1498.9) A Sand	6122.9 (1866.3) A Sand
	Pyrite	5600.0 (1706.9) Wick Sand	6122.9 (1866.3) A Sand
Lepidocrocite		5190.6 (1582.1) B Sand	7323.2 (2232.1) I Sand
Maghemite		3736.0 (1138.7) Pentland	3749.0 (1142.7) Pentland

well's OWC zone (Figure 6.70; Table 6.7). There are little to no clear patterns seen within the magnetic mineral distribution across the IMF, with goethite present in abundance in all wells, siderite present in nine of the twelve wells, in a mix of both oil- and water-saturated samples and iron sulphides present in a wide variety of scenarios (Figure 6.70; Table 6.7). The only differential is lepidocrocite, which solely occurs in the samples of the central IMF, across the Beatrice and Jacky Fields region, although there is also lepidocrocite in three samples from the oil-saturated samples in Well 12/27-2.

The relative abundance of minerals in the two saturating fluids varies across the basin, with goethite being the dominant mineral in eight out of ten oil-saturated sections, with the exceptions being in Wells 11/24a-2 and 12/21-2 (Figure 6.70; Table 6.7). Comparatively, siderite is a minor presence in the oil-saturated sections of five wells, and the dominant magnetic mineral in another. The only oil-saturated section to not be dominated by one of goethite or siderite is Well 11/24a-2, which contains a very high proportion of iron sulphides, mostly pyrite but with some pyrrhotite or greigite formed from alteration of other minerals. In comparison, beyond the wells within Beatrice Field, which have goethite dominated water-saturated samples, there is a higher proportion of siderite in the water-saturated sections of wells than in their related oil-saturated sections, most clearly seen in Wells 12/21-2 and 12/27-2, but Wells 11/24-1, 11/24a-2 and 12/25-3 all also show a relatively greater siderite presence in the water-saturated sections when compared to Wells 11/30-2, 11/30a-8 and 11/30a-B10 in the Beatrice Field.

The magnetic minerals occur at varying depths across the basin, with some forming in very constrained depths, and others being present across the entire depth sequence of the IMF (Table 6.8). The most tightly constrained mineral is maghemite, with its sole presence occurring in six samples around 3740 ft (1140 m) in Well 12/27-1. In comparison, goethite and siderite are present throughout large swathes of the basin, from 3656 ft (1114 m) to 7323.2 ft (2232 m) and 11148.7 ft (3398 m), respectively. Interestingly, beyond magnetite, siderite is the only magnetic mineral seen within samples from

the Devonian flagstones. In comparison, samples from the Pentland Formation show all magnetic minerals, and the KCF show evidence for magnetite, goethite and siderite. The shallowest presence of lepidocrocite is deceptive, as it is defined by three samples within Well 12/27-2 at 5190 ft (1582 m), however beyond these, the next presence is at 6752.3 ft (2058 m). The anomalous localised presence of lepidocrocite in Well 12/27-2, adjacent to the maghemite-bearing Well 12/27-1, could be a result of an alteration sequence between the two, as dehydration and dehydroxylation of lepidocrocite results in the formation of maghemite (Cheng *et al.*, 2019; Gendler *et al.*, 2005; Guyodo *et al.*, 2016; Song and Boily, 2016). However, this does not directly give reason as to why lepidocrocite is present in this region, approximately 1500 ft (500 m) shallower than the mineral's presence across the rest of the basin, although it could be an indicator of biodegradation.

6.5.2 | Magnetic mineral assemblages at oil-water contacts

Analysis of the magnetisation across the wells in this study identifies two clear differences in the magnetic responses around the oil-water contacts (OWCs). Some observations show that magnetisation is enhanced at the contact, in agreement with Badejo (2019) and Badejo *et al.* (2021b,c), however this study pinpoints further developments in this relationship. Beyond the initial identification of enhancements, this study discovers two different enhancements around the contacts. One set of wells experience magnetic enhancement above the contact, e.g. Well 12/29-1, and another set of wells experience magnetic enhancement below the contact, e.g. Wells 11/24-1 and 12/27-1 (Figure 6.71).

Of the twelve wells that were discussed in this study, ten contain OWCs, with two of the wells in Beatrice Field containing dual OWCs, resulting in twelve contacts being analysed (Figures 6.71 & 6.72; Table 6.9). Of these twelve contacts, three OWCs see increased magnetisation above the contact, and seven have increased magnetisation below the contact, plus there are two contacts, in Well 11/30a-8 and the upper OWC from Well 11/30a-B10, which show very subtle below-contact enhancement. The OWCs with enhanced magnetisation above the contact come from wells 11/24a-2, 12/25-3 and 12/29-1 and are relatively clear and well defined. In comparison, the OWCs with enhanced magnetisation below the contact come from wells 11/24-1, 11/30a-8, 11/30a-B10, 12/21-2, 12/27-1 and 12/27-2. Wells 11/24-1, 12/27-1 and 12/27-2 offer the best examples, whilst Well 11/30-2 is less conclusive due to the sampling constraints placed upon it. The strongest example, Well 11/24-1 shows a clear, uninterrupted sharp increase in magnetisation within the first 2 feet of the water column at the top of the OWC zone, which then proceeds to return back to baseline (Figure 6.71).

The two types of enhancements show evidence of goethite and siderite with strong consistency (Figures 6.71 & 6.72), however, only the wells showing above-contact enhancement, Wells 11/24a-2 and 12/25-3, have distinct and consistent presence of iron sulphides, alongside a small section of Well 11/30a-8, which has inconclusive OWC enhancement (Figure 6.71; Table 6.9). In contrast, there is no evidence of iron sulphides in any of the below-enhancement wells. Furthermore, the wells showing no evidence of iron sulphides show increased influence of magnetite (Fe_3O_4) around the OWC, interconnecting with decreasing influence of goethite, suggesting that goethite is unstable around the contact and alters to magnetite. As such, is it possible to broadly classify the two series of wells (Table 6.9):

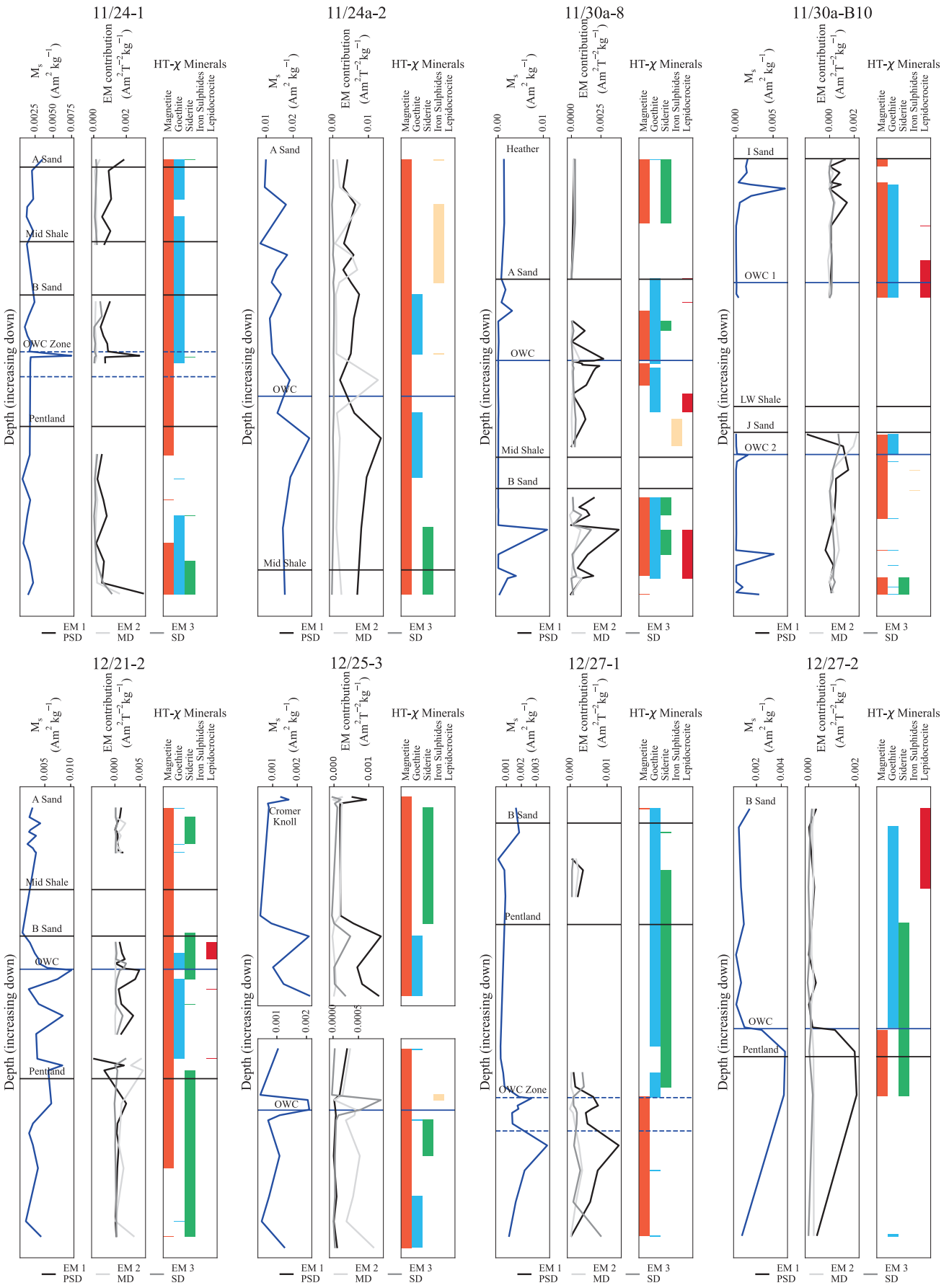


Figure 6.71: *Series of plots showing the room temperature M_s values, FORC PCA endmember contributions, and the high temperature susceptibility-identified minerals present in samples across wells in the IMF that both bear OWCs (highlighted) and show mineralogical variation. Note that the depth (Y axis) are not consistent between wells.*

- Goethite-rich wells – these wells show no evidence of iron sulphides and often show magnetite-derived enhancement at the OWC, with a below-OWC enhancement.
- Iron sulphide-rich wells – these wells show iron sulphide presence and are more goethite-poor, but still show presence of it and siderite, and have above-OWC enhancement.

Table 6.9: *Table summarising the OWC locations and depths (in MD, bar 11/30a-B10 which is TVD), magnetic responses and magnetic minerals present the wells studied in the IMF, ignoring the pervasive magnetite, separated by saturating fluid, and the classification of each OWC-bearing well, based on its characteristics. Goe = goethite, FeS = iron sulphides, Lep = lepidocrocite, Sid = siderite, Mgh = maghemite.*

Well	OWC-bearing Formation (& Depth)	Magnetic enhancement in relation to OWC	OWC PCA enhan-cement	HT-χ identified minerals		LT-identified minerals		Classi-fication
				Water	Oil	Water		
11/24-1	B Sand (4948 ft)	Below	PSD	Goe	Goe, Sid	Goe	Goe, Sid	Goe-rich
11/24a-2	A Sand (6130 ft)	Above	MD, PSD	FeS, Goe	Goe, Sid	n/a		FeS-rich
11/30-2	A Sand (6385 ft) H Sand (6879 ft)	Below Below	PSD	Goe	Goe, Sid, Lep	Goe	Goe	Goe-rich
11/30a-8	A Sand (6925 ft)	?Below	PSD, MD	Goe, Sid, Lep	Goe, Sid, Lep, FeS	Goe	Goe, Sid	?Goe-rich
11/30a-B10	I Sand (6643 ft) J Sand (6753 ft)	?Below Below	unclear	Goe, Lep	Goe, Sid, Lep, FeS	Goe, Sid	Goe, Sid	?Goe-rich
12/21-2	B Sand (7118 ft)	Below	PSD, SD	Sid, Goe, Lep	Sid, Goe, Lep	Goe	Sid	Goe-rich
12/25-3	Cromer Knoll (5603 ft)	Above	SD, MD	Goe, Sid	Goe, Sid, FeS	n/a		FeS-rich
12/27-1	Pentland (3735.8 ft)	Below	PSD	Goe, Sid, Mgh	Goe, Mgh	n/a		Goe-rich
12/27-2	B Sand (5207.8 ft)	Below	PSD	Goe, Sid, Lep	Sid, Goe	n/a		Goe-rich
12/29-1	Heather (6921.95 ft)	Above	PSD, (MD)	Goe	Goe	n/a		unclear

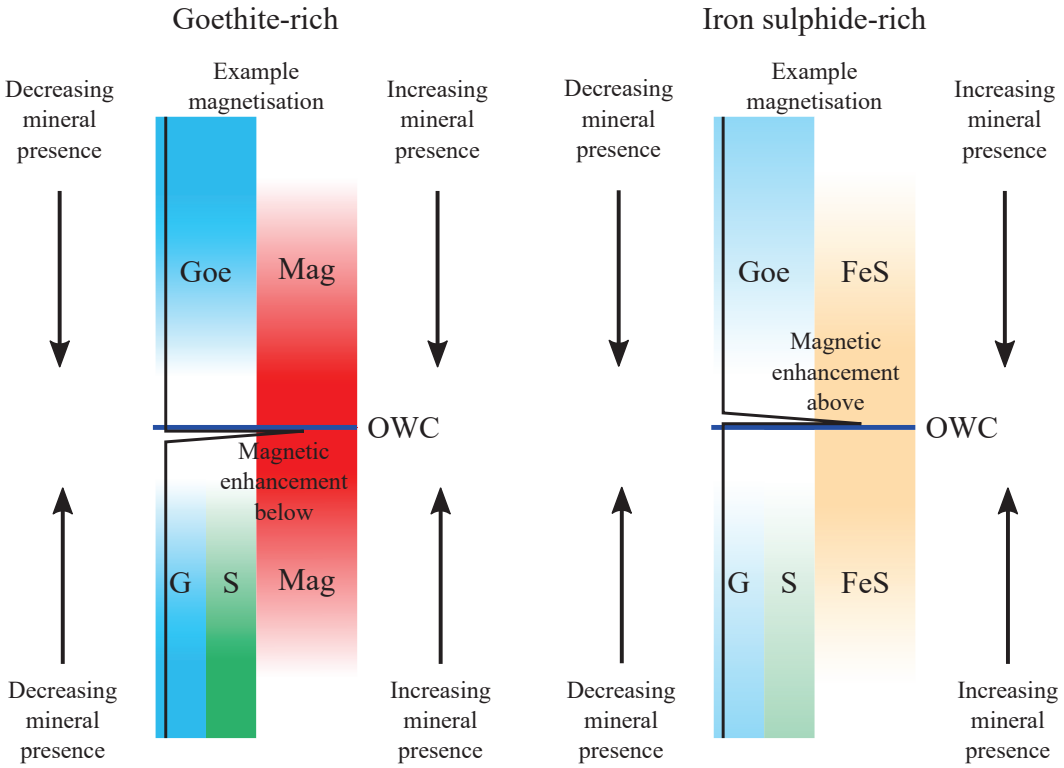


Figure 6.72: *Schematic showing how magnetic minerals interact around oil-water contacts in the IMF. Wells dominated by goethite (Goe, G) see decreasing goethite signals towards the OWC in tandem with increasing magnetite (Mag) presence towards the contact, with siderite (S) present in wells that experience extensive vertical migration of the hydrocarbons. Wells with low concentrations of goethite see this same pattern, but with increasing iron sulphide (FeS)-presence towards the OWC.*

Through this classification, the wells with OWCs can be separated and Wells 11/24-1, 11/30-2, 11/30a-B10, 12/21-2, 12/27-1 and 12/27-2 are all goethite-rich wells, whilst Wells 11/24a-2 and 12/25-3 are iron sulphide-rich wells, with Wells 11/30a-8 and 12/29-1 being unclassifiable as they show inconclusive OWC enhancement. This classification directly correlates to the location of the enhancements around the OWCs, with the goethite-rich wells being those that have below-contact enhancement, and the iron sulphide-rich wells being those that have above-contact enhancement. The iron sulphide-rich wells directly correlate to the behaviour seen in the Central North Sea study by Badejo *et al.* (2021c), who identify above-contact enhancement alongside high iron sulphide presence. This suggests that certain magnetic minerals cause certain magnetic enhancements, regardless of location. Furthermore, the lack of goethite identified in the Central North Sea study of Badejo *et al.* (2021c) suggests that magnetic mineral assemblages also do vary between locations. This raises the potential for environments impacted by petroleum systems to form similar magnetic mineral assemblages in similar conditions, regardless of location, but also for differing conditions to form alternate magnetic mineral assemblages. As such, there is the possibility that petroleum systems and their components could be identified through the magnetic minerals seen in the system.

The magnetic signals created by the samples also show broad trends that partially align with the well classification. Five wells, Wells 11/24-1, 11/30a-8, 11/30a-B10, 12/27-2 and 12/29-1, three of which are below-contact enhanced goethite-rich wells and the other two are unclassifiable, see broadly decreasing magnetic signals as the samples become closer to the OWC, with the signals increasing

into both oil- and water-saturated regions. In contrast, the other five wells, Wells 11/24a-2, 11/30-2, 12/21-2, 12/25-3 and 12/27-1, see the opposite trend, where magnetic signals broadly increase towards the OWC from both saturating fluids, with two of these being the two iron sulphide-rich wells with above-contact enhancement. Consequently, there is a rough correlation between magnetic enhancement and magnetic mineral presence and the trends of the magnetic signals, with the localised increase in magnetisation and decrease in coercivity around the OWCs suggesting that the the goethite-rich wells experience accumulation of a relatively large abundance of small magnetite grains (Figure 6.72).

The alteration of goethite to magnetite is complex, as typically goethite dehydroxylates directly into hematite (Cudennec and Lecerf, 2005; Till and Nowaczyk, 2018), however other studies have shown that dehydroxylation of goethite can also form magnetite (Goss, 1987; Ibrahim *et al.*, 1994; Lima-de Faria, 1967; Lowrie and Heller, 1982), whilst other work has shown that goethite can alter to magnetite in the presence of organic matter (Schwertmann and Fechter, 1984), as well as through reductive diagenetic alteration (Abrajevitch *et al.*, 2009; Peter D. Rude, 1989). As such, it is likely that the alteration of the pervasive goethite identified through the IMF could alter to magnetically stronger, ferromagnetic magnetite immediately below the redox boundary caused by the OWC. Furthermore, it could be possible for the magnetite to form within the water column during the migration of hydrocarbons, thus providing the required organic matter, and then being transported within the migration hydrocarbons before accumulating at the density boundary caused by the two fluids. In comparison, iron sulphides, predominantly pyrite, form and are stable, in reducing environments, such as those formed by hydrocarbon accumulations (Machel and Burton, 1991a,b; Machel, 1995), thus the magnetic enhancement seen in iron sulphide-rich wells being situated above the OWC is a result of accumulation and formation of stable minerals above the redox boundary.

Whilst FORC PCA analysis shows a limited relationship between magnetic minerals and grain domains, due to the majority of magnetic minerals in the system not contributing to FORCs, there are connections between the domains and the well classification seen in this study. The increase in magnetite presence at the OWC in the goethite-rich wells is reciprocated in the FORC PCA through the enhancement of PSD-domain grains, most clearly seen in the increase in PSD contributions in Wells 11/24-1 and 12/27-2 (Figure 6.71). In comparison, the iron sulphide-rich wells see enhancements at contacts of both MD (Well 11/24a-2) and SD (Well 12/25-3) domains (Figure 6.71). This further supports the classification of the wells and the behaviours seen within them at the OWCs, through increased PSD magnetite presence in goethite-rich wells, and MD or SD iron sulphide increases in the iron sulphide-rich wells.

6.5.3 | Mineral sources

Magnetite is the most prevalent magnetic mineral in the IMF system, despite often occurring in low levels, as it is the most dominant magnetic mineral in the vast majority of rocks on Earth (Stacey and Banerjee, 1974). Magnetite forms in a variety of conditions due to the extensive commonality of its two components, iron and oxygen, and remains in many environments due to its stable nature (Dunlop and Özdemir, 1997). Hematite is also widely common within geological environments due to its common formation occurring through the oxidation of numerous other minerals (Dunlop and Özdemir, 1997;

Evans and Heller, 2003; Kilgore and Elmore, 1989). Hematite also forms through heating of magnetite, thus is commonly the end-member of many magnetic mineral alteration chains (Dunlop and Özdemir, 1997). Consequently, the ubiquitous nature of both magnetite and hematite makes constraining their influence in the IMF difficult, however, there is a clear connection between the increased presence of magnetite around OWCs as an alteration product of goethite.

Iron hydroxides, present in this study as goethite and lepidocrocite, form through the oxidation of Fe^{2+}, commonly via the alteration of other magnetic minerals (Dunlop and Özdemir, 1997). There is also widespread evidence that iron hydroxides form within lacustrine deposits (Fortin *et al.*, 1993; van der Zee *et al.*, 2003) and red beds (Berner, 1969; Gendler *et al.*, 2005; Weibel, 1999). The presence of iron hydroxides in lacustrine environments and red beds originate through precipitation of reductively dissolved magnetic minerals in anaerobic sediments and the alteration of detrital magnetite, respectively (Berner, 1969; Fortin *et al.*, 1993; Gendler *et al.*, 2005; Weibel, 1999; van der Zee *et al.*, 2003). Furthermore, there is evidence that varying the volume of carbon, either in the form of carbon dioxide or carbonate, varies the ratios between lepidocrocite and goethite (Carlson and Schwertmann, 1990). Kars *et al.* (2014) shows that goethite forms in environments where burial temperatures are below 80 °C, which is typically peak hydrocarbon-generation temperature, further supporting the connection between goethite and hydrocarbons. It has been shown that lepidocrocite alters to maghemite through topotactic thermal dehydration as well as dehydroxylation (Cudennec and Lecerf, 2005; Gendler *et al.*, 2005). This alteration could explain the presence of maghemite within the OWC zone of Well 12/27-1, as there is evidence of lepidocrocite in this region in the neighbouring Well 12/27-2, potentially due to the development of a reducing environment caused by the present of hydrocarbons within the zone.

Siderite requires dissolved iron Fe^{2+} and carbonate ions ($CO_3{}^2$) to react in anoxic, reducing conditions, without the presence of hydrogen sulphides, to form (Bachan and Kump, 2015; Berner, 1981; Lin *et al.*, 2020). Consequently, the reducing conditions created in the presence of hydrocarbons provide ideal conditions to allow siderite to form (Emmerton, 2012; Machel and Burton, 1991a; Machel, 1995). Abdulkarim *et al.* (2022a) suggest that siderite forms in petroleum systems through vertical migration, connecting the presence of siderite in the IMF to potential charging mechanisms investigated within this study's petroleum systems modelling. Through this method, it can be inferred that all of the known hydrocarbon accumulations within the IMF, Beatrice, Lybster and Jacky Fields, could be charged to some degree by vertical migration, with wells in these fields showing evidence of siderite (Wells 11/24-1, 11/30-2, 11/30a-8, 11/30a-B10, 12/21-2). In addition, it can be hypothesised that vertical hydrocarbon migration has occurred in other regions of the IMF where siderite is present, for example Wells 11/24a-2, 12/25-3 and 12/27-1.

The formation of multiple iron sulphide phases, e.g. pyrite and pyrrhotite, is very common across numerous environments, as they are both stable and require only the addition of sulphur into a reducing, anoxic system to form (Berner, 1984; Canfield and Berner, 1987; Horng and Roberts, 2006; Sagnotti, 2007; Thiel *et al.*, 2019; Volk *et al.*, 2016). Sedimentary pyrite forms during early diagenesis, and the amount formed is related to the amount of available sulphur not iron, with the most common source being organic matter (Berner, 1984). In addition, pyrite can be formed by magnetotactic bacteria during biodegradation (Thiel *et al.*, 2019), however, the depths of most samples within the IMF limit biodegra-

dation potential, especially through the basin centre, which is supported by the geochemical analysis of Peters *et al.* (1989). In contrast, some samples and wells, e.g. Well 11/24-1 in Lybster Field, are shallow enough and of low enough temperature to aid the occurrence of biodegradation, although there is limited variation in the magnetic mineral assemblages to support this. In comparison, pyrrhotite forms slowly at temperatures below 180 °C, suggesting that, despite its typical formation in early diagenesis of anoxic sediments, akin to pyrite, it is unlikely to be prevalent (Horng and Roberts, 2006). In connection to hydrocarbon presence, Aubourg *et al.* (2008), Aubourg and Pozzi (2010) and Aubourg *et al.* (2012) show how pyrrhotite and iron sulphides are prevalent at low temperatures (below 85 °C), but when heated beyond this to around 250 °C, magnetite becomes more dominant in replacement of the iron sulphides. This variation in magnetic mineral formation as a function of temperature could be a cause of the differing well behaviour.

Geochemical analyses of the hydrocarbons of the IMF (Peters *et al.*, 1989) suggest that the Devonian and Pentland hydrocarbons have low sulphur content (maximum 0.62 wt%), as does the mixed oil itself (0.11 wt%). In contrast, Kimmeridge Clay Black Shales have a much higher sulphur content of 2.59 wt% (Peters *et al.*, 1989). This variance suggests that the Devonian and Pentland organic matters are not main sulphur contributors, but that the Black Shales could be. With literature suggesting that there is no Kimmeridgian influence on the hydrocarbon accumulations (Linsley *et al.*, 1980; Peters *et al.*, 1989; Stevens, 1991), the extensive presence of iron sulphides in some wells, most clearly Well 11/24a-2, means that basin and petroleum systems modelling is required to refine and clarify the hydrocarbon mixing and influence of Kimmeridge Clay Black Shales.

Beyond the possible Kimmeridge Clay contributions to iron sulphide formation, hydrocarbons produce anoxic, reducing environments, thus is is possible that minor presence of sulphur in the IMF could be a result of preferentially-formed iron sulphides when hydrocarbons entered the area. In contrast, the relatively strong presence of iron sulphides in Well 12/25-3 and the dominating presence of iron sulphides in Well 11/24a-2 is different (Figure 6.71). The Cretaceous-age Cromer Knoll sediments that bear the iron sulphides in 12/25-3 are stratigraphically shallower than the Kimmeridge Clay, thus any mature Black Shale hydrocarbons could have migrated upwards into the Cromer Knoll sediments, and aided the increased iron sulphide presence observed in this well. Well 11/24a-2 is complex, as the samples are taken from the reservoir sequence that is stratigraphically deeper than the Kimmeridge Clay Black Shales, however the well is located on the hanging wall side of the Great Glen Fault, so the reservoir sequence is at a shallower depth than the Black Shales. I hypothesise that the Great Glen Sub-Basin matured some Kimmeridge Clay Black Shale organic matter, and these hydrocarbons migrated up-fault and across the Great Glen Fault into the Well 11/24a-2 region, bringing an influx of sulphur as well as producing an anoxic, reducing environment; however, this must be tested in the BPSM.

6.5.4 | COMPARISONS TO PUBLISHED WORK

This study has shown the presence of numerous magnetic minerals that both correlate and contrast with other published studies. Abdulkarim *et al.* (2022a,b,c) identifies not only pervasive magnetite, alongside pyrrhotite and siderite, and the potential of vivianite, lepidocrocite, and other iron sulphides

including greigite. The extensive presence of iron sulphides in the Central North Sea (Abdulkarim *et al.*, 2022a,b,c; Badejo *et al.*, 2021a,b,c) partially correlates with the iron sulphides identified in the IMF, however, whilst the iron sulphides are present in the IMF, they are more minor than in the Central North Sea studies. Furthermore, neither Abdulkarim *et al.* (2022a,b,c) nor Badejo *et al.* (2021a,b,c) identify a decrease in iron hydroxide presence in correlation to increased iron sulphide presence. In contrast, the identification of siderite, and its proxy for vertical migration (Abdulkarim *et al.*, 2022a), directly correlates with the magnetic mineral assemblages across the IMF. However, the widespread presence of goethite in the IMF is not seen in the Central North Sea studies (Abdulkarim *et al.*, 2022a,b,c; Badejo *et al.*, 2021a,b,c), thus there is a clear difference between the magnetic mineral assemblages across the North Sea, potentially linked to differing source rock and petroleum system components.

Abubakar (2015) and Abubakar *et al.* (2020) identified iron sulphides, in association with Type II kerogen, deep marine-deposited source rocks in the Wessex Basin, UK. The magnetic minerals are identified in both immature and pyrolysed kerogen samples, thus indicating that the magnetic minerals are directly associated with the source rocks (Abubakar, 2015; Abubakar *et al.*, 2020). The identification of minor iron sulphides in the IMF and the presence of Kimmeridge Clay within it, including the potential influence through hydrocarbon charging, directly correlating to the work of Abubakar (2015) and Abubakar *et al.* (2020), however, the dominance of goethite in the IMF is a clear departure. In comparison, Emmerton *et al.* (2012) identify extensive siderite across Wessex Basin samples, alongside hematite and magnetite, which aligns with the IMF results.

The magnetic minerals and behaviours seen in the co-sourced system of De la Rosa *et al.* (2021), align with the work of this study, combining the presence of iron sulphides and iron hydroxides. Aldana *et al.* (2011) identify high hydrogen sulphide presence and the degradation of hydrocarbons that both directly correlate to greigite presence, although there is limited evidence of greigite presence in the IMF magnetic mineral assemblage Peters *et al.* (1989). Costanzo-Álvarez *et al.* (2019) also identify two diagenetic stages on the kerogens of the Vaca Muerta Shale in the Neuquén Basin, through which previously formed magnetite, titanomagnetite and pyrrhotite dissolve during the first stage, and the second stage sees the replacement of pyrite with pyrrhotite. This diagenetic alteration and formation of iron sulphides in the presence of sulphide-rich kerogens is a further connection between the magnetic minerals and certain source rocks.

6.5.5 | IMPLICATIONS ON THE PETROLEUM SYSTEM

Interconnections can be made between the magnetic mineral analysis conducted in this chapter and the petroleum system of the IMF. Firstly, and most importantly, the dominance of the iron hydroxides goethite and lepidocrocite in the IMF is a departure from the work of Abdulkarim *et al.* (2022a,b,c); Badejo (2019); Badejo *et al.* (2021a,b,c), which show more dominance of iron sulphides and iron carbonates in the Cenozoic systems of the Central North Sea. These petroleum systems were charged by the Type II kerogen, deep marine, Kimmeridge Clay, akin to the Kimmeridgian Black Shales seen within the IMF. Consequently, the presence of completely different magnetic mineral assemblages can initially suggest that the system within the IMF is not charged by the Kimmeridge Clay Black Shales,

which supports the geochemical analysis carried out on the basin by Peters *et al.* (1989, 1998). Whilst Abdulkarim *et al.* (2022b) note some indications of lepidocrocite presence, due to the mineral's readiness to form through alteration of numerous other magnetic minerals, and the relatively low presence seen in the IMF, this is not a strong correlation between the two systems.

Secondly, the dominance of iron hydroxides, which form within both lacustrine environments and iron-rich red beds (Berner, 1969; Fortin *et al.*, 1993; Gendler *et al.*, 2005; Weibel, 1999; van der Zee *et al.*, 2003), indicates that these iron hydroxides could well be produced by the Devonian Fish Beds, a Type I, lacustrine-formed hydrocarbon source rock that is thought to be the dominant source rock of the IMF (Peters *et al.*, 1989). Providing the basin and petroleum systems modelling correlates these findings (Chapter 7), it can be hypothesised that goethite forms in association with Type I source rocks, and thus could be used as a proxy for hydrocarbon source rock identification.

The work of Abdulkarim *et al.* (2022a) shows that siderite can be used as a proxy for vertical migration within a petroleum system, a connection established by Badejo *et al.* (2021a,b) and examined further in Abdulkarim *et al.* (2022b). The magnetic mineral assemblages of the IMF show broad presence of siderite, including within known accumulations, thus requires investigation within the basin and petroleum systems modelling to understand to what extent vertical migration has charged the petroleum system of the IMF. The relatively low presence of siderite in Beatrice and Lybster Fields compared to Jacky Field suggests that Jacky Field was charged through more vertical migration than the other two fields, with this pattern matched in the south eastern wells 12/27-1 and 12/27-2, that both show higher siderite presence.

The petroleum system of the Falcon Basin, NW Venezuela, is sourced predominantly by a Type II black shale (Agua Clara Formation), but shows potential influences of a continental source rock of the Cerro Pelado Formation. This mixed-source region shows evidence for numerous magnetic minerals including hematite, magnetite, maghemite, goethite and iron sulphides (De la Rosa *et al.*, 2021). Whilst these magnetic minerals are predominantly associated with hydrocarbon seepages, thus do not directly correlate to the IMF petroleum system, the presence of similar magnetic minerals in a multiple-source rock system indicates that a wide variety of magnetic minerals can coexist is a system charged by multiple hydrocarbon sources (De la Rosa *et al.*, 2021).

Beyond the direct implications of magnetic mineralogy and the understanding of the IMF petroleum system, Zhang *et al.* (2020) follows Zhang *et al.* (2018, 2019) in investigating the magnetic behaviours around breached reservoirs within petroleum systems and those that experienced extensive hydrocarbon loss post-peak accumulation. Most clearly seen within this work is the chemical remagnetisation of minerals during rift events which typically cause reservoir breaching. With the extensive rifting and late-stage evolution of the IMF, it is of critical importance to understand how the impact of potential hydrocarbon loss could influence the magnetic mineral assemblages and properties.

6.6 | Conclusion

In conclusion, the magnetic mineral assemblages of the IMF show minimal variation at basin-scale, with no distinct pattern seen across the IMF, however, at well-scale, there are localised patterns that are most likely a result of environmental changes and source rock influences. The magnetic mineral assemblages of the IMF are broadly consistent across the basin, with all twelve wells showing evidence of goethite, alongside nine wells showing evidence of siderite. In comparison, lepidocrocite is also seen in seven of the wells, six of which are located in the centre of the basin in and around Beatrice Field. There is also evidence of minor iron sulphide presence, through pyrite and pyrrhotite in four wells, one of which, Well 11/24a-2 is dominated by them, in a departure from the other magnetic mineral assemblages. There is also one occurrence of maghemite, in Well 12/27-1, across the well's oil-water contact zone, which can be attributed to dehydration or dehydroxylation of lepidocrocite.

In the wells that contain oil-water contacts, clear magnetic enhancements are seen at contacts in eight of the ten wells, with two wells showing no clear enhancement across them, Wells 11/30a-8 and 11/30a-B10. This enhancement supports the work of Badejo *et al.* (2021c), but goes further by identifying two different magnetic enhancements at the OWCs, some wells experience the magnetic enhancements above the contact, and others experience them below. These enhancement trends correlate to the magnetic minerals identified within the wells, allowing for classification of the wells into two groups.

The first group, goethite-rich, is the most dominant, with six of the ten OWC-bearing wells containing no iron sulphides, but strong presence of goethite and siderite and magnetic enhancements below the OWCs. The second group, iron sulphide-rich, is represented by two OWC-bearing wells, with both of these showing less goethite in tandem with clear iron sulphide presence, and an above-OWC magnetic enhancement, whilst two of the wells are unclassifiable. Furthermore, the goethite-rich wells show increasing ferromagnetic material around the OWCs in the form of magnetite, which the FORC PCA shows is PSD and this is the origin of the magnetic enhancement seen. The increased presence of magnetite at the contacts is connected to the alteration of unstable goethite into magnetite around the contact, due to the variable redox conditions surrounding it. The FORC PCA behaviour is expanded further in the iron sulphide-rich wells which see relative enhancements of MD and SD domain grains at the contacts, differing from the goethite-rich well behaviour. The presence of iron sulphides in place of iron hydroxides when sulphur is present, as seen in the iron sulphide-rich wells, infers that reducing, anoxic conditions exist within these wells, causing preferential formation of sulphur, and thus iron sulphides, instead of iron hydroxides. Alternatively, it is possible iron sulphides formed elsewhere, away from the wells, and migrated to them, potentially connecting to possible source rock variations.

The formation of goethite is linked to lacustrine depositional environments (Berner, 1969; Fortin *et al.*, 1993; Gendler *et al.*, 2005; Weibel, 1999; van der Zee *et al.*, 2003), and iron sulphides with Kimmeridge Clay-sourced hydrocarbon accumulations (Abdulkarim *et al.*, 2022a,b,c; Badejo, 2019; Badejo *et al.*, 2021a,b,c). As such, well classifications can indicate: 1) which source rocks charged the hydrocarbons present in the wells, and 2) how the hydrocarbons migrated into the well region. Consequently, correlating siderite presence within goethite-rich wells to migration methods, and any potential presence of Kimmeridge Clay-sourced hydrocarbons within iron sulphide-rich wells is of key importance

within the basin modelling. With the presence of siderite in numerous wells inferring the existence of vertical hydrocarbon migration, magnetic mineral assemblages aid the understanding of the petroleum system, however this must be supported by basin and petroleum systems modelling. In comparison, the magnetic mineral analysis in this chapter offers no clear indication for lateral migration.

CHAPTER 7 | BASIN & PETROLEUM SYSTEMS MODELLING

7.1 | INTRODUCTION

This chapter, covering this study's investigation into the Inner Moray Firth's (IMF) petroleum system, builds, analyses and develops a successful basin and petroleum systems model (BPSM) of the IMF. The BPSM is crucial to understanding the basin's petroleum system components, in order to analyse the impacts of the basin's complex geological history on the petroleum system and how the hydrocarbons have formed accumulations in localised pockets of the basin. Furthermore, it allows investigations into the magnetic variations seen in Chapter 6 and to what extent they may be directly related to the petroleum system. The BPSM also aims to build understanding into the different source rocks within the basin, what degree of maturity they each reach, and to what extent they may or may not contribute towards the hydrocarbons accumulated within the three known and produced fields within the IMF.

The BPSM is derived directly from the analysis undertaken in Chapter 5, as well as previous literature and scenario testing within the models themselves, to understand how variables in the basin impact the petroleum system. The BPSM framework, created in Schlumberger's PetroMod (Schlumberger, 2020) is a direct copy of the geological model's faults and depth maps that were created in Schlumberger's Petrel (Schlumberger, 2015) in Chapter 5, as the framework created in Petrel considers the basin's structure and filling, whilst the PetroMod model considers the petroleum system's timings and fluid movements. This chapter covers the results of the BPSM, the conclusions and interpretations drawn from them and the impacts it has on present knowledge of the IMF as a petroleum system. The model underwent extensive building with numerous inputs required to produce a viable BPSM, therefore for clarity, the framework and production of the BPSM is outlined within the Appendix of this study (Appendix A.1). However, several key components of the model that impact the results of it are outlined below.

7.2 | KEY COMPONENTS OF THE MODEL

7.2.1 | AGE ASSIGNMENT

The age assignment table of the BPSM, the delineation of events that occur, their timings and the relative impacts they have on the model's behaviour is of key importance, due to the chaotic structural history of the IMF. The age assignment of the BPSM in this study is seen in Table 7.1, and is derived from geological data (Chapter 5) and literature (e.g. Andrews *et al.* (1990) and Roberts *et al.* (1990)).

7.2.2 | BOUNDARY CONDITIONS

The boundary conditions of the model control the heat impacting the model from both above (Sediment-Water Interface Temperature; SWIT) and below (Heat Flow; HF), and the relative depth of the model controlled by sea level through time (Paleo-Water Depth; PWD). These conditions are key to the model and maintain influence over it, especially through the temperature controls, and as such, they are critical to the success of the petroleum system (Figure 7.1).

Table 7.1: *Table outlining the ages and main events assigned to the BPSM of the IMF in this study, and the facies assigned to layers. The facies are derived from the properties available within PetroMod, including mixing multiple facies, determined through core and wireline log analysis, and, where required, supported by literature (Andrews* et al.*, 1990; Brown* et al.*, 1988; Glennie* et al.*, 2003; Linsley* et al.*, 1980; Roberts* et al.*, 1990; Stevens, 1991).*

Age (Ma)	Horizon	Layer (activity below horizon)	PetroMod lithology assigned to layer
0.00	Present day	Non-deposition then Q deposits	Sandstone
23.00	End K & Cz subsidence, erosion & uplift	**Basin-forming Events 3 & 4**; variable sediment removed	-
66.00	Top Cretaceous	End K; start Cz deposition (removed during uplift & erosion)	Clay-rich sands
120.00	Top Cromer Knoll Group	Cromer Knoll deposition	Clay-rich sands
132.00	BCU	Hiatus event	-
133.00	Top Wick Sand	Wick Sand deposition	Sandstone
140.00	Top KCF	KCF deposition (& **Basin-forming Event 2**)	Mix of 50 % sandstone & 50 % sandy, organic lean shale
152.00	Top KCF Black Shales	KCF Black Shales deposition	Black Shale
157.30	Top Heather Formation	Heather Formation deposition	Shale
163.50	Top A Sand	A Sand deposition	Sandstone
164.70	Top Mid Shale	Mid Shale deposition	Shale
164.90	Top B Sand	B Sand deposition	Sandstone
166.10	Top Brora Coal	Brora Coal deposition	Pure coal
166.30	Pentland Formation	Pentland Formation deposition	75% sandstone, 25 % black shale
177.65	Top H Sand	H Sand deposition	Sandstone
180.15	Top I Sand	I Sand deposition	Sandstone with minor cementation
182.60	Toa-Pliens Unconformity	NSD-caused hiatus event	-
182.70	Top LW Shale	LW Shale deposition	Shale
183.40	Top J Sand	J Sand deposition	Clay-rich, partially cemented sands
192.35	Top Red Beds	Red Beds deposition	Clay-rich, partially cemented sands
201.30	Top Stotfield Chert	Stotfield Chert deposition	Equal mix of clay, sand, carbonates and chert
206.30	Triassic Unconformity	small erosive event; 500 m sediment removed	-
208.15	Top Triassic	Triassic deposition	Clay-rich sands
251.90	Top Zechstein	Zechstein deposition	40 % sandstone, 20 % carbonate, 10 % shale, 30 % halite/anhydrite
259.00	Top Rotliegend	Rotliegend deposition	Clay-rich sands
298.90	End of basin-forming inversion & erosion	**Basin-forming Event 1**; all 2000 m of C sediment removed	-
310.00	Top Carboniferous	Carboniferous deposition	Sandstone
377.50	Top Devonian	Old Red Sandstone flagstones and fish bed deposition	Flagstones – 47.5 % organic-lean, carbonaceousshales, 47.5 % silts, 5 % sandstone. Fish beds – 75 % organic-rich shales, 20 % carbonaceous silts, 5 % sandstone
392.50	Top Basement	Basement formation	Granite
420.00	Base of Model	-	-

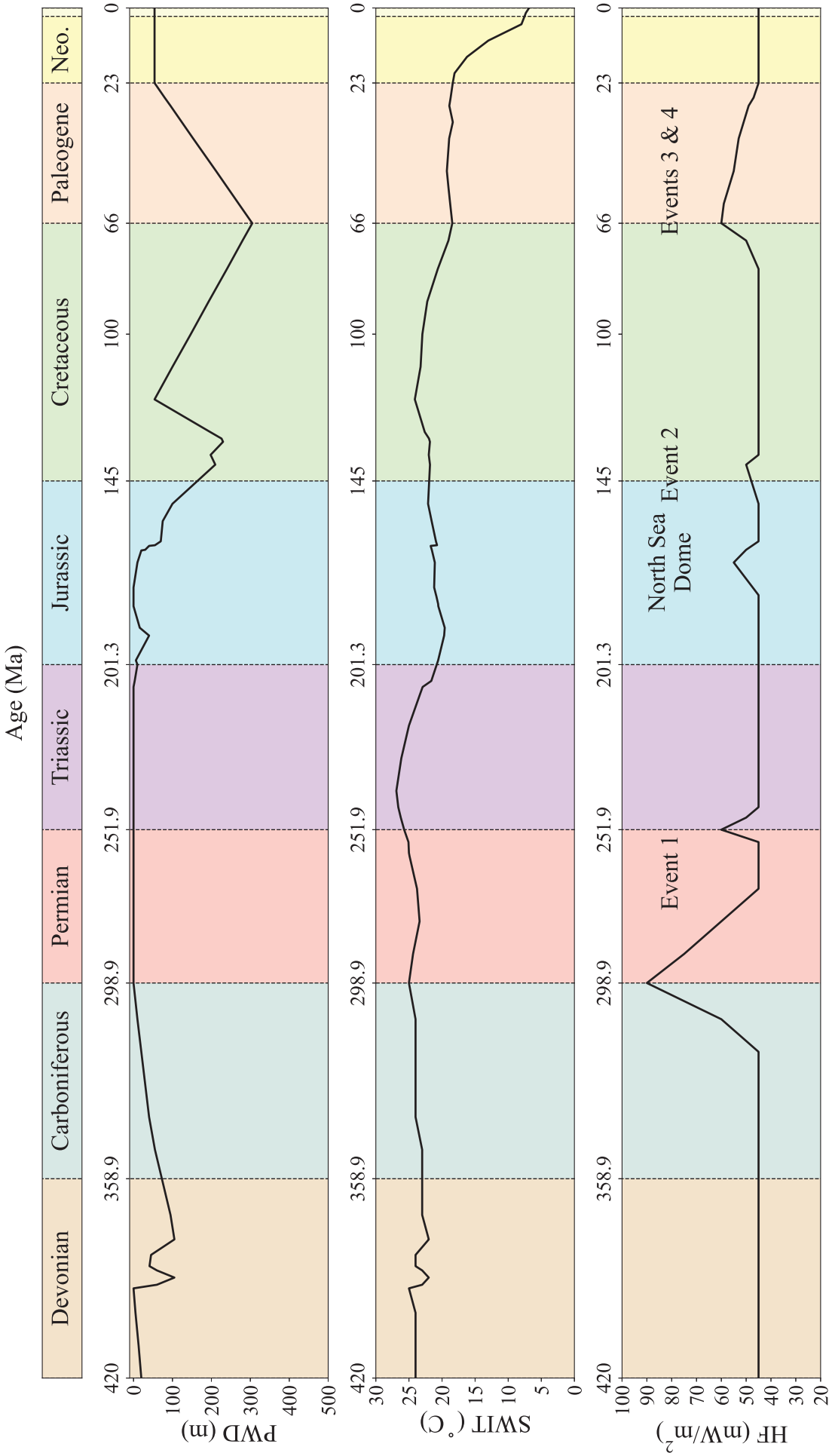


Figure 7.1: *Series of boundary condition plots of the three components and their properties used within the BPSM in this study. The paleo-water depth is a direct estimation on the water level of the area throughout time, and correlatable to the facies seen in the basin, whilst sediment-water interface temperatures relate to the temperature at seabed, thus is related to the PWD. Heat flow is directly connected to the basin's geological history and periods of rifting and instability that increase the temperatures across the basin, and the events seen in the IMF are visible in it. Conditions were collated and derived from Allen and Allen (2005); Andrews* et al. *(1990); Brown* et al. *(1988) and Wygrala (1989).*

7.2.3 | SOURCE ROCK PROPERTIES

In the BPSM, hydrocarbon generation properties must be assigned to potential source rocks. These properties, total organic carbon (TOC) content, hydrocarbon index (HI) and source rock kinetic, constrain the source rocks' amount of organic matter, and capability to mature the organic matter and generate hydrocarbons, respectively (Bjorlykke, 2010; Hantschel and Kauerauf, 2009). Within this BPSM, TOC and HI were taken from core analysis within well reports and published literature (Peters *et al.*, 1989), and were back-calculated (Jarvie *et al.*, 2007) to create original, pre-generation TOC (TOC_O) and HI (HI_O) values (Table 7.2). The kinetics used were taken from the analysis of Baur (2019) and di Primio and Horsfield (2006), and derived from the source rock types (Table 7.2).

Table 7.2: *Table of properties applied to the source rocks of the IMF in the BPSM. TOC and HI were derived from well report core analysis and Peters* et al. *(1989), and then back-calculated to define an original TOC (TOC_O) and HI (HI_O) value, using Jarvie* et al. *(2007), whilst the 4-component source rock kinetics were taken from the work of Baur (2019) (Ba) and di Primio and Horsfield (2006) (DP).*

Source Rock	TOC_O (%)	HI_O (mg HC/g TOC)	Kinetic
Devonian Fish Beds	5.5	930	Type I (Ba)
Pentland Formation	4.0	400	Type II-III (Ba)
Brora Coal	60.0	60	Type III (Ba)
KCF Black Shales	6.5	400	Type II (DP)

7.2.4 | FAULT PROPERTIES

Due to the extensive and pervasive nature of the faults in the IMF (Andrews *et al.*, 1990; Roberts *et al.*, 1990), accurate fault properties throughout time are a key component of the IMF BPSM. With faults' ability to trap or migrate fluids, they are crucial to how the petroleum system of the IMF operates, and those used within this study's BPSM can be seen in Table 7.3. Due to the IMF experiencing four basin-forming and -constraining events, reflected in three stages of instability interspersed between four of stability, various fault properties had to be considered. Faults are considered more open, fluid migration pathways during periods of instability, and more closed, barriers to fluids during periods of stability, with this reflected in the BPSM. This behavioural framework was then scenario tested (Appendix A.3) to determine the degree to which the faults were more open and more closed (fluid pathways or barriers) in the relevant time periods.

7.2.5 | EROSION VOLUMES

The amount of material eroded and removed from a basin throughout its geological history can be influential within a BPSM (Hantschel and Kauerauf, 2009), as it not only considers the removal of sediment, resulting in the shallowing of pre-existing lithologies, but also the initial deposition above what exists at present day, thus potentially burying lithologies deeper than they presently appear. Both of these impacts influence the petroleum system as they not only mature source rocks through burial, but also compact lithologies, release faults, create structural traps and assist hydrocarbon migration.

Table 7.3: *Table of properties applied to the faults within the IMF BPSM, showing the variation in fault behaviour – more closed during basin stability, thus acting as fluid migration barriers; and semi permeable-to-open during periods of rifting and instability, where the faults act as fluid pathways.*

Age From (Ma)	Age To (Ma)	Instability or stable	FCP (MPa)	Fault Perm. (mD)
23.00	0.00	Stable	11	-6.14
66.00	23.00	Cenozoic uplift	2.5	-3.48
206.30	66.00	Stable	11	-6.14
208.15	206.30	Triassic Rift	2.5	-3.48
298.90	208.15	Stable	11	-6.14
310.00	298.90	Carboniferous inversion	2.5	-3.48
421.00	310.00	Stable	11	-6.14

The erosion that occurred during the late-stage subsidence and associated uplift is uneven across the IMF, giving the basin a tilt (Andrews *et al.*, 1990; Argent *et al.*, 2002; Barr, 1985; Hillis *et al.*, 1994; Roberts *et al.*, 1990). Consequently, an erosion map specifying varying amounts of erosion, and thus the volume of extra material deposited, across the basin was produced, derived from well log analysis based on work by Thomson (1993), focused on wells in Figure 7.2. The erosion map produced (Figure 7.3) shows that the Great Glen Fault acts as the main axis for varying erosion volumes, with extensive erosion occurring to the fault's northern side and decreasingly less erosion occurring to the south east.

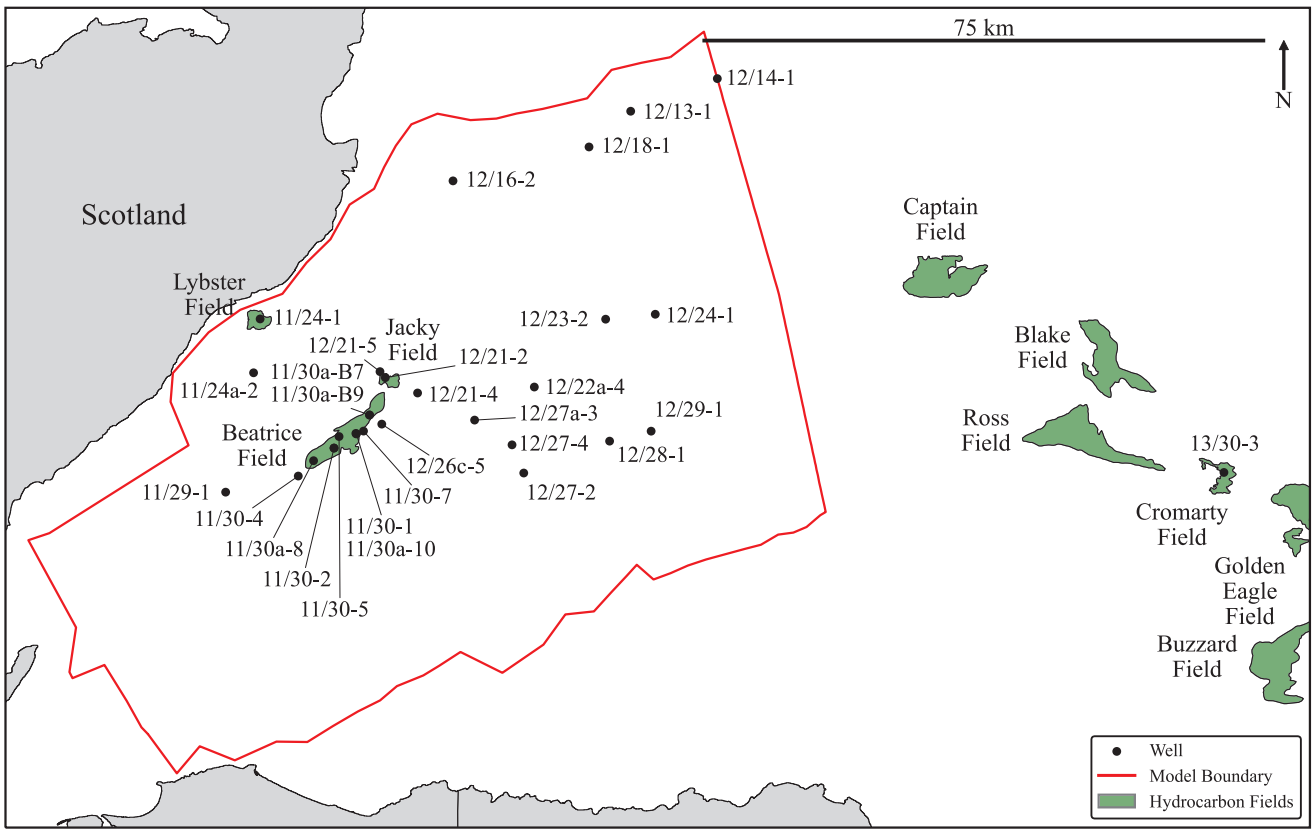


Figure 7.2: *Map showing the locations of the wells used to create the erosion map used for the late-stage uplift in the BPSM, including the reference well within Cromarty Field. Wells were selected through data availability, with limitations in certain regions as a result of reduced data coverage.*

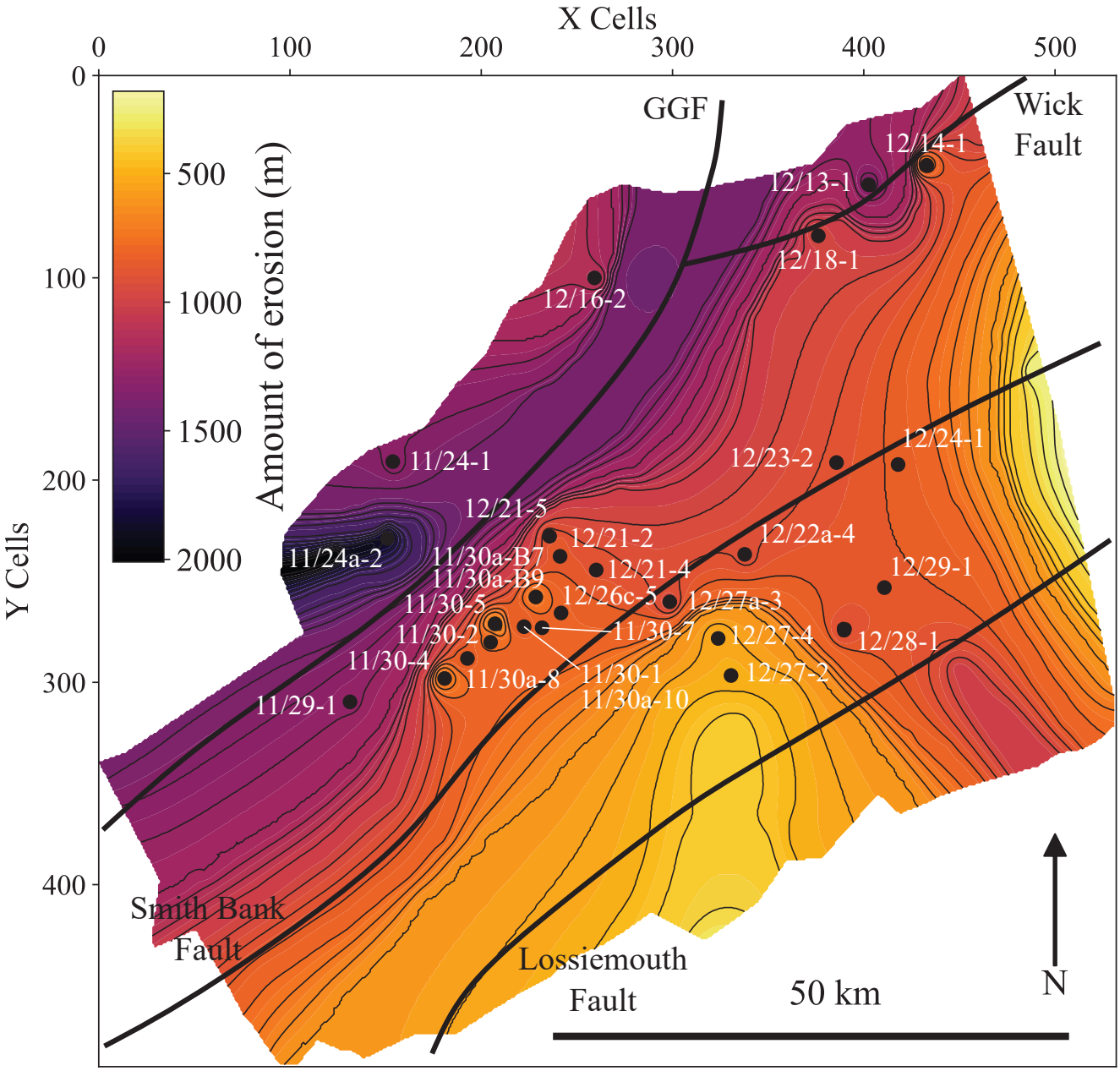


Figure 7.3: *Map showing the amount of sediment eroded across the IMF during the late stage Cenozoic uplift and erosion, estimated through well log analysis and calculations based on the work of Thomson (1993), with the locations of the wells used and the basin-bounding faults from which the erosion is centred. The majority of the erosion is bound to the Great Glen Fault (GGF) and the greatest volume of lost sediment occurs in the Sutherland Terrace to the north of the GGF.*

7.3 | ONE-DIMENSIONAL MODELLING

1D models are used to calibrate the basin's burial history at points across the basin, typically selected based on the availability of vitrinite reflectance data, the most crucial and widespread HF calibration dataset (Figure 7.4), and to investigate how these vary through geological time (Figure 7.5). 1D modelling is also used to identify the key components of petroleum systems, to develop and refine the boundary conditions, and to calibrate both these and other components of the models for scaling up to 2D and 3D (Hantschel and Kauerauf, 2009). 1D models are typically developed directly at well locations, but can also be at proxy "wells" on seismic lines where wells have not been drilled. 1D models take input data in the form of formation top depths, boundary condition data and any erosion or hiatus events, and then output series of time- and depth-orientated data. The output data is calculated by taking the depth inputs and expanding them into a 1 km diameter cylinder, with the input data, i.e., the well,

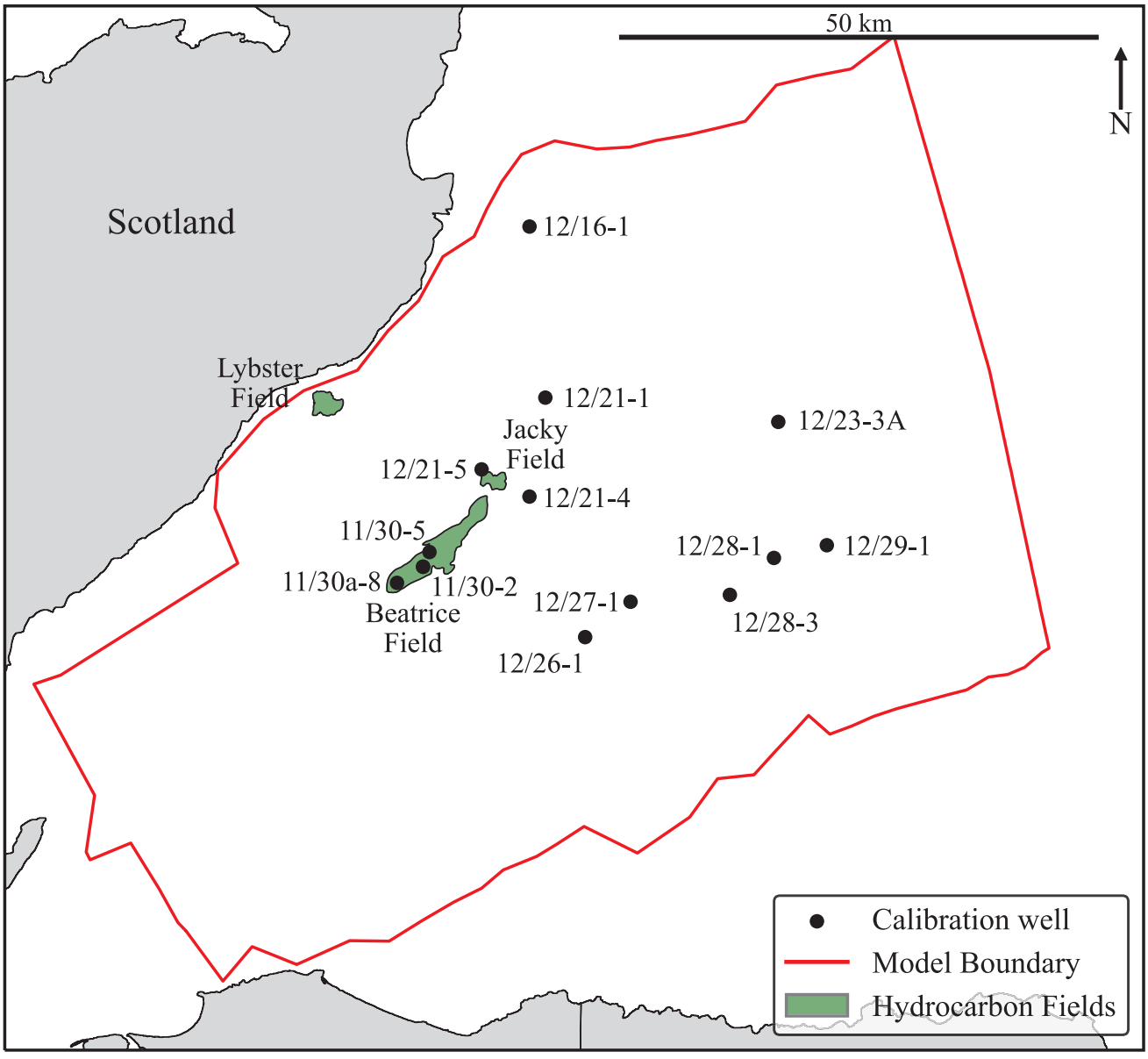


Figure 7.4: *Map of the IMF showing the location of the wells used for 1D modelling calibrations. The well distribution across the IMF is generally strong, however the wells available are limited to those with calibration data.*

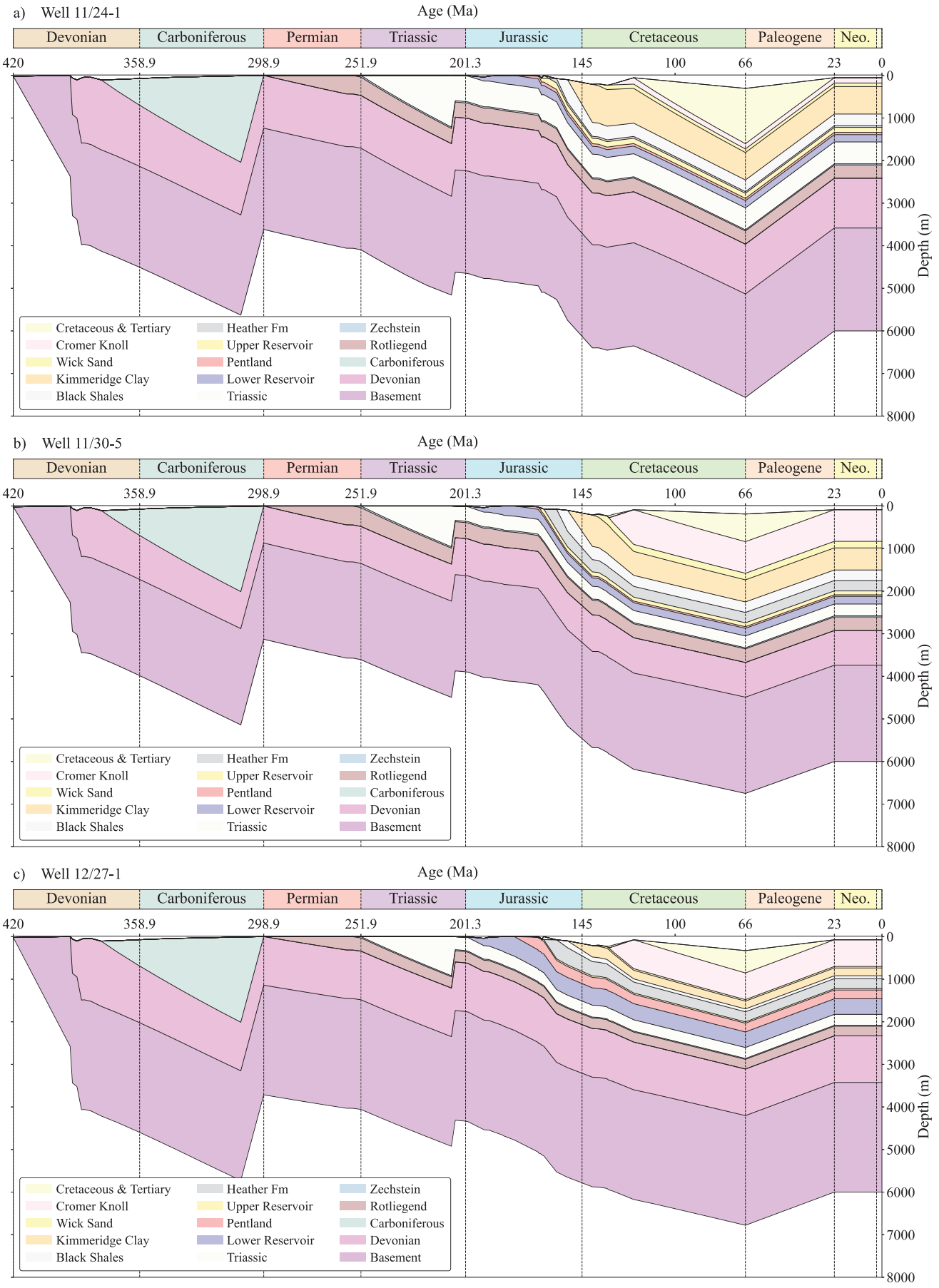


Figure 7.5: *Burial history plots of the formations seen in the IMF, created in this study, from Wells 11/24-1, in the Lybster Field, 11/30-5 in Beatrice Field, and 12/27-1 in the south west of the IMF. The burial histories in these three wells are the same throughout the Devonian-Triassic sequence, prior to variations from the Late Jurassic into the Cenozoic, where the influence from the erosion maps occurs.*

at its centre. Burial history plots offer insights into the depths and temperatures reached within the formations through time, and also show how variations in PWD can impact the system. The PWD is kept consistent across the basin as it varies through time, therefore it has minimal impact upon the system until the present day, where sea level is much more accurately measured during drilling.

The point where burial varies across the basin most extremely is within the late-stage Cretaceous and Cenozoic subsidence and uplift (Figure 7.5). This saw burial and erosion varying between 2 km and less than 500 m across the IMF, resulting in various degrees of burial within the formations below. This is most starkly seen within the burial history of Well 11/24-1 (Figure 7.5a), which experiences over 1.5 km of Cretaceous and Cenozoic sediments deposited and then eroded between 120 Ma and 23 Ma. In comparison, Well 12/27-1 experiences approximately 500 m of sediment shift within the same time frame (Figure 7.5c). In the same period, the region around the Beatrice Field, evidenced by Well 11/30-5 (Figure 7.5b) sees more sediment upheaval than at Well 12/27-1 to the south east, but significantly less than Well 11/24-1 to the northwest. This degree of burial likely contributed to the maturity of the source rocks around the reservoir to degrees not seen elsewhere within the basin, either being too low, and not offering sufficient depth and temperatures for maturity (in the southeast) or too great a burial, creating over-maturity in the northwest. The significant obstacle within this theory is the presence of Lybster Field, within which Well 11/24-1 is located, and thus is a key issue that requires attention within the 2D and 3D modelling. The likely over-maturity of the source rocks in the Lybster Field region suggests that the field was charged from another region of the IMF instead of directly beneath it.

The boundary conditions within the model are based on geological history and estimates, and thus need calibrating against known sample data. This requires 1D modelling of wells containing vitrinite reflectance data, which acts as a proxy for source rock maturity, as a result of temperature and depth, and identified the need for a lower heat flow than typically expected due to the thick crust within the IMF (Andrews *et al.*, 1990). 13 wells were used from various locations within the basin (Figure 7.4), and the results of the final calibrations can be seen in Figure 7.6. Overall, calibration via 1D wells was successful, with 9 of the 13 calibration wells successfully matching the simulated vitrinite reflectance curves to the core analysed data (Figure 7.6). The four that do not calibrate as strongly, Wells 12/21-1, 12/21-4, 12/21-5 and 12/23-3A, exist within the central eastern sector of the basin (Figure 7.7), with several possible reasons as to their miscalibration. Firstly, the quality of the data in these wells could be low, however this appears unlikely. Secondly, the wells are grouped within the same region, around the edges of the Smith Bank High horst, suggesting the presence of a localised geological variation. This is a more likely cause as two of the four wells (12/21-1 and 12/23-3A) only drill through the Cromer Knoll and Kimmeridge Clay Formation, both of which are heavily influenced by the late stage Cenozoic instability. It is possible that there was less burial and erosion in this region that was not reflected in the calculated erosion values. Despite testing all variables available to these wells, successfully calibrating these wells without causing erroneous calibration on the other wells was not possible, therefore these uncalibrated wells have been deemed anomalous.

In the 1D calibration, various sub-divisions of the different layers are developed to refine the model, add accuracy within the facies and to account for variations across the basin. Whilst the Cretaceous, Kimmeridge Clay, Black Shales and Heather Formations are not subdivided, those within the layers

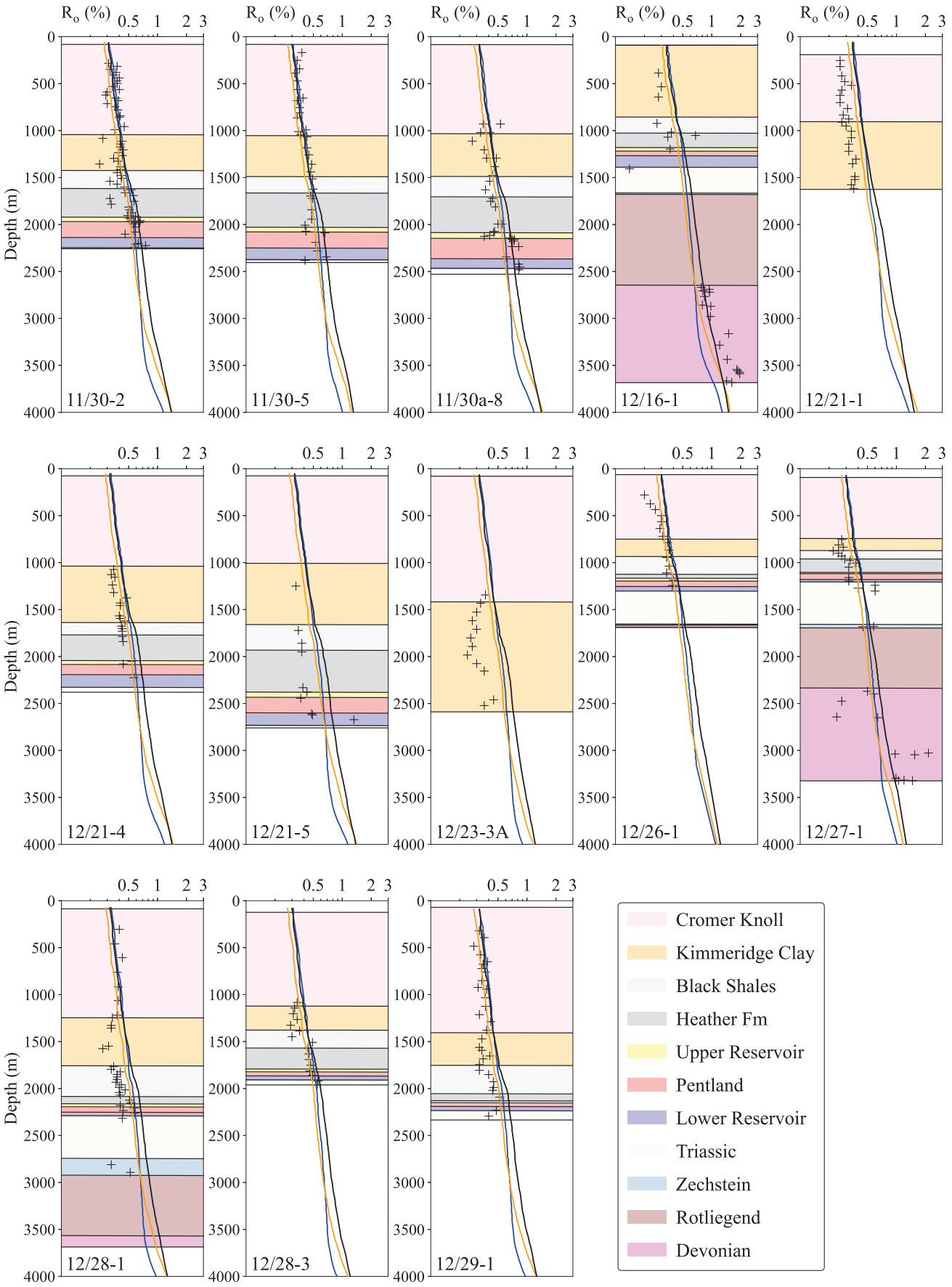


Figure 7.6: *Well calibration plots of calculated vitrinite reflectance curves (lines) plotted against the core sample tested vitrinite reflectance data (crosses) from the calibration wells used within the IMF model. Note that the model base is 6km, but the plots are limited to the drilled depths of the wells. The different calculated lines represent different calculation techniques from Burnham* et al. *(2016) (blue), Nielsen* et al. *(2015) (orange) and Sweeney and Burnham (1990) (black).*

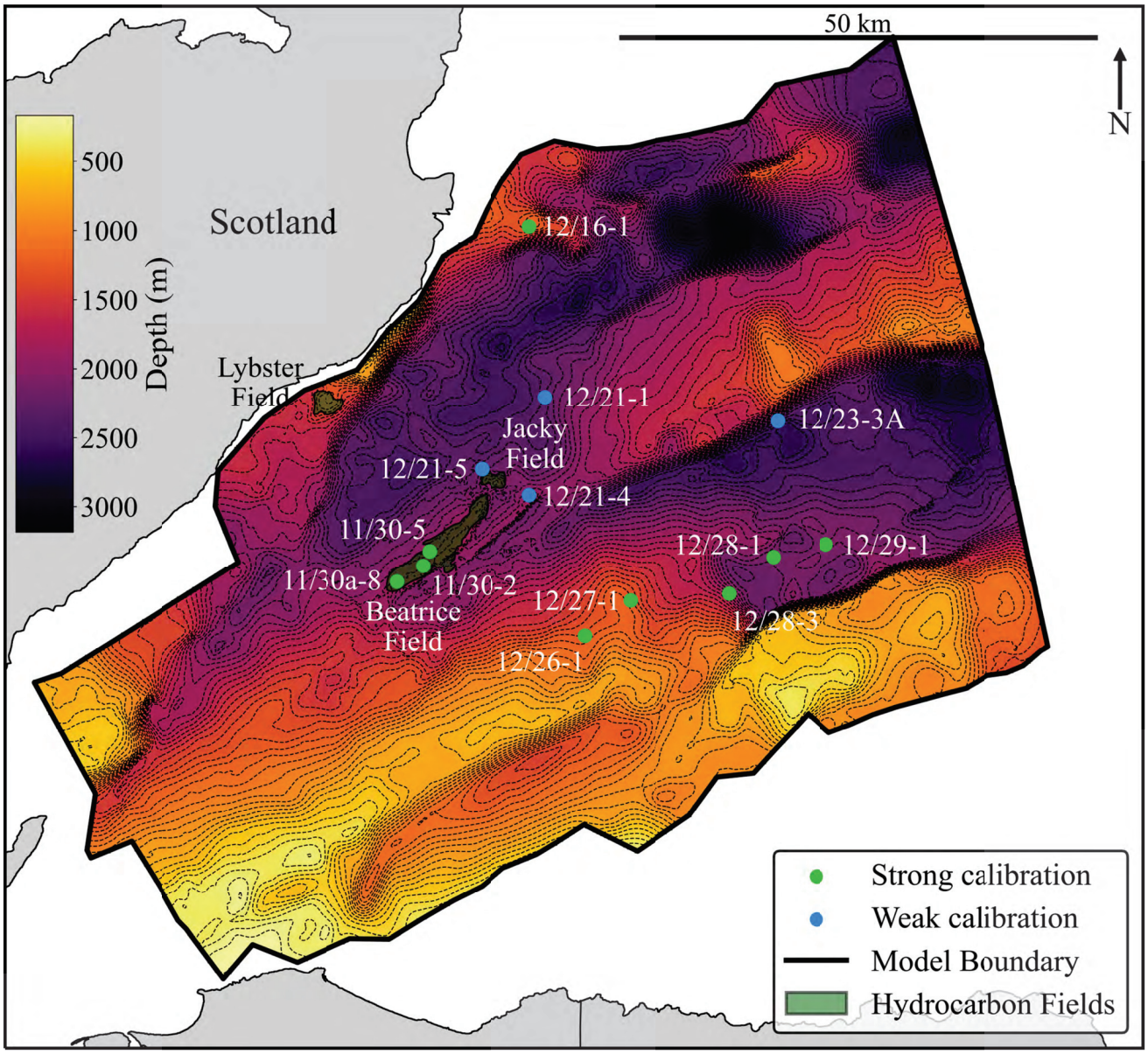


Figure 7.7: *Map of the IMF showing the wells used for calibration and their success in matching calibration data to calculated values against the backdrop of the depth map of the Top Reservoir. The majority of the wells see strong calibration between the simulated results and the calibration data, however several around the perimeter of the Smith Bank High, suggesting the formation of this horst.*

beneath these, from the reservoir to the Devonian, are. The Upper Reservoir section is divided into the A Sand, Mid Shale and B Sand, the Pentland Formation has a sub-5 m thick Brora Coal added to the top of it, and the Lower Reservoir is divided into the H Sand, I Sand, Lady's Walk Shale, J Sand and Red Beds. Below the reservoir section, the thin (sub-30 m) Stotfield Chert is added to the top of the Triassic, the Permian layer is split into the Zechstein and Rotliegend intervals, and the Devonian is sub-divided into the sandstone, flagstone and fish bed intervals that exist across the basin. The Devonian is topped by the John O'Groats Sandstone, which contains a thin fish bed at its centre, and the flagstones beneath have fish beds distributed somewhat evenly throughout (Andrews *et al.*, 1990; Newman and Dean, 2005). However, these thin fish bed layers are not suitable for the upscaled nature of PetroMod's BPSM, and create numerous issues that had to be resolved by condensing them into one unit and placing it at the average depth of all the Fish Beds within the Devonian.

7.4 | Multi-dimensional Modelling

In this study, modelling in two- and three-dimensions was conducted simultaneously to assess the testable variables. Models consist of grids with cell sizes of 200 m by 200 m, creating a 3D model over the IMF with a surface grid of 531 by 489 cells, totalling 259659 cells, covering an area equating to 106.2 km by 97.8 km. The move from 1D to 2D modelling introduces fluid flow into the model, whilst 2D modelling allows for relatively fast simulation and testing of different variables, alongside vertical and lateral analysis of the system (Hantschel and Kauerauf, 2009). 2D modelling is primarily utilised as a method of understanding lithological variations and fault properties and their relative influences on the petroleum system, with the tested variables then being applied to the 3D model. Due to the inability of 2D modelling to account for fluid flow across a second lateral axis that 3D does, the 2D models can develop inaccurate results, thus a constant feedback loop between the 2D and 3D models is required. The majority of 2D modelling in this study concentrates on cross-sections across the centre of the basin, from the north-west edge by Lybster Field, through Beatrice Field then to the south-east. This focus is a response to the locations of the known accumulations and to the seismic lines on which the 2D modelling was based. Furthermore, this orientation is orthogonal to the majority of the faults across the IMF, including the major basin-bounding faults, which typically trend north-east to south-west.

2D models were extracted from the 3D BPSM, allowing for the most accurate correlation between the two dimensions, however, this resulted in the same fault-derived artefacts that occur in 3D models where the BPSM struggles to replicate formation juxtaposition against faults (Figure 7.8). This juxtaposition is caused by the production of surfaces through geological modelling techniques and the need for each layer in the BPSM to have continuous top and basal surfaces with no overlap. As a result, faults within BPSMs act as less of a basin-forming process and more of a fluid flow component and it is common for faults to produce phantom accumulations where fluids trap against faults in artificial structures that do not represent the real-world counterpart. It is possible to create basin- and geologically-accurate fault juxtaposition, however it requires manual correction at each of the 259659 cells, thus demands a huge time input that far outweighs the comparative results it produces.

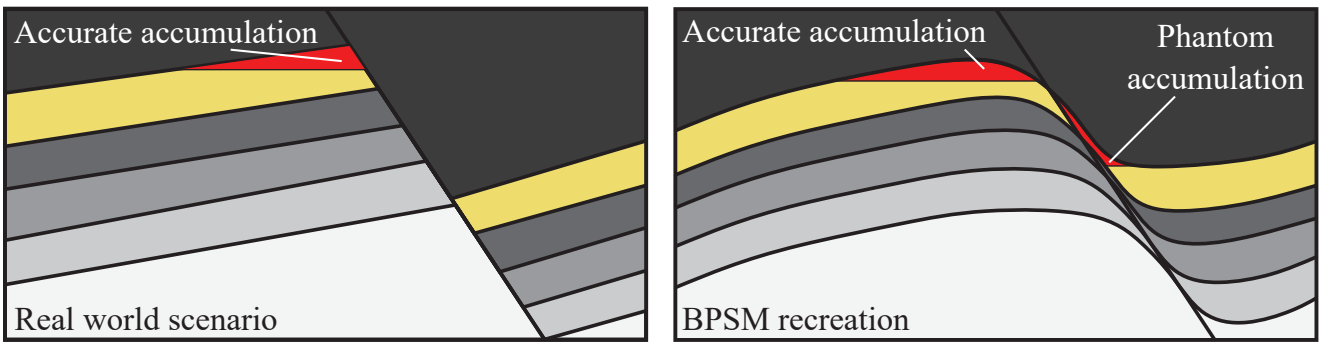


Figure 7.8: *Schematic diagrams showing how BPSMs recreate fault-lithology relationships compared to an idealised real-world example, and the potential for erroneous accumulations within the reservoir layer in the footwall of the modelled fault.*

7.4.1 | FINAL MODEL RESULTS

This section covers the outputs of the final, selected model, chosen from extensive sensitivity testing that is discussed in Appendix A.3 and what results, discoveries and understandings it can provide about the petroleum system within the IMF. The variables provide a successful BPSM that both accumulated hydrocarbons within the known fields of the IMF, as well as providing a mixing ratio within the fields that is similar to the estimated mixing ratio provided by geochemical analyses (Peters *et al.*, 1989). In summary, the refined scenarios used to create this model are as follows:

- Original thermal conductivities
- Heat flows peaking at 90 mW/m^2 in the Permian and 60 mW/m^2 at 66 Ma in the Cenozoic, with an overall low average heat flow of 45 mW/m^2 due to the thick crust.
- Erosion of 2000 m of additional Carboniferous sediments, and a variable amount of erosion, based on sonic-derived compaction trends in the Cenozoic.
- Two fault property systems, one where faults are more closed during stability, with an FCP of 11 MPa and permeability of -6.14 mD, and one with faults that are more open during rifting and instability, with an FCP of 2.5 MPa and permeability of -3.48 mD.
- Highly sealing facies being assigned the sealing capabilities of a shale, and varying volumes of differing lithologies in the formations.
- A Pentland Type II-III kinetic activation energy, but commencing at lower temperature.
- TOC values of 5.5 % in the Devonian Fish Beds, 4 % in the Pentland Formation, 60 % in the Brora Coal, and 6.5 % in the Kimmeridge Clay Black Shales.
- HI values of 930 mg HC/g TOC in the Devonian Fish Beds, 400 mg HC/g TOC in the Pentland Formation, 60 mg HC/g TOC in the Brora Coal, and 400 mg HC/g TOC in the Kimmeridge Clay Black Shales.

7.4.1.1 | HYDROCARBON GENERATION

The start of any BPSM is the effectiveness of the source rocks to produce the hydrocarbons necessary to flow through the system. Within the BPSM of the IMF, of the four source rocks, only two reach high levels of hydrocarbon generation, the Devonian Fish Beds and the Pentland Formation, but both the Brora Coal does not generate any hydrocarbons and the Kimmeridge Clay Black Shales experiences only partially generation (Figure 7.9; Table 7.4). In the IMF, source rock maturity in the formations besides the Fish Beds is mostly constrained to the deepest regions of the basin, the Great Glen and Wick Sub-Basins and eastern end of the Lossiemouth Sub-Basins, however the Fish Beds generally do not follow this trend, as the majority of the formation is sufficiently deep to ensure a high degree of hydrocarbon generation. The only exception to this is the southern edge of the basin, where the TR of the Fish Beds only reaches approximately 40 % (Figure 7.9; Table 7.4). The lack of generation in the Brora Coal and Black Shales confirms what past literature, Andrews *et al.* (1990); Greenhalgh (2016); Mackenzie *et al.* (1983); Peters *et al.* (1989); Stevens (1991), suggests – that the Black Shales are broadly immature in the IMF, contrary to in the central North Sea, where it operates as the dominant

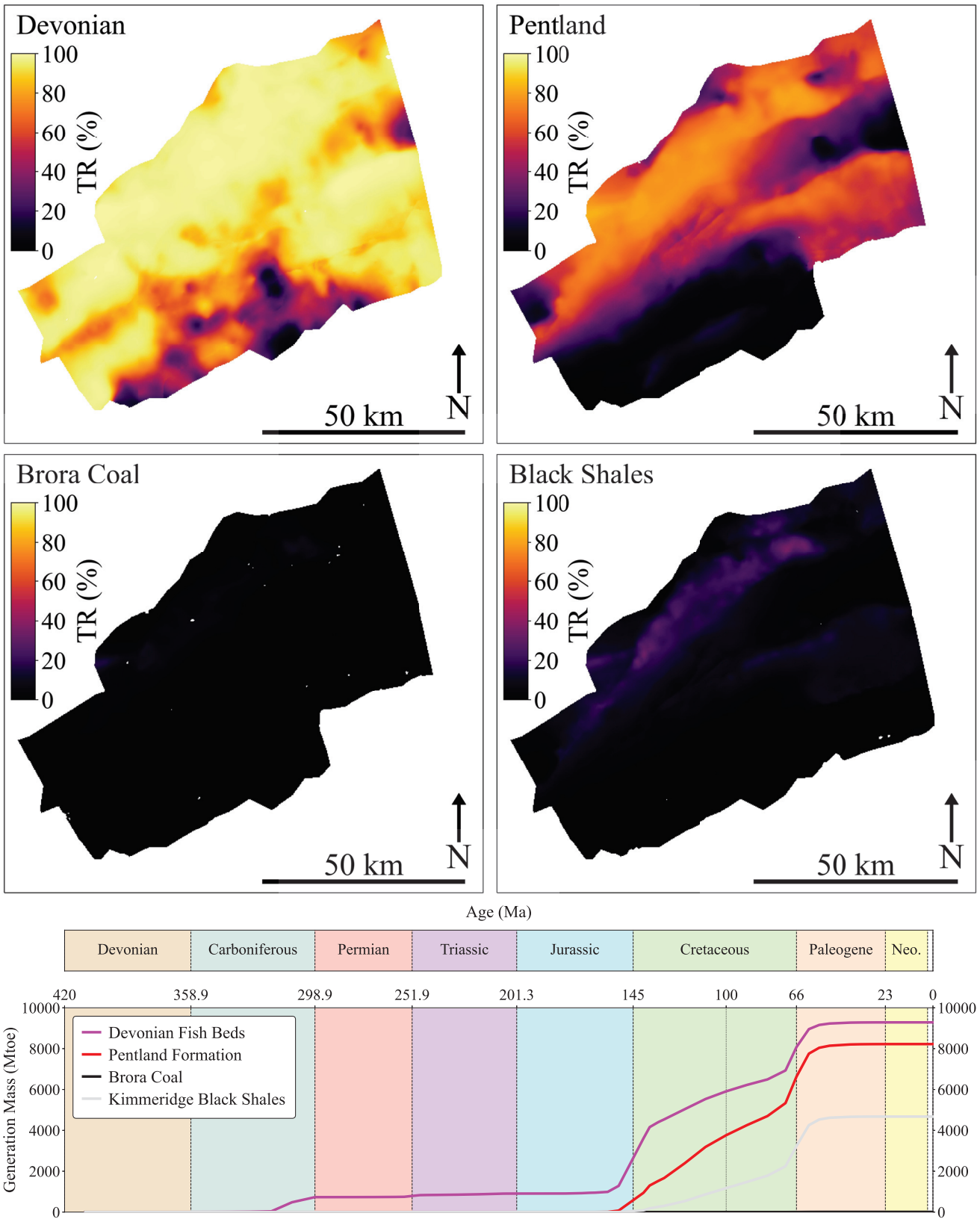


Figure 7.9: *Maps showing the average transformation ratio (TR) in the model cells of the four source rocks of the IMF at present day, and time plot showing the source rock maturity via generation mass, in Mtoe, through time across the entire IMF. The maps show how for the non-Devonian source rocks, the Great Glen Sub-basin is the main centre of maturity for the source rocks. For the generation mass, indicative of the ever-increasing maturity of a source rock, is that the Devonian Fish Beds begin to mature in the late-Carboniferous during the early basin-forming inversion, however, the bulk of maturity in the Fish Beds, alongside the other source rocks, occurs from approximately 150 Ma, due to the deposition of large volumes of sediment alongside the mid- and late-Jurassic rifting events.*

Table 7.4: *Table showing the rounded results from the final model of source rock hydrocarbon totals, generation, expulsion and accumulation totals across the entirety of the IMF, in gigatons of oil equivalent (Gtoe) and converted billion barrels of oil equivalent (Bboe), due to the very large totals involved, based on the conversion rate of 1 toe = 7.142857 boe. Results are rounded due to the degree of accuracy available in the BPSM.*

Source Rock	Total hydrocarbon mass		Total generated		Remaining potential		Accumulated in source		Total expelled	
	Gtoe	Bboe	Gtoe	Bboe	Gtoe	Bboe	Gtoe	Bboe	Gtoe	Bboe
Black Shales	62	441	5	33	57	408	2	15	3	18
Brora Coal	2	14	0	0	2	14	0	0	0	0
Pentland	20	144	8	59	12	85	6	40	3	19
Devonian	11	82	9	66	2	15	1	5	9	61
IMF Total	95	680	22	158	73	522	8	60	14	98

source rock, although very minor Kimmeridgian influences in the hydrocarbon mixing ratios shows that there is some maturation occurring, reflecting the marginal maturation seen in Figure 7.9. The lack of hydrocarbon generation in the Brora Coal offers a possible cause as to why there is little gas in the system, as coals are gas prone, thus had potential to flood the reservoir intervals with gas.

The model shows that the majority of hydrocarbon potential within the IMF comes from the Kimmeridge Clay Black Shales, which has approximately double the hydrocarbon potential of all other source rocks collectively. However, the Kimmeridge Clay Black Shales generate less than half the amount of hydrocarbons than the Pentland Formation and Devonian Fish Beds combined, with a further half of the Kimmeridge Clay Black Shale hydrocarbons generated not being expelled out of the source rock (Table 7.4). Of the nearly 62 Gtoe of potential hydrocarbons within the Kimmeridge Clay Black Shales, less than 5 Gtoe is generated, approximately 8 % (Table 7.4). Whilst the Kimmeridge Clay Black Shales contribute 21.4 % of the expelled hydrocarbons in the system, they lack an effective seal and trap which to contain the hydrocarbons, and thus also lack a sufficient pressure differential to force expulsion downward into the Mid-Jurassic reservoir sequence. Alongside the Kimmeridge Clay Black Shales, the immature Brora Coal do not generate any hydrocarbons from the potential hydrocarbons it contains (0 Gtoe generated from 2 Gtoe potential).

The Pentland Formation and Devonian Fish Beds in the BPSM generate large volumes of hydrocarbons, with the Pentland Formation generating 8 Gtoe of hydrocarbons from 20 Gtoe of potential hydrocarbons (40 %), whilst the Devonian Fish Beds generated 9 Gtoe of hydrocarbons from 11 Gtoe of potential hydrocarbons (81.8 %; Table 7.4). The Pentland Formation expels proportionally significantly less hydrocarbons than the Devonian Fish Beds, with this due to the high sand content within the Pentland offering an in-source reservoir rock, thus skewing results. The Pentland Formation is also overall less mature than the Devonian Fish Beds, further impacting expulsion volumes.

The generation of hydrocarbons from all of the source rocks bar the Devonian Fish Beds does not begin until after 150 Ma (Figure 7.9). The Fish Beds initially see generation beginning at around 330

Ma, but this plateaus after the end of the Carboniferous. The initial Fish Bed generation begins due to the Carboniferous sediment deposition, followed by the initial basin-forming inversion event that consequently removed the Carboniferous sediments. In comparison, the Pentland Formation and Kimmeridge Clay Black Shales do not see any hydrocarbon generation before 150 Ma, due to a lack of burial and the associated higher temperatures needed. These requirements are supplied at around 150 Ma by the deposition of the Kimmeridge Clay Formation as well as the late-Jurassic rifting event. This burial and temperature increase also restarts the stalled generation of the Devonian Fish Beds (Figure 7.9).

As the syn-rift deposition of the Kimmeridge Clay occurred, and the basin began building towards maximum burial at 66 Ma, the transformation ratio (TR) of both the Fish Beds and Pentland increase at steady rates. As the late-stage subsidence leads into the basin's maximum burial, prior to causing uplift and erosion, all three effective source rocks experience a relative sharp increase in TR. The uplift, caused by crustal flexure, results in the source rocks reaching peak hydrocarbon generation at maximum burial, and not during the uplift and consequential influx of heat. Therefore, it can be concluded that the main driver of maturity within the IMF is the extensive later-stage burial of the source rocks, not large influxes of heat from rifting and instability.

In summary, due to the lack of maturity within the Brora Coal, it is removed as a consideration for source rock contributions to the petroleum system of the IMF. However, the Kimmeridge Clay Black Shales are, and consequently, the Devonian Fish Beds, Pentland Formation and Kimmeridge Clay Black Shales are investigated regarding hydrocarbon expulsion during primary migration.

7.4.1.2 | MIGRATION PATHWAYS

Following hydrocarbon generation, the next stage of petroleum system analysis is hydrocarbon migration through the basin, both initially as primary migration through expulsion out of the source rock, then secondary migration through the system in carrier beds towards the reservoir formations and trap locations. As Section 7.4.1.1 shows, the Devonian Fish Beds and the Pentland Formation are the main contributors to generated hydrocarbons within the IMF, as the Brora Coal no hydrocarbons, and the Kimmeridge Clay Black Shales, whilst generating low amounts of hydrocarbons in the deeper regions of the formation, lacks sufficient hydrocarbon generation potential formation- and basin-wide to contribute as significant amounts of hydrocarbons as the Devonian and Pentland source rocks.

Hydrocarbon migration, through expulsion out of source rocks, occurs in a similar pattern and time sequence as hydrocarbon generation (Figure 7.9). The expulsion of Devonian-sourced hydrocarbons began early, between 320-310 Ma, shortly after generation was initiated, whilst the expulsion of Pentland Formation- and Kimmeridge Clay Black Shale-sourced hydrocarbons all commenced post-140 Ma, again approximately 10 million years after generation began. All source rocks show evidence of expulsion occurring at maximum burial at 66 Ma, suggesting that the hydrocarbons are generated during this time and near-immediately, on a geological time-scale, are expelled from the source rocks (Figure 7.10).

Early Devonian expulsion in the Late Carboniferous is a result of the initial basin-forming, Permian inversion that removed the entire Carboniferous sediment package, with the Carboniferous deposition moving the Devonian deeper into the beginning stages of maturation. However, once the Carboniferous

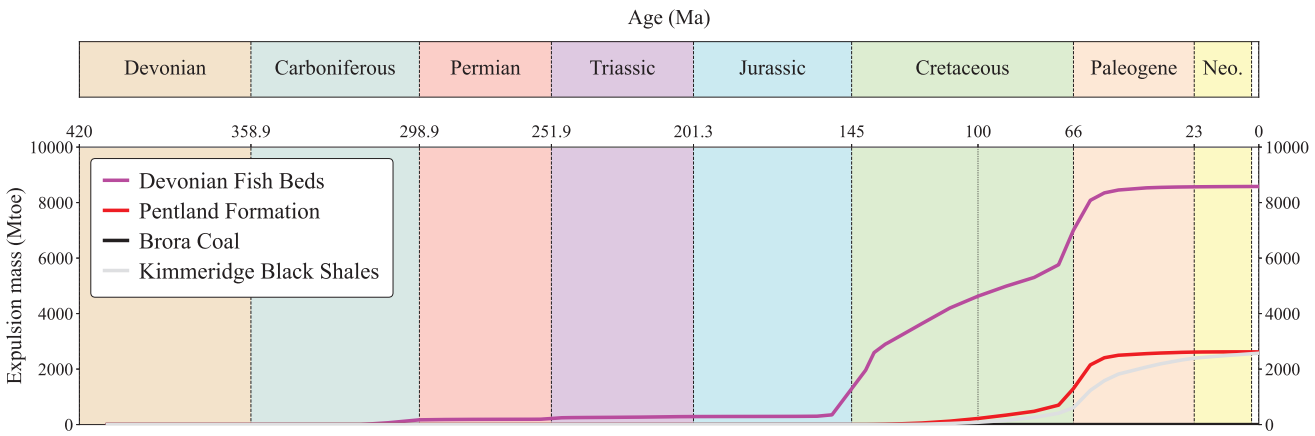


Figure 7.10: *Time plots of expulsion mass, in million tons of oil equivalent, of the three effective source rocks in the IMF, the Devonian Fish Beds, Pentland Formation and the Kimmeridge Clay Black Shales, alongside the immature Brora Coal. The expulsion masses of hydrocarbons broadly reflect the generation masses of the source rocks, outlined in Figure 7.9, but with a delay due to the time needed to generate and then expel the matured hydrocarbon. The expulsion masses show how there was an early stage of hydrocarbon production of the Devonian Fish Beds, but the vast majority of hydrocarbons were expelled after 150 Ma, especially in the Pentland Formation and Kimmeridge Clay Black Shales.*

sediments were eroded, Devonian expulsion was halted (Figure 7.10), and the early expelled hydrocarbons lacked any suitable reservoir or trap in which to accumulate, so were lost. However, the majority of expulsion occurs after 152-140 Ma, which coincides with two increases in heat flow, one preceding the expulsion at around 170 Ma caused by the North Sea Thermal Dome (Underhill and Partington, 1993), and then during the expulsion, between 152-140 Ma, as a result of the second stage of basin rifting. The initial heat influx increased hydrocarbon generation in the Devonian, before the hydrocarbons were then expelled during the rifting phase. This sequence of maturity followed by expulsion is matched around 66 Ma during the onset of the main generation and expulsion event that expels the majority of the Pentland and Black Shales hydrocarbons, except they occur together in the late-stage uplift sequence. Within the late-stage, Cenozoic tilting, the source rocks initially generate hydrocarbons during the subsidence and burial between 140-71 Ma, prior to being expelled during the uplift (Figure 7.10).

At the point when each source rock begins to expel their generated hydrocarbons, all three effective source rocks are overlain by porous and permeable lithologies. Whilst the Devonian Fish Bed source rocks are situated within the clay-rich Old Red Sandstone flagstones, these flagstones have a high enough sand content to facilitate migration (Figure 7.11; Andrews *et al.* (1990); Brown *et al.* (1988)). Once hydrocarbons breach the top of the Devonian, in the early stages of the basin, they would encounter the sand-bearing Carboniferous sediments and likely be lost to leakage, however hydrocarbons generated in the late generation and expulsion period post-150 Ma would encounter sand-bearing, porous and permeable lithologies in the Rotliegend, Zechstein and Triassic, which all facilitate migration through the basin. Within the Zechstein and the Triassic, salt and chert, ascertained through well log analysis and scenario testing, respectively, offer minor inhibitors to migration, however these may also implement more lateral than vertical migration, instead of complete hydrocarbon trapping.

Hydrocarbons migrating out of the Pentland Formation must pass through the Brora Coal to vertically migrate into the Upper Reservoir A and B Sands, but must also migrate vertically downwards

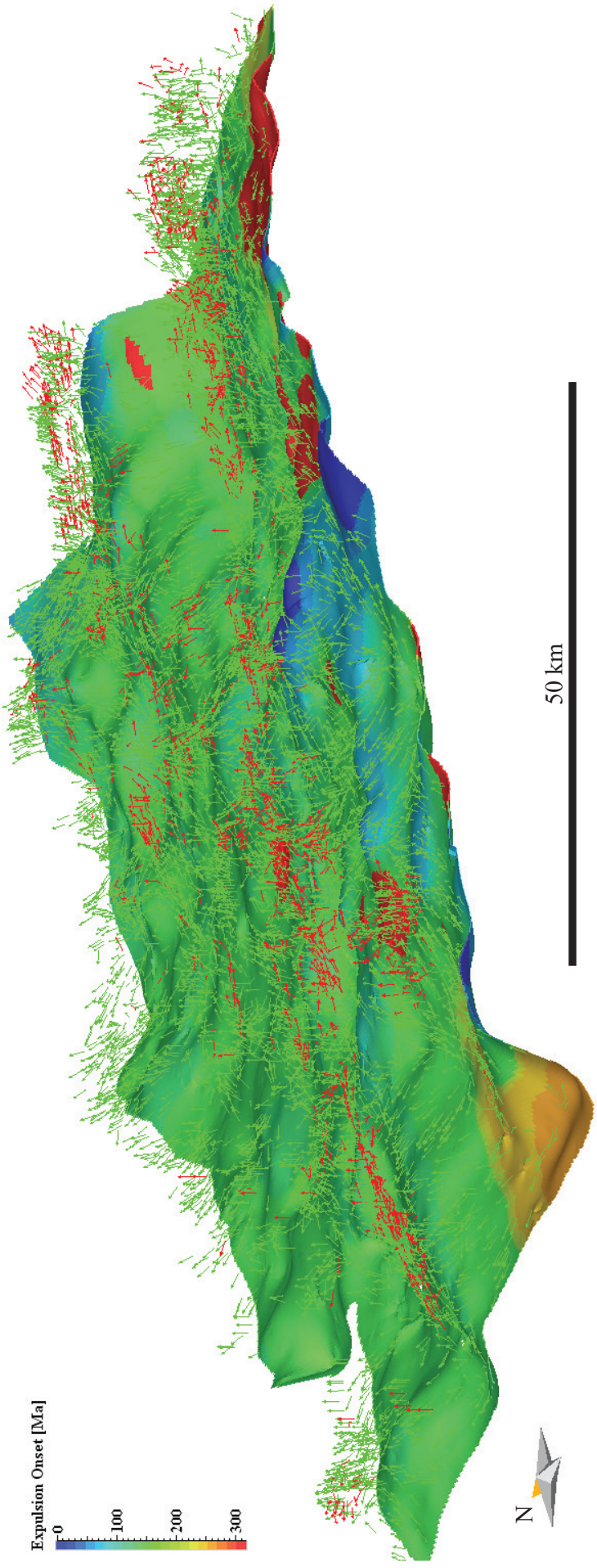


Figure 7.11: *Figure showing the Devonian Fish Beds and the expulsion onset time of the hydrocarbons generated in the source rock, alongside the migration vectors of the Devonian-sourced hydrocarbons within the Devonian ORS flagstones, Rotliegend and Zechstein sediment packages. Migration occurs laterally through the flagstones prior to seeing more vertical migration during the more permeable and porous sediments that overlay them. Green indicates oil migration and red indicates gas migration.*

into the Lower Reservoir H, I and J Sands. Whilst coals are typically not highly porous (sub-10 % porosity) or permeable (0.01-0.04 mD; Li *et al.* (2012)) and often have high capillary entry pressures (Dabbous *et al.*, 1976), the Brora Coal is very thin, typically less than 5 m thick, and thus is easily broken through by the pressure build up of the hydrocarbons beneath. This near immediate connection between reservoir sand above and source rock below, through a structurally limited thin bed means vertical migration from the Pentland directly into the Upper Reservoir is extensive within the IMF (Figure 7.12). Secondarily, downward migration out of the Pentland is also prevalent due to the presence of the Lower Reservoir directly beneath the source rock. The clay- and shale-rich nature of the source rock causes a higher capillary entry pressure across the source rock, limiting upward migration potential for the hydrocarbons generated in the deeper regions of the formation. As such, the hydrocarbons expel downward into the H and I Sands.

Whilst the Kimmeridge Clay Black Shales tend to be less mature than the Devonian and Pentland source rocks, the BPSM has proven that generation and expulsion of hydrocarbons occurs in deeper regions of the IMF, thus migration must be analysed. There lacks any sealing lithologies above the Black Shales, as it is followed by the sand-bearing Kimmeridge Clay Formation, the Wick Sand and the Cromer Knoll Group before reaching the seabed. Consequently, the majority of hydrocarbons generated within the Black Shales are likely to have vertically migrated upward out of the formation into these porous and permeable lithologies, before being lost at the surface due to the lack of seal (Figure 7.13). Despite this significant loss of hydrocarbons vertically, there is evidence through the hydrocarbon mixing ratios in several locations across the IMF BPSM of very small (sub-0.1 %) contributions of Black Shales in the reservoir sands, suggesting that downward migration from the Black Shales does occur. This downward migration is most likely developed through the same patterns seen in the Pentland Formation, however the Black Shales overlay the clay-rich Heather Formation, which seals the reservoir section, thus there is less likelihood of the hydrocarbons migrating downward out of the Black Shales into the Heather Formation, compared to the Pentland Formation.

To ascertain the locations of the hydrocarbons that charge the three fields of the IMF, migration analysis was carried out through differentiation of the source rock kinetics assigned to the source rock formations in the basin. For both the Devonian Fish Beds and Pentland Formations, two identical facies were assigned to the formations, a "deep-basin" one assigned to the most mature regions of the basin, the the Great Glen, Wick and Lossiemouth Sub-basins, acting as a proxy for lateral migration through carrier beds, and a "proximal" kinetic assigned everywhere else, acting as a proxy for vertical migration directly into the fields (Figure 7.14). Analysis shows that Beatrice Field is predominantly charged by proximal hydrocarbons, with these contributing 80 % of the hydrocarbons, compared to 20 % from the deep-basin regions (Table 7.5). In comparison, Jacky Field, despite its adjacency to Beatrice Field, shows an even 50:50 % split in its charge between proximal and deep-basin hydrocarbons, whilst Lybster Field sees a marginal control of proximal hydrocarbons over those from the deep-basin (Table 7.5). These differences seen across the fields hint at different charging mechanisms between them, most clearly between Beatrice and Jacky Fields. The analysis suggests that Jacky and Lybster Field rely more heavily on lateral and up-dip charging from the more mature Great Glen Sub-basin than Beatrice Field, which sees more vertical migration.

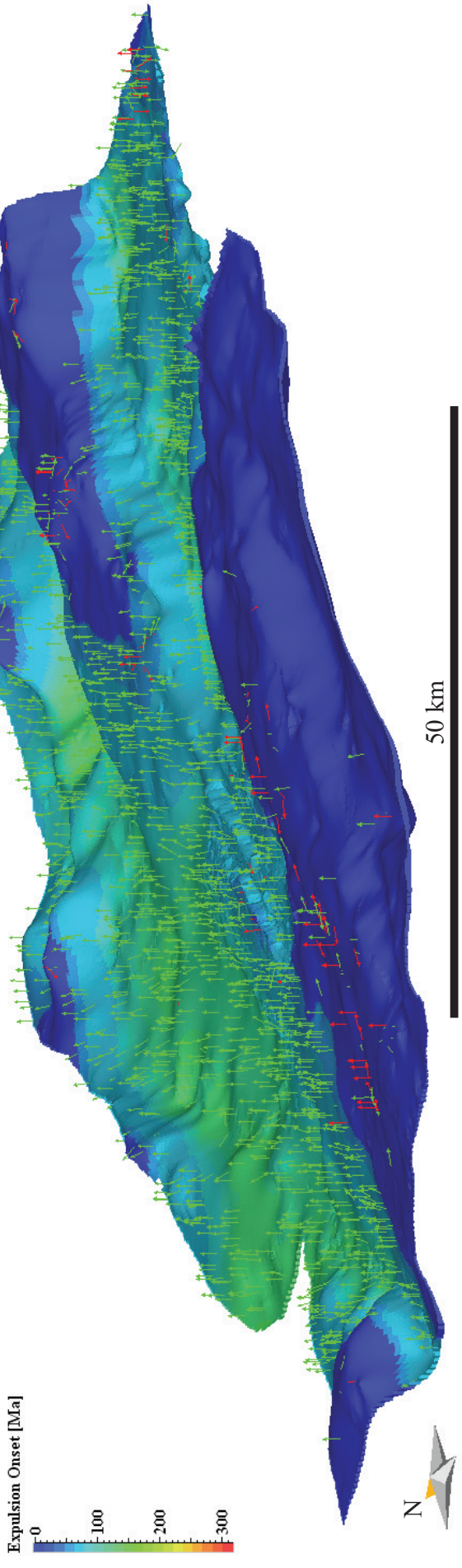


Figure 7.12: *Figure showing the Pentland Formation and the expulsion onset time of the hydrocarbons generated in the source rock, alongside the migration vectors of the Pentland-sourced hydrocarbons within the Pentland, Brora Coal, B and A Sand sediment packages. Migration occurs overwhelmingly vertically through the section. Green indicates oil migration and red indicates gas migration.*

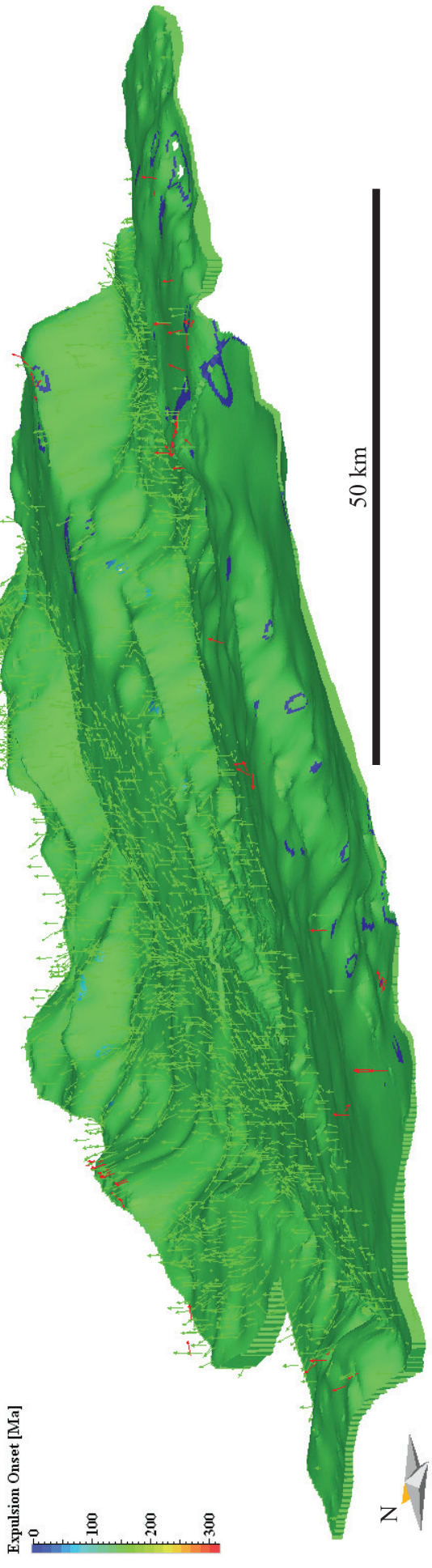


Figure 7.13: *Figure showing the Kimmeridge Clay Black Shales and the expulsion onset time of the hydrocarbons generated in the source rock, alongside the migration vectors of the Black Shale-sourced hydrocarbons within the Black Shales and Kimmeridge Clay Formation sediment packages. Migration occurs overwhelmingly vertically through the section but with lateral migration within the Black Shales initially due to the high clay and shale content. Green indicates oil migration and red indicates gas migration.*

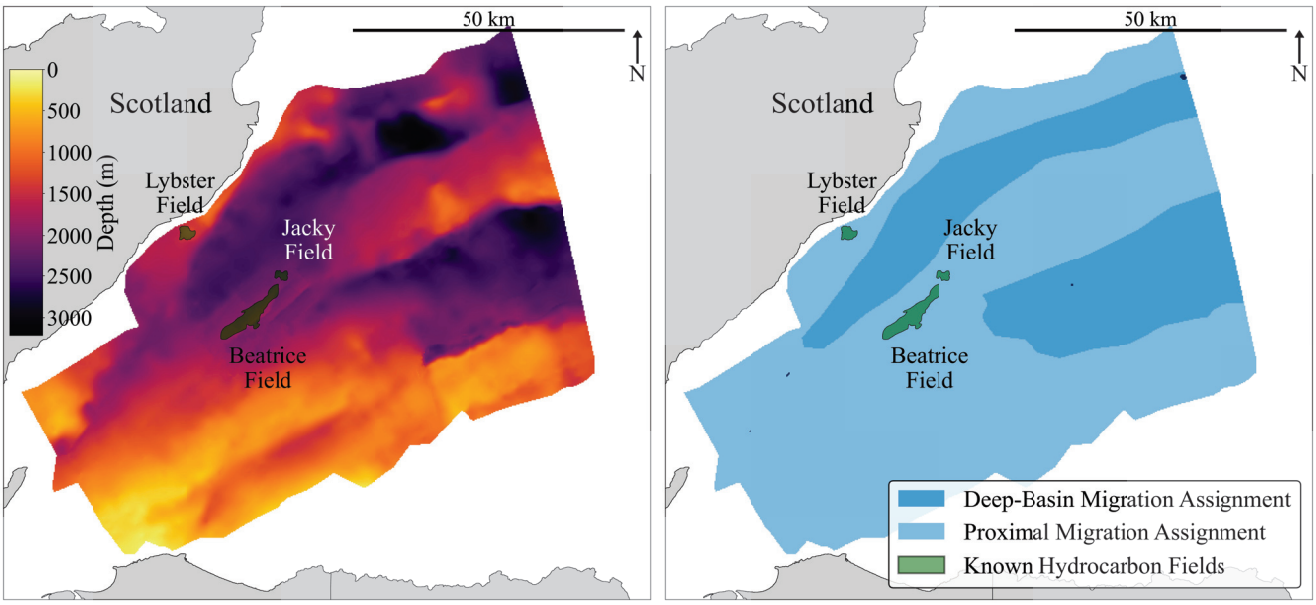


Figure 7.14: *Maps of the IMF showing the structure of the basin through a Top Reservoir depth map (left) and the regions of different migration methods used to determine the charge history of the known hydrocarbon accumulations in the basin (right). The deepest regions of the basin, through the Great Glen, Wick and Lossiemouth Sub-basins, are where the source rocks of the IMF reach highest maturity, but, as discussed, large swathes of the basin reach maturity in both the dominant source rocks.*

7.4.1.3 | KNOWN ACCUMULATION CHARGING

Charging of the three known fields in the IMF, Beatrice, Jacky and Lybster Fields, occurs both vertically and laterally (Section 7.4.1.2). The accumulated volumes of the three fields vary, from the large 480 Mboe accumulation in Beatrice Field, to the 40 Mboe in Lybster Field to the much smaller 5.2 Mboe estimated to be accumulated in Jacky Field (Kilvington and Gallivan, 1983; Izundu, 2008; Offshore Magazine, 2012; Oil and Gas Authority, 2018; Stevens, 1991). There is a lack of geochemical analysis investigating the hydrocarbon mixing ratios in each field, however the work of Peters *et al.* (1989) suggests the mixing ratios of the oils sampled in the IMF are approximately 60:40 % Devonian:Pentland. Whilst the mixing ratio likely varies across the basin, controlled by maturity variations

Table 7.5: *Table outlining the results of the differential migration methods used to analyse the hydrocarbon charging of the three known hydrocarbon accumulations within the IMF (Beatrice, Jacky and Lybster Fields). The table shows the split between deep-basin migration from the sub-basins, and proximal migration from beneath alongside the relevant contribution of each source rock to the field's hydrocarbon mixing ratio. Note that the relevant migration totals, or source contributions, in Lybster Field do not sum to 100 % due to the 1 % influence of the Kimmeridge Clay Black Shales.*

Hydrocarbon Field	Devonian Migration (%)			Pentland Migration (%)			Deep Basin Total (%)	Proximal Total (%)
	Deep Basin	Proximal	Total	Deep Basin	Proximal	Total		
Beatrice Field	12	55	67	8	25	33	20	80
Jacky Field	36	25	61	14	25	39	50	50
Lybster Field	37	30	67	9	23	32	46	53

of the source rocks, but especially the Pentland Formation, the analysis carried out by Peters *et al.* (1989) gives an approximate goal to focus on.

In the final model, successful charging of the three fields occurred and filling volumes closely match the estimated published volumes, with some minor but expected variations (Table 7.6). The filling of the Beatrice Field region closely matched the estimated published volume of 480 Mboe from Stevens (1991), with the BPSM calculating a filling volume of 481 Mboe, a sub-0.2 % variation, and a mixing ratio of 66:34 Devonian:Pentland, an approximately 10 % variation on the estimated ratio of Peters *et al.* (1989). However, the filling of Jacky Field in the BPSM (94 Mboe) is far greater than the estimated accumulation (5.2 Mboe; Izundu (2008)), however the mixing ratio matches the estimated ratio of Peters *et al.* (1989) – 61:39. The mismatch in filling volumes could be a result of a wide variety of reasons, such as minor, sub-seismic resolution faults around the field that allow hydrocarbon leakage, less porous or permeable migration pathways due to localised lithological variations or a lower quality reservoir compared to the Beatrice Field.

In comparison, the charging of Lybster Field, in the north west of the basin, was successful however the volumetric estimations calculated by the BPSM differ slightly to the published volume estimates from Offshore Magazine (2012). Unfortunately, no published literature exists on Lybster Field so finding an accurate estimate on its volume was not possible, however the calculated volume was close to the only published estimate found from Offshore Magazine (2012), of 40 Mboe, approximately 20 % greater than the calculated volume in the BPSM of 32 Mboe. The mixing ratio of the hydrocarbons within Lybster Field is also very similar to those of Peters *et al.* (1989), and to those of Beatrice Field, being 67:32:1 Devonian:Pentland:Black Shales. The minor presence of the Black Shales within Lybster is likely a result of vertical migration out of the Black Shales in the Great Glen Sub-basin, migration across the GGF and then into the relatively shallower reservoir sequences within the Sutherland Terrace, where Lybster Field is located (Table 7.6).

Table 7.6: *Table showing the basin and petroleum systems model simulated hydrocarbon mass (in million tons of oil equivalent; Mtoe), equivalent calculated volume (in million barrels of oil equivalent; Mboe) and hydrocarbon mixing ratio results from the three known accumulations within the IMF, Beatrice, Jacky and Lybster Fields, alongside their published estimated volumes, and mixing ratio, from Izundu (2008); Offshore Magazine (2012); Oil and Gas Authority (2018); Peters* et al. *(1989); Stevens (1991). Volume calculations are based on the conversion rate of 1 toe = 7.142857 boe. Bl. Sh. refers to the Kimmeridge Clay Black Shales.*

Hydrocarbon Field	Simulated hydrocarbon mass (Mtoe)	Calculated hydrocarbon vol. (Mboe)	Published hydrocarbon vol. (Mboe)	Accumulation contribution %		
				Devonian	Pentland	Bl. Sh.
Beatrice Field	67.32	481	480	66	34	0
Jacky Field	13.19	94	5.2	61	39	0
Lybster Field	4.42	32	40	67	32	1
Published estimates				60	40	0

Charging of all three fields begins at approximately 120 Ma, with varying changes in relative percentage of each hydrocarbon source rock throughout time (Figure 7.15). Beatrice Field charges at consistent ratios until 71.3 Ma, prior to a sharp increase in Pentland contribution to 66 Ma, before a large loss of hydrocarbons caused by the late-stage uplift and faults opening (Figure 7.15). Jacky Field initially charges with Devonian hydrocarbons, prior to the Pentland contribution increasing from approximately 110 Ma. The drop in accumulation volume after the peak volume at 66 Ma is relatively smaller one than within Beatrice Field (Figure 7.15). In comparison to the other two fields, Lybster Field sees a slow, limited charge prior to the faults opening at 66 Ma, at which it sees a rapid charging of the field via predominantly Devonian hydrocarbons (Figure 7.15). Once this significant charge post-fault opening occurs, Lybster Field experiences the same loss of hydrocarbons as the other fields until fault closure at

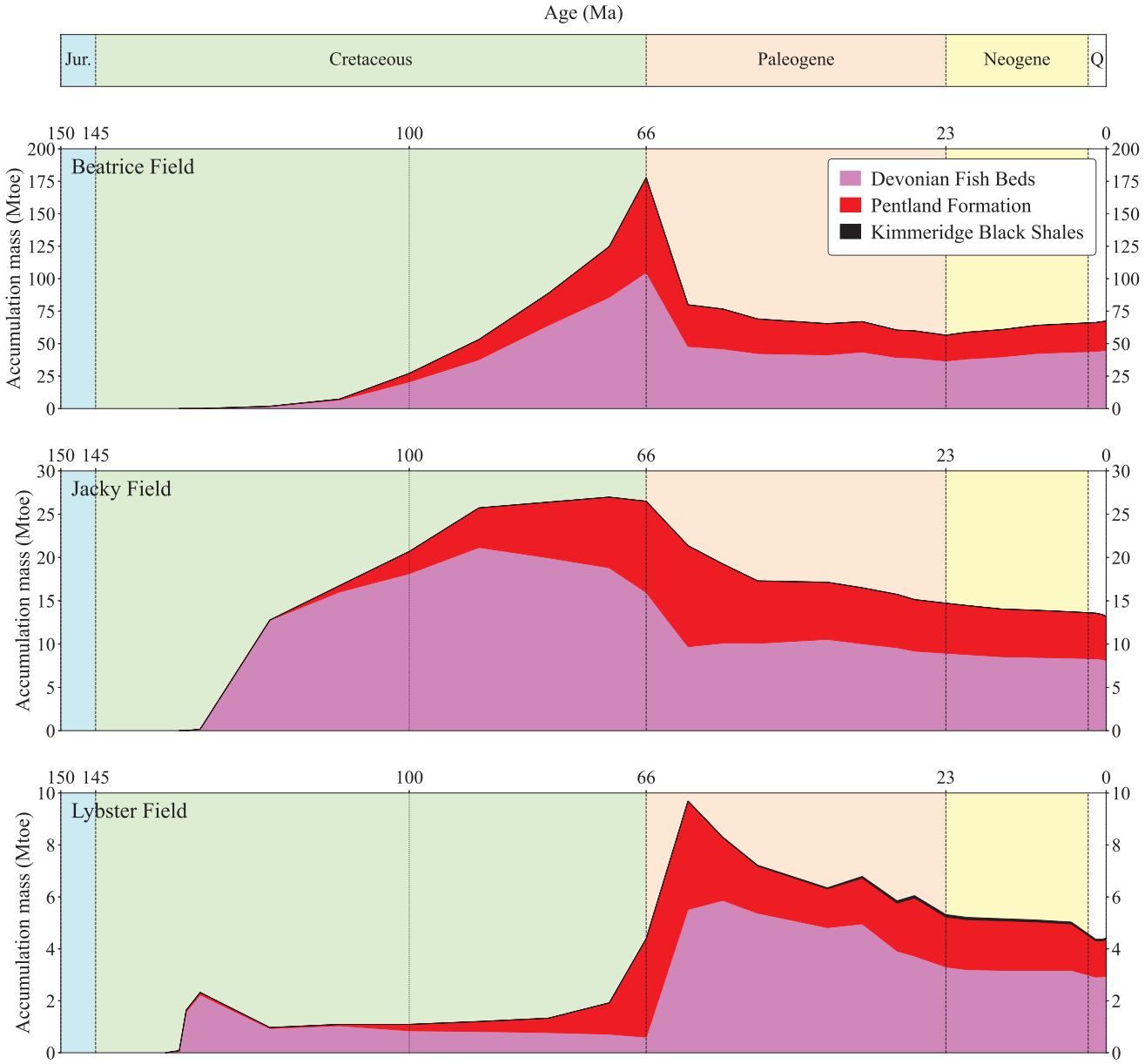


Figure 7.15: *Time plot showing the filling history, in mass (million tons of oil equivalent) of the three known accumulations in the IMF – Beatrice (top), Jacky (middle) and Lybster (bottom) Fields. The fields filled at varying rates throughout geological time, post-deposition of the sealing Heather Formation, with the filling histories split into the hydrocarbon components and their relative contributions, as calculated by the final model produced in the BPSM.*

23 Ma, showing how critical the faults are in both filling and leaking of Lybster Field.

In the central-IMF fields (Beatrice and Jacky), once the large loss of hydrocarbons occurs after 66 Ma, the hydrocarbon volumes and mixing ratios remain relatively stable until the faults close at 23 Ma, and in the case of Beatrice Field, this fault closure leads to marginal continuation of filling. This pattern is not reflected in Lybster Field, as discussed, which sees a continued loss of hydrocarbons that were initially charged through fault opening. However, the amount of hydrocarbons lost during the time period is roughly similar across the three fields. The steady decline in volumes beyond this initial loss within the central-IMF fields suggests that whilst the faults are the cause of the main loss of hydrocarbons in the region, the fields are not fully constrained by fault activity, although any hydrocarbons charging the fields during this open fault period between 66-23 Ma are lost. The large volume of lost hydrocarbons from faults is supported by Parnell *et al.* (2017) and Peters *et al.* (1998) who identified IMF-type oils in fault breccias onshore to the north of the IMF. At the peak filling of each field, at 66.01 Ma for the central-IMF fields and at 60 Ma for Lybster, the fields are filled to several multiples of the final, present day total (Table 7.7; Figure 7.16). In Beatrice Field, the present day simulated hydrocarbon volume of 481 Mboe is just over a third (37.9 %) of its peak filling volume, 1270 Mboe, which is a similar scenario in both Jacky and Lybster Fields, where Jacky loses just over half of its peak filling volume, with a final volume 49.7 % that of its peak, and and Lybster's present day simulated volume of 32 Mboe is 46.4 % of the field's maximum simulated volume of 69 Mboe (Table 7.7).

Table 7.7: *Table showing the basin and petroleum systems model simulated hydrocarbon masses (in Mtoe) and equivalent calculated volume (in Mboe) at both present day and at the peak of hydrocarbon charging, at 66.01 Ma, prior to faults opening during the late-stage uplift event in the IMF. Volume calculations are based on the conversion rate of 1 toe = 7.142857 boe.*

Hydrocarbon Field	Final hydrocarbon mass (Mtoe)	Peak hydrocarbon mass (Mtoe)	Final hydrocarbon volume (Mboe)	Peak hydrocarbon volume (Mboe)	Relative hydrocarbon loss (%)
Beatrice Field	67.32	177.83	481	1270	37.9 %
Jacky Field	13.19	26.49	94	189	49.7 %
Lybster Field	4.42	9.69	32	69	46.4 %

MIGRATION MIXING HISTORY

As discussed in Section 7.4.1.2, distinct separations can be made between the migration mixing types used to charge the different known accumulations. Whilst this showed that Beatrice Field at present day shows a hydrocarbon charge comprised of predominantly proximally migrated hydrocarbon, compared to the more even proximal-deep basin split seen in Jacky and Lybster Fields, analysis of the charging through time shows that this migration mix was not consistent throughout the fields' history. As Figure 7.15 has shown, the fields charge broadly in the same mixing ratios through their filling history, with a high Devonian Fish Bed component early before the Pentland Formation begins to influence the mix after approximately 110 Ma, however to fully understand the proximal-deep basin mix within each source rock, further refinement is necessary.

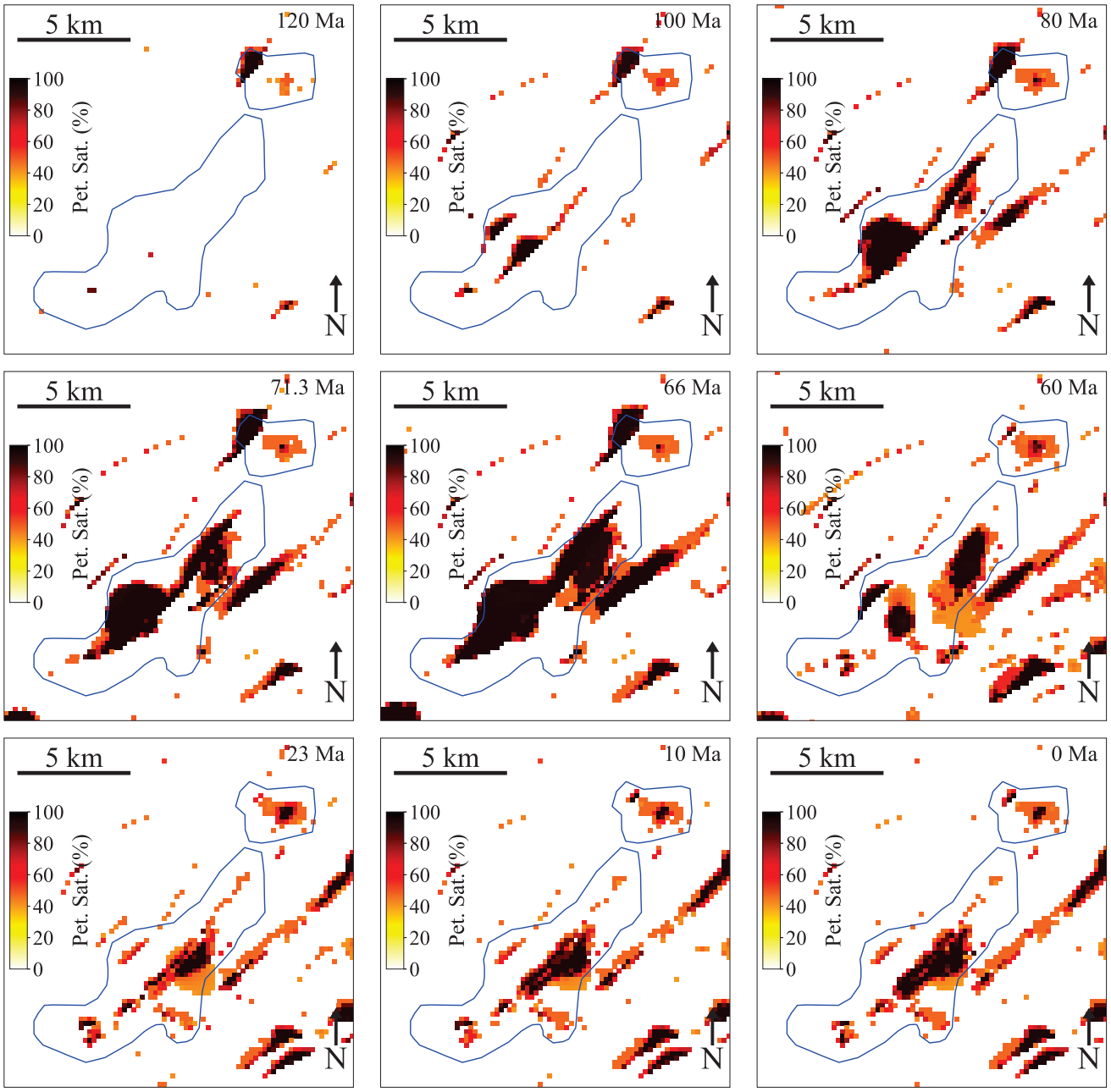


Figure 7.16: *Series of maps showing the changes in petroleum saturation percentage, above a threshold of 30 %, across the Beatrice and Jacky Field region of the IMF through geological time. The maps show the early stages of charging (120 Ma), through to the peak of filling (66 Ma), the significant losses post-uplift commencement, and then through to present day.*

In the Beatrice Field, the proximal- and deep basin-migration charge mix is heavily proximal-influenced, with an early dominance by proximal Devonian hydrocarbons, followed by an increasing amount of the other migration types (Figure 7.17). Prior to the faults opening at 66 Ma, the mix sees an early proximal dominance followed by an increasing amount of deep-basin influence, which peaks at 90 Ma, before slowly decreasing, and seeing a rapid drop when the faults open at 66 Ma. Post-fault opening, the mix of migration methods remains relatively stable, but the fault openings sees a small increase in proximal Devonian hydrocarbons and somewhat large increase in proximal Pentland hydrocarbons, whilst the influence of both deep-basin hydrocarbons diminished (Figure 7.17). This suggests that either the deep basin-migrated hydrocarbons leaked out via faults when the faults opened, or that they were

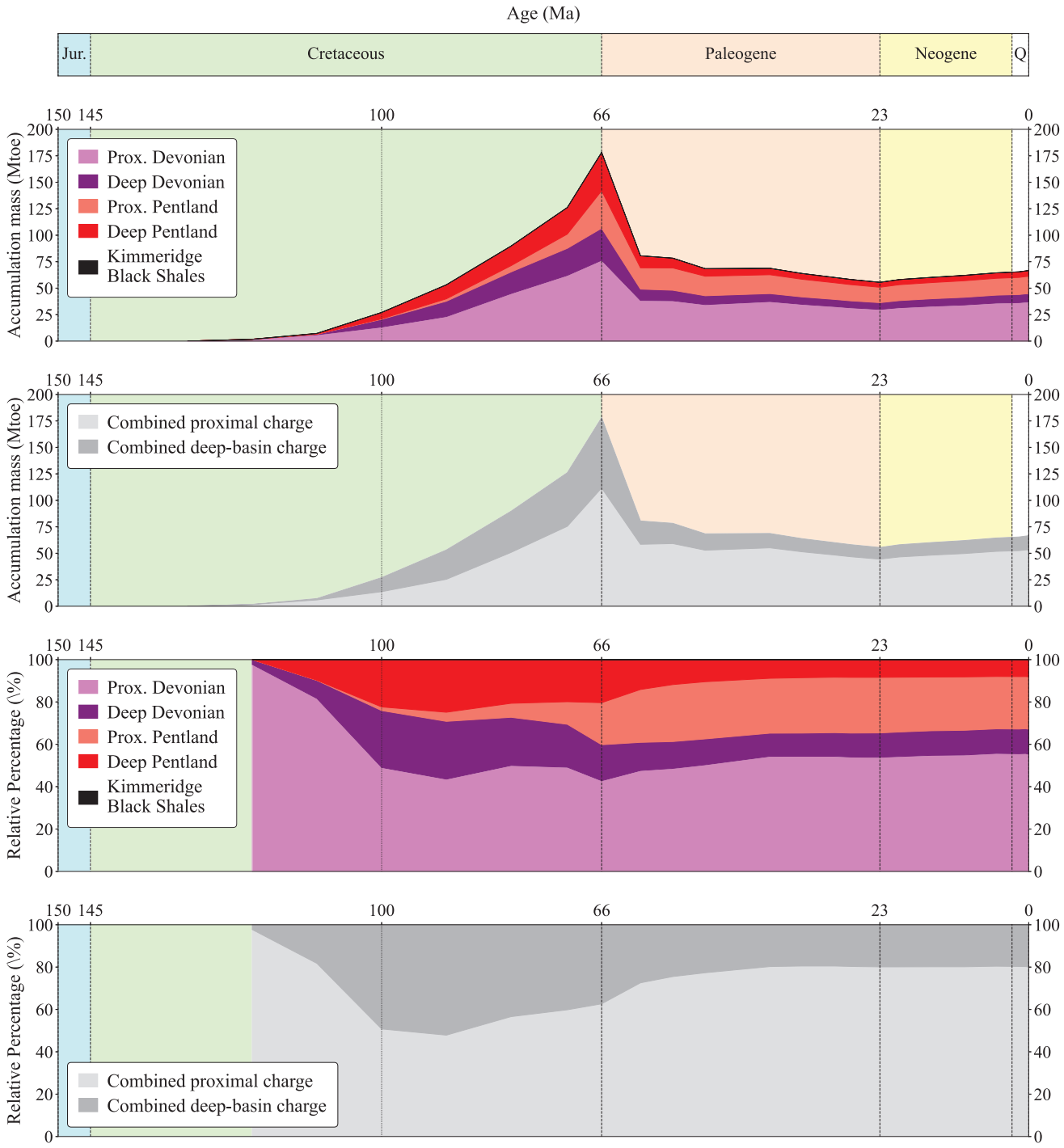


Figure 7.17: *Time plots from Beatrice Field showing the proximal and deep-basin migration mixing of the Devonian Fish Beds and Pentland Formation through time. The plots show both the regions and source rocks of the IMF where hydrocarbons migrated from and the combined totals of each migration region, in accumulated mass and relative percentages. The influence of deep-basin hydrocarbons is greatest prior to the opening of the faults at 66 Ma, before the dominance of proximal charge becomes clear.*

displaced by proximal-sourced hydrocarbons that migration up faults in the region to charge the field, or a combination of both. What is clear from the migration mixing analysis is that when the faults open, all types of sourced hydrocarbons see massive losses.

Jacky Field shows somewhat similar behaviour to Beatrice Field with its migration mixing through time, with an initial dominance by Devonian-sourced hydrocarbons, both proximal and deep-basin, prior

to more Pentland influence post-100 Ma (Figure 7.18). However, in the early charge of the field, prior to 100 Ma, where Beatrice experiences a dominance of proximal Devonian charge, Jacky sees a much greater influence from deep-basin migrated Devonian hydrocarbons. This suggests that Beatrice Field is initially sourced through more vertical migration than Jacky, which experiences a more lateral charge in its early stages. Post-100 Ma, when the influence of both Pentland methods increases, patterns between

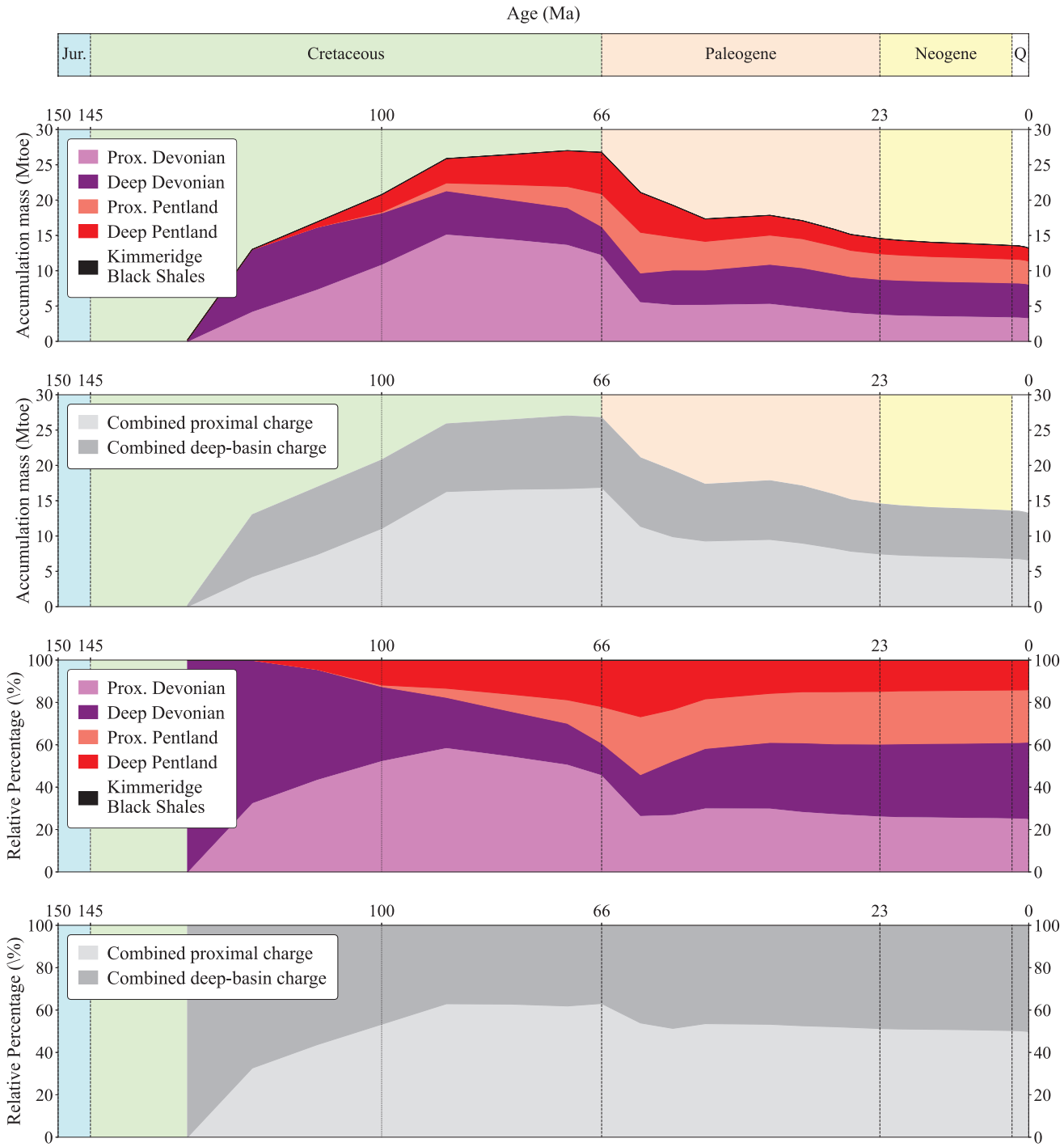


Figure 7.18: *Time plots from Jacky Field showing the proximal and deep-basin migration mixing of the Devonian Fish Beds and Pentland Formation through time. The plots show both the regions and source rocks of the IMF where hydrocarbons migrated from and the combined totals of each migration region, in accumulated mass and relative percentages. The relative influence of both migration types is somewhat consistent through the charge history after the initial dominance of deep-basin Devonian, with the migration mix post-66 Ma being relatively even across.*

the migration methods in Jacky Field approximately match those of Beatrice, however post-66 Ma, when Beatrice sees a small increase in proximal Devonian charge, Jacky experiences a more deep-basin Devonian influence increase that sees a marginal decrease in proximal Devonian influence.

In comparison to the central-IMF fields, the charging of Lybster Field occurs post-fault opening at 66 Ma, with this reflected in the migration mixing (Figure 7.19). The field sees a slow accumulation rate

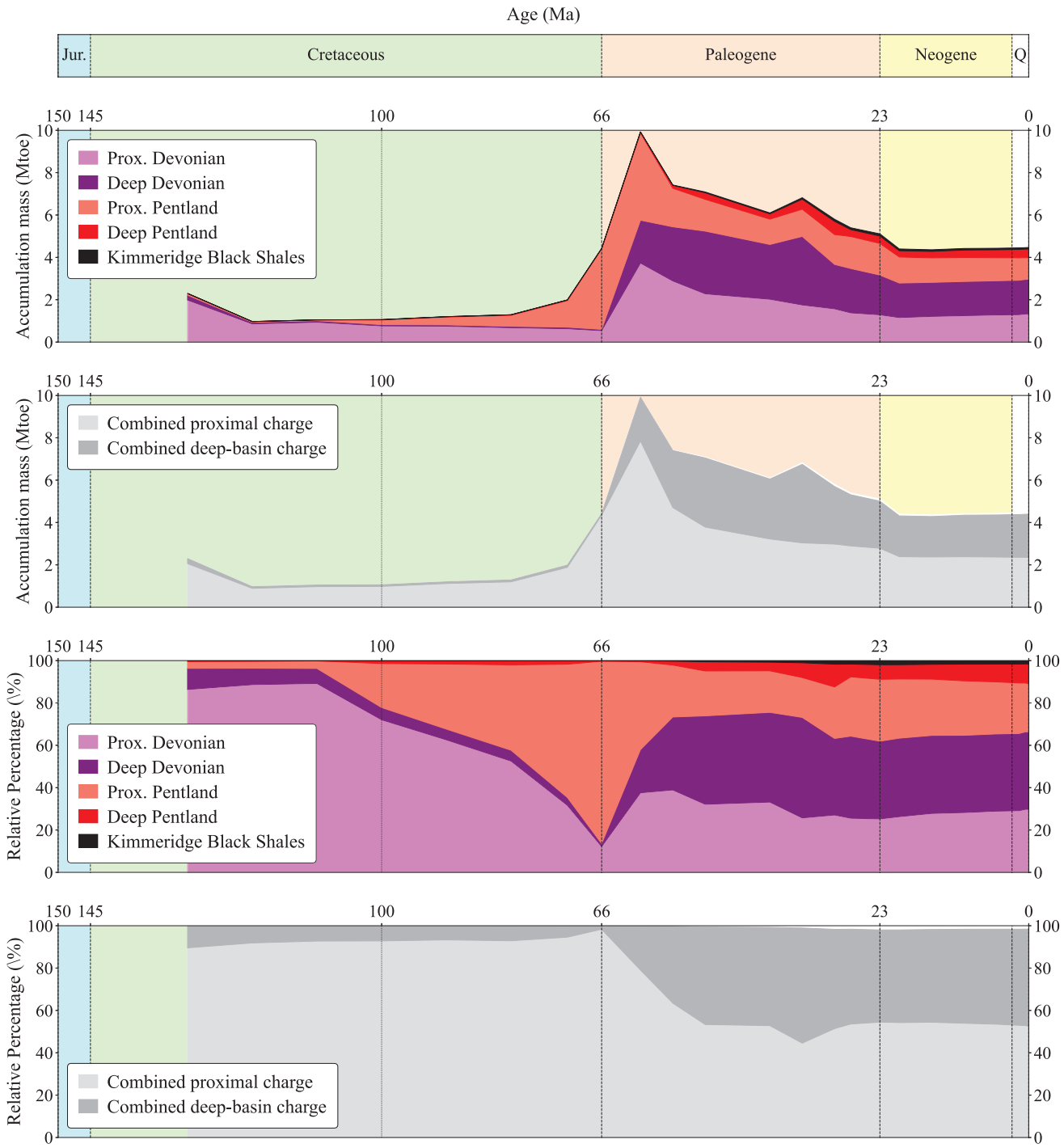


Figure 7.19: *Time plots from Lybster Field showing the proximal and deep-basin migration mixing of the Devonian Fish Beds and Pentland Formation through time. The plots show both the regions and source rocks of the IMF where hydrocarbons migrated from and the combined totals of each migration region, in accumulated mass and relative percentages. There is a near-total dominance on the charge by proximal migration until the faults open at 66 Ma, when the deep-basin migration charge enters and the two combine to create a near-even mix.*

prior to 66 Ma, where early proximal Devonian dominance gives way to proximal Pentland dominance by 66 Ma, with minimal deep-basin hydrocarbon influence. Once the faults open and the field reaches maximum fill at 60 Ma, the migration mix sees a rapid increase in proximal migration influences, but also a distinct influx of deep-basin hydrocarbons, reflected in the rapid increase in deep-basin Devonian hydrocarbons from 66 Ma which remain stable until present day. Post-peak fill, as with the other fields, Lybster sees a relative stability in the migration mix, despite the loss of hydrocarbons due to fault-derived leakage.

In summary, all fields see a stability in the migration mixing ratio once the faults have opened at 66 Ma, however, all three have distinct differences. Whilst Beatrice Field sees its greatest influence of deep basin-sourced hydrocarbons prior to the faults opening, and having a present day migration mix dominated by proximal-sourced hydrocarbons, the adjacent Lybster Field sees a much more deep basin-sourced hydrocarbon mix. In comparison, Lybster Field is heavily reliant on the fault opening and late-stage uplift to both charge the field and remove large volumes of hydrocarbon, but it experiences a mirror in influence to the central-IMF fields. This mirroring involves little to no deep basin-sourced hydrocarbons charging Lybster Field until the faults open and cross-fault migration can occur over the GGF, at which point the field is rapidly charged with both proximal and deep-basin hydrocarbons, and the mixing ratio between the two becomes more even.

7.4.1.4 | POSSIBLE UNKNOWN ACCUMULATIONS

Within a BPSM, identifying unknown but potentially present accumulations of hydrocarbons (unknown accumulations; UA) is a key aspect. Due to the age of the exploration that occurred in the IMF, initially in the 1970s through to the 1990s, basin and petroleum systems modelling was not a tool available at the time, or sufficiently widespread to be used during the later years of development. As such, the work in this study can be used as a tool to aid the identification of UAs and offer some potential new discoveries within the IMF that previously may have been missed. Several components of the BPSM are required to successfully identify potential accumulations, but most critically a lack of previous exploration in the area, through the drilling of wells, and a sufficient accumulation of hydrocarbons (over 10 Mboe) is required. Furthermore, potential accumulations that have been drilled before have been ignored as these have either been decreed as dry and not hydrocarbon-bearing, or not pursued. In this study, fifteen potential UAs have been identified and investigated, with these potential accumulations split into location across the basin (Figure 7.20; Table 7.8).

Of the fifteen UAs, five can be considered too small to be economically viable, with UAs 2, 7, 11, 12 and 13 all showing estimated accumulated volume less than 30 Mboe. Whilst initially UA 13 was selected for its location within the same region and geology as both Lybster Field and UAs 11 and 12, it lacks any distinct accumulated volume, despite the reservoir unit cells having simulated petroleum saturations. UA 2 and 7, alongside UA 9, are likely phantom accumulations, formed as artifacts of the conversion between seismic interpretations and surface production in Schlumberger's Petrel, and thus can be discounted. This artifact is also the likely cause of the very large phantom accumulation to the east of UAs 9 and 10, which has been drilled and was not oil-saturated.

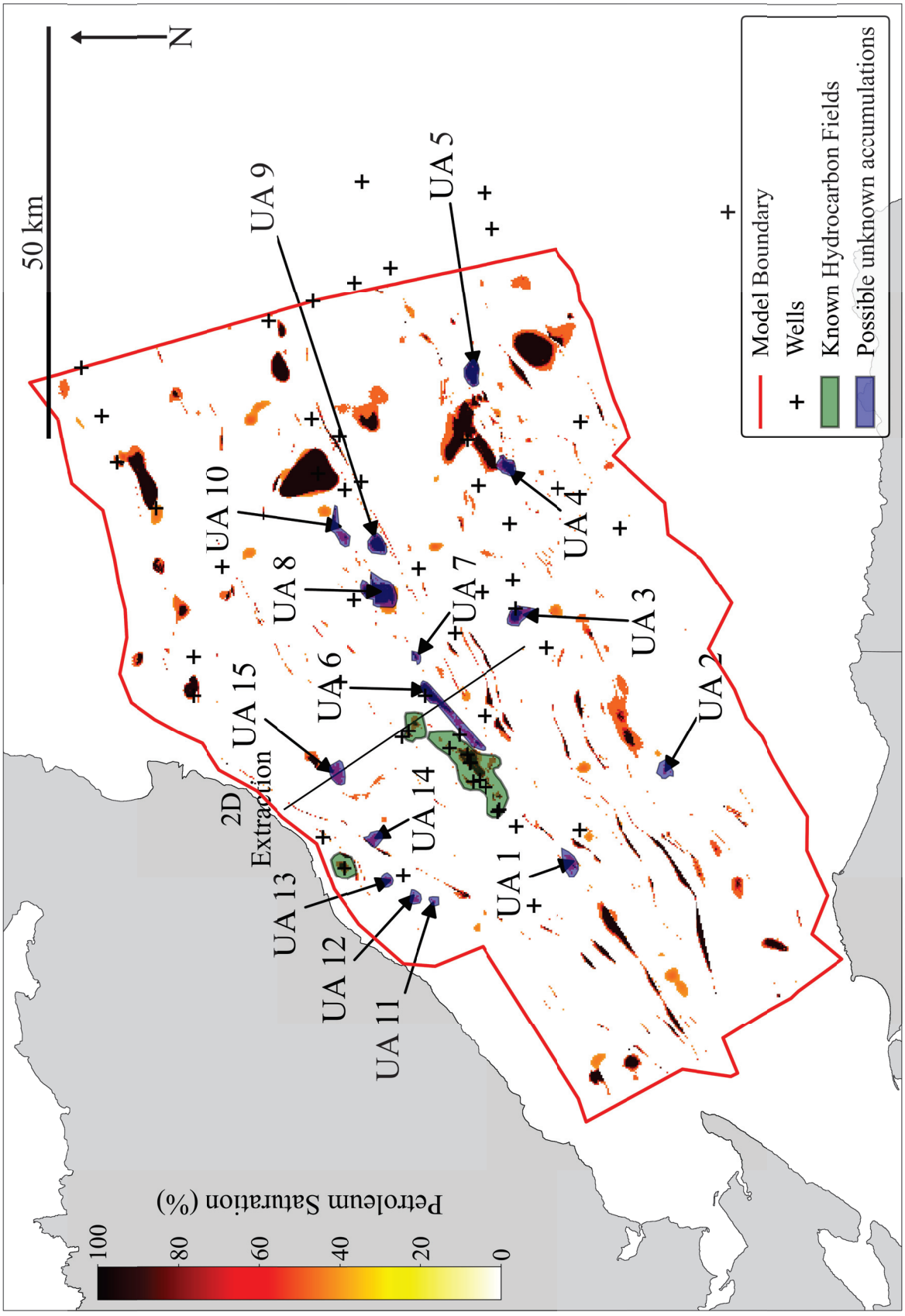


Figure 7.20: *Map of the study area within the IMF, containing a boundary identifying the region of the BPSM, showing petroleum saturation percentages of reservoir formations within the basin. Highlighted on the map are the known hydrocarbon accumulations (Beatrice, Jacky and Lybster Fields), the fifteen potential unknown accumulations identified in this study, and the 2D line extracted and shown in Figure 7.22. UA = unknown accumulation.*

Table 7.8: *Table outlining the properties of the various potential previously-unidentified accumulations highlighted within the BPSM of the IMF in this study. Volume calculations are based on the simulated mass, converted to barrels of oil through the conversion rate of 1 toe = 7.142857 boe.*

UA number	Accumulation mass (Mtoe)	Accumulation vol. (Mboe)	Accumulation contribution %			Comment
			Devonian	Pentland	Black Shales	
1	10.03	72	81	19	0	Good potential
2	3.94	28	100	0	0	Too small
3	15.89	114	79	21	0	Good potential
4	15.18	108	56	44	0	Phantom
5	12.58	90	78	22	0	Phantom
6	38.57	276	91	9	0	Unclear
7	1.59	11	88	12	0	Too small
8	39.04	279	70	30	0	Phantom
9	25.51	182	8	92	0	Phantom
10	12.37	88	44	56	0	Phantom
11	1.97	14	32	64	4	Too small
12	1.57	11	36	61	3	Too small
13	0	0	-	-	-	Too small
14	6.52	47	48	31	21	Phantom
15	15.48	111	82	16	2	Best potential

UA 3, adjacent to the oil-saturated Well 12/27-1, is a good potential accumulation, as it is estimated to have just over 100 Mboe (114 Mboe) of accumulated hydrocarbons, mixed in an 79:21 ratio between Devonian and Pentland source rocks, respectively. In comparison, UAs 4 and 5 sit in the depths of the Smith Bank Graben, and form solely due to their proximity and association to the Lossiemouth Fault, within no structural high, and as discussed, the faults remove extensive volumes of hydrocarbons during the late-stage uplift, thus these are likely phantom accumulations also. UA 6 is a complex potential accumulation, as despite it being situated in a structural high similar to that which forms Beatrice Field, it has been drilled by Well 12/21-4, which has no evidence of oil saturation, declared a dry well. However, the BPSM produces an accumulation along the length of the structure, with a very large accumulation (275 Mboe), but a very different mixing ratio of that seen in Beatrice Field, approximately 90:10 % Devonian:Pentland. The accuracy of UA 6 as an accumulation is very difficult to ascertain, as it is possible that Well 12/21-4 did not pass through the accumulated hydrocarbons, as it was not drilled into the peak of the structure, however it is also possible that the accumulation is phantom, and forms as a result of the structure, but was not charged due to one of any number of reasons beyond the ability of the model to determine. UAs 1, 8 and 10 show more potential as accumulations that others that run parallel to the central basin faults, as they all are located along the same structure, and same fault system as Beatrice and Jacky Fields. Whilst UA 1 is at the very end of the region of influence of the Beatrice and Smith Bank Faults, UAs 8 and 10 do not, however UA 8 is located on the opposite side, the footwall side, of the Beatrice Fault, thus is likely a phantom accumulation,

as UA 10 is also likely to be, however this is less conclusive. UAs 11, 12 and 13 all sit along the same structural and lithological line as Lybster Field, however unlike Lybster Field, as discussed, show very small accumulation volumes. Hypothetically, should these accumulations exist, they could be extracted in similar methods to Lybster Field via wells drilled from onshore, however this is still likely to produce very limited economic success, with a total estimated volume of approximately 25 Mboe. In comparison, UA 14, similarly to UA 4 and 5, are located in the footwall of a basin-forming fault, in this case the Great Glen Fault, thus is unlikely to be accurate in the same way as those other accumulations, with the GGF most likely removing the hydrocarbons during the late-stage uplift.

UA 15 shows strong potential for an accumulation, as whilst is sits against a fault, it is in the hanging wall, and thus is less likely to see as extensive hydrocarbon losses as the other UAs analysed. Furthermore, it has a large enough estimated volume (110 Mboe) to possibly be economically viable (Table 7.8; Figure 7.21). The mixing ratio of the accumulation is heavily Devonian-controlled (82:16 % Devonian:Pentland at present day), with minor Kimmeridge Clay Black Shale influences. The location of UA15 (Figures 7.20 & 7.22), in the fringes of Great Glen Sub-basin, provides it direct access to the most mature regions of the source rocks, and its position against a fault offers it charging capabilities similar to those that charged Beatrice and Jacky Fields (Figure 7.22). Consequently, UA 15 has the strongest potential to be an as-yet unproven accumulation in the IMF, determined by this study.

The mixing ratio and charging history of UA 15 follows the trends of the known fields, through early stage Devonian dominance in the charge, followed by increasing Pentland contributions to peak filling at 66 Ma. Following the opening of the faults, hydrocarbon volumes decrease but the mixing ratio does not vary extensively. One difference in the mixing history of UA 15 compared to the known fields is that the steady decline of hydrocarbon volume is predominantly Pentland-sourced hydrocarbons. At peak filling, 66 Ma, the mixing ratio was 75:23:2 Devonian:Pentland:Black Shales, however by present day this ratio had altered to 82:16:2, thus the relative volume of Devonian hydrocarbons showed little to no fluctuation or loss, but the Pentland hydrocarbons did (Figure 7.21).

Figure 7.22 shows how the structure of UA 15 is similar to Jacky Field, however mirrored, being located on the northern flank of the Great Glen Sub-basin compared to the south flank position of Jacky Field. The highs in which the reservoir formations are located are trapped against a large-scale fault,

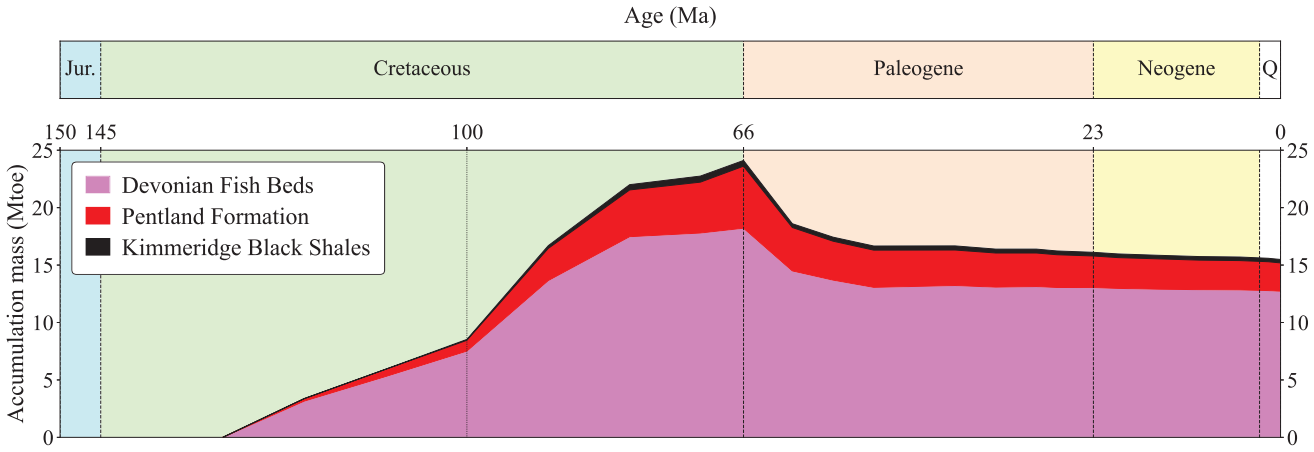


Figure 7.21: *Time plot showing the filling history of the unknown accumulation UA 15, in the northern region of the Great Glen Sub-basin, split into the relative hydrocarbon source rock contributions.*

again similar to Jacky Field, however as Table 7.8 indicates, it has a significantly smaller Pentland Formation contribution. This reduced Pentland contribution is likely due to the shape of the Great Glen Sub-basin and its position within it, where the deepest point of the reservoir formations in the sub-basin are to the immediate south of UA 15, therefore all Pentland-generated hydrocarbons from this point towards the south will preferentially migrate up-dip towards Jacky Field.

7.5 | DISCUSSION

7.5.1 | MODELLING IMPLICATIONS ON THE IMF

The BPSM in this study has proven that the Devonian and Pentland source rocks within the IMF are the dominant contributors to the hydrocarbons in the basin's petroleum system. The Kimmeridge Clay Black Shales, whilst producing minor hydrocarbon volumes that contribute to the Mid-Jurassic reservoir intervals, they do not exert a large influence over the known accumulations in the IMF. With the source rocks being below and within the reservoir unit, the majority of migration is vertical and direct expulsion from the source into the reservoirs.

The main influence on the petroleum system of the IMF is the late-stage subsidence, uplift and tilting with associated fault activity in the Cretaceous and Cenozoic. This was proved by fluctuating the properties of the faults, and varying their ability to trap or migrate fluids. Consequently, it can be hypothesised that should the faults have impacted the system less, and tilting of the basin had been less extensive, then the fields within the IMF could have accumulated much greater volumes of hydrocarbons. This was evidenced by the peak filling of Beatrice Field in the BPSM, at 66 Ma prior to the uplift, which was over 1200 Mboe, and the final filling volume of the field being less than 500 Mboe. This roughly 60 % decrease undoubtedly impacted the viability of the IMF as a petroleum system as productive and widespread as the other regions of the North Sea.

The hydrocarbon loss due to trap malfunction or fault leakage during the late-stage uplift could be the cause of the double-OWCs present within the Beatrice Field, seen in the cores. The Pentland Formation, alongside the Lady's Walk Shale and Mid Shale could have locally trapped bodies of hydrocarbons in the region as the faults opened and large volumes of hydrocarbons were lost. Whilst this hypothesis can not be directly proven, it is a strong possibility, as localised hydrocarbon trapping through small structures or lithological traps are common in petroleum systems, and the past extensive filling of Beatrice Field is proof that there were sufficiently high enough volumes of hydrocarbons in the region to trap.

7.5.2 | COMPARISONS TO PUBLISHED WORK

The BPSM-calculated mixing ratios of the hydrocarbons in the three fields of the IMF follow the geochemical analysis carried out by Peters *et al.* (1989), whilst both Aalund (1983) and Mackenzie *et al.* (1983) agree with Peters *et al.* (1989) that there is a lack of Kimmeridge Clay influence in the hydrocarbons, which is also supported by the BPSM calculations in this study. Whilst there is minor Kimmeridge Clay Black Shale presence in the basin, is is sufficiently small enough to not impact the geochemical composition of the hydrocarbons.

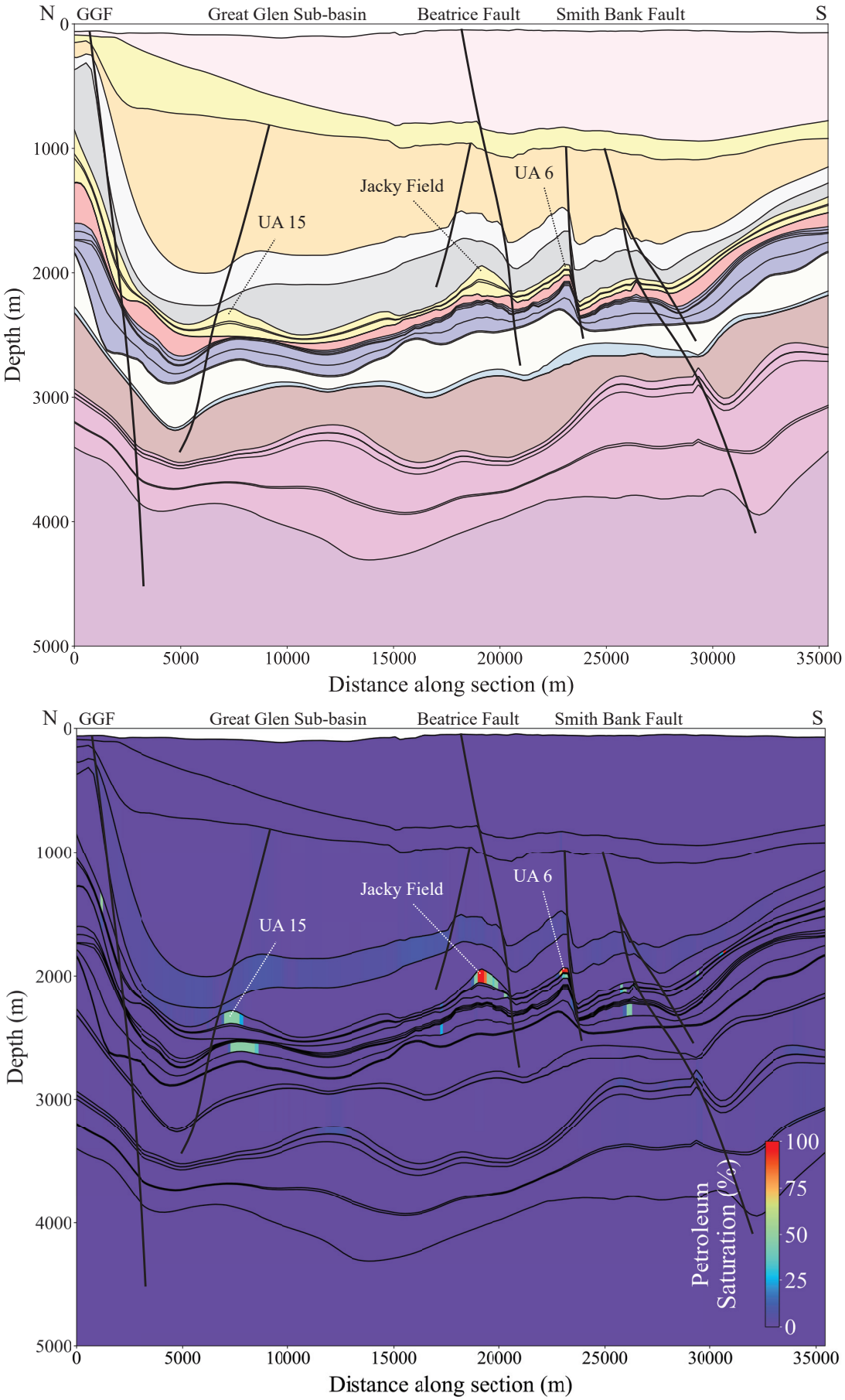


Figure 7.22: *Two 2D lines extracted from the central northern region of the IMF, see Figure 7.20, across the Great Glen Sub-basin, highlighting UAs 6 and 15, and Jacky Field. The upper 2D extraction shows the lithologies and structures present, and the lower 2D extraction shows the petroleum saturation of the section, highlighting the locations of accumulated modelled hydrocarbons.*

Prior to this study, Greenhalgh (2016) states that the source regions and migration history of the IMF has not been successfully accomplished. Hogan *et al.* (1978) suggests that long range Pentland migration is unlikely due to its low mobility caused by a high waxy content, and this is supported by this study's BPSM, especially for Lybster Field, which sees a very small contribution of deep-basin, laterally migrated Pentland Formation hydrocarbons, whilst both Beatrice and Jacky Fields show marginally greater deep-basin Pentland contributions, it is still the smallest contributor to the fields, bar the Kimmeridge Clay Black Shales. This is in direct opposition to Marshall (1998) who suggests that Beatrice Field-adjacent Devonian source maturation is unlikely, whereas this study's BPSM suggests that proximal Devonian charging is possible, and is the greatest contributor to the field. However, this study does agree with Marshall (1998) in the relative lack of maturation of the Devonian to the south and south west of Beatrice Field. Curran (1987a,b) and Underhill (1991) offers the likelihood that Devonian hydrocarbons could experience long-range migration, which is supported by this study which shows deep-basin Devonian sourcing of the fields. However, this study disagrees with the suggestion by Curran (1987a) that the region around Well 12/27-1 reaches sufficient Devonian maturity to be a source kitchen, where, whilst this region does reach some maturity, there are more preferential regions, such as the sub-basins, which is the theory of Underhill (1991).

Whilst Parnell *et al.* (2017) and Peters *et al.* (1998) attempt to constrain the location of IMF source kitchens through geochemical analysis, this study and its BPSM shows that large swatches of the Devonian in the IMF reach maturity, matched by the Pentland Formation reaching maturity most successfully in the Great Glen, Wick and Lossiemouth Sub-basins. This suggests that the deepest regions of the basin are most likely to be the optimal source kitchens, however the main impact on the petroleum system is not the location of greatest maturity, but the fault activity caused by rifting and instability. This theory is supported by Aydin (2000), Jonk *et al.* (2003) and Parnell *et al.* (2017) who all investigated the presence of fault-emplaced high-pressured fluids.

7.5.3 | Uncertainties and assumptions

Prior to the modelling, the depth maps were produced from the seismic interpretation carried out in this study (Chapter 5). As discussed, the interpretations were carried out on seismic data that was depth converted before being supplied for this study, and as such, there is a degree of uncertainty in the seismic dataset used to create the model. Whilst there are unlikely to be large-scale errors in the depth conversion, as the seismic-well ties show good correlation between the drilled wells and the seismic data, there could be erroneous areas of data that are not clear and obvious, however this is not something that can be easily corrected without the original time-domain seismic data.

The main uncertainties in the model creation revolving around the inputs for the BPSM. Whilst depth maps and fault presence are open to minor assumption based on the supra-reservoir sequence seismic resolution, and interpretations of seismic data is often subjective, these components of the models are more stable than those requiring scenario testing. All of the scenario-tested inputs are open to variance as a result of the potential for what are deemed correct results, but are based on compounded assumptions. For example, to create a similar hydrocarbon generation total to that within the final model in this

study, a decrease in heat flow and increase in TOC, or *vice versa*, could theoretically produce similar results. Whilst these variables were tested and constrained to well and core reports, alongside published estimates, they are still constrained estimates not guaranteed accurate values.

The main uncertainties in the model outputs are the fault properties and the facies continuity within formations. As the properties of the faults impact the volumes accumulated within the known hydrocarbon fields the most, these are crucial to the BPSM. As discussed in Section A.3.0.7, the fault properties were extensively tested and the confidence in the final choice is high, however the potential for further analysis via fault investigation would increase certainty. Furthermore, the upscaled nature of BPSMs lead to difficulties in accurately defining how facies and lithologies vary within a formation. Variations in facies, especially the sand and clay ratios in the Pentland Formation would have significant influences on the hydrocarbon source contributions in different areas of the basin, as well as impacting both migration routes and hydrocarbon generation. This is also reflected in the Brora Coal, as coals are very rarely continuous across large swathes of land, thus the Brora Coal is unlikely to be as consistent across the IMF as it is portrayed within the BPSM. Refining these variables is only possible through extensive drilling and coring of the basin, followed by sample analysis and core logging, leading to very high costs and time requirements.

7.5.4 | Implications on magnetic mineral analysis

The modelling undertaken in this study, whilst occurring independently, can aid the understanding of the magnetic mineral assemblages across the IMF that were discussed in Chapter 6. The understanding of the petroleum system through the BPSM allows for a base of evidence from which conclusions can be drawn between the petroleum system and the magnetic mineral assemblage. This will be discussed in greater detail in Chapter 8, however initial implications are outlined here. Firstly, the source rocks within the IMF are different to the majority of the hydrocarbon fields in the rest of the North Sea, with the IMF being dominated by Type I Devonian and Type II-III Pentland source rocks, compared to the Type II Kimmeridge Clay in the rest of the North Sea. This offers the ability to compare and contrast the magnetic mineral assemblages between the work in this study, and the work done in others, such as Abdulkarim *et al.* (2022a,b,c), Abubakar *et al.* (2020) and Badejo *et al.* (2021a,b,c).

Beyond comparisons to petroleum systems outside of the study area, analysis within the IMF is also possible. With the ability to estimate mixing ratios of the multiple hydrocarbon sources, this could be used to investigate any potential correlation between relative magnetic mineral presence or abundance and the different hydrocarbon sources. If there are clear differences between the magnetic minerals associated with different source rocks or kerogen types, then these could be used in correlation with the BPSM to narrow down the mixing ratios of hydrocarbons in the accumulations across the IMF.

7.6 | Conclusion

In conclusion, the BPSM created and analysed in this study confirms the literature on the IMF that indicates the petroleum system is charged by Devonian and Pentland source rocks with limited influence from the Kimmeridge Clay Black Shales (Linsley *et al.*, 1980; Peters *et al.*, 1989; Stevens,

1991). Furthermore, the mixing ratios between these hydrocarbon sources, as derived from analysis of the BPSM, align with the geochemical analysis carried out on the hydrocarbons and kerogens of the IMF by Peters *et al.* (1989) and Peters *et al.* (1998). The estimated mixing ratio of the hydrocarbons in the IMF by Peters *et al.* (1989) is 60:40 % Devonian:Pentland, which is reflected in similar mixing ratios within the known accumulations in the basin, of Beatrice, Jacky and Lybster Fields. The mixing ratios of these three accumulations are 66:34 %, 61:39 % and 67:32 % Devonian:Pentland, respectively, with Lybster Field having a minor 1 % Kimmeridge Clay Black Shale influence.

The model suggests that the majority of hydrocarbons charged vertically, both directly through the intermediate formations between the Devonian and the Jurassic reservoir sequences, but also vertically surface-ward through the numerous faults in the basin. Furthermore, the Pentland Formation, located in the middle of the reservoir sands, expel hydrocarbons vertically, both surface-ward and downward, and likely also migration laterally up-dip into the structural highs the reservoir sands occupy. The most dominant geological control on the hydrocarbon migration, filling, and accumulation is the pervasive faults across the basin, as these have been proven to remove vast volumes of hydrocarbons from the accumulations produced prior to 66 Ma. The loss of hydrocarbons caused by the faults and associated trap malfunction is likely why the IMF is not as productive a petroleum system as the other regions of the North Sea.

Beyond the three known accumulation in the basin, this study has identified several potential previously unidentified hydrocarbon accumulations of potential economic value, with the accumulation with the greatest potential located on the opposite flank of the Great Glen Sub-basin to Jacky Field. This unknown accumulation, UA 15, has a similar charge history pattern to the known accumulations, but with a significantly greater dominance of Devonian-sourced hydrocarbons, with a mixing ratio of 82:16:2 Devonian:Pentland:Black Shales. This Devonian dominance is likely a result of limited lateral migration of Pentland Formation from the Great Glen Sub-basin into the accumulation, with the majority of these hydrocarbons migrating to fill Beatrice and Jacky Fields.

By proving the contributions of multiple sources and their varying inputs into the hydrocarbon accumulations in the IMF, the model provides an area of focus within the magnetic mineral analysis carried out in this study. Comparisons between the magnetic mineral assemblages in the IMF and other regions of the North Sea can further expand on the understanding of the connections between hydrocarbons and magnetic minerals in different environments. Furthermore, the potential for utilising magnetic minerals to understand relative source rock contributions via varying magnetic mineral presence can be investigated through this study. In summary, the BPSM produced within this study both concurs with the dominant literature on the basin regarding the source rock components of the petroleum system, as well as successfully accumulating hydrocarbons in the correct regions and with mixing ratios similar to the published estimates derived through alternative techniques.

CHAPTER 8 | DISCUSSION

8.1 | INTRODUCTION

To achieve the aims of this study, set out in Chapter 1, it is necessary to correlate the results and findings from the magnetic mineral analysis (Chapter 6) to the basin and petroleum systems modelling (BPSM; Chapter 7), to identify the relationships that connect the two different disciplines. Whilst each discipline has stand-alone discoveries and conclusions, to fully achieve the objectives of this study, developing the interconnections between them is crucial, and is what this chapter covers. This chapter combines the previous chapters' analyses to build knowledge on the Inner Moray Firth's (IMF) petroleum system and how it is related to, and constrained by, the magnetic mineral behaviour, and further compares these findings to other systems and research.

8.2 | WELL-SCALE MAGNETISM-BPSM CORRELATIONS

Magnetic mineral analysis shows limited patterns in magnetic mineral behaviour across the IMF on a basin-scale (Chapter 6), however the analysis shows clear patterns of behaviour at well-scale, not only within the magnetic mineral assemblages but also in magnetic mineral behaviour around oil-water contacts within the wells. To investigate the comparisons between the BPSM and magnetic analyses at well-scale, extractions from the BPSM are analysed and used to produce well-scale data from petroleum system, including hydrocarbon mixing ratios, the region's charging history and local accumulation volumes. To produce the extractions, the cells in the model where the wells are located are identified, and a three-by-three grid cell area of interest is produced (Figure 8.1). The larger area of interest is necessary to not only remove the potential for anomalous results within a single cell, but to also obtain more data around the wells, as each model cell is 200 m^2. This small area produces limited BPSM results and creates the requirement for more data, therefore, by increasing the area of interest to 600 m^2, more accurate and effective model-derived data is available.

8.2.1 | MIXING RATIOS AND MAGNETIC MINERALS

Comparisons between the hydrocarbon mixing ratios and the magnetic minerals within wells are crucial to determine how the source rocks and their relative contributions may influence the magnetic mineral assemblages in the wells across the basin. The comparisons are carried out on wells where both oil- and water-saturated samples were collected and analysed. Goethite is present in all the wells, in both saturating fluids, with this reflected in the mixing ratios that contain Devonian and Pentland hydrocarbon contributions (Table 8.1). There are no correlations between mixing ratios and siderite presence, indicating that siderite within the magnetic mineral assemblage is a result of vertical migration, not differing hydrocarbon sources. In contrast, the clearest correlation between source rock contribution and magnetic mineral presence is seen in Well 11/24a-2, which is the only well that shows Kimmeridge Clay Black Shales contribution above 1 %, with the contribution in this well >50 % (Table 8.1). This dominance of Black Shale-sourced hydrocarbons within Well 11/24a-2 is reflected in the magnetic mineral assemblage in the oil-saturated samples, which are dominated by iron sulphides. The other wells containing iron sulphides only have minor presence of the magnetic minerals, likely caused by localised

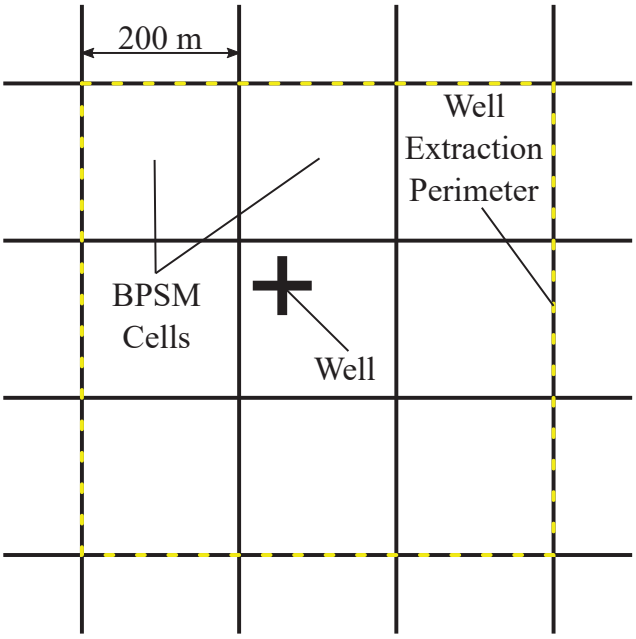


Figure 8.1: *Systematic figure outlining the method of delineating the region around each well for hydrocarbon mixing ratio analysis. The accurate extraction of a precise area around each well on a small scale within the BPSM is not possible, thus delineating the area based on the BPSM cells is the more accurate method, despite variations in distance from wells occurring in different directions.*

sulphur presence; no well has as high proportion of iron sulphides as 11/24a-2 (Table 8.1). Consequently, this enhances the connection between iron sulphides and deep marine, Type II kerogen source rocks, a connection evidenced by Abdulkarim *et al.* (2022a,b) and Badejo *et al.* (2021a,b,c).

Constraining the relationship between magnetic mineral abundance and hydrocarbon source rocks is difficult, as estimating the absolute abundance of magnetic minerals within samples is challenging. In this study, abundance was estimated through a mineral presence against total sample count, where if one of the indicator minerals (goethite, lepidocrocite or maghemite for Devonian and Pentland sources, iron sulphides for Black Shales) was present in a sample, it was counted against those samples where they did not, creating a percentage (Table 8.2). Whilst this method has drawbacks, such as sample distribution constraint, it does give an insight into the relationship. The Devonian and Pentland source-dominated oil-saturated sections of wells all have at least 50 % of samples containing one of the indicator minerals, with five of the eight wells having an indicator mineral present in over 90 % of the samples (Table 8.2). In comparison, the single well that was not dominated by a Devonian or Pentland source charge, Well 11/24a-2, shows only 27 % presence of a Devonian or Pentland indicator mineral (Table 8.2), but does have seven out of eleven samples (64 %) showing Black Shale-indicating iron sulphide presence, with this confirmed by the dominance of Black Shale-sourced hydrocarbons in the mixing ratio. The limited presence of Devonian and Pentland source indicators is reflected in the mixing ratio that shows no Devonian contribution and less than 50 % Pentland contribution (Table 8.2).

The most clear relationship between the magnetic mineral presence and hydrocarbon source rocks is related to the iron sulphide existence, which shows that the other magnetic minerals are highly sensitive to the presence of sulphur (Table 8.2). The high abundance of iron sulphides in Well 11/24a-2 (64 %;

Table 8.1: *Table summarising the hydrocarbon mixing ratios and magnetic minerals present in the wells sampled for magnetic analysis in the IMF that contain both oil- and water-saturated samples, and the dry well 12/21-4, for reference. The mixing ratios are calculated in the BPSM and the magnetic mineral presence is the percentage of samples containing the relevant magnetic mineral against the total number of samples in each well, note that minerals can occur concurrently within samples. Dashes indicate no presence of relevant magnetic mineral. Dev. = Devonian Fish Beds, Pent. = Pentland Formation, Bl. Sh. = Kimmeridge Clay Black Shales, Goe = goethite, Sid = siderite, FeS = iron sulphides (either pyrite or pyrrhotite), Lep = lepidocrocite, Mgh = maghemite.*

Well	Source mix (%)			Saturating Fluid	Magnetic mineral presence (%)				
	Dev.	Pent.	Bl. Sh.		Goe	Sid	FeS	Lep	Mgh
11/24-1	59	40	1	Oil	85	10	-	-	-
				Water	75	50	-	-	-
11/24a-2	0	49	51	Oil	23	-	64	-	-
				Water	60	40	-	-	-
11/30-2	57	43	0	Oil	60	-	-	-	-
				Water	42	8	-	8	-
11/30a-8	40	60	0	Oil	90	40	-	20	-
				Water	74	30	4	30	-
11/30a-B10	100	0	0	Oil	75	-	-	17	-
				Water	50	28	11	17	-
12/21-2	71	29	0	Oil	50	75	-	19	-
				Water	44	69	-	13	-
12/27-1	78	22	0	Oil	54	46	-	-	38
				Water	50	-	-	-	25
12/27-2	54	46	0	Oil	88	63	-	38	-
				Water	25	50	-	-	-
12/29-1	57	43	0	Oil	86	-	-	-	-
				Water	100	-	-	-	-
12/21-4	Dry Well			Water	100	-	-	75	-

Table 8.1) combines with a much lower presence of the other magnetic minerals in the samples (27 %; Table 8.2). This is in direct contrast to the other wells seen across the basin, which all show above 50 % abundance of non-iron sulphide minerals in association with low iron sulphide presence (Tables 8.1 & 8.2). This shows that the presence of sulphur within a region directly impacts the creation of magnetic minerals, either through direction formation, or alteration of other minerals.

Table 8.2: *Table outlining the comparison between the mixing ratio contributions of the Devonian Fish Beds and Pentland Formation source rocks and the relative abundance of goethite, lepidocrocite and maghemite in oil-saturated samples in wells across the IMF. The mixing ratios are calculated from the BPSM and the relative abundance is investigated through the presence in each sample of one of the three minerals, roughly equating to abundance in the magnetic mineral assemblages in each sample, as direct abundance estimates are not possible. Note that multiple minerals can occur concurrently within samples, but this does not impact the count. Dev. = Devonian Fish Beds, Pent. = Pentland Formation, Bl. Sh. = Kimmeridge Clay Black Shales, Goe = goethite, Lep = lepidocrocite, Mgh = maghemite.*

Well	Source mix (%)			Sum of Dev. & Pent. (%)	Total Samples	Number of samples showing Goe, Lep or Mgh	% samples showing Goe, Lep or Mgh
	Dev.	Pent.	Bl. Sh.				
11/24-1	59	40	1	99	16	15	94
11/24a-2	0	49	51	49	11	3	27
11/30-2	57	43	0	100	5	3	60
11/30a-8	40	60	0	100	10	9	90
11/30a-B10	100	0	0	100	12	9	75
12/21-2	71	29	0	100	17	9	53
12/27-1	78	22	0	100	15	14	93
12/27-2	54	46	0	100	8	8	100
12/29-1	57	43	0	100	7	7	100

8.2.2 | MIGRATION METHODS AND MAGNETIC MINERALS

To further refine the charging mechanisms of the petroleum system, separation of the Devonian and Pentland source rocks within the BPSM to produce both deep basin and proximal hydrocarbons shows where the hydrocarbons that charge the known accumulations is generated, and thus how they migrate into the fields (Figure 8.2). Deep basin hydrocarbons are sourced from the Great Glen and Lossiemouth Sub-basins, and require lateral migration to access the fields of the IMF, whereas proximal hydrocarbons represent direct vertical migration into each field. To further the work of Abdulkarim *et al.* (2022a), this refinement is also used to investigate if there is a direct connection between the amount of proximally charged (vertical) hydrocarbons and siderite within wells across the IMF.

Of the nine wells analysed, five show a dominant proximal charge – Wells 11/24-1 and 11/24a-2 in the NW of the basin, and Wells 11/30-2, 11/30a-8 and 11/30a-B10 in Beatrice Field. Of the other four, Wells 12/21-2, 12/27-1, 12/27-2 and 12/29-1, 12/21-2 and 12/27-1 sit outside the deep basin charge region (Figure 8.2), and this is represented in the similar mixing ratios seen between them (28:72 % proximal:deep basin for 12/21-2; 30:70 % proximal:deep basin for 12/27-1; Table 8.3). These migration ratios are starkly different to those in the deep basin regions, with 12/27-2 and 12/29-1 both being dominated by deep basin charge, at 7:93 % and 15:85 % proximal:deep basin, respectively (Table 8.3).

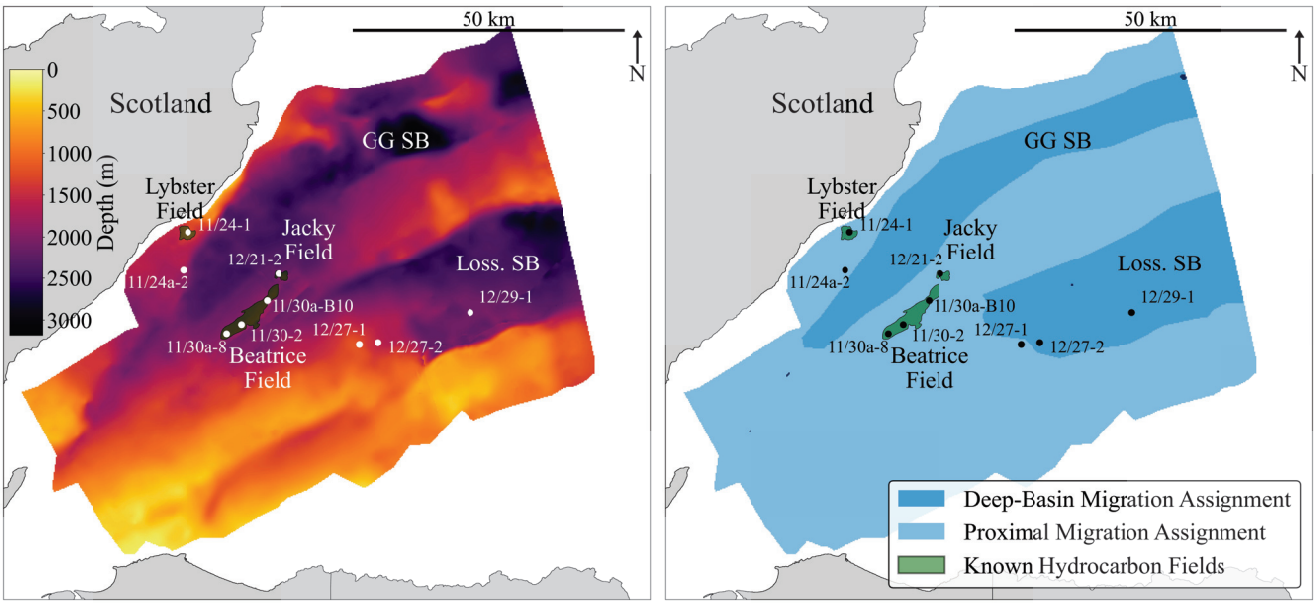


Figure 8.2: *Maps of the IMF identifying the regions separated for deep basin and proximal hydrocarbon charging, highlighting the Great Glen Sub-basin (GG SB) and the Lossiemouth Sub-basin (Loss. SB), and the wells utilised in this analysis. The majority of wells are located within the shallower, proximally charged regions of the basin, however two, Wells 12/27-2 and 12/29-1, sit within the deep basin-charge region of the Lossiemouth Sub-basin.*

Consequently, the migration mixes of Wells 12/27-2 and 12/29-1 are inconclusive, as their location within the Lossiemouth Sub-basin results in a high likelihood that hydrocarbons generated from deep basin sources, used elsewhere as a proxy for lateral migration, actually charges the wells, leaving seven wells with varying migration mixing ratios for analysis.

The connection between siderite presence and proximally sourced hydrocarbons within wells is consistent across the IMF, with all wells that contain siderite also being at least partially charged by proximally sourced hydrocarbons, bar Well 12/29-1 which has consistently proven inconclusive evidence across all magnetic analysis (Table 8.3). The dominant proximal contribution in Wells 11/24-1, 11/24a-2, 11/30a-8 and 11/30a-B10 is matched by high siderite presence in the water-saturated samples. This is further correlated by the presence of siderite in the water-saturated samples of Well 11/30-2 (Table 8.3). In contrast, whilst there is extensive presence of siderite in Well 12/21-2, this is not corroborated by a proximal-dominant hydrocarbon charge, with this also reciprocated by Well 12/27-1. In comparison to the proximal-dominated wells, the extensive presence of siderite in Well 12/27-2 contrasts to the heavily deep basin-charged hydrocarbon mix. However, as discussed, due to the location of the well in a deep basin region, there is uncertainty in the migration mixing ratios (Table 8.3). Consequently, it can be concluded that whilst proximally charged hydrocarbons closely associate with siderite presence, there is no clear link between degree of proximal charge and extent of siderite presence.

8.3 | Hydrocarbon Prospectivity

Whilst analysis of the BPSM has shown potential for accumulations at locations across the basin, they all consist of small hydrocarbon bodies with the majority bearing limitations and therefore having limited chance of success. However, the BPSM has shown how the petroleum system has formed

Table 8.3: *Table outlining the source rock mixing percentages, mixing percentages of the source locations of the Devonian and Pentland source rocks, and magnetic mineral presence at wells across the IMF. The mixing ratios and migration ratios are calculated in the BPSM and the magnetic mineral presence is the percentage of samples containing the relevant magnetic mineral against the total number of samples in each well, note that minerals can occur concurrently within samples. Dashes indicate no presence of relevant magnetic mineral. Dev. = Devonian Fish Beds, Pent. = Pentland Formation, Bl. Sh. = Kimmeridge Clay Black Shales, O = oil, W = water, Goe = goethite, Sid = siderite, FeS = iron sulphides (either pyrite or pyrrhotite), Lep = lepidocrocite, Mgh = maghemite.*

Well	Source mix (%)			Migration mix (%)		Fluid	Mineral presence (%)				
	Dev.	Pent.	Bl. Sh.	Proximal	Deep B.		Goe	Sid	FeS	Lep	Mgh
11/24-1	59	40	1	51	49	O	85	10	-	-	-
						W	75	50	-	-	-
11/24a-2	0	49	51	53	47	O	23	-	64	-	-
						W	60	40	-	-	-
11/30-2	57	43	0	79	21	O	60	-	-	-	-
						W	42	8	-	8	-
11/30a-8	40	60	0	67	33	O	90	40	-	20	-
						W	74	30	4	30	-
11/30a-B10	100	0	0	65	35	O	75	-	-	17	-
						W	50	28	11	17	-
12/21-2	71	29	0	28	72	O	50	75	-	19	-
						W	44	69	-	13	-
12/27-1	78	22	0	30	70	O	54	46	-	-	38
						W	50	-	-	-	25
12/27-2	54	46	0	7	93	O	88	63	-	38	-
						W	25	50	-	-	-
12/29-1	57	43	0	15	85	O	86	-	-	-	-
						W	100	-	-	-	-

and evolved, with broad hydrocarbon prospectivity possible. The hydrocarbon generation proven in the Devonian Fish Beds and Pentland Formation have shown the likely sources of hydrocarbons within the IMF, but with evidence that the Kimmeridge Clay Black Shales reach low levels of maturation, shown through transformation ratios and generation masses, this offers the possibility of other hydrocarbon accumulations existing, especially within shallower lithologies such as the Wick Sand and Cromer Knoll. This potential source rock-reservoir combination would rely heavily on localised lithological trapping, as the Cromer Knoll and other Cretaceous sediments are likely too sand-rich to be successful seals. However, thick sand bodies of the Wick Sand in the north of the Great Glen Sub-basin could offer hydrocarbon accumulation potential, charged by a combination of the hydrocarbon generating source rocks, including the Kimmeridge Clay.

8.4 | COMPARISONS TO OTHER WORK

The interactions between the magnetic minerals across the IMF and the petroleum system within it agree with past work identifying a connection between the two (Abdulkarim *et al.*, 2022a,b; Abubakar, 2015; Abubakar *et al.*, 2020; Badejo *et al.*, 2021a,b,c; Costanzo-Álvarez *et al.*, 2006, 2019; Donovan *et al.*, 1979, 1982; Elmore *et al.*, 1987; Elmore and Crawford, 1990; Emmerton *et al.*, 2012, 2013; Kilgore and Elmore, 1989; Machel and Burton, 1991a,b; Machel, 1995). Whilst many of the previous investigations were influenced by biodegradation (Badejo *et al.*, 2021b,c; Costanzo-Álvarez *et al.*, 2006; Emmerton *et al.*, 2012, 2013), and the IMF lacks biodegradation of the hydrocarbons (Peters *et al.*, 1989), this is solely one area of influence over the magnetic minerals. Initial predictions by Machel (1995) shows how different magnetic minerals form in different depths and different conditions due to the environments impacting formation, with magnetite, hematite and pyrrhotite the most likely minerals to be present away from the hydrocarbon influence, compared to more pyrite and siderite the closer to the hydrocarbons the investigations become. Whilst the lack of definitively dry, hydrocarbon-free wells limited the investigation of background signals in this study, the presence of siderite and iron sulphides, among other minerals, in the hydrocarbon-influenced regions of the IMF is broadly correlative with the predictions of Machel (1995). This work was also corroborated by Abubakar *et al.* (2015, 2020) who also showed that hydrocarbon generation can also directly form magnetic minerals, which aids the connections from this study between varying magnetic minerals and different source rocks.

8.4.1 | BURIAL ESTIMATIONS, TEMPERATURE AND MAGNETIC MINERALS

Via the work of Aubourg *et al.* (2008, 2012), Aubourg and Pozzi (2010) and Kars *et al.* (2012, 2014), the remagnetisation of magnetic minerals as they pass through various temperatures offers the possibility of creating a pseudo-burial history, and in turn, to conduct organic matter maturity analysis. They show how pyrrhotite is common from 40-85 °C, before magnetite occurs through the alteration of pyrrhotite up to 250 °C. Above this, to 320 °C, pyrrhotite dominates prior to pyrite occurring above 320 °C. The lack of pyrrhotite across the IMF, extensive abundance of magnetite and minor pyrite presence suggests that the basin typically experienced temperatures between 85-250 °C, or above 320 °C. However, the presence of hydrocarbons in the pyrite-bearing regions, and the relative lack of both over-maturity and hydrocarbon cracking in the basin (Peters *et al.*, 1989), suggests that it is unlikely the basin reached these temperatures within the hydrocarbon-bearing sequences. In contrast, the extensive presence of magnetite, albeit in low concentrations, both across the basin and increasingly towards the oil-water contacts in wells, (Chapter 6), indicates that the majority of the hydrocarbon-bearing formations of the IMF experienced temperatures between 85-250 °C at points during its history, likely during rifting or maximum burial. In comparison, the present day temperature gradient calculated from the BPSM is approximately 28 °C/km (Figure 8.3). Consequently, the presence of pyrrhotite, based on the estimates of Aubourg *et al.* (2008, 2012), Aubourg and Pozzi (2010) and Kars *et al.* (2012, 2014) would occur between approximately 1.4 km and 3 km, encapsulating all reservoir units, reaffirming the iron sulphide presence within the magnetic mineral assemblages.

The Devonian Fish Beds reach the highest maximum temperature of any of the source rocks (191

°C), yet remain in the magnetite range of Aubourg *et al.* (2008, 2012), Aubourg and Pozzi (2010) and Kars *et al.* (2012, 2014). Furthermore, the lowest maximum temperature reached in the formation (99 °C) is above the lower threshold (Figure 8.3). In comparison, the two other source rocks, the Pentland Formation and Kimmeridge Clay Black Shales, experience similar maximum temperature ranges of 39.25-148.00 °C and 32-125 °C, respectively. Whilst the lowest maximum temperatures seen within these formations is below the magnetite threshold, there are significant regions of the formations that are above the 85 °C threshold (Figure 8.3). In the oil-bearing reservoir sequence, the maximum temperature range is similar to the non-Devonian source rocks (37-143 °C), with the regions of known accumulations, in the centre and north of the basin, consistently showing magnetite-forming temperatures (Figure 8.3). This temperature indication directly relates not only to the widespread presence of magnetite in the samples of this study, but also to the increasing magnetite presence towards OWCs, although it should be noted that, as discussed, magnetite very readily forms in a variety of environments (Dunlop and Özdemir, 1997), so this correlation is more corroborative than it is definitive.

In contrast to the works of Aubourg *et al.* (2008, 2012), Aubourg and Pozzi (2010) and Kars *et al.* (2012, 2014), Abdulkarim *et al.* (2022c) offers a different temperature-centred analytical method for understanding petroleum systems, offering two different enhancements at oil-water contacts, referenced therein as oil-water transition zones, akin to this study. Whilst the enhancements shown by Abdulkarim *et al.* (2022c) are defined by pyrrhotite at shallow depths (<80 °C) and lepidocrocite at deeper depths (>80 °C), these are also iron sulphide- and iron hydroxide-defined enhancements that match those seen in this study. However, the model in this study estimates temperatures at the OWCs of each well to be below 80 °C, and as such, it cannot directly correlate the pyrrhotite-lepidocrocite relationship seen by Abdulkarim *et al.* (2022c). Furthermore, the temperature at the iron sulphide-rich Well 11/24a-2 (63 °C) is the highest seen within this study of the IMF, with the wells across Beatrice and Jacky Fields being closest to this temperature at between 58-61 °C. Consequently, the relationship seen in the IMF is the inverse of that seen within the Central North Sea region of Abdulkarim *et al.* (2022c). However, Abdulkarim *et al.* (2022c) offers the suggestion that the relationship seen within the Central North Sea is a result of biodegradation in the cooler regions forming the pyrrhotite, with no biodegradation seen within the IMF (Peters *et al.*, 1989), it is possible that the relationship shown by Abdulkarim *et al.* (2022c) is critically controlled by biodegradational processes.

8.4.2 | Source rocks and magnetic minerals

Badejo *et al.* (2021c) highlighted the enhancement of magnetisation at oil-water contacts, attributing it not to the concentration of grains between the saturating fluids, but of the precipitation of new grains, either through diagenetic changes or biodegradation. The identification of enhancements at the OWCs across the IMF, and the lack of biodegradation seen within the IMF (Peters *et al.*, 1989), suggests that in the IMF, the magnetic enhancement at the OWCs is a result of diagenetic influences on the region around the fluid contacts. Whilst there is no consistent correlation between enhancements and OWCs, there are many occasions where enhancements occur as found by Badejo *et al.* (2021c), and suggests that enhancement occurs across petroleum systems, regardless of the system and the differences between them. Abdulkarim *et al.* (2022a) also outline how siderite can be a direct proxy for vertical migration,

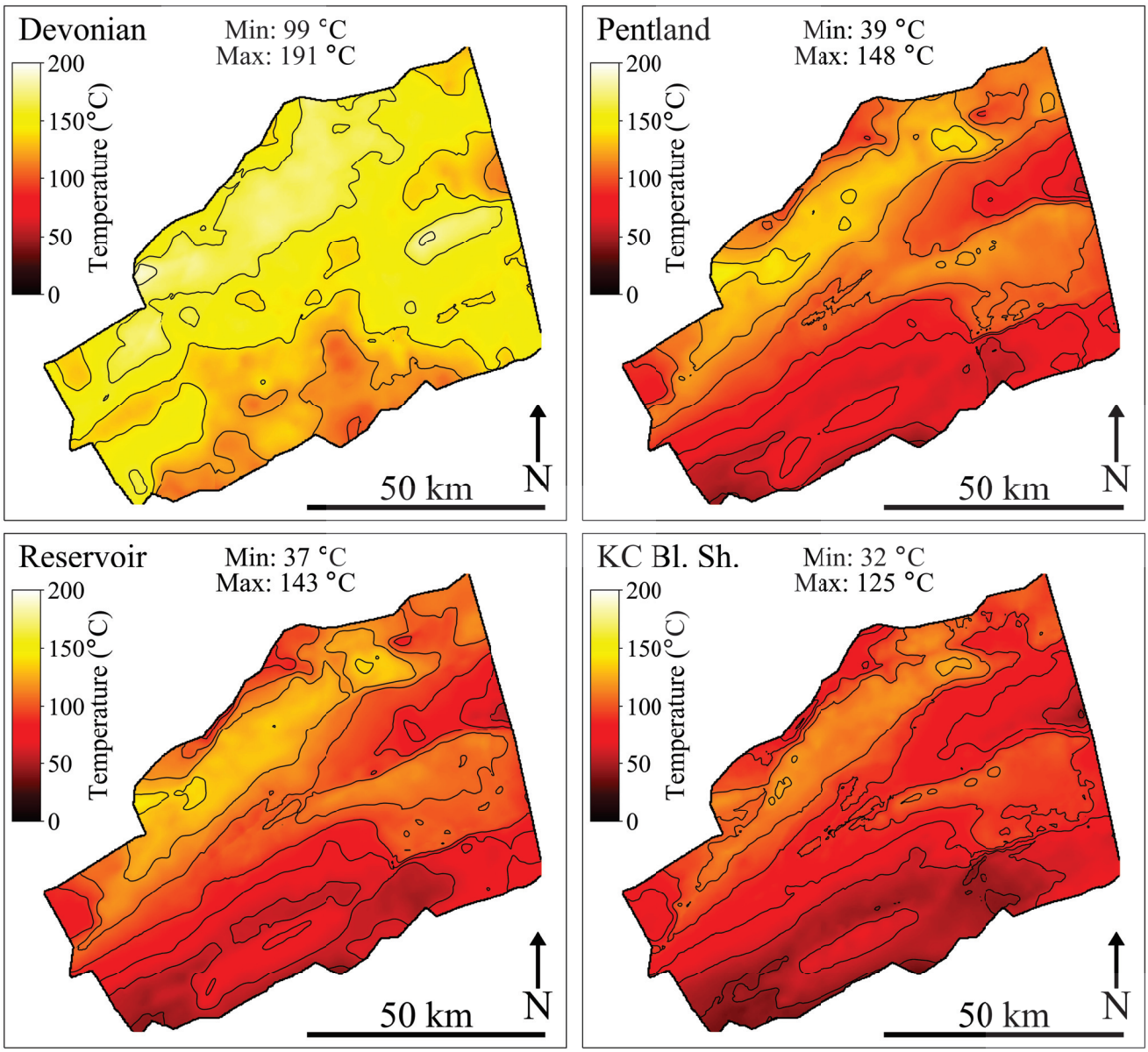


Figure 8.3: *Contour maps of varying sequences through the BPSM of the IMF showing the maximum temperature reached across the basin, highlighting the highest and lowest maximum temperatures reached. These temperatures are derived from the BPSM and show that all sequences exist within the magnetite-formation window between 85-250 °C defined by Aubourg* et al. *(2008, 2012), Aubourg and Pozzi (2010) and Kars* et al. *(2012, 2014). KC Bl. Sh. = Kimmeridge Clay Black Shale.*

which is reflected in this study, where siderite is seen in numerous samples across the IMF basin, and the BPSM in this study proves that vertical migration occurs across the basin, from both the Devonian Fish Beds and Pentland Formation source rocks.

Work by Badejo *et al.* (2021a,b,c) showed the interconnection of iron sulphides with the petroleum system of the central North Sea, where these magnetic minerals were not present in non-hydrocarbon-bearing samples. Whilst the magnetic mineral assemblages in the work of Badejo *et al.* (2021b,c) are dominated by these iron sulphides, this contradicts the magnetic mineral assemblages of this study, which have been shown to contain widespread goethite, alongside magnetite, siderite, lepidocrocite and more minor iron sulphides, alongside very minor maghemite. Furthermore, the studies of Abubakar *et al.* (2020) and Abdulkarim *et al.* (2022a,b,c) all show presence of magnetite and pyrrhotite, and

siderite, iron sulphides and titanium oxides, respectively. The starkly contrasting magnetic mineral assemblages between this study and those presented suggest that there is not a set group of magnetic minerals that form within all petroleum systems, and that the petroleum system and the basin geology control the assemblages to a certain extent, suggesting the potential for different source rocks to form, and exert influence over, magnetic minerals. Beyond this, it is clear that the presence of sulphur within a petroleum system has critical control over the magnetic signal and presence of other magnetic minerals. Consequently, it is likely that the dominance of iron sulphides seen in other studies (Abdulkarim *et al.*, 2022a,b,c; Abubakar *et al.*, 2015, 2020; Badejo *et al.*, 2021a,b,c) limits the ability for alternative magnetic minerals to be present in those regions.

With Abubakar *et al.* (2020) showing that hydrocarbon generation forms magnetic minerals, and Badejo *et al.* (2021a,b,c) showing direct connections between iron sulphides and the deep marine, Type II kerogen, Kimmeridge Clay-sourced hydrocarbons of the Central North Sea, and numerous works (Berner, 1969; Fortin *et al.*, 1993; Gendler *et al.*, 2005; Weibel, 1999; van der Zee *et al.*, 2003) showing how red beds, alongside lacustrine (Type I kerogen) and lagoonal, shallow marine (Type II-III kerogen) depositional environments can form iron hydroxides (goethite, lepidocrocite), it can be concluded that different kerogen type source rocks deposited in different depositional environments could form different magnetic minerals that can be used as a proxy for source rock kerogen type identification. This conclusion is supported by the presence of extensive iron sulphides in the oil-saturated samples of Well 11/24a-2, where BPSM-derived hydrocarbon mixing ratios show how Kimmeridge Clay Black Shales dominate the hydrocarbon contribution in the area around the well. As such, this study proposes that Type I kerogen, lacustrine-deposited and Type II-III, lagoon- and shallow marine-deposited source rocks can be identified through the dominance of goethite, and possibly lepidocrocite, formed during source rock deposition. Furthermore, this study also proposes that Type II kerogen, deep marine-deposited source rocks can be identified through the dominance of iron sulphides in the assemblage, linked directly to the sulphur content of the source rock, however these correlations must be tested further.

The increased presence of sulphur in Type II kerogen source rocks compared to Type I or III is a result of the depositional environments in which each source rock forms (Peters *et al.*, 2004). Whilst all source rocks require anoxic conditions to preserve organic matter, and sulphate-reducing, H_2S-forming bacteria are widespread in these anoxic environments, different environments contain different amounts of other minerals that readily combine with the H_2S to create new compounds that remove the sulphur from the system, most typically dissolved iron which produces iron monosulphides (Peters *et al.*, 2004). When sulphur is not combined into new compounds, it is typically absorbed by the kerogen and organic matter of the source rock (Peters *et al.*, 2004). As such, the greater the amount of sulphur-combining minerals and compounds in the system, the lower the sulphur of the source rock, and *vice versa*, with deep marine, Type II kerogen-forming environments often lacking in these compounds compared to the other source rock-forming environments that are often in much shallower water (Dembicki, 2009; Dembicki Jr, 2017; Peters *et al.*, 2004).

8.4.3 | Migration, accumulation and magnetic minerals

The magnetic mineral analysis within this study identifies widespread magnetite across samples, with scanning electron microscopy showing the presence of magnetite in framboidal form, and also sees the iron sulphide presence in Well 11/24a-2 extensively impacting the other magnetic minerals within the samples. This relationship was also shown initially by Elmore *et al.* (1987), Elmore and Crawford (1990) and Kilgore and Elmore (1989), who identify the formation of magnetite as a result of hydrocarbon influx. Further analysis by González *et al.* (2002), Aldana *et al.* (2003, 2011), Costanzo-Álvarez *et al.* (2006) and De la Rosa *et al.* (2021) also see this magnetite correlation as well as iron sulphide formation during hydrocarbon influx in petroleum systems across South America. Aldana *et al.* (2003) and Costanzo-Álvarez *et al.* (2006) also experience the formation of secondary framboidal magnetite in association with initial magnetite caused by the creation of a reducing environment from hydrocarbon migration. Aldana *et al.* (2003) continue to suggest that iron sulphides form solely where there is a source of sulphur from migrating hydrocarbons, supporting the iron sulphide-magnetite relationship seen within the IMF in this study. The correlations between magnetite formation, and where sulphur is present, iron sulphide formation, not only in this study in the IMF but in other petroleum systems across the globe, suggests that this connection is a result of the environments created by migrating and accumulating hydrocarbons rather than petroleum system-specific conditions.

Research into paleo-reservoirs and the tectonism-derived destruction of hydrocarbon reservoirs by Zhang *et al.* (2018, 2019, 2020) reaffirm how hydrocarbon migration causes widespread remagnetisation within an area, regardless of the post-accumulation evolution of the reservoir. Akin to the analysis in this study, and previously discussed other research, Zhang *et al.* (2018, 2019, 2020) identify magnetite formation during hydrocarbon migration, and also identify the formation of pyrite and pyrrhotite when sulphur is present in the system. Zhang *et al.* (2018, 2019) shows the formation of magnetite during hydrocarbon influx, as a result of the change in environmental conditions, and also identify iron sulphide mineral formation solely when sulphur is present within the hydrocarbons of the system. This directly correlates to the magnetic minerals identified in this study, with the Kimmeridge Clay Black Shales providing sulphur to initiate iron sulphide formation in Well 11/24a-2 and not in any other well, as well as other research previously outlined. In contrast to this study, Zhang *et al.* (2020) experiences the alteration of pyrite into magnetite as a result of fluid migration, whereas this study sees both minerals present together where sulphur exists in sufficient amounts to produce iron sulphides.

8.5 | Summary

When collating all of the data from this study and combining it with other research in this chapter, a clear image is produced regarding the behaviour of the petroleum system and how the magnetic minerals associated with components of it align. Firstly, different potential source rocks in the IMF, and possibly beyond, bear different magnetic minerals depending on their depositional environments, which directly relate to varying magnetic mineral assemblages within the IMF petroleum system (Figure 8.4). The presence of goethite and lepidocrocite in association with the Type I and Type II-III source rocks of the lacustrine-deposited Devonian Fish Beds and lagoonal-deposited Pentland Formation, respectively,

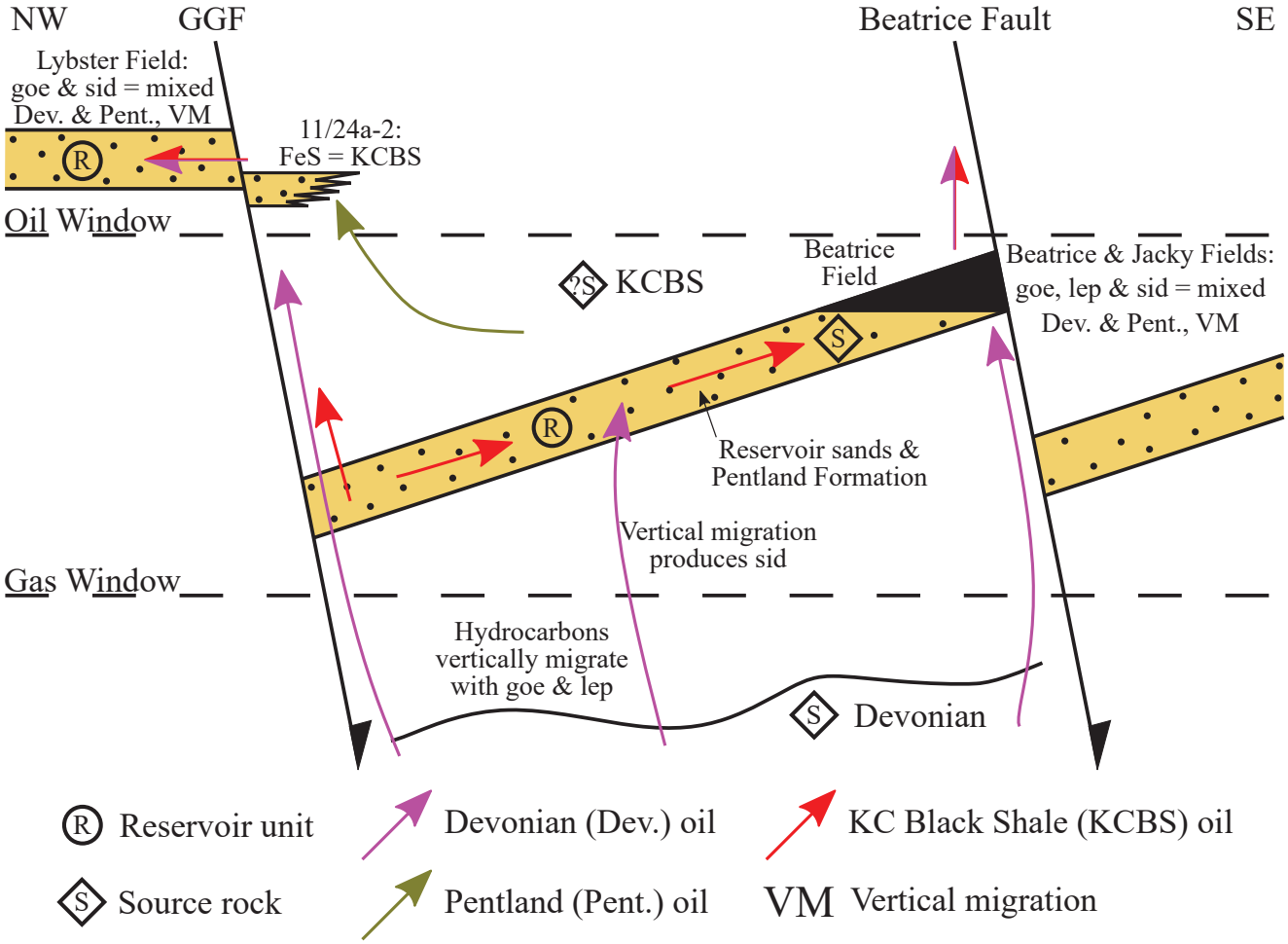


Figure 8.4: *Cross-section across the Great Glen Sub-basin showing the relationships and behaviours between the petroleum system and the hydrocarbon-generating source rocks, and the magnetic minerals within the basin.*

are seen across the basin, including in Beatrice, Jacky and Lybster Fields. In comparison, iron sulphides associated with the Type II, deep marine-deposited Kimmeridge Clay Black Shales are only seen in certain areas of the IMF, due to a combination of a lack of hydrocarbon generation and structural constraints (Figure 8.4). Furthermore, both modelling and magnetic mineral analysis combine to affirm the presence of siderite formed during vertical hydrocarbon migration, with this predominantly occurring in association with the migration of Devonian- and Pentland-sourced hydrocarbons (Figure 8.4).

8.6 | Conclusion

The presence of the iron hydroxides goethite and lepidocrocite contradict the magnetic mineral assemblages found for Type II-source petroleum systems which are more iron sulphide-dominant (Peters *et al.*, 2004). This infers a connection between the formation of iron hydroxides and Type I and II-III source rocks, a connection supported by literature which indicates the lacustrine and lagoonal-to-shallow marine depositional environments of the IMF source rocks are ideal environments for iron hydroxides to form. The connection between iron sulphides and Type II kerogen, deep marine-deposited source rocks is evidenced within the IMF, where Well 11/24a-2 is shown to have Kimmeridge Clay Black Shale-dominated hydrocarbons present in its vicinity, and is the only well that has significantly high

proportional presence of iron sulphides in oil-saturated samples in the IMF.

The presence of siderite as a proxy for vertical migration is further supported by this study, as siderite is identified across the IMF, and the BPSM has shown how vertical migration is widespread within the IMF petroleum system, moving hydrocarbons from both the Devonian Fish Beds and the Pentland Formation into the mid-Jurassic reservoir sands. The presence of siderite across the IMF in alignment with the consistent proximal-sourced hydrocarbon charging supports the effectiveness of siderite presence as a vertical migration proxy. However, this study shows that there is less of a correlation between the relative proportion of vertical migration and extent of siderite presence, although there is room for further investigation into this connection beyond the scope of this study.

When compared to other research, consistent conclusions can be drawn across numerous study areas globally. The formation of magnetite and iron sulphides as a result of hydrocarbon migration is consistent, and typically as a result of the changing of environments and the formation of reducing environments when hydrocarbons influx into a region. Furthermore, this study supports findings of other studies that suggest iron sulphides form preferentially when sulphur is brought into a region via sulphur-bearing hydrocarbons. The iron sulphide behaviour directly connects to the Kimmeridge Clay Black Shale-charged well 11/24a-2, with geochemical analysis showing that the Kimmeridge Clay source rocks are typically more sulphur-rich than the Devonian and Pentland source rocks of the IMF. However, with the challenge in deriving magnetic mineral abundance, it is difficult to assess if there is a direct correlation between iron sulphide abundance and degree of source rock contribution.

CHAPTER 9 | CONCLUSIONS

9.1 | Introduction

The aims outlined in Chapter 1 have been successfully achieved, with an effective basin and petroleum systems model producing conclusive results surrounding the petroleum system of the IMF. Furthermore, the interconnection between the BPSM and the magnetic mineral analysis has shown direct links between components of the petroleum system and various magnetic minerals and magnetic mineral behaviour. As such, it can be concluded that the aims set out prior to this study have been met and that this work successfully contributes to the knowledge surrounding magnetic minerals and their relationships with hydrocarbons.

This sequence of conclusions covers the analytical work conducted in this study. Whilst conclusions have been drawn and outlined at the end of each of the main chapters of this work, Chapters 5, 6 and 7, this chapter compiles them and connects them together to complete this body of work. This study has proven successful, and the Inner Moray Firth (IMF) has been a strong candidate for this project, through good seismic data and core availability, alongside numerous wells and well data through which analysis has occurred. Furthermore, the identification of non-Kimmeridge Clay-sourced hydrocarbons offered this study and the study area as a whole the opportunity to correlate and compare the IMF to the Central North Sea not only through their petroleum systems but also through their magnetic mineral assemblages. This study has added a new layer of investigation and discovery onto not only other research from Imperial College London into the connections between magnetic minerals and hydrocarbons (Abdulkarim *et al.*, 2022a,b; Abubakar *et al.*, 2015, 2020; Badejo *et al.*, 2021a,b,c; Emmerton *et al.*, 2012, 2013), but also from other institutions on other areas of the globe.

9.2 | Geological Appraisal

Chapter 5 investigates the structure and sediments of the IMF through well log analysis and seismic data interpretation, and creates a geological model of the basin from them. Well log analysis shows how relatively consistent the formations are across the IMF, through both well log data and core logging, proving that the basin exists as a structurally complex layer cake sequence. In tandem with this, seismic interpretation supports the consistency of units across the basin, but also shows how complex and fault-reliant the basin is. The development of depth and thickness maps for the sequences of the IMF also produced initial understanding of the petroleum system and its components, and suggest that the Kimmeridge Clay and Brora Coal source rocks are likely too shallow to effectively generate hydrocarbons when compared to the deeper Pentland Formation and the Devonian Fish Beds. Comparatively, seismic interpretation shows the structural highs and potential fault-trapped locations of the basin into which hydrocarbons could migrate and accumulate.

9.3 | Magnetic Analysis

In Chapter 6, this study presents and discusses the extensive magnetic analysis conducted on core-derived samples from across the Inner Moray Firth. Through room temperature magnetic hysteresis

property, high temperature magnetic susceptibility and low temperature magnetic remanence analysis, this study proved the presence of seven magnetic minerals in the basin. Pervasive magnetite and goethite are seen across the basin, supported by extensive siderite presence, and lesser iron sulphide, lepidocrocite, hematite and maghemite presence.

The magnetic minerals show broadly consistent trends across the IMF, with no clear variation identified on a basin-scale, however, at well-scale, there are localised patterns that are likely a result of environmental changes. At basin scale, all twelve wells discussed in Chapter 6 show evidence of magnetite and goethite, and nine contain siderite, whilst lepidocrocite is within seven wells, iron sulphides are identified in four, and maghemite is seen in one. Whilst siderite is seen in wells across the basin, and iron sulphides are seen in wells in the north west, east and central IMF, only lepidocrocite is constrained into a part of the basin, through the central region of the IMF.

At well scale, magnetic enhancement, seen most clearly by increases in room temperature magnetisation (M_s), is experienced at oil-water contacts across the basin, reflecting the work of Badejo *et al.* (2021c). Of the twelve analysed wells in Chapter 6, ten show evidence of oil-water contacts, identified through the methods discussed in Chapter 3, and of these ten wells, eight show clear enhancement of their magnetic responses at their oil-water contacts through increases in M_s. Beyond this identification, however, is the discovery of different types of magnetic enhancement in tandem with differing magnetic mineralogy. This study has shown that the majority of magnetic enhancement-experiencing, OWC-bearing wells, six out of eight, have below-OWC magnetic enhancement and two out of ten have above-OWC magnetic enhancement. The enhancement behaviours of the wells align with the magnetic mineral assemblages identified within the wells, as the six below-contact magnetically enhanced wells show dominant goethite and magnetite, often with siderite. In comparison, alongside the two wells that do not experience magnetic enhancement, the above-contact magnetically enhanced wells are the only wells to show evidence of iron sulphide presence. This shows that the magnetic enhancement is directly influenced either by the magnetic minerals present in the region, or by the environments necessary to facilitate the formation of specific magnetic minerals.

The classification of the two groups of wells, the "goethite-rich", below-OWC enhanced wells and the "iron sulphide-rich", above-OWC enhanced wells, shows that whilst mineralogy does fluctuate across the basin, there is a lack of pattern in the magnetic mineralogy when looked at from a purely magnetic analysis standpoint. This is proven by the locations of the wells, with the two iron sulphide-rich wells being located in the north west and east of the basin, whilst the two non-enhanced wells are situated in Beatrice Field. As such, location relative to the basin cannot be defined as the cause of the magnetic mineral and enhancement variations alone, with variations in material presence the likely cause.

The goethite-rich group of wells show evidence of increased ferromagnetic material around the OWC, identified as magnetite through the low temperature analysis and the FORC PCA, with this attributed to the pervasive goethite altering to magnetite around the contact. The direct cause of this alteration is unclear, however the instability of goethite around OWCs compared to further away from the contact suggests that the change in environment from oxidising to reducing conditions, or *vice versa*,

is the cause. In comparison, this behaviour is not seen in the iron sulphide-rich wells, where enhancement at the contacts comes in the form of MD- and SD-domain grains, thus likely representing a direct increase in the iron sulphides, with this behaviour, enhancement and mineralogy matching those of Badejo *et al.* (2021c). Consequently, it can be concluded that the change in magnetic enhancement and magnetic mineral presence is a direct result of sulphur presence in a region, which not only preferentially forms ahead of other more unstable minerals, but also impacts the alteration of minerals when present.

Beyond the investigation in well-scale magnetic behaviour, broadly understanding the environments required to form and stabilise the various magnetic minerals identified in the basin is crucial to understanding their implications. In this study, this is done through analysing literature, and has shown that there are direct connections between the depositional environments of the formations in the IMF and the environments required to form the dominant minerals of the basin's magnetic mineral assemblage. Due to its ability to form in a wide variety of environments, magnetite is the most commonly formed and observed magnetic mineral on Earth, forming in locations where there are iron and oxygen molecules present (Dunlop and Özdemir, 1997; Emmerton *et al.*, 2012). This relatively simple formation is also seen in hematite, as it is a end-product of the oxidation of a wide range of magnetic minerals (Dunlop and Özdemir, 1997; Evans and Heller, 2003). Goethite has been shown to form in abundance in lacustrine sediments and red beds, predominantly due to its relationship with hematite, and is also capable of forming within swamp and lagoonal environments (Berner, 1969; Fortin *et al.*, 1993; Gendler *et al.*, 2005; Klein and Hurlbut, 1985; Weibel, 1999; van der Zee *et al.*, 2003), and has also been shown to alter into magnetite if given the necessary environments (Abrajevitch *et al.*, 2009; Cudennec and Lecerf, 2005; Goss, 1987; Till and Nowaczyk, 2018; Ibrahim *et al.*, 1994; Lima-de Faria, 1967; Lowrie and Heller, 1982; Peter D. Rude, 1989; Schwertmann and Fechter, 1984). Siderite requires Fe^{2+} ion- and carbonate-rich, anoxic, reducing environments lacking in hydrogen sulphides (Bachan and Kump, 2015; Berner, 1981; Lin *et al.*, 2020). The production of reducing environments and the supply of carbon by the presence of hydrocarbons offer the ideal environment for siderite formation (Emmerton, 2012; Machel and Burton, 1991a; Machel, 1995), whilst Abdulkarim *et al.* (2022a) show how the depressurisation of molecules during vertical migration also forms siderite. Iron sulphides form in highly reducing, organic-rich deep marine environments, most commonly as pyrrhotite and pyrite Kobayashi and Nomura (1972). Following this, Abdulkarim *et al.* (2022a,b); Badejo *et al.* (2021b,c) identify widespread presence of iron sulphides in Kimmeridge Clay-sourced petroleum systems.

9.4 | BASIN AND PETROLEUM SYSTEMS MODELLING

The basin and petroleum systems modelling conducted in this study, as covered in Chapter 7, was utilised to understand how the petroleum system of the Inner Moray Firth formed and evolved throughout its geological history. Modelling was undertaken in two- and three-dimensions, and has proven that of the four source rocks present within the IMF, one, the Brora Coal, is immature for gas, one, the Kimmeridge Clay Black Shales, is nearly wholly immature, and two, the Devonian Fish Beds and the Pentland Formation, generate nearly all of the hydrocarbons within the system.

Modelling shows that the majority of hydrocarbons have charged vertically, not only directly through the intermediate formations between the source rocks and the reservoir sequences, but also vertically surface-ward through the pervasive faults in the basin. Vertical charging from the Pentland Formation occurred both surface- and down-ward into the reservoir sands within which it is located. Lateral migration is also extensive, typically occurring up-dip into the structural highs of the basin.

The most dominant control on the hydrocarbon migration, filling and accumulation is the faults that exist across the basin, as proven by the modelling which shows how significant volumes of hydrocarbons are lost from accumulations post-66 Ma when faults opened and traps malfunctioned. This fault-derived loss of hydrocarbons, alongside the tilting of the basin during its late-stage rifting is likely why the IMF is not as productive a petroleum system as the other regions of the North Sea. The basin modelling has shown that the hydrocarbon generation of the source rocks is sufficient to form extensive accumulations should the rest of the components be in place, however this is not the case due to the late-stage evolution of the basin.

Modelling shows that accumulation of hydrocarbons in the known fields of the IMF, Beatrice, Jacky and Lybster Fields, begins at approximately 120 Ma, with variations in each source rock contribution occurring from this until present day. At present day, the mixing ratios between the Devonian and Pentland source rocks differs between each field, but all three broadly correlate with the geochemical analysis of Peters *et al.* (1989), who suggested that the petroleum system is comprised of 60 % Devonian and 40 % Pentland hydrocarbons. The modelling refines the mixing ratios of the three fields to be 66:34 % Devonian:Pentland in Beatrice Field, 61:39 % Devonian:Pentland in Jacky Field, and 67:32 % Devonian:Pentland in Lybster Field, which also contains a 1 % contribution of the Kimmeridge Clay Black Shale-sourced hydrocarbons.

The modelling in this study has identified several potential previously unidentified hydrocarbon accumulations of potential economic value, with one showing the greatest potential, located on the opposite flank of the Great Glen Sub-basin to Jacky Field. This unknown accumulation has a similar charge history to the known accumulations but modelling suggests a much more Devonian-dominated hydrocarbon mixing ratio of 82 %, compared to the 16 % and 2 % Pentland and Kimmeridge Clay contributions, respectively. Beyond this potential accumulation, the discovery of partially mature and low hydrocarbon generating Kimmeridge Clay Black Shales within the sub-basins of the IMF offer the potential for Late Jurassic and Early Cretaceous hydrocarbon accumulations bearing a, likely partial, Kimmeridge Clay hydrocarbon contribution. The potential of the Wick Sand in the north of the IMF, within the Great Glen Sub-basin to accumulate hydrocarbons is reasonable, however it is heavily dependant on clay-rich lithological constraints in the overlying Cromer Knoll Group sediments.

The hydrocarbon mixing ratios produced in the modelling of this study aligns with the analysis of Peters *et al.* (1989), as do Aalund (1983) and Mackenzie *et al.* (1983). Various estimates of the source kitchen locations have been produced and published, with this study agreeing with Hogan *et al.* (1978) in suggesting that long-range Pentland-sourced hydrocarbon migration is unlikely due to its high wax content. This study opposes Marshall (1998) who suggest that Beatrice Field-adjacent Devonian source maturation is unlikely, as the modelling of this study shows that proximal Devonian charging is not only

possible, but is the greatest contributor to the field. This study agrees with the suggestion of long-range Devonian-sourced hydrocarbons from Curran (1987a,b) and Underhill (1991), supported by the work of Parnell *et al.* (2017) and Peters *et al.* (1998), who offer potential regions of maturation away from the accumulations. This long-ranged migration is likely assisted by the extensive faults and their activity, as shown by this study's modelling and is supported by the work of Aydin (2000) and Jonk *et al.* (2003).

9.5 | CONNECTIONS BETWEEN MAGNETISM AND MODELLING

Deriving connections between the separate magnetic mineral behaviour and BPSM analysis proved critical to the understanding of both components, with this covered in Chapter 8. With the formation of goethite in lacustrine and swamp/lagoonal depositional environments, there is a direct connection between the extensive presence of goethite in all wells and the near-total Devonian Fish Beds and Pentland Formations contributions to the hydrocarbons of the petroleum system. Whilst this connection may be purely coincidental, the differences seen between the majority of the wells and the iron sulphide-rich Well 11/24a-2 suggest that there is a correlation. This is supported by the connection between the magnetic mineral assemblage of Well 11/24a-2 and the modelled hydrocarbon mixing ratios in the same region, which show dominance of Kimmeridge Clay-sourced hydrocarbons. This correlation is the same as the hydrocarbon source and magnetic mineral assemblages seen in the work of Abdulkarim *et al.* (2022a,b,c) and Badejo *et al.* (2021a,b,c) in the Central North Sea. As such, this study proposes tentative connections between iron sulphides and Kimmeridge Clay-type hydrocarbons, thus potentially extended to Type II, deep marine-deposited source rocks, and iron hydroxides and Devonian Fish Bed- or Pentland Formation-type hydrocarbons, thus also potentially kerogen Type I or II-III hydrocarbons.

This study found limited connections between magnetic mineral abundance and hydrocarbon source rocks due to the difficulty in estimating the abundance of magnetic minerals in samples. In this study, the Devonian- and Pentland- dominated oil-saturated regions of wells have 50 % of samples containing one of the indicator minerals (goethite, lepidocrocite or maghemite for Devonian and Pentland sources, iron sulphides for Black Shales), with the majority having indicator mineral presence in over 90 % of samples. In contrast, the only well that was not dominated by a Devonian or Pentland charge, Well 11/24a-2, shows 27 % of samples containing a Devonian or Pentland indicator mineral, but seven of eleven samples (64 %) show the Black Shale indicator mineral (iron sulphides). This correlates to the over-50 % contribution to the well of Kimmeridge Clay Black Shale-sourced hydrocarbons, as shown by the modelling. Attempts to constrain the relationship between siderite presence and vertical migration were successful, as all wells that experience BPSM-derived vertical migration showing siderite. However, this study shows a lack of connection between siderite abundance and percentage of vertical migration in comparison to lateral migration, although this is likely due to the limitations of estimating mineral abundance and the production of migration contribution calculations within the modelling.

The interactions between the magnetic minerals across the IMF and its petroleum system reflect past work identifying a connection between the two components (Abdulkarim *et al.*, 2022a,b; Abubakar, 2015; Abubakar *et al.*, 2020; Badejo *et al.*, 2021a,b,c; Costanzo-Álvarez *et al.*, 2006, 2019; Donovan *et al.*, 1979, 1982; Elmore *et al.*, 1987; Elmore and Crawford, 1990; Emmerton *et al.*, 2012, 2013;

Kilgore and Elmore, 1989; Machel and Burton, 1991a,b; Machel, 1995). This study correlates with the work of Badejo *et al.* (2021c) followed by Abdulkarim *et al.* (2022a), who show how siderite is formed as a result of vertical migration. The widespread vertical migration shown by the modelling within this study and the extensive presence of siderite identified in the well analysis. Beyond this connection, the identification of Kimmeridge Clay-sourced hydrocarbons is supported by the work of Badejo *et al.* (2021a,b,c) followed by Abdulkarim *et al.* (2022a,b), who find extensive iron sulphides in association of Kimmeridge Clay-sourced petroleum systems of the Central North Sea, furthering the correlation this study finds between varying magnetic minerals and the source rocks producing the hydrocarbons they are associated with. This study also directly correlates to the research conducted across petroleum systems in South America (Aldana *et al.*, 2003, 2011; González *et al.*, 2002; Costanzo-Álvarez *et al.*, 2006; De la Rosa *et al.*, 2021) that follow original work by Elmore *et al.* (1987), Kilgore and Elmore (1989) and Elmore and Crawford (1990) in identifying secondary framboidal magnetite as a result of alteration of pre-existing minerals when not in the presence of sulphur, which preferentially forms non-magnetite forming iron sulphides. However, this study goes beyond those works by linking this magnetite formation to the altering conditions around oil-water contacts.

BIBLIOGRAPHY

Aalund, L. R. **1983**. Guide to export crudes of the 80s-3. North Sea now offers 14 export crudes. *Oil and Gas Journal*. 81 (2): 75–79.

Abdulkarim, M. A., Muxworthy, A. R., Fraser, A., Neumaier, M., Hu, P., and Cowan, A. **2022**a. Siderite occurrence in petroleum systems and its potential as a hydrocarbon-migration proxy: A case study of the Catcher Area Development and the Bittern area, UK North Sea. *Journal of Petroleum Science and Engineering*. 212: 110248. doi:10.1016/j.petrol.2022.110248.

Abdulkarim, M. A., Muxworthy, A. R., Fraser, A., Sims, M., and Cowan, A. **2022**b. Effect of Hydrocarbon Presence and Properties on the Magnetic Signature of the Reservoir Sediments of the Catcher Area Development Region, UK North Sea. *Frontiers in Earth Science*. 10: 1–20. doi:10.3389/feart.2022.818624.

Abdulkarim, M. A., Muxworthy, A. R., and Fraser, A. J. **2022**c. High temperature susceptibility (HT-χ) measurements: A potential tool for the identification of oil water transition zone (OWTZ) in petroleum reservoirs. *Frontiers in Earth Science*. doi:10.3389/feart.2022.973385.

Abrajevitch, A., Van der Voo, R., and Rea, D. K. **2009**. Variations in relative abundances of goethite and hematite in Bengal Fan sediments: Climatic vs. diagenetic signals. *Marine Geology*. 267 (3-4): 191–206. doi:10.1016/j.margeo.2009.10.010.

Abubakar, R. **2015**. *Mapping petroleum migration pathways using magnetics, geochemistry and seismic mapping. Case study: Wessex Basin, southern England, UK*. PhD Thesis. Imperial College London.

Abubakar, R., Muxworthy, A. R., Fraser, A. J., Sephton, M. A., Watson, J. S., Heslop, D., Paterson, G. A., and Southern, P. **2020**. Mapping hydrocarbon charge-points in the Wessex Basin using seismic, geochemistry and mineral magnetics. *Marine and Petroleum Geology*. 111: 510–528. doi:10.1016/j.marpetgeo.2019.08.042.

Abubakar, R., Muxworthy, A. R., Sephton, M. A., Southern, P., Watson, J. S., Fraser, A. J., and Almeida, T. P. **2015**. Formation of magnetic minerals at hydrocarbon-generation conditions. *Marine and Petroleum Geology*. 68: 509–519. doi:10.1016/j.marpetgeo.2015.10.003.

Ai, Y., Liu, L., Zhang, C., Qi, L., He, M., Liang, Z., Sun, H. B., Luo, G., and Liang, Q. **2018**. Amorphous Flowerlike Goethite FeOOH Hierarchical Supraparticles: Superior Capability for Catalytic Hydrogenation of Nitroaromatics in Water. *ACS Applied Materials and Interfaces*. 10 (38): 32180–32191. doi:10.1021/acsami.8b10711.

Aldana, M., Costanzo-Álvarez, V., and Diaz, M. **2003**. Magnetic and mineralogical studies to characterize oil reservoirs in Venezuela. *The Leading Edge*. 22 (6): 526–529. doi:10.1190/1.1587674.

Aldana, M., Costanzo-Álvarez, V., Gómez, L., González, C., Díaz, M., Silva, P., and Rada, M. **2011**. Identification of magnetic minerals related to hydrocarbon authigenesis in venezuelan oil fields using an alternative decomposition of isothermal remanence curves. *Studia Geophysica et Geodaetica*. 55 (2): 343–358. doi:10.1007/s11200-011-0019-0.

Allen, P. A. and Allen, J. R. **2005**. *Basin analysis: principles and applications*. 2nd edn.. Oxford: Blackwell.

Andrews, I. J., Long, D., Richards, P. C., Thomson, A. R., Brown, S., Chesher, J. A., and McCormac, M. **1990**. The geology of the Moray Firth. Tech. rep.. British Geological Survey. Keyworth, Nottingham.

Antonova, A., Chistyakova, N., Gracheva, M., Rusakov, V., Koksharov, Y., Zhilina, T., and Zavarzina, D. **2020**. Mössbauer and EPR study of ferrihydrite and siderite biotransformations by a syntrophic culture of alkaliphilic bacteria. *Journal of Molecular Structure*. 1206: 127606. doi:10.1016/j.molstruc.2019.127606.

Argent, J. D., Stewart, S. A., Green, P. F., and Underhill, J. R. **2002**. Heterogeneous exhumation in the Inner Moray Firth, UK North Sea: constraints from new AFTA(R) and seismic data. *Journal of the Geological Society*. 159 (6): 715–729. doi:10.1144/0016-764901-141.

Athy, L. F. **1930**. Density, porosity and compaction of sedimentary rocks. *AAPG Bulletin*. 14 (1): 1–24. doi:10.1126/science.58.1489.27.b.

Aubourg, C. and Pozzi, J. P. **2010**. Toward a new <250 °C pyrrhotite-magnetite geothermometer for claystones. *Earth and Planetary Science Letters*. 294 (1-2): 47–57. doi:10.1016/j.epsl.2010.02.045.

Aubourg, C., Pozzi, J. P., Janots, D., and Sahraoui, L. **2008**. Imprinting chemical remanent magnetization in claystones at 95 °C. *Earth and Planetary Science Letters*. 272 (1-2): 172–180. doi:10.1016/j.epsl.2008.04.038.

Aubourg, C., Pozzi, J. P., and Kars, M. **2012**. Burial, claystones remagnetization and some consequences for magnetostratigraphy. In: R.D. Elmore, A.R. Muxworthy, M. Aldana, and M. Mena, eds., *Remagnetisation and Chemical Alteration of Sedimentary Rocks*. vol. 371. 1st edn.. London: Geological Society Special Publications. pp. 181–188.

Aydin, A. **2000**. Fractures, faults, and hydrocarbon entrapment, migration and flow. *Marine and Petroleum Geology*. 17: 797–814. doi:10.1016/S0264-8172(00)00020-9.

Bachan, A. and Kump, L. R. **2015**. The rise of oxygen and siderite oxidation during the Lomagundi event. *Proceedings of the National Academy of Sciences of the United States of America*. 112 (21): 6562–6567. doi:10.1073/pnas.1422319112.

Badejo, S. A. **2019**. *Using magnetic techniques to calibrate lateral hydrocarbon migration in basin modelling: A case study from the Lower Tertiary, UK Central North Sea*. PhD Thesis. Imperial College London.

Badejo, S. A., Fraser, A. J., Neumaier, M., Muxworthy, A. R., and Perkins, J. R. **2021**a. 3D petroleum systems modelling as an exploration tool in mature basins: A study from the Central North Sea, UK. *Marine and Petroleum Geology*. 133: 1–15. doi:10.1016/j.marpetgeo.2021.105271.

Badejo, S. A., Muxworthy, A. R., Fraser, A. J., Neumaier, M., Perkins, J. R., Stevenson, G. R., and Davey, R. **2021**b. Using magnetic techniques to calibrate hydrocarbon migration in petroleum systems modelling: A case study from the Lower Tertiary, UK Central North Sea. *Geophysical Journal International*. 227 (1): 617–631. doi:10.1093/gji/ggab236.

Badejo, S. A., Muxworthy, A. R., Fraser, A. J., Stevenson, G. R., Zhao, X., and Jackson, M. **2021**c. Identification of magnetic enhancement at hydrocarbon-fluid contacts. *AAPG Bulletin*. 105 (10): 1973–1991. doi:10.1306/07062019207.

Badley, M. E. **1985**. *Practical Seismic Interpretation*. Hoboken: Prentice Hall.

Baechle, G. T., Colpaert, A., Eberli, G. P., and Weger, R. J. **2008**. Effects of microporosity on sonic velocity in carbonate rocks. *The Leading Edge*. 1: 1–5. doi:10.17730/praa.3.3.1245ulmr62264266.

Barr, D. **1985**. 3-D palinspastic restoration of normal faults in the Inner Moray Firth: implications for extensional basin development. *Earth and Planetary Science Letters*. 75 (2-3): 191–203. doi:10.1016/0012-821X(85)90101-3.

Barr, D., McQuillin, R., and Donato, J. A. **1985**. Footwall uplift in the Inner Moray Firth basin, offshore Scotland. *Journal of Structural Geology*. 7 (2): 267–268. doi:10.1016/0191-8141(85)90137-3.

Baur, F. **2019**. Predicting petroleum gravity with basin modeling: New kinetic models. *AAPG Bulletin*. 103 (8): 1811–1837. doi:10.1306/12191818064.

Becquey, M., Lavergne, M., and Willm, C. **1979**. Acoustic impedance logs computed from seismic traces. *Geophysics*. 44 (9): 1485–1501. doi:10.1190/1.1441020.

Berner, R. A. **1969**. Goethite stability and the origin of red beds. *Geochimica et Cosmochimica Acta*. 33 (2): 267–273. doi:10.1016/0016-7037(69)90143-4.

Berner, R. A. **1981**. A New Geochemical Classification of Sedimentary Environments. *SEPM Journal of Sedimentary Research*. 51 (2): 359–366. doi:10.1306/212F7C7F-2B24-11D7-8648000102C1865D.

Berner, R. A. **1984**. Sedimentary pyrite formation: An update. *Geochimica et Cosmochimica Acta*. 48 (4): 605–615. doi:10.1016/0016-7037(84)90089-9.

Berry, J. E. **1959**. Acoustic Velocity in Porous Media. *Petroleum Transactions, AIME*. 216 (1): 262–270. doi:10.2118/1231-g.

Besnus, M. J. and Meyer, A. J. **1964**. Nouvelles donnees experimentales sur le magnetisme de la pyrrhotine naturelle. In: *Proceedings of the International Conference on Magnetism*. Nottingham: Institute of Physics and the Physical Society. pp. 507–511.

Bill, E. **2019**. 57Fe-mössbauer spectroscopy and basic interpretation of mössbauer parameters. *Practical Approaches to Biological Inorganic Chemistry*: 201–228. doi:10.1016/B978-0-444-64225-7.00006-7.

Bina, M. and Daly, L. **1994**. Mineralogical change and self-reversed magnetizations in pyrrhotite resulting from partial oxidation; geophysical implications. *Physics of the Earth and Planetary Interiors*. 85: 83–99. doi:10.1016/0031-9201(94)90009-4.

Bird, T. J., Bell, A., Gibbs, A. D., and Nicholson, J. **1987**. Aspects of strike-slip tectonics in the Inner Moray Firth Basin, offshore Scotland. *Norsk Geologisk Tidsskrift*. 67: 353–369.

Bjorlykke, K. **2010**. *Petroleum Geoscience*. 1st edn.. Berlin: Springer-Verlag.

Bleaney, B. I. and Bleaney, B. **2013**. *Electricity And Magnetism*. 1st edn.. Oxford: Oxford University Press.

Brown, S., Richards, P. C., Andrews, I. J., and Thomson, J. R. **1988**. Stratigraphic Evolution and Reservoir Sedimentology, Moray Firth Basin: a core workshop. Tech. rep.. British Geological Survey. Edinburgh.

Burke, J. A., Campbell Jr, R. L., and Schmidt, A. W. **1969**. The Litho-Porosity Cross Plot. In: *SPWLA Tenth Annual Logging Symposium*. 3. pp. 1–27.

Burnham, A. K., Peters, K. E., and Schenk, O. **2016**. Evolution of Vitrinite Reflectance Models. In: Calgary, ed., *AAPG 2016 Annual Convention*. AAPG. pp. 1–22.

Bustamante, A., Lovera, D., Quille, R., Arias, A. V., and Quiñones, J. **2010**. Mössbauer spectroscopy study of a mineral sample from Oshno hill, District of Chavín de Pariarca, Huanuco Region, Peru. *Hyperfine Interactions*. 195 (1): 63–68. doi:10.1007/s10751-009-0102-x.

Butler, R. **1982**. Magnetic mineralogy of continental deposits, San Juan Basin, New Mexico, and Clark's Fork Basin, Wyoming. *Journal of Geophysical Research*. 87 (B9): 7843–7852. doi:10.1029/JB087iB09p07843.

Butler, R. F. **1992**. *Paleomagnetism: magnetic domains to geologic terranes*. September. 1st edn.. Portland: University of Portland.

Butler, R. F. and Banerjee, S. K. **1975**. Theoretical single-domain grain size range in magnetite and titanomagnetite. *Journal of Geophysical Research*. 80 (29): 4049–4058. doi:10.1029/jb080i029p04049.

Canfield, D. E. and Berner, R. A. **1987**. Dissolution and pyritization of magnetite in anoxie marine sediments. *Geochimica et Cosmochimica Acta*. 51 (3): 645–659. doi:10.1016/0016-7037(87)90076-7.

Carlson, L. and Schwertmann, U. **1990**. The effect of CO 2 and oxidation rate on the formation of goethite versus lepidocrocite from an Fe(II) system at pH 6 and 7 . *Clay Minerals*. 25 (1): 65–71. doi:10.1180/claymin.1990.025.1.07.

Carneiro, C. E., Ivashita, F. F., De Souza, I. G., De Souza, C. M., Paesano, A., Da Costa, A. C., Di Mauro, E., De Santana, H., Zaia, C. T., and Zaia, D. A. **2013**. Synthesis of goethite in solutions of artificial seawater and amino acids: A prebiotic chemistry study. *International Journal of Astrobiology*. 12 (2): 149–160. doi:10.1017/S1473550413000013.

Chakraborty, S., Mondal, S., and Yadav, A. **2015**. Rock physical diagnostic of diagenetic cement with additional input from M-N lithology Cross- Plot : Study from wells in East coast of India . In: *SPG India 11th Biennial International Conference and Exposition*. Jaipur. pp. 1–3.

Cheng, Y., Xing, J., Bu, C., Zhang, J., Piao, G., Huang, Y., Xie, H., and Wang, X. **2019**. Dehydroxylation and structural distortion of kaolinite as a high-temperature sorbent in the furnace. *Minerals*. 9 (10). doi:10.3390/min9100587.

Chorneyko, D. M. **2006**. Real-time reservoir surveillance utilizing permanent downhole pressures-an operator's experience. *Proceedings - SPE Annual Technical Conference and Exhibition*. 7: 4436–4443. doi:10.2523/103213-ms.

Clifford, P. J. and Duthie, A. **1987**. Analysis of a polymer well treatment in the Beatrice Field. In: *Society of Petroleum Engineers - Offshore Europe, OE 1987*. pp. 1–14.

Costanzo-Álvarez, V., Aldana, M., Díaz, M., Bayona, G., and Ayala, C. **2006**. Hydrocarbon-induced magnetic contrasts in some Venezuelan and Colombian oil wells. *Earth, Planets and Space*. 58 (10): 1401–1410.

doi:10.1186/BF03352636.

Costanzo-Álvarez, V., Rapalini, A. E., Aldana, M., Díaz, M., Kietzmann, D., Iglesia-Llanos, M. P., Cabrera, A., Luppo, T., Vallejo, M. D., and Walther, A. M. **2019**. A combined rock-magnetic and EPR study about the effects of hydrocarbon-related diagenesis on the magnetic signature of oil shales (Vaca Muerta formation, southwestern Argentina). *Journal of Petroleum Science and Engineering*. 173 (September 2018): 861–879. doi:10.1016/j.petrol.2018.10.082.

Cudennec, Y. and Lecerf, A. **2005**. Topotactic transformations of goethite and lepidocrocite into hematite and maghemite. *Solid State Sciences*. 7 (5): 520–529. doi:10.1016/j.solidstatesciences.2005.02.002.

Curran, P. M. **1987**a. A Geochemical Study of the Inner Moray Firth, Quadrants 11-13, UCKS. Tech. rep.. BP Petroleum Development Ltd.

Curran, P. M. **1987**b. Timing of Hydrocarbon Generation and Volumes of Oil Generated in the Inner Moray Firth. Tech. rep.. BP.

Curry, M. R. and Fisher, M. J. **1982**. Coastal plain deposits in the Beatrice oilfield, UK, North Sea. In: *11th International Congress of the International Association of Sedimentologists*. Hamilton, Ontario: Congress of the International Association of Sedimentologists. p. 150.

Dabbous, M. K., Reznik, A. A., Mody, B. G., Fulton, P. F., and Taber, J. J. **1976**. Gas-Water Capillary Pressure in Coal At Various Overburden Pressures. *Soc Pet Eng AIME J*. 16 (5): 261–268. doi:10.2118/5348-pa.

Davies, R. J., Stephen, K. J., and Underhill, J. R. **1996**. A re-evaluation of Middle and Upper Jurassic stratigraphy and the flooding history of the Moray Firth Rift System, North Sea. *Geological Society, London, Special Publications*. 114 (1): 81–108. doi:10.1144/GSL.SP.1996.114.01.04.

Day, R., Fuller, M., and Schmidt, V. A. **1977**. Hysteresis properties of titanomagnetites: Grain-size and compositional dependence. *Physics of the Earth and Planetary Interiors*. 13 (4): 260–267. doi:10.1016/0031-9201(77)90108-X.

de Grave, E. and Vandenberghe, R. E. **1986**. 57Fe Mössbauer effect study of well-crystallized goethite (α-FeOOH). *Hyperfine Interactions*. 28 (1-4): 643–646. doi:10.1007/BF02061530.

De la Rosa, R., Aldana, M., Costanzo-Alvarez, V., Yepez, S., and Amon, C. **2021**. The surface expression of hydrocarbon seeps characterized by satellite image spectral analysis and rock magnetic data (Falcon basin, western Venezuela). *Journal of South American Earth Sciences*. 106 (November 2020): 103036. doi:10.1016/j.jsames.2020.103036.

Dekkers, M. J. **1989**. Magnetic properties of natural pyrrhotite. II. High- and low-temperature behaviour of Jrs and TRM as function of grain size. *Physics of the Earth and Planetary Interiors*. 57 (3-4): 266–283. doi:10.1016/0031-9201(89)90116-7.

Dekkers, M. J. **1990**. Magnetic monitoring of pyrrhotite alteration during thermal demagnetisation. *Geophysical Research Letters*. 17: 779–782. doi:10.1029/GL017i006p00779.

Dekkers, M. J., Passier, H. F., and Schoonen, M. A. A. **2000**. Magnetic properties of hydrothermally synthesized-greigite (Fe3S4)–II. High- and low-temperature characteristics. *Geophysical Journal International*. 141: 809–819. doi:10.1046/j.1365-246x.2000.00129.x.

Dembicki, H. **2009**. Three common source rock evaluation errors made by geologists during prospect or play appraisals. *AAPG Bulletin*. 93 (3): 341–356. doi:10.1306/10230808076.

Dembicki Jr, H. **2017**. *Practical Petroleum Geochemistry for Exploration and Production*. 1st edn.. New York: Elsevier.

di Primio, R. and Horsfield, B. **2006**. From petroleum-type organofacies to hydrocarbon phase prediction. *American Association of Petroleum Geologists Bulletin*. 90 (7): 1031–1058. doi:10.1306/02140605129.

Díaz, M., Aldana, M., Costanzo-Álvarez, V., Silva, P., and Pérez, A. **2000**. EPR and magnetic susceptibility studies in well samples from some Venezuelan oil fields. *Physics and Chemistry of the Earth, Part A: Solid Earth and Geodesy*. 25 (5): 447–453. doi:10.1016/S1464-1895(00)00069-7.

Dimitropoulos, K. and Donato, J. A. **1981**. The Inner Moray Firth Central Ridge, a geophysical interpretation. *Scottish Journal of Geology*. 17 (1): 27–38. doi:10.1144/sjg17010027.

Dodrill, B. C. **2015**. First-Order-Reversal-Curve (FORC) Measurements of Magnetic Minerals. Tech. rep.. Lake Shore Cryogenics Inc.. Westerville.

Donovan, T. J., Forgey, R. L., and Roberts, A. A. **1979**. Aeromagnetic detection of diagenetic magnetite over oil fields. *American Association of Petroleum Geologists Bulletin*. 63 (2): 245–248.

Donovan, T. J., Hendricks, J. D., Roberts, A. A., and Eliason, P. T. **1982**. Low-level aeromagnetic surveying for petroleum in Arctic Alaska. In: G. Gryc, ed., *Geology and Exploration of the National Petroleum Reserve in Alaska, 1974-1982*. Washington: U.S. Geological Survey Professional Papers. p. 940.

Duncan, A. D. and Hamilton, R. F. M. **1988**. Palaeolimnology and organic geochemistry of the Middle Devonian in the Orcadian Basin. In: A.J. Fleet, K. Kelts, and M.R. Talbot, eds., *Lacustrine Petroleum Source Rocks*. London: Geological Society Special Publications. pp. 173–201.

Dunlop, D. J. **2014**. High-temperature susceptibility of magnetite: A new pseudo-single-domain effect. *Geophysical Journal International*. 199 (2): 707–716. doi:10.1093/gji/ggu247.

Dunlop, D. J. and Özdemir, Ö. **1997**. *Rock Magnetism: Fundamentals and Frontiers*. Cambridge: Cambridge University Press.

Ellis, D. and Singer, J. **2007**. *Well Logging for Earth Scientists*. Dordrecht: Springer.

Elmore, R. D. and Crawford, L. **1990**. Remanence in authigenic magnetite: testing the hydrocarbon-magnetite hypothesis. *Journal of Geophysical Research*. 95 (B4): 4539–4549. doi:10.1029/JB095iB04p04539.

Elmore, R. D., Engel, M. H., Crawford, L., Nick, K., Imbus, S., and Sofert, Z. **1987**. Evidence for a relationship between hydrocarbons and authigenic magnetite. *Nature*. 325 (29): 428–430. doi:10.1038/325428a0.

Elmore, R. D., Kelley, J., Evans, M., and Lewchuk, M. T. **2001**. Remagnetization and orogenic fluids: Testing the hypothesis in the central Appalachians. *Geophysical Journal International*. 144 (3): 568–576. doi:10.1046/j.0956-540X.2000.01349.x.

Elmore, R. D., Muxworthy, A. R., and Aldana, M. **2012**. Remagnetization and chemical alteration of sedimentary rocks. *Geological Society, London, Special Publications*. 371 (1): 1–21. doi:10.1144/SP371.15.

Emmerton, S. A. **2012**. *Investigating the relationship between magnetisation and oil geochemistry*. PhD Thesis. Imperial College London.

Emmerton, S. A., Muxworthy, A. R., and Sephton, M. A. **2012**. Magnetic characterization of oil sands at Osmington Mills and Mupe Bay, Wessex Basin, UK. *Geological Society, London, Special Publications*. 371 (1): 189–198. doi:10.1144/sp371.6.

Emmerton, S. A., Muxworthy, A. R., Sephton, M. A., Aldana, M., Costanzo-Álvarez, V., Bayona, G., and Williams, W. **2013**. Correlating biodegradation to magnetization in oil bearing sedimentary rocks. *Geochimica et Cosmochimica Acta*. 112: 146–165. doi:10.1016/j.gca.2013.03.008.

Evans, B. H. T., Milton, C., Chao, E. C. T., Adler, I., Mead, C., Ingram, B., and Berner, R. A. **1964**. Valleriite and the new iron sulphide, mackinawite. *U.S. Geological Survey Professional Paper*. 475 D: 64=69.

Evans, B. J., Johnson, R. G., Senftle, F. E., Cecil, C. B., and Dulong, F. **1982**. The 57Fe Mössbauer parameters of pyrite and marcasite with different provenances. *Geochimica et Cosmochimica Acta*. 46 (5): 761–775. doi:10.1016/0016-7037(82)90028-X.

Evans, D., Graham, C., Armour, A., and Bathurst, P. **2003**. *The Millennium Atlas: petroleum geology of the central and corthern North Sea*. London: Geological Society of London.

Evans, M. E. and Heller, F. **2003**. *Environmental magnetism: principles and applications of enviromagnetics*. Amsterdam: Academic Press.

Fielder, M. and Johnson, R. W. **1986**. Use of Pour-Point Depressant Additive in the Beatrice Field. *Society of Petroleum Engineers of AIME*: 363–372. doi:10.2118/15888-ms.

Fortin, D., Leppard, G. G., and Tessier, A. **1993**. Characteristics of lacustrine diagenetic iron oxyhydroxides.

Geochimica et Cosmochimica Acta. 57 (18): 4391–4404. doi:10.1016/0016-7037(93)90490-N.

Fysh, S. A. and Clark, P. E. **1982**. Aluminous goethite: A mössbauer study. *Physics and Chemistry of Minerals*. 8 (4): 180–187. doi:10.1007/BF00308241.

Gao, X., Hao, Q., Oldfield, F., Bloemendal, J., Deng, C., Wang, L., Song, Y., Ge, J., Wu, H., Xu, B., Li, F., Han, L., Fu, Y., and Guo, Z. **2019**. New High-Temperature Dependence of Magnetic Susceptibility-Based Climofunction for Quantifying Paleoprecipitation From Chinese Loess. *Geochemistry, Geophysics, Geosystems*. 20 (8): 4273–4291. doi:10.1029/2019GC008401.

Geldart, L. P. and Sheriff, R. E. **2004**. *Problems in Exploration Seismology and their Solutions*. 1st edn.. Tulsa: Society of Exploration Geophysicists.

Gendler, T. S., Shcherbakov, V. P., Dekkers, M. J., Gapeev, A. K., Gribov, S. K., and McClelland, E. **2005**. The lepidocrocite-maghemite-haematite reaction chain - I. Acquisition of chemical remanent magnetization by maghemite, its magnetic properties and thermal stability. *Geophysical Journal International*. 160 (3): 815–832. doi:10.1111/j.1365-246X.2005.02550.x.

Giles, M. R., Indrelid, S. L., and James, D. M. D. **1998**. Compaction - the great unknown in basin modelling. *Geological Society Special Publication*. 141 (1): 15–43. doi:10.1144/GSL.SP.1998.141.01.02.

Glennie, K., Higham, J., and Stemmerik, L. **2003**. Chapter 8 - Permian. In: D. Evans, C. Graham, A. Armour, and P. Bathurst, eds., *The Millenium Atlas: petroleum geology of the central and northern North Sea*. chap. 8. London: Geological Society of London. pp. 91–103.

Gluyas, J. and Swarbrick, R. **2004**. *Petroleum Geoscience*. Oxford: Blackwell.

González, F., Aldana, M., Costanzo-Álvarez, V., Díaz, M., and Romero, I. **2002**. An integrated rock magnetic and EPR study in soil samples from a hydrocarbon prospective area. *Physics and Chemistry of the Earth*. 27 (25-31): 1311–1317. doi:10.1016/S1474-7065(02)00125-0.

Goss, C. J. **1987**. The kinetics and reaction mechanism of the goethite to hematite transformation. *Mineralogical Magazine*. 51: 437–451. doi:10.1180/minmag.1987.051.361.11.

Greenhalgh, E. E. **2016**. Literature Review of Devonian Source Rocks and Devonian-Sourced Hydrocarbons in the Orcadian Basin. Tech. rep.. British Geological Survey. Keyworth, Nottingham.

Guyodo, Y., Bonville, P., Till, J. L., Ona-Nguema, G., Lagroix, F., and Menguy, N. **2016**. Constraining the origins of the magnetism of lepidocrocite (γ-FeOOH): A mössbauer and magnetization study. *Frontiers in Earth Science*. 4 (March): 1–9. doi:10.3389/feart.2016.00028.

Hantschel, T. and Kauerauf, A. I. **2009**. *Fundamentals of basin and petroleum system modelling*. Dordrecht: Springer.

Harker, S. D. and Rieuf, M. **1996**. Genetic stratigraphy and sandstone distribution of the Moray Firth Humber Group (Upper Jurassic). In: A. Hurst, ed., *Geology of the Humber Group; Central Graben and Moray Firth, UKCS.*. vol. 114. London: Geological Society Special Publications. pp. 109–130.

Harrison, R. J. and Lascu, I. **2014**. FORCulator: A micromagnetic tool for simulating first-order reversal curve diagrams. *Geochemistry, Geophysics, Geosystems*. 15: 4671–4691. doi:10.1002/2014GC005582.

Harrison, R. J., Muraszko, J., Heslop, D., Lascu, I., Muxworthy, A. R., and Roberts, A. P. **2018**. An Improved Algorithm for Unmixing First-Order Reversal Curve Diagrams Using Principal Component Analysis. *Geochemistry, Geophysics, Geosystems*. 19 (5): 1595–1610. doi:10.1029/2018GC007511.

Hillis, R. R., Thomson, K., and Underhill, J. R. **1994**. Quantification of Tertiary erosion in the Inner Moray Firth using sonic velocity data from the Chalk and the Kimmeridge Clay. *Marine and Petroleum Geology*. 11 (3): 283–293. doi:10.1016/0264-8172(94)90050-7.

Hogan, J. A., Jones, T. P., and Mills, S. J. **1978**. Evaluation of the Beatrice Field and reappraisal of the Inner Moray Firth Basin. Tech. rep.. British National Oil Corporation.

Horng, C. S. and Roberts, A. P. **2006**. Authigenic or detrital origin of pyrrhotite in sediments?: Resolving a paleomagnetic conundrum. *Earth and Planetary Science Letters*. 241 (3-4): 750–762.

doi:10.1016/j.epsl.2005.11.008.

Hunger, S. and Benning, L. G. **2007**. Greigite: A true intermediate on the polysulfide pathway to pyrite. *Geochemical Transactions*. 8: 1–20. doi:10.1186/1467-4866-8-1.

Ibrahim, M. M., Edwards, G., Seehra, M. S., Ganguly, B., and Huffman, G. P. **1994**. Magnetism and spin dynamics of nanoscale FeOOH particles. *Journal of Applied Physics*. 75 (10): 5873–5875. doi:10.1063/1.355545.

Ivakhnenko, O. P. and Potter, D. K. **2004**. Magnetic susceptibility of petroleum reservoir fluids. *Physics and Chemistry of the Earth*. 29 (13-14 Spec. Iss.): 899–907. doi:10.1016/j.pce.2004.06.001.

Izundu, U. **2008**. Ithaca Energy to develop Jacky field.

Jankowsky, W. **1962**. Diagenese und Ölinhalt als Hilfsmittel für die strukturgeschichtliche Analyse des Norwestdeutschen Beckens. *Zeitschrift der Deutschen Geologischen Gesellschaft*. 114 (1): 452–460.

Jarvie, D. M., Hill, R. J., Ruble, T. E., and Pollastro, R. M. **2007**. Unconventional shale-gas systems: The Mississippian Barnett Shale of north-central Texas as one model for thermogenic shale-gas assessment. *American Association of Petroleum Geologists Bulletin*. 91 (4): 475–499. doi:10.1306/12190606068.

Johnson, H., Leslie, A. B., Wilson, C. K., Andrews, I. J., and Cooper, R. M. **2005**. Middle Jurassic, Upper Jurassic and Lower Cretaceous of the UK Central and Northern North Sea. Tech. rep.. British Geological Survey. Keyworth, Nottingham.

Johnson, H., Warrington, G., and Stoker, S. J. **1994**. 6. Permian and Triassic of the Southern North Sea. In: R.W.O. Knox and W.G. Cordey, eds., *Lithostratigraphic nomenclature of the UK North Sea*. chap. 6. Keyworth, Nottingham: British Geological Survey. p. 172.

Jonk, R., Duranti, D., Parnell, J., Hurst, A., and Fallick, A. **2003**. The structural and diagenetic evolution of injected sandstones: examples from the Kimmeridgian of NE Scotland. *Journal of the Geological Society*. 160 (6): 881–894. doi:10.1144/0016-764902-091.

Kar, S., Mandal, S. K., Das, D., and Chaudhuri, S. **2004**. Wet chemical synthesis of iron pyrite and characterization by Mössbauer spectroscopy. *Materials Letters*. 58 (22-23): 2886–2889. doi:10.1016/j.matlet.2004.05.012.

Kars, M., Aubourg, C., Labaume, P., Berquo, T. S., and Cavailhes, T. **2014**. Burial diagenesis of magnetic minerals. *Minerals*. 4 (July 2015): 0–24. doi:10.3390/min40x000x.

Kars, M., Aubourg, C., Pozzi, J. P., and Janots, D. **2012**. Continuous production of nanosized magnetite through low grade burial. *Geochemistry, Geophysics, Geosystems*. 13 (8): 1–12. doi:10.1029/2012GC004104.

Kilgore, B. and Elmore, R. D. **1989**. A study of the relationship between hydrocarbon migration and the precipitation of authigenic magnetic minerals in the Triassic Chugwater Formation, southern Montana. *Geological Society of America Bulletin*. 101 (10): 1280–1288. doi:10.1130/0016-7606(1989)101<1280:ASOTRB>2.3.CO;2.

Kilvington, L. J. and Gallivan, J. D. **1983**. Beatrice Field: electrical submersible pump and reservoir performance 1981-1983. In: *Society of Petroleum Engineers - Offshore Europe, OE 1983*. Aberdeen. pp. 1934–1940.

Kilvington, L. J., Thomson, J. Y., and Brown, J. K. **1987**. Electrical submersible pumping success in the North Sea, Beatrice field. *Proceedings of the Annual Offshore Technology Conference*. 1987-April (November): 229–238.

Kittel, C. **1949**. Physical theory of ferromagnetic domains. *Reviews of Modern Physics*. 21 (4): 541–583. doi:10.1103/RevModPhys.21.541.

Kittel, C. **1967**. Ferromagnetism and antiferromagnetism. In: S. Johnson and P. McFadden, eds., *Introduction to Solid State Physics*. 3rd edn.. New York: John Wiley & Sons, Inc. pp. 321–357.

Klein, C. and Hurlbut, C. S. **1985**. *Manual Of Mineralogy (after J. D. Dana)*. 20th edn.. Wiley.

Kobayashi, K. and Nomura, M. **1972**. Iron sulfides in the sediment cores from the Sea of Japan and their geophysical implications. *Earth and Planetary Science Letters*. 16 (2): 200–208. doi:10.1016/0012-821X(72)90190-2.

Krupp, R. E. **1994**. Phase relations and phase transformations between the low-temperature iron sulfides mackinawite, greigite, and smythite. *European Journal of Mineralogy*. 6 (2): 265–278. doi:10.1127/ejm/6/2/0265.

Kumar, A. **2012**. *Petroleum Engineering Handbook*. New Delhi: SBS Publishing.

Kwon, K. D., Refson, K., Bone, S., Qiao, R., Yang, W. L., Liu, Z., and Sposito, G. **2011**. Magnetic ordering

in tetragonal FeS: Evidence for strong itinerant spin fluctuations. *Physical Review B - Condensed Matter and Materials Physics*. 83 (6). doi:10.1103/PhysRevB.83.064402.

Lang, W. H. **1978**. The determination of prior depth of burial (uplift and erosion) using interval transit time. In: *SPWLA 19th Annual Logging Symposium 1978*. El Paso: SPWLA. pp. 1–17.

Lanza, R. and Meloni, A. **2006**. *The Earth's Magnetism: An Introduction for Geologists*. Berlin: Springer.

Lascu, I., Einsle, J. F., Ball, M. R., and Harrison, R. J. **2018**. The Vortex State in Geologic Materials: A Micromagnetic Perspective. *Journal of Geophysical Research: Solid Earth*. 123 (9): 7285–7304. doi:10.1029/2018JB015909.

Lascu, I., Harrison, R. J., Li, Y., Muraszko, J. R., Channell, J. E., Piotrowski, A. M., and Hodell, D. A. **2015**. Magnetic unmixing of first-order reversal curve diagrams using principal component analysis. *Geochemistry, Geophysics, Geosystems*. 16 (9): 2900–2915. doi:10.1002/2015GC005909.

Lennie, A. R., England, K. E., and Vaughan, D. J. **1995**. Transformation of synthetic mackinawite to hexagonal pyrrhotite: a kinetic study. *American Mineralogist*. 80 (9-10): 960–967. doi:10.2138/am-1995-9-1012.

Lennie, A. R., Redfern, S. A., Champness, P. E., Stoddart, C. P., Schofield, P. F., and Vaughan, D. J. **1997**. Transformation of mackinawite to greigite: An in situ X-ray powder diffraction and transmission electron microscope study. *American Mineralogist*. 82 (3-4): 302–309. doi:10.2138/am-1997-3-408.

Li, G., Zhang, B., Yu, F., Novakova, A. A., Krivenkov, M. S., Kiseleva, T. Y., Chang, L., Rao, J., Polyakov, A. O., Blake, G. R., De Groot, R. A., and Palstra, T. T. **2014**. High-purity Fe3S4 greigite microcrystals for magnetic and electrochemical performance. *Chemistry of Materials*. 26 (20): 5821–5829. doi:10.1021/cm501493m.

Li, H. Y. and Zhang, S. H. **2005**. Detection of mineralogical changes in pyrite using measurements of temperature-dependence susceptibilities. *Acta Geophysica Sinica*. 48 (6): 1384–1391. doi:10.1002/cjg2.794.

Li, S., Tang, D., Xu, H., Yang, Z., and Guo, L. **2012**. Porosity and permeability models for coals using low-field nuclear magnetic resonance. *Energy and Fuels*. 26 (8): 5005–5014. doi:10.1021/ef300432m.

Lima-de Faria, J. **1967**. Anomalous orientations of cubic close packing in the dehydration of Goethite in an inert atmosphere. *Acta Crystallographica*. 23: 733–736. doi:10.1107/s0365110x67003615.

Lin, C. Y., Turchyn, A. V., Krylov, A., and Antler, G. **2020**. The microbially driven formation of siderite in salt marsh sediments. *Geobiology*. 18 (2): 207–224. doi:10.1111/gbi.12371.

Linsley, P. N., Potter, H. C., McNab, G., and Racher, D. **1980**. The Beatrice Field, Inner Moray Firth, UK., North Sea. In: M.T. Halbouty, ed., *Giant Oil and Gas Fields of the Decade 1968-1978*. Houston: American Association of Petroleum Geologists. pp. 117–129.

Liu, Q., Yu, Y., Torrent, J., Roberts, A. P., Pan, Y., and Zhu, R. **2006**. Characteristic low-temperature magnetic properties of aluminous goethite [α-(Fe, Al)OOH] explained. *Journal of Geophysical Research: Solid Earth*. 111 (B12). doi:10.1029/2006JB004560.

Lloyd's Register. **2018**. Interactive Petrophysics.

Lowrie, W. **2012**. *Fundamentals of Geophysics*. 2nd edn.. Cambridge: Cambridge University Press.

Lowrie, W. and Heller, F. **1982**. Magnetic properties of marine limestones. *Reviews of Geophysics*. 20 (2): 171–192. doi:10.1029/RG020i002p00171.

Machel, H. G. **1995**. Magnetic mineral assemblages and magnetic contrasts in diagenetic environments - with implications for studies of palaeomagnetism, hydrocarbon migration and exploration. In: P. Turner and A. Turner, eds., *Palaeomagnetic Applications in Hydrocarbon Exploration and Production*. London: Geological Society Special Publications. pp. 9–29.

Machel, H. G. and Burton, E. A. **1991**a. Causes and spatial distribution of anomalous magnetization in hydrocarbon seepage environments. *American Association of Petroleum Geologists Bulletin*. 75 (12): 1864–1876. doi:10.1306/0C9B2A5B-1710-11D7-8645000102C1865D.

Machel, H. G. and Burton, E. A. **1991**b. Chemical and microbial processes causing anomalous magnetization in environments affected by hydrocarbon seepage. *Geophysics*. 56 (5): 598–605. doi:10.1190/1.1443076.

Mackenzie, A. S., Maxwell, J. R., Coleman, M. L., and Deegan, C. E. **1983**. Biological marker and isotope studies of North Sea crude oils and sediments. In: *11th World Petroleum Congress*. London: World Petroleum Congress. pp. 45–56.

Marshall, J. E. A. **1998**. The recognition of multiple hydrocarbon generation episodes : an example from Devonian lacustrine sedimentary rocks in the Inner Moray Firth , Scotland. *Journal of the Geological Society*. 155 (1): 335–352. doi:10.1144/gsjgs.155.2.0335.

McQuillin, R., Donato, J. A., and Tulstrup, J. **1982**. Development of basins in the Inner Moray Firth and the North Sea by crustal extension and dextral displacement of the Great Glen Fault. *Earth and Planetary Science Letters*. 60 (1): 127–139. doi:10.1016/0012-821X(82)90028-0.

Minyuk, P. S., Subbotnikova, T. V., and Plyashkevich, A. A. **2011**. Measurements of thermal magnetic susceptibility of hematite and goethite. *Izvestiya, Physics of the Solid Earth*. 47 (9): 762–774. doi:10.1134/S1069351311080052.

Minyuk, P. S., Tyukova, E. E., Subbotnikova, T. V., Kazansky, A. Y., and Fedotov, A. P. **2013**. Thermal magnetic susceptibility data on natural iron sulfides of northeastern Russia. *Russian Geology and Geophysics*. 54 (4): 464–474. doi:10.1016/j.rgg.2013.03.008.

Morin, F. J. **1950**. Magnetic susceptibility of α-Fe2O3 and α-Fe2O3 with added titanium. *Physical Review*. 78 (6): 819–820. doi:10.1103/PhysRev.78.819.2.

Morton-Thompson, D., Woods, A. M., and American Association of Petroleum Geologists. **1993**. *Development Geology Reference Manual: AAPG Methods in Exploration Series, No. 10*. Methods in Exploration Series. American Association of Petroleum Geologists.

Mössbauer, R. L. **1958**. Kernresonanzfluoreszenz von Gammastrahlung in Ir191. *Zeitschrift für Physik*. 151 (2): 124–143. doi:10.1007/BF01344210.

Murad, E. **1982**. The characterization of goethite by Mossbauer spectroscopy. *American Mineralogist*. 67 (9-10): 1007–1011.

Muxworthy, A., Heslop, D., and Williams, W. **2004**. Influence of magnetostatic interactions on first-order-reversal-curve (FORC) diagrams: A micromagnetic approach. *Geophysical Journal International*. 158 (3): 888–897. doi:10.1111/j.1365-246X.2004.02358.x.

Muxworthy, A. R. and Baker, E. **2022**. Revisiting the non-heating Preisach paleointensity method using remanence-based FORC diagrams. In Prep.

Muxworthy, A. R. and Williams, W. **2006**. Critical single-domain/multidomain grain sizes in noninteracting and interacting elongated magnetite particles: Implications for magnetosomes. *Journal of Geophysical Research: Solid Earth*. 111 (12). doi:10.1029/2006JB004588.

Newman, M. J. and Dean, M. T. **2005**. A biostratigraphical framework for geological correlation of the Middle Devonian strata in the Moray-Ness Basin Project area. Tech. rep.. British Geological Survey. Keyworth, Nottingham.

Nielsen, S. B., Clausen, O. R., and McGregor, E. **2015**. basin%Ro: A vitrinite reflectance model derived from basin and laboratory data. *Basin Research*. 29 (1): 515–536. doi:10.1111/bre.12160.

Offshore Magazine. **2012**. Trapoil reports Lybster onstream, discovery at Orchid.

Ohfuji, H. and Rickard, D. **2005**. Experimental syntheses of framboids - A review. *Earth-Science Reviews*. 71 (3-4): 147–170. doi:10.1016/j.earscirev.2005.02.001.

Oil and Gas Authority. **2018**. Oil and Gas Authority Production Data from PPRS - Beatrice Field.

Oil and Gas Authority. **2021**. UK National Data Repository.

Paleoservices. **1978**. Sedimentological, palentological, petrographic and environmental study with SEM and XRD analyses of Well 11/30-5, UK North Sea. Tech. rep.. Paleoservices. Watford.

Parnell, J., Baba, M., Bowden, S., and Bullock, L. **2017**. Geochemistry and origin of organic-rich sediment veins in fractured granitic basement, Helmsdale, Sutherlandshire, UK. *Marine and Petroleum Geology*. 88: 107–114.

doi:10.1016/j.marpetgeo.2017.08.013.

Pepper, A. S. and Corvi, P. J. **1995**a. Simple kinetic models of petroleum formation. Part I: Oil and gas generation from kerogen. *Marine and Petroleum Geology*. 12 (3): 291–319. doi:10.1016/0264-8172(95)98381-E.

Pepper, A. S. and Corvi, P. J. **1995**b. Simple kinetic models of petroleum formation. Part III: Modelling an open system. *Marine and Petroleum Geology*. 12 (4): 417–452. doi:10.1016/02648-1729(59)69045-.

Pepper, A. S. and Dodd, T. A. **1995**. Simple kinetic models of Petroleum formation. Part II: Oil-gas cracking. *Marine and Petroleum Geology*. 12 (3): 321–340. doi:10.1016/0264-8172(95)98382-F.

Perkins, J. R. **2017**. *Post-mortem reservoir quality assessment: reservoir characterisation through well log analysis, calculated porosity & permeability curves and geological modelling - The Hutton Field, East Shetland Basin, Northern North Sea*. MSc Thesis. University of Portsmouth.

Peter D. Rude, R. C. A. **1989**. Early Diagenetic Alteration of Lateritic Particle Coatings in Amazon Continental Shelf Sediment. *Journal of Sedimentary Research*. 59 (5): 704–716. doi:10.1306/212F9052-2B24-11D7-8648000102C1865D.

Peters, K. E., Clutson, M. J., and Robertson, G. **1998**. Mixed marine and lacustrine input to an oil-cemented sandstone breccia from Brora, Scotland. *Organic Geochemistry*. 30 (4): 237–248. doi:10.1016/S0146-6380(98)00216-2.

Peters, K. E., Moldowan, J. M., Driscole, A. R., and Demaison, G. J. **1989**. Origin of Beatrice Oil by Co-Sourcing from Devonian and Middle Jurassic Source Rocks, Inner Moray Firth, United Kingdom. *The AAPG Bulletin*. 73 (4): 454–471. doi:10.1306/44B49FCE-170A-11D7-8645000102C1865D.

Peters, K. E., Walters, C. C., and Moldowan, J. M. **2004**. *The Biomarker Guide*. 2nd edn.. Cambridge: Cambridge University Press.

Pike, C. R., Roberts, A. P., and Verosub, K. L. **1999**. Characterizing interactions in fine magnetic particle systems using first order reversal curves. *Journal of Applied Physics*. 85 (9): 6660–6667. doi:10.1063/1.370176.

Poelchau, H. S. **2001**. Modeling an exhumed basin: A method for estimating eroded overburden. *Natural Resources Research*. 10 (1): 73–84. doi:10.1023/A:1011537632624.

Ponomar, V. P., Dudchenko, N. O., and Brik, A. B. **2017**. Phase transformations of siderite ore by the thermomagnetic analysis data. *Journal of Magnetism and Magnetic Materials*. 423: 373–378. doi:10.1016/j.jmmm.2016.09.124.

Qu, X. F., Yao, Q. Z., and Zhou, G. T. **2011**. Synthesis of siderite microspheres and their transformation to magnetite microspheres. *European Journal of Mineralogy*. 23 (5): 759–770. doi:10.1127/0935-1221/2011/0023-2134.

Raymer, L. L., Hunt, E. R., and Gardner, J. S. **1980**. An improved sonic transit time-to-porosity transform. In: *SPWLA Twenty-First Anuual Logging Symposium*. Lafayette: SPWLA. pp. 1–13.

Richards, R. P., Lott, G. K., Johnson, H., Knox, R. W. O., and Riding, J. B. **1993**. 3 . Jurassic of the central and northern North Sea. In: R.W.O. Knox and W.G. Cordey, eds., *Lithostratigraphic nomenclature of the UK North Sea*. chap. 3. Keyworth, Nottingham: British Geological Survey. p. 252.

Rickard, D. **2013**. *The Sedimentary Sulfur System: Biogeochemistry and Evolution through Geologic Time*. vol. 9. 2nd edn.. Elsevier Ltd.

Rijal, M. L., Appel, E., Petrovský, E., and Blaha, U. **2010**. Change of magnetic properties due to fluctuations of hydrocarbon contaminated groundwater in unconsolidated sediments. *Environmental Pollution*. 158 (5): 1756–1762. doi:10.1016/j.envpol.2009.11.012.

Rijal, M. L., Porsch, K., Appel, E., and Kappler, A. **2012**. Magnetic signature of hydrocarbon-contaminated soils and sediments at the former oil field Hänigsen, Germany. *Studia Geophysica et Geodaetica*. 56 (3): 889–908. doi:10.1007/s11200-010-0040-8.

Ristić, M., Krehula, S., Reissner, M., and Musić, S. **2017**. 57Fe mössbauer, XRD, FT-IR, FE SEM analyses of natural goethite, hematite and siderite. *Croatica Chemica Acta*. 90 (3): 499–507. doi:10.5562/cca3233.

Roberts, A. M., Badley, M. E., Price, J. D., and Huck, I. W. **1990**. The structural history of a transtensional basin: Inner Moray Firth, NE Scotland. *Journal of the Geological Society*. 147 (1): 87–103. doi:10.1144/gsjgs.147.1.0087.

Roberts, A. P., Almeida, T. P., Church, N. S., Harrison, R. J., Heslop, D., Li, Y., Li, J., Muxworthy, A. R., Williams, W., and Zhao, X. **2017**. Resolving the Origin of Pseudo-Single Domain Magnetic Behavior. *Journal of Geophysical Research: Solid Earth*. 122 (12): 9534–9558. doi:10.1002/2017JB014860.

Roberts, A. P., Chang, L., Rowan, C. J., Horng, C. S., and Florindo, F. **2011**. Magnetic properties of sedimentary greigite (Fe3S4): An update. *Reviews of Geophysics*. 49 (1). doi:10.1029/2010RG000336.

Roberts, A. P., Heslop, D., Zhao, X., and Pike, C. R. **2014**. Understanding fine magnetic particle systems through use of first-order reversal curve diagrams. *Reviews of Geophysics*. 52 (4): 557–602. doi:10.1002/2014RG000462.

Roberts, A. P., Pike, C. R., and Verosub, K. L. **2000**. First-order reversal curve diagrams: A new tool for characterizing the magnetic properties of natural samples. *Journal of Geophysical Research: Solid Earth*. 105 (B12): 28461–28475. doi:10.1029/2000JB900326.

Roberts, A. P., Zhao, X., Harrison, R. J., Heslop, D., Muxworthy, A. R., Rowan, C. J., Larrasoana, J. C., and Florinado, F. **2018**. Signatures of Reductive Magnetic Mineral Diagenesis From Unmixing of First-Order Reversal Curves. *Journal of Geophysical Research: Solid Earth*. 123 (1): 1–23. doi:10.1029/2018JB015706.

Robertson Research International. **2001**. Moray Firth Basins, Hydrocarbon Provenance and Modelling Vol.1. Tech. rep.. Robertson Research International.

Rochette, P. **1987**. Metamorphic control of the magnetic mineralogy of black shales in the Swiss Alps: toward the use of "magnetic isograde". *Earth and Planetary Science Letters*. 84 (4): 446–456. doi:10.1016/0012-821X(87)90009-4.

Rochette, P., Fillion, G., Mattéi, J. L., and Dekkers, M. J. **1990**. Magnetic transition at 30-34 Kelvin in pyrrhotite: insight into a widespread occurrence of this mineral in rocks. *c*. 98 (3-4): 319–328. doi:10.1016/0012-821X(90)90034-U.

Sagnotti, L. **2007**. Iron Sulfides. In: D. Gubbins and E. Herrero-Bervera, eds., *Encyclopedia of Geomagnetism and Paleomagnetism*. 1st edn.. Dordrecht: Springer-Verlag. pp. 454–459.

Schlumberger. **2015**. Petrel.

Schlumberger. **2020**. PetroMod.

Schröder, C., Wan, M., Butler, I. B., Tait, A., Peiffer, S., and McCammon, C. A. **2020**. Identification of mackinawite and constraints on its electronic configuration using mössbauer spectroscopy. *Minerals*. 10 (12): 1–13. doi:10.3390/min10121090.

Schwertmann, U. and Fechter, H. **1984**. The Influence of Aluminum on Iron Oxides: XI. Aluminum-Substituted Maghemite in Soils and Its Formation. *Soil Science Society of America Journal*. 48 (6): 1462–1463. doi:10.2136/sssaj1984.03615995004800060054x.

Simm, R. and Bacon, M. **2014**. *Seismic Amplitude*. Cambridge: Cambridge University Press.

Song, X. and Boily, J. F. **2016**. Surface and Bulk Thermal Dehydroxylation of FeOOH Polymorphs. *Journal of Physical Chemistry A*. 120 (31): 6249–6257. doi:10.1021/acs.jpca.6b04294.

Stacey, F. and Banerjee, S. K. **1974**. *The Physical Principles of Rock Magnetism*. Amsterdam: Elsevier.

Stevens, V. **1991**. The Beatrice Field, Block 11/30a, UK North Sea. *Geological Society, London, Memoirs*. 14 (1): 245–252. doi:10.1144/GSL.MEM.1991.014.01.30.

Stewart, S. A. and Clark, J. A. **1999**. Impact of salt on the structure of the Central North Sea hydrocarbon fairways. *Petroleum Geology Conference Proceedings*. 5 (0): 179–200. doi:10.1144/0050179.

Sweeney, J. J. and Burnham, A. K. **1990**. Evaluation of a Simple Model of Vitrinite Reflectance Based on Chemical Kinetics. *AAPG Bulletin*. 74 (10): 1559–1570.

Tauxe, L. **2009**. *Essentials of Paleomagnetism*. La Jolla: UC San Diego.

Thiel, J., Byrne, J. M., Kappler, A., Schink, B., and Pester, M. **2019**. Pyrite formation from FeS and H 2 S is mediated through microbial redox activity. *Proceedings of the National Academy of Sciences of the United States of America*. 116 (14): 6897–6902. doi:10.1073/pnas.1814412116.

Thomson, K. **1993**. *Tertiary tectonics and uplift of the Inner Moray Firth and adjacent areas.* PhD Thesis. University of Edinburgh.

Thomson, K. and Hillis, R. R. **1995**. Tertiary structuration and erosion of the Inner Moray Firth. In: R.A. Scrutton, M.S. Stoker, G.B. Shimmield, and A.W. Tudhope, eds., *The Tectonics, Sedimentation and Palaeoceanography of the North Atlantic Region*. vol. 90. London: Geological Society Special Publications. pp. 249–269.

Till, J. L. and Nowaczyk, N. **2018**. Authigenic magnetite formation from goethite and hematite and chemical remanent magnetization acquisition. *Geophysical Journal International*. 213 (3): 1818–1831. doi:10.1093/gji/ggy083.

Tissot, B. P. and Welte, D. H. **1984**. *Petroleum Formation and Occurrence*. 2nd edn.. Berlin: Springer-Verlag.

Trewin, N. H. **1989**. The petroleum potential of the Old Red Sandstone of northern Scotland. *Scottish Journal of Geology*. 25 (2): 201–225. doi:10.1144/sjg25020201.

Tucker, M. **2011**. *Sedimentary Rocks in the Field: A Practical Guide*. 4th edn.. Chichester: Wiley.

Underhill, J. R. **1991**. Implications of Mesozoic-Recent basin development in the western Inner Moray Firth, UK. *Marine and Petroleum Geology*. 8: 359–369. doi:10.1016/0264-8172(91)90089-J.

Underhill, J. R. and Partington, M. A. **1993**. Jurassic thermal doming and deflation in the North Sea: implications of the sequence stratigraphic evidence. In: *Petroleum Geology of Northwest Europe: Proceedings of the 4th Conference*. London: Geological Society of London. pp. 337–345.

Valdez-Grijalva, M. A. and Muxworthy, A. R. **2019**. First-order reversal curve (FORC) diagrams of nanomagnets with cubic magnetocrystalline anisotropy: A numerical approach. *Journal of Magnetism and Magnetic Materials*. 471 (October 2017): 359–364. doi:10.1016/j.jmmm.2018.09.086.

Valdez-Grijalva, M. A., Muxworthy, A. R., Williams, W., Ó Conbhuí, P., Nagy, L., Roberts, A. P., and Heslop, D. **2018**. Magnetic vortex effects on first-order reversal curve (FORC) diagrams for greigite dispersions. *Earth and Planetary Science Letters*. 501: 103–111. doi:10.1016/j.epsl.2018.08.027.

van der Zee, C., Roberts, D. R., Rancourt, D. G., and Slomp, C. P. **2003**. Nanogoethite is the dominant reactive oxyhydroxide phase in lake and marine sediments. *Geology*. 31 (11): 993–996. doi:10.1130/G19924.1.

Vandenberghe, R. E., De Grave, E., De Geyter, G., and Landuydt, C. **1986**. Characterization of goethite and hematite in a Tunisian soil profile by Mossbauer spectroscopy. *Clays & Clay Minerals*. 34 (3): 275–280. doi:10.1346/CCMN.1986.0340307.

Vaughan, D. J. and Craig, J. R. **1978**. *Mineral Chemistry of Metal Sulphides*. Cambridge: Cambridge University Press.

Veeken, P. **2007**. *Seismic Stratigraphy, Basin Analysis and Reservoir Characterisation*. Oxford: Elsevier.

Verwey, E. J. W. **1939**. Electronic conduction of magnetite (Fe3O4) and its transition point at low temperatures.

Volk, M. W., Gilder, S. A., and Feinberg, J. M. **2016**. Low-temperature magnetic properties of monoclinic pyrrhotite with particular relevance to the Besnus transition. *Geophysical Journal International*. 207 (3): 1783–1795. doi:10.1093/gji/ggw376.

Walsh, J. J., Childs, C., Imber, J., Manzocchi, T., Watterson, J., and Nell, P. A. R. **2002**. Strain localisation and population changes during fault system growth within the Inner Moray Firth, northern North Sea. *Journal of Structural Geology*. 25 (2): 307–315. doi:10.1016/S0191-8141(02)00028-7.

Wang, L., Pan, Y., Li, J. H., and Qin, H. F. **2008**. Magnetic properties related to thermal treatment of pyrite. *Science in China, Series D: Earth Sciences*. 51 (8): 1144–1153. doi:10.1007/s11430-008-0083-7.

Wang, M., Chou, I. M., Lu, W., and De Vivo, B. **2015**. Effects of CH4 and CO2 on the sulfidization of goethite and magnetite: an in situ Raman spectroscopic study in high-pressure capillary optical cells at room temperature. *European Journal of Mineralogy*. 27 (2): 193–201. doi:10.1127/ejm/2015/0027-2432.

Waters, K. E., Rowson, N. A., Greenwood, R. W., and Williams, A. J. **2008**. The effect of heat treatment on the magnetic properties of pyrite. *Minerals Engineering*. 21 (9): 679–682. doi:10.1016/j.mineng.2008.01.008.

Weibel, R. **1999**. Pseudomorphous Transformation of Goethite Needles into Hematite in Sediments of the Triassic Skagerrak Formation, Denmark. *Clay Minerals*. 34 (4): 657–660. doi:10.1180/claymin.1999.034.4.11.

Whitbread, K. and Kearsey, T. **2016**. Devonian and Carboniferous stratigraphical correlation and interpretation in the Orcadian area, Central North Sea, Quadrants 7-22. Tech. rep.. BGS. Keyworth, Nottingham.

Wygrala, B. P. **1989**. *Integrated study of an oil field in the southern Po basin, northern Italy*. PhD Thesis. University of Koln.

Yilmaz, O. **2001**. *Seismic Data Analysis: Processing, Inversion and Interpretation of Seismic Data*. Istanbul: Society of Exploration Geophysicists.

Zavarzina, D. G., Kochetkova, T. V., Chistyakova, N. I., Gracheva, M. A., Antonova, A. V., Merkel, A. Y., Perevalova, A. A., Chernov, M. S., Koksharov, Y. A., Bonch-Osmolovskaya, E. A., Gavrilov, S. N., and Bychkov, A. Y. **2020**. Siderite-based anaerobic iron cycle driven by autotrophic thermophilic microbial consortium. *Scientific Reports*. 10 (1): 1–11. doi:10.1038/s41598-020-78605-7.

Zhang, Y., Jia, D., Muxworthy, A. R., Li, Y., Xia, B., Xie, Z., Hu, J., Zi, J., and Liu, W. **2018**. The Chemical Remagnetization of Ediacaran Dolomite in the Taishan Paleo-Reservoir, South China. *Journal of Geophysical Research: Solid Earth*. 123 (8): 6161–6175. doi:10.1029/2018JB015547.

Zhang, Y., Jia, D., Muxworthy, A. R., Zhang, Y., Li, Y., Yin, H., Chen, Z., Brzozowski, M. J., Li, W., Wang, M., and Li, Z. **2020**. Fluid Migration and Widespread Remagnetization in the Dabashan Fold and Thrust Belt, China. *Journal of Geophysical Research: Solid Earth*. 125 (11): 1–14. doi:10.1029/2020JB019989.

Zhang, Y., Muxworthy, A. R., Jia, D., Wei, G., Xia, B., Wen, B., Wang, M., Liu, W., and Brzozowski, M. J. **2019**. Identifying and Dating the Destruction of Hydrocarbon Reservoirs Using Secondary Chemical Remanent Magnetization. *Geophysical Research Letters*. 46 (20): 11100–11108. doi:10.1029/2019GL084812.

Zhao, X., Roberts, A. P., Heslop, D., Paterson, G. A., Li, Y., and Li, J. **2017**. Magnetic domain state diagnosis using hysteresis reversal curves. *Journal of Geophysical Research: Solid Earth*. 122 (7): 4767–4789. doi:10.1002/2016JB013683.

APPENDIX

A.1 | BPSM FRAMEWORK

This section of the Appendix covers the generation of, and inputs required to develop, a working basin and petroleum systems model (BPSM), as carried out in production of the model in this study, discussed in Chapter 7. The following discusses the various inputs used to build the BPSM, from geological properties such as formation ages, depth maps, facies and rifting events, to fault presence and properties, and the external basinal events such as the seabed-depth defining paleo-water depths (PWD) and the model-bounding temperatures - the sediment-water interface temperature (SWIT) from above, and underlying heat flow (HF) from beneath. The geological properties of formation ages and depths are stable across all models and are directly taken from the geological model built in Petrel (Schlumberger, 2015) and outlined in Chapter 5. The other inputs, which are discussed here, can vary and ultimately are testable properties rather than directly known or completely provable, and are the basis of the different testing scenarios undertaken in this study through 1D, 2D and 3D models. When compiled and then simulated within the various models, these inputs are calibrated against a range of known datasets collated from core and well log analysis.

A.1.1 | STABLE GEOLOGICAL MODEL INPUTS

The first layer of the BPSM is the stable inputs which do not change across model scenarios taken directly from the geological model. These stable inputs act as the skeleton for which every other variable is built upon, and therefore are crucial to the success of the models. Due to these inputs being created directly from data, beyond the issues with depth map interpolation between 2D seismic lines, they are the most reliable model inputs and are rarely subject to change once created.

A.1.1.1 | DEPTH MAPS

The interpreted depth maps, built in Petrel and exported into PetroMod were previously discussed within Chapter 5, see Figure 5.21. The interpreted depth maps of the Triassic and Jurassic from the geological model were augmented in the BPSM by the addition of further depth maps created by splitting the layers between the original depth maps, to add finer detail of formations that were too thin to interpret directly, as they exist below seismic resolution. The thin (sub-30 m thick) Stotfield Chert was added into the top of the Triassic layer, whilst the upper and lower reservoirs and the Pentland Formation layers were also subdivided further. Splitting of the reservoir layers allowed for the addition of the mid-reservoir shales, the Mid Shale in the Upper Reservoir and the Lady's Walk Shale in the Lower Reservoir, and to refine the reservoir sand facies, which varied in quality across the section. Furthermore, the splitting of the Pentland Formation allowed for the addition of the thin (maximum 5 m thick) formation-topping Brora Coal. The splitting was controlled and aided by the well log data, which showed extensive presence of the Stotfield Chert across the basin, the varying reservoir quality in the lower reservoir, predominantly the J Sand, and the consistent presence of shales and coals in the relevant regions of the reservoir section.

A.1.1.2 | FAULT PRESENCE

Akin to the depth maps, the faults are exported, as part of the geological model, out of Petrel and into PetroMod, and as they are direct interpretations from seismic data, are stable within the models and are not subject to change. Whilst the existence of the faults is not a variable to test, the properties applied to the faults is, such as timings, fault capillary pressures and fault permeabilities, however these will be discussed in a following section.

A.1.1.3 | AGE ASSIGNMENT

The age assignment inputs are the connection between geological time and the formation layers, and are linked to the formation depth maps, which indicate both the top of the formation, and thus the age of final deposition. They are the PetroMod equivalent of a chronostratigraphic chart. The BPSM uses the ages of the depth maps above and below the layer, and the thickness of the layer, to calculate a constant deposition rate of the layer throughout its period of formation. These deposition rates, ages and present day depth maps (those from the geological model) create a burial history of the model, which can be further altered and impacted by rifting, extra deposition and erosional events. Whilst the burial history is subject to fluctuation depending on the inputs, the age assignment of the formations do not change.

The age assignment table created for this study's BPSM is outlined in Table A.1, and contains a complete sequence of the events the IMF experienced throughout its post-basement formation and development. The table is separated into both below-, above- and within-reservoir sections and after each major rifting event. In total, 30 events and ages are included, from the beginning of basin formation at the base of the model at 420 Ma which began the formation of the basement, prior to the rest of the basin-forming events to present day (0 Ma). As discussed within Section A.1.1.1, the reservoir section was heavily subdivided, resulting in a very finely detailed series of events through the Jurassic.

A.1.2 | TESTABLE GEOLOGICAL MODEL INPUTS

The testable model inputs from a geological perspective are the properties assigned to the layers and the faults. Whilst these are known and understood from literature and well log and core analysis, there is uncertainty in basin-wide consistency and variation where analysis was not possible. As such, there is testing different scenarios must be conducted to refine model accuracy and results.

A.1.2.1 | FAULT PROPERTIES

The faults properties in the BPSM control the fluid flow across and up faults through time, and ac as either fluid seals or pathways, and thus can heavily influence the petroleum system. Producing accurate information about fault properties is time consuming, thus they are typically tested through scenario analysis. In this study, several scenarios were analysed, however the starting point for the fault properties is thus: the faults act as more of a barrier to fluids during periods of stability, and act as more of a pathway for fluids during periods of rifting, and the degree to which these occur (more or less of a barrier and more or less of a pathway) is the testable property. As such, a framework of periods of stability and rifting was created and applied through testing (Table A.2).

Table A.1: *Table outlining the ages and main events assigned to the BPSM of the IMF in this study, and the facies assigned to layers. The facies are derived from the properties available within PetroMod, including mixing multiple facies, determined through core and wireline log analysis, and, where required, supported by literature (Andrews* et al.*, 1990; Brown* et al.*, 1988; Glennie* et al.*, 2003; Linsley* et al.*, 1980; Roberts* et al.*, 1990; Stevens, 1991).*

Age (Ma)	Horizon	Layer (activity below horizon)	PetroMod lithology assigned to layer
0.00	Present day	Non-deposition then Q deposits	Sandstone
23.00	End K & Cz subsidence, erosion & uplift	**Basin-forming Events 3 & 4**; variable sediment removed	-
66.00	Top Cretaceous	End K; start Cz deposition (removed during uplift & erosion)	Clay-rich sands
120.00	Top Cromer Knoll Group	Cromer Knoll deposition	Clay-rich sands
132.00	BCU	Hiatus event	-
133.00	Top Wick Sand	Wick Sand deposition	Sandstone
140.00	Top KCF	KCF deposition (& **Basin-forming Event 2**)	Mix of 50 % sandstone & 50 % sandy, organic lean shale
152.00	Top KCF Black Shales	KCF Black Shales deposition	Black Shale
157.30	Top Heather Formation	Heather Formation deposition	Shale
163.50	Top A Sand	A Sand deposition	Sandstone
164.70	Top Mid Shale	Mid Shale deposition	Shale
164.90	Top B Sand	B Sand deposition	Sandstone
166.10	Top Brora Coal	Brora Coal deposition	Pure coal
166.30	Pentland Formation	Pentland Formation deposition	75% sandstone, 25 % black shale
177.65	Top H Sand	H Sand deposition	Sandstone
180.15	Top I Sand	I Sand deposition	Sandstone with minor cementation
182.60	Toa-Pliens Unconformity	NSD-caused hiatus event	-
182.70	Top LW Shale	LW Shale deposition	Shale
183.40	Top J Sand	J Sand deposition	Clay-rich, partially cemented sands
192.35	Top Red Beds	Red Beds deposition	Clay-rich, partially cemented sands
201.30	Top Stotfield Chert	Stotfield Chert deposition	Equal mix of clay, sand, carbonates and chert
206.30	Triassic Unconformity	small erosive event; 500 m sediment removed	-
208.15	Top Triassic	Triassic deposition	Clay-rich sands
251.90	Top Zechstein	Zechstein deposition	40 % sandstone, 20 % carbonate, 10 % shale, 30 % halite/anhydrite
259.00	Top Rotliegend	Rotliegend deposition	Clay-rich sands
298.90	End of basin-forming inversion & erosion	**Basin-forming Event 1**; all 2000 m of C sediment removed	-
310.00	Top Carboniferous	Carboniferous deposition	Sandstone
377.50	Top Devonian	Old Red Sandstone flagstones and fish bed deposition	Flagstones – 47.5 % organic-lean, carbonaceousshales, 47.5 % silts, 5 % sandstone. Fish beds – 75 % organic-rich shales, 20 % carbonaceous silts, 5 % sandstone
392.50	Top Basement	Basement formation	Granite
420.00	Base of Model	-	-

Table A.2: *Table of the fault property framework in the BPSM, from which testing was carried out. Testing was based on the correlation between faults becoming more permeable and more capable of migrating fluids during periods of basin rifting and instability, and faults being less permeable and more of a barrier to fluids during periods of stability.*

Fault property period	Age From (Ma)	Age To (Ma)	Rifting or stable	Fault property (variable)
1	421.00	310.00	Stable	Barrier
2	310.00	298.90	Carboniferous Rifting	Pathway
3	298.90	208.15	Stable	Barrier
4	208.15	206.30	Jurassic Rifting	Pathway
5	206.30	66.00	Stable	Barrier
6	66.00	23.00	Cenozoic Rifting	Pathway
7	23.00	0.00	Stable	Barrier

A.1.2.2 | FACIES

The facies applied to layers within the BPSM are a series of calculable properties that are assigned to the cells within the model, and these properties vary with the facies. The facies of a formation is crucial to the modelling as they control the geological properties of the formations, such as compaction rate, and in turn porosity, permeability, thermal conductivity, capillary pressure and rock stresses, all of which impact the formations contributions to the petroleum system. Whilst the overarching facies of each formation is known, there are localised geological variations that cannot be ascertained as data is not present across the entire basin. This results in a need to test both localised changes in certain regions, as well as testing mixing ratios of the lithologies used within the layers. Within the models created in this study, several facies were applied to the formations, but variations on these were tested, and discussed within Chapter 7 (Table A.3).

Table A.3: *Table outlining the facies assigned to layers in the BPSM, derived from the properties available within PetroMod. All facies, such as sandstone, shales, carbonates, etc. are assigned geological properties in PetroMod, produced through calculations and literature, and mixing these facies will create new ones with updated and refined properties reflective of the lithologies they replicate.*

Layer	Baseline Facies
Quaternary	Typical sandstone
Cretaceous/Cenozoic	Typical sandstone
Cromer Knoll	Typical sandstone
Wick Sand	Typical sandstone
Kimmeridge Clay Fm	50:50 % mix of sandstone and sandy, organic lean shale
Kimmeridge Clay Black Shales	Black shale
Heather Fm	Typical shale
A Sand	Typical sandstone
Mid Shale	Typical shale
B Sand	Typical sandstone
Brora Coal	Pure coal
Pentland Fm sands & shales	Mix of 75% sands and 25 % black shale
H Sand	Typical sandstone
I Sand	Typical sandstone with minor cementation
LW Shale	Typical shale
J Sand	Clay-rich, partially cemented sands
Red Beds	Clay-rich, partially cemented sands
Stotfield Chert	Equal mix of clay, sand, carbonates and minor chert
Triassic	Clay-rich sands
Zechstein	Mix of 40 % sands, 20 % carbonates, 10 % clays and 30 % halite and anhydrite
Rotliegend	Clay-rich sands
Carboniferous	Typical sandstone
Devonian	Flagstones – mix of 47.5:47.5:5 % organic-lean carbonaceous shales and silts and typical sandstone Fish beds – mix of 75 % organic rich shales, 20 % carbonaceous silts and 5 % sandstone
Basement	Granite

A.1.3 | EROSION MAPS

Erosion maps in PetroMod control the amount of sediment removed during erosive events through adding then subtracting specified volumes of material. This volume is a further testable input, but differs from those covered previously as it relates to the basin's structure rather than the properties of the cells within it. Consequently, the erosion events within the IMF were tested during calibration and then kept constant across all further models. Erosion of the Carboniferous at the beginning of the IMF's formation was estimated to have removed approximately 2 km of sediments within the IMF (Andrews *et al.*, 1990; Brown *et al.*, 1988; Johnson *et al.*, 2005; Roberts *et al.*, 1990; Whitbread and Kearsey, 2016), and as the calibration fitted this value, it was kept as this and applied to the erosive, rifting event at 298.9 Ma. Similarly, the smaller erosion associated with the late-Triassic unconformity saw 500 m of Triassic sediment removed across the entire system at 206.3 Ma.

In comparison to the other erosive events, rifting within the Cretaceous and Cenozoic saw uneven removal of sediment from the basin, resulting in tilting of the system (Andrews *et al.*, 1990; Argent *et al.*, 2002; Barr, 1985; Hillis *et al.*, 1994; Roberts *et al.*, 1990). To create an accurate erosion map relating to this tilted, uneven erosive event, apparent erosion at various wells was calculated and converted into a calibrated map, following the methods of Thomson (1993).

The method is underpinned by the theory that porosity decreases as depth, temperature and compaction increases, which results in lower than expected porosities post-exhumation, evidenced by faster sonic velocities, as seen in the wells within the IMF (Baechle *et al.*, 2008; Berry, 1959; Giles *et al.*, 1998; Hillis *et al.*, 1994; Jankowsky, 1962; Lang, 1978; Poelchau, 2001; Raymer *et al.*, 1980; Thomson, 1993)). The amount of erosion in over-compacted sediments is estimated through the difference in sonic velocities between the compaction-altered well under consideration and the undisturbed, "normal" compaction trends seen in a reference well (Hillis *et al.*, 1994; Thomson, 1993)).

To maintain consistency and accuracy, all calculations are undertaken in a sand-rich formation that is prevalent within each analysed well and the reference well. Within this study, the Kimmeridge Clay Formation was selected as the formation for analysis, and Well 13/03-3, in the Outer Moray Firth, was chosen as the reference well (Figure A.1. To determine the validity of Well 13/30-3 as a reference well that hasn't been impacted by uplift or erosion, Athy's Law (Athy, 1930) was used to determine a porosity versus depth curve, which was used to produce a sonic transit time curve for typical sandstones in the same depth region as Well 13/30-3, based on the work of Geldart and Sheriff (2004), which can be seen in Figure A.2. For each well analysed, apparent erosion (E_A) is calculated by the following equation, where Δt_U and Δt_R are the mean sonic velocity of the analysed well and the reference well, respectively, m is the gradient of the sonic-depth relationship in the analysed well, and d_U and d_R are the depths to the formation midpoint below seabed of the analysed well and the reference well, respectively:

$$E_A = \frac{(\Delta t_U - \Delta t_R)}{m} - d_U + d_R \tag{A.1}$$

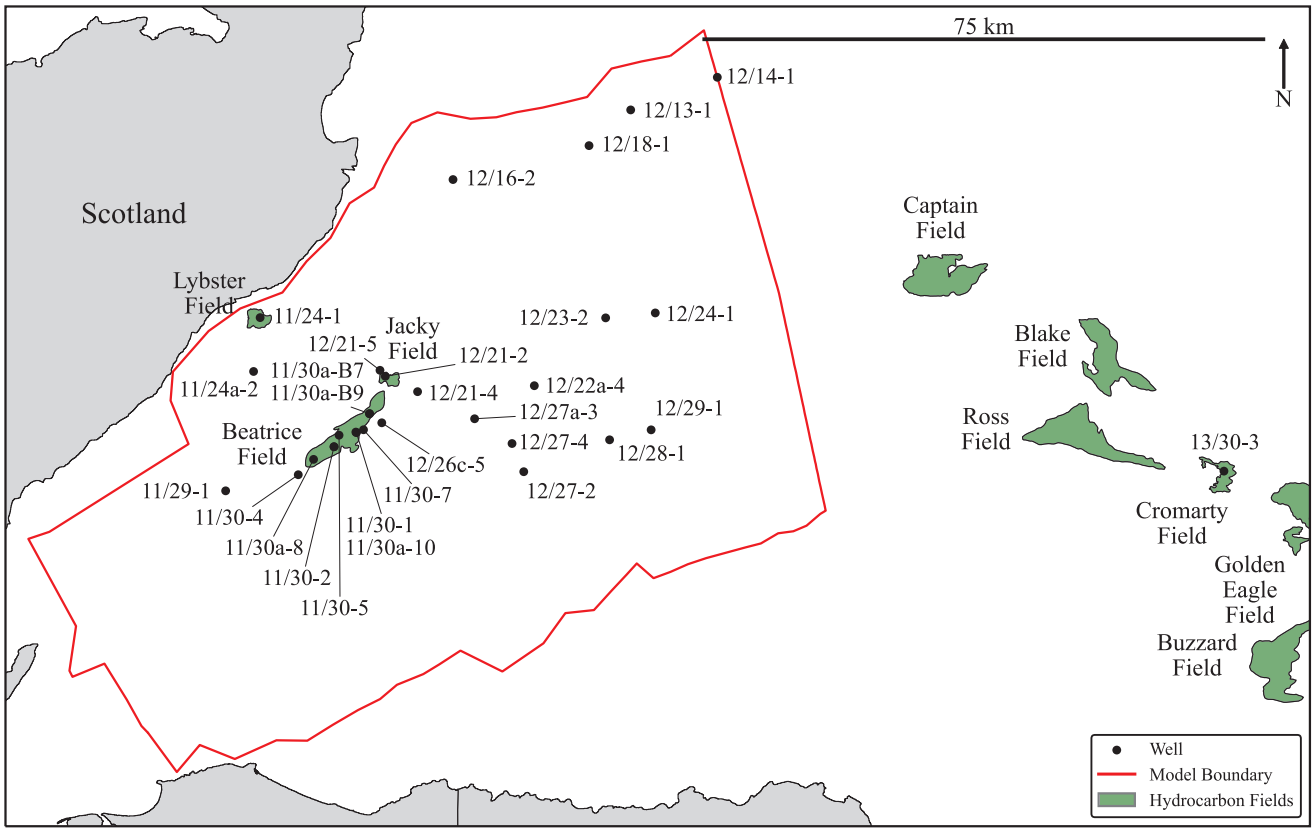


Figure A.1: *Map of the Inner and Outer Moray Firths, and Northern North Sea showing the locations of the wells used to build the erosion map of the sediments removed during the late-stage rifting event in the IMF. Highlighted are the hydrocarbon fields across the region, and the positions of the wells cused to calculate the erosion volume and the location of the non-erosion impacted reference well, 13/30-3.*

Smoothing of the data is necessary for the equation, and in this study is done via a 130-point rolling average, which not only removes anomalous data but also removes the first and last 65 datapoints from the logs, thus removing any potential influence from other formations. Following the smooth, Δt_U, Δt_R and m are calculated, the latter through the calculation of a trendline of the smoothed data. Once E_A is calculated (Table A.4), the values are plotted on a map and contoured (Figure A.3). The main limitations to this method are well log availability, evidenced by the lack of wells in the SW of the IMF, and confidence in the reference well. However, as the Athy's Law-calculated curve shows, Well 11/30-3 was does not greatly differ from the calculated compaction-formed sonic transit time, proving that it is a good reference well.

The wells in the IMF have extensive sonic offsets compared to the reference well (Figure A.2). The reference well is both significantly deeper than the wells of the IMF, and also has slower sonic velocities at relative depths to the IMF wells, shown by its trendline in Figure A.2. The offset between the reference well trendline and those of the IMF wells is used to develop the apparent erosion values in Table A.4, and the erosion map of Figure A.3. The calculated erosion values within the IMF show distinct variations between the northwest, south and east of the basin, with the highest areas of erosion, in the northwest, being in the vicinity of the GGF to the northwest and Wick Fault to the north. In comparison, the south and east of the basin has seen much lower sediment loss, although this may be skewed due to the previously discussed lack of wells. The erosion map successfully calibrates against the calibration data, and thus represents the erosion within the rifting event occurring at 66-23 Ma, as

a result of epeirogenic subsidence and flexural uplift. As this event is in the later stages of the basin's evolution, the erosion of material within the Cretaceous and Cenozoic, which this map removes, exerts significant control on the late-stage evolution of the basin, causing extensive tilting and variations in compaction, source rock maturity and migration pathways between the greater burial-then-erosion in the northwest and the lesser burial-then-erosion in the southwest.

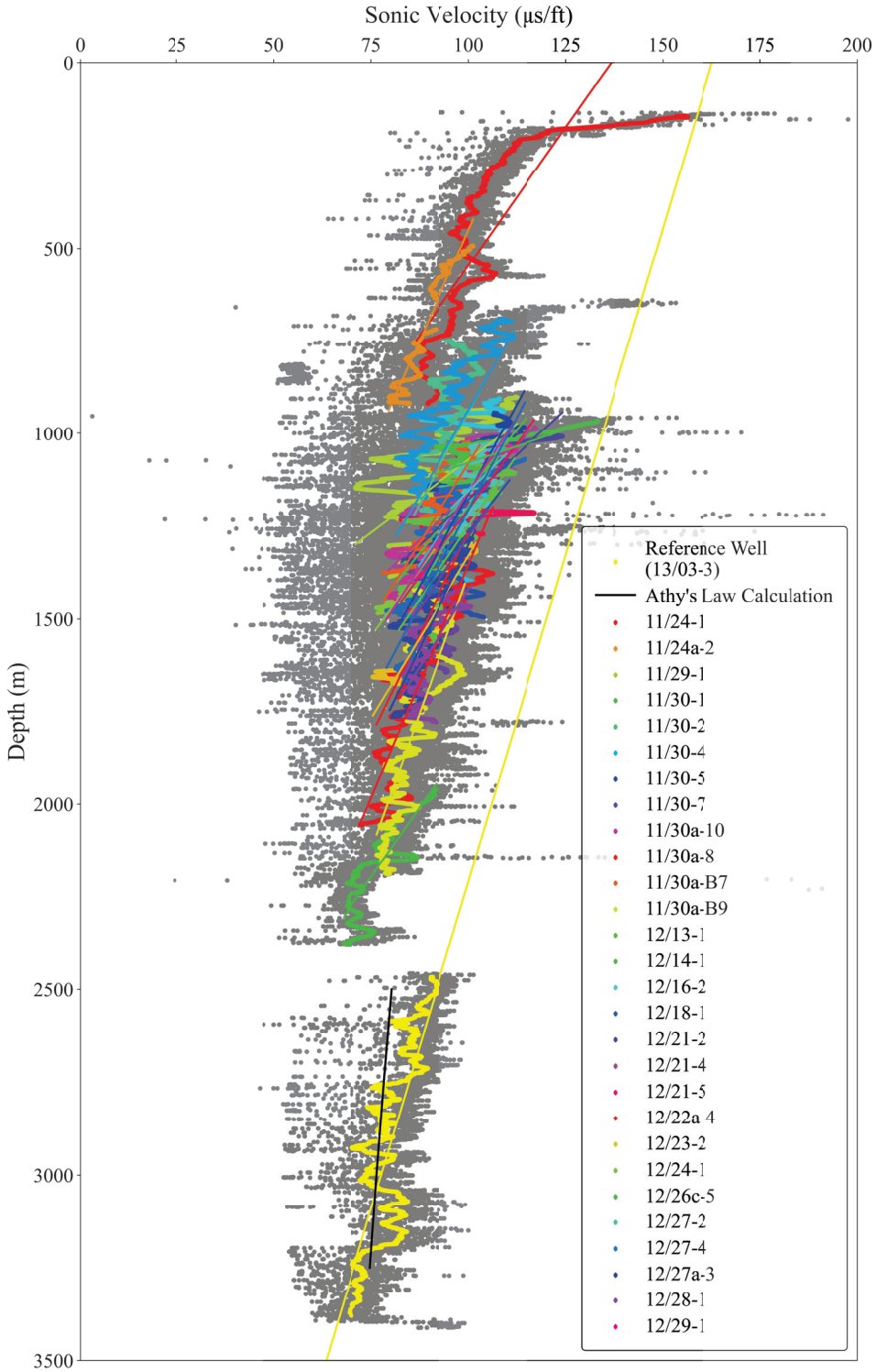


Figure A.2: *Sonic-Depth plot of all wells used to calculate apparent erosion, and both their original sonic velocities (grey) and rolling average results (coloured), alongside their m gradient line. Note reference Well 13/03-3 is plotted in yellow, and its midpoint sonic velocity is highly correlatable with the Athy's Law calculation estimate. The reference well is significantly deeper but has a slower relative sonic velocity than the wells from the IMF.*

Table A.4: *Table outlining the inputs to calculate the apparent erosion within the Cenozoic of the IMF used in the BPSM, and the reference well (13/30-3) alongside the Athy's Law calculation used to confirm the lack of erosion in the reference well.*

Well	Sonic-depth gradient (*m*)	Mean sonic velocity (Δt_U; µs/ft)	KCF midpoint depth (d_U; m)	Apparent erosion (E_A; m)
Ref. Well (13/03-3)	-0.01888	79.586	2870.99	-
Athy Calc.	-0.00647	77.386	2875	-
11/24-1	-0.02960	101.056	422.13	1312
11/24a-2	-0.03800	90.798	417.03	1860
11/29-1	-0.04510	90.837	999.61	1275
11/30-1	-0.05690	97.520	1086.56	835
11/30-2	-0.04126	97.318	1156.24	776
11/30-4	-0.02884	100.128	1104.39	679
11/30-5	-0.01604	99.003	1194.22	648
11/30-7	-0.05660	99.368	1102.79	720
11/30a-10	-0.05550	97.360	1086.22	843
11/30a-8	-0.05013	95.438	1199.12	832
11/30a-B7	-0.03410	92.109	1470.83	737
11/30a-B9	-0.04640	91.596	1501.45	733
12/13-1	-0.05071	86.860	1153.63	1332
12/14-1	-0.04832	76.773	2055.02	965
12/16-2	-0.01182	94.940	619.52	1438
12/18-1	-0.02663	97.835	930.84	974
12/21-2	-0.02521	95.185	1187.07	858
12/21-4	-0.02343	93.332	1266.40	877
12/21-5	-0.04999	93.132	1262.28	891
12/22a-4	-0.03191	86.802	1582.26	907
12/23-2	-0.03882	92.799	1079.01	1092
12/24-1	-0.02052	85.792	1723.82	818
12/26c-5	-0.03590	94.682	1243.82	828
12/27-2	-0.15570	105.683	986.96	502
12/27-4	-0.05425	104.620	1036.53	509
12/27a-3	-0.03772	91.894	1282.84	936
12/28-1	-0.03093	89.908	1420.84	903
12/29-1	-0.02628	89.150	1502.50	862

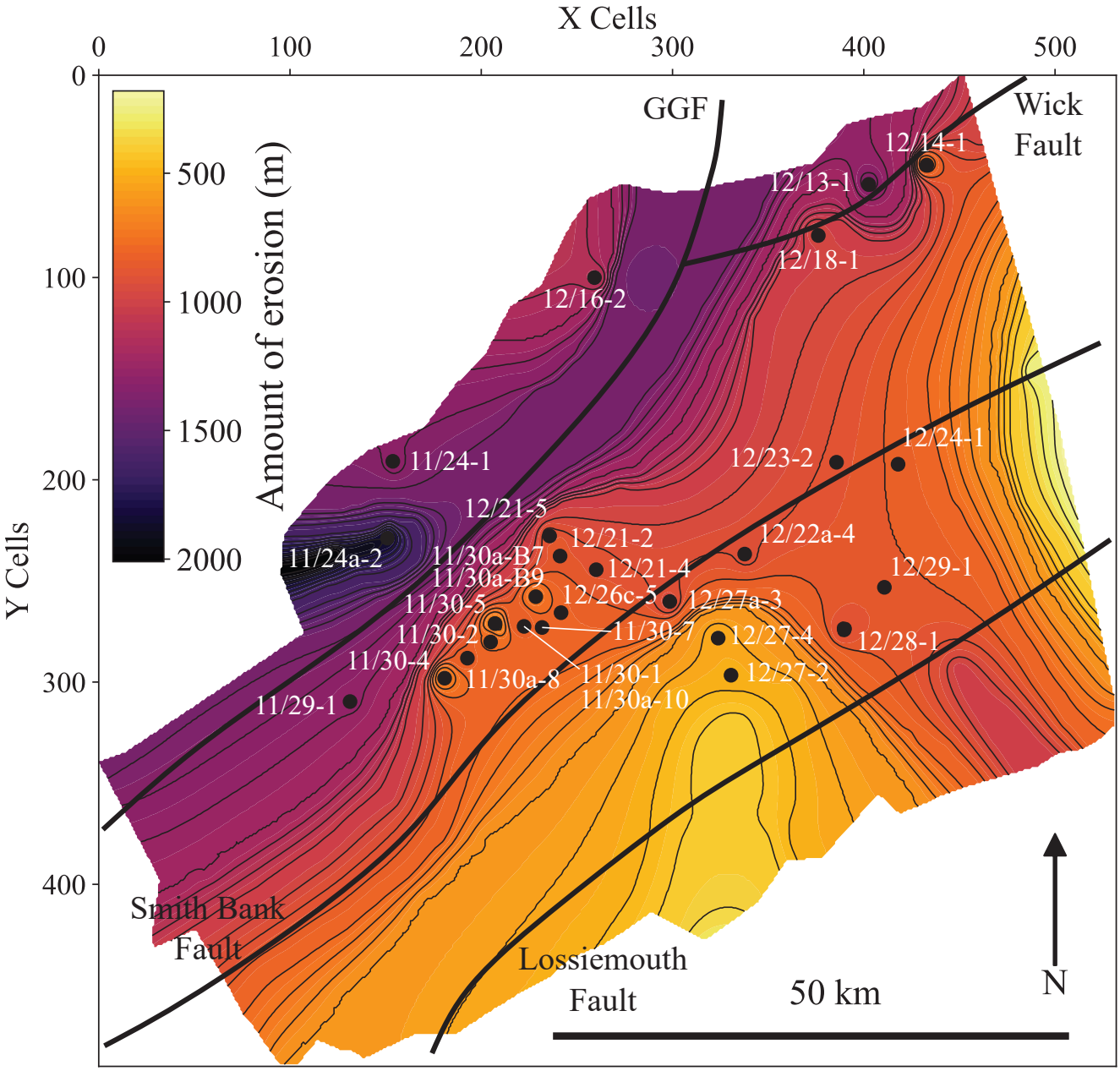


Figure A.3: *Map showing the calculated variation in volume of eroded material across the IMF and the locations of the wells used to calculate it, based on the offset from the relevant wells in the IMF to the reference well, 13/30-3 in the Outer Moray Firth. Locations of the wells used to develop the map are shown, including locations of the known hydrocarbon fields within the IMF, and the basin-forming faults that the erosion is influenced by. Note that X and Y Cells refers to the grid of the BPSM.*

A.1.4 | Model boundary conditions

Basin-bounding properties in the BPSM control the conditions around the model through three different components - paleo-water depth (PWD), sediment-water interface temperature (SWIT), and heat flow (HF). PWD is the depth of the seabed throughout the geological history of the basin, and controls the height of the model with respect to overlying water. SWIT is derived directly from PWD, and is the temperature at the top of the model, imposing heat from above as a result of varying sea levels. HF in the opposing condition to SWIT, in that it controls the underlying heat beneath the model, controlled by geological processes, most significantly the heat created through rifting. As PWD and HF are estimated values, and SWIT is calculated from PWD, the conditions are subject to variation and require testing,

but once they are calibrated successfully, they are kept consistent throughout the models.

PWD is typically estimated through facies variations through geological time, where depositional environments are used as proxies from sea level. Whilst this gives an estimation of the PWD, there is variation that must be tested. Post-calibration, the PWD developed and assigned to the models in this study sees relatively shallow water within the Devonian through to the Triassic, before seeing much deeper water levels through the late Jurassic and the Cretaceous (Figure A.4).

The SWIT is calculated directly through the PWD, using methods developed by Wygrala (1989). The SWIT is calculated by estimating temperatures throughout geological time, which vary by latitude, and factoring in the PWD values. This calculation is built into PetroMod, and is known as Auto-SWIT, where the inputs required are the PWD throughout time, and the present day latitude of the model, in this case, 51°N. Once the calculation is complete, the temperature throughout time is assigned to the model (Figure A.4). As the SWIT is controlled by the PWD, it is not a directly testable input, but does impact the model and needs to be calibrated as a function of the PWD.

The most dominant boundary condition on petroleum systems is the HF, as it controls the most impacting condition on the models, and consequently, HF demands intense calibration. HF is estimated based on work by Allen and Allen (2005), who determine average HF values for a variety of basin-forming processes, as well as typical baseline, stable values. These values are then applied to the events within the BPSM, and calibrated against the calibration data in the models, to ensure that the temperatures within the basin, and the maturity that the source rocks reach, is accurate. Within this study, a HF was created and successfully calibrated, and contains high HF influxes during the basin-forming rift in the Permian, and more minor HF influxes within the later rifting events (Figure A.4).

Within this study, whilst the boundary conditions were tested, analysed and altered based on calibration results, this was done prior to the addition of any petroleum systems-based variables. This was because it was imperative to limit the amount of variables within the models once the petroleum systems components (e.g. source rock kinetics and facies heterogeneity) were involved, and as such, once calibration was complete, the conditions were maintained.

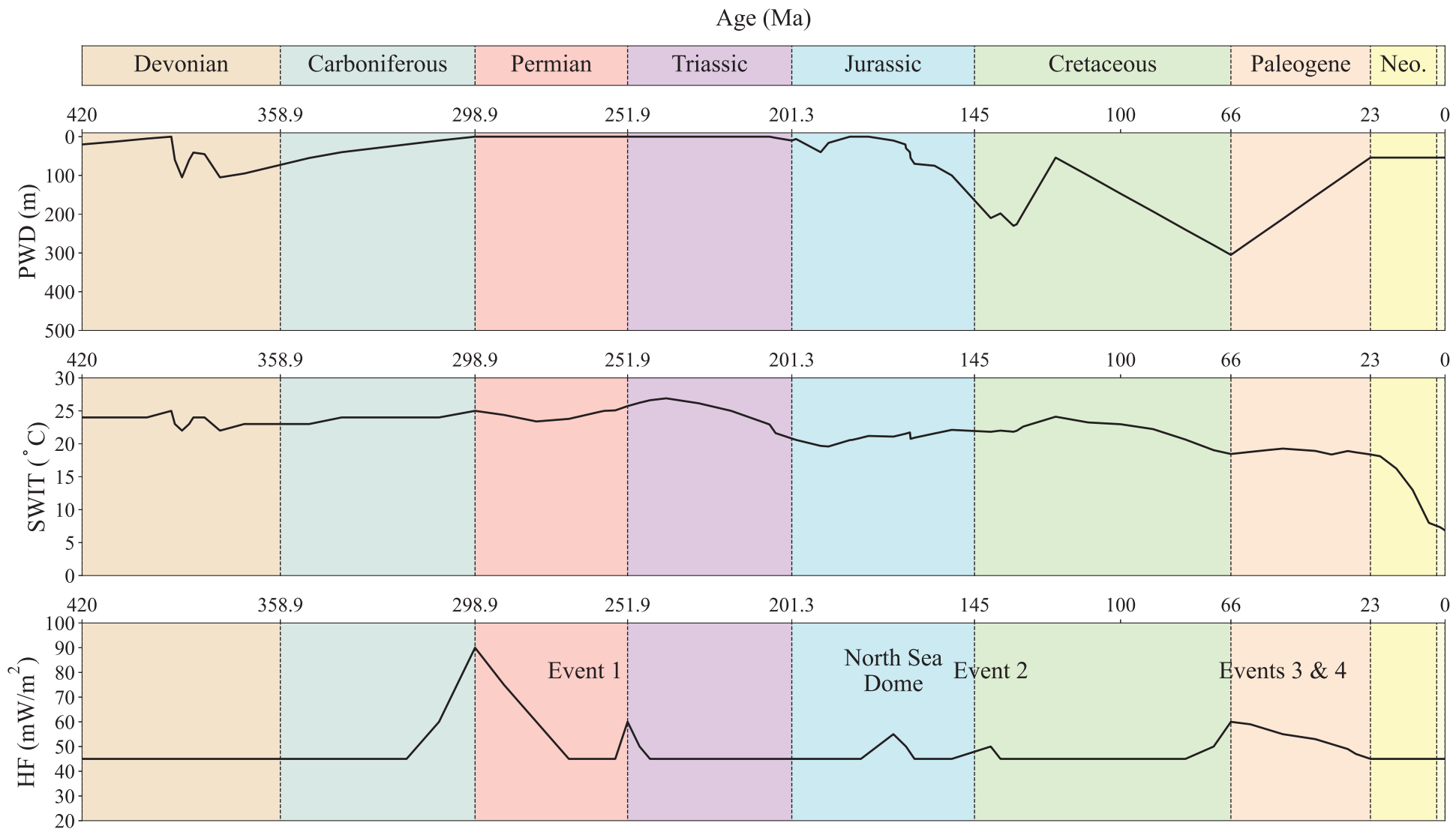


Figure A.4: *Series of boundary condition plots of the three components and their properties used within the BPSM in this study. The paleo-water depth is an estimation on the water level of the area throughout time, and somewhat correlatable to the facies seen in the basin, whilst sediment-water interface temperatures relate to the temperature at seabed, thus is related to the PWD. Heat flow is connected to the basin's geological history and periods of rifting that increase the temperatures across the basin, and the rifting events seen in the IMF are visible in it, and is estimated from work by Allen and Allen (2005).*

A.1.5 | SOURCE ROCK PROPERTIES

Transforming source rocks from simple facies into productive components of the BPSM requires additional geochemical inputs in the form of source rock properties. These properties – a source rock kinetic, total organic carbon content and hydrogen index – control the volume and ability of a source rock to generate hydrocarbons. These properties, akin to the others within the BPSM are variable and rarely known in complete totality, and as such, are tested to various degrees within the models.

A.1.5.1 | SOURCE ROCK KINETICS

Source rock kinetics are sets of characteristics and properties that define how source rocks mature, thus how they generate and expel hydrocarbons (Bjorlykke, 2010; Dembicki Jr, 2017; Hantschel and Kauerauf, 2009; Tissot and Welte, 1984). These properties are applied to the cells of the model attributed to the source rock formations, which in turn are used to simulate and calculate maturity levels in the formations. Kinetics vary between different source rocks and the kerogen types within them, and due to variations in both of these across geological time, location and depositional environment, they are subject to alteration and thus must be tested (Bjorlykke, 2010; Dembicki Jr, 2017; Hantschel and Kauerauf, 2009; Pepper and Corvi, 1995a,b; Pepper and Dodd, 1995; Tissot and Welte, 1984). In this study, four kinetics were collated, assessed and applied to the four potential source rocks in the Devonian Fish Beds, Pentland Formation, Brora Coal and Kimmeridge Clay Black Shales.

The Devonian Fish Beds, Pentland Formation and its topping Brora Coal all lack peer-reviewed and published kinetics developed for their unique source rock properties, and as such, were assigned the standardised kinetics produced by Baur (2019). The Devonian Fish Beds were assigned the lacustrine-depostied Type I kerogen kinetic, the Pentland Formation was assigned the oil-prone, lagoon and shallow-marine deposited Type II-III kinetic, and the Brora Coal was assigned the gas-producing, marsh- and swamp-deposited Type III kinetic Baur (2019). In contrast to these, the deep marine, Type II Kimmeridge Clay Black Shales do have a unique kinetic, developed by di Primio and Horsfield (2006), which was used and allowed the Black Shales to be modelled more closely to its real-world properties.

A.1.5.2 | TOTAL ORGANIC CARBON (TOC) CONTENT

TOC is the relative percentage of organic carbon in a source rock and is therefore directly relevant to the amount of hydrocarbons that can be generated from in the source rock. Furthermore, due to this relationship, TOC decreases as hydrocarbon generation increases as the organic matter is converted into hydrocarbons. Consequently, a mature source rock's present day TOC is typically lower than it would be prior to hydrocarbon generation, thus TOC requires either analysis of immature samples or a back calculation to estimate the original TOC (Jarvie *et al.*, 2007). The downside with back calculations is that no one calculation can be applied to all source rocks and their varying kerogen types (Jarvie *et al.*, 2007), thus making the back calculation an estimation in itself. Consequently, in this study more simple estimates were created and scenario tested, based on estimates from geochemical work carried out by Peters *et al.* (1989) who offered present day TOC values within the IMF source rocks of 4.68 %, 3.40 % and 5.78 %, in the Devonian, Pentland Formation and Kimmeridge Clay Black Shales, respectively.

A.1.5.3 | HYDROCARBON INDEX (HI)

HI is the amount of hydrogen relative to the amount of organic matter within a source rock, in mg/g TOC, and varies depending on the source rock, kerogen type and depositional environment (Dembicki Jr, 2017; Hantschel and Kauerauf, 2009; Tissot and Welte, 1984). It is similar to TOC in the BPSM in that it controls the amount of hydrocarbons generated in the source rocks, and a higher HI typically results in greater amounts of hydrocarbons being generated. As with TOC, it decreases as hydrocarbons are generated and it is calculable through source rock sample analysis, or through calculations. As original, pre-generation HI is typically more stable than TOC, it is easier to estimate values to apply to the source rocks within the models. However, as HI does vary, both due to kerogen type and source rock formation, it is crucial that it is also tested. Again similar to the TOC estimations, the HI testing originated from the work of Peters *et al.* (1989) who calculated present day HI values of 933, 222 and 387 mg/g TOC for the Devonian, Pentland Formation and Kimmeridge Clay Black Shales, respectively.

A.1.6 | HYDROCARBON MIGRATION METHODS

When modelling hydrocarbon migration, the methods of how the fluids migrate are vitally important to the model, as methods vary in their calculations, requirements, results and usefulness, with three methods being the most used – Darcy Flow, Flowpath and Invasion Percolation (Hantschel and Kauerauf, 2009). Darcy Flow is the most accurate, using multi-component phase flow calculations based on relative permeabilities and capillary pressures to move molecules through pore spaces using Darcy's Law. However, due to the complexity of the calculations, Darcy Flow requires extensive simulation time within lots of short-spanned time-sequences, and consequently, takes far longer than deemed acceptable to be used on large scales (Hantschel and Kauerauf, 2009). Flowpath is a more simple migration technique that relies on buoyancy to move hydrocarbon molecules surface-ward, and as such is comparatively very fast, although struggles to perform within complex basins as it ignores lateral migration within low permeability regions and flow through time, resulting in very fast hydrocarbon migration through the models that may be somewhat inaccurate. Invasion Percolation also centres on buoyancy-derived migration, however it includes geological timescales within the migration, as well as capillary pressures, giving a more accurate migration calculation than Flowpath.

Due to the mixed accuracies of the migration methods, typically two are combined within a model, with Darcy Flow used to migrate fluids out of low permeability source rocks, and either Flowpath or Invasion Percolation used to migrate the fluids through the carrier beds and into the reservoirs (Hantschel and Kauerauf, 2009; Schlumberger, 2020). In PetroMod, these combinations are called Hybrid Migration (Darcy Flow and Flowpath) and Combined Migration (Darcy Flow and Invasion Percolation). Typically Hybrid is fastest and recommended, however it struggles to calculate migration within sub-layered model layers (e.g. an interbedded shale and sand layer), and as the IMF is geologically complex, whilst hybrid was used to more quickly analyse the tested scenarios, Combined Migration was used within the vast majority of the models.

A.1.7 | Calibration Data

Calibration data is data collected from sample analysis from wells. Typically calibration data is taken directly from core analysis, and includes predominantly petroleum system data as well as geological data that cannot be directly calculated by well log data, such as porosity and permeability. Calibration data is used to control the simulated, calculated outputs from the BPSM with real-world, collected data to improve the accuracy of the models, bringing them away from hypothetical, idealised models into grounded, accurate, interpretable, analytical tools.

Within this study, calibration data was collected from analysis carried out then published in well reports procured through the Oil and Gas Authority (2021), with no calibration data collected directly. Predominantly, calibration of the models is done through vitrinite reflectance data, as this is the closest proxy to petroleum system maturity widely tested through analytical methods. Whilst TOC, HI and Tmax (maximum temperature at which hydrocarbon generation has occurred) are used as typically more accurate calibration techniques, these are less widely available within the wells of the IMF, due to the wells being drilled before these methods were used more consistently. The calibration data used within this study is outlined in Table A.5. Other data was included in the well reports, such as initial TOC estimates, S1 and S2 data (source rock quality values from pyrolysis), formation density and hydrocarbon saturation, however these were not used to calibrate the models as they were in very few wells, thus could not be relied upon to reflect the properties of the entire basin.

Table A.5: *Table outlining the calibration data, and wells containing it, within this study.*

Calibration Data	Well
Porosity	11/24-1, 11/24a-2z, 11/25-1, 11/30-1, 11/30-2, 11/30-5, 11/30-6, 11/30-7, 11/30a-8, 11/30a-9, 11/30a-10, 11/30a-A29, 11/30a-B7, 11/30a-B9, 11/30a-B10, 12/13-1, 12/14-1, 12/16-1, 12/21-2, 12/21-3, 12/21-4, 12/21-5, 12/22-2, 12/24-2, 12/25-3, 12/26-2, 12/27-1, 12/27-2, 12/27-4, 12/29-1
Permeability	11/24-1, 11/25-1, 11/30-1, 11/30-2, 11/30-5, 11/30-7, 11/30a-8, 11/30a-9, 11/30a-10, 11/30a-A29, 11/30a-B7, 11/30a-B9, 11/30a-B10, 12/13-1, 12/14-1, 12/16-1, 12/21-2, 12/21-3, 12/21-4, 12/21-5, 12/22-2, 12/24-2, 12/25-3, 12/26-2, 12/27-2, 12/27-4, 12/29-1
Vitrinite Reflectance	11/30-2, 11/30-5, 11/30a-8, 12/16-1, 12/21-1, 12/21-3, 12/21-4, 12/21-5, 12/22-2, 12/23-3A, 12/24-2, 12/26-1, 12/27-1, 12/28-1, 12/28-3, 12/29-1
Temperature	11/24a-2z, 11/25-1, 11/30-1, 11/30-2, 11/30-5, 11/30-6, 11/30-7, 11/30a-8, 11/30a-9, 12/21-1, 12/21-2, 12/21-3, 12/21-4, 12/21-5, 12/22-2, 12/23-3A, 12/24-2, 12/26-1, 12/27-1, 12/27-2, 12/28-1, 12/28-3, 12/29-1, 12/29-2, 13/26a-2, 13/26a-4
TOC	11/30-1, 11/30-2, 11/30-5, 11/30-6, 11/30-7, 11/30a-8, 12/16-1, 12/18-1, 12/21-1, 12/21-2, 12/21-3, 12/21-4, 12/21-5, 12/22-2, 12/23-3A, 12/24-2, 12/26-1, 12/27-1, 12/28-1, 12/28-3, 12/29-1, 12/29-2
HI	11/30a-8, 12/16-1, 12/18-1, 12/21-1, 12/21-3, 12/21-4, 12/21-5, 12/22-2, 12/24-2, 12/27-1, 12/28-3
Tmax	11/30-6, 12/16-1, 12/18-1, 12/21-3, 12/21-4, 12/24-2, 12/28-3

A.2 | BPSM Field Volumetric Extents

In the 2D and 3D modelling, initial understanding of the basin and the locations of the hydrocarbon fields was carried out through shapefiles collated from Oil and Gas Authority (2018), which delineate the known extents of the fields. However, there are small-scale variations between these delineated extents and those within the BPSM in this study, most likely due to the seismic resolution limiting the extent and accuracy of the interpretations. As a result, the outputs of the models within this study do not directly correlate to the shape and size of the known delineated fields' extents, and as investigating localised model results requires constraining the outputs through polygons, the published shapefiles were not applicable and new ones were required. These new delineations were derived from the final model extents, but controlled by the most extreme outputs where extensive filling of the fields occurred, so that the results and investigations therein were accurate to all scenarios tested (Figure A.5). As such, note that, where applicable, all volumetric comparisons outlined within this study are constrained through these more refined delineations.

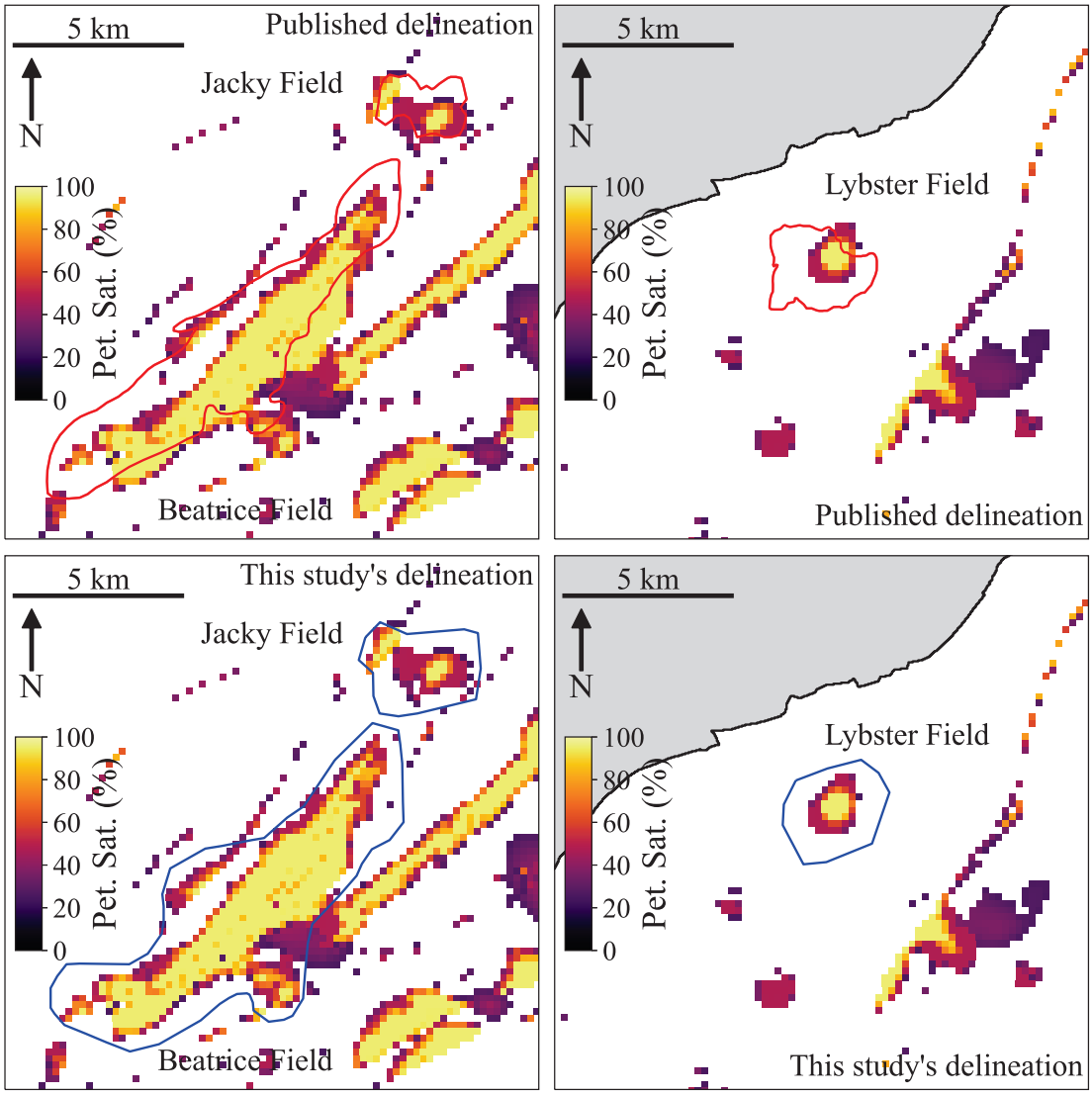


Figure A.5: *Figures showing the published (upper; red) and this study's (lower; blue) delineations of the three hydrocarbon fields within the IMF for accurate volumetric comparisons against the greatest petroleum saturation volume created in BPSM testing.*

A.3 | BPSM SCENARIO TESTING

This section covers the route through model scenario testing that resulted in the successful production of a 3D BPSM of the IMF, what variables were required to make it function as expected, what components are key to the system and what are the results of the source mixing assessment. To reach the final model, as outlined in Figure A.6, iterative processes were implemented, tested and altered where required. Within the process, several variables were altered within each component and these are outlined in Table A.6. It should be noted that whilst Table A.6 outlines a large number of tested variables in terms of the upper, lower and median inputs, the table does not reflect the total number of variables tested within this study for each component, due to the need for concision. Furthermore, the variables within each component that combined for the successful, final model are highlighted in italics. Within the scenario testing phase, all modelling was carried out on upscaled models, in both 2D and 3D, where cells were "merged" on a sampled grid of 400 m by 400 m cells, significantly speeding up the simulation processes without losing significant data quality.

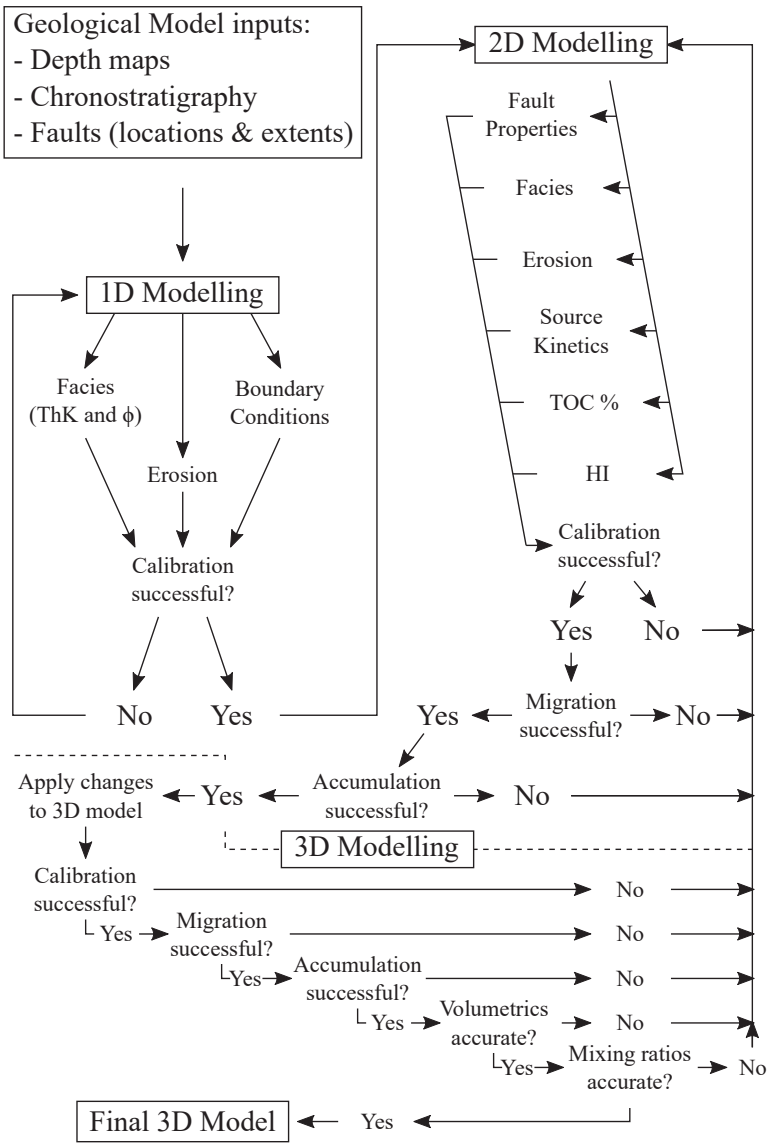


Figure A.6: *Flow chart outlining the iterative processes involved in the creation of this study's final 3D BPSM. ThK refers to thermal conductivity and Φ refers to porosity.*

Table A.6: *Table outlining the components and variables tested within the modelling carried out in this study, with variables in bold italics being those used in the successful final model.*

Component	Point of Implementation	Tested Variables		
		Upper Limit	**Median**	**Lower Limit**
Thermal Conductivity	All formations	30% increase	***No Change***	30% decrease
	Only Fms below reservoir	30% increase	No Change	30% decrease
	Only Fms above reservoir	30% increase	No Change	30% decrease
	Only Basement	30% increase	No Change	30% decrease
Heat Flow	Permian rift peak	110 mW/m^2	***90 mW/m^2***	70 mW/m^2
	K-P rift - peaking at 23 Ma	80 mW/m^2	60 mW/m^2	40 mW/m^2
	K-P rift - peaking at 66 Ma	80 mW/m^2	***60 mW/m^2***	40 mW/m^2
Erosion	Permian rift	3000 m	***2000 m***	1000 m
	K-P rift	2000 m	***Erosion Map (Figure A.3)***	500 m
Fault Capillary Pressure & permeability	Open stage (more open)	3 MPa & -3.90 mD	***2.5 MPa & -3.48 mD***	1 MPa & -1.80 mD
	Open stage (less open)	6 MPa & -5.00 mD	5 MPa & -4.75 mD	4 MPa & -4.50 mD
	Closed stage	12 MPa & -6.30 mD	***11 MPa & -6.14 mD***	10 MPa & -5.80 mD
Formation Facies	Devonian Fish Beds	As 7 beds	As 2 units	***As 1 unit***
	Zechstein salt %	40 %	***30 %***	20 %
	Zechstein sealing capability	Original (full seal)	***As shale***	As sand
	Stotfield Chert sealing capability	Original (full seal)	***As shale***	As sand
	Mid-reservoir shale sand %	40 %	***20 %***	0 %
	Pentland Fm clay-silt ratio	100-0 % C-S	50-50 % C-S	***0-100 % C-S***
	Pentland Fm sand %	75 %	***50 %***	25 %
	Brora Coal sealing capability	Original (strong seal)	***as shale***	as sand
Kinetic Type	Pentland Formation	Baur (2019) Type II	Baur (2019) Type IIS	***Baur (2019) Type II-III***
Kinetic Type II-III Activation Energy	Pentland Formation	Original Type II-III	***Mix of Types II-III & IIS***	Like Type II or IIS
TOC	Devonian Fish Beds	10 %	***5.5 %***	2 %
	Pentland Formation	7.5 %	***4 %***	2.5 %
	Brora Coal	70 %	***60 %***	50 %
	KC Black Shales	8 %	***6.5 %***	5 %

A.3.0.1 | THERMAL CONDUCTIVITY

Testing the thermal conductivity of facies in the model is necessary for accurate calibration, and varying it by 30% above and below the original values of the facies allowed for testing how the heat fluctuations impact the model (Table A.6). Both increases and decreases of the thermal conductivity lead to less well calibrated results than the original, unchanged thermal conductivities (Figure A.7). Furthermore, only varying parts of the basin, e.g. either above or below the Jurassic section, did not improve the calibration enough to warrant varying from the original values (Figure A.7). As such, despite the calibration with unchanged thermal conductivity not matching perfectly, as outlined previously, no changes to the thermal conductivity were necessary in the final model.

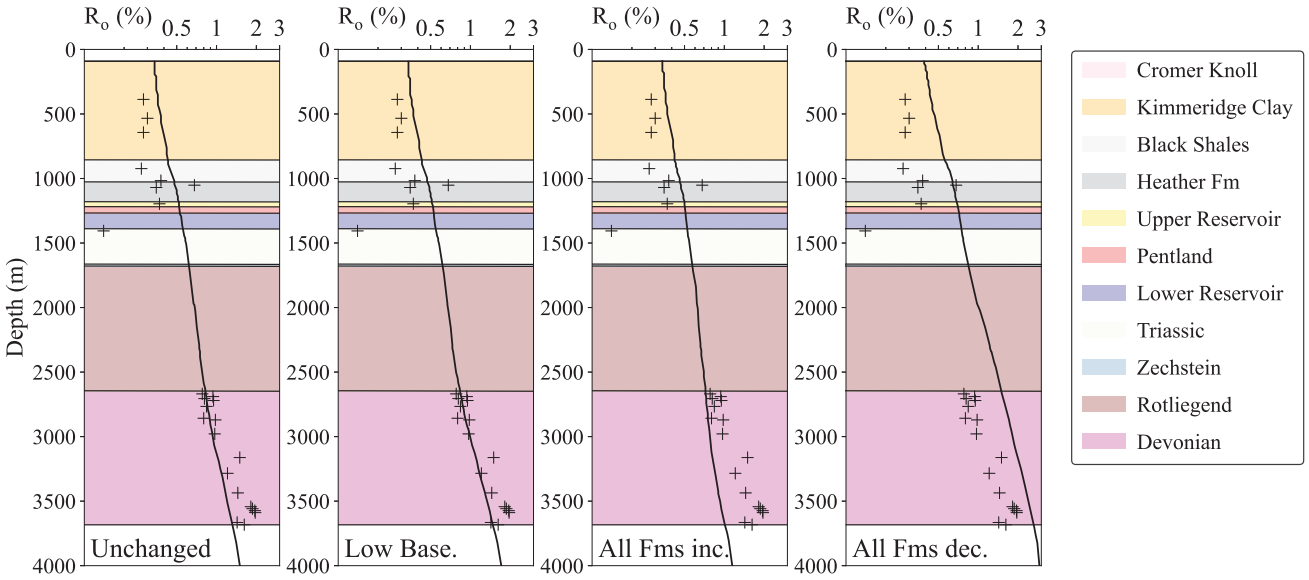


Figure A.7: *Series of depth plots from Well 12/16-1, in the North of the IMF, showing the results of varying thermal conductivities on calculated vitrinite reflectance curves and their relationships to calibration data.*

A.3.0.2 | HEAT FLOW

Heat flow, being the main, direct influence on basin temperatures required extensive scenario testing. Based on the estimated heat flow values from Allen and Allen (2005), the upper and lower limits of the various rifting phases were estimated and tested. The lower limits of the heat flows resulted in insufficient temperatures to both meet the vitrinite reflectance calibration data and mature the source rocks of the basin. In contrast, the upper limit of the heat flows resulted in temperatures greater than necessary for the calibration, and also overmatured the source rocks, especially the Devonian Fish Beds. This resulted in the use of the median value of the estimated heat flow, that accurately matured the basin and matched calibration data (Table A.6).

A.3.0.3 | RIFT TIMINGS

Rifting timings are also a area of uncertainty as there are no post-Early Cretaceous sediments to analyse, increasing the importance of regional understanding to its constraints (Andrews *et al.*, 1990; Bird *et al.*, 1987; Thomson, 1993). Two different scenarios of when this rifting occurred were tested

within the heat flow variables. Whilst rifting is constrained to the Late Cretaceous and Cenozoic, the peak of rifting is unknown. Testing the peak at 23 Ma and at 66 Ma resulted in the peak at 23 Ma, finishing at 2.53 Ma, being discarded as not viable for both basin temperatures and hydrocarbon migration. In contrast, peaking the rift at 66 Ma and finishing at 23 Ma was highly successful for both (Table A.6).

A.3.0.4 | EROSION AMOUNTS

Erosion during rifting events, akin to the uncertainty around timings, is not directly calculable, thus required testing. Due to the total removal of the previously extensive and thick Carboniferous sediments in the basin during the Permian rift, estimates of the amount of removal were necessary. Testing the removal of between 1000 m and 3000 m of Carboniferous sediments led to accurate results through the removal of 2000 m of sediment (Table A.6). The addition and removal of 1000 m of sediment did not bury the Devonian sufficiently for it to achieve maturity, and also led to insufficient maturity of the vitrinite reflectance estimates compared to the sub-Jurassic calibration data points. In opposition to this, addition and removal of 3000 m of sediment overmatured the Devonian and calibration estimates, resulting in a very gas-dominated Devonian hydrocarbon contribution.

A.3.0.5 | FORMATION FACIES

The facies applied to the formations in the BPSM exerted extensive influence over the petroleum system, and numerous testing scenarios were carried out to refine these facies within the IMF. The first facies scenario tested was the presence of the Devonian Fish Beds within the flagstones in the basin, as whilst there are believed to be seven thin fish beds spread somewhat evenly through the Devonian (Newman and Dean, 2005), this refined nature is difficult to replicate within a BPSM. The difficulties are due to BPSMs typically existing as upscaled versions of known properties, and the implementation of seven sub-5m thick formations, as outlined by Andrews *et al.* (1990); Brown *et al.* (1988); Greenhalgh (2016); Newman and Dean (2005); Peters *et al.* (1989), proved unsuccessful. The fish beds in the BPSM acted as intra-Devonian hydrocarbon seals, with each fish bed trapping the hydrocarbons produced from the fish bed below it, creating a tiered system of traps within the Devonian with no hydrocarbons migrating out of the formation. Several tests were carried out to ascertain the best combination of the number of fish beds and their performance in the BPSM, but the only successful result came with all fish beds combined thickness being merged into one unit positioned at their average depth within the Devonian (Table A.6). This clearly creates some uncertainty in the model, as differing maturities would occur in differently located fish beds, however the thickness of the unit matches the total estimated thickness of the combined fish beds, thus limiting this uncertainty as much as possible.

The Zechstein facies in the IMF are of some debate, as whilst the Zechstein in the North Sea proper is salt dominated, in its fringes, as in the IMF, there is ever increasing clastic influences (Glennie *et al.*, 2003). Whilst it is believed that salt is present in the Zechstein of the IMF (Andrews *et al.*, 1990), it is unclear what percentage of the facies is salt-based, and as salt plays a extensively controlling part in the North Sea petroleum systems (Stewart and Clark, 1999), it is necessary to test its impact. No wells show direct salt presence, however this is likely a result of the salt being mixed within other facies (Andrews *et al.*, 1990), and no cores analysed were cored in the Permian, so defining a salt percentage

is difficult. Initial salt estimates of 30 % of the facies (Andrews *et al.*, 1990), 15 % each anhydrite and halite proved successful, both partially controlling hydrocarbon migration but also not acting as a seal trapping the Devonian hydrocarbon surface-ward progress. Further variations, both lower and higher percentages proved to have limited impacts beyond minor variations in sealing capability, as such, the initial estimates, taken from literature, were used. The secondary consideration in the Zechstein is the sealing capability of the mixed clastic-salt facies, as PetroMod automatically makes a facies containing salt a perfect seal, which is not the case within the IMF. Consequently, whilst this perfect seal was tested, it naturally produced a trapping scenario that sealed all Devonian hydrocarbons within the Rotliegend, so two other seal scenarios were investigated, one where the facies had the seal capability of a shale, and one of sand's sealing capability (Table A.6). The sand seal properties proved inadequate as some degree of sealing within the Zechstein is required to focus the hydrocarbons towards the structural highs and faults, and the sand-based properties were both geologically inaccurate and allowed significantly greater and easier vertical migration through the system than needed to fill the structures. Therefore, the shale-based sealing properties were chosen as these act as both sufficiently sealing and controlling, but weak enough to allow fluid migration through the formation, unlike a perfect seal would do.

Akin to the Zechstein salt sealing capabilities, the presence of Chert within a PetroMod facies also results in the assignment of that facies as a perfect seal. Within the Stotfield Chert, at the top of the Triassic, the chert presence, despite only contributing to 25 % of the facies, therefore resulted in the Stotfield Chert acting as a perfect seal at the base of the Jurassic reservoir unit, limiting the surface-ward migration of the Devonian hydrocarbons. Similarly to the Zechstein sealing testing, shale- and sand-based seal properties were tested, and again, the shale-derived sealing properties were ideal in both focussing the hydrocarbon accumulations yet allowing migration through formation to occur (Table A.6).

As the log analysis showed in Chapter 5, whilst the mid reservoir shales, the Mid Shale in the Upper Reservoir and Lady's Walk Shale in the Lower Reservoir, are mostly clay-dominated, there is localised sand influences. Whilst these sand influences are difficult to model as they vary across the basin, a general addition of an amount of sand within the facies accounts for this well, but this sand contribution must be tested (Table A.6). Initially mid reservoir shales with 0 % sand were tested however these drastically limited through-reservoir migration, especially of the Devonian hydrocarbons, preventing any discernible volume of hydrocarbons accumulating within the Upper Reservoir section. In contrast, having 40 % sand in these shales did not produce the localised sealing affects seen in the various reservoir formations that created localised pockets of hydrocarbons, as well as controlling the accumulations within the formations. Furthermore, 40 % sand resulted in the mid-reservoir shales beginning to act as reservoir formations also, which is inaccurate. As a result, a sand contribution of 20 % provided both the requisite sand component in the shales, whilst also allowing them to act as the local seals they need to be.

In the Pentland Formation, there are three variables that demand testing within the facies properties – the shale properties, the amount of sand, and the sealing capabilities of the topping Brora Coal (Table A.6). Similar to the issues faced within the Devonian and the Fish Beds, the shale in the Pentland Formation acts as an intra-formational seal between the interbedded sands where the generated hydrocarbons

accumulate. As such, a shale facies acts as both source rock and seal, preventing expulsion out of the formation into the reservoir lithologies of the IMF, and required alteration. To maintain the very fine grained nature of the source rock portion of the Pentland, the scenarios were constrained between shale and silt, with varying ratios of the two grains the focus of the tests. Any degree of shale contribution resulted in limited outward migration of the hydrocarbons into the surrounding reservoirs, and as such, the source rock components of the Pentland Formation were altered to be completely silty in nature. Whilst this is not totally accurate to the geology seen within the logged cores outlined previously, it is a function of the way the basin models operate that cannot be avoided. Secondly, the source to sand ratio in the Pentland is of some uncertainty also, as the formation is chaotically interbedded with no accurate correlation between the interbeds possible between wells. Consequently, it was necessary to assess how much sand was present within the formation in a general sense across the basin, and the testing proved that too much sand resulted in large hydrocarbon accumulations within the Pentland between the more sealing source rock, limiting outward migration and too little sand limited outward migration due to the dominant sealing source rock. The successful ratio of source rock to sand was 50:50 %, as this allowed for both accumulation within the formation and expulsion outward, whilst also not biasing the model towards either facies without the proof required to justify one being more dominant over the other. The final variable in the Pentland was one seen deeper in the basin in the Zechstein and the Stotfield Chert, with the coals of the Brora Coal acting as a very successful seal preventing hydrocarbon migration from below into the Upper Reservoir section, due to the high capillary pressures generated within coals. Consequently, as with the other sealing formations, altering the sealing properties of the coal to a shale-based seal property system, this removed the strong sealing capabilities of the coals whilst also retaining a degree of seal needed to balance the system.

A.3.0.6 | KINETIC TYPES

Kinetic type and activation energy are two variables that control the extent to which hydrocarbons are generated from the source rocks, thus variations in these can lead to fluctuations in the results. The activation energy is the energy required to begin generation of various hydrocarbon fractions, and is most heavily influenced by temperature. As such, the effectiveness of activation energies on a source rock is often shown through a plot of temperature against transformation ratio (TR), with TR being the percentage of hydrocarbons generated from a variable number of hydrocarbon components within the source rock at that location (or cell, in BPSM terms). The assessment of these variables were primarily focussed on the Type II-III Pentland Formation, with this being the source rock subject to the most uncertainty in its properties (Figure A.8). Whilst initially a Type II kinetic was employed, the accuracy was poor, and testing switched to an oil-prone Type II-III kinetic, reflecting the mixed terrestrial/marine nature of the source rock. Initially, the original activation energy for the Type II-III kinetic was used (Figure A.8a), however the Pentland Formation is on the borderline of maturity in large swathes of the basin, and this combined with its low TOC (sub 3%) meant the original activation energy was insufficient to mature the source rock enough to generate the necessary amount of hydrocarbons reported in the known fields (Izundu, 2008; Offshore Magazine, 2012; Oil and Gas Authority, 2018; Stevens, 1991). In response, the slightly higher activation energy of the original Type II kinetic was

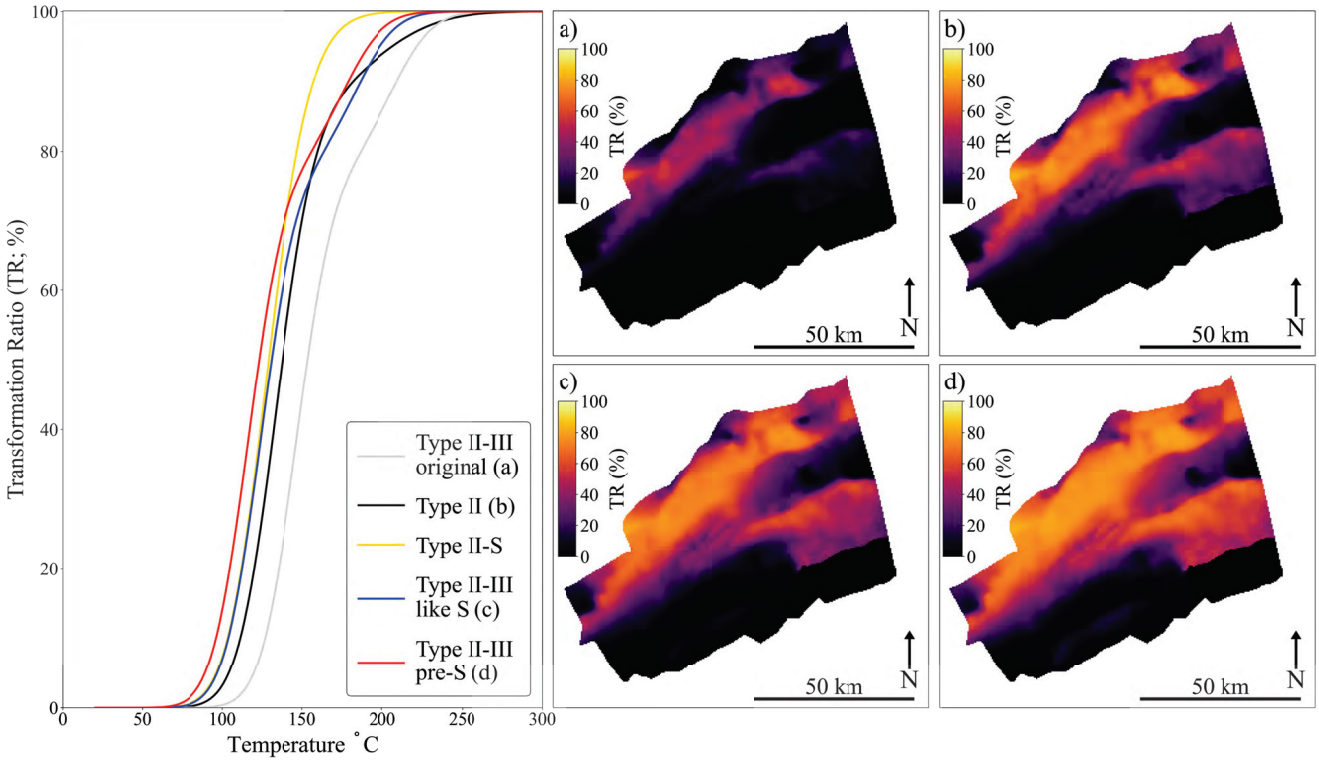


Figure A.8: *Graph showing the transformation ratios and the temperatures they require of the different kinetics used to test hydrocarbon generation in the Pentland Formation, and their associated maps showing the degrees of maturity the Pentland Formation reached using them, based on the final model's Pentland Formation TOC of 4 %.*

applied, but again this proved insufficient for generating adequate hydrocarbon volumes as the onset of maturity was too late (Figure A.8b). The Type II-III activation energy was then shifted to match the activation energy onset of a sulphur-rich Type II, but with the trend of the Type II-III, and whilst this was somewhat successful, it was still not fully acceptable (Figure A.8c). Consequently, the activation energy was shifted to begin prior to the sulphur-rich Type II kinetic, allowing for early onset of hydrocarbon transformation, and this provided the necessary charge of early generation needed to produce sufficient volumes of hydrocarbons (Figure A.8d).

A.3.0.7 | FAULT PROPERTIES

Testing the properties of the pervasive faults across the IMF shows how crucial they are to the petroleum system. Fault Capillary Pressure (FCP) and associated fault permeabilities, calculated by Schlumberger geoscientists and conveyed to this author (O. Schenk, personal communications, Jan 31st, 2022), control how easily fluids flow across and up faults. Within this study, two sets of faults were required – those during periods of fault closure, during basin stability, and open faults, during periods of rifting. As such, several combinations were tested, and whilst the closure period tests showed no variation in results, the openness of the faults did (Table A.6). Testing showed that a closed period requires an FCP of 11 MPa and permeability of -6.14 mD, and an open period requires an FCP of 2.5 MPa and permeability of -3.48 mD (Table A.7; Figure A.9).

Despite the petroleum saturation-derived geometries of the accumulations in the FCP 3-6 MPa models appearing to be a strong fit to the field geometry (Figure A.9), the volumes of these accumulations

Table A.7: *Table showing the results of varying FCP and fault permeability scenarios in the Beatrice Field in both BPSM-simulated masses and calculated converted volume, based on the conversion rate of 1 toe = 7.142857 boe, and the percentage contributions of each source rock to the accumulation. Bl. Sh. = Kimmeridge Clay Black Shales.*

FCP (MPa)	Fault Permeability (mD)	Simulated hydrocarbon mass (Mtoe)	Calculated hydrocarbon volume (Mboe)	Accumulation contribution %		
				Devonian	Pentland	Bl. Sh.
1	-1.80	24.76	176.86	67.71	32.29	0.00
2	-3.05	51.34	366.71	62.19	37.79	0.02
2.5	-3.48	67.32	480.86	66.24	33.76	0.00
3	-3.90	84.03	600.21	68.22	31.77	0.01
4	-4.50	141.59	1011.36	68.45	31.53	0.02
5	-4.75	170.04	1214.57	64.70	35.26	0.04
6	-5.00	178.32	1273.71	62.24	37.69	0.07
Published estimates*		67.20	480	60	40	0

**Published estimates from Peters* et al. *(1989); Stevens (1991)*

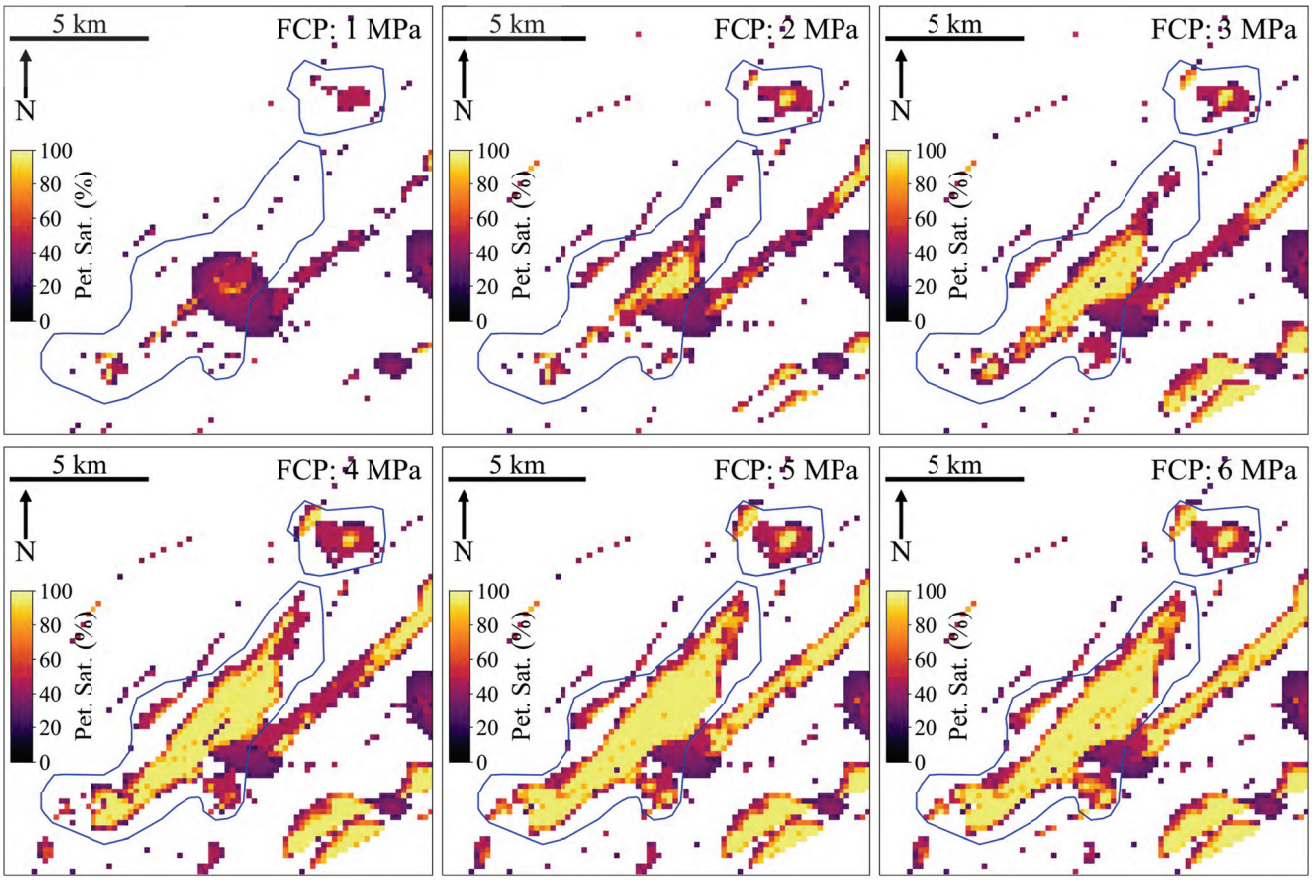


Figure A.9: *Series of maps over Beatrice and Jacky Fields in the centre of the IMF showing the petroleum saturation percentage of each cell, over a threshold of 25%, developed via various FCP and permeability scenarios, with consistent TOC values of 4 % and 5.5 % for the Pentland and Devonian, respectively. The threshold is to remove any unsaturated cells from the figures, which show how much influence the fault properties have on the accumulations.*

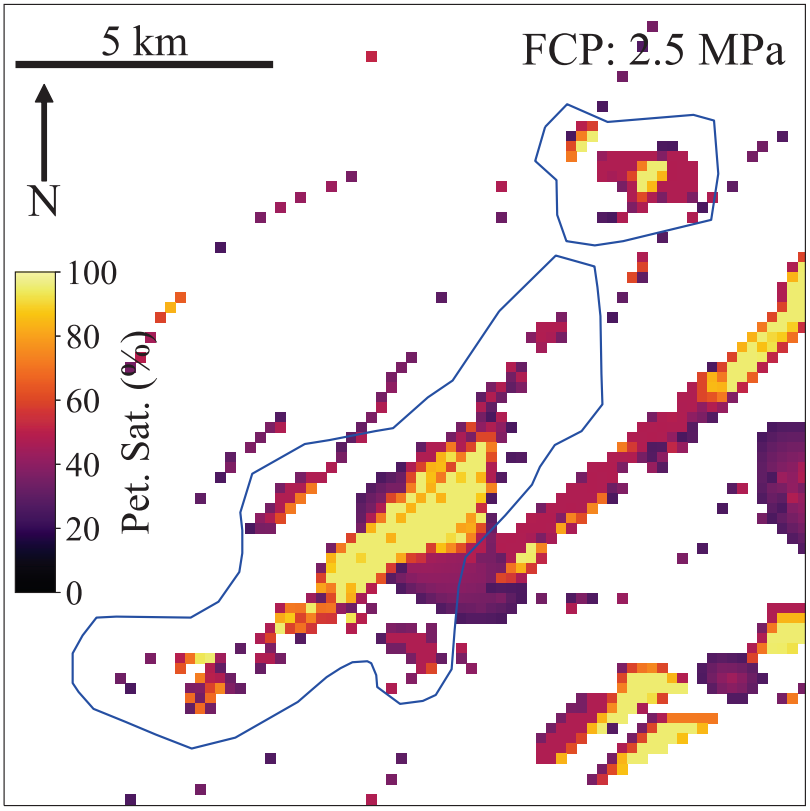


Figure A.10: *Map over Beatrice and Jacky Fields showing the petroleum saturation percentage of each cell, over a threshold of 25%, of the final model derived through the FCP 2.5 MPa model, with consistent TOC values of 4 % and 5.5 % for the Pentland and Devonian, respectively.*

are far greater than the estimated volume of Beatrice Field, 480 million barrels of oil equivalent (Mboe, 67.20 million tons of oil equivalent; Mtoe; Table A.7; Stevens (1991)). Consequently, it is necessary to view the models' accumulations through their volume rather than geographical extent (Table A.7). Whilst the FCP 4-6 MPa models fill the field geometry, the volume of hydrocarbons accumulated in the Beatrice Field in these scenarios is far greater than the estimated field volume, and the FCP 1 and 2 MPa models do not fill it sufficiently, whereas the FCP 2.5 MPa model does not appear to fill the geometry but is within 1 Mboe of the estimated volume (Table A.7; Figure A.10).

Whilst the faults act as conduits for fluids, this acts as both beneficial and detrimental to accumulations in the IMF. Even though the faults appear to be necessary to bring hydrocarbons from depth out of the Devonian into the Jurassic reservoirs, they also appear to allow leakage from the accumulations, especially in Beatrice Field (Figure A.11). All fault scenarios initially accumulate hydrocarbons within Beatrice Field at the same rate, and all to a peak mass of approximately 170 Mtoe (1200 Mboe) at 132 Ma, with this likely a result of maturation caused by the mid-Kimmeridgian rifting. However, when the faults open at the beginning of the late stage rifting at 66 Ma, clear deviations occur in the differing scenarios (Figure A.11). The more open scenarios, models with FCPs of 1-3 MPa lose significant volumes of accumulated hydrocarbons, whilst the less open scenarios (FCP 5-6 MPa models) see accumulations continuing to increase in size as more hydrocarbons are trapped instead of lost. This is most clearly seen in the disparity between the FCP 1 MPa and 6 MPa models, where the more permeable fault system loses over 80 % (approximately 140 Mtoe) of its peak volume at 132 Ma, whereas the less permeable fault system gains an extra 15 % (25 Mtoe) of hydrocarbons compared to the 170 Mtoe at

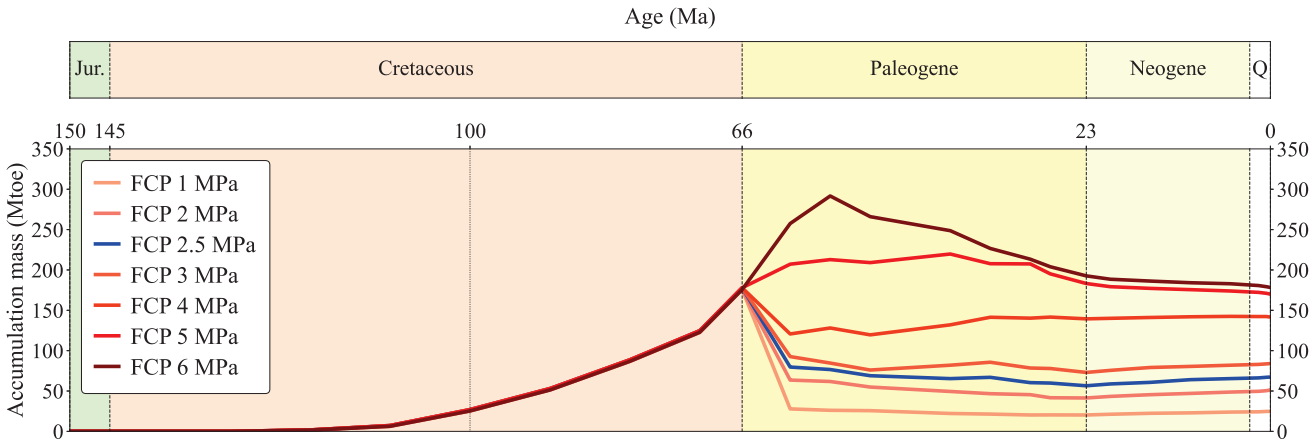


Figure A.11: *Time plots showing the accumulation history of Beatrice Field throughout geological time, post-deposition of the sealing Heather Formation, under various FCP and fault permeability conditions. The initial filling of the field occurs at the same rate regardless of fault properties due to it occurring during a period of stability and closed fault properties. Beyond 66 Ma, when the faults open to varying degrees, based on their properties, the significant difference in accumulation volumes caused by the faults becomes clear.*

132 Ma (Table A.7; Figure A.11).

The fault properties also exert an important control over the mixing ratios between the Pentland and Devonian source rocks in the accumulations (Table A.7). The Devonian contribution is more fault-dependant as it requires them to provide a route for the hydrocarbons to reach the reservoirs, but also to bypass them, and also as it is the more dominant contribution, it is the most displaced when the faults open. The impact of the faults is most clearly evidenced in the mixing ratio differences between the FCP 2 MPa and 4 MPa models, where the 4 MPa model not only accumulates over twice as much hydrocarbons as the 2 MPa model, but also experiences a 20 % difference in mixing ratio, with the 4 MPa ratio being 67:33 % Devonian:Pentland compared to the 2 MPa's ratio of 57:43 %.

A.3.0.8 | Total Organic Carbon

Varying the TOC, predominantly of the Pentland and Devonian source rocks, leads to drastic changes in both the hydrocarbon volumes and mixing ratios between the sources within accumulations. Initial testing, based on the TOC estimates from Peters *et al.* (1989), proved overall successful once back-calculated to their pre-generation content. Whilst the Black Shales and Brora Coal proved to be generally under-mature, and thus little testing was required, the Devonian and Pentland sources proved to be somewhat variable. Devonian Fish Beds with 5.5% TOC proved the most accurate as any TOC below this did not generate sufficient hydrocarbons, and TOCs over 7% proved to preferentially accumulate large volumes of late stage gas, displacing the oil within accumulations.

In comparison, the Pentland Formation has lower TOCs and lower maturity than the Devonian Fish Beds, but due to its location within the reservoir sequence, the Pentland Formation TOC variations have less impact on the accumulated hydrocarbon volumes and more impact on the hydrocarbon mixing ratios (Table A.8). Scenario testing shows that with each additional 1 % TOC in the Pentland Formation, the Beatrice Field accumulations increase by only 10 Mboe, a less than 2 % increase in total volume, but the Pentland Formation contribution to mixing ratio increases by 2 %, thus also reducing the Devonian

Table A.8: *Table showing the results of scenario tests of Pentland TOC in the Beatrice Field, with a FCP of 2 MPa and Devonian TOC of 5.5%, through the BPSM-simulated hydrocarbon mass and the calculated converted volume, based on the conversion rate of 1 toe = 7.142857 boe.*

Pentland TOC (%)	Simulated hydrocarbon mass (Mtoe)	Calculated hydrocarbon volume (Mboe)	Accumulation contribution %		
			Devonian	Pentland	Bl. Sh.
2.5	64.49	460.64	72.39	27.60	0.01
3.0	65.74	469.57	70.25	29.74	0.01
4.0	67.32	480.86	66.24	33.76	0.00
4.5	67.81	484.36	64.37	35.59	0.04
5.0	68.42	488.71	62.46	37.53	0.01
6.0	69.70	497.86	59.39	39.59	0.02
7.5	71.18	508.43	55.18	44.80	0.02
Published estimates*		480	60	40	0

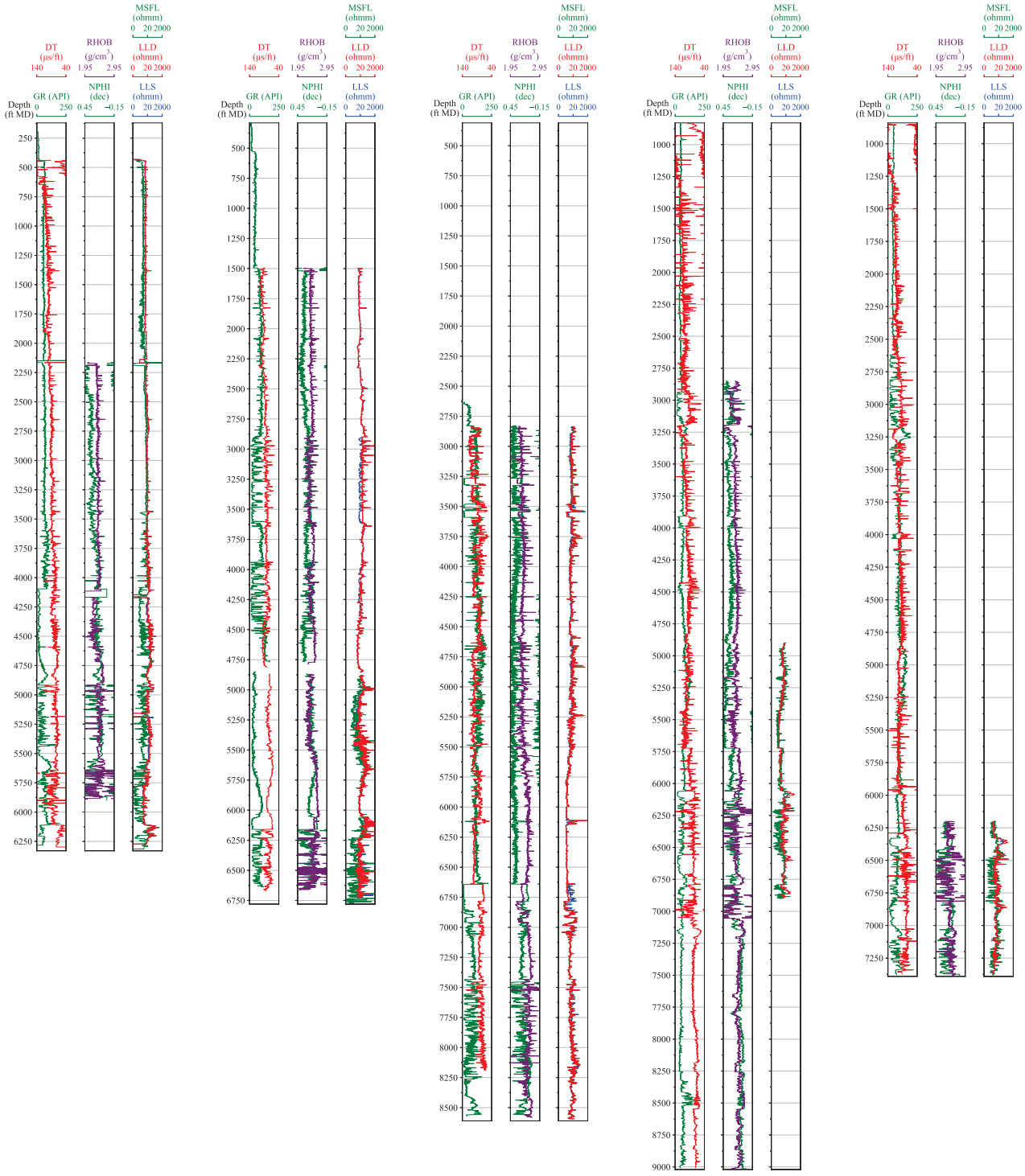
**Published estimates from Peters* et al. *(1989); Stevens (1991)*

contribution by 2 % (Table A.8). This relatively large swing in mixing ratios but relatively small change in total hydrocarbon volume is evidence that the maturity and TOC of the Pentland Formation has much more control on the mixing ratio than it does the accumulation volume. This is proven by a 3 % TOC increase in Pentland TOC adding only 30 Mboe to the Beatrice Field accumulation volume, but changing the mixing ratios from approximately 70:30 to 60:40 Devonian:Pentland (Table A.8). Due to the extensive variations in mixing ratios created by the minor fluctuations in the Pentland Formation TOC, assigning a definitive Devonian-Pentland TOC pair is not possible through solely the BPSM as it was not built for this purpose, however it does confirm the approximate mixing ratio of the two source rocks suggested by Peters *et al.* (1989). The final model was assigned a Pentland Formation TOC of 4 % as this produced the most accurate volumetric estimation of Beatrice Field from Stevens (1991). However, it should be noted that all of the volumetrics, mixing ratios and TOC amounts within both this study and in published literature are estimations, thus the results of the scenario testing should be viewed through a more holistic approach regarding the impacts of the scenario testing, rather than directly focussing on the numbers produced within it.

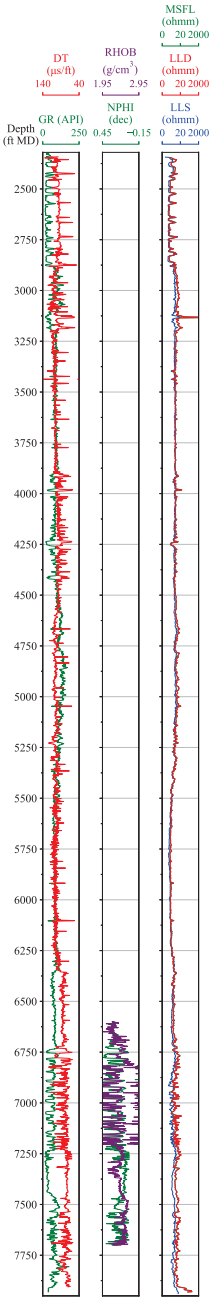
A.4 | WELL LOGS

This section of the Appendix presents all of the well logs used in this study that are located inside the BPSM boundary and that have all the necessary log data, in a typical "Triple Combo" structure, consisting of gamma ray, sonic velocity, density, neutron porosity and resistivity logs. All logs have the same depth scale, presented in feet MD BRT, with this the domain used during drilling and logging. Note not all logs have the full resistivity data suite.

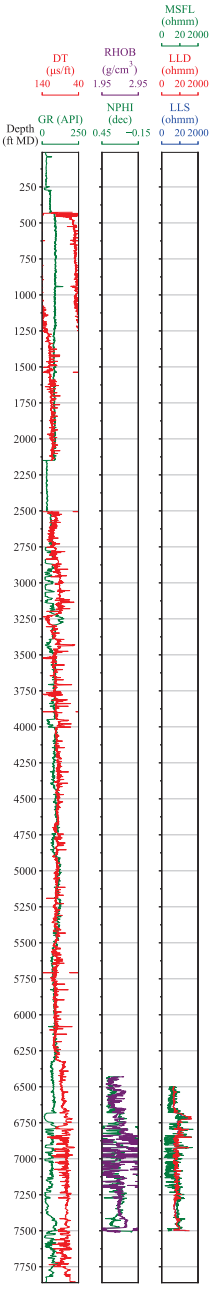
11/24-1 **11/24a-2** **11/29-1** **11/30-1** **11/30-2**



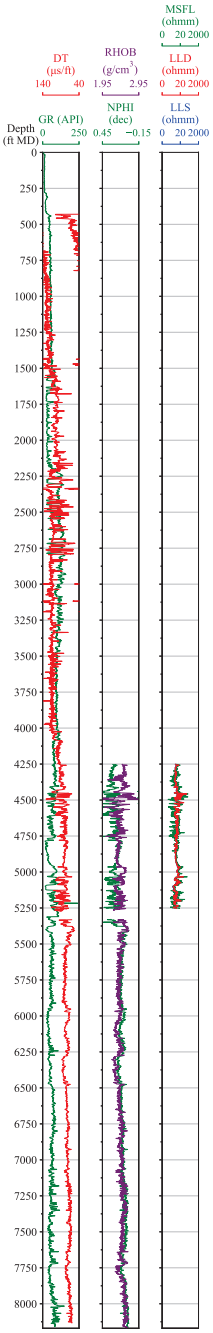
11/30-4



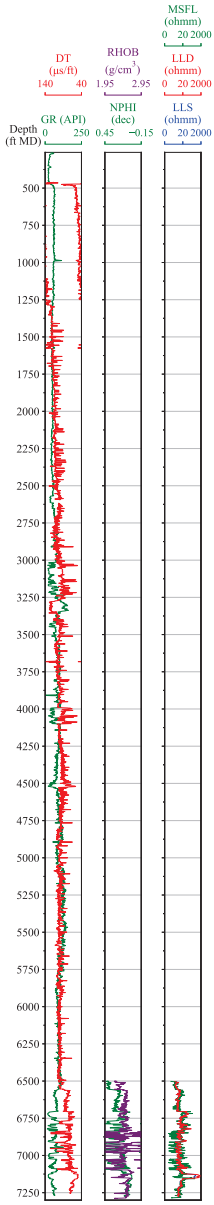
11/30-5



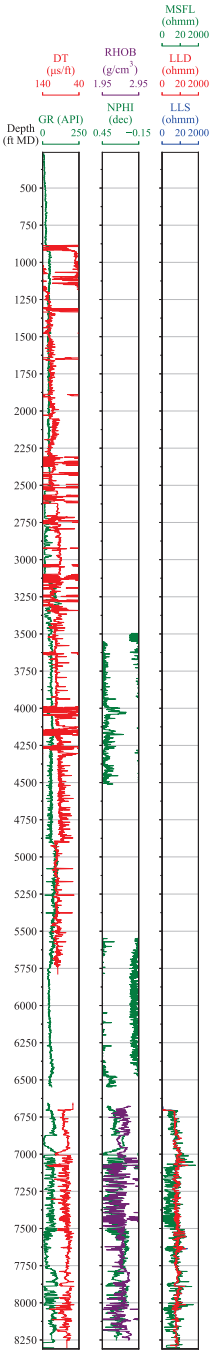
11/30-6



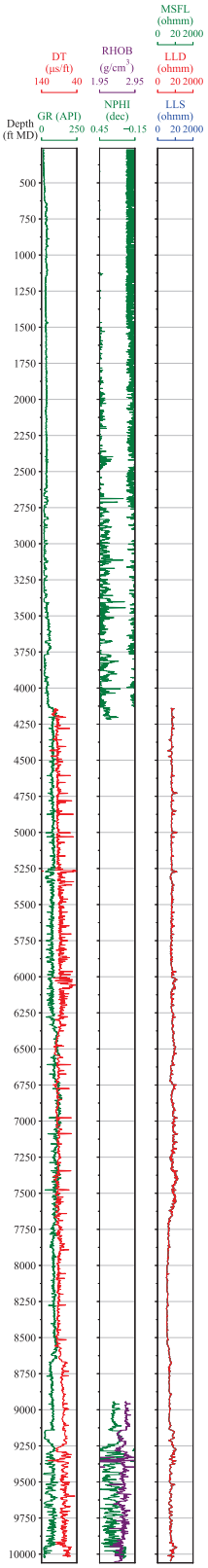
11/30-7



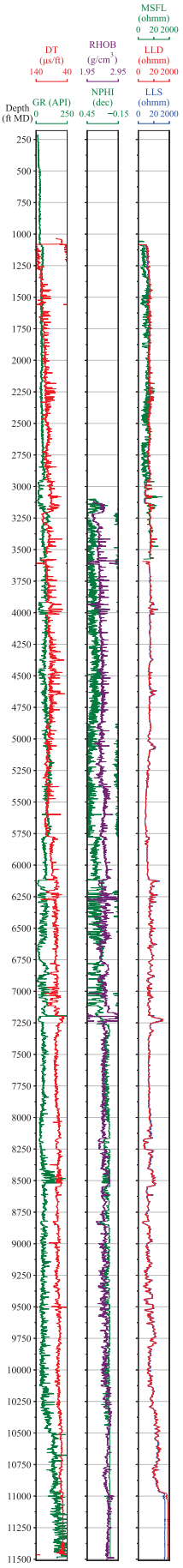
11/30a-8



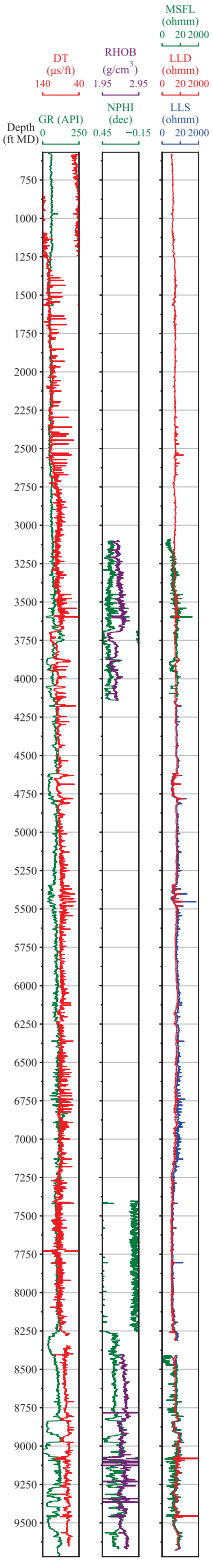
11/30a-9



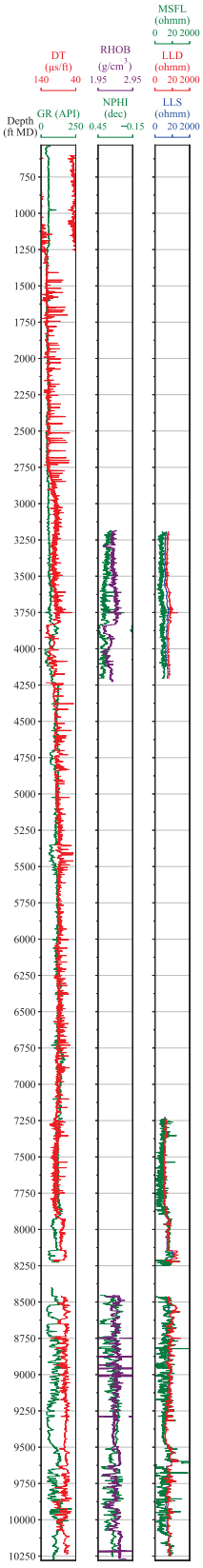
11/30a-10



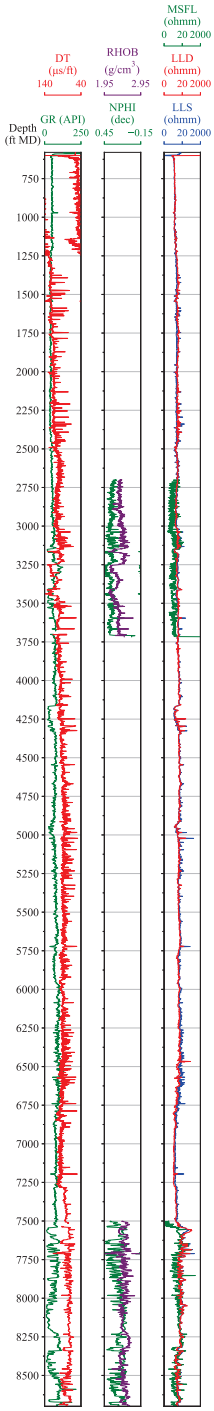
11/30a-B7



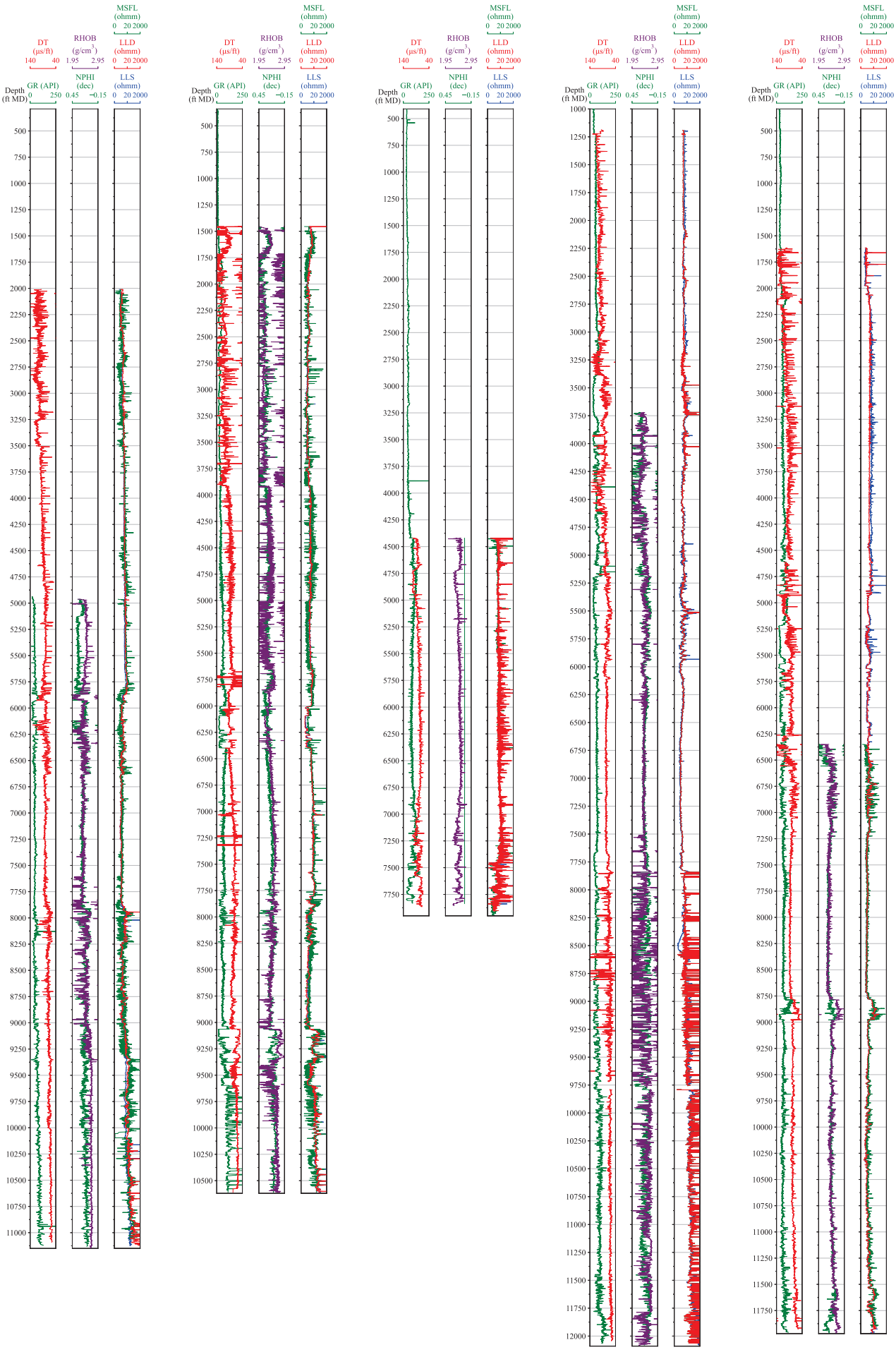
11/30a-B9



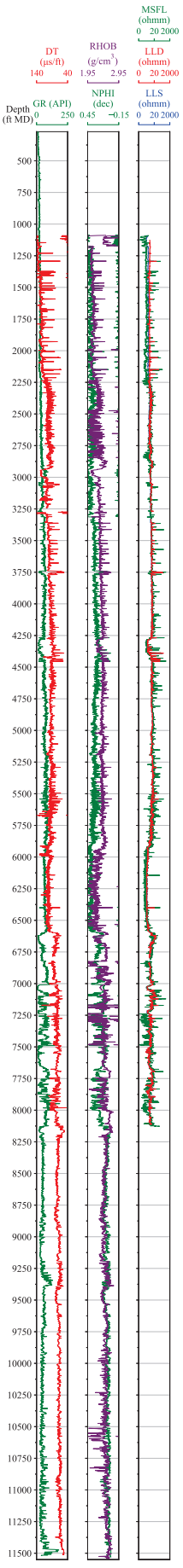
11/30a-B10



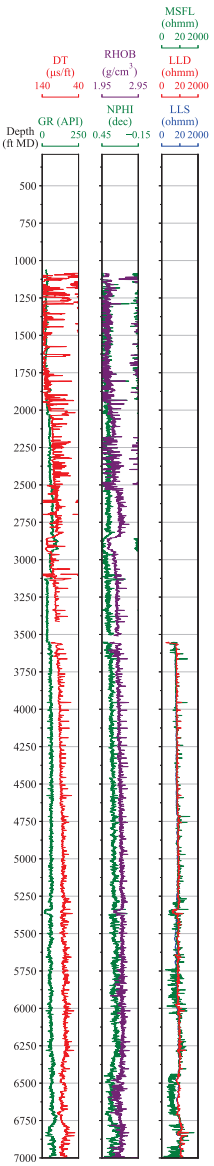
12/13-1 **12/14-1** **12/14-2** **12/16-1** **12/18-1**



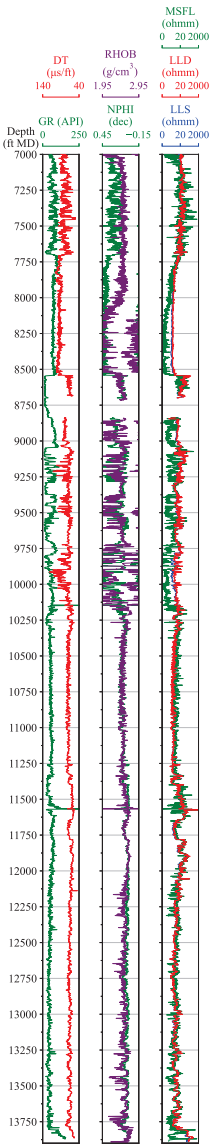
12/21-2



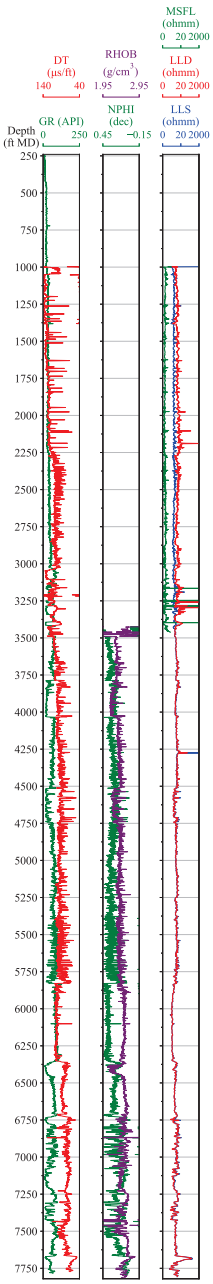
12/21-3 Upper



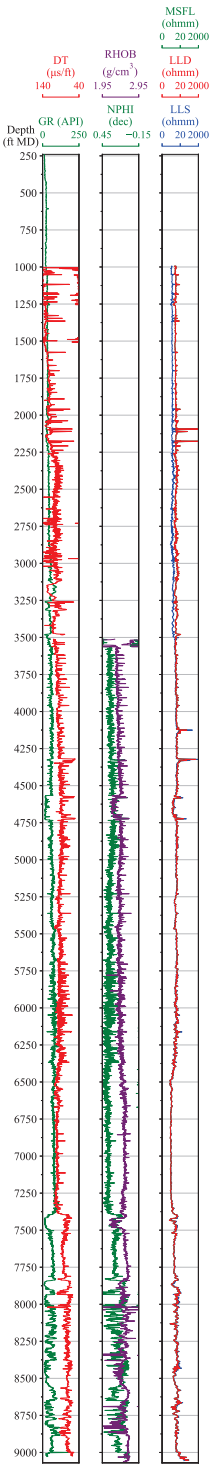
12/21-3 Lower

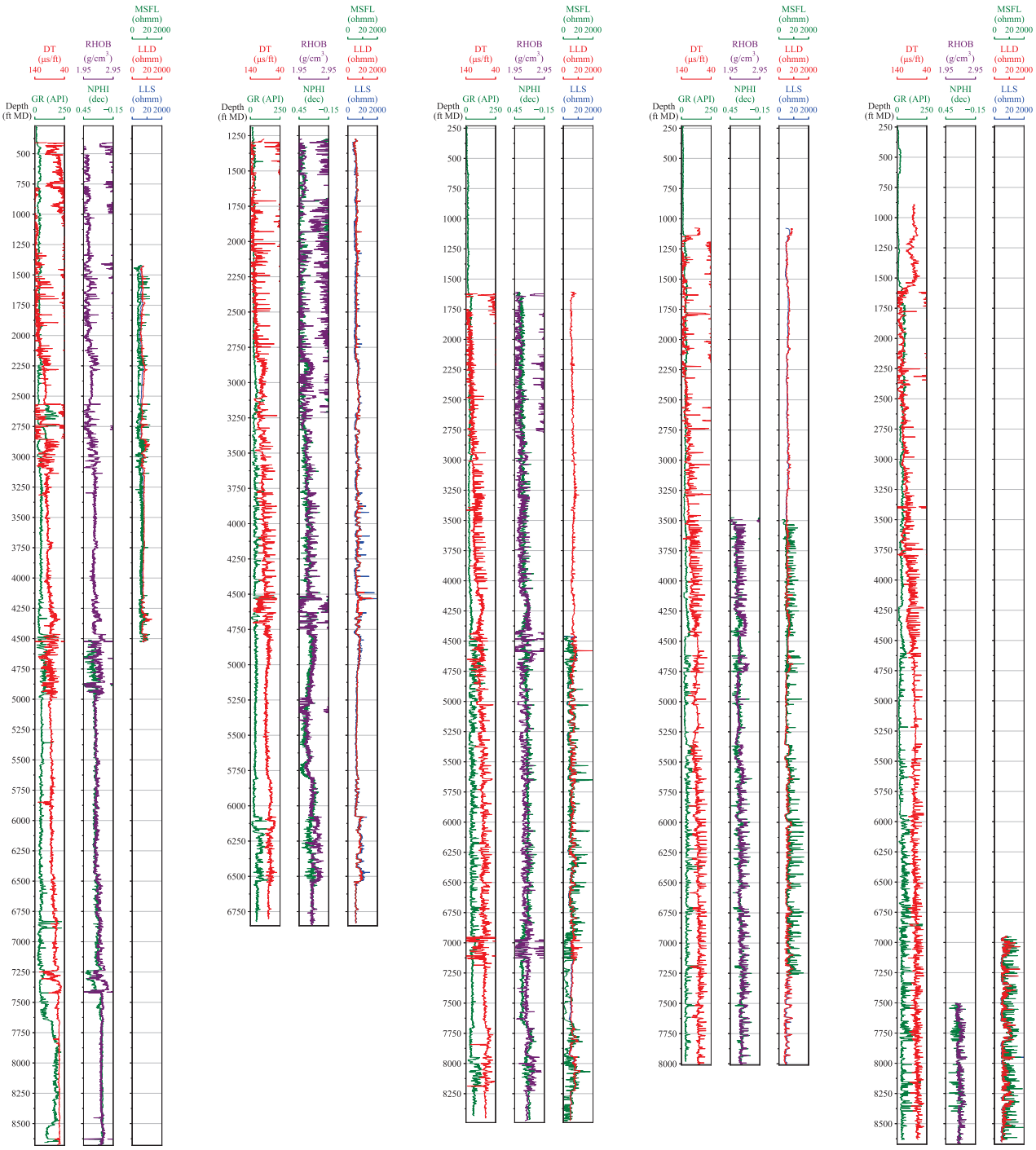


12/21-4

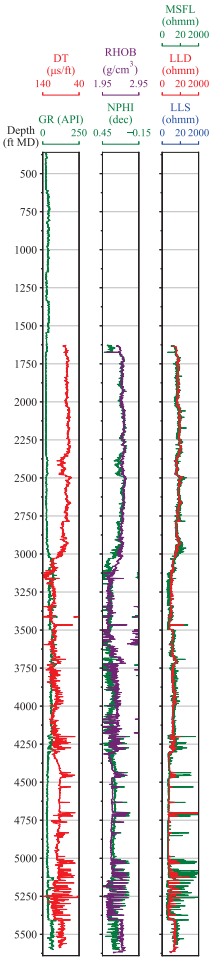


12/21-5

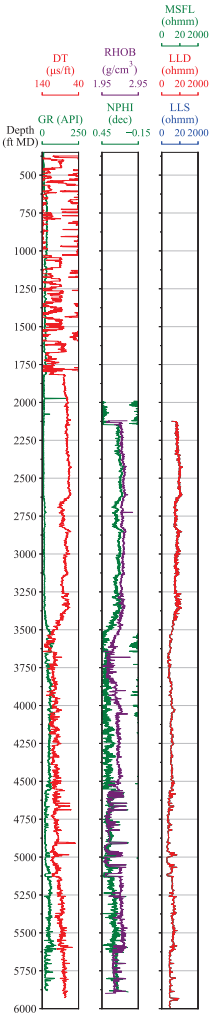



12/23-1
12/23-2
12/23-3A
12/24-1
12/24-1
MSFL (ohmm) 0 20 2000
DT (µs/ft) 140 40
RHOB (g/cm3) 1.95 2.95
LLD (ohmm) 0 20 2000
GR (API) 0 250
NPHI (dec) 0.45 −0.15
LLS (ohmm) 0 20 2000
Depth (ft MD)

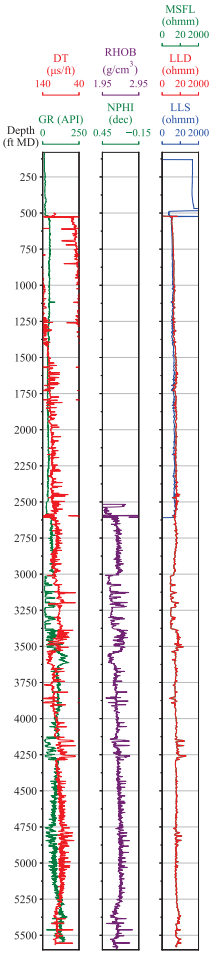
12/25-1



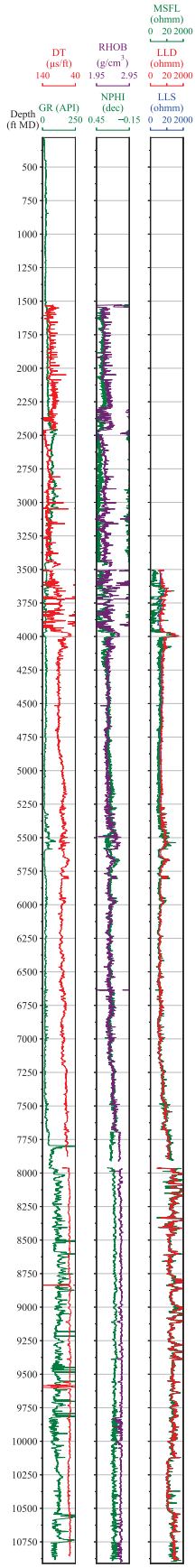
12/25-3



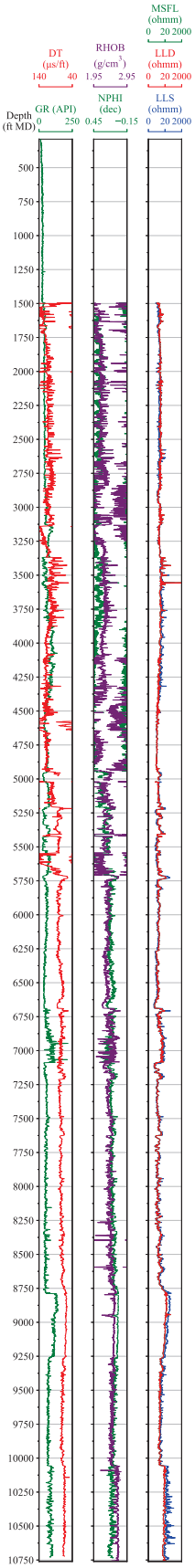
12/26-2

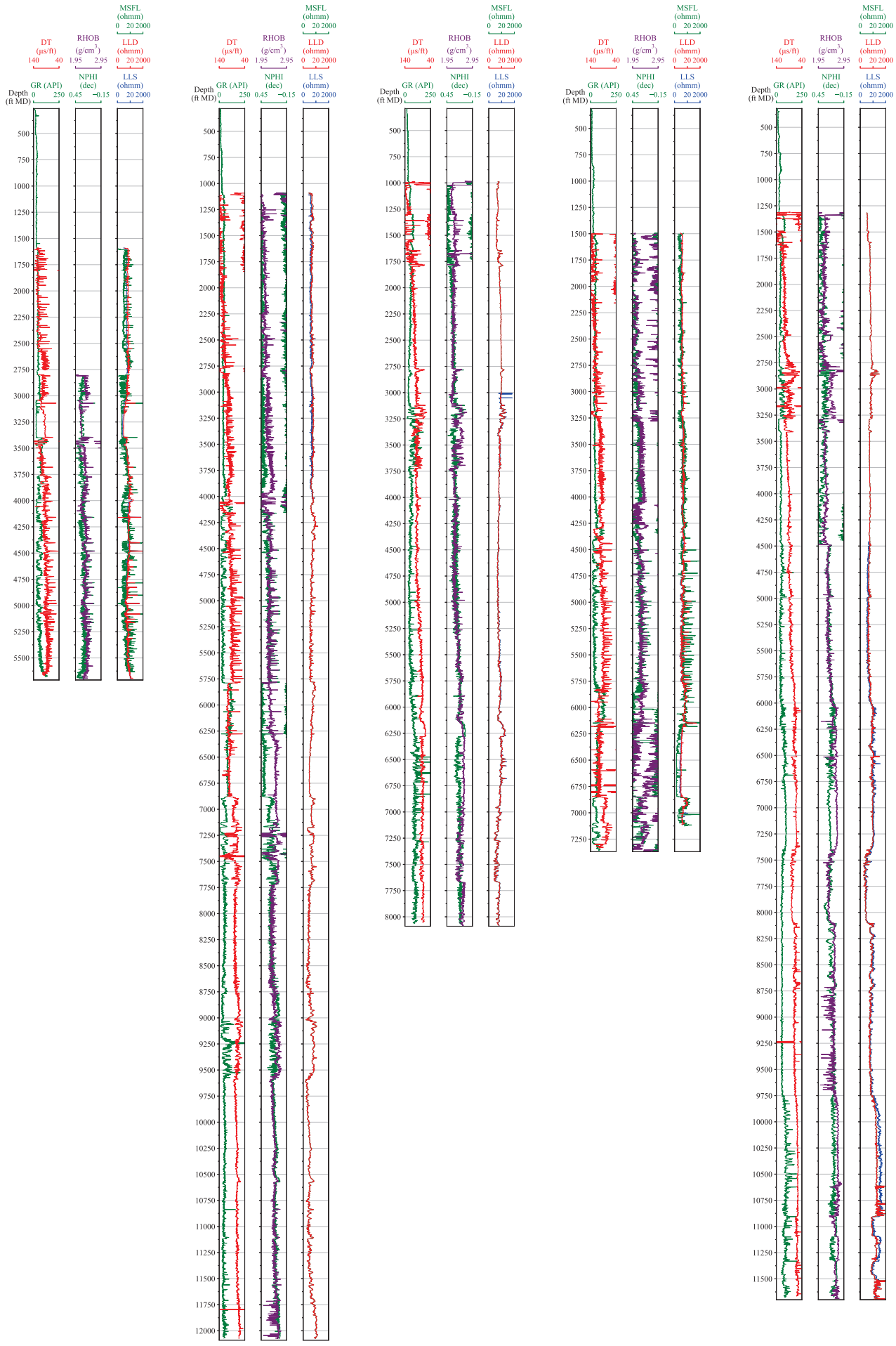


12/27-1



12/27-2




12/27a-3
12/28-1
12/28-2
12/29-1
12/29-2
MSFL (ohmm)
RHOB (g/cm3)
LLD (ohmm)
DT (µs/ft)
NPHI (dec)
LLS (ohmm)
GR (API)
Depth (ft MD)

A.5 | Complete magnetic dataset access

All raw and, where necessary, processed magnetic data produced in this study is available on GitHub at github.com/JosephRPerkins/Magnetic_data (doi:10.5281/zenodo.6977236).

A.6 | Basin and petroleum systems model access

The BPSM with which conclusions were predominantly drawn from in this work is available on GitHub at github.com/JosephRPerkins/BPSM_model (doi:10.5281/zenodo.6977149).